Stacking and migration in an/isotropic media

Habilitationsschrift von
Dr. Claudia Vanelle

May 29, 2012

Für Dirk Gajewski:

Frau Nachbarin dankt.

Contents

Abstract and introduction

Traveltimes and amplitudes of elastic waves are the foundation of the seismic world. Our ultimate goal, detailed knowledge of the structure and material parameters of the subsurface, can only be obtained from the measurement of the time a wave needs to travel from one place to another, as well as the amplitude changes the wave undergoes while propagating through Earth.

In a typical seismic experiment, a wave is excited by a source. Depending on the subsurface properties, the wave is reflected, refracted, and diffracted at interfaces and through changes in the velocity distribution, before it is registered by a network of receivers. Although the conduction of such an experiment is expensive and can pose a logistical challenge, from the point of view of achieving our goal, the acquisition is not the most demanding step.

This work deals with the processing of seismic data. The raw output from the experiment needs to be pre-processed first, which includes filtering, static corrections, setting up the geometry, and sorting from common shot into common midpoint (CMP) gathers. These are the input for subsequent processing steps.

The CMP-sorted data are stacked into simulated zero-offset sections, which already are images of the subsurface in which the structure of reflectors and diffractors can be recognised. However, these images are distorted because the 'positions' of reflectors and diffractors are given not at depth but in time, and furthermore, their lateral positions do not coincide with their real locations.

Therefore, the data need to be *migrated*, i.e., the reflectors and diffractors are moved to their correct position and, finally, given at depth. In order to migrate the data, a velocity model is required. Since the trajectory for the previously carried out stack is determined by a velocity parameter, it is possible to use this parameter for the migration. The stacking velocity is not the 'real' medium velocity that we are interested in, but we can use it to collapse diffractions and triplications in the wavefield caused by syn- and anticline structures, and thus obtain a less distorted subsurface image than the zero-offset section provides. This will usually be achieved by performing a *time migration*, where the migration operator is computed analytically under the assumption of a constant velocity.

Considerably more effort is required to obtain a *depth-migrated* image. Here, the 'true' velocity model is needed, and traveltimes are computed by numerical means, e.g., ray tracing. Usually, the initial model has to be refined through several migration steps, each of which is followed by a velocity analysis and update.

Finally, once a velocity model has been determined that is consistent with the data, a *true-amplitude migration* can be performed. Only with this method, it is possible to gain not only information about the structure and velocities, but also the reflection strengths. The latter can be very important for reservoir characterisation or a means to constrain shear velocities if only a PP survey was carried out.

Stacking and migration are powerful methods. It is not surprising that they are also very costly in terms of computer time and storage. Therefore, a lot of work has been invested in developing efficient strategies. More sophisticated stacking methods have been introduced as well as techniques to reduce the computational effort in migration, particularly of the true-amplitude type.

The author of this work is proud to have contributed to developments in the mentioned fields. In this thesis, I catalogue the main results of my work over the past fifteen years.

The thesis is structured into three parts. Beginning with the introduction of a hyperbolic traveltime interpolation method that is valid for media of arbitrary heterogeneity, anisotropy, and wavetype, I set a foundation for the subsequent chapters. The interpolation method is closely-related to multiparameter stacking formulations, which I investigate before introducing a new, non-hyperbolic operator, the *i-CRS* that is applicable to heterogeneous and anisotropic media and leads to better results than the classic stacking methods.

In the second part, I dedicate a chapter to the determination of geometrical spreading, a measure for seismic amplitudes. I suggest a method to obtain the spreading directly from traveltime information. As for the traveltimes in the first part, the spreading computation can be carried out in all types of media, including anisotropy. Since the geometrical spreading is a key ingredient for true-amplitude migration, I have developed a migration method that requires only traveltimes on coarse grids for the computation of all auxiliary quantities needed for the migration. This *traveltime-based strategy* has significant advantages over conventional migration methods, in particular if anisotropy has to be considered.

I demonstrate the superiority of the new stacking and migration methods with numerous meaningful examples, beginning with simple generic isotropic and anisotropic models in order to evaluate the accuracy. Application to complex media and field data shows that the new migration technique leads to equivalent results as obtained by standard methods, but with highly-increased efficiency and significantly lower demands on the input velocity model. This is especially true if seismic anisotropy has to be considered. The new stacking operator results in a highly-improved image in comparison to classic stacks. The reflector continuity and, particularly, the resolution of small structures like diffractors are significantly enhanced if the new i-CRS operator is applied.

Finally, a third part supplies an appendix with useful background information that would have been out of proportion in the main text.

Many of the results put forward in this thesis have already been published in journals or at conferences. However, it is my aim to present them as a comprehensive work in synoptic form, and I hope that my audience will enjoy reading it.

Part I

Traveltimes and stacking: the kinematic problem

Chapter 1

Introduction

Traveltimes of elastic waves are the key ingredient to any step in seismic data processing. First, analytic expressions are used during stacking to obtain a first image. At the end of the processing chain, after velocity model building has been carried out, traveltimes are generated numerically for the model to be used in prestack depth migration for the final image. In this first part of my thesis, I am providing insight and a means to express and interpolate traveltimes for any of the processing applications.

Over the years, a large variety of fast traveltime tools have been developed. Most of these tools are either based on ray methods, see, e.g., Červený (2001) or Appendix A, or finite-difference solutions of the eikonal equation (for an overview of both, see, e.g., Leidenfrost et al. 1999).

Several methods for traveltime interpolation have also been proposed, the simplest of them being trilinear interpolation, which does, however, not acknowledge the curvature of the wavefronts. Therefore, higher-order methods have been introduced, e.g., parabolic and hyperbolic approximations (Ursin, 1982; Gjøystdal et al., 1984; Schleicher et al., 1993b) or Fourier (sinc) interpolation (Brokešová, 1996) to name only a few.

A general second-order approximation of traveltimes in seismic systems was established by Bortfeld (1989). His work is based on the paraxial ray approximation (Červený, 2001) and can be used to interpolate traveltimes for sources and receivers which are located in the surfaces bordering the seismic system. Schleicher et al. (1993b) linked the Bortfeld theory to the ray propagator formalism and introduced a hyperbolic variant of paraxial traveltime interpolation. Both methods are, however, restricted to source and receiver reference surfaces and require the application of dynamic ray tracing. Mendes (2000) suggested traveltime interpolation using the Dix hyperbolic equation (Dix, 1955). Since the Dix equation is valid only for horizontally layered media, this technique is not justified for other models.

Brokešová (1996) stated the superiority of the paraxial (parabolic) interpolation compared with linear and Fourier (sinc-) interpolation of traveltimes. Gajewski (1998) not only found the hyperbolic variant of paraxial approximation to be far superior to trilinear interpolation but also introduced a technique to determine the interpolation coefficients directly from traveltimes, thus providing a means of avoiding dynamic ray tracing. The algorithm is, however, restricted to horizontal interpolation. Although the procedure can be repeated for vertical receiver lines, this does not allow for data reduction on to vertical coarse grids.

The method of traveltime interpolation that I present in this work is restricted neither to laterally homogeneous media nor to interpolation in reference surfaces, i.e. horizontal layers, only. I overcome the latter problem by introducing a technique that also computes coefficients for vertical interpolation. With all properties being determined from traveltimes only, our method corresponds to an extension of the well-known $T^2 - X^2$ technique to arbitrary heterogeneous media. No dynamic ray tracing is necessary.

Following the derivation of the parabolic and hyperbolic traveltime expansion in 3D, I give a detailed description of the implementation of the algorithm. Interpolation coefficients are determined from coarsely-gridded traveltimes including coefficients necessary for vertical interpolation and for the interpolation not only for the receivers but also inbetween shots. Using properties of the ray propagator, I also establish relations between the interpolation coefficients.

I then demonstrate the quality of the method by applying it to a variety of velocity models, ranging from generic examples for which analytical solutions are known to a 3D extension of the highly complex Marmousi model and anisotropic media. I compare the accuracy and performance of the results for both parabolic and hyperbolic interpolation to those for trilinear interpolation. I also investigate the influence of the size of the coarse grid spacing and the behaviour in the vicinity of non-smooth zones in the traveltime data, i.e., where later arrivals exist, and introduce an extension of the method to handle these regions correctly.

The applications so far were based on traveltime tables as source for the required quantities in terms of traveltime coefficients. Chapter 3 suggests an alternative process to determine the coefficients directly from data. The process is based on the common-reflection-surface (CRS) stack (Jäger et al., 2001; Zhang et al., 2001). The operator used for this stack is a hyperbolic formula describing the reflection move-out, which is closely-related to my hyperbolic traveltime expression.

Chapter 3 begins with an introduction of the image space concept (Höcht et al., 1999), which makes it possible to describe the reflection moveout in the real, usually arbitrarily heterogeneous, model by an auxiliary homogeneous medium. This concept enables me to present two derivations of the CRS operator. One is based on geometrical properties and follows the lines of Shah (1973) and Hubral and Krey (1980). The other derivation is carried out in image space based on a suggestion by B. Kashtan (personal communication) and allows for converted waves as well.

Once I have properly explained the CRS operator, I introduce the hyperbolic traveltime expression derived in Chapter 2 as general normal move-out operator, which contains the CRS formula as a subset, but has the advantage over CRS that it is applicable in any measurement configuration and in the presence of anisotropy. I demonstrate the general NMO operator with an example of stacking in the source-receiver domain.

Although the CRS and with it the general NMO operator have a multitude of applications, they do not provide good results for diffractions. This is because the reflection response can be well-approximated by a hyperbola, but diffractions are better described by double square root (DSR) type operators. This has led to the development of a non-hyperbolic traveltime operator that uses the same parameters or wavefield attributes as the CRS method. It can therefore be considered as an extension of the CRS technique. Since the resulting traveltime expression is implicit, I refer to it as the implicit common reflection surface, in short i-CRS, operator.

I demonstrate that the i-CRS operator provides a highly-accurate description of reflection traveltimes for curved interfaces ranging from the diffractor limit to nearly plane reflectors, and carry out a detailed error analysis. The accuracy holds for isotropic as well as anisotropic media. The application of the i-CRS operator to a complex data set proves that it leads to far superior results, particularly for diffraction-type structures like rugged top of salt.

Finally, I will give an outlook to further investigations of the i-CRS operator for heterogeneous anisotropic media. These have gained importance over the years because, for examples, shale gas is considered a major future energy source, and shales exhibit strong anisotropy. Chapter 5 suggests how the anisotropic i-CRS can be applied for anisotropy parameter determination.

Chapter 2

Traveltime interpolation

Using finite difference (FD) eikonal solvers or the wavefront construction method (for an overview of both, see, e.g., Leidenfrost et al. 1999), traveltime tables can be computed efficiently. This is one foundation for the summation stack along diffraction surfaces for a Kirchhoff type migration. For a 3-D depth migration, however, large amounts of fine gridded traveltime maps are required. The effort in computational time as well as in data storage can be significantly reduced if a fast and accurate traveltime interpolation routine can be applied. Then only few original traveltime tables must be computed and stored on coarse grids, whereas fast interpolation is carried out onto a finer grid during migration of data.

In 1982, Ursin introduced a hyperbolic approximation for reflection traveltimes where the wavefront curvature matrix is determined by dynamic ray tracing. Gjøystdal et al. (1984) compared parabolic and hyperbolic traveltime approximations for a variety of general inhomogeneous 3-D models with curved interfaces, also employing dynamic ray tracing. They concluded that a hyperbolic traveltime approximation is more accurate than a parabolic one. A general second order approximation of traveltimes in seismic systems was established by Bortfeld (1989). His work is based on the paraxial ray approximation (Červený, 2001) and can be used to interpolate traveltimes for sources and receivers which are located in the bordering surfaces of the seismic system. Schleicher et al. (1993b) link the Bortfeld theory to the ray propagator formalism and introduce a hyperbolic variant of the paraxial traveltime interpolation. Both methods are, however, restricted to source and receiver reference surfaces.

Mendes (2000) suggests traveltime interpolation using the Dix hyperbolic equation. Since the Dix equation is only valid for horizontally layered media, this technique is not justified for other models. Brokešová (1996) states the superiority of the paraxial (parabolic) interpolation compared to linear and Fourier (sinc-) interpolation of traveltimes.

Gajewski (1998) not only finds the hyperbolic variant of the paraxial approximation far superior to trilinear interpolation but also introduces a technique to determine the interpolation coefficients directly from traveltimes, therefore providing a means to avoid dynamic ray tracing. That algorithm is, however, restricted to horizontal interpolation. Although the procedure can be repeated for vertical receiver lines, this does not allow for data reduction onto vertical coarse grids.

The traveltime interpolation algorithm that I present here is neither restricted to laterally homogeneous media nor to interpolation in reference surfaces respectively horizontal layers only. In contrast to most other methods, it also allows for the interpolation of sources, not only receivers. Since no assumptions are made on the velocities of the medium, the method can be applied to arbitrary 3-D heterogeneous and even anisotropic media.

Following the derivation of a parabolic and hyperbolic traveltime expansion in arbitrary 3-D media, I give a detailed description on the determination of the Taylor coefficients. In the following section I give examples for the coefficients in media where an analytic solution is available. They demonstrate that the coefficients can be determined from traveltimes with high accuracy. Application of the resulting traveltime interpolation to a variety of velocity models is shown in the next sections. The models range from isotropic and anisotropic examples for which analytic solutions are known to a 3-D extension of the highly complex Marmousi model. The results of both parabolic and hyperbolic interpolation are compared to trilinear interpolation. As expected the hyperbolic variant is superior to the parabolic one. This is not surprising because it confirms that any wavefront can locally be approximated by a sphere. Also, the accuracy of second order interpolation is far better than trilinear interpolation, because the latter neglects the curvature of the wavefront.

In addition, I find that the required amount of computational time is of the same order for all three interpolation methods. I also investigated the influence of the size of the coarse grid spacing. In conclusion, if traveltimes for only every tenth grid point are stored, savings of up to a factor of 10^6 are possible with no significant loss in accuracy and significant gains in CPU time.

Finally I take a closer look at the behaviour of the method in the vicinity of discontinuities in the traveltime data as well as in the presence of later arrivals. The traveltime coefficients determined during the interpolation can be used for the detection of such discontinuities. The traveltimes in regions surrounding these points can be correctly dealt with in two ways, depending on whether later-arrival traveltimes or only first arrivals are available. This is demonstrated in a section before I conclude with an analysis as to how and why the traveltime interpolation method can also be applied to reflected traveltimes.

2.1 Parabolic traveltime expansion

The following considerations are based upon the existence of first and second order continuous spatial derivatives for the traveltime fields. Traveltimes that satisfy these conditions can be expanded into a Taylor series up to second degree. Provided that the distance to the expansion point is small, the Taylor series yields a good approximation for the original traveltime function. The size of the vicinity describing "small" distances depends on the scale of velocity variations in the input model.

For the 3-D case, the Taylor expansion has to be carried out in 6 variables: the 3 components of the source position vector $\hat{\boldsymbol{s}} = (s_1, s_2, s_3)^\top$ and those of the receiver position $\hat{\boldsymbol{g}} = (g_1, g_2, g_3)^\top$. The values of $\hat{\boldsymbol{s}}$ and $\hat{\boldsymbol{g}}$ at the expansion point are $\hat{\boldsymbol{s}}_0$ and $\hat{\boldsymbol{g}}_0$ with the traveltime τ_0 from $\hat{\boldsymbol{s}}_0$ to $\hat{\boldsymbol{g}}_0$. The variations in source and receiver positions $\Delta\hat{\boldsymbol{s}}$ and $\Delta\hat{\boldsymbol{g}}$ are such that $\hat{\boldsymbol{s}} = \hat{\boldsymbol{s}}_0 + \Delta\hat{\boldsymbol{s}}$ and $\hat{\boldsymbol{g}} = \hat{\boldsymbol{g}}_0 + \Delta\hat{\boldsymbol{g}}$. The Taylor expansion for $\tau(\hat{\boldsymbol{s}}_0 + \Delta\hat{\boldsymbol{s}}, \hat{\boldsymbol{g}}_0 + \Delta\hat{\boldsymbol{g}})$ up to second order written in index notation (i, j=1,2,3) is

$$
\begin{aligned}
\tau(s_i, g_i) &= \tau_0 + \Delta s_i \left.\frac{\partial \tau}{\partial s_i}\right|_{\hat{\boldsymbol{s}}_0, \hat{\boldsymbol{g}}_0} + \Delta g_i \left.\frac{\partial \tau}{\partial g_i}\right|_{\hat{\boldsymbol{s}}_0, \hat{\boldsymbol{g}}_0} + \Delta s_i \, \Delta g_j \left.\frac{\partial^2 \tau}{\partial s_i \partial g_j}\right|_{\hat{\boldsymbol{s}}_0, \hat{\boldsymbol{g}}_0} \\
&+ \frac{1}{2} \Delta s_i \, \Delta s_j \left.\frac{\partial^2 \tau}{\partial s_i \partial s_j}\right|_{\hat{\boldsymbol{s}}_0, \hat{\boldsymbol{g}}_0} + \frac{1}{2} \Delta g_i \, \Delta g_j \left.\frac{\partial^2 \tau}{\partial g_i \partial g_j}\right|_{\hat{\boldsymbol{s}}_0, \hat{\boldsymbol{g}}_0} + \mathcal{O}(3) \qquad (2.1.1)
\end{aligned}
$$

(summation convention is applied). I introduce the following notation for the slowness vectors $\hat{\boldsymbol{p}}_0$ and $\hat{\boldsymbol{q}}_0$ at $\hat{s}_0$ and $\hat{\boldsymbol{g}}_0$, respectively

$$
p_{i_0} = -\left.\frac{\partial \tau}{\partial s_i}\right|_{\hat{\boldsymbol{s}}_0, \hat{\boldsymbol{g}}_0} \quad , \qquad q_{i_0} = \left.\frac{\partial \tau}{\partial g_i}\right|_{\hat{\boldsymbol{s}}_0, \hat{\boldsymbol{g}}_0} \quad , \qquad (2.1.2)
$$

and the second order derivative matrices $\underline{\hat{\mathsf{S}}}$, $\underline{\hat{\mathsf{G}}}$ and $\underline{\hat{\mathsf{N}}}$ with

$$
\begin{aligned}
S_{ij} &= - \left.\frac{\partial^2 \tau}{\partial s_i \partial s_j}\right|_{\hat{\boldsymbol{s}}_0, \hat{\boldsymbol{g}}_0} = S_{ji} \quad , \\
G_{ij} &= \left.\frac{\partial^2 \tau}{\partial g_i \partial g_j}\right|_{\hat{\boldsymbol{s}}_0, \hat{\boldsymbol{g}}_0} = G_{ji} \quad , \\
N_{ij} &= - \left.\frac{\partial^2 \tau}{\partial s_i \partial g_j}\right|_{\hat{\boldsymbol{s}}_0, \hat{\boldsymbol{g}}_0} \neq N_{ji} \quad . \qquad (2.1.3)
\end{aligned}
$$

With these the Taylor series (2.1.1) reads

$$
\begin{aligned}
\tau(\hat{\boldsymbol{s}}, \hat{\boldsymbol{g}}) &= \tau_0 - \hat{\boldsymbol{p}}_0^\top \Delta \hat{\boldsymbol{s}} + \hat{\boldsymbol{q}}_0^\top \Delta \hat{\boldsymbol{g}} - \Delta \hat{\boldsymbol{s}}^\top \underline{\hat{\mathsf{N}}} \, \Delta \hat{\boldsymbol{g}} \\
&- \frac{1}{2} \Delta \hat{\boldsymbol{s}}^\top \underline{\hat{\mathsf{S}}} \, \Delta \hat{\boldsymbol{s}} + \frac{1}{2} \Delta \hat{\boldsymbol{g}}^\top \underline{\hat{\mathsf{G}}} \, \Delta \hat{\boldsymbol{g}} + \mathcal{O}(3) \quad . \qquad (2.1.4)
\end{aligned}
$$

Equation (2.1.4) describes the *parabolic* traveltime expansion. The signs were chosen in a form, that for growing distance between source and receiver the traveltime (e.g., in a homogeneous medium) increases.

Equation (2.1.4) states that for small variations of $\Delta \hat{\boldsymbol{s}}$ and $\Delta \hat{\boldsymbol{g}}$, traveltimes can be approximated by a parabola with high accuracy. If the $\mathcal{O}(3)$ term is neglected, Equation (2.1.4) can be used for the determination of the coefficients. This requires that traveltimes for certain source-receiver combinations are given, which can be substituted in Equation (2.1.4) and then solved for the coefficients. The aim is to apply this interpolation to migration, where the seismic reflection data is stacked along diffraction traveltime surfaces. To compute these stacking surfaces traveltime tables need to be computed in any event. Therefore I assume that such data is available. Application of the traveltime interpolation will, however, reduce the need to compute these traveltime tables on fine grids. Before discussing the traveltime interpolation I will demonstrate how to obtain the coefficients from traveltimes sampled on a coarse grid.

In the following, Cartesian grids for both source and receiver positions are used. Sources are located in the x-y-plane with x, y, and z corresponding to the indices 1, 2, and 3. To determine the slowness vectors $\hat{\boldsymbol{p}}_0$ and $\hat{\boldsymbol{q}}_0$ as well as the second order derivative matrices $\underline{\hat{\mathsf{S}}}$, $\underline{\hat{\mathsf{G}}}$, and $\underline{\hat{\mathsf{N}}}$, tables containing traveltimes from the source to each subsurface coarse grid point are required for nine different source positions: the central source at $\hat{s}_0$ and eight surrounding source positions (for a

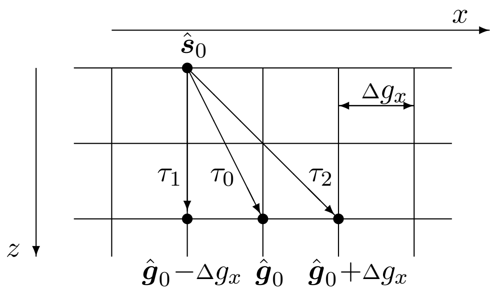

Figure 2.1: Determination of the coefficients q_{x_0} and G_{xx}: the traveltimes τ_0 from $\hat{\boldsymbol{s}}_0$ to $\hat{\boldsymbol{g}}_0$, τ_1 from $\hat{\boldsymbol{s}}_0$ to $\hat{\boldsymbol{g}}_0-\Delta g_x$, and τ_2 from $\hat{\boldsymbol{s}}_0$ to $\hat{\boldsymbol{g}}_0+\Delta g_x$ are required.

2-D model the number of additional sources reduces to two). These additional sources are placed on the x-y-grid with a distance to the central source that in my example coincides with the coarse grid spacing Δx and Δy. Note that the method is neither restricted to cubical grids nor to equal grid spacing for sources and receivers.

To compute q_{x_0} and G_{xx} from the traveltime tables, only the traveltimes τ_0, τ_1, and τ_2 are required, as shown in Figure 2.1. The traveltimes τ_1 and τ_2 are inserted into the parabolic expansion (2.1.4), respectively. Building the sum and the difference of the resulting expressions yields

$$
\begin{array}{lrl}
 & \tau_1 = & \tau_0 - q_{x_0}\Delta g_x + \tfrac{1}{2} G_{xx}\Delta g_x^2 \\
 & \tau_2 = & \tau_0 + q_{x_0}\Delta g_x + \tfrac{1}{2} G_{xx}\Delta g_x^2 \\
\hline
\text{Sum:} & \tau_1+\tau_2 = & 2\tau_0 \qquad\qquad + G_{xx}\Delta g_x^2 \\
\text{Difference:} & \tau_1-\tau_2 = & \quad -2q_{x_0}\Delta g_x \quad .
\end{array}
$$

This can be solved for q_{x_0} and G_{xx}

$$
q_{x_0} = \frac{\tau_2 - \tau_1}{2\,\Delta g_x} \quad \text{and} \quad G_{xx} = \frac{\tau_1 + \tau_2 - 2\,\tau_0}{\Delta g_x^2} \quad . \tag{2.1.5}
$$

The expressions for the remaining coefficients follow accordingly.

The y- and z-components of $\hat{\boldsymbol{q}}_0$ and $\hat{\underline{\mathsf{G}}}$ can be found in the same way by varying g_y, respectively g_z. Varying both g_x and g_y leads to G_{xy}; G_{yz} and G_{zx} follow accordingly. The determination of the x- and y-components of $\hat{\underline{\mathsf{S}}}$ and $\hat{\boldsymbol{p}}_0$ is straightforward: instead of varying the receiver position, different source positions in the x-y-surface are used. For the xx-, yy-, xy- and yx-components of $\hat{\underline{\mathsf{N}}}$, both source and receiver positions have to be varied in x and y. The z-components of $\hat{\boldsymbol{p}}_0$, $\hat{\underline{\mathsf{S}}}$, and $\hat{\underline{\mathsf{N}}}$ can be determined from traveltimes for sources at different depths, following the same lines as for the x- and y-components. For isotropic media, however, I propose a different approach without having to compute these additional traveltime tables for sources in the subsurface. The eikonal equation

$$
\left(\frac{\partial\tau}{\partial x}\right)^2 + \left(\frac{\partial\tau}{\partial y}\right)^2 + \left(\frac{\partial\tau}{\partial z}\right)^2 = \frac{1}{V^2} \tag{2.1.6}
$$

can be solved for the z-component of the slowness vector $\hat{\boldsymbol{p}}$

$$p_z = \sqrt{\frac{1}{V_s^2} - p_x^2 - p_y^2} \quad . \tag{2.1.7}$$

This requires that the source lies in the top surface of the model, otherwise the sign of p_z must be taken into account. This case is, however, not considered here. The velocity V_s in (2.1.6) is the phase velocity at the source. With the definitions (2.1.2) and (2.1.3), $\hat{\underline{\mathsf{S}}}$ and $\hat{\underline{\mathsf{N}}}$ can be rewritten to

$$S_{ij} = \left.\left(\frac{\partial p_i}{\partial s_j}\right)\right|_{\hat{\boldsymbol{s}}_0,\hat{\boldsymbol{g}}_0} \quad , \tag{2.1.8}$$

$$N_{ij} = -\left.\left(\frac{\partial q_j}{\partial s_i}\right)\right|_{\hat{\boldsymbol{s}}_0,\hat{\boldsymbol{g}}_0} = \left.\left(\frac{\partial p_i}{\partial g_j}\right)\right|_{\hat{\boldsymbol{s}}_0,\hat{\boldsymbol{g}}_0} \quad . \tag{2.1.9}$$

Substituting p_z in Equations (2.1.8) and (2.1.9) by (2.1.7), the second order derivatives of τ with respect to s_z can be determined from the already known x-y-matrix elements and derivatives of the velocity. If the velocity field under consideration is continuous, the velocity derivatives can be determined with a second order FD operator on the coarse grid.

The results for the z elements of $\hat{\underline{\mathsf{S}}}$ and $\hat{\underline{\mathsf{N}}}$ are as follows:

$$\begin{aligned}
S_{xz} &= \frac{\partial p_z}{\partial s_x} = \frac{\partial}{\partial s_x}\sqrt{\frac{1}{V_s^2} - p_x^2 - p_y^2} \\
&= \frac{1}{2\,p_{z_0}}\frac{\partial}{\partial s_x}\left(\frac{1}{V_s^2} - p_x^2 - p_y^2\right) \\
&= -\frac{1}{V_s^3\,p_{z_0}}\frac{\partial V_s}{\partial s_x} - \frac{p_{x0}}{p_{z_0}}\frac{\partial p_x}{\partial s_x} - \frac{p_{y0}}{p_{z_0}}\frac{\partial p_y}{\partial s_x} \\
&= -\frac{1}{V_s^3\,p_{z_0}}\frac{\partial V_s}{\partial s_x} - \frac{p_{x0}}{p_{z_0}}S_{xx} - \frac{p_{y0}}{p_{z_0}}S_{xy} \quad = \quad S_{zx} \quad , && (2.1.10)\\
S_{yz} &= -\frac{1}{V_s^3\,p_{z_0}}\frac{\partial V_s}{\partial s_y} - \frac{p_{x0}}{p_{z_0}}S_{xy} - \frac{p_{y0}}{p_{z_0}}S_{yy} \quad = \quad S_{zy} \quad , && (2.1.11)\\
S_{zz} &= -\frac{1}{V_s^3\,p_{z_0}}\frac{\partial V_s}{\partial s_z} - \frac{p_{x0}}{p_{z_0}}S_{xz} - \frac{p_{y0}}{p_{z_0}}S_{yz} \quad , && (2.1.12)\\
N_{zx} &= -\frac{p_{x0}}{p_{z_0}}N_{xx} - \frac{p_{y0}}{p_{z_0}}N_{yx} \quad , && (2.1.13)\\
N_{zy} &= -\frac{p_{x0}}{p_{z_0}}N_{xy} - \frac{p_{y0}}{p_{z_0}}N_{yy} \quad , && (2.1.14)\\
N_{zz} &= -\frac{1}{p_{z_0}}\left(p_{x_0}\,N_{xz} + p_{y_0}\,N_{yz}\right) && (2.1.15)
\end{aligned}$$

(derivatives are taken at $\hat{\mathbf{s}}_0, \hat{\boldsymbol{g}}_0$). These expressions will not yield results if p_{z_0} equals zero. This case has, however, no practical relevance for the applications that the method was developed for.

For anisotropic media, the eikonal equation corresponds to Equation (2.1.6), but V_s is a function of the phase normal (i.e. V_s depends on the direction of wave propagation). To obtain the appropriate derivatives, results of Gajewski (1993) can be used. Until these formulae exist the anisotropic coefficients can be determined from traveltimes, however, for the derivatives with respect to the z component of the source position traveltime tables for sources at different depths are required. Then these derivatives can be computed in the same way as the derivatives with respect to other components of the source and receiver position, as shown above.

2.2 Hyperbolic traveltime expansion

Considering the simplest medium that we can think of, a homogeneous medium with constant velocity, it appears that there might be an even better approximation than the parabolic one: in a constant velocity medium the wavefronts are circles that translate into hyperbolic traveltimes. Therefore, it should be possible to locally approximate wavefronts in heterogeneous media by spheres[1]. This corresponds to a hyperbolic traveltime interpolation. For the constant velocity model the hyperbolic approximation is not only an approximation but equals the exact result.

To derive a hyperbolic traveltime approximation not τ is expanded into a Taylor series but its square, τ^2. As for the parabolic approximation, the expansion is carried out up to order two

$$\begin{aligned}\tau^2(s_i, g_i) \;&=\; \tau_0^2 + \Delta s_i \left.\frac{\partial \tau^2}{\partial s_i}\right|_{\hat{\boldsymbol{s}}_0,\hat{\boldsymbol{g}}_0} + \Delta g_i \left.\frac{\partial \tau^2}{\partial g_i}\right|_{\hat{\boldsymbol{s}}_0,\hat{\boldsymbol{g}}_0} + \Delta s_i\,\Delta g_j \left.\frac{\partial^2 \tau^2}{\partial s_i \partial g_j}\right|_{\hat{\boldsymbol{s}}_0,\hat{\boldsymbol{g}}_0} \\ &\quad + \frac{1}{2}\,\Delta s_i\,\Delta s_j \left.\frac{\partial^2 \tau^2}{\partial s_i \partial s_j}\right|_{\hat{\boldsymbol{s}}_0,\hat{\boldsymbol{g}}_0} + \frac{1}{2}\,\Delta g_i\,\Delta g_j \left.\frac{\partial^2 \tau^2}{\partial g_i \partial g_j}\right|_{\hat{\boldsymbol{s}}_0,\hat{\boldsymbol{g}}_0} + \mathcal{O}(3) \quad . \qquad (2.2.1)\end{aligned}$$

Applying the chain rule, $[f(g(x))]' = f'(g) \cdot g'(x)$, and inserting the abbreviations (2.1.2) and (2.1.3) into Equation (2.2.1), this yields

$$\begin{aligned}\tau^2(\hat{\boldsymbol{s}}, \hat{\boldsymbol{g}}) \;&=\; (\tau_0 - \hat{\boldsymbol{p}}_0^\top \Delta\hat{\boldsymbol{s}} + \hat{\boldsymbol{q}}_0^\top \Delta\hat{\boldsymbol{g}})^2 + \tau_0 \left(-2\,\Delta\hat{\boldsymbol{s}}^\top \underline{\hat{\mathsf{N}}}\,\Delta\hat{\boldsymbol{g}}\right. \\ &\quad \left. -\Delta\hat{\boldsymbol{s}}^\top \underline{\hat{\mathsf{S}}}\,\Delta\hat{\boldsymbol{s}} + \Delta\hat{\boldsymbol{g}}^\top \underline{\hat{\mathsf{G}}}\,\Delta\hat{\boldsymbol{g}}\right) + \mathcal{O}(3) \quad . \qquad (2.2.2)\end{aligned}$$

This equation is the *hyperbolic* traveltime expansion. As above for the parabolic form, the coefficients can be determined from traveltime tables. I give the same example as above, using the traveltimes τ_0, τ_1, and τ_2 (cf. Figure 2.1) and inserting them into (2.2.2):

$$\begin{array}{lllll} & \tau_1^2 = & \tau_0^2 + q_{x0}^2 \Delta g_x^2 & -2\tau_0 q_{x0} \Delta g_x & + \tau_0 G_{xx} \Delta g_x^2 \\ & \tau_2^2 = & \tau_0^2 + q_{x0}^2 \Delta g_x^2 & +2\tau_0 q_{x0} \Delta g_x & + \tau_0 G_{xx} \Delta g_x^2 \\ \hline \text{Sum:} & \tau_1^2 + \tau_2^2 = & 2\tau_0^2 + 2 q_{x0}^2 \Delta g_x^2 & & + 2\tau_0 G_{xx} \Delta g_x^2 \\ \text{Difference:} & \tau_1^2 - \tau_2^2 = & & -4\tau_0 q_{x0} \Delta g_x & . \end{array}$$

Solving for q_{x0} and G_{xx} yields

$$q_{x0} = \frac{\tau_2^2 - \tau_1^2}{4\,\tau_0\,\Delta g_x} \quad \text{and} \quad G_{xx} = \frac{\tau_2^2 + \tau_1^2 - 2\,\tau_0^2}{2\,\tau_0\,\Delta g_x^2} - \frac{q_{x0}^2}{\tau_0} \quad . \qquad (2.2.3)$$

The remaining coefficients can be determined accordingly. For the z derivatives Equations (2.1.7) and (2.1.10) to (2.1.15) apply without changes in isotropic media.

[1] This is a simplification. In 3-D, an ellipse would be more appropriate. However, the method approximates the local wavefront by a general surface of second order, meaning, that the two main radii of curvature can even have different sign.

2.3 Accuracy of the coefficients

I have tested the accuracy of the method on two analytic models: a homogeneous model, and a gradient model with $V = a + bz$. The velocity at the source (at depth z_s) is given by $V_s = a + bz_s$. The coefficients that were determined from the traveltime expansions were compared to analytic coefficients. Expressions for the analytic coefficients for both models are given in Appendix B.
The constant velocity medium has a velocity V=3000m/s, and the gradient model has a=3000m/s and b=0.5s^{-1}. Traveltimes for both models were given on a 100m grid, i.e. a grid with 100m spacing. To test the accuracy of the method itself analytic traveltimes have been used. Since an analytic solution is not generally available, a second test was carried out with traveltimes computed with a finite differences eikonal solver (FDES) using the Vidale (1990) algorithm. These traveltimes were computed on a 10m fine grid and resampled to the 100m grid. This was necessary because FDES need fine grids to provide sufficient accuracy. For both models and both sets of traveltime tables the coefficients were determined twice: from the hyperbolic and the parabolic variant as shown above. The results were compared to the analytic coefficients. For the gradient model the analytic coefficients are shown in Figure 2.2.

Tables 2.1 and 2.2 show that the hyperbolic results are superior to the parabolic ones. This confirms that any wavefront can locally be well approximated by a sphere, or, more generally, a surface of second order. The coefficients from the numerically computed input traveltimes are less accurate than for analytic traveltimes. Figure 2.3 demonstrates the spatial distribution of the errors for both hyperbolic and parabolic coefficients from analytic traveltimes and hyperbolic coefficients from analytic traveltimes for the gradient model. Figure 2.4 shows relative errors of the hyperbolic coefficients from Vidale traveltimes, also for the gradient model.

Table 2.1 gives the median relative errors for the coefficients of the constant velocity model, in Table 2.2 the same is found for the gradient model. I use median errors rather than average errors because they are less sensitive to outliers. The errors given are relative errors, meaning

$$\triangle f_{\rm rel} = \frac{f - f_0}{f_0} \quad , \tag{2.3.1}$$

where $\triangle \, f_{\rm rel}$ is the relative error of the quantity f compared with the reference value f_0. There are regions with small reference value (e.g., if f is a traveltime near the source) where the relative errors appear higher due to the division by the small f_0. This should be kept in mind when dealing with relative errors.

Figure 2.3 also states that the hyperbolic form yields smaller errors than the parabolic one. This is most obvious in the near source region but not restricted to it. The same holds for the coefficients from Vidale traveltimes: Figure 2.4 shows the errors of the hyperbolic coefficients from Vidale traveltimes. In all plots, there exist regions with higher errors, as, for example, the stripe in the front of G_{zz} or the top surface of q_z (see Figures 2.3 and 2.4). Comparing these errors with the values of G_{zz} and q_z in Figure 2.2 explains them with the exaggerated impact of very small values of G_{zz} and q_z (see the discussion on relative errors above). Figure 2.4 shows that the coefficients from Vidale traveltimes suffer from more errors than those from analytic traveltimes. For nearly all coefficients a region of higher error is visibly present which follows a 45° line starting from the source position. This region coincides with errors of the input traveltimes from the Vidale algorithm given in Figure 2.9. The error distribution of the parabolic coefficients from Vidale traveltime corresponds to that of the parabolic coefficients from analytic traveltimes with additional contributions due to the errors in

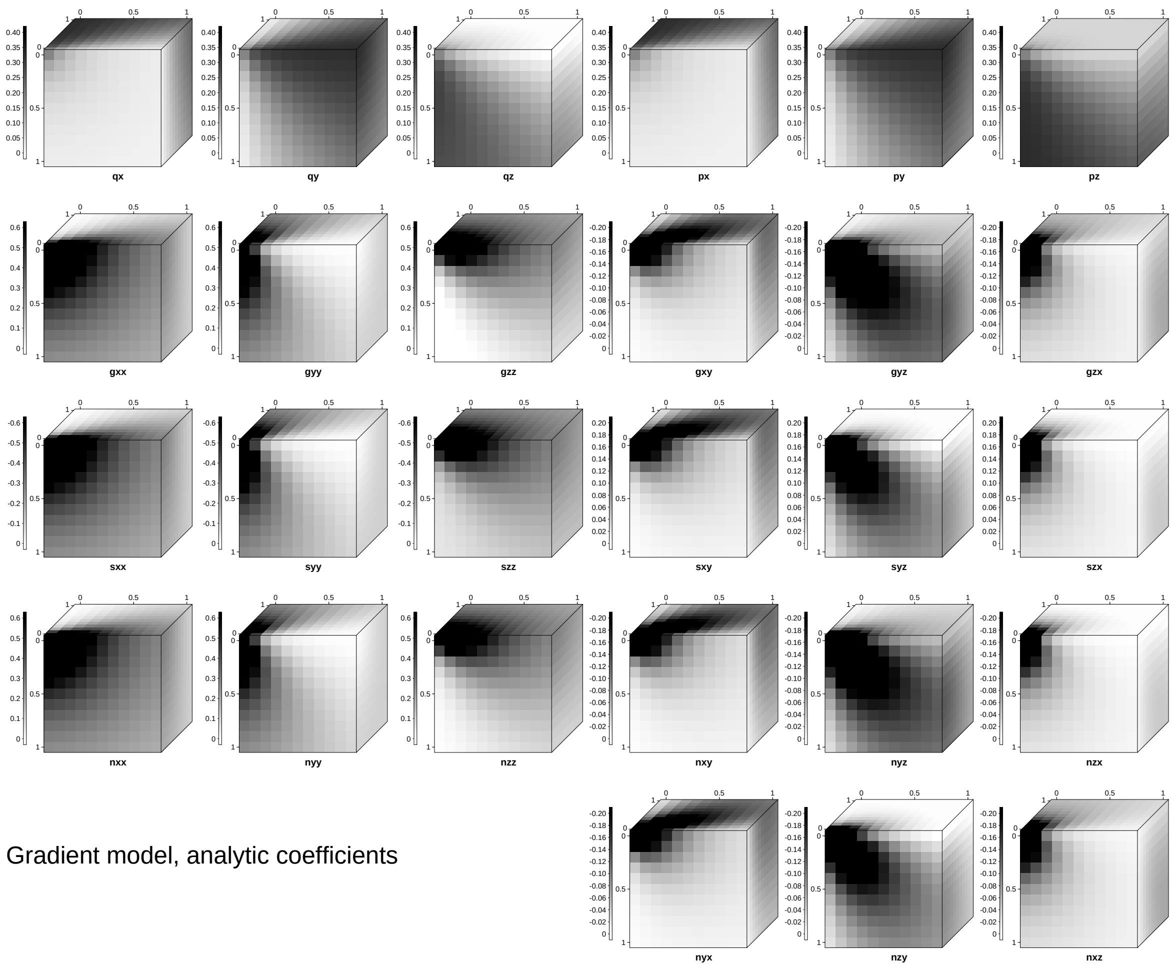

Figure 2.2: Analytic coefficients for a gradient model: the slownesses in [s/km] are given in the top row, followed by the second order derivatives in [s/km^2]. Absolute values are given. Axis labels are omitted to save space. The z axis corresponds to the vertical direction (depth), the y axis to the horizontal direction. The x axis is perpendicular to the page. Distances are given in [km]. The source is located at –100m in either direction.

Table 2.1: Median of relative errors in percent of the coefficients for the constant velocity model. Hyperbolic coefficient errors from analytic traveltimes reflect the numerical noise of 32 bit words.

	Analytic traveltimes		Vidale traveltimes	
	hyperbolic $\cdot 10^{-3}$	parabolic	hyperbolic	parabolic
q_x	0.040	0.245	0.229	0.436
q_y	0.040	0.245	0.229	0.436
q_z	0.040	0.245	0.136	0.264
p_x	0.040	0.245	0.229	0.436
p_y	0.040	0.245	0.229	0.436
p_z	0.055	0.451	0.147	0.406
G_{xx}	1.190	0.162	1.63	1.73
G_{yy}	1.190	0.162	1.63	1.73
G_{zz}	1.210	0.162	1.62	1.57
G_{xy}	0.725	0.886	1.17	2.13
G_{yz}	0.720	0.886	1.40	1.96
G_{zx}	0.720	0.886	1.40	1.96
S_{xx}	1.190	0.162	1.63	1.73
S_{yy}	1.190	0.162	1.63	1.73
S_{zz}	2.860	0.361	1.86	2.00
S_{xy}	0.725	0.886	1.17	2.13
S_{yz}	3.16	0.455	2.05	2.10
S_{zx}	3.16	0.455	2.05	2.10
N_{xx}	0.291	0.637	0.931	1.61
N_{yy}	0.291	0.637	0.931	1.61
N_{zz}	0.509	1.48	0.976	1.65
N_{xy}	0.725	0.886	1.17	2.13
N_{yz}	0.720	0.886	1.40	1.96
N_{zx}	1.14	1.33	1.57	2.66
N_{yx}	0.725	0.886	1.17	2.13
N_{zy}	1.14	1.33	1.57	2.66
N_{xz}	0.720	0.886	1.40	1.96

Table 2.2: Median of relative errors in percent of the coefficients for the gradient model.

	Analytic traveltimes		Vidale traveltimes	
	hyperbolic $\cdot 10^{-3}$	parabolic	hyperbolic	parabolic
q_x	4.17	0.248	0.206	0.41
q_y	4.17	0.248	0.206	0.41
q_z	131.0	0.367	0.139	0.305
p_x	4.17	0.248	0.206	0.41
p_y	4.17	0.248	0.206	0.41
p_z	6.73	0.316	0.098	0.306
G_{xx}	2.07	0.165	1.21	1.32
G_{yy}	2.07	0.165	1.21	1.32
G_{zz}	111.0	0.204	1.46	1.48
G_{xy}	8.64	0.884	0.913	1.79
G_{yz}	94.9	0.767	1.05	1.40
G_{zx}	94.9	0.767	1.05	1.40
S_{xx}	2.07	0.165	1.21	1.32
S_{yy}	2.07	0.165	1.21	1.32
S_{zz}	7.65	0.209	0.664	0.688
S_{xy}	8.64	0.884	0.913	1.79
S_{yz}	5.56	0.578	1.46	1.60
S_{zx}	5.56	0.578	1.46	1.60
N_{xx}	8.16	0.643	0.772	1.48
N_{yy}	8.16	0.643	0.772	1.48
N_{zz}	106.0	1.22	0.913	1.34
N_{xy}	8.64	0.884	0.913	1.79
N_{yz}	94.9	0.767	1.05	1.40
N_{zx}	18.6	1.45	1.37	2.55
N_{yx}	8.64	0.884	0.913	1.79
N_{zy}	18.6	1.45	1.37	2.55
N_{xz}	94.9	0.767	1.05	1.40

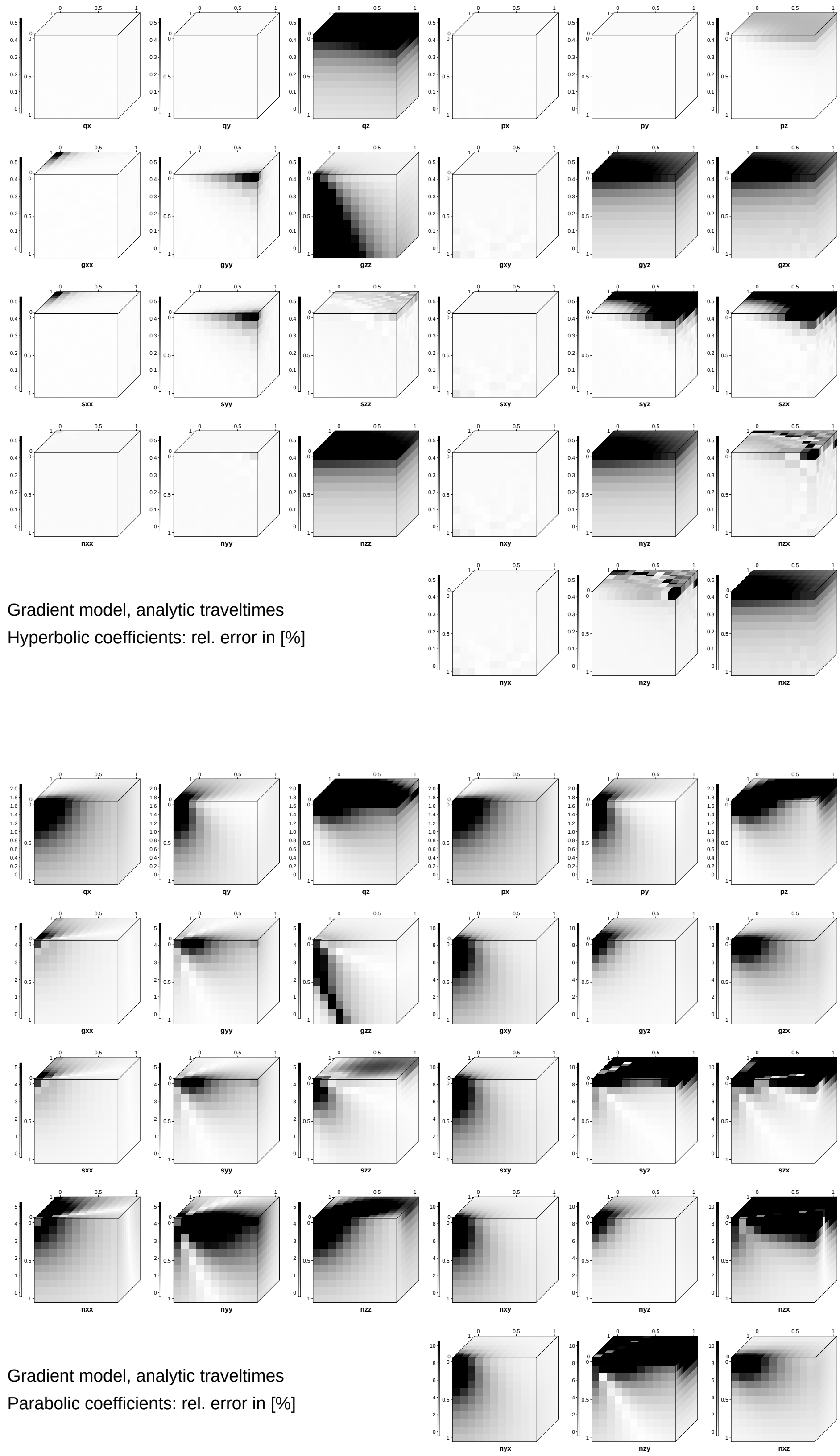

Figure 2.3: Relative errors of coefficients from analytic traveltimes for the gradient model. On top for the hyperbolic, bottom for parabolic coefficients. Note the different error scales. The source is at –100m in either direction.

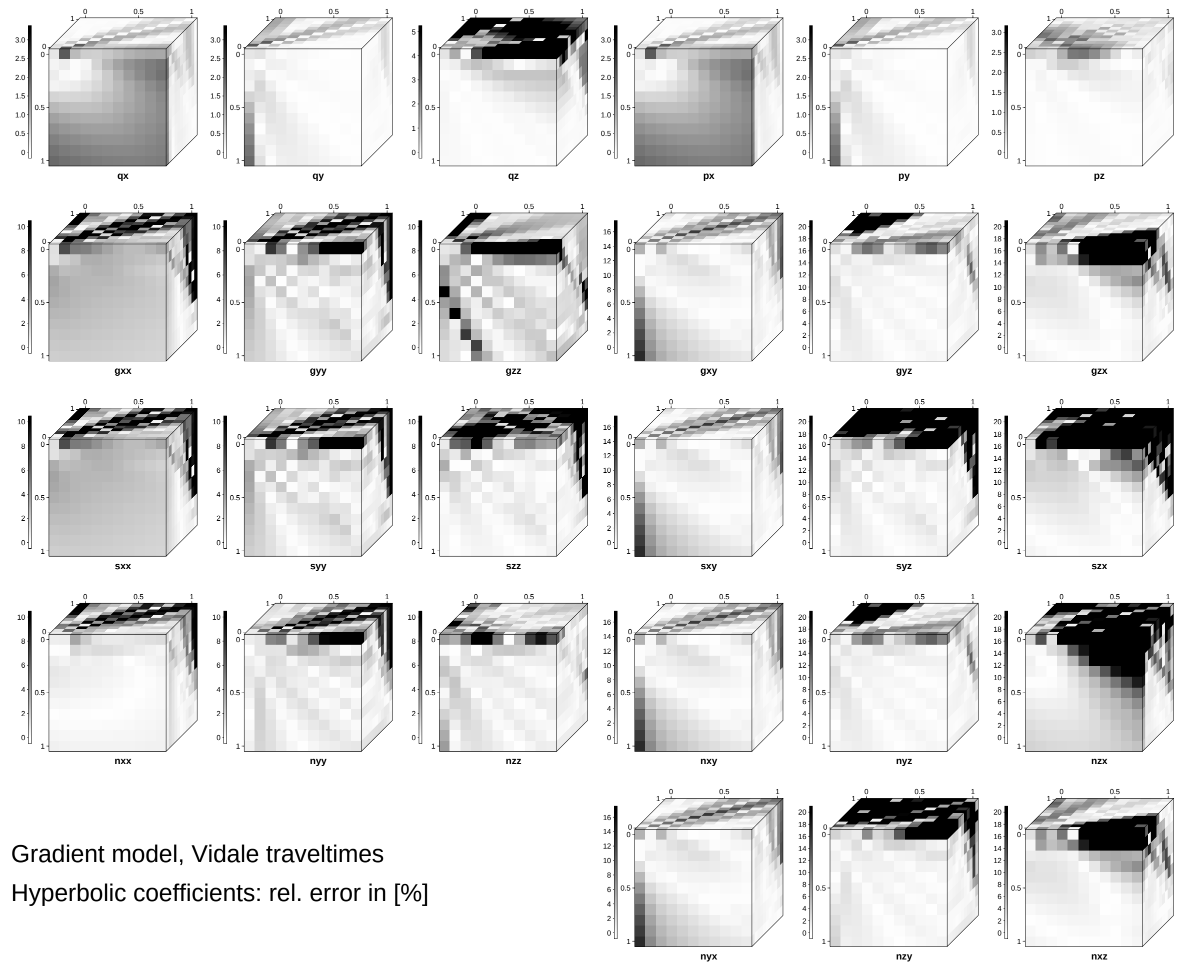

Figure 2.4: Relative errors of coefficients from Vidale traveltimes for the gradient model. In addition to regions with higher relative errors caused by small values of the coefficients under consideration, other regions with higher errors follow the errors of the Vidale input traveltimes, see Figure 2.9.

the Vidale traveltimes. Since no new insights can be gained from it, the parabolic error distribution of coefficients from Vidale traveltimes is not displayed in a Figure.

Error plots for the homogeneous model are not given here. The spatial distribution of the errors looks similar to the gradient model. The hyperbolic variant has again much smaller errors than the parabolic one. It would be, however, misleading to base the superiority of the hyperbolic variant only on the homogeneous example, because in this case the hyperbolic traveltime expansion up to second order yields the exact traveltime (see Appendix B). Therefore, the accuracy of the hyperbolic coefficients from analytic traveltimes is expected to be within machine precision, which is confirmed by Table 2.1. Similarly, the accuracy of the hyperbolic coefficients from Vidale traveltimes is dominated by errors in the input traveltimes.

2.4 Isotropic examples

The parabolic and hyperbolic expressions for traveltimes can be used for traveltime interpolation with high accuracy, once the according coefficient sets are known. This includes interpolation not only in between receivers but also in between sources. For each of the following examples both parabolic and hyperbolic coefficients were determined using the procedure described in Sections 2.1 and 2.2. Subsequent interpolation with the parabolic formula (2.1.4) respectively the hyperbolic variant (2.2.2) was applied.

Constant velocity model

The first example is a model with a constant velocity of 3000m/s. I have used analytic traveltimes and traveltimes from an FDES using the Vidale algorithm (see Section 2.3) as input data to validate the accuracy. Errors from analytic input traveltimes are only due to the method itself and possibly roundoff errors whereas the errors from Vidale traveltimes (shown in Figure 2.9 for a gradient model) give an estimate of the accuracy under more realistic conditions.

The example model is a cube of 101×101×101 grid points with 10m grid spacing. The source is centred in the top surface. Input traveltimes were given on a cubical 100m coarse grid. The distances in source position were also 100m in either direction. The interpolations onto a 10m fine grid were each carried out twice: for the original source position and for a source shifted by 50m in x and y. The results are compared to analytic and Vidale reference traveltimes, respectively, on a fine 10m grid.

The resulting relative traveltime errors are displayed in Figure 2.5 for the analytic input traveltimes and in Figure 2.6 for the Vidale input traveltimes. The results look similar for analytic and Vidale traveltimes: hyperbolic coefficients yield higher accuracy than parabolic ones. The magnitude of the errors from Vidale traveltime is the same as those from analytic input traveltimes for the parabolic variant. For the hyperbolic variant analytic traveltimes lead to exact coefficients, therefore the errors from the interpolation are within machine precision. The results from hyperbolic interpolation of Vidale input traveltimes give a more realistic estimate.

The pattern in the error distribution can be explained as follows: traveltimes were interpolated onto the fine grid using the coefficients of the nearest coarse grid point. This leads to the discontinuities in the error plots where the area of fine grid points surrounding the coarse grid point under consideration ends. The traveltime errors are summarised in Table 2.3 together with results

Table 2.3: Errors of traveltime interpolation for the homogeneous velocity model excluding a layer of 100m thickness under the source.

Interpolation	Source shift $\Delta s_x = \Delta s_y$	Median of rel. error	Maximum rel. error	Median of abs. error	Maximum abs. error
Analytic input traveltimes					
hyperbolic	0 m	$<10^{-6}$ %	$2.2 \cdot 10^{-5}$ %	$<10^{-6}$ ms	$5.96 \cdot 10^{-5}$ ms
hyperbolic	50 m	$<10^{-6}$ %	$3.35 \cdot 10^{-5}$ %	$<10^{-6}$ ms	$8.94 \cdot 10^{-5}$ ms
parabolic	0 m	0.0088 %	4.90 %	0.023 ms	2.00 ms
parabolic	50 m	0.0137 %	8.38 %	0.035 ms	4.44 ms
trilinear	0 m	0.4080 %	36.3 %	0.878 ms	8.54 ms
Vidale input traveltimes					
hyperbolic	0 m	0.0017 %	0.82 %	0.0038 ms	0.446 ms
hyperbolic	50 m	0.0048 %	2.18 %	0.0118 ms	0.952 ms
parabolic	0 m	0.0102 %	4.37 %	0.0257 ms	1.83 ms
parabolic	50 m	0.0150 %	8.39 %	0.0381 ms	4.47 ms
Rel. errors of the Vidale input traveltimes					
		0.0638 %	0.824 %	0.17 ms	0.752 ms

for a trilinear interpolation (without source shift) using the 100m coarse grid traveltimes as input data.

A layer of 100m thickness under the source was excluded from the statistics since the errors near the source are dominated by small traveltimes (see the discussion of relative errors in Section 2.3). The hyperbolic interpolation is superior to the parabolic variant. Both exceed the trilinear interpolation by far. Note that *median* errors are used rather than mean errors. This is due to the stability of the median concerning outliers. Therefore, the median error is a more reliable value compared to the mean error.

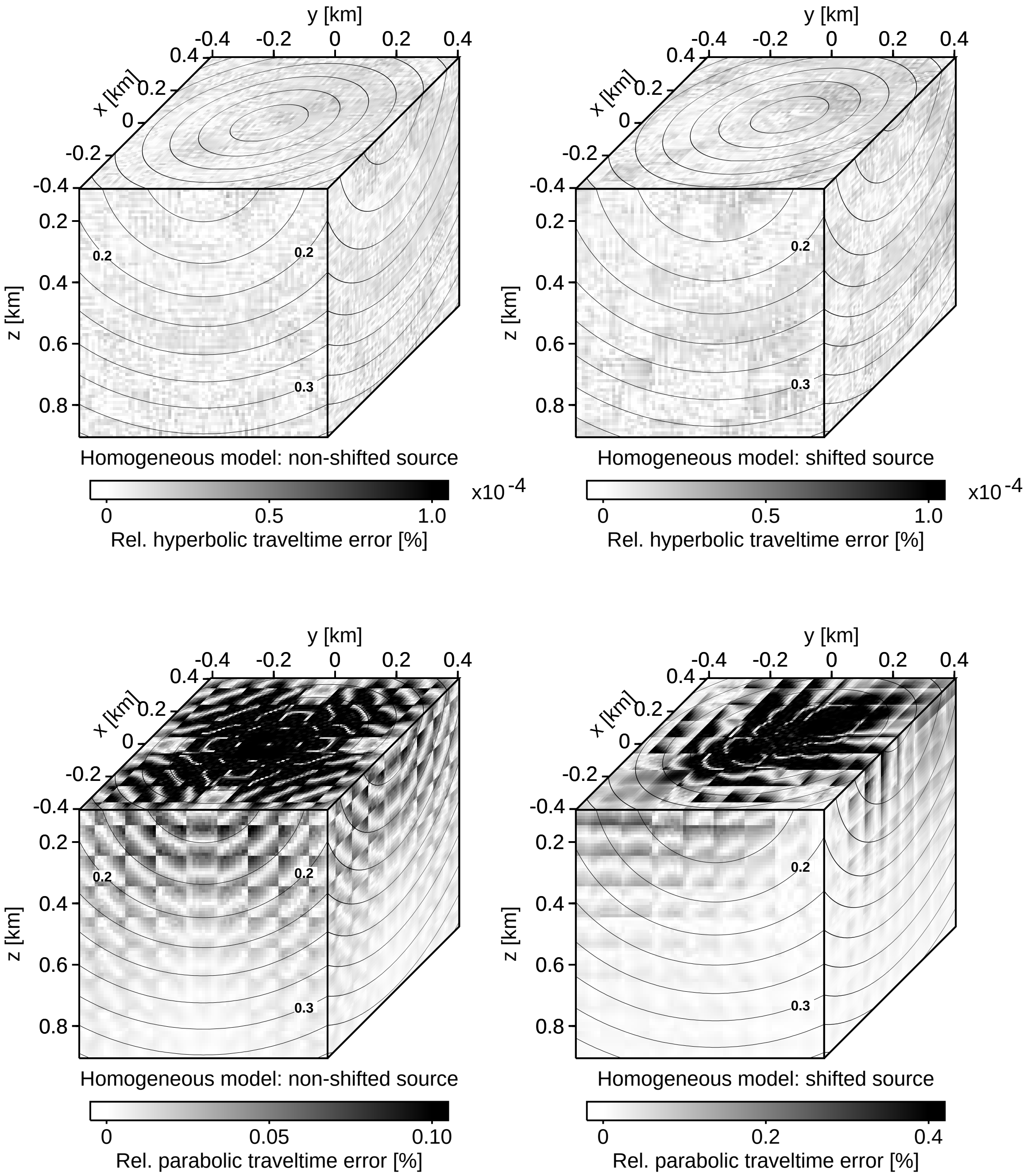

Figure 2.5: Relative traveltime errors for a homogeneous velocity model using analytic input traveltimes. Top: errors using the hyperbolic interpolation if only receivers are interpolated (left) and for both source and receiver interpolation (right). Isochrones are given in seconds. Bottom: the same as above but using the parabolic variant. The relative errors near the source appear exaggerated because there the traveltimes are very small. Note the different error scales.

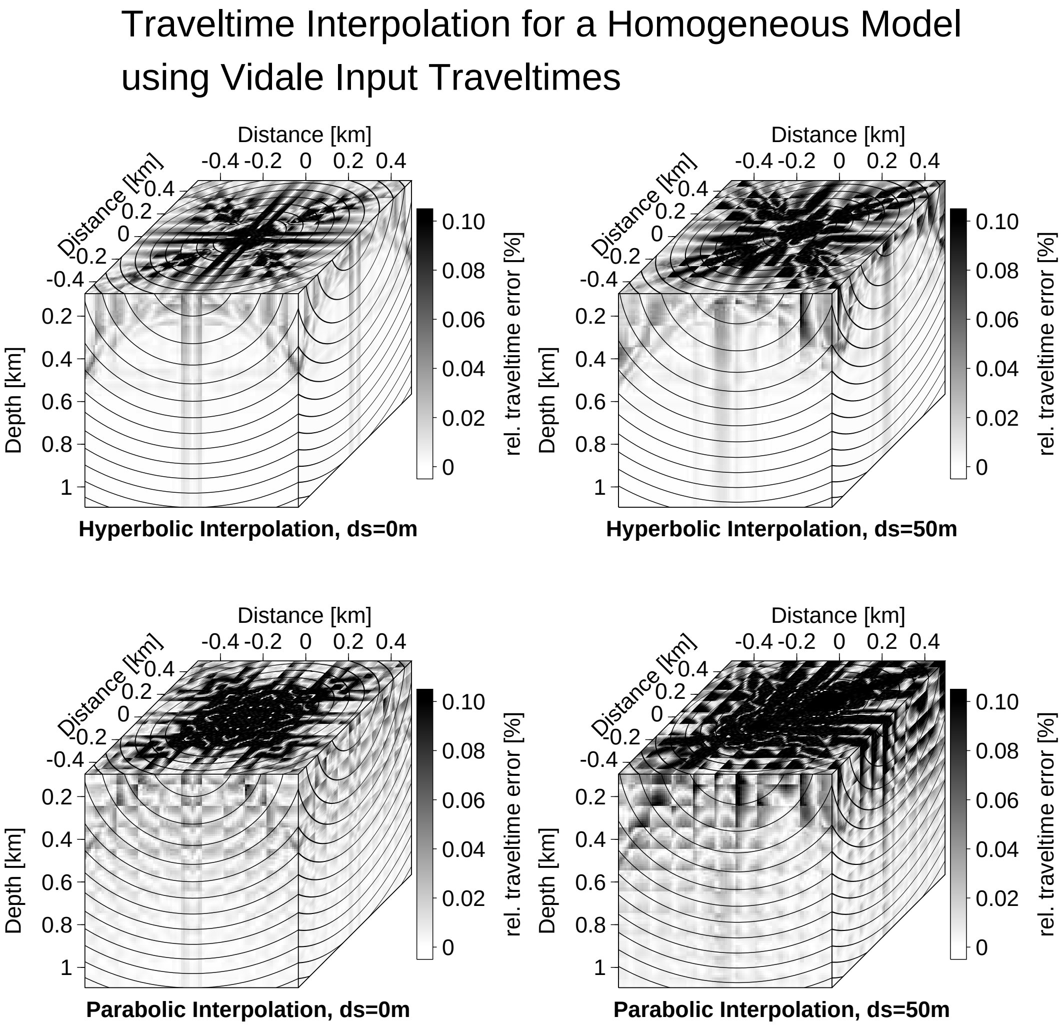

Figure 2.6: Relative traveltime errors for a homogeneous velocity model using Vidale input traveltimes. Top: errors using the hyperbolic interpolation if only receivers are interpolated (left) and for both source and receiver interpolation (right). Isochrones are given in seconds. Bottom: the same as above but using the parabolic variant. The relative errors near the source appear exaggerated because there the traveltimes are very small.

Constant velocity gradient model

The second model is again an example where the analytic solution is known. It consists of 121×121×121 grid points with 10m grid spacing and has a constant velocity gradient of $\partial V/\partial z$=0.5s^{-1}. The velocity at the source is 3000m/s. The source is positioned in the centre of the top surface. As before, a coarse grid of 100m was used for the analytic and Vidale input traveltimes.

The results are shown in Figure 2.7 and Figure 2.8, and in Table 2.4, where a layer of 100m depth under the source was excluded from the statistics. Again the hyperbolic results are more accurate than the parabolic ones and both second order interpolations are far superior to trilinear interpolation. Table 2.5 gives result for a model with the same geometry and gradient as the previous one, but with a velocity of 1500m/s at the source (given for analytic traveltimes only).

For both gradient models, the errors of the hyperbolic variant using analytic input traveltimes are smaller for the shifted source case. This is correct – although it seems counter-intuitive at first sight. The reason is that the errors caused by the change in receiver position have different sign than those caused by the source interpolation. Therefore in this special case the errors from source and receiver interpolation compensate each other.

The difference in quality between hyperbolic and parabolic interpolation for the gradient models is less than for the constant velocity model. This is due to the fact that for a homogeneous medium the hyperbolic approximation is equal to the analytic result (see the proof in Appendix B). The reason for the much higher accuracy of the parabolic and hyperbolic interpolation compared to trilinear interpolation is that the latter neglects the wavefront curvature. Unlike in the previous examples this is not only a problem in the near-source region but anywhere where locally higher wavefront curvatures occur. It is especially very common for more complex velocity models.

Table 2.4: Errors for the constant velocity gradient model (V_s=3000m/s) with 100m coarse grid spacing excluding a layer of 100m depth under the source.

Interpolation	Source shift $\Delta s_x = \Delta s_y$	Median of rel. error	Maximum rel. error	Median of abs. error	Maximum abs. error
Analytic input traveltimes					
hyperbolic	0 m	0.002 %	0.137 %	0.004 ms	0.064 ms
hyperbolic	50 m	0.001 %	0.320 %	0.002 ms	0.148 ms
parabolic	0 m	0.009 %	4.9 %	0.021 ms	1.99 ms
parabolic	50 m	0.015 %	8.38 %	0.036 ms	4.47 ms
trilinear	0 m	0.282 %	14.5 %	0.677 ms	5.52 ms
Vidale input traveltimes					
hyperbolic	0 m	0.003 %	0.822 %	0.0065 ms	0.479 ms
hyperbolic	50 m	0.005 %	2.1 %	0.0110 ms	0.905 ms
parabolic	0 m	0.010 %	4.36 %	0.0248 ms	1.83 ms
parabolic	50 m	0.016 %	8.4 %	0.0375 ms	4.50 ms
Rel. errors of the Vidale input traveltimes					
		0.0719 %	0.829 %	0.181 ms	0.745 ms

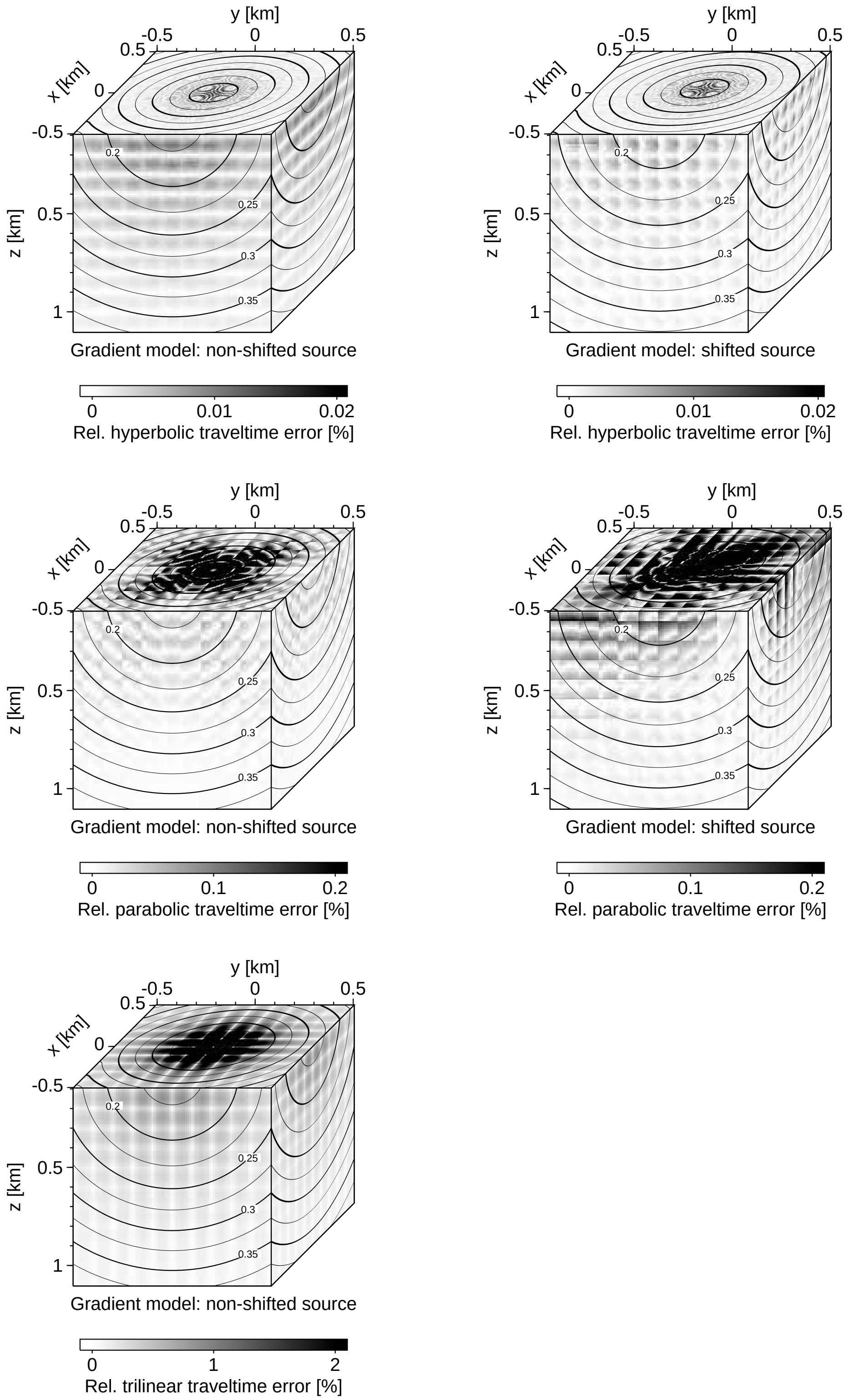

Figure 2.7: Relative traveltime errors for a constant velocity gradient model using analytic input traveltimes. Top: errors using the hyperbolic interpolation for the original source position (left) and for a shifted source (right). Middle: the same as above using parabolic interpolation. Bottom: as before but with trilinear interpolation. Note the different error scales on the plots.

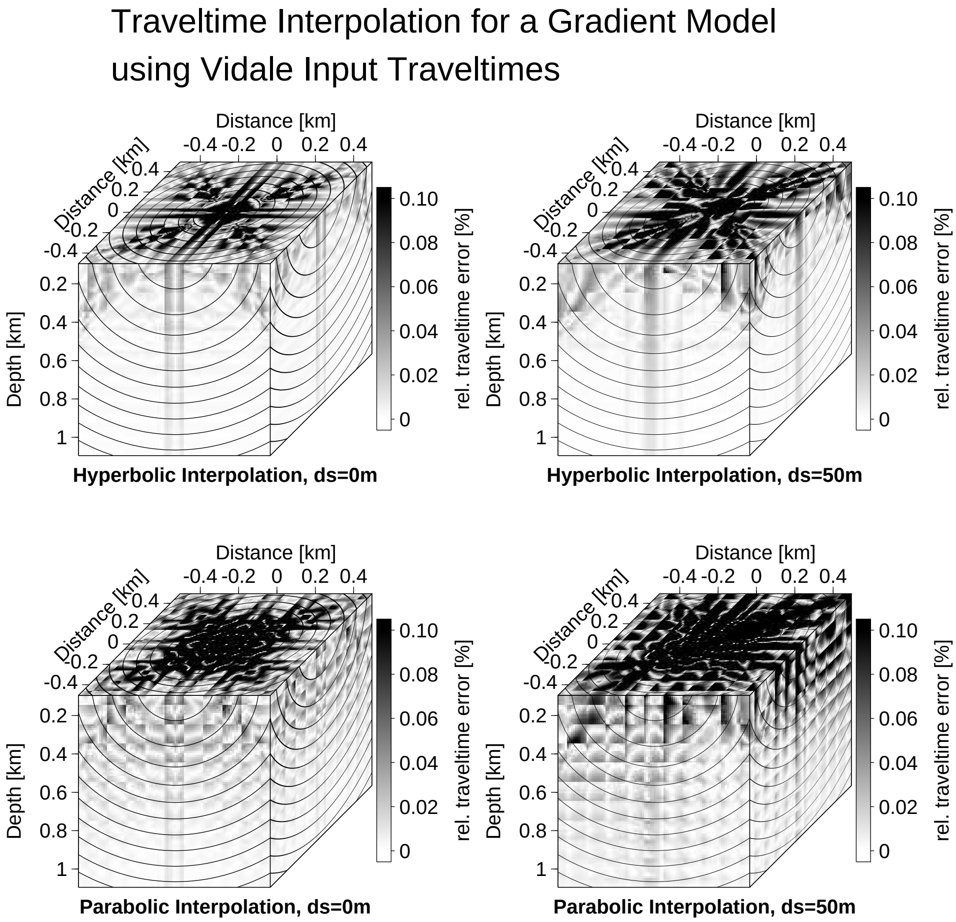

Figure 2.8: Relative traveltime errors for a constant velocity gradient model using Vidale input traveltimes. Top: errors using the hyperbolic interpolation for the original source position (left) and for a shifted source (right). Bottom: the same as above using parabolic interpolation.

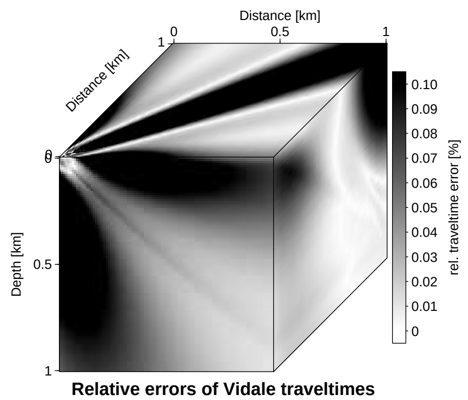

Figure 2.9: Relative errors of traveltimes computed with the Vidale algorithm for the gradient model.

Table 2.5: Errors for the constant velocity gradient model (V_s=1500m/s) with 100m coarse grid spacing excluding a layer of 100m depth under the source.

Interpolation	Source shift $\Delta s_x = \Delta s_y$	Median of rel. error	Maximum rel. error	Median of abs. error	Maximum abs. error
hyperbolic	0 m	0.003 %	0.263 %	0.012 ms	0.240 ms
hyperbolic	50 m	0.002 %	0.616 %	0.008 ms	0.566 ms
parabolic	0 m	0.009 %	4.91 %	0.042 ms	3.94 ms
parabolic	50 m	0.015 %	8.39 %	0.071 ms	9.0 ms

Marmousi model

As an example for a complex velocity model I have employed a 3-D extension of the Marmousi model (Versteeg and Grau, 1991), shown in Figure 2.10. The model was 100-fold smoothed using a three point operator with a central weight of 0.5 (cf., e.g., Ettrich and Gajewski 1996). This corresponds to removing all wavelengths below 667m from the model. Smoothing of velocities is required if traveltime generators based on the ray method are used. Traveltimes were computed with a 3-D-FD eikonal solver using the Vidale (1990) algorithm on a 12.5m fine grid. These were used as reference data as well as for the input traveltime tables which were obtained from the fine grid data by resampling them onto a 125m coarse grid. The resulting interpolated traveltimes were compared to the reference data on the fine grid. The relative traveltime errors for the hyperbolic interpolation (no source shift) are shown in Figure 2.11. Figure 2.12 shows the absolute traveltime errors using the hyperbolic interpolation (again, the source was not shifted). Table 2.6 summarises the errors. A layer of 62.5m depth under the source was excluded from the statistics.

In this example there are high maximum errors. These are no measure for the accuracy of the interpolation scheme because they only occur in the vicinity of discontinuities in the isochrones. These indicate triplications of the wavefronts. The resulting errors are no surprise, since the assumption of smooth traveltimes is not valid anymore: a triplication consists of wavefronts belonging to two different branches. These must be interpolated separately. The obvious solution to overcome this problem is to employ later arrivals in the input traveltime scheme and to apply the interpolation to first and later arrivals separately. If traveltimes are computed, e.g., by the method of Coman and Gajewski (2001), which outputs traveltime tables sorted for different arrivals, the identification and interpolation of separate branches is only a matter of implementation. On the other hand, the method presented here itself provides means to detect and account for triplications. This will be addressed below in Section 2.7.

Compared to the generic models, both interpolations for the Marmousi model yield similar quality. One reason is that for this model errors due to the different algorithms are dominated by errors caused by the quality of the input data, i.e. insufficient accuracy and particularly smoothness of the input traveltimes (see Figure 2.11). The fact that all wavelengths below 667m were removed from the velocity model does not mean that a coarse grid spacing for the input traveltimes of 667m will be sufficient. The required grid spacing for the traveltime interpolation depends on the wavenumbers in the input traveltimes, not the velocity model. Smoothing of the velocities is required for traveltime generators based on the ray method. This aspect will also be addressed in Section 10.1.

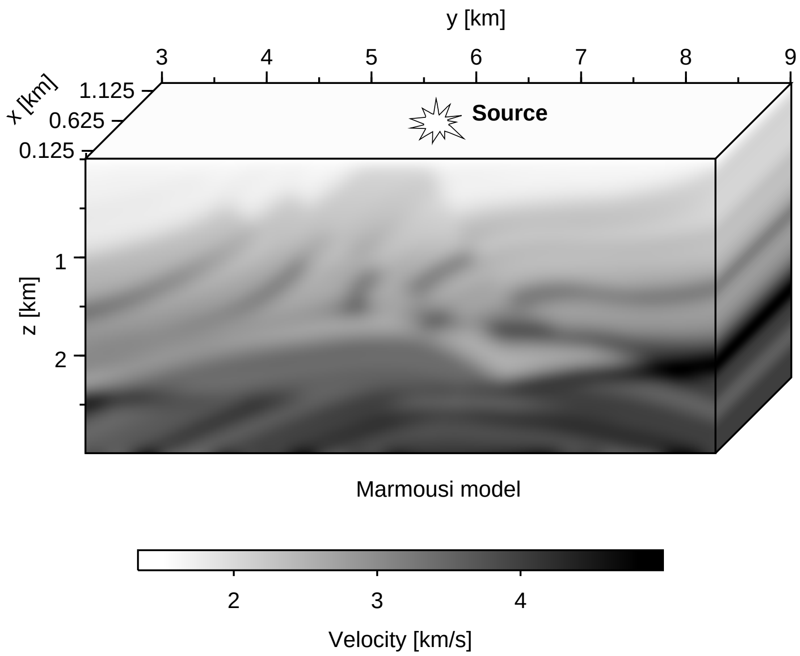

Figure 2.10: Marmousi model extended to three dimensions. The model was 100-fold smoothed. Only a part of the original model was used. The grid spacing is 12.5m in either direction. The source is placed on top of the model at 625m in x- and 6km in y-direction.

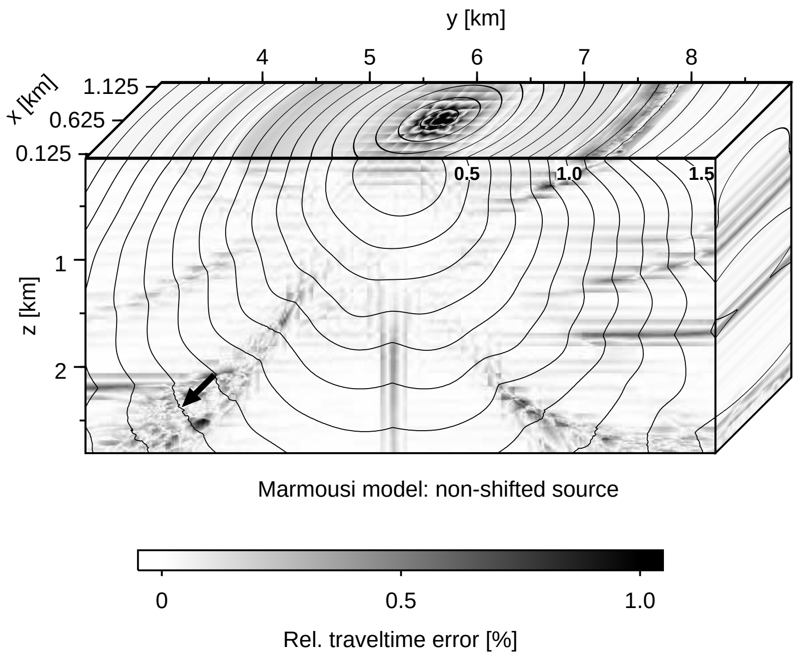

Figure 2.11: Relative traveltime errors for the Marmousi model using hyperbolic interpolation. Isochrones are given in seconds. The correlation of errors and discontinuities in the isochrones is clearly visible. The arrow at the 1.2s isochrone in the lower left region indicates a higher error area that is caused by bad quality of the input traveltimes (due to a deficiency of the FD implementation used). This can be compensated by smoothing the input traveltimes.

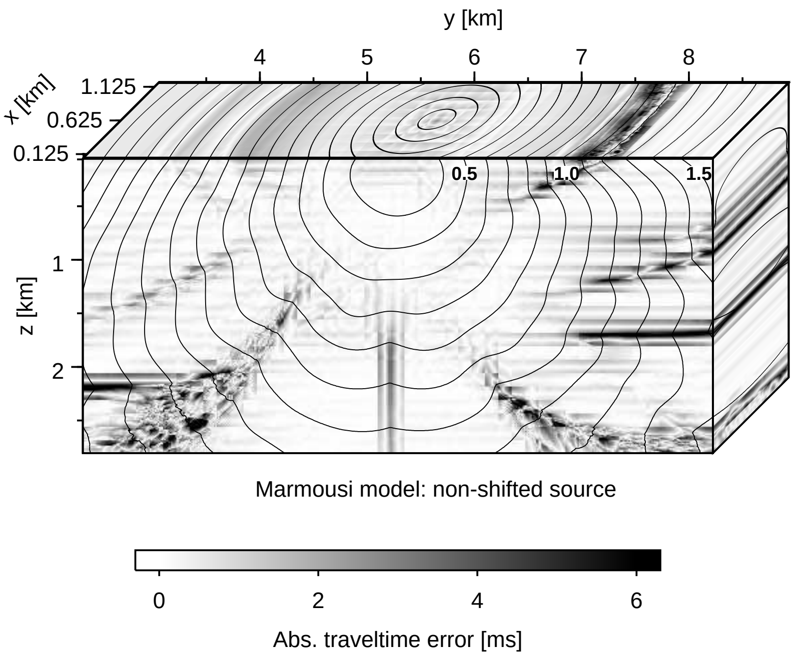

Figure 2.12: Absolute errors for the hyperbolic interpolation on the Marmousi model. Apart from regions in the vicinity of discontinuities in the wavefronts and areas with corrupted reference traveltimes (see Figure 2.11) the errors are well below a millisecond.

Table 2.6: Errors for the Marmousi model with 125m coarse grid spacing excluding a layer of 62.5m depth under the source. Maximum errors are associated with triplications of the wavefront and therefore do not represent the method's accuracy.

Interpolation	Source shift $\Delta s_x = \Delta s_y$	Median of rel. error	Maximum rel. error	Median of abs. error	Maximum abs. error
hyperbolic	0 m	0.025 %	7.04 %	0.214 ms	14.3 ms
hyperbolic	50 m	0.033 %	45.1 %	0.279 ms	301 ms
parabolic	0 m	0.026 %	21.3 %	0.223 ms	14.3 ms
parabolic	50 m	0.035 %	62.4 %	0.299 ms	308 ms
trilinear	0 m	0.087 %	32.6 %	0.833 ms	18.6 ms

2.5 Anisotropic examples

Since no assumptions on the model were made for the derivation of Equation (2.2.2) it is equally valid in isotropic as in anisotropic media, and it is expected to yield results of the same order of accuracy for anisotropic media as for isotropic media. Nevertheless, I will demonstrate the accuracy with examples also for the anisotropic case.

There is, however, one difference compared to the isotropic situation, where the derivatives with respect to the third (z) component of the source coordinates can be determined directly from the eikonal equation, as shown above. If the source position lies in an anisotropic medium, this is not possible, and expressions of the type (2.1.5) or (2.2.3) must be used.

I will demonstrate the method with three examples for the traveltime interpolation. The first example is a homogeneous model with elliptical symmetry with the density normalised elastic coefficients A_{11}=A_{22}=15.96 km^2/s^2 and A_{33}=11.4 km^2/s^2. P-wave traveltimes were computed on a 10 m fine grid using the FDES perturbation implementation of Soukina et al. (2003) and resampled to a 100 m coarse storage grid. These coarsely-gridded traveltimes were the input data for the interpolation using Equation (2.2.2) to a 10 m fine grid. The results were compared to the original fine grid traveltime tables to determine the accuracy of the interpolation. Interpolation was carried out twice, (1) only for receivers while maintaining the original source position, and (2) for the receivers and additionally the source position was changed by 50 m in x and y.

The median of the relative errors for the interpolation of receivers alone is 0.002 % (corresponding to 0.004 ms) and the maximum absolute error is 0.7 ms. For the interpolation of source and receiver positions the median of the relative errors is 0.014 % (0.025 ms), the maximum absolute error is 2.1 ms. Figure 2.13 shows the error distribution for both cases. The highest errors occur in the near source vicinity. However, the source region is of lower interest for migration purposes and even there the absolute errors are small. The errors following the x=0, y=0, x=y, and z=0.5 km lines are caused by errors in the input traveltimes which are inherent to the FD algorithm used.

In order to demonstrate the influence of the FD traveltime errors, Figure 2.14 shows another homogeneous example with elliptical symmetry, but using analytical traveltimes as input. For this type of medium, analytical traveltimes are available (see Appendix C). As for the isotropic homogeneous case, the hyperbolic interpolation corresponds to the exact solution. The resulting errors are small, as expected: for both source positions, the median of the relative errors is below 7$\times$10^{-6} %. The maximum error is smaller than 10^{-4} % except in the vicinity of the source, where the division by τ_0=0 during the determination of the coefficients leads to a wrong result. This region is, however, not of interest for practical applications.

The second example is a homogeneous Vosges sandstone with triclinic symmetry. The original elasticity tensor given by Mensch and Rasolofosaon (1997) was density normalised, leading to (values are given in km^2/s^2):

$$\underline{\mathsf{A}} = \begin{pmatrix} 6.77 & 0.62 & 1.00 & -0.48 & 0.00 & -0.24 \\ & 4.95 & 0.43 & 0.38 & 0.67 & 0.52 \\ & & 5.09 & -0.28 & 0.09 & -0.09 \\ & & & 2.35 & 0.09 & 0.00 \\ & & & & 2.45 & 0.00 \\ & & & & & 2.88 \end{pmatrix} .$$

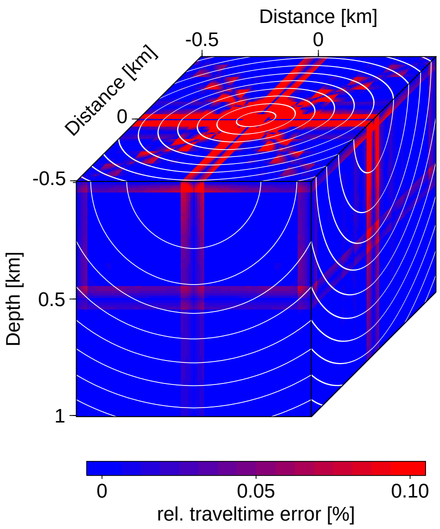

Figure 2.13: Relative traveltime errors and isochrones for a homogeneous model with elliptical symmetry using FD input traveltimes. Left: errors resulting from the hyperbolic interpolation if only receivers are interpolated. On the right the source position is changed by 50m in x and y. The relative errors near the source appear exaggerated because here the traveltimes are very small.

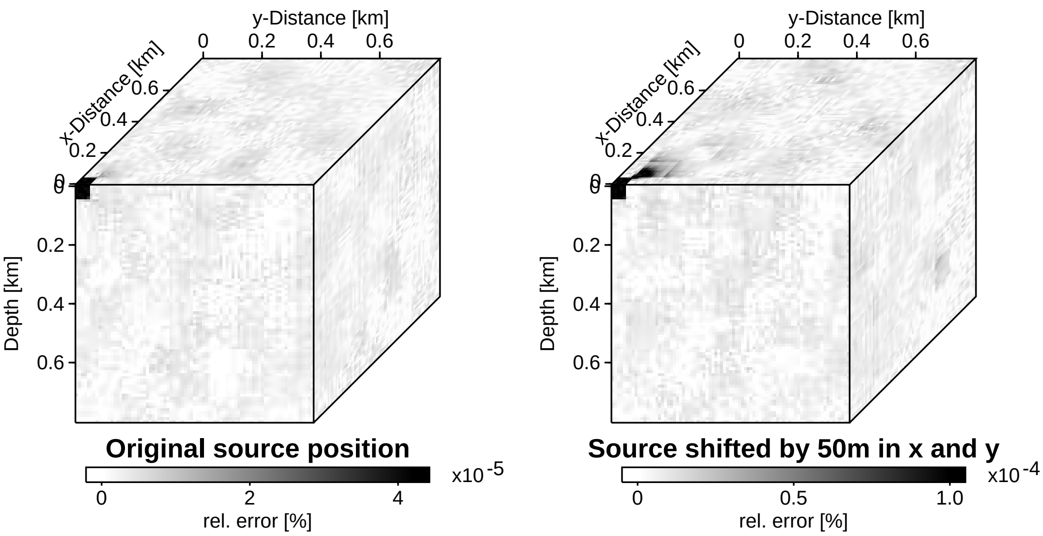

Figure 2.14: Traveltime errors for a homogeneous velocity model with elliptical anisotropy, where analytical input traveltimes were used. Left: traveltimes were interpolated from a 100m coarse grid onto a 10m fine grid without a change of the source position. Right: as before, but additionally, the source was shifted 50m in x- and y-direction. The errors are within machine precision apart from the near source vicinity. In this region, the hyperbolic coefficients are wrong, because of the division by τ_0, which is zero at the source.

Traveltimes were generated and interpolated in the same manner as for the first example. The results are given in Figure 2.15. The median of the relative errors for the interpolation of receivers only is 0.01 % (corresponding to 0.04 ms) with a maximum absolute error of 2.7 ms near the source. If the source position is also interpolated, the median of the relative error rises to 0.04 % (0.1 ms) with a maximum absolute error of 6 ms, again near the source.

My third model is a factorised medium consisting of a velocity lens. It is embedded in a background medium with triclinic symmetry that corresponds the Vosges sandstone already introduced for the homogeneous second example. The same codes and geometries as for the previous examples were applied for the generation of input and reference traveltime tables. The resulting traveltime errors from the interpolation are displayed in Figure 2.16.
The median of the relative error for the interpolation to receivers only is 0.015 %, corresponding to 0.044 ms. If the position of the source is also interpolated, the median of the relative error becomes 0.041 % (0.119 ms). Owing to numerical artifacts in the reference traveltime tables (e.g. grid-points with zero traveltime), I do not give maximum errors here since these would not correctly reflect the accuracy of the method. Also, I have chosen the median instead of the average error because it is more stable concerning these outliers. As I show in the next figure, Figure 2.17, the higher errors in some regions are not due to the method itself.

Figure 2.17 displays the traveltime errors for both experiments in a section through the centre of the model. It illustrates that high errors occur only in the vicinity of discontinuities in the isochrones. In these regions, the assumption of continuous first- and second-order derivatives (the condition for a Taylor expansion) is not fulfilled. The discontinuities are manifestations of triplications of the wavefront. If later-arrival traveltimes are available, it is possible to interpolate the left and right branches of the traveltime curve individually, as will be shown further below in Section 2.7. Then the errors in these regions reduce to the same magnitude as in the rest of the model. Since a finite-difference scheme was used for the generation of the input traveltimes, later arrivals were not available. Apart from these regions high accuracy is achieved.

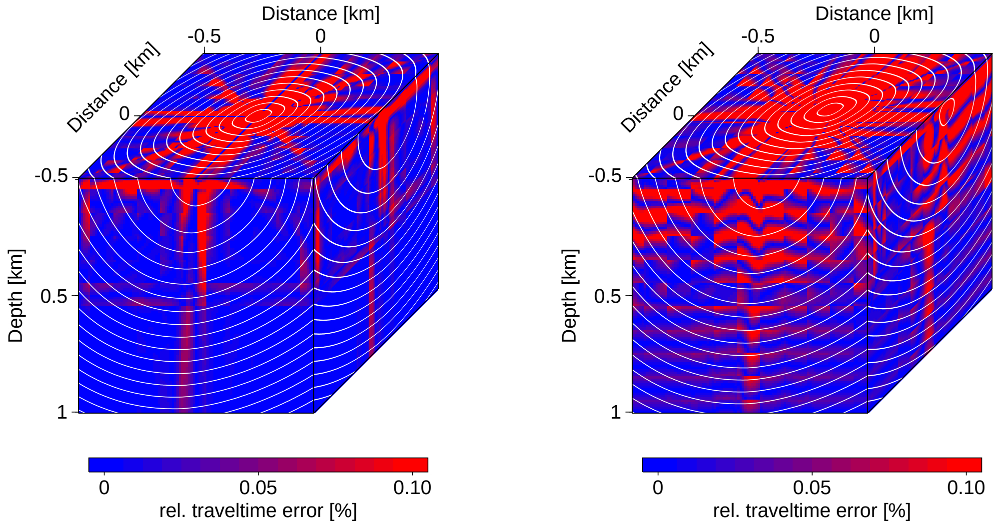

Figure 2.15: Relative traveltime errors and isochrones for a homogeneous triclinic model. Left: errors resulting from the hyperbolic interpolation if only receivers are interpolated. On the right the source position is changed by 50m in x and y. The relative errors near the source appear exaggerated because here the traveltimes are very small.

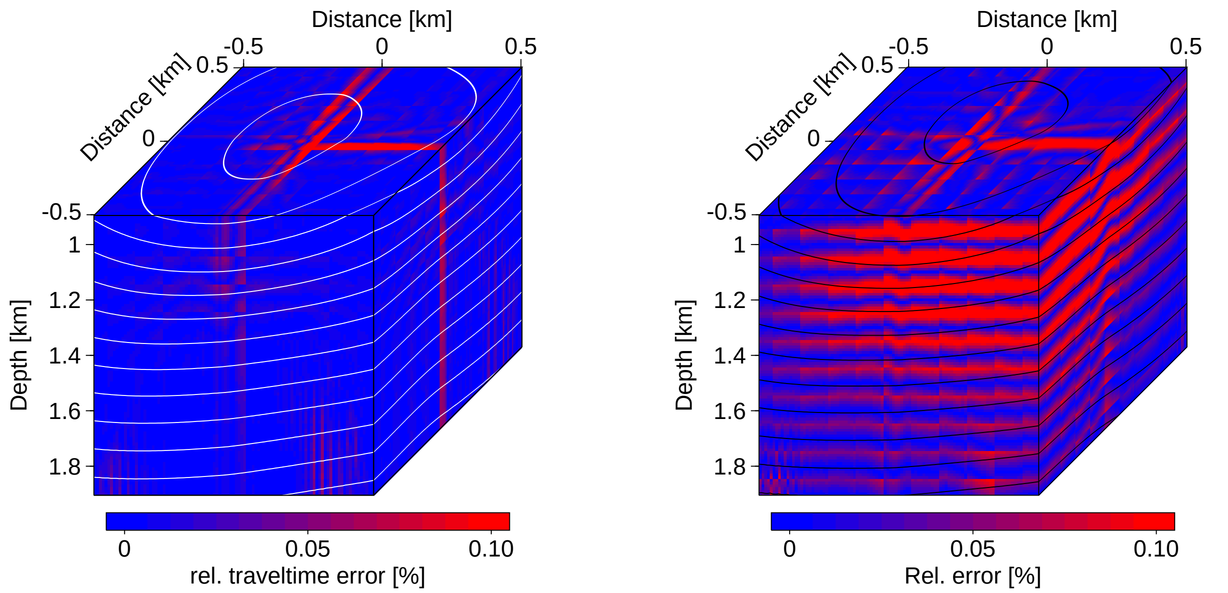

Figure 2.16: Traveltime errors from the hyperbolic interpolation for the velocity lens model. Values are given in milliseconds. Left: traveltime errors for the original source position at (0 m, 0 m, 0m). Right: traveltime errors for an interpolated source at (50 m, 50 m, 0m). Isochrones illustrate the un-interpolated wavefronts. The cross-shaped error distribution centred at the distances of 0 km is caused by errors in the finely-gridded reference traveltimes due to the Vidale scheme. The pattern near the edges of both cubes at higher depths are caused by ripples in the reference traveltimes.

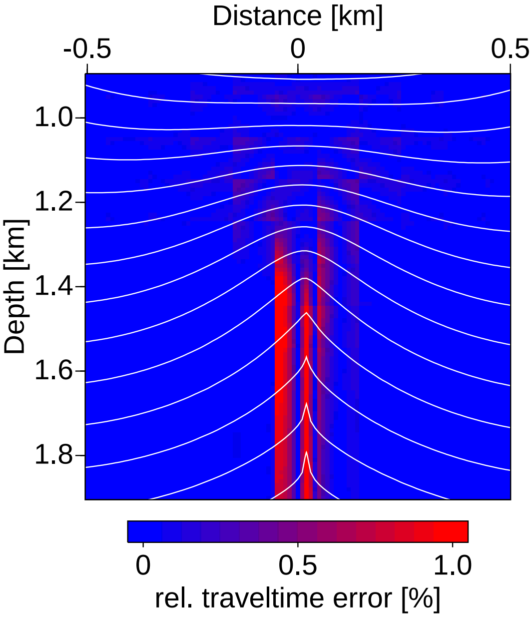

Figure 2.17: Traveltime errors from hyperbolic interpolation for a section through the lens model, on the left for the original source position, on the right the source position was also interpolated. The sections were extracted at the distance $x = 0$ km. The isochrones indicate the positions of triplications of the wavefront, leading to errors in the traveltime interpolation if only first-arrival traveltimes are considered. The shape of the triplicated wavefront at higher depths is caused by artifacts in the reference traveltimes.

2.6 Influence of the grid spacing

The constant velocity gradient model with V_s=3000m/s (see above) was further used to investigate the influence of the coarse grid spacing on the accuracy. Traveltime interpolation was carried out for coarse grid spacings ranging from 20 to 100m using hyperbolic, parabolic, and trilinear interpolation. The fine grid spacing remained fixed at 10m. The resulting errors are displayed in Figure 2.18. I found the same quality relation between the three interpolation schemes as before and, as expected, the accuracy increasing for smaller coarse to fine grid ratio.

It must, however, be taken into account that the finer the coarse grid is made, the smaller the move-out becomes. This means that for very small grids the difference in traveltimes may be contaminated by round-off errors and the accuracy of the coefficients may degrade. This problem may also occur for very large distances to the source or any other situation where small move-out occurs.

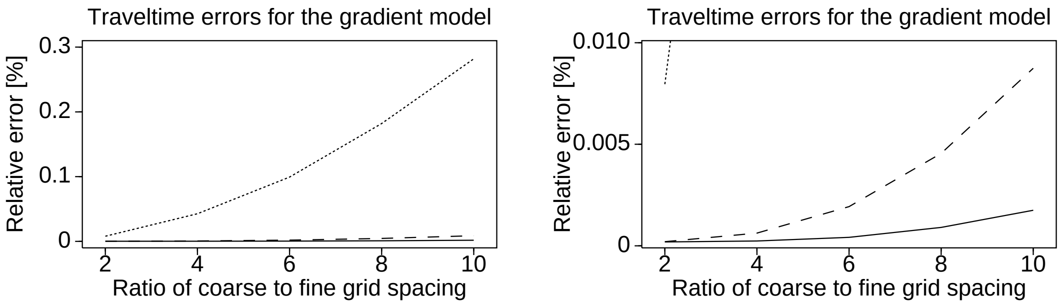

Figure 2.18: Relative traveltime errors vs. ratio of fine to coarse grid spacing for a constant velocity gradient model shown for trilinear (dotted line) parabolic (dashed line) and hyperbolic interpolation (solid line). The plot is displayed twice using different scales to illustrate the differences between trilinear and second-order interpolations (left), and between parabolic and hyperbolic interpolation (right).

2.7 Triplications and later arrivals

For the derivation of the traveltime expansions (2.1.4) and (2.2.2), I have assumed that the traveltime fields under consideration are smooth with continuous first and second order derivatives. This is not always the case. In this section a method is proposed to detect regions where discontinuities arise. This is not only necessary to correct the errors resulting from traveltime interpolation, but also because these discontinuities are associated with later arrivals, which need to be considered in migration (Geoltrain and Brac, 1993), particularly for the amplitude-preserving type, since a lot of energy is carried by events with later arrival-traveltime (Operto et al., 2000).

In this section, I will discuss a means of locating a wavefront triplication and suggest two different ways to correct for its effect on the traveltime interpolation, depending on the availability of traveltime tables for first arrivals only, or the existence of multi-valued traveltime tables. After describing the two techniques, I will demonstrate both with an example.

Method

Let us assume that traveltimes are given on coarse grids, as depicted in Figure 2.19. We can determine the coefficients in (2.2.2) from these coarsely-gridded traveltimes as shown above, provided that the traveltimes are a smooth function. Subsequent interpolation onto finer grids usually leads to high accuracy, because the curvature of the wavefront is acknowledged. However, there are cases where the interpolation fails, namely in the vicinity of first-order discontinuities of the wavefronts: Figure 2.20 displays errors of the hyperbolic interpolation for first- and second-arrival traveltimes in a model with a low-velocity lens. This leads to a pronounced triplication of the wavefronts. If only first-arrival traveltimes are considered, the triplication shows as a cusp in the wavefront that represents the discontinuity (see Figures 2.20, left, and 2.21). Figure 2.20 shows that regions with higher errors follow the positions of the cusps. The reason is that the Taylor expansion that leads to Equation (2.2.2) requires continuity of the first- and second-order derivatives of the traveltimes. This criterion is not fulfilled in regions with cusps in the wavefronts as these are associated with cusps in the traveltime functions, and thus discontinuities in the traveltime gradients. Therefore application of Eq. (2.2.2) leads to errors in these regions, at which we will now take a closer look.

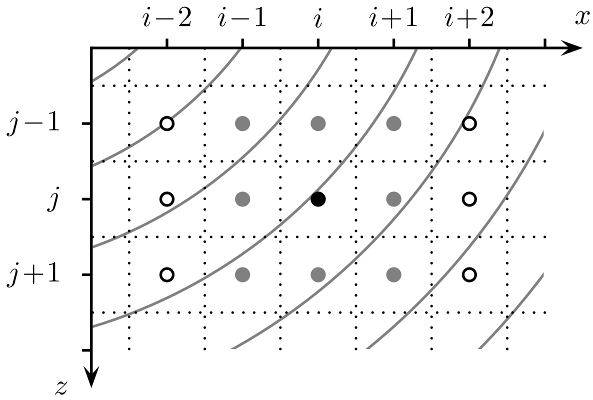

Figure 2.19: Traveltime grid in the x-z-plane: gray lines denote isochrones; the black circle is the point of expansion. The surrounding gray circles designate coarse grid points with traveltimes required to determine the coefficients in the expansion point. Dotted lines indicate the regions in which traveltimes are interpolated around each coarse grid point.

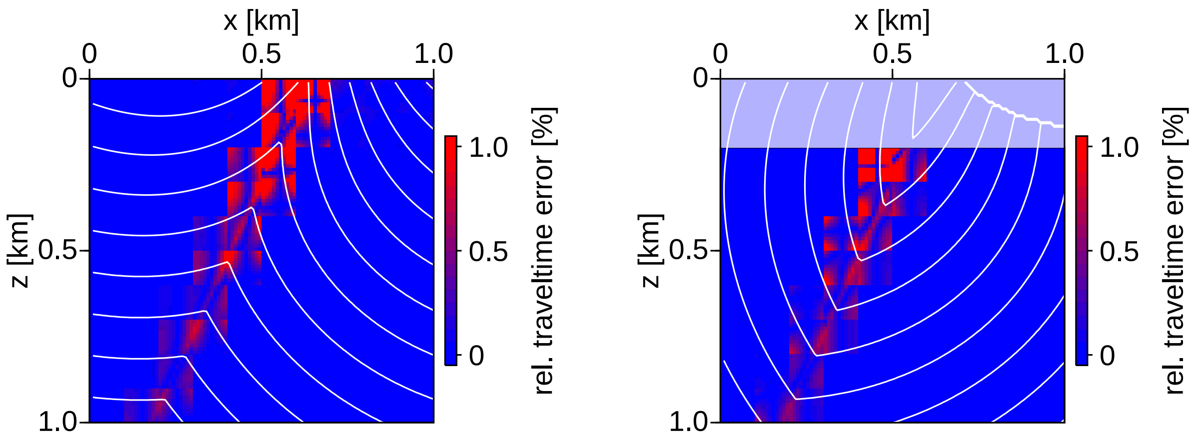

Figure 2.20: Interpolation of first (left) and second arrival (right) traveltimes for a model with a low velocity lens. Relative errors are given in percent. Regions with higher errors are associated with cusps in the wavefronts, illustrated by the isochrones.

Figure 2.21 shows a triplicated traveltime curve with first, second, and third arrivals. A cusp is formed at the point P if only the first arrivals are considered, as they belong to different branches (denoted by 1 and 2, see Figure 2.21) of the traveltime curve. The point P is the intersection point of the two branches. The positions of the cusps in the first-arrival traveltimes coincide with those in the isochrones in Figure 2.20. Likewise, the second arrivals also form a cusp, if considered separately. For the third arrivals, that type of discontinuity does not occur, i.e., in contrast to the first and second arrivals, no special treatment is required.

In Figure 2.21, the grid point denoted by the index i is close to the point P. Therefore, the coefficients q_x and G_{xx}, determined from the first-arrival traveltimes at the grid points $i \pm 1$ will be wrong if (2.2.3) is used, because these traveltimes belong to different branches. Consequently, the traveltime interpolation will fail in the vicinity of the grid point at i: the dotted line in Figure 2.21, that represents the interpolated traveltimes, does not match the real traveltime curve.

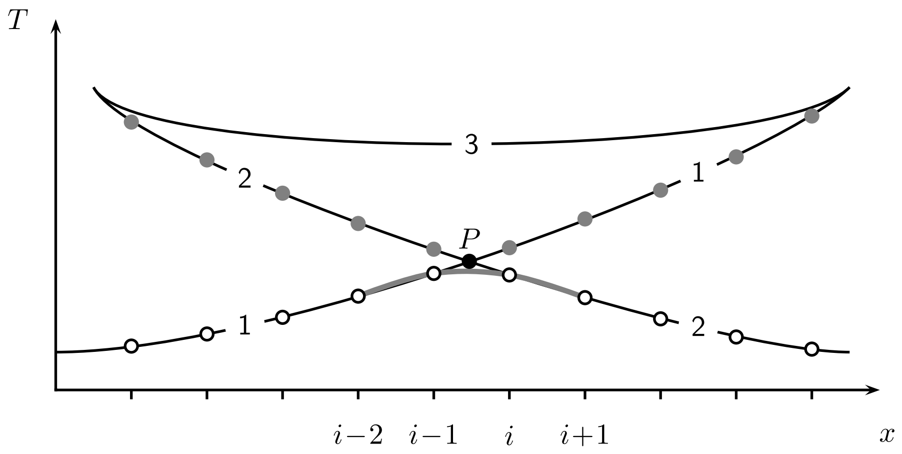

Figure 2.21: Triplication of a traveltime curve. The traveltime curve consists of three branches. The white circles indicate first-arrival traveltimes on the coarse grid, whereas the gray circles correspond to second arrivals. The black circle at P denotes the intersection point of the branches 1 and 2. The gray line describes the hyperbolic interpolation if only first arrivals are considered, leading to a mis-fit around the grid points at i and $i-1$. Please note that, whereas the traveltime branches 1 and 2 show convex behaviour, the hyperbolic curve is concave.

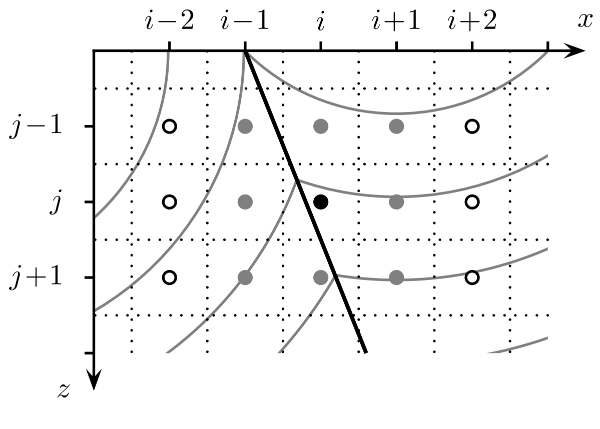

Figure 2.22: First-arrival wavefronts in the x-z-plane: gray lines denote isochrones; the black circle is the point of expansion. The surrounding gray circles designate coarse grid points with traveltimes required to determine the coefficients in the expansion point. The black line marks the cusp made by the intersection between the two traveltime branches (corresponding to the point P in Figure 2.21). Dotted lines indicate the regions in which traveltimes are interpolated around each coarse grid point.

Figure 2.22 depicts the same situation in the x-z-plane. The isochrones, i.e. wavefronts, corresponding to the first-arrival traveltimes are indicated by gray lines. Circles mark the coarse grid points at which traveltimes are given. The black circle at (i, j) denotes the expansion point. Grid points with traveltimes required for the determination of the coefficients in that expansion point are marked gray. The black line corresponds to the position of the cusps. Since the traveltimes at the gray points, which surround the expansion point, do not all belong to the same branch, all coefficients obtained from combining these traveltimes are wrong. Also, the coefficients for an expansion point at $(i-1, j)$ are wrong, for the same reason. Hence the interpolation fails in the region surrounding these two expansion points. The regions covered by the interpolation around each expansion point is indicated by the dotted lines in Figure 2.22. The expected width (in x-direction) of the region with incorrectly interpolated traveltimes is therefore twice the coarse grid spacing, following from the squares around the points (i, j) and $(i-1, j)$. This is confirmed by the error distribution in Figure 2.20.

The strategy to solve the problem caused by the cusps is the separate treatment of the two traveltime branches 1 and 2. Thus the first step is the identification of the individual branches. To do so, we have to determine the location P of the cusp. From the position P we can then deduce at which grid points the traveltime coefficients are affected by the cusp. The next step depends on the availability of later-arrival traveltime tables. If only first arrivals are given, traveltimes for both branches can be extrapolated until P, using the coefficients from the nearest unaffected grid point, from both sides of the cusp. If later arrivals are available, the coefficients in the affected region can be correctly obtained from appropriate combination of first- and second-arrival traveltimes. We will explain both approaches in detail now.

A region with a cusp can be detected by evaluating the traveltime curve. Figure 2.21 demonstrates that, whereas the traveltime curves of the branches 1 and 2 are convex, the traveltime curve following from the hyperbolic interpolation shows concave behaviour in the vicinity of a cusp. Mathematically, this corresponds to a negative value of the coefficient G_{xx}, if the wavefront propagates mainly in the vertical direction, as in Figures 2.21 and 2.22. In the case of mainly horizontal wave propagation G_{zz} is investigated accordingly.

To ensure the reliability of the detection, we choose only these points whose G_{xx} values are significantly more negative than those of the surrounding points. If only the sign would be evaluated, we might unintentionally select also grid points on nearly plane wavefronts, where $G_{xx} \approx 0$ may take slightly negative values due to round-off errors. Also, concave wavefronts may occur, where no cusp exists. In this case, however, the G_{xx} value of a single grid point will not be significantly more negative than those of the surrounding points. To determine whether a grid point with negative G_{xx} has a significantly negative value of G_{xx}, we compute the quartiles Q_k of G_{xx} from 14 points, in a rectangle of 5 points width and 3 points height, centred around the grid point under consideration. For a set of 14 values, the quartile Q_1 is the fourth smallest value, and Q_3 is the fourth greatest value. The median Q_2 here is the average of the two middle values. If

$$G_{xx} + \kappa\,(Q_3 - Q_1) < Q_2 \tag{2.7.1}$$

is fulfilled, then most likely a cusp is present. We have investigated a large variety of velocity models ranging from simpler models consisting of layers with different vertical velocity gradients or low velocity lenses to highly complex media like the Marmousi model (Versteeg and Grau, 1991). From these models we have concluded that a value of κ=0.74 can provide a reliable detection, as shown in Figure 2.24 for the Marmousi model. This value corresponds to one standard deviation in a Gaussian distribution. Smaller values of κ can lead to selecting grid points on nearly plane wavefronts, as mentioned above, whereas too large values of κ make the algorithm too insensitive. Although we have found that for the variety of models mentioned above κ=0.74 is a reliable criterion, this value may not lead to a detection in certain situations. For

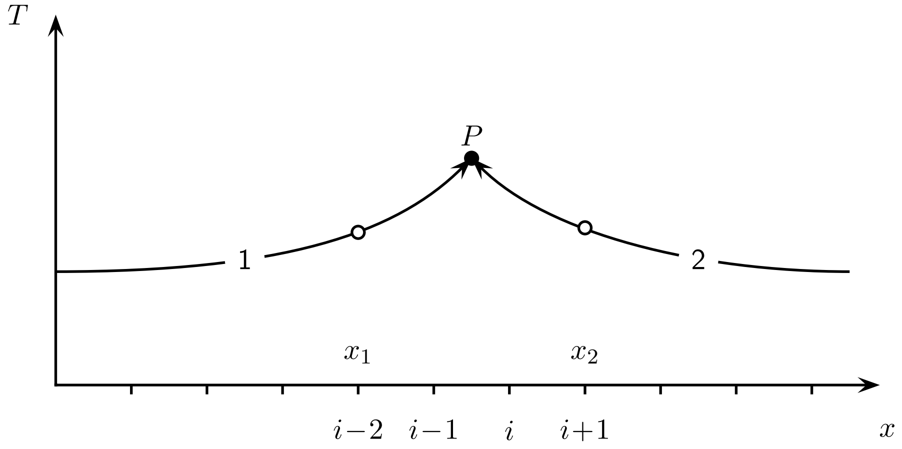

Figure 2.23: Determining the location of P: Traveltimes are extrapolated from the unaffected grid points (white circles) at $i-2$ and $i+1$. The intersection point of the two extrapolated traveltime curves is marked P.

example, κ=0.74 fails at the intersection of two locally plane waves in a locally homogeneous medium.

If traveltime tables for later arrivals are available, the detection can be improved by additionally requiring that a second arrival exists at the grid point under consideration.

The detection algorithm will select those two coarse grid points that frame the cusp. For example, in Figures 2.21 and 2.22 the points at $(i-1,j)$ and (i,j) will be detected. With this information, we can now determine the location of P. As the cusp lies between the points at $(i-1,j)$ and (i,j), the coefficients at $(i-2,j)$ and $(i+1,j)$ are not affected. Denoting $x(i-2,j)$ by x_1 (for branch 1) and $x(i+1,j)$ by x_2 (for branch 2), the coefficients at $(i-2,j)$ by q_{x_1} and G_{xx_1}, and those at $(i+1,j)$ by q_{x_2} and G_{xx_2}, we can extrapolate the traveltimes from x_1 and x_2 until P, as shown in Figure 2.23, by

$$\begin{aligned} T_P^2 &= (T_1 + q_{x_1}(P-x_1))^2 \ + G_{xx_1}(P-x_1)^2 \\ &= (T_2 + q_{x_2}(P-x_2))^2 \ + G_{xx_2}(P-x_2)^2 \quad . \end{aligned} \tag{2.7.2}$$

This system of equations is then solved for P.

Only first-arrival traveltimes are required to determine the location of P. If later-arrival traveltimes are not available, the correct first-arrival traveltimes in the region surrounding P can be obtained from extrapolation until P, using the coefficient sets from the grid points at $(i-2,j)$ and $(i+1,j)$, respectively. To obtain the position of the cusp on the fine grid for the interpolation, we assume a straight line between the position P at the depth index j and the values for P at $j\pm1$, respectively. This line corresponds to the black line shown in Figure 2.22. We will demonstrate the extrapolation with an example in the next section.

If second-arrival traveltime tables are available, two sets of coefficients are required for the interpolation of first and second arrivals. As discussed above, both coefficient sets will be wrong in the vicinity of a cusp. Although it is possible to apply the extrapolation approach indicated above also for the second arrivals, we suggest an alternative, that leads to correct coefficients at the affected grid points. We use the location of the points P at the depths $i-1$, i, and $i+1$ to separate the traveltime branches 1 and 2 (note that the branch indices 1 and 2 do not denote first and second arrivals, see Figure 2.21). Now, let $T_1(i,j)$ denote the traveltime of the first arrival at (i,j), and $T_2(i,j)$ that of the second arrival. We can now obtain the coefficients from Equation (2.2.3) with the appropriate traveltime combinations according to Figure 2.22. For example, the coefficients at (i,j) (on branch 2) for the first-arrival traveltimes are determined as

$$
\begin{aligned}
q_x &= \frac{T_1^2(i+1,j) - T_2^2(i-1,j)}{4\,T_1(i,j)\,d} \quad, \\
q_z &= \frac{T_2^2(i,j+1) - T_1^2(i,j-1)}{4\,T_1(i,j)\,d} \quad, \\
G_{xx} &= \frac{T_1^2(i+1,j) + T_2^2(i-1,j) - 2\,T_1^2(i,j)}{2\,T_1(i,j)\,d^2} - \frac{q_x^2}{T_1(i,j)} \quad, \\
G_{zz} &= \frac{T_2^2(i,j+1) + T_1^2(i,j-1) - 2\,T_1^2(i,j)}{2\,T_1(i,j)\,d^2} - \frac{q_z^2}{T_1(i,j)} \quad, \\
G_{xz} &= \frac{T_1^2(i+1,j+1) + T_2^2(i-1,j-1) - T_1^2(i+1,j-1) - T_2^2(i-1,j+1)}{8\,T_1(i,j)\,d^2} - \frac{q_x\,q_z}{T_1(i,j)} \quad.
\end{aligned}
$$

When the coefficients of the first and second arrivals have been correctly determined for both branches, the interpolation is carried out until P with the appropriate set of coefficients.

Figure 2.24 displays isochrones for a 2-D version of the Marmousi model (see Figure 2.10) and the negative values of the second order derivative matrix elements G_{xx} and G_{zz}. The coincidence between the triplications and the negative curvature is obvious (although only first arrivals are shown, I will further use the term triplications for these discontinuities). Figure 2.24 also shows that in regions where the wavefront has a more horizontal orientation G_{xx} is more suitable for identification of triplications, whereas for vertical wavefronts the behaviour of G_{zz} is the better indicator. Therefore, the decision whether to investigate G_{xx} or G_{zz} is made automatically from the direction of the associated ray, i.e. the slowness vector, since it is perpendicular to the wavefront. The slowness is not only taken from a single point, but also from its vicinity as it would not yield sensible results at a triplication. In the 2-D case, this would mean that for $q_{0_z} > q_{0_x}$ the matrix element G_{xx} will be taken and *vice versa*. However, the sign of G alone is not enough for a reliable triplication detection algorithm. For example, in the vicinity of near plane wavefronts the curvature becomes very small and G may undergo a change in sign there.

In 3-D we must theoretically account for two types of cusps caused by first arrivals of triplicated wavefronts. These correspond to point and line foci, as shown in Figure 2.25. For 3-D wavefronts with mainly horizontal orientation, as in Figure 2.25, the derivatives G_{xx} and G_{yy} must be investigated. For a point focus both, G_{xx} and G_{yy}, will be negative, whereas for a line focus only G_{xx} will be negative. However, due to the high symmetry of a model required to create a point focus, point foci are unlikely to play an important role in the earth.

The case of a multi-valued traveltime curve which has a triplication in a later arrival can be handled in the same manner as a triplicated first arrival: Figure 2.26 shows an example with five arrivals and a triplication of the first and second arrival. The triplication of the first arrival is treated as described above. For the triplication of the second arrival between the branches

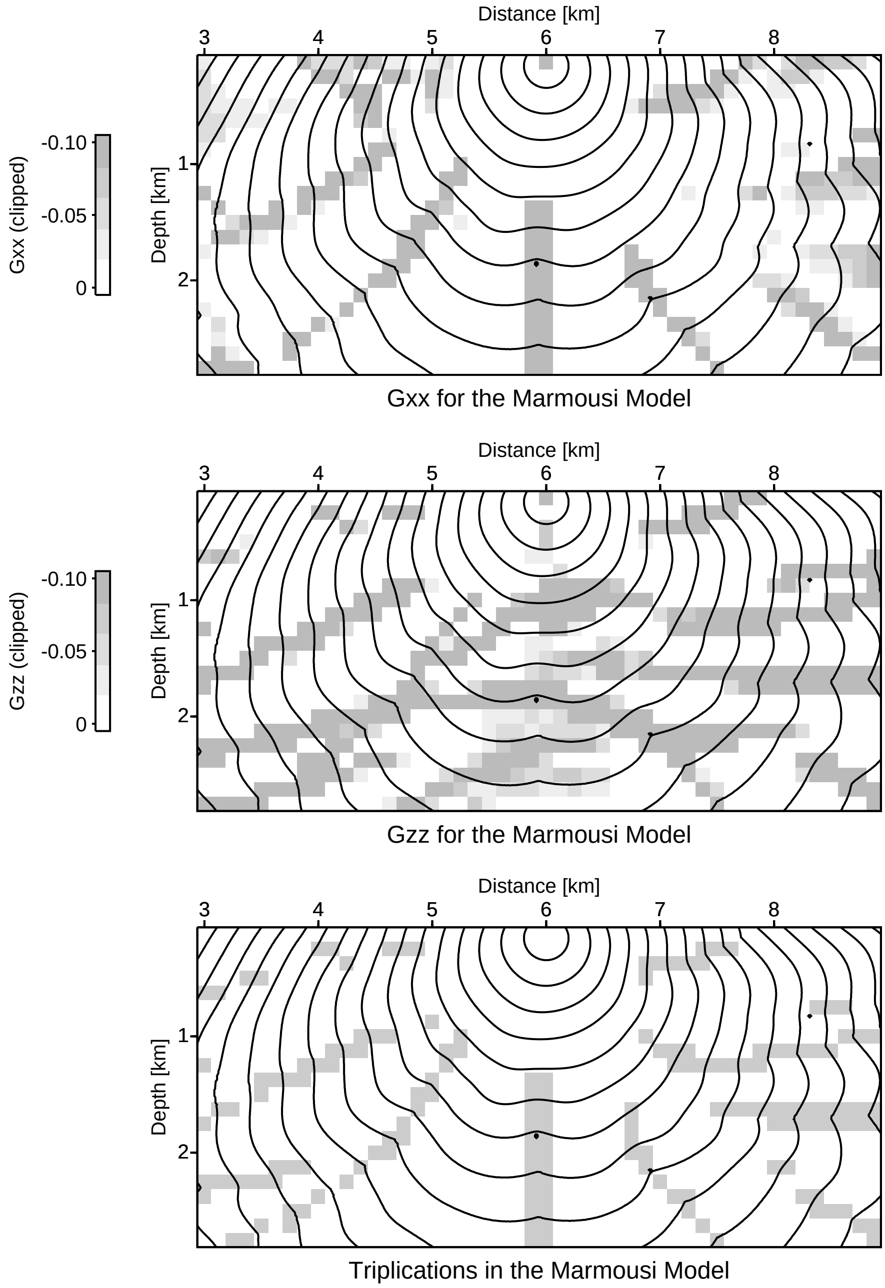

Figure 2.24: Matrix elements G_{xx} (top) and G_{zz} (middle) for the Marmousi model. Only negative values are displayed. They follow the triplications. Bottom: Triplications found by applying the quartile criterion in addition to the signs of G.

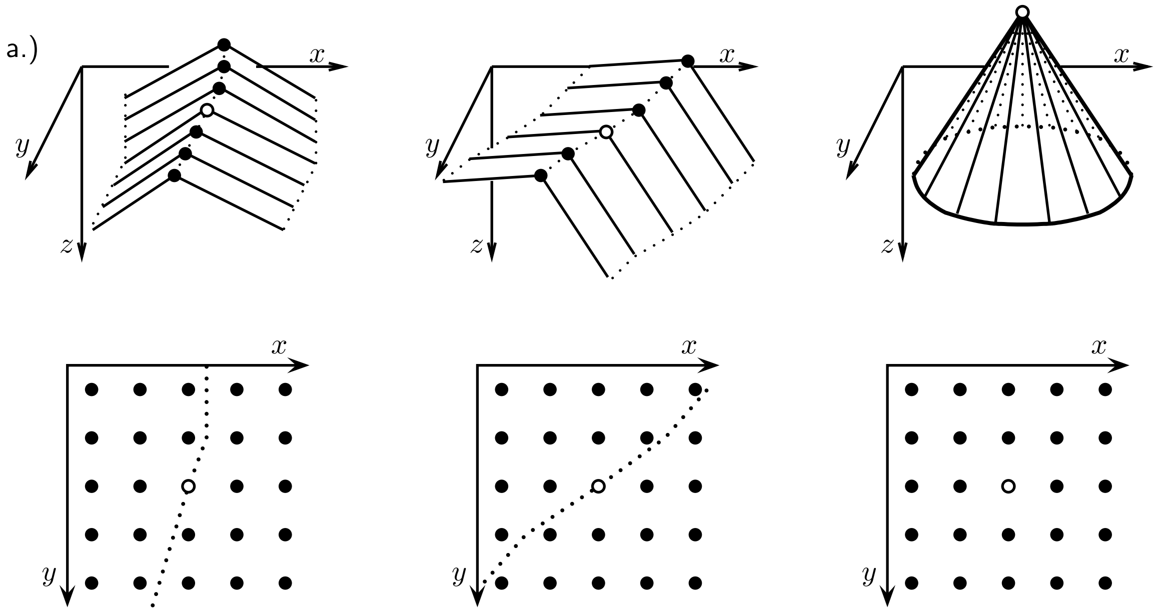

Figure 2.25: The two types of cusps that can occur in first arrivals of triplicated wavefronts (top) and their projection onto the grid (bottom). The cusp on the left is caused by a line focus with predominant orientation in y-direction, while the one in the centre represents a line focus mainly in $x - y$ direction. The cusp on the right corresponds to a point focus.

2 and 3 we note again, that the coefficient G_{xx} has a negative value at the grid nodes which frame the intersection point between the two branches. This means that we can apply the same algorithm as for the first arrivals to correctly treat the triplicated second-arrival traveltime curve: we now investigate the coefficients of the second arrivals to detect the intersection point. Then the correct coefficients are determined by separate treatment of the branches 2 and 3 and the interpolation is carried out. Triplications of other arrivals can he handled in the same fashion.

The method can also be applied to interpolate traveltimes between shots. In this case, the locations of the cusps are determined for each shot point on the input coarse grid individually. The coefficients are again determined from the appropriate combination of traveltimes, according to the different branches. Examples for the interpolation of first and second arrivals in the presence of cusps will be given in the next section.

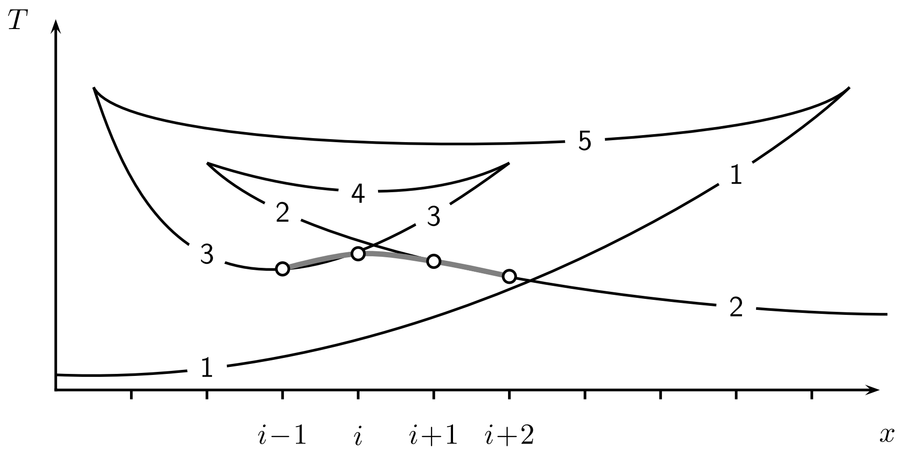

Figure 2.26: Multi-valued traveltime curve. The traveltime curve consists of five branches. The white circles indicate second-arrival traveltimes on the branches 2 and 3 which form a cusp between grid points i and $i + 1$. The gray line describes the result of hyperbolic interpolation if only second arrivals are considered, leading to a mis-fit around the grid points at i and $i-1$. As for the triplicated first-arrival traveltime shown in Figure 2.21 the hyperbolic curve is concave, whereas the branches 2 and 3 show convex behaviour. This means that the triplication of the second-arrival traveltime can be treated in the same way as a triplicated first arrival by investigation of the corresponding second-order derivatives followed by separate interpolation of the individual branches.

Examples

We have applied the method to a 2-D example. The model used for this example is a parabolic lens with a negative velocity perturbation embedded in a homogeneous background medium. First- and second-arrival traveltimes were generated, using the wavefront-oriented ray tracing technique introduced by Coman and Gajewski (2005), on a 100 m $\times$ 100 m coarse grid. The same algorithm was used to compute reference first- and second-arrival traveltimes on a 10 m $\times$ 10 m fine grid. The coarsely-gridded traveltime table was the input for the interpolation algorithm. Coefficients were determined from these traveltimes and used for the hyperbolic interpolation onto the 10 m $\times$ 10 m fine grid. The interpolated traveltimes on the fine grid were compared to the reference traveltimes. The resulting relative errors of the first-arrival traveltimes without consideration of cusps are shown in Figure 2.20. Their mean (average) relative error is 0.113 % with a maximum of 11.5 %.

In the first example we have applied our method assuming that only first-arrival traveltimes are available. The cusps were searched and the traveltimes in their vicinities were extrapolated until the position of the cusp, using the coefficients from the surrounding unaffected grid points. Figure 2.27 shows the relative traveltime errors resulting from this scheme. The mean error was reduced to 0.014 %, with a maximum of 0.8 %.

In the second example we have combined first- and second-arrival traveltime tables to correct the coefficients in regions with cusps in the wavefronts. Figure 2.28 displays the resulting errors for the interpolation of the first-arrival traveltimes, using these coefficients. The mean relative error is 0.014 %, with a maximum of 9.2 %. Compared to the uncorrected case the maximum error

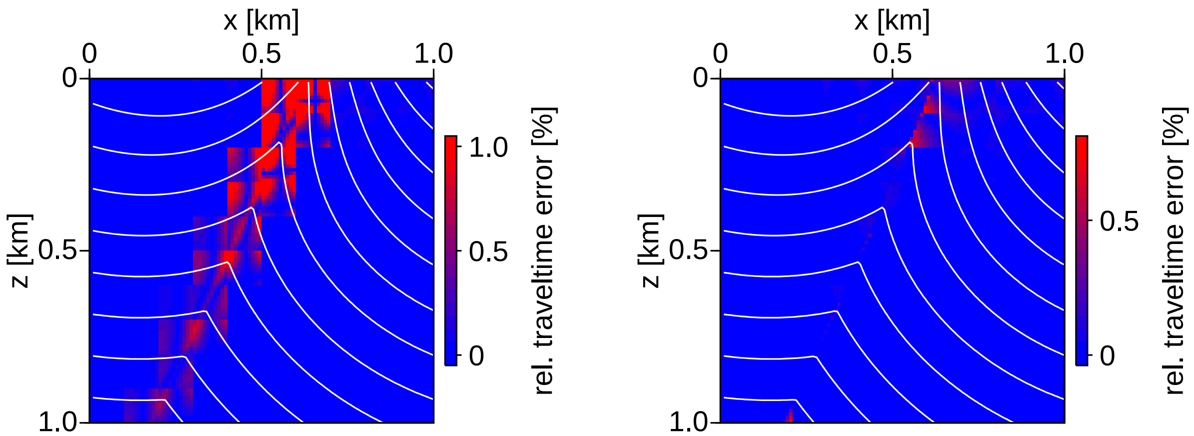

Figure 2.27: Relative errors of first-arrival traveltimes for the velocity lens model. On the left, the results from traveltime interpolation without considering cusps in the wavefronts are shown for comparison. For the right hand figure, first-arrival traveltimes were extrapolated until the position of the cusp, using coefficients from unaffected grid points.

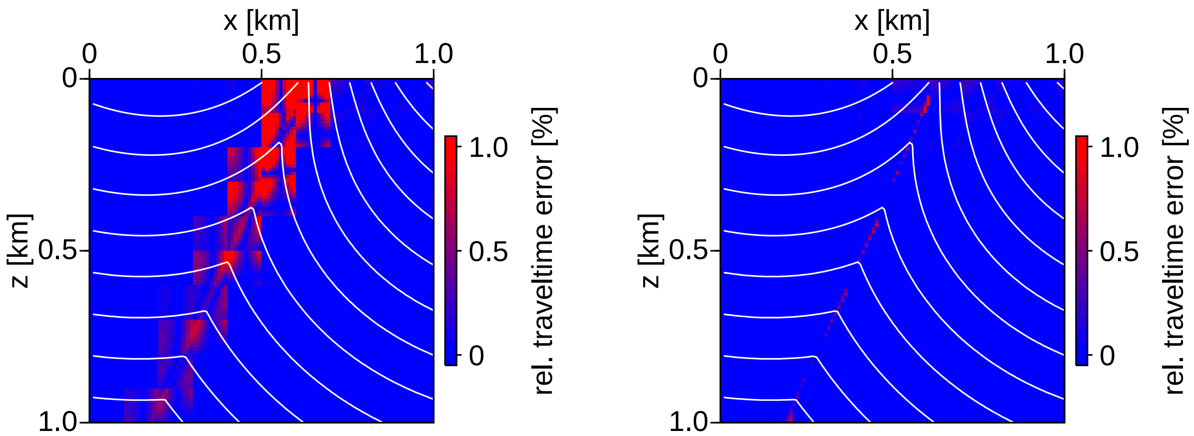

Figure 2.28: Relative errors of first-arrival traveltimes for the velocity lens model. On the left, errors of interpolation without considering cusps are shown for comparison. For the right hand figure, first-arrival traveltimes were interpolated, using corrected coefficients computed from first- and second-arrival traveltime tables.

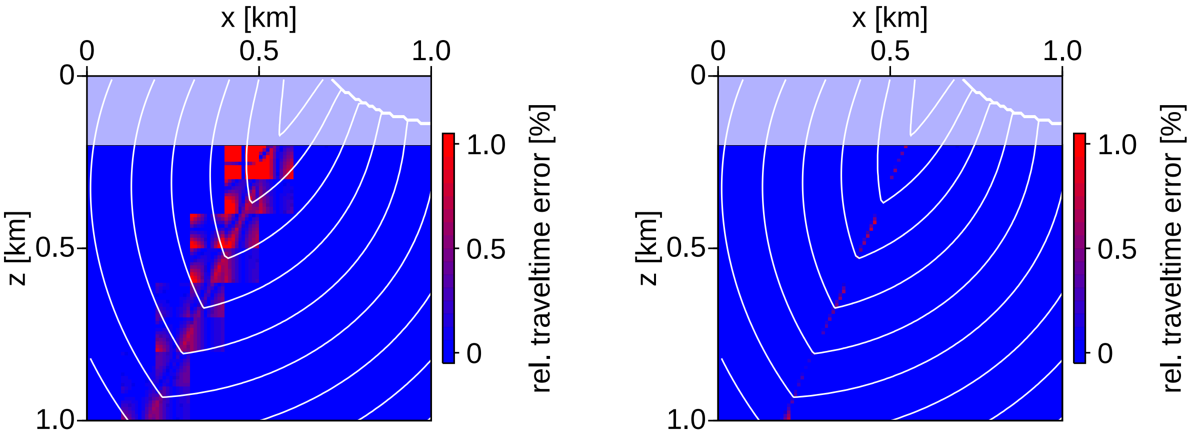

Figure 2.29: Relative errors of second-arrival traveltimes in the velocity lens model. Since second arrivals occur only in the lower part of the model, only the region below the horizontal black line was considered. Left: errors from the uncorrected interpolation of second arrivals. Right: errors from the interpolation of second arrivals with corrected coefficients.

was not considerably reduced, however, whereas errors of that magnitude arise within a broad region around the cusp in the uncorrected case, there are now only single points with higher errors, as Figure 2.28 shows. The overall accuracy is of the same magnitude as for the example where only first-arrival traveltimes were used, yet in the upper 200 m, where the two wavefront branches meet in the steepest angles, the corrected coefficients lead to higher accuracy than the extrapolation.

The error distribution for the uncorrected second-arrival interpolation, Figure 2.29 (left) looks similar to that of the uncorrected first-arrival interpolation in Figure 2.20, with a mean error of 0.249 % and a maximum of 79.9 %. The right part of Figure 2.29 shows the relative errors of the second-arrival traveltimes, if the coefficients in the affected region are corrected by combining the appropriate first- and second-arrival traveltimes. The mean relative error here is 0.006 %, with a maximum of 0.8 %. As mentioned above, third arrivals, that are also present in this example, need no special treatment, as they do not show discontinuities.

Conclusions

The traveltime coefficients discussed here have a much broader range of application than just the interpolation of traveltimes. Since the second-order traveltime derivatives are closely related to the curvature of the wavefront, the coefficients can be applied to determine the geometrical spreading from traveltimes as will be described later in this work. Like for the interpolation of the traveltimes, the same problem due to cusps arises for the geometrical spreading. The separate treatment of the individual traveltime branches suggested in this work will also improve the algorithm for the determination of geometrical spreading from traveltimes. Another closely related application of the suggested method lies in the traveltime-based strategy to true-amplitude migration, which is also introduced later in this work. In that strategy, all quantities, namely the migration weight functions, required for a true-amplitude migration of the Kirchhoff type are expressed in terms of the traveltime coefficients discussed above. Thus, high savings in computer time and storage can be achieved. Since later-arrivals need to be included in true-amplitude migration, the traveltime-based strategy will also greatly benefit from the method suggested in this section.

2.8 Reflection traveltimes

This section introduces a 6×6 matrix $\hat{\underline{\underline{\mathsf{T}}}}$ that is formed by the matrices $\hat{\underline{\mathsf{S}}}$, $\hat{\underline{\mathsf{G}}}$, and $\hat{\underline{\mathsf{N}}}$ introduced in this chapter. Although $\hat{\underline{\underline{\mathsf{T}}}}$ bears a strong similarity to the 4×4 Bortfeld propagator matrix $\underline{\underline{\mathsf{T}}}$ that was introduced in Section A.9, it is not a propagator matrix, i.e. the solution to a differential equation like (A.6.2) under additional conditions (see Section A.6). The matrix $\hat{\underline{\underline{\mathsf{T}}}}$ is useful, because its relation to $\underline{\underline{\mathsf{T}}}$ links the 3×3 matrices $\hat{\underline{\mathsf{S}}}$, $\hat{\underline{\mathsf{G}}}$, and $\hat{\underline{\mathsf{N}}}$ to the 2×2 matrices $\underline{\mathsf{A}}$, $\underline{\mathsf{B}}$, $\underline{\mathsf{C}}$, and $\underline{\mathsf{D}}$. The latter build the Bortfeld propagator $\underline{\underline{\mathsf{T}}}$ which is defined in reference surfaces, e.g., the reflector or registration surface. With $\hat{\underline{\underline{\mathsf{T}}}}$, it is possible to express certain properties, e.g., the geometrical spreading of a reflected event, or a traveltime expansion into the reflector surface, directly in terms of the matrices $\hat{\underline{\mathsf{S}}}$, $\hat{\underline{\mathsf{G}}}$, and $\hat{\underline{\mathsf{N}}}$. This requires the relationship between $\hat{\underline{\underline{\mathsf{T}}}}$ and $\underline{\underline{\mathsf{T}}}$ which I will derive. It leads to another, useful notation for the submatrices of $\underline{\underline{\mathsf{T}}}$.

I will begin by introducing the 6×6 matrix $\hat{\underline{\underline{\mathsf{T}}}}$. I will then develop the relationship between the matrix $\hat{\underline{\underline{\mathsf{T}}}}$ and the propagator $\underline{\underline{\mathsf{T}}}$. This relationship comprises the rotation of the 3×3 matrices involved in $\hat{\underline{\underline{\mathsf{T}}}}$ into the tangent planes of the surfaces in which $\underline{\underline{\mathsf{T}}}$ is defined. The curvature of these surfaces is also acknowledged in the relations given here. Finally, I will treat reflected events in terms of propagator matrices, which lead to an expression for paraxial reflection traveltimes. The matrices in this expression can be decomposed into those of the two ray branches that build the reflected ray.

The matrix $\hat{\underline{\underline{\mathsf{T}}}}$

The matrix $\hat{\underline{\underline{\mathsf{T}}}}$ negotiates between changes in positions and changes in slownesses, similar as the propagator $\underline{\underline{\mathsf{T}}}$, but for 3-D vectors. The slownesses are determined by taking the gradient with respect to source and receiver coordinates, respectively, of the parabolic traveltime expansion, Equation (2.1.4):

$$\tau(\hat{\boldsymbol{s}},\hat{\boldsymbol{g}}) = \tau_0 + \hat{\boldsymbol{q}}_0\,\Delta\hat{\boldsymbol{g}} - \hat{\boldsymbol{p}}_0\,\Delta\hat{\boldsymbol{s}} - \Delta\hat{\boldsymbol{s}}^\top \hat{\underline{\mathsf{N}}}\,\Delta\hat{\boldsymbol{g}} + \frac{1}{2}\,\Delta\hat{\boldsymbol{g}}^\top \hat{\underline{\mathsf{G}}}\,\Delta\hat{\boldsymbol{g}} - \frac{1}{2}\,\Delta\hat{\boldsymbol{s}}^\top \hat{\underline{\mathsf{S}}}\,\Delta\hat{\boldsymbol{s}} \quad . \tag{2.8.1}$$

The slowness at the source is

$$\hat{\boldsymbol{p}} = -\vec{\nabla}_s\tau = \hat{\boldsymbol{p}}_0 + \hat{\underline{\mathsf{S}}}\,\Delta\hat{\boldsymbol{s}} + \hat{\underline{\mathsf{N}}}\,\Delta\hat{\boldsymbol{g}} \quad , \tag{2.8.2}$$

and the slowness at the receiver is

$$\hat{\boldsymbol{q}} = \vec{\nabla}_g\tau = \hat{\boldsymbol{q}}_0 + \hat{\underline{\mathsf{G}}}\,\Delta\hat{\boldsymbol{g}} - \hat{\underline{\mathsf{N}}}^\top\,\Delta\hat{\boldsymbol{s}} \quad . \tag{2.8.3}$$

Rearranging of Equations (2.8.2) and (2.8.3) gives

$$\begin{pmatrix} \Delta\hat{\boldsymbol{g}} \\ \hat{\boldsymbol{q}} - \hat{\boldsymbol{q}}_0 \end{pmatrix} = \begin{pmatrix} -\hat{\underline{\mathsf{N}}}^{-1}\hat{\underline{\mathsf{S}}} & \hat{\underline{\mathsf{N}}}^{-1} \\ -\hat{\underline{\mathsf{N}}}^\top - \hat{\underline{\mathsf{G}}}\,\hat{\underline{\mathsf{N}}}^{-1}\hat{\underline{\mathsf{S}}} & \hat{\underline{\mathsf{G}}}\,\hat{\underline{\mathsf{N}}}^{-1} \end{pmatrix} \begin{pmatrix} \Delta\hat{\boldsymbol{s}} \\ \hat{\boldsymbol{p}} - \hat{\boldsymbol{p}}_0 \end{pmatrix} . \tag{2.8.4}$$

I define the matrix $\hat{\underline{\underline{\mathsf{T}}}}$ as

$$\hat{\underline{\underline{\mathsf{T}}}} = \begin{pmatrix} -\hat{\underline{\mathsf{N}}}^{-1}\hat{\underline{\mathsf{S}}} & \hat{\underline{\mathsf{N}}}^{-1} \\ -\hat{\underline{\mathsf{N}}}^\top - \hat{\underline{\mathsf{G}}}\,\hat{\underline{\mathsf{N}}}^{-1}\hat{\underline{\mathsf{S}}} & \hat{\underline{\mathsf{G}}}\,\hat{\underline{\mathsf{N}}}^{-1} \end{pmatrix} \tag{2.8.5}$$

The next section will establish the relationship between the 6×6 matrix $\hat{\underline{\underline{\mathsf{T}}}}$ and the 4×4 propagator matrix $\underline{\underline{\mathsf{T}}}$.

Curved surfaces

The matrices $\underline{\underline{\mathsf{T}}}$ and $\hat{\underline{\underline{\mathsf{T}}}}$ have some common properties. In this section I introduce the 2×2 matrices $\tilde{\underline{\mathsf{G}}}$, $\tilde{\underline{\mathsf{S}}}$, and $\tilde{\underline{\mathsf{N}}}$ and write the propagator $\underline{\underline{\mathsf{T}}}$ in terms of these matrices, similar as $\hat{\underline{\underline{\mathsf{T}}}}$ is formed by $\hat{\underline{\mathsf{G}}}$, $\hat{\underline{\mathsf{S}}}$, and $\hat{\underline{\mathsf{N}}}$:

$$\underline{\underline{\mathsf{T}}} = \begin{pmatrix} -\tilde{\underline{\mathsf{N}}}^{-1}\tilde{\underline{\mathsf{S}}} & \tilde{\underline{\mathsf{N}}}^{-1} \\ -\tilde{\underline{\mathsf{N}}}^{\top} - \tilde{\underline{\mathsf{G}}}\,\tilde{\underline{\mathsf{N}}}^{-1}\tilde{\underline{\mathsf{S}}} & \tilde{\underline{\mathsf{G}}}\,\tilde{\underline{\mathsf{N}}}^{-1} \end{pmatrix} \quad . \tag{2.8.6}$$

Referring to Appendix A, where the propagator $\underline{\underline{\mathsf{T}}}$ is introduced as

$$\underline{\underline{\mathsf{T}}} = \begin{pmatrix} \underline{\mathsf{A}} & \underline{\mathsf{B}} \\ \underline{\mathsf{C}} & \underline{\mathsf{D}} \end{pmatrix} \quad , \tag{2.8.7}$$

the relationship between the matrices $\tilde{\underline{\mathsf{G}}}$, $\tilde{\underline{\mathsf{S}}}$, $\tilde{\underline{\mathsf{N}}}$ and $\underline{\mathsf{A}}$, $\underline{\mathsf{B}}$, $\underline{\mathsf{C}}$, $\underline{\mathsf{D}}$ is

$$\begin{aligned} \underline{\mathsf{A}} &= -\tilde{\underline{\mathsf{N}}}^{-1}\tilde{\underline{\mathsf{S}}} \quad , \\ \underline{\mathsf{B}} &= \tilde{\underline{\mathsf{N}}}^{-1} \quad , \\ \underline{\mathsf{C}} &= -\tilde{\underline{\mathsf{N}}}^{\top} - \tilde{\underline{\mathsf{G}}}\,\tilde{\underline{\mathsf{N}}}^{-1}\tilde{\underline{\mathsf{S}}} \quad , \\ \underline{\mathsf{D}} &= \tilde{\underline{\mathsf{G}}}\,\tilde{\underline{\mathsf{N}}}^{-1} \quad , \end{aligned} \tag{2.8.8}$$

and

$$\begin{aligned} \tilde{\underline{\mathsf{S}}} &= -\underline{\mathsf{B}}^{-1}\underline{\mathsf{A}} \quad , \\ \tilde{\underline{\mathsf{G}}} &= \underline{\mathsf{D}}\,\underline{\mathsf{B}}^{-1} \quad , \\ \tilde{\underline{\mathsf{N}}} &= \underline{\mathsf{B}}^{-1} \quad . \end{aligned} \tag{2.8.9}$$

Here, I have also used the fact that $\underline{\underline{\mathsf{T}}}$ must obey the symplecticity relation (A.6.12). The matrix $\hat{\underline{\underline{\mathsf{T}}}}$ is also a symplectic matrix.

To find a relationship between $\tilde{\underline{\mathsf{G}}}$, $\tilde{\underline{\mathsf{S}}}$, $\tilde{\underline{\mathsf{N}}}$ and $\hat{\underline{\mathsf{G}}}$, $\hat{\underline{\mathsf{S}}}$, $\hat{\underline{\mathsf{N}}}$, I use Equation (2.8.1), the parabolic traveltime expansion in the Cartesian coordinate system in which the traveltime tables are given. Since the traveltimes must not depend on the coordinate system, I can use a similar traveltime expansion in a coordinate system that coincides with the system in which the propagator $\underline{\underline{\mathsf{T}}}$ is defined by the anterior and posterior surfaces. These correspond to the reflector's tangent plane and the registration surface and that system is denoted with a tilde ˜. The according 3-D vectors carry an additional hat. In this coordinate system associated with the surfaces, the traveltime expansion reads

$$\tau(\hat{\tilde{\boldsymbol{s}}},\hat{\tilde{\boldsymbol{g}}}) = \tau_0 + \hat{\tilde{\boldsymbol{q}}}_0\,\Delta\hat{\tilde{\boldsymbol{g}}} - \hat{\tilde{\boldsymbol{p}}}_0\,\Delta\hat{\tilde{\boldsymbol{s}}} - \Delta\hat{\tilde{\boldsymbol{s}}}^{\top}\hat{\tilde{\underline{\mathsf{N}}}}\,\Delta\hat{\tilde{\boldsymbol{g}}} + \frac{1}{2}\,\Delta\hat{\tilde{\boldsymbol{g}}}^{\top}\hat{\tilde{\underline{\mathsf{G}}}}\,\Delta\hat{\tilde{\boldsymbol{g}}} - \frac{1}{2}\,\Delta\hat{\tilde{\boldsymbol{s}}}^{\top}\hat{\tilde{\underline{\mathsf{S}}}}\,\Delta\hat{\tilde{\boldsymbol{s}}} \quad . \tag{2.8.10}$$

The anterior surface coordinate system has the 1- and 2-axes in the surface's tangent plane at $\hat{\tilde{\boldsymbol{s}}}_0 = \hat{\boldsymbol{s}}_0$ and the 3-axis perpendicular to it. The vector $\Delta\hat{\tilde{\boldsymbol{s}}} = (\Delta\tilde{\boldsymbol{s}},\Delta\tilde{s}_3)^{\top} = (\Delta\tilde{s}_1,\Delta\tilde{s}_2,\Delta\tilde{s}_3)^{\top}$ describes a point on the anterior surface. Its 3-component is given by

$$\Delta\tilde{s}_3 = \frac{1}{2}\,\Delta\tilde{\boldsymbol{s}}^{\top}\underline{\mathsf{F}}_s\Delta\tilde{\boldsymbol{s}} \quad , \tag{2.8.11}$$

where the 2×2 matrix $\underline{\mathsf{F}}_s$ is the curvature matrix of the anterior surface. It is zero for a plane, therefore the 3-component vanishes in this case. The 2-D vector $\Delta\tilde{\boldsymbol{s}}$ is computed by

$$\Delta\tilde{\boldsymbol{s}} = \underline{1}_{2\times 3}\,\hat{\underline{\mathsf{Z}}}_s\,\Delta\hat{\boldsymbol{s}} \quad , \tag{2.8.12}$$

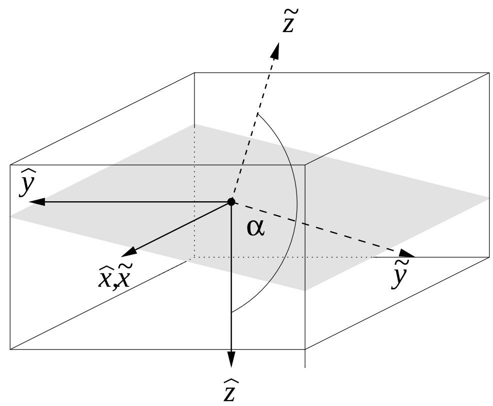

Figure 2.30: Rotation of 3-D second-order derivative matrices into the anterior surface's tangent plane: the coordinate system of the anterior surface (gray) is denoted by a tilde ˜. The Cartesian system that coincides with the system in which the traveltime tables are given is indicated by a hat ˆ. The angle α is the angle between the 3-axes (z) of both systems. In this plot the 1-axes (x) of both systems coincide and the curvature of the anterior surface is zero. The rotation matrix for this case is given in the text. (The index s was omitted in the figure.)

where the matrix $\underline{1}_{2\times 3} = \underline{1}^{\top}_{3\times 2}$ is

$$\underline{1}_{2\times 3} = \begin{pmatrix} 1 & 0 & 0 \\ 0 & 1 & 0 \end{pmatrix} \quad . \tag{2.8.13}$$

The matrix $\hat{\underline{Z}}_s$ in Equation (2.8.12) describes the rotation into the tangent plane of the anterior surface. It is defined corresponding to Equation (A.8.1),

$$Z_{ij} = \frac{\partial x_i}{\partial \tilde{x}_j} = \frac{\partial \tilde{x}_j}{\partial x_i} = \hat{\vec{\boldsymbol{x}}}_i \cdot \hat{\tilde{\vec{\boldsymbol{x}}}}_j \quad . \tag{2.8.14}$$

Vectors $\hat{\vec{\boldsymbol{x}}}_i$ are the base vectors of the global Cartesian coordinate system, $\hat{\tilde{\vec{\boldsymbol{x}}}}_i$ ($=\vec{\boldsymbol{\imath}}_i$) are those of the interface coordinates. It follows that the 1-component of the vector $\tilde{\boldsymbol{s}}$ lies in the plane defined by the emerging wave and the anterior surface (see Section A.8). These considerations also apply to the posterior surface with the appropriate index g instead of s. Figure 2.30 gives an example where the 1-components of the two systems coincide and the angle α lies between the 3-components. For this example the rotation matrix $\hat{\underline{Z}}$ becomes

$$\hat{\underline{Z}} = \begin{pmatrix} 1 & 0 & 0 \\ 0 & \cos\alpha & \sin\alpha \\ 0 & -\sin\alpha & \cos\alpha \end{pmatrix} \quad . \tag{2.8.15}$$

Since the traveltime must not depend on the coordinate system, expressions (2.8.1) and (2.8.10) must be equal for points in the corresponding surfaces. Applying Equations (2.8.11) and (2.8.12) for both anterior and posterior surface, and retaining only terms up to second order yields

$$\tau(\tilde{\boldsymbol{s}},\tilde{\boldsymbol{g}}) = \tau_0 + \tilde{\boldsymbol{q}}_0\,\Delta\tilde{\boldsymbol{g}} - \tilde{\boldsymbol{p}}_0\,\Delta\tilde{\boldsymbol{s}} - \Delta\tilde{\boldsymbol{s}}^{\top}\underline{\tilde{N}}\,\Delta\tilde{\boldsymbol{g}} + \frac{1}{2}\,\Delta\tilde{\boldsymbol{g}}^{\top}\underline{\tilde{G}}\,\Delta\tilde{\boldsymbol{g}} - \frac{1}{2}\,\Delta\tilde{\boldsymbol{s}}^{\top}\underline{\tilde{S}}\,\Delta\tilde{\boldsymbol{s}} \quad . \tag{2.8.16}$$

The 2×2 matrices $\underline{\tilde{N}}$, $\underline{\tilde{G}}$, and $\underline{\tilde{S}}$ are the same as in Equation (2.8.8) and are computed from the matrices $\underline{\hat{\mathsf{N}}}$, $\underline{\hat{\mathsf{G}}}$, and $\underline{\hat{\mathsf{S}}}$ as follows:

$$\begin{aligned}
\underline{\tilde{\mathsf{N}}} &= \underline{1}_{2\times3}\,\underline{\hat{\mathsf{Z}}}_s^\top\,\underline{\hat{\mathsf{N}}}\,\underline{\hat{\mathsf{Z}}}_g\,\underline{1}_{3\times2} \quad , \\
\underline{\tilde{\mathsf{S}}} &= \underline{1}_{2\times3}\,\underline{\hat{\mathsf{Z}}}_s^\top\,\underline{\hat{\mathsf{S}}}\,\underline{\hat{\mathsf{Z}}}_s\,\underline{1}_{3\times2} + \frac{\cos\theta_s}{v_s}\,\underline{\mathsf{F}}_s \quad , \\
\underline{\tilde{\mathsf{G}}} &= \underline{1}_{2\times3}\,\underline{\hat{\mathsf{Z}}}_g^\top\,\underline{\hat{\mathsf{G}}}\,\underline{\hat{\mathsf{Z}}}_g\,\underline{1}_{3\times2} + \frac{\cos\theta_g}{v_g}\,\underline{\mathsf{F}}_g \quad .
\end{aligned} \tag{2.8.17}$$

The angle θ_g is the incidence angle at the posterior surface at $\hat{\tilde{\boldsymbol{g}}}_0 = \hat{\boldsymbol{g}}_0$ and θ_s is the emergence angle at the anterior surface at $\hat{\tilde{\boldsymbol{s}}}_0 = \hat{\boldsymbol{s}}_0$. The quantity $\cos\theta_s/v_s$ is the 3-component of the slowness vector in the anterior surface coordinate system (accordingly for $\cos\theta_g/v_g$). The 2-D slowness vectors in Equation (2.8.16), $\tilde{\boldsymbol{p}}_0$ and $\tilde{\boldsymbol{q}}_0$, are given by

$$\begin{aligned}
\tilde{\boldsymbol{p}}_0 &= \underline{1}_{2\times3}\,\underline{\hat{\mathsf{Z}}}_s\,\hat{\boldsymbol{p}}_0 \quad , \\
\tilde{\boldsymbol{q}}_0 &= \underline{1}_{2\times3}\,\underline{\hat{\mathsf{Z}}}_g\,\hat{\boldsymbol{q}}_0 \quad .
\end{aligned} \tag{2.8.18}$$

One useful application of the propagator $\underline{\underline{\mathsf{T}}}$ is the decomposition of the ray that describes a reflected event into two individual ray branches. This decomposition is demonstrated in the next section.

Reflected events

For any point M on a smooth interface along the central ray, the propagator $\underline{\underline{\mathsf{T}}}$ satisfies the following chain rule (Hubral et al., 1992b):

$$\underline{\underline{\mathsf{T}}}(\tilde{\mathbf{g}}_\mathbf{0}, \tilde{\mathbf{s}}_\mathbf{0}) = \underline{\underline{\mathsf{T}}}(\tilde{\mathbf{g}}_\mathbf{0}, M)\,\cdot\,\underline{\underline{\mathsf{T}}}(M, \tilde{\mathbf{s}}_\mathbf{0}) = \underline{\underline{\mathsf{T}}}_2\,\cdot\,\underline{\underline{\mathsf{T}}}_1 \quad , \tag{2.8.19}$$

where I denote the matrices from $\tilde{\mathbf{s}}_\mathbf{0}$ to M with the index 1, i.e.

$$\underline{\underline{\mathsf{T}}}_1 = \begin{pmatrix} -\underline{\tilde{\mathsf{N}}}_1^{-1}\underline{\tilde{\mathsf{S}}}_1 & \underline{\tilde{\mathsf{N}}}_1^{-1} \\ -\underline{\tilde{\mathsf{N}}}_1^\top - \underline{\tilde{\mathsf{G}}}_1\underline{\tilde{\mathsf{N}}}_1^{-1}\underline{\tilde{\mathsf{S}}}_1 & \underline{\tilde{\mathsf{G}}}_1\underline{\tilde{\mathsf{N}}}_1^{-1} \end{pmatrix} \quad . \tag{2.8.20}$$

For the ray from M to $\tilde{\mathbf{g}}_\mathbf{0}$ I use the reverse propagator $\underline{\underline{\mathsf{T}}}^*(M, \tilde{\mathbf{g}}_\mathbf{0})$ for the reverse ray from $\tilde{\mathbf{g}}_\mathbf{0}$ to M instead of $\underline{\underline{\mathsf{T}}}(\tilde{\mathbf{g}}_\mathbf{0}, M)$. The relationship between a propagator matrix and that of its reverse ray which is given by Hubral et al. (1992a) leads to

$$\underline{\underline{\mathsf{T}}}_2 = \begin{pmatrix} \underline{\tilde{\mathsf{N}}}_2^{-\top}\underline{\tilde{\mathsf{G}}}_2 & \underline{\tilde{\mathsf{N}}}_2^{-\top} \\ -\underline{\tilde{\mathsf{N}}}_2 - \underline{\tilde{\mathsf{S}}}_2\underline{\tilde{\mathsf{N}}}_2^{-\top}\underline{\tilde{\mathsf{G}}}_2 & -\underline{\tilde{\mathsf{S}}}_2\underline{\tilde{\mathsf{N}}}_2^{-\top} \end{pmatrix} \quad . \tag{2.8.21}$$

Inserting these two propagators into Equation (2.8.19) yields the resulting matrices

$$\begin{aligned}
\underline{\tilde{\mathsf{N}}} &= \underline{\tilde{\mathsf{N}}}_1\left(\underline{\tilde{\mathsf{G}}}_1 + \underline{\tilde{\mathsf{G}}}_2\right)^{-1}\underline{\tilde{\mathsf{N}}}_2^\top \\
\underline{\tilde{\mathsf{G}}} &= -\underline{\tilde{\mathsf{S}}}_2 - \underline{\tilde{\mathsf{N}}}_2\left(\underline{\tilde{\mathsf{G}}}_1 + \underline{\tilde{\mathsf{G}}}_2\right)^{-1}\underline{\tilde{\mathsf{N}}}_2^\top \\
\underline{\tilde{\mathsf{S}}} &= \underline{\tilde{\mathsf{S}}}_1 + \underline{\tilde{\mathsf{N}}}_1\left(\underline{\tilde{\mathsf{G}}}_1 + \underline{\tilde{\mathsf{G}}}_2\right)^{-1}\underline{\tilde{\mathsf{N}}}_1^\top
\end{aligned} \tag{2.8.22}$$

which form $\underline{\underline{\mathsf{T}}}(\tilde{\mathbf{g}}_\mathbf{0}, \tilde{\mathbf{s}}_\mathbf{0})$.

If I assume a reflector at M, the resulting propagator $\underline{\underline{\mathsf{T}}}(\tilde{\mathbf{g}}_{\mathbf{0}}, \tilde{\mathbf{s}}_{\mathbf{0}})$ leads to the paraxial reflection traveltime

$$\tau_R(\tilde{\boldsymbol{s}}, \tilde{\boldsymbol{g}}) = \tau_0 + \tilde{\boldsymbol{q}}_0 \,\Delta\tilde{\boldsymbol{g}} - \tilde{\boldsymbol{p}}_0 \,\Delta\tilde{\boldsymbol{s}} - \Delta\tilde{\boldsymbol{s}}^{\top} \underline{\tilde{\mathsf{N}}} \,\Delta\tilde{\boldsymbol{g}} + \frac{1}{2} \,\Delta\tilde{\boldsymbol{g}}^{\top} \underline{\tilde{\mathsf{G}}} \,\Delta\tilde{\boldsymbol{g}} - \frac{1}{2} \,\Delta\tilde{\boldsymbol{s}}^{\top} \underline{\tilde{\mathsf{S}}} \,\Delta\tilde{\boldsymbol{s}} \quad , \tag{2.8.23}$$

with the matrices $\underline{\tilde{\mathsf{N}}}$, $\underline{\tilde{\mathsf{G}}}$, and $\underline{\tilde{\mathsf{S}}}$ given by Equation (2.8.22).

Chapter 3

Multiparameter stacking

In the previous chapter I have considered applications based on traveltime tables as input information. These traveltimes were used to compute the first and second order spatial derivatives required for the applications. Another possibility not mentioned before is the determination of the coefficients directly from data. Reflection traveltimes may be obtained from seismic data by picking of events. Due to noise, however, picked traveltimes will in all likelihood not match the requirements for sufficiently accurate coefficients. In this chapter I will discuss an alternative for the determination of the coefficients.

Stacking is a fundamental concept in exploration seismics. Its goal is the transformation of multicoverage, i.e., prestack data, into a simulated zero-offset section. Over the years, methods have been developed that extend the classic NMO stacking technique, where the normal move-out velocity is the stacking parameter. The NMO-velocity is directly related to the curvature of the wavefront, and thus to the traveltime derivatives serving as coefficients in the traveltime expressions introduced in Chapter 2.

This chapter deals with multiparameter stacking, focusing mainly on hyperbolic operators like the Common Reflection Surface (CRS, e.g., Jäger et al., 2001) stack operator. Whereas the NMO formula can be applied for a single parameter stack, multiparameter expressions employ more than one parameter or wavefield attribute. The number of attributes depends on the situation, e.g., 2D or 3D, zero-offset or common-offset data, or whether converted waves are considered.

I begin with an overview of stacking of seismic reflection data where I will briefly review the classical methods. This first section is followed by an introduction to the image space concept (Höcht et al., 1999), which is fundamental for the understanding of the physical properties of multiparameter stacking parameters. In the next two sections, I derive the zero-offset CRS formula based on geometric considerations as suggested by Shah (1973) and Hubral and Krey (1980), as well as from a Taylor expansion of the traveltime (B. Kashtan, personal communication). The latter section also considers converted waves.

In the section following thereafter, I introduce a so-called general NMO operator, which is based on the hyperbolic traveltime formula derived in Chapter 2. I discuss the equivalence between the general NMO and zero-offset and common-offset CRS operators, as well as a qualitative comparison of their results in the section on stacking in the source-receiver domain. It turns out that although multiparameter stacking is best carried out in the midpoint and half-offset domain, the general NMO operator, which can be applied in arbitrary coordinates, has advantages when it comes to the offset situation, converted waves, or seismic anisotropy.

3.1 Introduction

The classical $T^2 - X^2$ formula was derived for a horizontally stratified medium. Taner and Koehler (1969) showed that the reflection traveltime in the short spread approximation corresponds to a hyperbola of the form

$$T^2 = T_0^2 + \frac{X^2}{V_{RMS}^2} \quad . \tag{3.1.1}$$

In Equation (3.1.1) V_{RMS} is the RMS velocity controlling the move-out, T_0 is the vertical two way traveltime, and X is the distance between the source and the receiver. The move-out in the $T^2 - X^2$ domain is linear. It can be directly determined from the slope of the $T^2 - X^2$ graph, which is equal to the inverse of V_{RMS}^2.

Since X is the offset, the distance between source and receiver, we can use the coordinate h instead, which defines the half-offset, i.e., $2\,h = X$. As I will demonstrate with a simple example, analysing data in common midpoint (CMP) gathers, where the coordinate is the half-offset, is advantageous over common shot gathers with the receiver position as coordinate.

Figure 3.1 shows ray paths for a reflection from a horizontal interface in a shot (a) and a CMP gather (b) for a constant velocity V_0. Observe that the reflections in the CMP gather all belong to the same point on the reflector, the CMP. This implies that by considering all traces in the CMP gather, we can make use of the redundant information in the data: by stacking along the CMP traveltime curve (in 2D) and assigning the result to the zero-offset time, we obtain a simulated zero-offset trace for the reflection point associated with the CMP with a signal to noise ration that has been improved by a factor of $\sqrt{n}$ with n the number of traces, compared to the unstacked zero-offset trace (if it even exists). The traveltime curve is in this case given by

$$T^2 = T_0^2 + \frac{4\,h^2}{V_0^2} \quad . \tag{3.1.2}$$

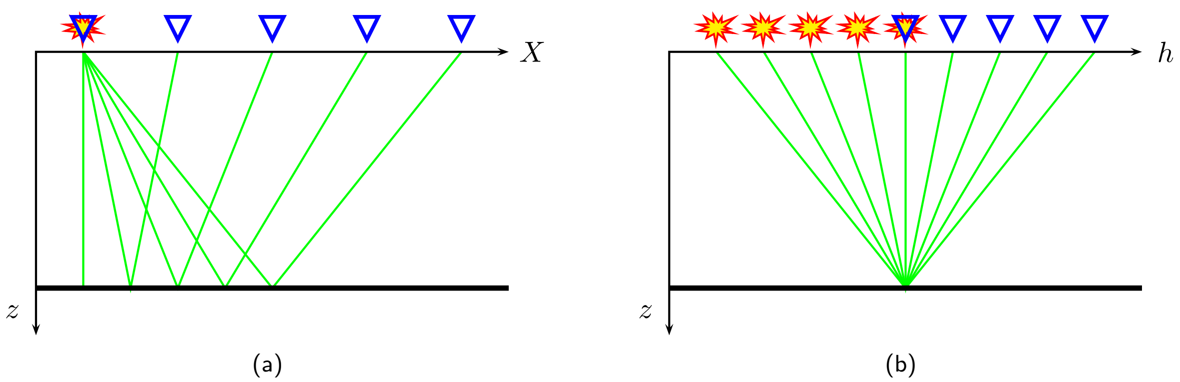

Figure 3.1: Ray paths for a horizontal reflector in a homogeneous medium. (a) Common source gather. (b) Common midpoint gather.

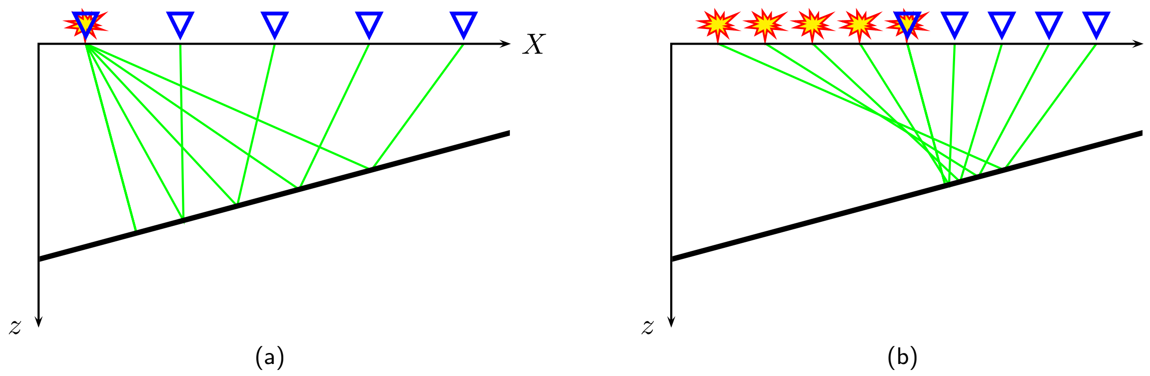

Figure 3.2: Ray paths for a plane inclined reflector in a homogeneous medium. (a) Common source gather. (b) Common midpoint gather.

For a horizontally-layered medium, we find that this traveltime is also given by Equation (3.1.1) if we substitute X with $2\,h$.

Let us now take a look at a single inclined reflector with an inclination angle ϑ, as depicted in Figure 3.2. In this case, we find that the ray paths in the CMP section (b) do not coincide in a single subsurface point on the reflector, but that there is still considerably less dispersal than in the shot gather (a). It can be shown that the traveltime in the CMP gather is described by

$$T^2 = T_0^2 + \frac{4\,h^2\,\cos^2\vartheta}{V_0^2} \quad . \tag{3.1.3}$$

This has led to the idea of generally expressing CMP traveltimes by the hyperbolic formula

$$T^2 = T_0^2 + \frac{4\,h^2}{V_{NMO}^2} \quad . \tag{3.1.4}$$

This equation contains the thus-defined normal move-out, NMO, velocity, V_{NMO} (Mayne, 1962; Hubral and Krey, 1980). In contrast to (3.1.1), Equation (3.1.4) is not restricted to models with horizontal layering, as can be seen from the traveltime expression for the inclined reflector. Hubral and Krey (1980) have also shown that the NMO velocity is related to the wavefront curvature.

In summary, we find that the NMO velocity

- for a single horizontal reflector in a homogeneous medium where the medium velocity is V_0: $V_{NMO} = V_0$,
- for a single inclined plane reflector in a homogeneous medium with the medium velocity V_0 and the inclination angle ϑ: $V_{NMO} = V_0/\cos\vartheta$,
- for a horizontally-stratified medium: $V_{NMO} = V_{RMS}$,
- for an arbitrary medium (with the offset $X = 2\,h$): $V_{NMO} = \sqrt{T_0\,\frac{d^2T}{dX^2}}^{\,-1}$,

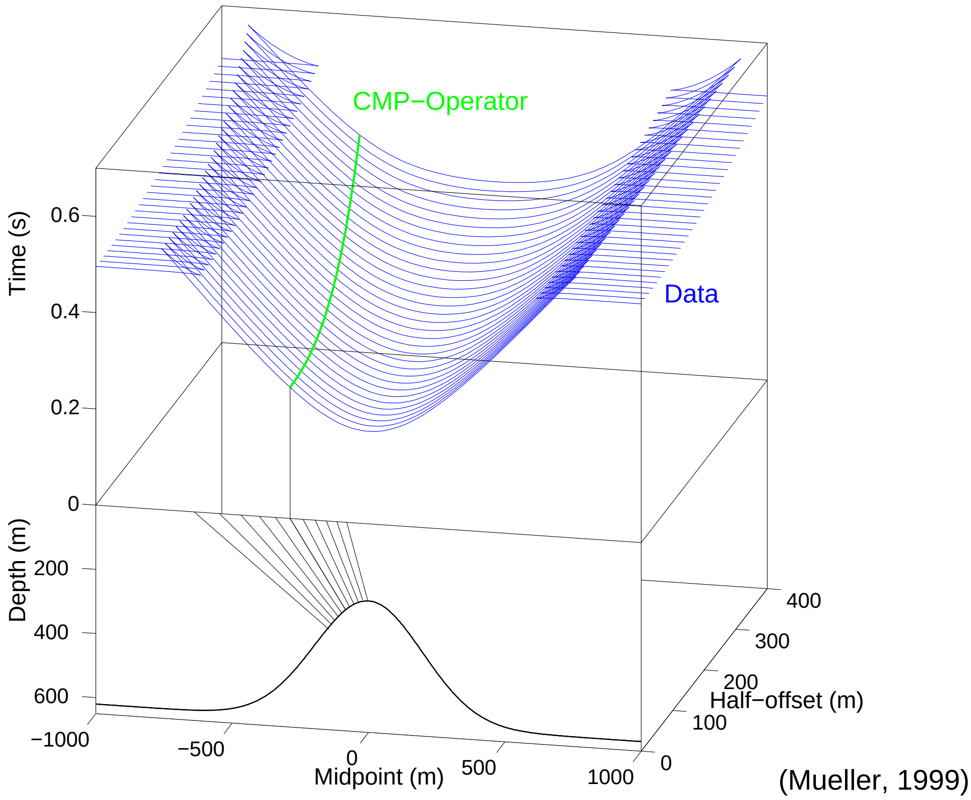

Figure 3.3: Multicoverage data in the midpoint and half-offset domain (blue) and the CMP operator (green), a line along the half-offset direction.

is a processing parameter for the single parameter NMO stack. It contains information about the model, which is, however, not in all cases suited for an inversion process. Only for relatively simple subsurface structures like horizontal or inclined layering is it possible to invert for the model, e.g., by determining interval velocities using the Dix-Dürbaum-Krey formula (Dix, 1955; Hubral and Krey, 1980).

Figure 3.3 shows multicoverage data in the midpoint and half-offset domain and the CMP stacking trajectory. As has already been mentioned above, stacking increases the signal to noise ratio depending on the number of traces. The CMP traveltime curve is but a line. Therefore, it is only logical to conclude that an extension of the stacking curve to a stacking surface, as shown in Figure 3.4 would serve to further increase the signal to noise ratio.

At the same time, we need more than a single parameter to describe said surface. Knowing that the NMO velocity from the single parameter stack can be useful for recovering subsurface information, it is straight forward to assume that the wavefield attributes obtained from a multiparameter stack will be useful not only to gain a simulated zero-offset section with an even higher signal to noise ratio, but also to obtain further information about the subsurface.

One example for such a multiparameter traveltime expression is the Common-Reflection-Surface (CRS) stack. It provides a simulated zero-offset section[1] from seismic multi-coverage reflection data.

[1]The offset situation will be discussed in Section 3.7.

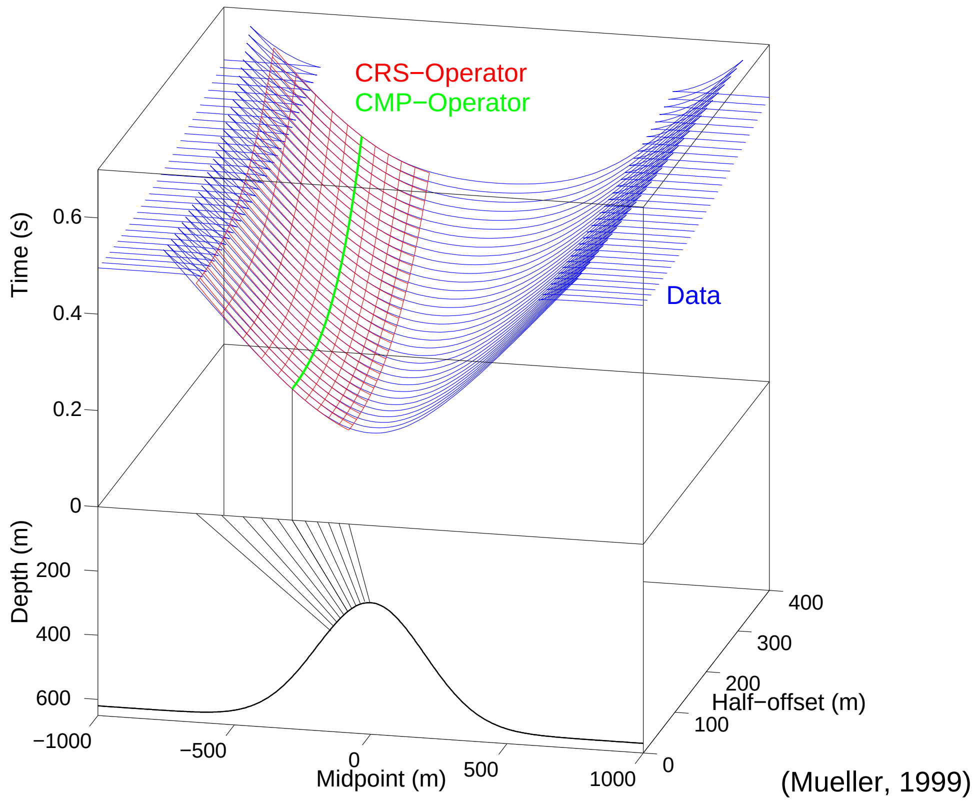

Figure 3.4: Multicoverage data in the midpoint and half-offset domain (blue), CMP operator (green), and the CRS operator (red), a surface in the midpoint and half-offset directions.

In contrast to conventional reflection imaging like NMO-DMO processing or depth migration the CRS stack does not even depend on a macro-velocity model. The output from the zero-offset CRS stack provides three kinematic wavefield attribute sections which can be used for a broad variety of applications. An overview is given by Baykulov et al. (2011). Examples are:

- Simulated ZO-section with high S/N ratio (e.g., Mann, 2002)
- Geometrical spreading (e.g., Mann, 2002)
- Migration weights (e.g., Mann, 2002)
- Fresnel zones (e.g., Vieth, 2001)
- Attribute-based time migration (Mann, 2002; Spinner, 2007)
- Multiple suppression (e.g., Dümmong, 2010)
- CRS supergather (pre-stack data enhancement) (Baykulov and Gajewski, 2009)
- Data regularisation (Baykulov, 2009)
- NIP-wave tomography (Duveneck, 2004)
- Diffractions (e.g., Dell and Gajewski, 2011)

The zero-offset CRS formula (see, e.g., Jäger et al. 2001) is a hyperbolic three-parameter traveltime expression in midpoint and half-offset coordinates. It is closely related to the Polystack (de Bazelaire, 1988) and the multi-focusing operator (Gelchinsky et al., 1999; Landa et al., 2010). Since the CRS stacking surface provides a fit to the reflection events covering a larger area than the 1D stacking trajectories in conventional stacking methods, the resulting simulated zero-offset section is of high quality. The three kinematic attributes for the zero-offset CRS formula are (see Figure 3.5c)

- the emergence angle of the zero-offset ray, β_0,
- the curvature or radius of curvature of a wavefront that corresponds to a wave emitted from a point source at the normal-incidence-point, the emerging normal-incident-point (NIP) wave, $K_{NIP} = 1/R_{NIP}$,
- the curvature or radius of curvature of the emerging normal (N) wave, $K_N = 1/R_N$, a wavefront that corresponds to a wave generated by an exploding reflector element.

These properties will be explained in more detail in Section 3.3. For more details on N and NIP waves, please refer to Hubral (1983). The zero-offset CRS formula is given by (Jäger et al., 2001)

$$T^2_{ZO-CRS} = \left[T_0 + \frac{2\sin\beta_0}{V_0}\,\Delta x_m\right]^2 + \frac{2\,T_0\,\cos^2\beta_0}{V_0}\left[K_N\,\Delta x_m^2 + K_{NIP}\,h^2\right] \quad , \tag{3.1.5}$$

where the velocity V_0 at the zero-offset position in the registration surface is assumed to be known, and $\Delta x_m = x_m - x_0$ is the deviation from the CMP under consideration, x_0.

A derivation of (3.1.5) will be given in Section 3.3. Before getting to the derivation, however, the important concept of model space and image space needs to be introduced, which I will do in the following section.

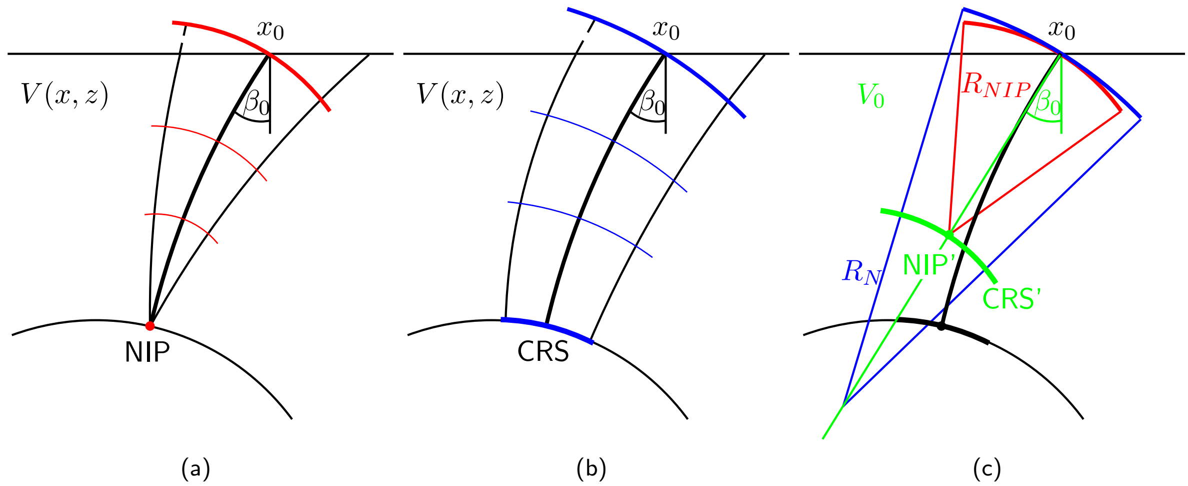

Figure 3.5: (a) NIP experiment in model space, (b) N experiment in model space, (c) image space. (Adapted and extended from Höcht et al., 1999.) The normal incidence point and common reflection surface in the model space are denoted by NIP and CRS, respectively. Their counterparts in image space are distinguished from model space by a prime, i.e., NIP' and CRS'.

3.2 Model space and image space

One important concept of the CRS method is that it is macro-model independent. This concept works because the model space, in which the real wave propagation takes place, can be replaced by an auxiliary medium denoted as image space (Höcht et al., 1999). In contrast to the arbitrarily heterogeneous model, $V(x,z)$, the image space assumes a homogeneous isotropic model with a velocity V_0. In summary, for each CMP, two wavefront curvatures and an angle measured at the registration surface coincide for both spaces and are used to describe the wavefield. I will explain these spaces in more detail in this section.

Figure 3.5 shows rays and wavefronts in the heterogeneous model (a,b) as well as in the homogeneous image space (c). Figure 3.5a describes a fictitious experiment in the model space, where rays emerge from a source located at the normal incident point (NIP) and propagate through the medium with the velocity $V(x,z)$. The wavefront created by this experiment is that of the so-called NIP-wave. It is measured in the registration surface. At the considered CMP location x_0, it has the radius of curvature R_{NIP}. In a second fictitious experiment shown in Figure 3.5b, we consider an exploding reflector element. This curved reflector element is the actual common reflection surface, which led to the name of the CRS method. The wavefront belonging to this so-called normal wave, or short N-wave, is also measured in the registration surface. Its radius is denoted R_N. Finally, the emergence angle β_0 of the central ray from the NIP to the CMP is also taken in the registration surface.

If we replace the heterogeneous medium with a homogeneous auxiliary medium that has the velocity $V_0 = V(x_0, z = 0)$ at the CMP location, we find that the now straight rays corresponding to the angle β_0 and the wavefront radii R_N and R_{NIP} also describe the reflection from a curved interface, denoted by CRS' in Figure 3.5c, with a corresponding normal incidence point at NIP'. Seen from the registration surface, both media are kinematically equivalent for the CMP under consideration in terms of β_0, R_N, and R_{NIP}. It should, however, be noted that although the wavefield parameters β_0, R_N, and R_{NIP} coincide, the zero-offset traveltimes in the real and auxiliary medium are different. Höcht et al. (1999) have shown this for a seismic system, i.e., a system of homogeneous layers, but it is equally applicable for media with arbitrary heterogeneity.

Wave propagation in image space is closely related to time imaging. This enables us to refer to the auxiliary medium or image space for any time processing. As we will see further below, the wavefield properties determined from CRS processing can also be used for velocity model building.

At this point, we should keep in mind that both wavefront curvatures and the angle follow from a one-way process, as we have placed our sources at the NIP/NIP' and CRS/CRS', respectively. This is appropriate as long as we are dealing with kinematic aspects and a zero-offset situation for monotypic waves. In the following section, I will use the image space concept for a geometric derivation of the zero-offset CRS operator.

3.3 Derivation of the CRS operator from geometric considerations

In this section, I derive the CRS operator for monotypic waves from geometric principles. The derivation assumes a one-way process in image space. I begin by considering the Taylor expansion of the traveltime in midpoint and half-offset coordinates, where the derivatives are determined in an approach that is closely related to those suggested by Shah (1973) and Hubral and Krey (1980).

Taylor expansion in midpoint and half-offset coordinates

In midpoint and half-offset coordinates, (x_m, h), the Taylor expansion of the traveltime T up to second order reads

$$T = T_0 + \frac{\partial T}{\partial x_m}\Delta x_m + \frac{\partial T}{\partial h}h + \frac{\partial^2 T}{\partial x_m^2}\Delta x_m^2 + \frac{\partial^2 T}{\partial h^2}h^2 + 2\,\frac{\partial^2 T}{\partial x_m \partial h}\Delta x_m\, h + \mathcal{O}(3) \quad , \tag{3.3.1}$$

where $\Delta x_m = x_m - x_0$ with the CMP position in the expansion point $x_m = x_0, h = 0$, and T_0 is the traveltime in the expansion point. Note that T_0 is the zero-offset traveltime in model space, not image space. The derivatives describe the move-out, which is independent from the space under consideration. Since we are considering monotypic waves, reciprocity applies, meaning that interchange of source and receiver position preserves the traveltime. Interchanging of source and receiver corresponds to changing the sign of the half-offset h. Therefore, $t(x_m, h) = t(x_m, -h)$ must be fulfilled. This requires that

$$\frac{\partial T}{\partial h} = 0 \quad \text{and} \quad \frac{\partial^2 T}{\partial x_m \partial h} = 0 \quad , \tag{3.3.2}$$

and our Taylor expansion reduces to (higher order terms will be neglected from here on):

$$T = T_0 + \frac{\partial T}{\partial x_m}\Delta x_m + \frac{\partial^2 T}{\partial x_m^2}\Delta x_m^2 + \frac{\partial^2 T}{\partial h^2}h^2 \quad . \tag{3.3.3}$$

In the following steps, I will investigate a ZO and a CMP experiment in order to find the partial derivatives that serve as coefficients in (3.3.3).

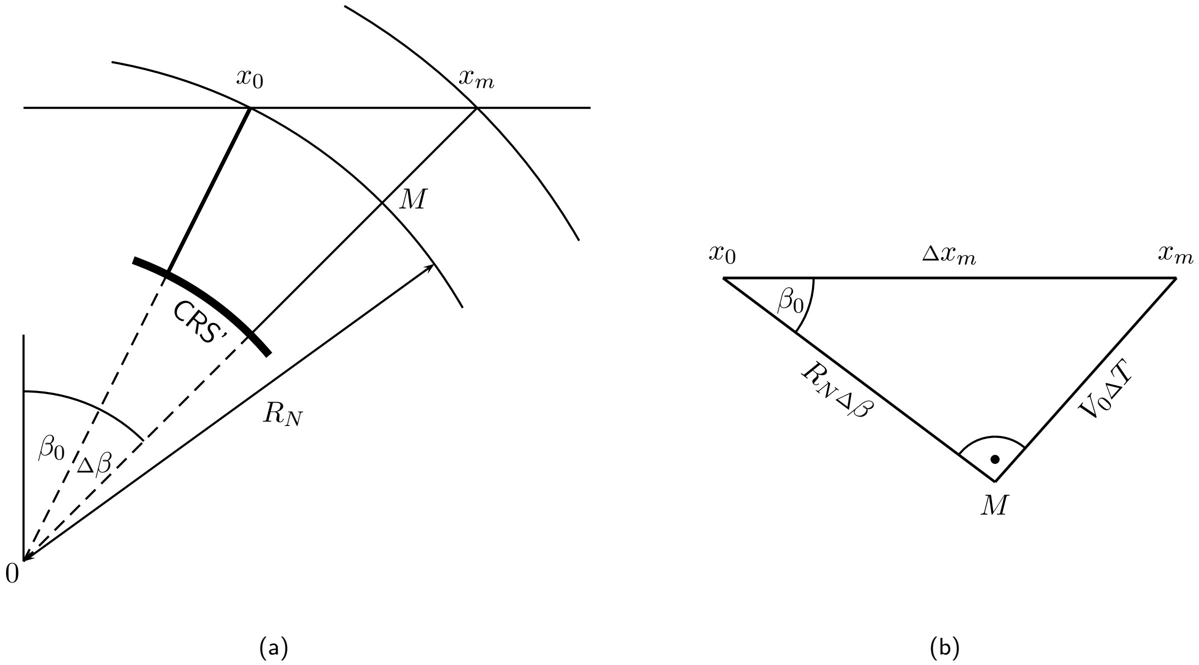

Figure 3.6: Zero-offset experiment: (a) a central ray and a paraxial ray are emitted from a curved reflector element, the image of the Common Reflection Surface, CRS'. (b) Close-up on the triangle $x_0 M x_m$.

Zero-offset experiment

Figure 3.6a shows a curved exploding reflector element in image space, CRS', resulting in two zero-offset rays whose associated wavefronts reach the registration surface at the locations x_0 and $x_m = x_0 + \Delta x_m$. The ray arriving at x_0 is denoted the central ray, whereas the one at x_m is a paraxial ray (see Appendix A). Since we assume that wave propagation takes place in image space, we have a constant velocity V_0 and the centres of both wavefronts coincide at a point 0. The central ray at x_0 arrives with the emergence angle β_0, the paraxial one at x_m with $\beta = \beta_0 + \Delta\beta$. The spatial distance between the two wavefronts at M and x_m is $\overline{M x_m} = V_0 \Delta T$. The radius of curvature of the wavefront of the central ray at x_0 corresponds to the radius of curvature of the normal wave, R_N.

Provided that all distances are small, we can approximately substitute the arc $\widehat{x_0 M} = R_N \, \Delta\beta$ by a straight line $\overline{x_0 M}$ with a length equal to the arc length, i.e., $\overline{x_0 M} = R_N \, \Delta\beta$. Since the rays are perpendicular to the wavefronts, we obtain a triangle $x_0 M x_m$ (see Figure 3.6b) with a right angle at M, $\angle x_0 M x_m$=90°. From the geometry we can see that

$$\sin\beta_0 = \frac{\overline{M x_m}}{\Delta x_m} = \frac{V_0 \, \Delta T}{\Delta x_m} \quad \text{and} \quad \cos\beta_0 = \frac{\overline{x_0 M}}{\Delta x_m} = \frac{R_N \, \Delta\beta}{\Delta x_m} \quad . \tag{3.3.4}$$

If we now let Δx_m go toward zero, we can rewrite these expressions to

$$\sin\beta_0 = V_0 \, \frac{\partial T}{\partial x_m} \quad \text{and} \quad \cos\beta_0 = R_N \, \frac{\partial \beta}{\partial x_m} \quad . \tag{3.3.5}$$

From the first of these, we obtain the first-order derivative $\partial T / \partial x_m$. The second-order derivative[2]

[2] These derivatives differ from the ones in the Taylor expansion (3.3.3) by a factor of two because (3.3.3) describes a two-way process and the derivatives here correspond to a one-way process.

is determined from

$$\frac{\partial^2 T}{\partial x_m^2} = \frac{\partial}{\partial x_m}\left(\frac{\sin\beta}{V_0}\right) = \frac{\cos\beta_0}{V_0}\,\frac{\partial\beta}{\partial x_m} = \frac{\cos^2\beta_0}{V_0\,R_N} \quad , \tag{3.3.6}$$

where the second expression from Equation (3.3.5) was substituted for the derivative of β. Remembering that the derivatives describe the move-out, these expressions lead to the following result for the traveltime:

$$T = T_0 + 2\,\frac{\sin\beta_0}{V_0}\Delta x_m + \frac{\cos^2\beta_0}{V_0\,R_N}\Delta x_m^2 \quad . \tag{3.3.7}$$

As mentioned before, T_0 is the zero-offset traveltime in model space, not image space. The factors of two had to be introduced because the results in this section were derived for a one-way process, whereas the Taylor expansion in (3.3.3) describes a two-way process.

In the next part, I will derive the remaining coefficient in (3.3.3).

CMP experiment

Instead of the ZO experiment in Figure 3.6 in the previous section, we now consider a CMP experiment for the same situation. This is shown in Figure 3.7: three rays are emitted from the image space normal incidence point NIP' to locations $x_0 - h$, x_0, and $x_0 + h$ in the registration surface. Note that the traveltime of the central ray from the NIP' to x_0 in image space is R_{NIP}/V_0, and not $T_0/2$. The traveltimes of the paraxial rays from the NIP to $x_0 \pm h$ are denoted T_1 and T_2, respectively. Their move-outs with respect to x_0 are ΔT_1 and ΔT_2.

We can apply the results from the previous section, namely Equation (3.3.7), to both paraxial rays with $\Delta x_1 = -h$ and $\Delta x_2 = h$. The radius R_N must now be replaced by R_{NIP}, as can be seen in

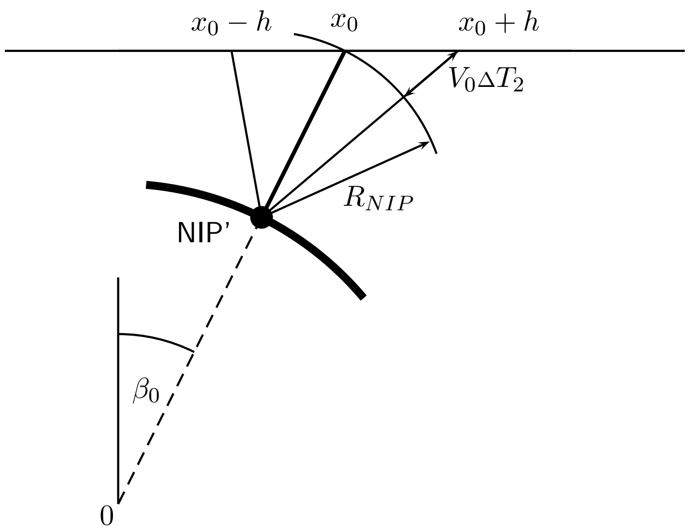

Figure 3.7: CMP experiment: a central ray and two paraxial rays are emitted from the normal incidence point in image space, NIP'.

Figure 3.7. Keeping in mind that (3.3.7) describes a two-way process, we obtain the traveltimes

$$\begin{aligned} \Delta T_1 &= -\frac{\sin\beta_0}{V_0}h + \frac{\cos^2\beta_0}{2\,V_0\,R_{NIP}}h^2 \\ \Delta T_2 &= \frac{\sin\beta_0}{V_0}h + \frac{\cos^2\beta_0}{2\,V_0\,R_{NIP}}h^2 \quad . \end{aligned} \tag{3.3.8}$$

In order to obtain the paraxial traveltime T of the reflected ray from $x_0 - h$ to $x_0 + h$, we add the move-outs ΔT_1 and ΔT_2 to T_0. We can immediately see that the linear terms cancel out, and we obtain the two-way traveltime as a sum of the zero-offset traveltime in model space, T_0, and the move-out in the CMP gather:

$$T = T_0 + \frac{\cos^2\beta_0}{V_0\,R_{NIP}}h^2 \quad . \tag{3.3.9}$$

Parabolic and hyperbolic CRS expressions

Since we see from the results from the previous sections that Equation (3.3.7) depends only on Δx_m and (3.3.9) only on h, we can add them to arrive at the parabolic CRS expression,

$$T = T_0 + 2\,\frac{\sin\beta_0}{V_0}\Delta x_m + \frac{\cos^2\beta_0}{V_0}\left(\frac{\Delta x_m^2}{R_N} + \frac{h^2}{R_{NIP}}\right) \quad . \tag{3.3.10}$$

However, it is well-known that hyperbolic expressions are better suited to approximate traveltimes than parabolic ones. Therefore, Equation (3.3.10) is squared. Neglecting terms of higher order than two leads to the hyperbolic and final CRS formula,

$$T^2 = \left(T_0 + 2\,\frac{\sin\beta_0}{V_0}\Delta x_m\right)^2 + \frac{2\,T_0\,\cos^2\beta_0}{V_0}\left(\frac{\Delta x_m^2}{R_N} + \frac{h^2}{R_{NIP}}\right) \quad . \tag{3.3.11}$$

3.4 Mathematical derivation of the CRS operator

In this section, I provide a mathematical derivation of the CRS formula. Since I will address converted waves later, the derivation is carried out for the case that the velocities of the down- and up-going rays do not coincide; however, this ansatz does not consider directional dependency of the velocities, i.e., anisotropy.

Coordinates and ansatz

In order to derive the CRS traveltime formula, I begin with defining the coordinates, parameters, and angles. They are depicted in Figure 3.8.

The circular reflector is defined by its radius R, the depth of its centre, H, and the lateral coordinate of its centre, x_c (see Figure 3.8a). The acquisition is described by x_1 and x_2, the coordinates of the source and receiver, which are assumed to lie on a flat datum at $z = 0$. The CMP position at which the zero-offset ray emerges is again denoted by x_0, see Figure 3.8b. The quantities $\epsilon_i = x_i - x_0$ are assumed to be small.

It is important to distinguish between the angles α, which describes the point on the circle $(R\sin\alpha, H - R\cos\alpha)$ where the zero-offset reflection takes place, and θ, which describes the point

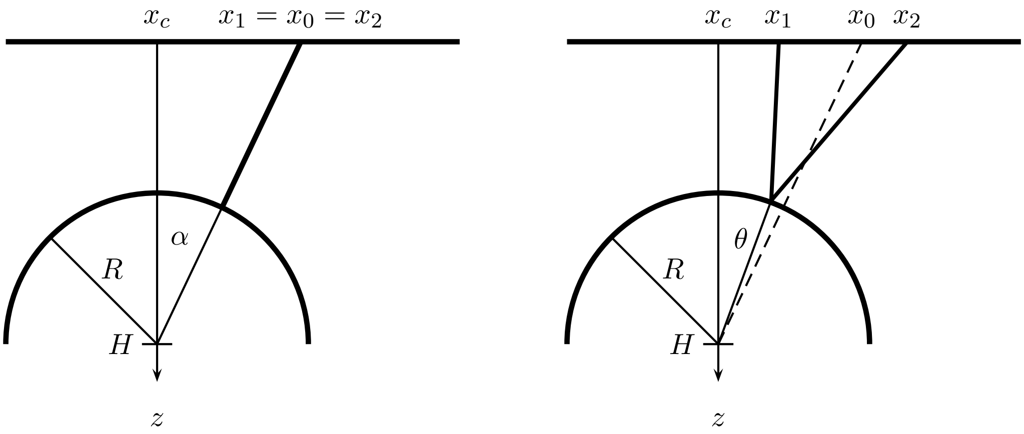

(a) (b)

Figure 3.8: Reflection from a circle with radius R and centre (x_c, H). (a) The angle α describes the point on the circle where the zero-offset reflection takes place. (b) The angle θ describes the reflection point on the circle in the offset case.

on the circle $(R\sin\theta, H - R\cos\theta)$ where the reflection occurs in the offset case.

Furthermore, I introduce the ray length of the one-way zero-offset ray,

$$D = \frac{H}{\cos\alpha} - R \quad . \tag{3.4.1}$$

The zero-offset coordinate is related to the angle α and the depth H by

$$x_0 = H\,\tan\alpha + x_c \quad . \tag{3.4.2}$$

For this geometry, the traveltime in terms of the reflection angle θ, $T(\theta)$ is given by

$$T(\theta) = T_1(\theta) + T_2(\theta) \quad , \tag{3.4.3}$$

where the traveltimes $T_1(\theta)$ and $T_2(\theta)$ are those of the down- and up-going rays, i.e.,

$$T_i(\theta) = \frac{1}{V_i}\sqrt{(x_i - x_c - R\sin\theta)^2 + (H - R\cos\theta)^2} \quad , \tag{3.4.4}$$

or, rewritten in terms of ϵ_i,

$$T_i(\theta) = \frac{1}{V_i}\sqrt{(\epsilon_i + H\tan\alpha - R\sin\theta)^2 + (H - R\cos\theta)^2} \quad . \tag{3.4.5}$$

In the first step of the derivation of the new traveltime expression, I expand $T(\theta)$ in the vicinity of the zero-offset angle α, up to second order:

$$T(\theta) \approx T(\theta=\alpha) + \frac{\partial T(\theta=\alpha)}{\partial\theta}(\theta-\alpha) + \frac{1}{2}\frac{\partial^2 T(\theta=\alpha)}{\partial\theta^2}(\theta-\alpha)^2 \quad . \tag{3.4.6}$$

In order to describe the traveltime of a reflected wave, Snell's law must be fulfilled. This requires that $\partial T(\theta)/\partial\theta = 0$:

$$\frac{\partial T(\theta)}{\partial\theta} \approx \frac{\partial T(\theta=\alpha)}{\partial\theta} + \frac{\partial^2 T(\theta=\alpha)}{\partial\theta^2}(\theta-\alpha) = 0 \quad , \tag{3.4.7}$$

or:

$$\theta - \alpha = -\frac{\partial T(\theta = \alpha)}{\partial \theta} \Bigg/ \frac{\partial^2 T(\theta = \alpha)}{\partial \theta^2} \quad . \tag{3.4.8}$$

Substituting (3.4.8) into (3.4.6), I find that

$$T(\theta) \approx T(\theta = \alpha) - \left[\frac{\partial T(\theta = \alpha)}{\partial \theta}\right]^2 \Bigg/ 2\, \frac{\partial^2 T(\theta = \alpha)}{\partial \theta^2} \quad . \tag{3.4.9}$$

To evaluate (3.4.9), we need to find expressions for $T_i(\theta = \alpha)$, $\partial T_i(\theta = \alpha)/\partial \theta$, and $\partial^2 T_i(\theta = \alpha)/\partial \theta^2$. These will be derived in the following sections.

Derivation of the zero-order term

In this section, I derive an expression of second order in ϵ_i for the traveltime $T_i(\alpha) \equiv T_i(\theta = \alpha)$. I begin by setting $\theta = \alpha$ in (3.4.5) and rewriting it with the help of the expression for D, Equation (3.4.1):

$$\begin{aligned}
T_i(\alpha) &= \frac{1}{V_i}\sqrt{(\epsilon_i + H\tan\alpha - R\sin\alpha)^2 + (H - R\cos\alpha)^2} \\
&= \frac{1}{V_i}\sqrt{\left(\epsilon_i + \left[\frac{H}{\cos\alpha} - R\right]\sin\alpha\right)^2 + (H - R\cos\alpha)^2} \\
&= \frac{1}{V_i}\sqrt{(\epsilon_i + D\sin\alpha)^2 + D^2\cos^2\alpha} \\
&= \frac{1}{V_i}\sqrt{\epsilon_i^2 + 2\,D\epsilon_i\sin\alpha + D^2}
\end{aligned} \tag{3.4.10}$$

In the next step, I expand Equation (3.4.10) until second order in ϵ_i:

$$T_i(\alpha;\epsilon_i) \approx T_i(\alpha;\epsilon_i = 0) + \frac{\partial T_i(\alpha;\epsilon_i = 0)}{\partial \epsilon_i}\,\epsilon_i + \frac{1}{2}\,\frac{\partial^2 T_i(\alpha;\epsilon_i = 0)}{\partial \epsilon_i^2}\,\epsilon_i^2 \tag{3.4.11}$$

For the zero-order term we find

$$T_i(\alpha;\epsilon_i = 0) = \frac{D}{V_i} \quad . \tag{3.4.12}$$

Now I determine the first-order term:

$$\frac{\partial T_i(\alpha;\epsilon_i)}{\partial \epsilon_i} = \frac{\epsilon_i + D\sin\alpha}{V_i^2\,T_i} \quad , \tag{3.4.13}$$

which for $\epsilon_i = 0$ becomes

$$\frac{\partial T_i(\alpha;\epsilon_i = 0)}{\partial \epsilon_i} = \frac{\sin\alpha}{V_i} \quad , \tag{3.4.14}$$

where (3.4.12) was substituted.

For the second-order term, we obtain

$$\begin{aligned}
\frac{\partial^2 T_i(\alpha;\epsilon_i)}{\partial \epsilon_i^2} &= \frac{1}{V_i^2}\,\frac{\partial^2}{\partial \epsilon_i^2}\left(\frac{\epsilon_i + D\sin\alpha}{T_i}\right) \\
&= \frac{1}{V_i^2\,T_i^2}\left(T_i - \frac{(\epsilon_i + D\sin\alpha)^2}{V_i^2\,T_i}\right).
\end{aligned} \tag{3.4.15}$$

Setting $\epsilon_i = 0$ leads to

$$\frac{\partial^2 T_i(\alpha; \epsilon_i = 0)}{\partial \epsilon_i^2} = \frac{1}{D^2} \left(\frac{D^2 - D^2 \sin^2 \alpha}{V_i\, D} \right) = \frac{\cos^2 \alpha}{V_i\, D} \quad . \tag{3.4.16}$$

Substituting these derivatives into Equation (3.4.11) I arrive at a second-order expression in ϵ_i for the traveltime $T_i(\alpha)$:

$$T_i(\alpha) \approx \frac{D}{V_i} \left(1 + \frac{\sin \alpha}{D}\, \epsilon_i + \frac{\cos^2 \alpha}{2\, D^2}\, \epsilon_i^2 \right) \quad . \tag{3.4.17}$$

Derivation of the first-order term

In this section, I derive an expression for the first derivative of the traveltime, $\partial T_i(\theta = \alpha)/\partial\theta$. Using (3.4.5), we find that

$$\begin{aligned} \frac{\partial T_i(\theta)}{\partial \theta} &= \frac{1}{2\, V_i^2\, T_i}\, 2 \left[R \sin\theta (H - R\cos\theta) - R\cos\theta(\epsilon_i + H\tan\alpha - R\sin\theta) \right] \\ &= \frac{R}{V_i^2\, T_i} \left[H\sin\theta - (\epsilon_i + H\tan\alpha)\cos\theta \right] \quad , \end{aligned} \tag{3.4.18}$$

which, for $\theta = \alpha$ reduces to

$$\begin{aligned} \frac{\partial T_i(\theta = \alpha)}{\partial \theta} &= \frac{R}{V_i^2\, T_i} \left[H\sin\alpha - \epsilon_i\cos\alpha - H\sin\alpha \right] \\ &= -\frac{R\cos\alpha}{V_i^2\, T_i}\, \epsilon_i \\ &\approx -\frac{R\cos\alpha}{V_i\, D}\, \epsilon_i \quad . \end{aligned} \tag{3.4.19}$$

The substitution of the last step in (3.4.19) is motivated by the search for a second-order expression and the fact that the first derivative appears in squared form in (3.4.9).

Derivation of the second-order term

In this section, I derive an expression for the second-order derivative of the traveltime, $\partial^2 T_i(\theta = \alpha)/\partial\theta^2$:

$$\begin{aligned} \frac{\partial^2 T_i(\theta)}{\partial \theta^2} &= \frac{R}{V_i^2} \frac{\partial}{\partial\theta} \frac{H\sin\theta - (\epsilon_i + H\tan\alpha)\cos\theta}{T_i} \\ &= \frac{R}{V_i^2\, T_i} \left[H\cos\theta + (\epsilon_i + H\tan\alpha)\sin\theta - \frac{R}{V_i^2\, T_i^2} \Big(H\sin\theta - (\epsilon_i + H\tan\alpha)\cos\theta \Big)^2 \right] \quad . \end{aligned} \tag{3.4.20}$$

Since we are interested in an expansion of $T(\theta)$ up to second order in ϵ_i, we need to consider only constant terms in $\partial^2 T_i(\theta = \alpha)/\partial\theta^2$, as the first-order derivative is linear in ϵ_i and it enters the final traveltime equation in squared form (see (3.4.9)). Therefore, (3.4.20) can be reduced to

$$\frac{\partial^2 T_i(\theta = \alpha)}{\partial \theta^2} \approx \frac{R(R + D)}{V_i\, D} \quad . \tag{3.4.21}$$

Final result in CMP coordinates

Substituting the results from the previous sections, Equations (3.4.17), (3.4.19), and (3.4.21) into (3.4.9), we find that the traveltime expansion up to second order is

$$
\begin{aligned}
T(\theta) \quad &\approx \quad D\left(\frac{1}{V_1}+\frac{1}{V_2}\right)+\sin\alpha\left(\frac{\epsilon_1}{V_1}+\frac{\epsilon_2}{V_2}\right) \\
&\quad +\frac{\cos^2\alpha}{2\,D}\left(\frac{\epsilon_1^2}{V_1}+\frac{\epsilon_2^2}{V_2}\right)-\frac{R\,\cos^2\alpha}{2\,D(R+D)}\,\frac{\left(\frac{\epsilon_1}{V_1}+\frac{\epsilon_2}{V_2}\right)^2}{\frac{1}{V_1}+\frac{1}{V_2}} \quad .
\end{aligned} \tag{3.4.22}
$$

I will now rewrite this result in midpoint and half-offset coordinates, and then reformulate it in CRS parameters. With

$$
\begin{aligned}
\epsilon_1 &= x_m-h-x_0 \\
\epsilon_2 &= x_m+h-x_0
\end{aligned}
$$

I compute

$$
\begin{aligned}
\frac{\epsilon_1}{V_1}+\frac{\epsilon_2}{V_2} &= \frac{x_m-x_0-h}{V_1}+\frac{x_m-x_0+h}{V_2} \\
&= \Delta x_m\left(\frac{1}{V_1}+\frac{1}{V_2}\right)-h\left(\frac{1}{V_1}-\frac{1}{V_2}\right) \quad ;
\end{aligned}
$$

$$
\begin{aligned}
\frac{\epsilon_1^2}{V_1}+\frac{\epsilon_2^2}{V_2} &= \frac{\Delta x_m^2+h^2-2\,h\,\Delta x_m}{V_1}+\frac{\Delta x_m^2+h^2+2\,h\,\Delta x_m}{V_2} \\
&= \Delta x_m^2\left(\frac{1}{V_1}+\frac{1}{V_2}\right)+h^2\left(\frac{1}{V_1}+\frac{1}{V_2}\right)-2\,h\,\Delta x_m\left(\frac{1}{V_1}-\frac{1}{V_2}\right) \quad ;
\end{aligned}
$$

$$
\left(\frac{\epsilon_1}{V_1}+\frac{\epsilon_2}{V_2}\right)^2 = \Delta x_m^2\left(\frac{1}{V_1}+\frac{1}{V_2}\right)^2+h^2\left(\frac{1}{V_1}-\frac{1}{V_2}\right)^2-2\,h\,\Delta x_m\left(\frac{1}{V_1}+\frac{1}{V_2}\right)\left(\frac{1}{V_1}-\frac{1}{V_2}\right) \quad .
$$

Now I introduce the abbreviations

$$
\frac{2}{V^{\pm}}=\frac{1}{V_1}\pm\frac{1}{V_2}
$$

and evaluate (3.4.22) in terms of the powers of Δx_m and h:

$$\begin{aligned}
const. &: \frac{2\,D}{V^+} \\
\Delta x_m &: \frac{2\,\sin\alpha}{V^+} \\
h &: \frac{-2\,\sin\alpha}{V^-} \\
\Delta x_m^2 &: \frac{\cos^2\alpha}{V^+(R+D)} \\
h^2 &: \frac{\cos^2\alpha}{V^+\,D} - \frac{V^+\,R\,\cos^2\alpha}{(V^-)^2\,D\,(R+D)} \\
\Delta x_m\,h &: \frac{-2\,\cos^2\alpha}{V^-(R+D)}
\end{aligned}$$

In order to express these coefficients by the CRS parameters β_0, R_{NIP}, and R_N, I consider the monotypic case, where $V_1 = V_2 = V_0$, leading to $V^+ = V_0$, and $1/V^- = 0$. By comparison with the (parabolic) CRS formula we see immediately that

$$\beta_0 = \alpha \quad , \tag{3.4.23a}$$

$$R_{NIP} = D \quad , \tag{3.4.23b}$$

$$R_N = D + R \quad . \tag{3.4.23c}$$

Note that this result also follows from geometrical considerations (see Figure 3.8).

With (3.4.23), the coefficients for the (parabolic) CRS equation for converted waves become

$$\begin{aligned}
T_0 &: \frac{2\,R_{NIP}}{V^+} \\
\Delta x_m &: \frac{2\,\sin\beta_0}{V^+} \\
h &: \frac{-2\,\sin\beta_0}{V^-} \\
\Delta x_m^2 &: \frac{\cos^2\beta_0}{V^+\,R_N} \\
h^2 &: \frac{\cos^2\beta_0}{V^+\,R_{NIP}} - \frac{\cos^2\beta_0}{V^-}\left(\frac{R_N - R_{NIP}}{R_N\,R_{NIP}}\right)\frac{V^+}{V^-} \\
\Delta x_m\,h &: \frac{-2\,\cos^2\beta_0}{V^-\,R_N}
\end{aligned}$$

In order to obtain a hyperbolic traveltime expression, I square the parabolic formula and neglect terms of higher order than two. This leads us to the final equation,

$$\begin{aligned} T^2 &\approx \left(T_0 + \frac{2\,\sin\beta_0}{V^+}\,\Delta x_m - \frac{2\,\sin\beta_0}{V^-}\,h\right)^2 \\ &\quad +2\,T_0\cos^2\beta_0\left(\frac{\Delta x_m^2}{V^+R_N} + \frac{h^2}{V^+R_{NIP}}\right) \\ &\quad -2\,T_0\cos^2\beta_0\left(\frac{(R_N - R_{NIP})}{R_N R_{NIP}}\frac{V^+\,h^2}{(V^-)^2} + \frac{2\,\Delta x_m\,h}{V^-R_N}\right) \end{aligned} \tag{3.4.24}$$

Note that in addition to the velocities, only three parameters are required. The reason is that in my derivation, I have assumed a constant ratio of V_p/V_s. In this case, the zero-offset reflections stem from the same subsurface point for monotypic as for converted waves. Bergler et al.'s equation (2002) has five independent parameters because it is not restricted by such an assumption.

Equation (3.4.24) includes the monotypic case as a subset with $V^+ = V_0$ and $1/V^- = 0$. It can therefore be simplified to

$$T^2 \approx \left(T_0 + \frac{2\,\sin\beta_0}{V_0}\,\Delta x_m\right)^2 + 2\,\frac{T_0\cos^2\beta_0}{V_0}\left(\frac{\Delta x_m^2}{R_N} + \frac{h^2}{R_{NIP}}\right) \quad . \tag{3.4.25}$$

Result in γ-CMP coordinates

The choice of an alternate coordinate system can lead to a considerable simplification of (3.4.24). Abakumov et al. (2011) have introduced γ-CMP coordinates, i.e.,

$$\tilde{x}_m = \frac{x_1 + \gamma x_2}{1+\gamma} \qquad \tilde{h} = \frac{x_2 - x_1}{1+\gamma} \quad , \tag{3.4.26}$$

where $\gamma = V_1/V_2$. With these coordinates, we can express ϵ_1 and ϵ_2 as

$$\begin{aligned} \epsilon_1 &= \tilde{x}_m - x_0 - \gamma\tilde{h} \\ \epsilon_2 &= \tilde{x}_m - x_0 + \tilde{h} \quad . \end{aligned} \tag{3.4.27}$$

As for the 'standard' CMP coordinates, we formulate

$$\frac{\epsilon_1}{V_1} + \frac{\epsilon_2}{V_2} \quad , \qquad \frac{\epsilon_1^2}{V_1} + \frac{\epsilon_2^2}{V_2} \quad , \qquad \left(\frac{\epsilon_1}{V_1} + \frac{\epsilon_2}{V_2}\right)^2$$

in terms of γ-CMP coordinates:

$$\begin{aligned} \frac{\epsilon_1}{V_1} + \frac{\epsilon_2}{V_2} &= (\tilde{x}_m - x_0)\left(\frac{1}{V_1} + \frac{1}{V_2}\right) \quad ; \\ \frac{\epsilon_1^2}{V_1} + \frac{\epsilon_2^2}{V_2} &= \left((\tilde{x}_m - x_0)^2 + \gamma\tilde{h}^2\right)\left(\frac{1}{V_1} + \frac{1}{V_2}\right) \quad ; \\ \left(\frac{\epsilon_1}{V_1} + \frac{\epsilon_2}{V_2}\right)^2 &= (\tilde{x}_m - x_0)^2\left(\frac{1}{V_1} + \frac{1}{V_2}\right)^2 \quad . \end{aligned}$$

Substituting these expressions and the representation of the CRS parameters, (3.4.23), into (3.4.22), we find after some algebra that the linear term in $\tilde{h}$ vanishes, as well as the mixed quadratic term $(\tilde{x}_m - x_0)\tilde{h}$. The final (hyperbolic) result is

$$T^2 \approx \left(T_0 + \frac{2\,\sin\beta_0}{V^+}\,(\tilde{x}_m - x_0)\right)^2 + 2\,T_0\cos^2\beta_0\left(\frac{(\tilde{x}_m - x_0)^2}{V^+ R_N} + \frac{\gamma\tilde{h}^2}{V^+ R_{NIP}}\right) \quad . \tag{3.4.28}$$

This equation is identical to the one derived by Abakumov et al. (2011). It is also formally identical to the monotypic CRS expression in standard CMP coordinates: for $V_1 = V_2$ the γ-CMP and standard CMP coordinates coincide, and (3.4.28) reduces to the original, i.e., monotypic, CRS expression.

The wavefield attributes β_0, R_N, and R_{NIP} are determined from data. The following section addresses corresponding search strategies.

3.5 CRS parameter determination

The 2D zero-offset CRS formula has three parameters. For the offset situation, the number of parameters is five in 2D. In 3D, we have eight parameters in the zero-offset case and fourteen for common offsets. It is easy to see that a simultaneous search for at most fourteen independent parameters is not feasible. Even in the 2D zero-offset situation, it is sensible to develop an efficient search strategy. This has already been recognised when the CRS method was introduced. In the following, I will describe the pragmatic search strategy for the 2D zero-offset CRS as it was published by, e.g., Jäger et al. (2001).

The strategy makes use of the fact that the searches in midpoint and half-offset direction can be decoupled. For example, in the CMP domain with $\Delta x_m = 0$ the zero-offset formula (3.3.11) reduces to the well-known CMP hyperbola (3.1.4) with

$$T^2(h) = T_0^2 + \frac{2\,T_0\cos^2\beta_0}{V_0}\,\frac{h^2}{R_{NIP}} \quad , \tag{3.5.1}$$

whereas in the ZO domain with $h = 0$ (3.3.11) becomes

$$T^2(\Delta x_m) = \left(T_0 + 2\,\frac{\sin\beta_0}{V_0}\,\Delta x_m\right)^2 + \frac{2\,T_0\cos^2\beta_0}{V_0}\,\frac{\Delta x_m^2}{R_N} \quad . \tag{3.5.2}$$

Equations (3.5.1) and (3.5.2) permit to split the search procedure into three search steps:

Step 1: automatic CMP stack

In this initial step, the parameter search is carried out in the CMP domain according to Equation (3.5.1). By defining a new interim parameter q[3] as a combined parameter of β_0 and R_{NIP},

$$q = \frac{\cos^2\beta_0}{R_{NIP}} \quad , \tag{3.5.3}$$

and comparison with the NMO Equation (3.1.4), we see that the parameter q relates to the NMO velocity as

$$q = 2\,\frac{V_0}{T_0\,V_{NMO}^2} \quad . \tag{3.5.4}$$

[3]This parameter is not to be confused with the slowness component q used in other parts of this thesis.

In other words, the search for the combined parameter q corresponds to a CMP stack: the data are stacked along the traveltime trajectory given by (3.5.1), while the semblance for each value of q is computed. Analysis of the semblance then leads to the q that best fits the data in the CMP domain.

The stacking result from the automatic CMP stack is a simulated zero-offset section and already provides a first image.

Step 2: Zero-offset stack

The second step is carried out in the simulated zero-offset section obtained in the first step. There are two possible approaches:

1. a two-parametric search according to (3.5.2), where the parameters β_0 and R_N are determined simultaneously by evaluating the semblance, or,

2. the search can be split into two one-parametric searches. In this case, the radius R_N is first set to infinity, i.e., (3.5.2) reduces to

$$T(\Delta x_m) = T_0 + 2\,\frac{\sin\beta_0}{V_0}\,\Delta x_m \quad . \tag{3.5.5}$$

   This means that plane waves are assumed in this step, and the search is restricted to small values of Δx_m. Once the angle β_0 has been determined, Equation (3.5.2) is used in full to find the R_N that best fits the data.

Step 3: Global or final optimisation

The first two steps serve mainly to determine suitable starting values for a simultaneous three-parametric search, which is the third step in the pragmatic search strategy.

With computer resources increasing over the past years, the pragmatic strategy has lost some of its former importance, in particular when it became apparent that results from the simultaneous optimisation are superior to results from the pragmatic search (P. Marchetti, personal communication). However, with respect to 3D offset CRS, the need for efficient search strategies has not yet become obsolete.

Meanwhile, not only search strategies are investigated, but also the means of evaluating the stack results. For example, Das and Gajewski (2011) have compared different measures of coherence for velocity analysis. Another important issue is the optimisation algorithm that is applied for the search. So far, the searches have been conducted using algorithms based on the Nelder-Mead technique (Nelder and Mead, 1965). Minarto (2012) demonstrates that a hybrid method applying a conjugate gradient scheme may be better-suited than the simplices used in the Nelder-Mead approach.

In the next section, I will introduce an alternative formulation of a hyperbolic operator, based on the results from Chapter 2, for the description of traveltime surfaces that is suited for monotypic as well as converted waves, and in any measurement configuration.

3.6 The general NMO operator

In Section 2.8 I have shown how the parabolic traveltime expansion, Equation (2.1.4), can also be applied to reflection traveltimes. Similarly, the hyperbolic traveltime expansion, Equation (2.2.2), can be rewritten for reflection traveltimes. Whereas the classical $T^2 - X^2$ method was derived for horizontally stratified media, the hyperbolic traveltime expansion resulting from Equation (2.2.2) can be considered as an extension of the $T^2 - X^2$ method to arbitrary 3-D heterogeneous media. Since no assumptions were made on the model in the derivation of Equation (2.2.2), it even applies to anisotropic media.

In the following I assume that the registration surface in which sources and receivers are located coincides with the x-y plane of the hyperbolic traveltime expansion given by (2.2.2). With the Δz components of the source and receiver coordinates equal to zero, Equation (2.2.2) for the reflection traveltime becomes

$$T^2(\boldsymbol{s},\boldsymbol{g}) = \left(T_0 - \boldsymbol{p}_0^\top \Delta\boldsymbol{s} + \boldsymbol{q}_0^\top \Delta\boldsymbol{g}\right)^2 + T_0 \left(-2\,\Delta\boldsymbol{s}^\top \underline{\mathsf{N}}\,\Delta\boldsymbol{g} - \Delta\boldsymbol{s}^\top \underline{\mathsf{S}}\,\Delta\boldsymbol{s} + \Delta\boldsymbol{g}^\top \underline{\mathsf{G}}\,\Delta\boldsymbol{g}\right) \quad . \qquad (3.6.1)$$

Vectors and matrices are defined in the recording surface and have dimension two. Equation (3.6.1) is valid in arbitrary, including anisotropic, 3-D media. Regardless of the wave type it applies to monotypic reflections (PP, SS) as well as to converted waves (PS, SP). It is, therefore, a *general* hyperbolic move-out equation.

Midpoint and half-offset coordinates

Equation (3.6.1) can be rewritten for the use of midpoint and half-offset coordinates. The midpoint coordinate is

$$\boldsymbol{x}_m = \frac{\boldsymbol{g}+\boldsymbol{s}}{2} \quad , \qquad (3.6.2)$$

and the half-offset coordinate is

$$\boldsymbol{h} = \frac{\boldsymbol{g}-\boldsymbol{s}}{2} \quad . \qquad (3.6.3)$$

Substituting these into (3.6.1) leads to

$$\begin{aligned} T^2 \;=\; & \left(T_0 + (\boldsymbol{q}_0+\boldsymbol{p}_0)^\top \Delta\boldsymbol{x}_m + (\boldsymbol{q}_0-\boldsymbol{p}_0)^\top \Delta\boldsymbol{h}\right)^2 + 2\,T_0\,\Delta\boldsymbol{h}^\top \left(\underline{\mathsf{G}} + \underline{\mathsf{S}} - 2(\underline{\mathsf{N}}^\top - \underline{\mathsf{N}})\right) \Delta\boldsymbol{x}_m \\ & + T_0\,\Delta\boldsymbol{x}_m^\top (\underline{\mathsf{G}} - \underline{\mathsf{S}} - 2\underline{\mathsf{N}})\,\Delta\boldsymbol{x}_m \;+\; T_0\,\Delta\boldsymbol{h}^\top (\underline{\mathsf{G}} - \underline{\mathsf{S}} + 2\underline{\mathsf{N}})\,\Delta\boldsymbol{h} \quad . \end{aligned} \qquad (3.6.4)$$

Equation (3.6.4) will now be investigated for the CMP and zero-offset configurations.

Arbitrary medium in CMP configuration

For the CMP configuration $\Delta\boldsymbol{s} = -\Delta\boldsymbol{g}$. The CMP coordinates for a 3-D medium are the offset r and the azimuth angle φ. They relate to the vectors $\Delta\boldsymbol{s}$ and $\Delta\boldsymbol{g}$ as follows:

$$\begin{aligned} -\Delta s_x =& \Delta g_x = \frac{r}{2}\cos\varphi \\ -\Delta s_y =& \Delta g_y = \frac{r}{2}\sin\varphi \quad . \end{aligned} \qquad (3.6.5)$$

Substituting these into the hyperbolic traveltime expansion and introducing the abbreviations

$$P = \frac{1}{2}\left[(p_x + q_x)\cos\varphi + (p_y + q_y)\sin\varphi\right] \tag{3.6.6}$$

$$N = \frac{1}{4}\Big[(G_{xx} - S_{xx} + 2N_{xx})\cos^2\varphi + (G_{yy} - S_{yy} + 2N_{yy})\sin^2\varphi$$
$$+2\,(G_{xy} - S_{xy} + N_{xy} + N_{yx})\sin\varphi\,\cos\varphi\Big] \tag{3.6.7}$$

leads to

$$\begin{aligned} T^2 &= (T_0 + Pr)^2 + T_0 N r^2 \\ &= T_0^2 + 2T_0 P r + (P^2 + T_0 N)\, r^2 \quad . \end{aligned} \tag{3.6.8}$$

This equation is generally valid for the CMP configuration, regardless of the model under consideration. It is even valid for converted waves. It is the equation of a shifted hyperbola.

Zero-offset situation for a monotypic wave

Here the hyperbolic equation must be symmetric with respect to exchange of $\Delta\boldsymbol{s}$ and $\Delta\boldsymbol{g}$. This requires that

$$\begin{aligned} \boldsymbol{q}_0 &= -\boldsymbol{p}_0 \\ \underline{\mathsf{G}} &= -\underline{\mathsf{S}} \\ \underline{\mathsf{N}} &= \underline{\mathsf{N}}^\top \quad . \end{aligned} \tag{3.6.9}$$

Therefore Equation (3.6.1) reduces to

$$T^2 = \left(T_0 + \boldsymbol{q}_0^\top(\Delta\boldsymbol{s} + \Delta\boldsymbol{g})\right)^2 + T_0\,\left((\Delta\boldsymbol{s} + \Delta\boldsymbol{g})^\top \underline{\mathsf{G}}\,(\Delta\boldsymbol{s} + \Delta\boldsymbol{g}) - 2\Delta\boldsymbol{s}^\top(\underline{\mathsf{G}} + \underline{\mathsf{N}})\Delta\boldsymbol{g}\right) \quad . \tag{3.6.10}$$

It can also be expressed in midpoint and half-offset coordinates:

$$T^2 = \left[T_0 + 2\boldsymbol{q}_0^\top \Delta\boldsymbol{x}_m\right]^2 + 2T_0\,\left[\Delta\boldsymbol{x}_m^\top(\underline{\mathsf{G}} - \underline{\mathsf{N}})\,\Delta\boldsymbol{x}_m + \Delta\boldsymbol{h}^\top(\underline{\mathsf{G}} + \underline{\mathsf{N}})\Delta\boldsymbol{h}\right] \quad . \tag{3.6.11}$$

Zero-offset CMP configuration

Using again the symmetric properties for zero-offset and monotypic waves given by (3.6.9), Equation (3.6.8) can be simplified to

$$T^2 = T_0^2 + T_0\,N\,r^2 \quad , \tag{3.6.12}$$

where N is

$$N = \frac{1}{2}\,\left[(G_{xx} + N_{xx})\cos^2\varphi + (G_{yy} + N_{yy})\sin^2\varphi + 2\,(G_{xy} + N_{xy})\sin\varphi\,\cos\varphi\right] \quad . \tag{3.6.13}$$

Comparing Equation (3.6.12) to the NMO Equation (3.1.4) rewritten to midpoint and half-offset coordinates

$$T^2 = T_0^2 + \frac{r^2}{V_{NMO}^2} \quad , \tag{3.6.14}$$

leads to an expression for the NMO velocity in terms of second order traveltime derivatives:

$$V_{NMO}^2 = \frac{1}{T_0 N} \quad . \tag{3.6.15}$$

For a $V(z)$ (homogeneously layered) medium N can be further simplified: in this case the matrices $\underline{\mathsf{G}}$ and $\underline{\mathsf{N}}$ are identical. The mixed components N_{xy} vanish and $N_{xx} = N_{yy} = N$.

Examples for the zero-offset CMP configuration

For a homogeneous medium with the velocity V_0 and a single horizontal reflector at the depth z_0 the traveltime is

$$T = \frac{1}{V_0} \sqrt{(g_x - s_x)^2 + (g_y - s_y)^2 + 4 z_0^2} \quad . \tag{3.6.16}$$

The second order derivatives are given by

$$N = \frac{1}{2\, V_0\, z_0} \quad . \tag{3.6.17}$$

The T_0 time is the two-way-traveltime

$$T_0 = \frac{2\, z_0}{V_0} \quad . \tag{3.6.18}$$

From this follows Equation (3.6.15) with $V_{NMO} = V_0$. For a layered medium above the reflector the NMO velocity becomes V_{RMS}. This corresponds to Equation (3.1.1), the $T^2 - X^2$ equation.

For a 2-D homogeneous model with an inclined reflector (inclination angle ϑ) and s_x and g_x the distances of the source and receiver to the point where the reflector intersects the x-surface, the traveltime is

$$T = \frac{1}{V_0} \sqrt{(g_x - s_x)^2 + 4\, g_x\, s_x \sin^2 \vartheta} \quad . \tag{3.6.19}$$

The second derivative $N = N_{xx}$ for $s_x = g_x = x$ is

$$N = \frac{1}{2\, V_0\, x} \frac{\cos^2 \vartheta}{\sin \vartheta} \tag{3.6.20}$$

and furthermore with

$$T_0 = \frac{2\, x \sin \vartheta}{V_0} \quad , \tag{3.6.21}$$

the NMO velocity is

$$V_{NMO} = \frac{V_0}{\cos \vartheta} \quad . \tag{3.6.22}$$

3.7 Equivalence of the general NMO and the CRS operator

In this section, I take a closer look at several special situations and compare the CRS and the general NMO operators. I begin with the zero-offset CRS, followed by the offset CRS formulation for monotypic waves and the CRS formula for converted waves.

Zero-offset CRS operator for monotypic waves

The zero-offset CRS expression derived in Equations (3.3.11) and (3.4.25) is equivalent to the 2-D variant of Equation (3.6.11), i.e.,

$$\begin{aligned} T^2 &= (T_0 + 2\, q_0\, \Delta x_m)^2 + 2\, T_0 [(G - N)\, \Delta x_m^2 + (G + N)\, h^2] \\ &= \left(T_0 + \frac{2\, \sin \beta_0}{V_0}\, \Delta x_m\right)^2 + 2\, \frac{T_0 \cos^2 \beta_0}{V_0} \left(\frac{\Delta x_m^2}{R_N} + \frac{h^2}{R_{NIP}}\right) \quad . \end{aligned} \tag{3.7.1}$$

Comparison of the coefficients yields immediately that $q_0 = \sin\beta_0/V_0$ and

$$
\begin{aligned}
K_{\mathrm{N}} &= \frac{V_0}{\cos^2\beta_0}\,(G-N) \qquad N = \frac{\cos^2\beta_0}{2\,V_0}\,(K_{NIP}-K_N) \\
K_{NIP} &= \frac{V_0}{\cos^2\beta_0}\,(G+N) \qquad G = \frac{\cos^2\beta_0}{2\,V_0}\,(K_{NIP}+K_N) \quad .
\end{aligned} \tag{3.7.2}
$$

Common-offset CRS operator for monotypic waves

The common-offset CRS formula is an extension of Equation (3.1.5) which yields a simulated common-offset section (Zhang et al., 2001). It uses the following five kinematic attributes

- the emergence angle at the source, β_s,
- the incidence angle at the receiver, β_g,
- the wavefront curvature K^G_{CS} of a wave generated by a point source at the source position and measured at the receiver position, corresponding to a common-shot experiment,
- the wavefront curvature K^G_{CMP} of a wave from a fictitious CMP experiment, measured at the receiver,
- the wavefront curvature K^S_{CMP} of a wave from a fictitious CMP experiment, measured at the source.

The common-offset CRS formula is given by (Zhang et al., 2001)

$$
\begin{aligned}
T^2_{CO-CRS} &= \left[T_0 + \left(\frac{\sin\beta_g}{V_g} - \frac{\sin\beta_s}{V_s}\right)\Delta x_m + \left(\frac{\sin\beta_g}{V_g} + \frac{\sin\beta_s}{V_s}\right)\Delta h\right]^2 \\
&\quad + T_0\left[\left(4\,K^G_{CS} - 3K^G_{CMP}\right)\frac{\cos^2\beta_g}{V_g} - K^{\mathrm{S}}_{CMP}\frac{\cos^2\beta_s}{V_s}\right]\Delta x_m^2 \\
&\quad + T_0\left[K^G_{CMP}\frac{\cos^2\beta_g}{V_g} - K^{\mathrm{S}}_{CMP}\frac{\cos^2\beta_s}{V_s}\right]\,h^2 \\
&\quad + 2T_0\left[K^G_{CMP}\frac{\cos^2\beta_g}{V_g} + K^{\mathrm{S}}_{CMP}\frac{\cos^2\beta_s}{V_s}\right]\,h\,\Delta x_m
\end{aligned} \tag{3.7.3}
$$

where the velocities V_g and V_s at the registration surface are again assumed to be known a priori.

Equation (3.7.3) is equivalent to the 2-D variant of Equation (3.6.4),

$$
\begin{aligned}
T^2 &= (T_0 + (q_0 - p_0)\,\Delta x_m + (q_0 + p_0)\,h)^2 + 2T_0(G+S)\Delta x_m\,h \\
&\quad + T_0[(G-S-2N)\,\Delta x_m^2 + (G-S+2N)\,h^2] \quad .
\end{aligned} \tag{3.7.4}
$$

Again, comparison of the coefficients leads to the following correspondences: $q_0 = \sin\beta_g/V_g$, $p_0 = \sin\beta_s/V_s$, and

$$
\begin{aligned}
K^S_{CMP} &= \frac{V_s}{\cos^2\beta_s}\,(S-N) \\
K^G_{CMP} &= \frac{V_g}{\cos^2\beta_g}\,(G+N) \\
K^G_{CS} &= \frac{V_g}{\cos^2\beta_g}\,G \quad .
\end{aligned}
\tag{3.7.5}
$$

The inverse relations between G, N, S and K^S_{CMP}, K^G_{CMP}, and K^G_{CS} are

$$
\begin{aligned}
G &= \frac{\cos^2\beta_g}{V_g}\,K^G_{CS} \\
N &= \frac{\cos^2\beta_g}{V_g}\,\left(K^G_{CMP} - K^{\mathrm{G}}_{CS}\right) \\
S &= \frac{\cos^2\beta_s}{V_s}\,K^S_{CMP} + \frac{\cos^2\beta_g}{V_g}\,\left(K^G_{CMP} - K^{\mathrm{G}}_{CS}\right) \quad .
\end{aligned}
\tag{3.7.6}
$$

Of course, the common-offset CRS formula, Equation (3.7.3) is also applicable to the zero-offset situation, where $q_0{=}{-}p_0$ and $G{=}{-}S$, see (3.6.9). The relationships between the CRS attributes are in this case given by

$$
\begin{aligned}
\beta_g &= -\beta_s \quad = \quad \beta_0 \\
K^G_{CS} &= \frac{K_{NIP}+K_N}{2} \\
K^G_{CMP} &= -K^S_{CMP} \quad = \quad K_{NIP} \quad .
\end{aligned}
\tag{3.7.7}
$$

CRS Formula for converted waves

Even for the zero-offset case of a converted wave, five parameters are required to describe the traveltime surface in two dimensions. This follows immediately because interchanging the source and receiver coordinates does not preserve the ray paths, and thus not the traveltime. The symmetry relations (3.6.9) no longer apply. In terms of a Taylor expansion in midpoint and half-offset coordinates, this means that the mixed second-order derivative and the first derivative with respect to h no longer vanish, as was the case in our derivation in Section 3.3.

Bergler et al. (2002) have introduced a CRS formula for converted waves. They parametrise their operator in terms of Bortfeld matrices (see Bortfeld, 1989 and Appendix A). It reads

$$
\begin{aligned}
T^2(\Delta x_m, h) &= \left[T_0 + \left(\frac{\sin\beta_S}{V_S} + \frac{\sin\beta_P}{V_P}\right)\Delta x_m + \left(\frac{\sin\beta_S}{V_S} - \frac{\sin\beta_P}{V_P}\right) h\right]^2 \\
&+ \; 2\,T_0\,\left(DB^{-1} - B^{-1}A\right)\Delta x_m h \\
&+ \; T_0\,\left(B^{-1}A + DB^{-1} - 2\,B^{-1}\right)\Delta x_m^2 \\
&+ \; T_0\,\left(B^{-1}A + DB^{-1} + 2\,B^{-1}\right) h^2 \quad .
\end{aligned}
\tag{3.7.8}
$$

This formulation is equivalent to the 2D version of the general NMO Equation (3.6.4) with

$$\begin{aligned}
\left(\frac{\sin\beta_S}{V_S} + \frac{\sin\beta_P}{V_P}\right) &= q_0 + p_0 \\
\left(\frac{\sin\beta_S}{V_S} - \frac{\sin\beta_P}{V_P}\right) &= q_0 - p_0 \\
\left(DB^{-1} - B^{-1}A\right) &= G + S \\
\left(B^{-1}A + DB^{-1} - 2\,B^{-1}\right) &= G - S - 2N \\
\left(B^{-1}A + DB^{-1} + 2\,B^{-1}\right) &= G - S + 2N \quad . \qquad (3.7.9)
\end{aligned}$$

If the V_P/V_S ratio is constant throughout the medium, the second-order terms in this equation can be expressed in terms of zero-offset monotypic CRS parameters as shown in Section 3.4. This is possible because in this case, the zero-offset ray paths of the PP and the PS reflection coincide. We then find that

$$\begin{aligned}
\left(\frac{\sin\beta_S}{V_S} + \frac{\sin\beta_P}{V_P}\right) &= \frac{2\,\sin\beta_0}{V^+} \\
\left(\frac{\sin\beta_S}{V_S} - \frac{\sin\beta_P}{V_P}\right) &= \frac{-2\,\sin\beta_0}{V^-} \\
\left(DB^{-1} - B^{-1}A\right) &= -\frac{2\,\cos^2\beta_0}{V^-\,R_N} \\
\left(B^{-1}A + DB^{-1} - 2\,B^{-1}\right) &= \frac{2\,\cos^2\beta}{V^+\,R_N} \\
\left(B^{-1}A + DB^{-1} + 2\,B^{-1}\right) &= \frac{2\,\cos^2\beta_0}{V^+\,R_{NIP}} - \frac{2\,\cos^2\beta_0}{V^-}\left(\frac{R_N - R_{NIP}}{R_N\,R_{NIP}}\right)\frac{V^+}{V^-} \quad . \qquad (3.7.10)
\end{aligned}$$

Although in realistic situations we cannot expect a constant V_P/V_S ratio, the parameters derived under this assumption may prove to be very useful when carrying out a PS-converted wave CRS stack: since for constant V_P/V_S they are identical to the CRS parameters of the PP stack, the values determined from the PP stacking procedure can be used to constrain the search even if V_P/V_S varies. As an alternative, the parameters obtained from the PP stack could be used as starting values for an initial converted wave stack as input for a simultaneous five parameter search or optimisation process.

It is possible to use the combined CRS PP and PS parameters for the determination of a shear velocity model by tomography. This is outlined in Appendix G.
In the next section, I will discuss the application of the general NMO formula for stacking in the source-receiver domain instead of the midpoint half-offset domain.

3.8 Stacking in the source-receiver domain

Considering the equivalence of the CRS and general NMO operators, the question arises if a search carried out in the source-receiver domain leads to similar results as in the midpoint and half-offset domain. We have investigated the potential of the general NMO operator with regards to this question for the zero-offset case in a diploma thesis by Dümmong (2006). The project came to

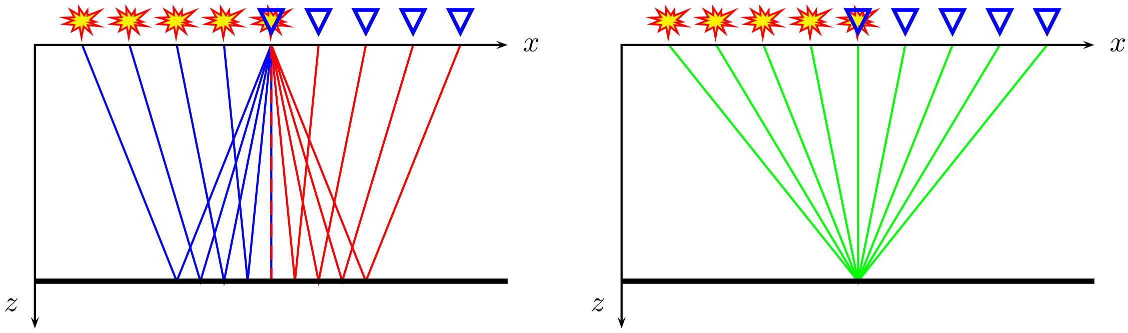

Figure 3.9: Search gathers for the parameter search in the source-receiver domain. (a) combined common-shot/common-receiver gather: the red ray paths describe the common-shot traces and the blue ray paths correspond to the common-receiver traces. (b) CMP gather.

the conclusion that although this is generally possible, the stacking procedure in the midpoint and half-offset domain has several advantages. I will summarise the results in this section. Details can be found in Dümmong (2006).

Like the search procedure in midpoint and half-offset coordinates, the search in the source-receiver domain is split into sub-searches. In the first step, the data are analysed in combined common-shot-receiver gathers (see Figure 3.9a) to determine the coefficients $q_0 = -p_0$ and $G = -S$, with $\Delta s = 0$ and $\Delta g = \Delta x$ for the common-source part of the gather and $\Delta g = 0$ and $\Delta s = \Delta x$ for the common-receiver part. The (squared) stacking trajectory in this combined gather is

$$T_{SG}^2 = (T_0 + q_0\,\Delta x)^2 + T_0\,G\,\Delta x^2 \quad . \tag{3.8.1}$$

In the second step, the data are stacked in common-midpoint gathers (Figure 3.9b) with $\Delta s = \Delta g = h$ along T_{CMP}, where

$$T_{CMP}^2 = T_0^2 + 2\,T_0\,(G + N)\,h^2 \quad . \tag{3.8.2}$$

Finally, a three-dimensional search procedure using the so far determined parameters as starting values is performed, leading to an optimised stack result.

Figure 3.10 shows a field data example. The data set was acquired along the profile BGR99-07 by the Bundesamt für Geowissenschaften und Rohstoffe (BGR) in 1999 before the coast of Costa Rica. The aim of the survey was the acquisition of a seismic profile in the vicinity of a suggested borehole in the framework of the Ocean Drilling Project (ODP). The profile covers the subduction zone separating the Cocos plate and the Caribbean plate (see Figure 3.10a). The acquisition and pre-processing are described in Dümmong (2006), as is the interpretation. I refer the interested reader to that work, whereas I will here concentrate only on the differences between the two stacking domains.

Both methods lead to a subsurface image in which the key features are visible. They are shown in Figure 3.10b and c. A closer look reveals differences, though. For example, in the region around CMP 1500, the reflectors between the bottom simulating reflector (BSR) and the multiple show better continuity if the stacking parameters are obtained in the midpoint-half-offset domain (from

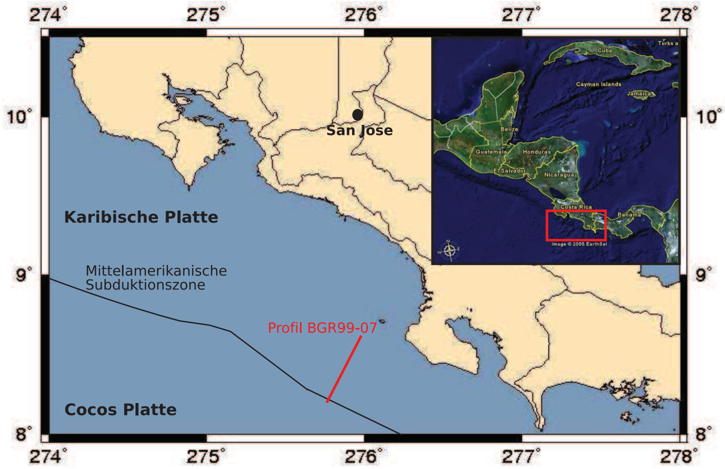

(a)

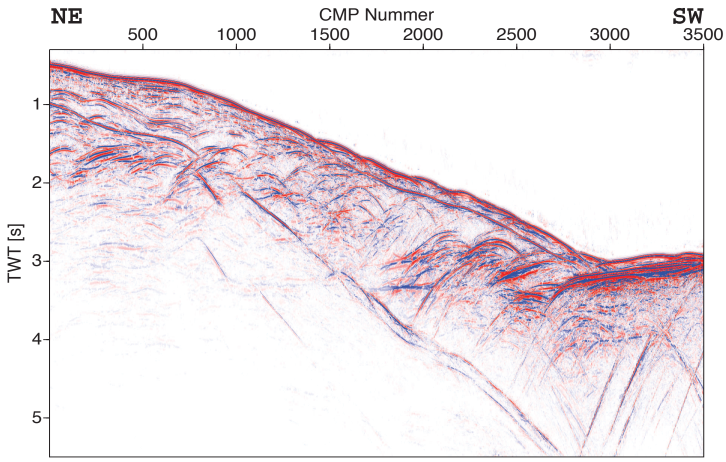

CRS stack in source and receiver coordinates

(b)

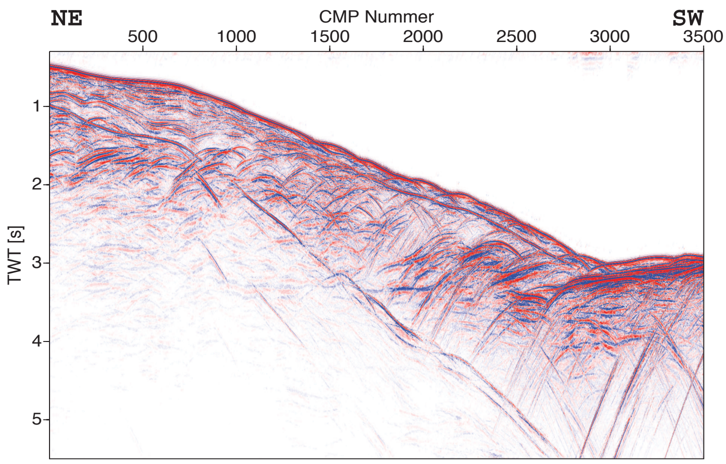

CRS stack in midpoint and half-offset coordinates

(c)

Figure 3.10: Comparison of CRS stacks in source and receiver coordinates (b) and midpoint and half-offset coordinates (c) for the profile BGR99-07 (a).

here on denoted by $x_m - h$ domain) than for the source-receiver or $s - g$ domain. The seemingly strong inferiority of the $s - g$ approach may, however, be overemphasised because the $x_m - h$ implementation is able to deal with conflicting dip situations, i.e., crossing events. This eventuality was not considered in the $s - g$ code.

We also recognise that weaker reflections are better imaged by the $x_m - h$ approach. Since the parameter search in the $x_m - h$ domain is partially carried out in stacked sections, whereas the $s - g$ search takes place in the prestack data, this explains why weak reflectors benefit from the $x_m - h$ implementation. Furthermore, since the density of receivers in the acquisition is usually higher than that of the sources, the trace numbers in the common shot and common receiver gathers used in the $s - g$ approach was not the same.

In general, it is easier to constrain the search intervals in the $x_m - h$ domain than in the $s - g$ domain because the CRS parameters are more physically intuitive. This may in particular have led to better imaging of steep dips in the $x_m - h$ case. While this poses a problem for handling diffractions and steeply-inclined reflectors with the $s - g$ approach, the $s - g$ method may turn out to be advantageous in the presence of anisotropy, where a CRS, i.e., $x_m - h$, theory with a physical interpretation of parameters does not yet exist. With the non-hyperbolic i-CRS operator introduced in the next chapter, this obstacle may, however, be soon overcome.

Chapter 4

i-CRS: a non-hyperbolic operator

Over the past years, a number of multiparameter stacking operators have been introduced as an extension of the CMP stacking technique. Examples of such operators are the common reflection surface stack from the previous chapter (CRS, Müller, 1999), multifocusing (MF, e.g., Landa et al., 2010), and the shifted hyperbola (de Bazelaire, 1988). These operators describe the traveltime surface for a reflected event in the short offset limit. The accuracy of the individual methods differs and depends not only on the considered offset but also on the reflector curvature.

Generally, operators based on double-square-root expressions like multifocusing are better suited for the description of diffraction traveltimes than hyperbolic formulae. Recently, the potential of diffractions for seismic processing has become more recognised. Since diffracted energy is scattered in all spatial directions, taking diffractions into account can considerably enhance illumination, which is of particular interest in the presence of anisotropy. Furthermore, diffractions are the link between active and passive seismics. Therefore, traveltime descriptions that fit diffractions well are an important feature not only in reflection seismics but also for the localisation of microseismic events.

The author is convinced that diffractions will in the near future play a substantial role in velocity model determination, or more general, in the determination of elastic parameters. Whereas the multifocusing operator is better-suited than CRS for the description of diffractions, none of the above-mentioned operators considers seismic anisotropy.

In order to overcome the limits of CRS with regards to diffractions and anisotropy, we have developed a new non-hyperbolic operator with the aim to make it applicable in the most general sense imaginable, to media with arbitrary heterogeneity and anisotropy, and for the description of reflected and diffracted events likewise, with the same degree of accuracy.

As I will show later during the derivation, the new operator is based on the same principle as the CRS operator, but in an implicit fashion. It is, therefore, called the 'i-CRS', as short for implicit common reflection surface, operator.

Although it was originally derived under the assumption of a homogeneous anisotropic medium, a recent diploma thesis under the author's supervision (Schwarz, 2011) has shown that the method can be successfully extended to arbitrarily heterogeneous media. This is possible because of the image space concept discussed in Section 3.2.

So far, this part of the theory exists only for heterogeneous isotropic media, but the extension to anisotropy is currently investigated. First results already suggest that it can even be applied for anisotropic parameter estimation (see Section 5).

After deriving the new i-CRS operator based on an idea by B. Kashtan (personal communication), I demonstrate that it leads to reliable and consistent results for a wide range of reflector curvatures from nearly planar reflectors to the diffraction limit for homogeneous isotropic and anisotropic media. The examples in this section are thoroughly investigated and analysed with regards to potential error sources. A comparison to results obtained with the conventional CRS and multifocusing operators in the isotropic case shows that the i-CRS method leads to higher accuracy than the other techniques.

In the section following after these simple generic examples serving for the verification and understanding of the method, I present the extension to isotropic heterogeneous media. The results and derivations of this section were obtained in the afore-mentioned diploma thesis by Schwarz (2011). It introduces a new parametrisation in terms of the CRS attributes, which makes it possible to carry out the entire processing chain within the CRS workflow (see Baykulov et al., 2011, and Chapter 3.1), where only the traveltime expression needs to be changed. The results confirm again the superiority of the i-CRS formulation over the classical CRS operator, in particular in regions with rugged topography, i.e., in the presence of diffracted energy.

4.1 Derivation of the i-CRS formula

We consider a spherical reflector in a homogeneous medium. The radius of the reflector is R, with its centre at the location $(x_c, 0, H)$, as shown in Figure 4.1a. The coordinates x_1 and x_2 are those of a source and a receiver, respectively, both at the depth z=0 and y=0. The angle θ defines the reflection point at $\vec{r} = (R\sin\theta, 0, H - R\cos\theta)$. The ray/group velocities of the down- and upgoing ray segments are $v_i(\vartheta_i)$ with the group angles ϑ_i (see Figure 4.1b).

The traveltimes T_i of the down and upgoing ray segments are given by

$$T_i^2 = \frac{(x_i - x_c - R\sin\theta)^2 + (H - R\cos\theta)^2}{v_i^2(\vartheta_i)} \quad , \qquad (4.1.1)$$

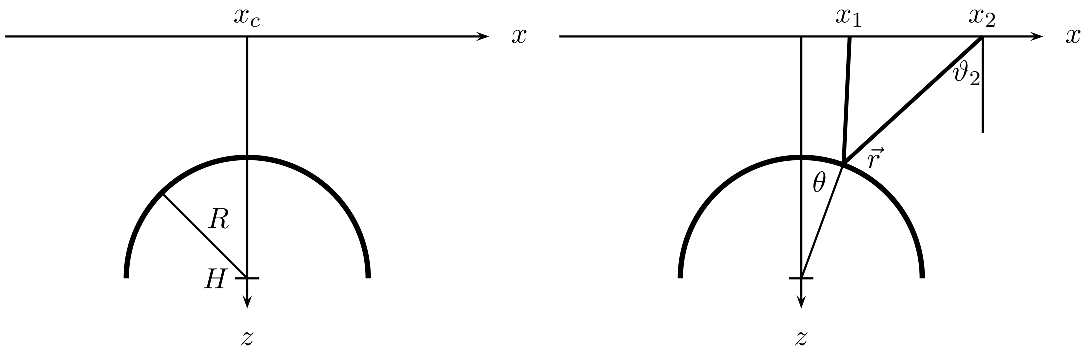

(a) (b)

Figure 4.1: Reflector geometry (a) and acquisition (b) for the spherical reflector. The reflection point $\vec{r}$ is defined by the angle θ. The angles ϑ_i are the ray/group angles.

or, in midpoint and half-offset coordinates (x_m, h):

$$T_1^2 = \frac{(x_m - h - x_c - R\sin\theta)^2 + (H - R\cos\theta)^2}{v_1^2(\vartheta_1)} \quad ,$$

$$T_2^2 = \frac{(x_m + h - x_c - R\sin\theta)^2 + (H - R\cos\theta)^2}{v_2^2(\vartheta_2)} \quad ,$$

$$T_{i-CRS} = T_1 + T_2 \quad .$$

The sum of T_1 and T_2 must fulfil Snell's law, i.e., $\partial T_{i-CRS}/\partial\theta = 0$. The derivatives of T_1 and T_2 with respect to θ are

$$\frac{\partial T_i}{\partial\theta} = \frac{1}{2\,T_i}\frac{\partial T_i^2}{\partial\theta} = \frac{R}{v_i^2\,T_i}\Big[H\sin\theta - (x_i - x_c)\cos\theta\Big] - \frac{T_i}{v_i}\frac{\partial v_i}{\partial\theta} \quad , \tag{4.1.2}$$

where

$$\frac{\partial v_i}{\partial\theta} = \frac{\partial v_i}{\partial\vartheta_i}\frac{\partial\vartheta_i}{\partial\theta} \quad . \tag{4.1.3}$$

From the geometry of the ray paths shown in Figure 4.1b, we have that

$$\tan\vartheta_i = \frac{x_i - x_c - R\sin\theta}{H - R\cos\theta} \quad , \tag{4.1.4}$$

which leads us to

$$\frac{\partial\vartheta_i}{\partial\theta} = \frac{R}{v_i^2\,T_i^2}\Big(R - H\cos\theta - (x_i - x_c)\sin\theta\Big) \quad , \tag{4.1.5}$$

and finally to

$$\begin{aligned}
\frac{\partial t}{\partial\theta} \;=\; & \underbrace{\left[\frac{H}{v_1^2T_1} + \frac{H}{v_2^2T_2} + \frac{x_1 - x_c}{v_1^3T_1}\frac{\partial v_1}{\partial\vartheta_1} + \frac{x_2 - x_c}{v_2^3T_2}\frac{\partial v_2}{\partial\vartheta_2}\right]}_{A} R\sin\theta \\
& + \underbrace{\left[\frac{H}{v_1^3T_1}\frac{\partial v_1}{\partial\vartheta_1} + \frac{H}{v_2^3T_2}\frac{\partial v_2}{\partial\vartheta_2} - \frac{x_1 - x_c}{v_1^2T_1} - \frac{x_2 - x_c}{v_2^2T_2}\right]}_{B} R\cos\theta \\
& + \underbrace{\left[-\frac{R}{v_1^3T_1}\frac{\partial v_1}{\partial\vartheta_1} - \frac{R}{v_2^3T_2}\frac{\partial v_2}{\partial\vartheta_2}\right]}_{C} R \quad .
\end{aligned} \tag{4.1.6}$$

Introducing the abbreviations A, B, and C as shown above this equation can be shortened to

$$A\sin\theta + B\cos\theta + C = 0 \quad . \tag{4.1.7}$$

Its solution is

$$\sin\theta = -\frac{AC}{A^2 + B^2} \pm \frac{B}{A^2 + B^2}\sqrt{A^2 + B^2 - C^2} \quad , \tag{4.1.8}$$

where the negative sign must be chosen, as will be shown below.

If the velocities do not depend on direction, Equation (4.1.7) simplifies considerably. Since the quantity C vanishes we find that

$$\tan\theta = -\frac{B}{A} \quad \Rightarrow \quad \sin\theta = -\frac{B}{\sqrt{A^2+B^2}} \quad . \tag{4.1.9}$$

The sign of $\sin\theta$ is negative because the cosine is positive for a reflection from the sphere. Equation (4.1.8) collapses to

$$\sin\theta = \pm\frac{B}{\sqrt{A^2+B^2}} \quad . \tag{4.1.10}$$

Comparing the coefficients of these expressions lets us recognise that the negative sign must be chosen in (4.1.8).

Note that until here, all expressions are exact. Since the angles ϑ_i and thus the velocities v_i and traveltimes T_i implicitly depend on θ, Equation (4.1.8) cannot be directly solved for θ. We can, however, apply (4.1.8) in a recursive fashion using an angle θ_0 defined for the zero-offset as initial angle to obtain an update for θ from (4.1.8), which can then be used to compute the traveltimes T_i with (4.1.1). Further iterations can be applied to enhance the accuracy.

Before demonstrating the implicit operator on isotropic and anisotropic examples, I very briefly touch the special case of converted waves.

4.2 Converted waves

All expressions derived in the previous section are equally applicable to converted waves. In this section, I consider isotropic velocities. Expressing the x_i by midpoint and half-offset coordinates (x_m, h) and substituting A and B into (4.1.7), we obtain for converted waves that

$$\tan\theta = \frac{(x_m - x_c)\,(v_2^2\,T_2 + v_1^2\,T_1) - h\,(v_2^2\,T_2 - v_1^2\,T_1)}{H\,(v_2^2\,T_2 + v_1^2\,T_1)} \quad , \tag{4.2.1}$$

where v_1 and v_2 are now the P- and S-wave velocities. For zero offset, the angle is

$$\tan\theta_0 = \frac{x_m - x_c}{H} \quad . \tag{4.2.2}$$

With the help of θ_0, we can also write $\tan\theta$ as

$$\tan\theta = \tan\theta_0 - \frac{h\,(v_2^2\,T_2 - v_1^2\,T_1)}{H\,(v_2^2\,T_2 + v_1^2\,T_1)} \quad . \tag{4.2.3}$$

The converted-wave i-CRS is currently investigated in a B.Sc. thesis (Bauer, 2012) under the author's supervision.

4.3 Accuracy studies for isotropic PP reflections

In the monotypic isotropic case, the velocities v_1 and v_2 coincide and Equation (4.2.1) can be further reduced to

$$\tan\theta = \frac{(x_m - x_c)\,(T_2 + T_1) - h\,(T_2 - T_1)}{H\,(T_2 + T_1)} = \tan\theta_0 - \frac{h\,(T_2 - T_1)}{H\,(T_2 + T_1)} \quad , \tag{4.3.1}$$

where the zero-offset angle is again

$$\tan\theta_0 = \frac{x_m - x_c}{H} \quad . \tag{4.3.2}$$

In order to investigate the feasibility of the new operator, we will now apply it to a homogeneous isotropic medium where the exact solution for the reflection traveltime is available (see Appendix F). Since we are also interested in the performance of i-CRS compared to other multiparameter operators, we need to relate the i-CRS parameters to the CRS wavefield attributes used by the CRS and multifocusing method.

From the geometry in Figure 4.1, we can see that for a zero-offset reflection with $x_1 = x_2 = x_0$ in our homogeneous test case, the corresponding homogeneous CRS[1] parameters would be

$$\begin{aligned} \beta_0 &= \theta \\ R_N &= \frac{H}{\cos\theta} \\ R_{NIP} &= \frac{H}{\cos\theta} - R \quad . \end{aligned} \tag{4.3.3}$$

Since it is part of the comparative accuracy studies, I give a brief introduction to the multifocusing operator in the next section.

Multifocusing

The multifocusing operator describes the traveltime of a reflected event in terms of the traveltime of a central ray and corrections applied at the source and receiver for a paraxial ray. This results in the double square root expression (e.g., Landa et al., 2010),

$$T(x_s, x_g) = \frac{1}{V_0}\sqrt{R_s^2 + 2\,R_s \Delta x_s \sin\beta_0 + \Delta x_s^2} + \frac{1}{V_0}\sqrt{R_g^2 + 2\,R_g \Delta x_g \sin\beta_0 + \Delta x_g^2} \quad , \tag{4.3.4}$$

with the source and receiver positions x_s and x_g, respectively, and $\Delta x_s = x_s - x_0$ and $\Delta x_g = x_g - x_0$. The quantities R_s and R_g are related to the radii of the N- and NIP-wave by

$$R_s = \frac{1+\sigma}{R_N^{-1} + \sigma\, R_{NIP}^{-1}} \quad \text{and} \quad R_g = \frac{1-\sigma}{R_N^{-1} - \sigma\, R_{NIP}^{-1}} \quad , \tag{4.3.5}$$

where σ is the so-called focusing parameter. For a detailed discussion of its meaning, please refer to Landa et al. (2010). If the reflector is locally plane, the focusing parameter can be expressed by

$$\sigma = \frac{\Delta x_s - \Delta x_g}{\Delta x_s + \Delta x_g + 2\,\dfrac{\Delta x_s\,\Delta x_g}{R_{NIP}}\sin\beta_0} \quad . \tag{4.3.6}$$

In a recently-published paper, Landa et al. (2010) state that the accuracy of multifocusing traveltimes can be enhanced by using the focusing parameter σ accordingly for a spherical reflector. However, the computation of the parameter σ even for the spherical case is not straightforward. Therefore, we have restricted our traveltime comparison to planar multifocusing, i.e., using the planar focusing parameter given by (4.3.6).

[1]denoted by a tilde here in order to distinguish them from the CRS parameters for the arbitrarily heterogeneous situation

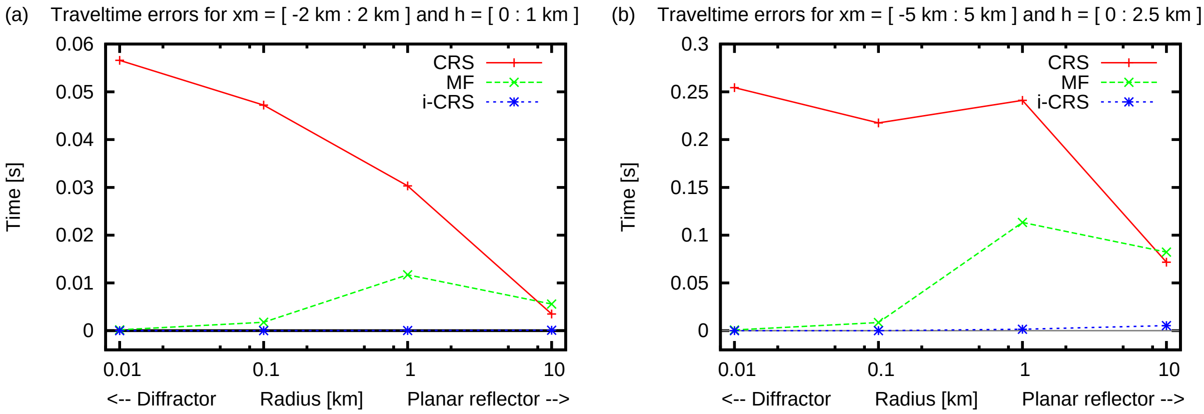

Figure 4.2: RMS traveltime errors for spherical reflectors with different radii for an aperture of (a) x_m in [-2 km:2 km] and h in [0:1 km], and (b) x_m in [-5 km:5 km] and h in [0:2.5 km]. For both apertures, we observe that the accuracy of CRS deteriorates for smaller radii, i.e. toward the diffraction limit. Planar MF is highly accurate for diffractions, but less so for larger radii. i-CRS maintains its high accuracy both in the diffraction as well as in the planar reflection limit.

Examples

We have computed traveltime surfaces for four different spherical reflectors with the CRS, planar multifocusing (MF), and the new implicit stacking operator (i-CRS) expressions. For the latter, we have only considered a single iteration as it already leads to high accuracy. An investigation of the accuracy of i-CRS for more iteration steps was carried out by Schwarz (2011). The results were compared with the exact solution (see Appendix F). In all cases, we chose V_0=2 km/s, β=0 and R_{NIP}=1 km, and only the radius of the sphere was varied from R=10 m, corresponding to a diffractor-like structure, to R=10 km, describing an almost plane reflector.

The RMS errors compared in Figure 4.2 were computed for two different apertures: the first one, (a), includes x_m in [-2 km:2 km] and h in [0:1 km], which is equivalent to a maximum offset over reflector depth ratio of two. The second aperture, shown in (b), covering x_m in [-5 km:5 km] and h in [0:2.5 km] was chosen in order to evaluate the accuracy far outside the usually-applied range. Figures 4.3–4.5 display the error distributions of the traveltime operators for the different reflector curvatures.

In Figure 4.2 as well as in Figures 4.3–4.5, we observe that within a realistic midpoint and offset range, all three methods perform reasonably well. The accuracy of the CRS expression deteriorates for smaller radii, i.e. toward the diffraction limit. Surprisingly, because this is counter-intuitive, MF is very accurate for diffractions despite the assumption of a planar focusing parameter, and shows higher errors for larger radii. i-CRS maintains its overall higher accuracy both in the diffraction as in the planar reflection limit over a wide range of midpoints and offsets.

Since the error distributions of all operators are very distinct, we have further investigated what causes the shape of the errors for the i-CRS operator in Figure 4.5. The error distribution for $R = 1$km and a fixed half-offset at h=2.5 km is plotted in the lower part of Figure 4.6. The upper part of Figure 4.6 shows ray paths for three different CMP's at 0, 2, and 4 km lateral distance from the centre of the sphere. Thick lines correspond to the zero-offset rays and thin lines are rays for the

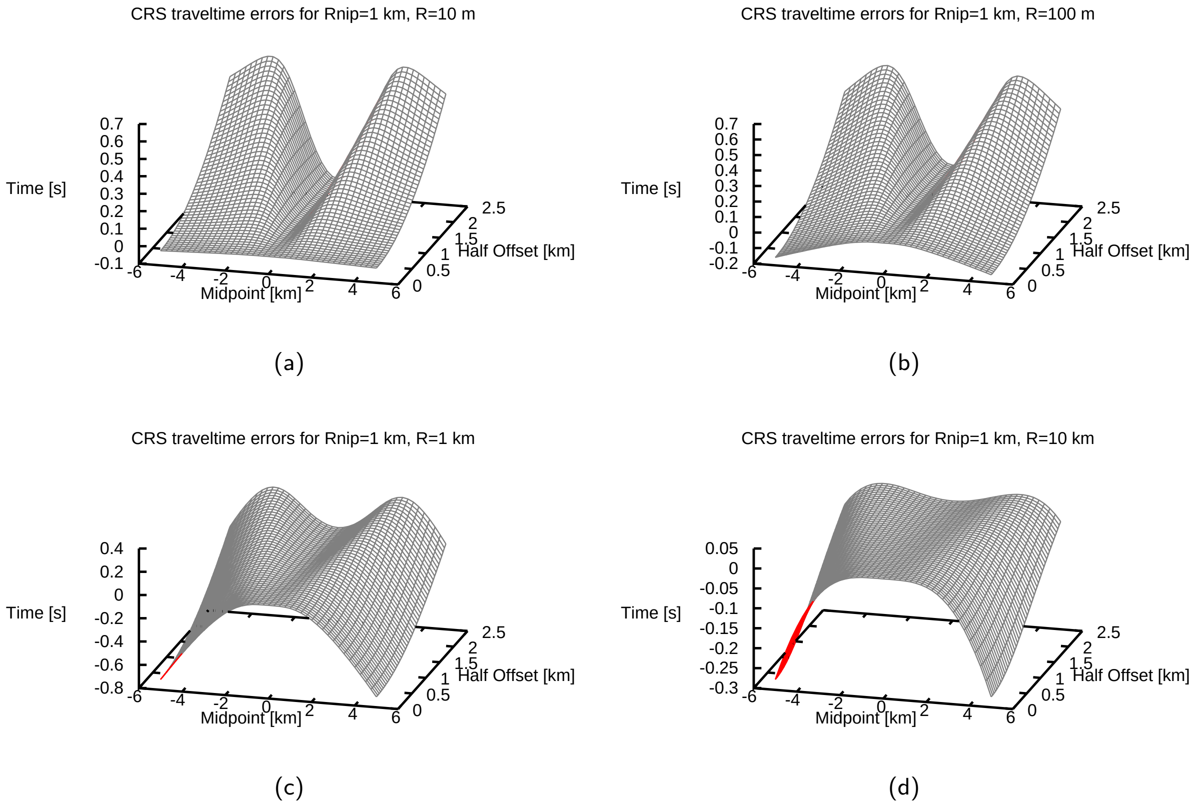

Figure 4.3: Traveltime errors for the CRS operator for spherical reflectors with (a) R=10 m, (b) R=100 m, (c) R=1 km, (d) R=10 km. The errors decrease for larger radii. Note the different scales.

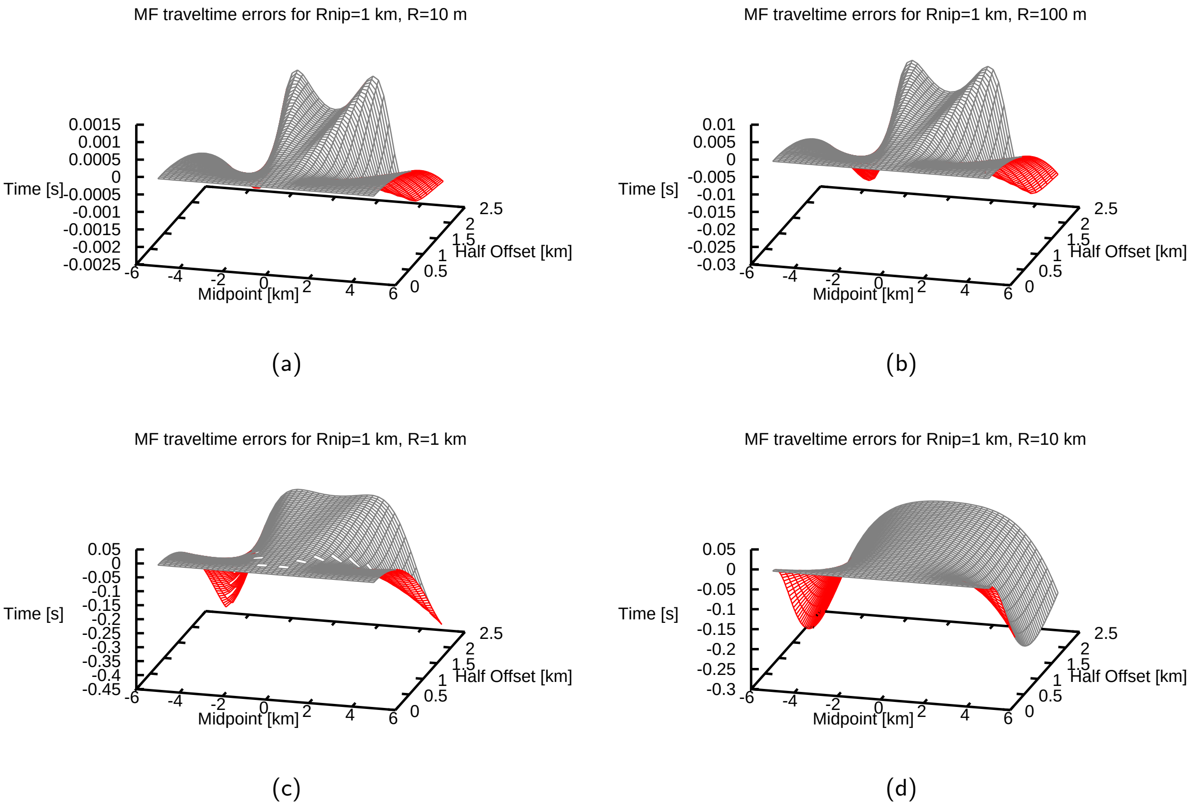

Figure 4.4: Traveltime errors for the planar MF operator for spherical reflectors with (a) R=10 m, (b) R=100 m, (c) R=1 km, (d) R=10 km. The errors increase for larger radii. Note the different scales.

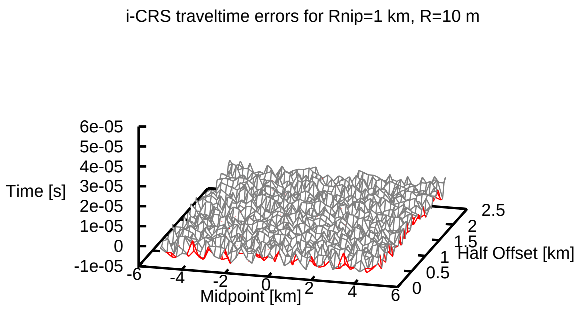

(a)

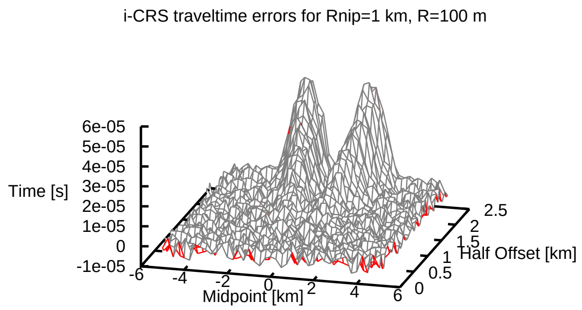

(b)

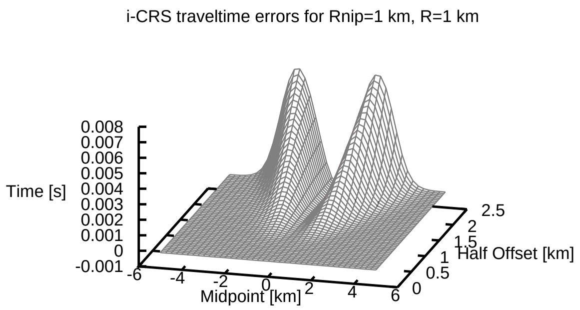

(c)

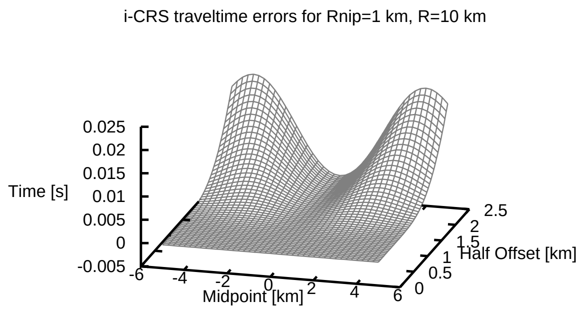

(d)

Figure 4.5: Traveltime errors for the i-CRS operator for spherical reflectors with (a) R=10 m, (b) R=100 m, (c) R=1 km, (d) R=10 km. The errors increase very mildly for larger radii. For the diffraction limit, errors are within machine precision. Note the different scales.

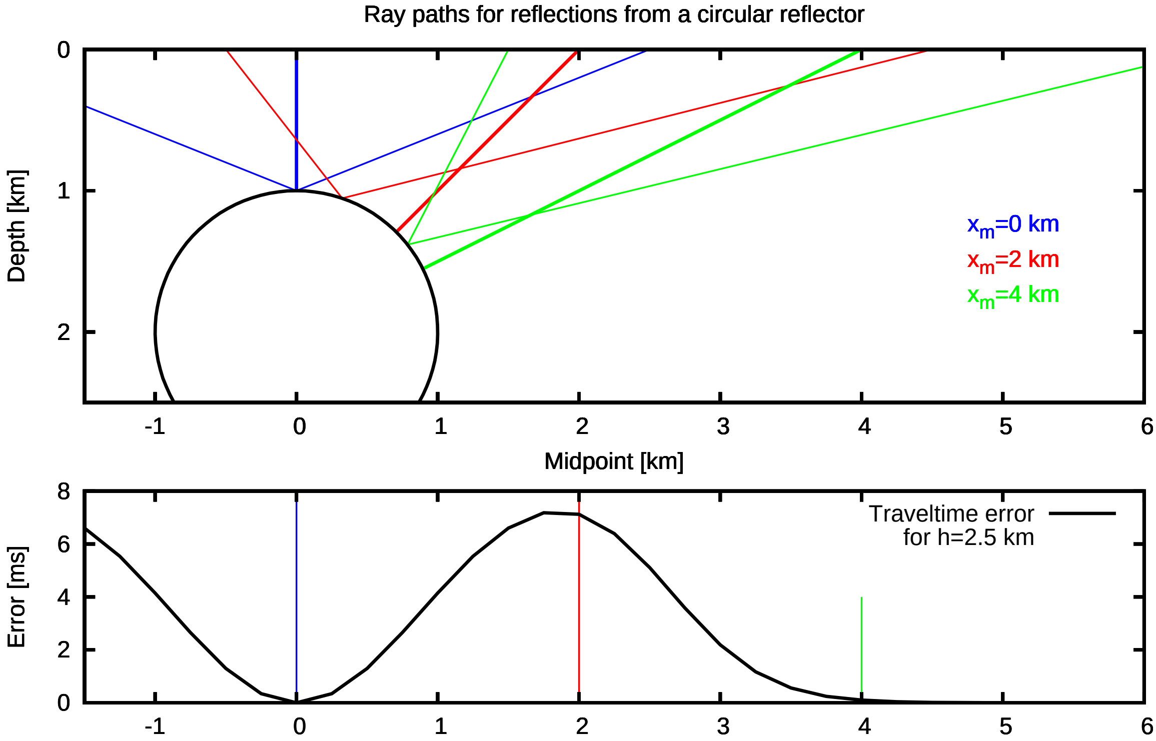

Figure 4.6: Ray paths for zero-offset and offset reflections (top) and their relation to traveltime errors (bottom). The traveltime error reaches a maximum where the deviation between the zero-offset and offset reflection point on the sphere is largest.

respective half-offsets at h=2.5 km. We can see that the traveltime error reaches a maximum where the deviation between the zero-offset and the offset reflection point on the sphere is largest. This observation is in good agreement with the derivation of the i-CRS operator as search for the angle θ, which describes the reflection point. It is therefore expected that the largest errors would occur in regions where the angle deviates most from the zero-offset angle, which is confirmed by the ray paths in Figure 4.6 Note that the accuracy is improved if more iteration steps are carried out (Schwarz, 2011).

From these simple numerical examples we can conclude that whereas existing approaches (CRS, planar multifocusing) lead to reasonable accuracy if applied within a realistic midpoint and offset range, the new i-CRS operator is not only superior to these approaches for larger offsets and midpoint distances, but it also maintains the high accuracy for a wide range of reflector curvatures, from the diffraction limit to quasi-plane reflectors.

After we have shown that the i-CRS operator leads to promising results for the isotropic case, we will now examine its applicability in the presence of anisotropy.

4.4 Anisotropic examples

Although Equation (4.1.8) was derived and is valid for arbitrary anisotropy, its application in the general case is not straightforward: in order to solve Equation (4.1.8) in the anisotropic case, the group velocities and their derivatives with respect to the group angle must be known. These quantities are not generally available. A closed-form expression exists only in the case of elliptical anisotropy, i.e. $\varepsilon = \delta$.

Therefore, we limit our examples here to media with weak polar anisotropy and the descriptions introduced by Thomsen (1986) to express the group velocity and its derivative. This is not a principal restriction of our method in particular but a general problem when anisotropic media are concerned. It is common to make assumptions that the degree of anisotropy is weak. A weak anisotropy parametrisation for arbitrary symmetry was introduced by Mensch and Rasolofosaon (1997).

For polar media with a vertical symmetry axis, we have the group velocities in terms of the group angles given by Thomsen (1986)

$$v_i = v_{i_0} \left(1 + a\, \sin^2 \vartheta_i + b\, \sin^4 \vartheta_i\right) \quad , \tag{4.4.1}$$

where

- for qP-waves: $v_{i_0} = \alpha$, $a = \delta$, and $b = (\varepsilon - \delta)$,
- for qSV-waves: $v_{i_0} = \beta$, $a = \sigma$, and $b = -\sigma$,
- for SH-waves: $v_{i_0} = \beta$, $a = \gamma$, and $b = 0$,

and α and β are the vertical velocities of P- and S-waves, respectively. For the velocity derivatives, we find

$$\frac{\partial v_i}{\partial \vartheta_i} = 2\, v_{i_0} \sin \vartheta_i \cos \vartheta_i \, \left(a + 2\, b\, \sin^2 \vartheta_i\right) \quad . \tag{4.4.2}$$

For polar media with a tilted symmetry axis and tilt angle ϕ, the angle θ is replaced by $\theta - \phi$.

Examples

As we can deduce from the previous section, there are two possible sources of contributions to traveltime errors. The first is the new operator itself, and the second is the introduction of the weak anisotropy approximation.

In order to investigate the influence of these contributions separately, we have chosen media with elliptical symmetry, where $\varepsilon = \delta$. For these media, a closed form solution exists for the group velocity and its derivative (see, e.g., Appendix C). Reference traveltimes were generated using the NORSAR ray tracing package for values of $\varepsilon = \delta$ ranging from 0.0 (i.e. isotropic) to 0.4. Reflector radii were 100 m, 1 km, and 10 km. The top of the reflector was located at x_c =0 and $H{-}R$ =1 km in each case. The simulated acquisition scheme covered midpoints from 0 to 1 km from x_c and half-offsets up to 1 km.

We have applied the new i-CRS operator twice, first using the exact velocity and derivative, and then using their weak anisotropy approximation. In both cases, we have chosen the isotropic

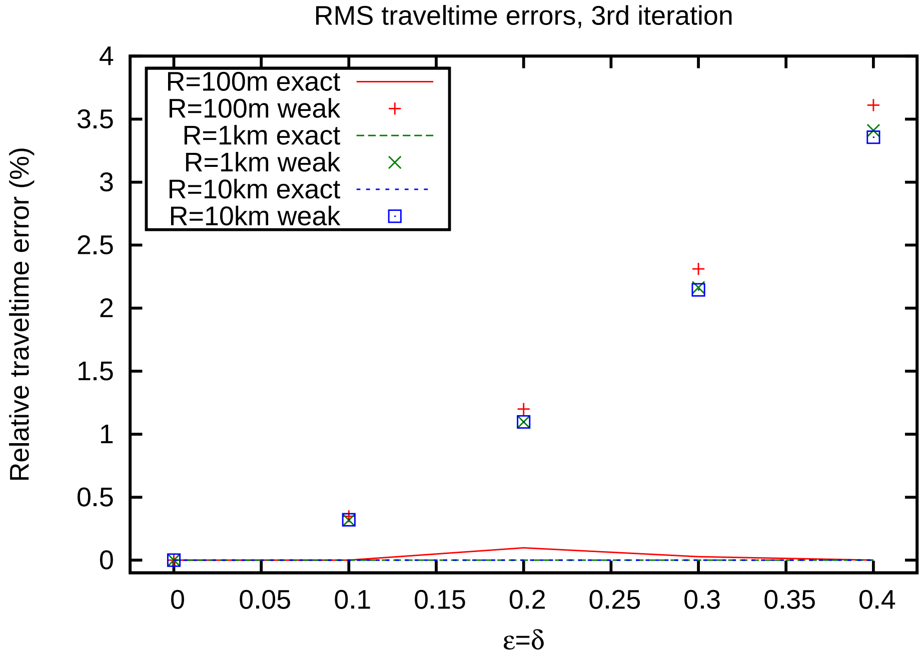

Figure 4.7: Accuracy of the i-CRS stacking operator after three iterations in the presence of elliptical anisotropy. Solid lines indicate that the new operator performs with high accuracy for all reflector radii if exact velocities and derivatives are chosen. If these are expressed by their weakly anisotropic counterpart, the accuracy degrades with increasing strength of anisotropy. Note that the slightly higher errors for the 100 m radius are introduced by errors in the reference traveltimes because the limit of applicability of the ray method is reached in this case.

zero-offset reflection angle θ_0 as starting angle. In the anisotropic case, the zero-offset ray is not perpendicular to the reflector. Therefore, the zero-offset ray angle ϑ_0 and the angle θ_0, which is the phase angle in this case with the phase normal perpendicular to the reflector do not coincide. There is no closed form solution for the determination of ϑ_0. Since the recursive application of the operator converges after two or at most three iterations, we nevertheless used θ_0 as starting angle.

The results after the third iteration are shown in Figure 4.7. If exact velocities and velocity derivatives are used, the new operator is highly accurate for all reflector curvatures under consideration. If the weak anisotropy approximation is applied, the accuracy decreases with the strength of anisotropy. This result is not surprising. As for the exact case, the accuracy remains independent of the reflector curvature. In conclusion, the degree of accuracy obtained in the presence of anisotropy is of the same order as for isotropic media.

As one important application of the CRS parameters is the tomographic inversion for velocities, the NIP wave tomography suggested by Duveneck (2004), the anisotropic i-CRS operator has a tremendous potential to provide an extension of Duveneck's work to anisotropic parameter estimation. First tests on homogeneous VTI media (see 5) suggest that anisotropy parameters can be estimated using i-CRS, but further work is needed.

Our experiments have so far successfully been carried out in homogeneous media in terms of a feasibility study. The next section deals with the extension of the theory to heterogeneity.

4.5 Parametrisation and examples for heterogeneous media

Introduction

The real challenge of any method is its performance in the case of heterogeneity. The equations in this chapter were derived for a spherical reflector in a homogeneous background. In this section, the theory is extended to heterogeneous isotropic media. The extension was carried out in the framework of a diploma thesis by Schwarz (2011) under the author's supervision. All derivations and examples in this section are taken from Schwarz's (2011) work.

Since the CRS formula derived from geometric principles for arbitrary media as in Section 3.3 as well as the CRS equation for a homogeneous medium derived in Section 3.4 are formally identical in their description of the move-out[2], it is suggestive to assume that an i-CRS formulation for media with arbitrary heterogeneity can be found.

The link between the homogeneous and heterogeneous i-CRS is again the image space concept (Höcht et al., 1999) introduced in Section 3.2. In his thesis, Schwarz (2011) has thoroughly investigated two approaches to obtain a heterogeneous i-CRS formulation. Both lead to relations between the original i-CRS parameters, i.e., R, H, x_c for the homogeneous case, and the CRS parameters β_0, R_N, and R_{NIP}. Furthermore, for heterogeneous media, the no longer constant velocity v and the near-surface velocity V_0 employed in the CRS also need to be considered. Finally, in order to carry out the actual i-CRS stack, we need an explicit expression for T_0.

All these issues are accomplished by Schwarz's resulting transformations. Moreover, the expressions he derived reduce to well-known formulae for particular subsurface geometries and acquisition schemes, e.g., for diffractions, horizontally-stratified media in CMP gathers, and the zero-offset situation.

During his research, Schwarz (2011) has investigated the performance of both transformations regarding the accuracy of the traveltime as well as the wavefield attributes in the presence of varying degrees of heterogeneity, for generic examples where analytic solutions were available for comparison, as well as the quality of the resulting stack, evaluated by the semblance and the stacked amplitudes.

He found that one of the transformations leads to consistently superior results. Therefore, I will only discuss this transformation here. For more details, I refer the reader to the original work by Schwarz (2011).

Parametrisation

Schwarz's ansatz is based on the comparison of coefficients of the CRS and the i-CRS formula. Since both operators have different shapes, he has expanded the i-CRS expression into a Taylor series of second order. The resulting expression can then be compared to its CRS counterpart.

[2]mind that although the move-outs coincide, whereas the zero-offset traveltimes differ for both descriptions

From now on, we will treat the i-CRS parameters as effective parameters. To distinguish them from the parameters for the homogeneous case in Section 4.1, we denote the effective parameters with a tilde. Note that the velocity $\tilde{v}$ is also an effective parameter now. For convenience, we introduce the abbreviation $\Delta\tilde{x}_c = \tilde{x}_c - x_0$, and use Equation (4.3.3) in the following variant:

$$\begin{aligned} \sin\tilde{\theta} &= \frac{\Delta\tilde{x}_c}{\sqrt{\Delta\tilde{x}_c^2 + \tilde{H}^2}} \\ \tilde{R}_{NIP} &= \sqrt{\Delta\tilde{x}_c^2 + \tilde{H}^2} - \tilde{R} \\ \tilde{R}_N &= \sqrt{\Delta\tilde{x}_c^2 + \tilde{H}^2} \quad . \end{aligned} \tag{4.5.1}$$

Carrying out the Taylor expansion of the i-CRS traveltime[3] and comparing the coefficients leads to the system of equations

$$\begin{aligned} \frac{\sin\tilde{\theta}}{\tilde{v}} &= \frac{\sin\beta_0}{V_0} \\ \frac{\cos^2\tilde{\theta}}{\tilde{v}\,\tilde{R}_{NIP}} &= \frac{\cos^2\beta_0}{V_0\,R_{NIP}} \\ \frac{\cos^2\tilde{\theta}}{\tilde{v}\,\tilde{R}_N} &= \frac{\cos^2\beta_0}{V_0\,R_N} \\ \frac{2\,\tilde{R}_{NIP}}{\tilde{v}} &= T_0 \quad , \end{aligned} \tag{4.5.2}$$

which can be solved for

$$\begin{aligned} \tilde{v} &= \frac{V_{NMO}}{\sqrt{1 + \frac{V_{NMO}^2}{V_0^2}\sin^2\beta_0}} \\ \Delta\tilde{x}_c &= -\frac{R_N\sin\beta_0}{\cos^2\beta_0\left(1 + \frac{V_{NMO}^2}{V_0^2}\sin^2\beta_0\right)} \\ \tilde{H} &= \frac{V_0\,R_N}{V_{NMO}\cos^2\beta_0\left(1 + \frac{V_{NMO}^2}{V_0^2}\sin^2\beta_0\right)} \\ \tilde{R} &= \frac{\frac{V_0\,R_N}{V_{NMO}\cos^2\beta_0} - \frac{V_{NMO}\,T_0}{2}}{\sqrt{1 + \frac{V_{NMO}^2}{V_0^2}\sin^2\beta_0}} \quad . \end{aligned} \tag{4.5.3}$$

In (4.5.3), the normal moveout velocity is given by

$$V_{NMO} = \sqrt{\frac{2\,V_0\,R_{NIP}}{T_0\cos^2\beta_0}} \quad . \tag{4.5.4}$$

Note that although these transformation relations were obtained from a Taylor expansion of the i-CRS operator, the resulting i-CRS traveltime expression is again non-hyperbolic, following Equation (4.1.2), with

$$T = T_{i-CRS}(\tilde{v}, \Delta\tilde{x}_c, \tilde{H}, \tilde{R}) \quad , \tag{4.5.5}$$

[3]For more details, I again refer the reader to the original work by Schwarz (2011).

or,

$$T = T_{i-CRS}(T_0, \beta_0, R_{NIP}, R_N) \quad , \tag{4.5.6}$$

Special case: diffractions

Several special cases have been investigated by Schwarz (2011). One of them is the application of i-CRS for diffractions, where conventional CRS shows weak performance, but which is of great interest. For diffractions, the CRS parameters R_N and R_{NIP} coincide. In the case of normal incidence and varying velocity in the overburden, we find that

$$\begin{aligned}
\tilde{v} &= V_{NMO} \\
\Delta\tilde{x}_c &= 0 \\
\tilde{H} &= \frac{T_0\, V_{NMO}}{2} \\
\tilde{R} &= 0 \quad .
\end{aligned} \tag{4.5.7}$$

Substituting these into the i-CRS operator, we obtain the double square root equation for the diffraction,

$$T_{\text{diff}} = \sqrt{\frac{T_0^2}{4} + \frac{(\Delta x_m - h)^2}{V_{NMO}^2}} + \sqrt{\frac{T_0^2}{4} + \frac{(\Delta x_m + h)^2}{V_{NMO}^2}} \quad . \tag{4.5.8}$$

For horizontal layering, V_{NMO} can be substituted by the root-mean-square velocity V_{RMS}. In this case, (4.5.8) is equivalent to the Kirchhoff time migration operator. Furthermore, we observe that T_{diff} becomes the exact diffraction response for the homogeneous case where $V_{NMO} = V_0$.

Examples

We have applied the CRS and i-CRS operators to the complex synthetic data set Sigsbee 2A. The model shown in Figure 4.8 represents a complex geological setting with a large salt body as the main feature. In addition, the model contains two rows of diffractors. These and additional diffractions resulting from the very rugged top-of-salt make the data set particularly suited as an example for our new operator. More details on the model and the data set are given in Schwarz (2011).

Already during the stack, Schwarz (2011) found significantly higher semblance values, up to an increase by 0.6, for the i-CRS method, particularly for the diffraction tails. This is not surprising as it is known that CRS has issues with diffractions.

Figure 4.9 displays the result of the i-CRS stack. Since it is overall similar to the CRS stack, only the i-CRS result is shown here. The differences between i-CRS and CRS become apparent if we take a more detailed look. In Figure 4.10, a close-up on a part of the top-of-salt is shown. Although the overall appearance is, as already stated, similar, we can see that particularly the diffraction tails in the i-CRS section have higher continuity, which can best be described by a 'smoother' look.

The difference between the i-CRS and CRS becomes much more distinct if we now examine the post-stack time-migrated section, shown in Figure 4.11 for the entire i-CRS section, and in Figure 4.12 for i-CRS (a) and CRS (b) close-ups. In the i-CRS case, the rugged top-of-salt is much better imaged with a considerably better continuity of the reflector. In particular, the structure of the

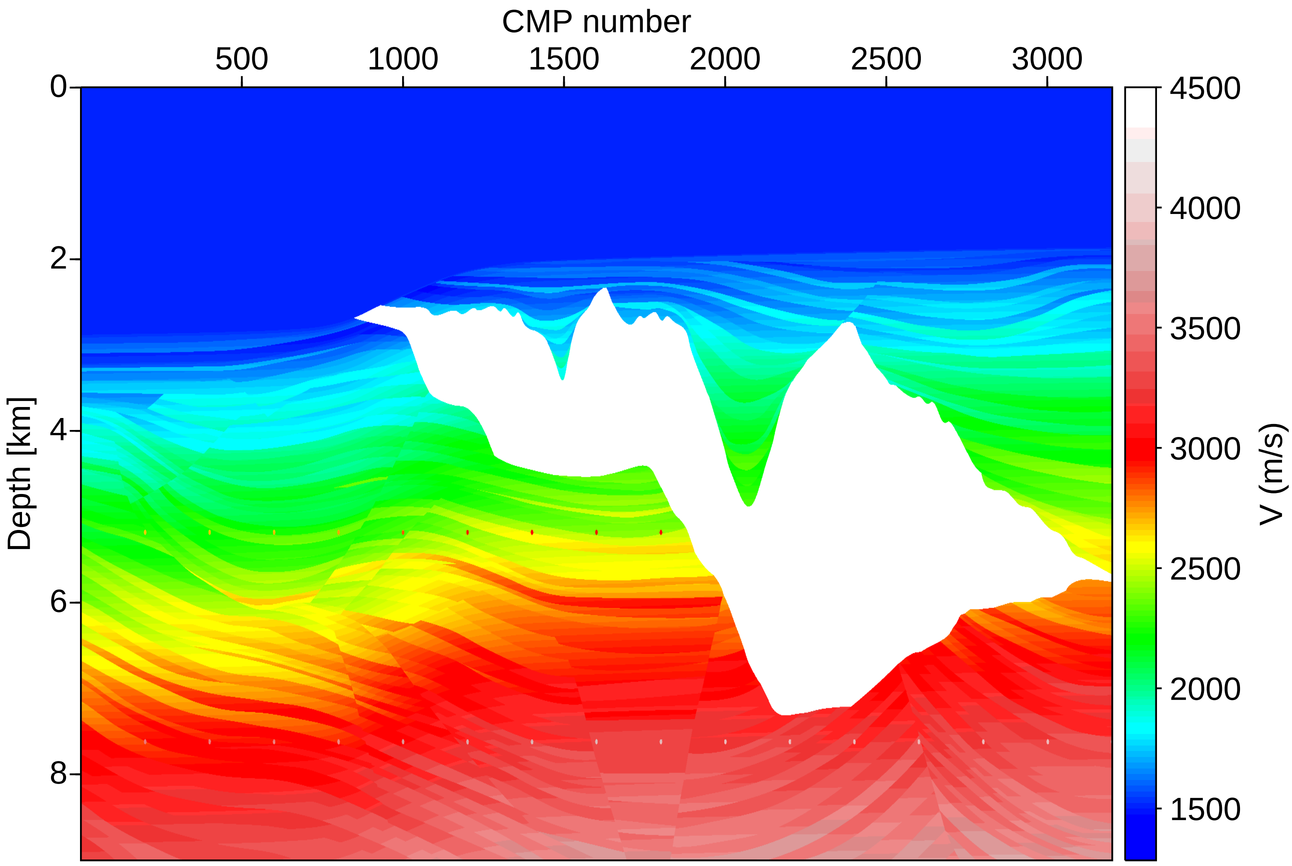

Figure 4.8: The Sigsbee 2A velocity model.

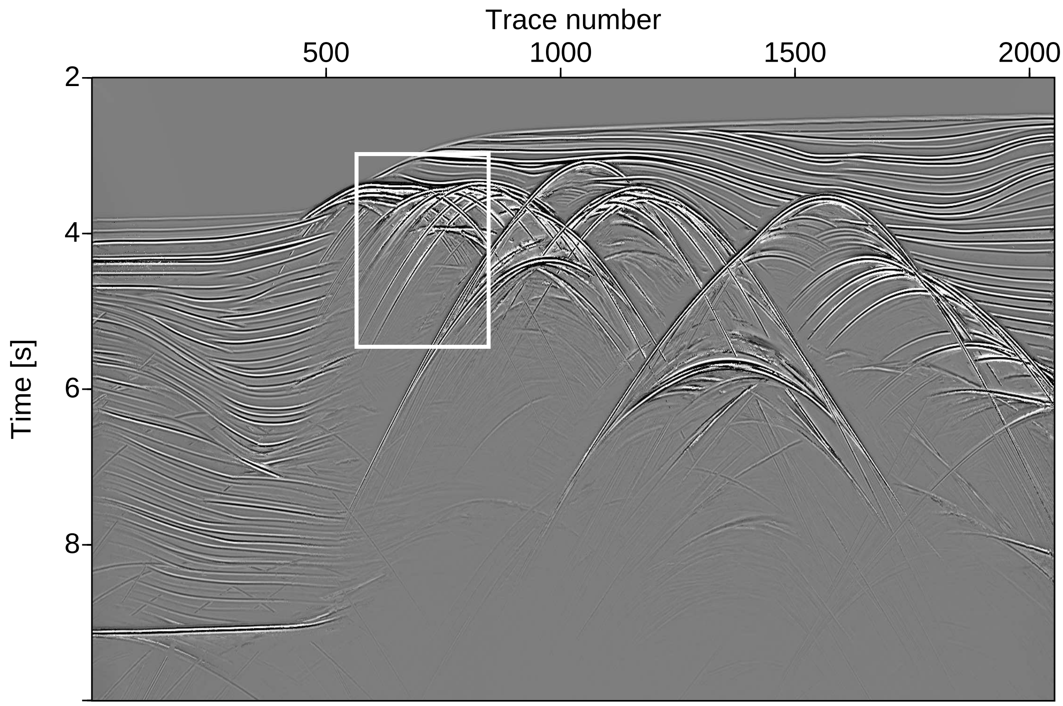

Figure 4.9: i-CRS-stack of the Sigsbee 2A data set. The section outlined by the white frame is shown in more detail in Figure 4.10.

top-of-salt around trace 1200 can only be clearly discerned in the i-CRS migrated section, whereas the CRS-migrated section suggests an altogether very different structure. Also, the steep flank at trace 1000 is much better imaged by the i-CRS.

In conclusion, we find the results from the homogeneous case studies confirmed such that the new i-CRS operator provides a much better traveltime fit in the case of diffractions than does the conventional CRS. The extension of the i-CRS to heterogeneous media has been successfully implemented and verified, leading to stack and PSTM results that are far superior than those obtained with the original CRS method, particularly in the presence of diffractors or small-scale structures like rugged salt topography.

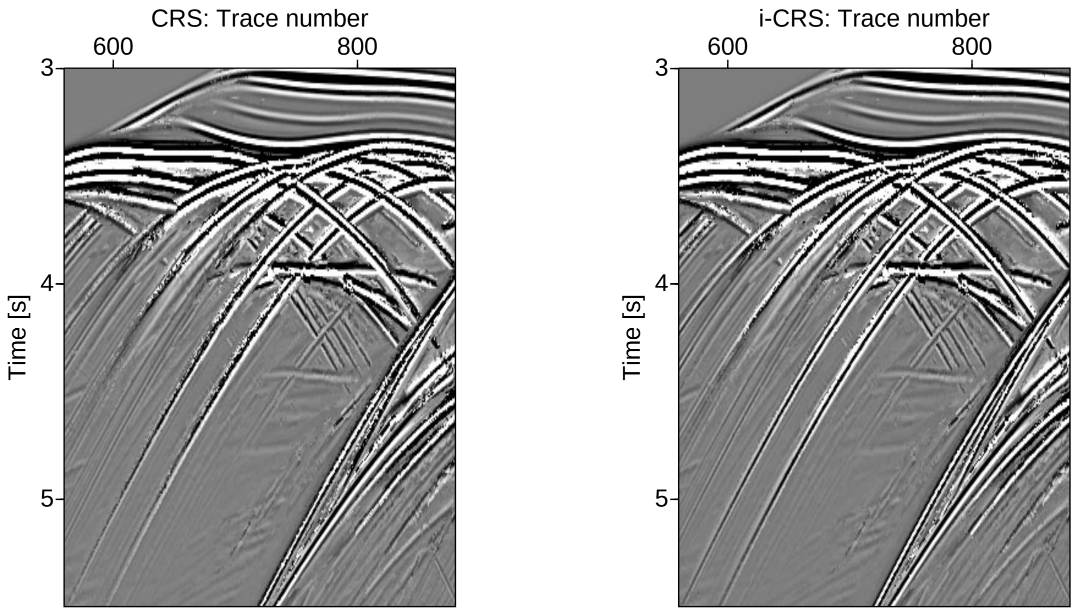

(a)

(b)

Figure 4.10: Close-up on the stack for the top-of-salt: (a) CRS and (b) i-CRS result. Note the better continuity in the i-CRS stack, particularly for the diffraction tails.

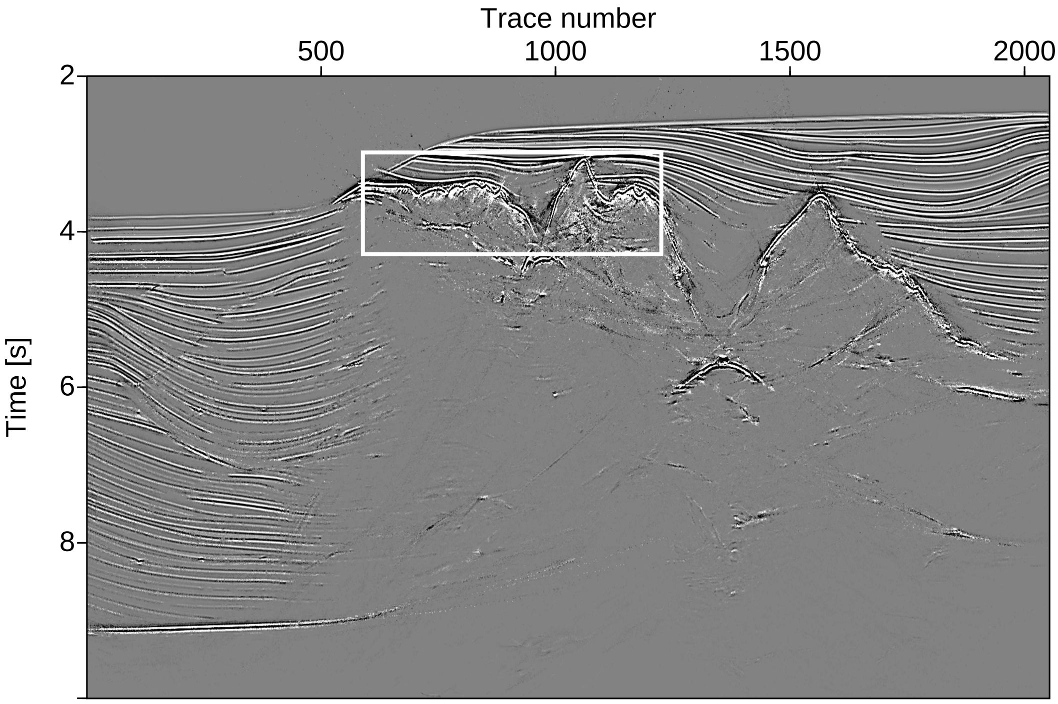

Figure 4.11: Post-stack time migration of the i-CRS-stacked Sigsbee 2A data set. The section outlined by the white frame is shown in more detail in Figure 4.12.

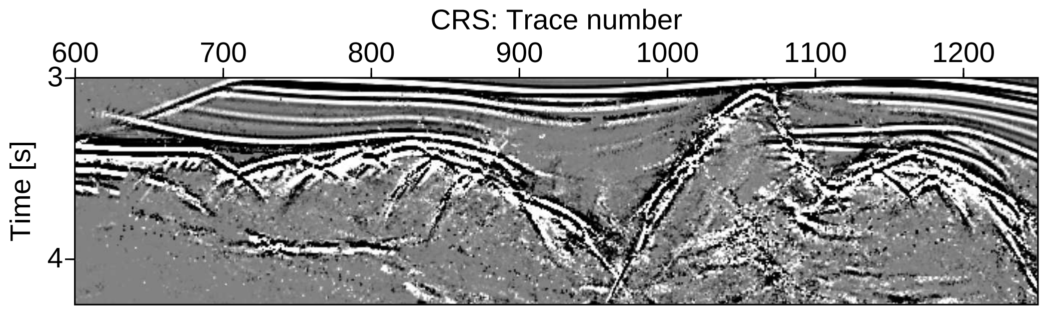

(a)

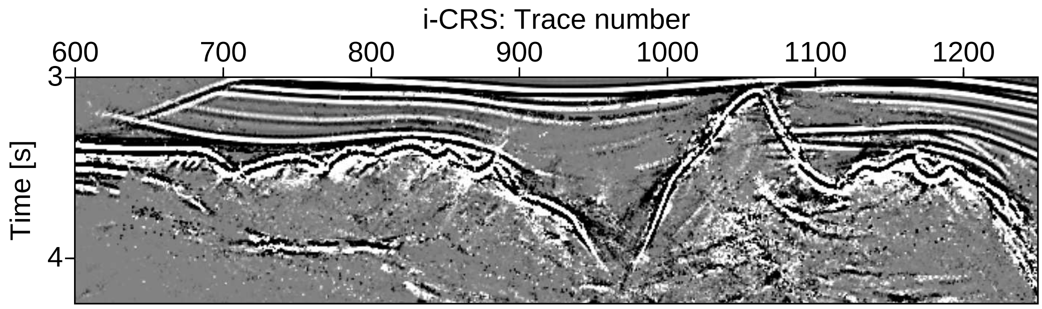

(b)

Figure 4.12: Close-up on the post-stack migration of the top-of-salt: (a) CRS and (b) i-CRS result. The rugged top-of-salt is much better resolved by the i-CRS method, as is, for example the steep flank at trace 1000.

Chapter 5

Outlook

As I have stated in Chapter 3, the CRS method has a multitude of applications. One of the future (and current) tasks is the study of these applications in combination with the new i-CRS operator. Since i-CRS has been shown to provide better stacks and coefficients, we expect that this will translate into advantages in the CRS processing chain, too. Notable examples where we expect improvement are the prestack data enhancement with partial stacks and the differentiation between reflections and diffractions, or diffraction processing in general.

Partial CRS stacks have been introduced by Baykulov and Gajewski (2009) to enhance seismic prestack data by, e.g., reconstructing traces. Baykulov and Gajewski (2009) have successfully applied their method for missing traces at moderate offsets, although this has been challenged because the parameters they use were determined for the zero-offset case. Since the i-CRS and its parameters provide a better fit than CRS, and over a larger offset range, we expect that the new operator will perform even better for the reconstruction of offset traces.

The application of i-CRS for the recognition and separation of diffracted events has large potential because the operator provides a much better fit for diffractions than does the classic CRS. Diffraction processing has begun to play a major role in seismic data processing and analysis and will continue to do so in the future. One recent example is the CRS-based workflow for diffraction imaging published by Dell and Gajewski (2011), where the authors suggest how diffractions can be employed not only for image enhancement but also for velocity model determination. Since the i-CRS is superior to the classic CRS used in that work, we expect even better results with the new operator.

Although model building with diffractions is a relatively new and highly promising discipline, reflection model building is still of utmost importance. The NIP-wave tomography introduced by Duveneck (2004) has been confirmed to be a powerful tool for the generation of a starting model for, e.g., migration. It is based on an inversion scheme that uses the CRS parameters β_0 and R_{NIP} as well as the traveltimes T_0.

In Appendix G, I introduce an extension of Duveneck's tomographic inversion method to shear velocities, using PS-converted waves. It combines parameters obtained from a PP and a PS stack in order to simulate SS CRS parameters, which can be inverted in the same fashion as the PP parameters, as suggested by Duveneck (2004).

Since the CRS expression for converted waves has five parameters, the search strategy is more demanding than for the PP case (see Section 3.5). If the ratio of V_P/V_S were constant, a simplified search could be carried out using the parameters from the PP stack because in this case, the zero-offset ray paths coincide and only three parameters enter the PS stack: there are still five parameters, but they can be expressed by the PP attributes, as I have shown in Section 3.4. If V_P/V_S varies, as we would expect in the real Earth, the PP parameters in conjunction with the PS CRS expression in Section 3.4 can still be used as starting values in order to simplify the search.

So far, the i-CRS method was extended to heterogeneous media only for P waves. A corresponding expression for converted waves is currently investigated in a B.Sc. thesis under the author's supervision (Bauer, 2012). The results from that ongoing work in combination with those from Section 3.4 and Appendix G will lead to a processing chain for converted waves resulting in a shear velocity model.

Another topic that is currently studied in a B.Sc. thesis under the author's supervision is the extension of anisotropic i-CRS to heterogeneity (Sager, 2012). As an important subtopic, we are currently investigating the potential of the anisotropic i-CRS operator for the estimation of anisotropy parameters. In the following, I will present first results obtained by Sager (2012).

Sager (2012) has extended the i-CRS code by Schwarz (2011) to include VTI anisotropy. It uses a Nelder-Mead optimisation scheme (Nelder and Mead, 1965) for the determination of the parameters.

M. Bobsin, a student under the author's supervision, has generated P-wave reflection traveltimes for two homogeneous VTI examples using the NORSAR package. Midpoints from 0 to 1 km and offsets up to 2 km were considered. The first medium is 'Mesaverde Shale (350)', taken from Thomsen (1986) and characterised by the following Thomsen's parameters and reflector geometry:

$$v_0 = 3383 \text{ m/s} \qquad \epsilon = 0.065 \qquad \delta = 0.059 \quad ,$$

$$x_c = 0 \text{ m} \qquad H = 2000 \text{ m} \qquad R = 1000 \text{ m} \quad .$$

Several optimisation tests were carried out for this medium. In a first test, the anisotropy parameters were assumed to be known and the optimisation was performed for the geometry. The second test kept the geometry parameters fixed and determined the anisotropy parameters. Then, a search was conducted where neither the anisotropy nor the reflector geometry was known. Finally, we have conducted a search where we prescribed the correct vertical velocity.

Table 5.1 shows that for the given starting values and known anisotropy parameters, the geometry can be determined with good accuracy. The same holds for the determination of the anisotropy parameters if the geometry is known (see Table 5.2). In the general case, where neither the geometry nor the anisotropy is known a priori, we find that the reflector shape is still well reconstructed in Table 5.3, however, at the cost of large errors in the anisotropy parameters. This situation improves if the vertical velocity is known a priori, as shown in Table 5.4.

These results are not only encouraging for the determination of anisotropy parameters, but they also suggest that application of our new operator may help us decide whether anisotropy is present at all, and, in consequence, how further processing steps are carried out. This is, however, a topic that still needs more detailed investigation.

Table 5.1: Determination of the geometrical parameters for Mesaverde Shale (350) if the anisotropy parameters are known.

	x_c [m]	H [m]	R [m]
Starting value	-2.5	2018	957
Result	-0.57	2001.65	1000.25
Correct value	0	2000	1000

Table 5.2: Determination of the anisotropy parameters for Mesaverde Shale (350) if the geometry parameters are known.

	v_0 [m/s]	ϵ	δ
Starting value	2000	0	0
Result	3383.04	0.0631	0.0524
Correct value	3383	0.065	0.059

Table 5.3: Determination of all parameters for Mesaverde Shale (350).

	x_c [m]	H [m]	R [m]	v_0 [m/s]	ϵ	δ
Starting value	-2.5	2018	957	3588	0	0
Result	-0.21	2002.22	987.48	3432.89	0.0478	0.0394
Correct value	0	2000	1000	3383	0.065	0.059

Table 5.4: Determination of all parameters for Mesaverde Shale (350) if the vertical velocity is prescribed.

	x_c [m]	H [m]	R [m]	ϵ	δ
Starting value	-2.5	2018	957	0	0
Result	0.03	1999.85	999.86	0.0631	0.0525
Correct value	0	2000	1000	0.065	0.059

Altogether, these results are promising for the determination of the model parameters for this example with relatively weak anisotropy. Therefore, we have repeated the experiment with a second medium, 'Shale (500)', also from Thomsen (1986), exhibiting stronger anisotropy:

$$v_0 = 3048 \text{ m/s} \qquad \epsilon = 0.255 \qquad \delta = -0.050 \quad ,$$
$$x_c = 0 \text{ m} \qquad H = 2000 \text{ m} \qquad R = 1000 \text{ m} \quad .$$

The results shown in Tables 5.5 to 5.8 display a similar behaviour as observed for the first example, however, the overall accuracy is lower, in particular for the anisotropy parameter ϵ. There are two possible reasons for this: in this second example, ϵ is rather large. Therefore, the assumption of weak anisotropy for the determination of the group velocity is violated. Furthermore, in order to obtain a reliable estimate of ϵ, large offsets are required, which were not provided with the acquisition considered in the examples.

In order to develop an anisotropic inversion scheme, e.g., based on NIP-wave tomography, we first need to extend the anisotropic i-CRS to heterogeneity. Although this step is still a current work in progress, these first simple results already confirm the potential of the application of i-CRS to anisotropy parameter estimation.

Table 5.5: Determination of the geometrical parameters for Shale (500) if the anisotropy parameters are known.

	x_c [m]	H [m]	R [m]
Starting value	-84	2333	1246
Result	-51.6	2305.4	1299.32
Correct value	0	2000	1000

Table 5.6: Determination of the anisotropy parameters for Shale (500) if the geometry parameters are known.

	v_0 [m/s]	ϵ	δ
Starting value	2000	0	0
Result	3047.28	0.1821	-0.0382
Correct value	3048	0.255	-0.05

Table 5.7: Determination of all parameters for Shale (500).

	x_c [m]	H [m]	R [m]	v_0 [m/s]	ϵ	δ
Starting value	-84	2333	1246	3316	0	0
Result	-0.93	2005.6	1005.52	3093.3	0.1684	-0.0505
Correct value	0	2000	1000	3048	0.255	-0.05

Table 5.8: Determination of all parameters for Shale (500) if the vertical velocity is prescribed.

	x_c [m]	H [m]	R [m]	ϵ	δ
Starting value	-84	2333	1246	0	0
Result	-1.18	2005.65	1005.52	0.1821	-0.0387
Correct value	0	2000	1000	0.255	-0.05

Chapter 6

Conclusions

This first part of my work was dedicated to kinematic aspects of seismic data processing. I have presented a new method for the hyperbolic interpolation of traveltimes. It is based on move-out, and therefore closely-related to stacking formulae. In consequence, my interpolation method represents a general NMO formulation, which contains classical formulae as subsets.

Whereas hyperbolic expressions are highly accurate for the interpolation of traveltimes as long as the spatial distance to the expansion point is kept small, they are less suited for the description of diffraction traveltimes. For this reason, I have also introduced a new non-hyperbolic stacking operator, the implicit common reflection surface (i-CRS) operator.

The technique for the interpolation of traveltimes is based on the traveltime differences (i.e., move-out) between neighbouring sources and receivers of a multi-coverage experiment. All coefficients for the interpolation are computed from traveltimes on coarse grids. The interpolation has a high accuracy since it acknowledges the curvature of the wavefront and is thus exact up to the second order.

Following from the investigation of the accuracy of the coefficients I recommend the hyperbolic rather than parabolic traveltime interpolation. This commendation is supported by the generic examples. Both hyperbolic and parabolic variants are, however, far superior to the often used trilinear interpolation. The difference in computational time for the three variants is insignificant.

One important feature of the technique is its possibility to interpolate between sources, not only between receivers. The fact that all necessary coefficients can be computed on a coarse grid leads to considerable savings in computational time and computer memory since traveltime tables for less sources need to be generated as well as kept in storage. If, e.g., every tenth grid point in three dimensions is used, this corresponds to a factor of 10^5 (if the sources are located in the x-y surface) less in storage requirement for interpolation of shots and receivers at no significant loss in accuracy. As the method is not restricted to cubical grids the coarse grid spacing can be adapted to the model under consideration. It is even possible to use the method on irregular grids; this will be demonstrated in Chapter 10 in the second part of this thesis.

I have applied the traveltime interpolation to a multitude of isotropic and anisotropic simple and complex models. The results clearly show the high accuracy of the method with the exception of regions where the wavefield is non-unique, i.e., the presence of triplications. In these regions, the requirements for the Taylor expansion on which my method is based, are not fulfilled. It was, therefore, necessary to extend the technique to the presence of later arrivals. If these are taken into account, I have shown that irregularities of the wavefield do not lead to errors any longer. Furthermore, the traveltime coefficients can be employed to detect such regions.

Since hyperbolic expressions are widely applied operators for multiparameter stacking, I have established the link between my hyperbolic formulation and the commonly-used CRS multiparameter stacking operator. I have shown that my formulation contains the CRS as a subset; however, my operator is applicable in a more general sense since it provides a description not only for isotropic media sorted in midpoint and half-offset coordinates, as does the CRS, but also for arbitrary measurement configurations and including anisotropy. It is therefore a *general* NMO operator.

An example on multiparameter stacking in the source-receiver domain using the general NMO operator demonstrates that it is possible to obtain good stacking results compared to the classic CRS method; however, stacking in midpoint and half-offsets is still superior because more parameters can be determined in the poststack domain. Since the classic CRS cannot account for anisotropy, however, use of the general NMO operator may still be a better solution in such media.

Although hyperbolic operators are widely used, they have disadvantages in the presence of diffractions. It is only fairly recently that the importance of diffractions in seismic data processing has been recognised, amongst others, as the link between active and passive seismics. In order to find a better description for diffraction traveltimes, I have developed a new, implicit CRS operator.

Its main advantages are that it leads to high accuracy over a wide range of reflector curvatures, from the diffraction limit to the plane reflector case, and that it can be formulated in terms of the classic CRS wavefield attributes, which have been implemented in a workflow starting with the stack to velocity model building and, finally, depth migration.

We have shown with generic examples that the i-CRS operator leads to better wavefield attributes and thus a better stack. In the context of the CRS processing, it does not matter how these attributes were determined, therefore the superior attributes from the i-CRS stack can lead to higher quality of the results of the CRS workflow.

Application of the new operator to a complex model with salt structures proves the superiority over the classic CRS and CMP methods. The resolution of the rugged top of salt, which leads to many diffractions in the data, is astonishingly high compared to the classic results. This result is very important for diffraction processing, e.g., also for the separation of diffraction and reflection events.

Another important result of my work presented here is that the i-CRS operator leads to convincing results in the presence of anisotropy. Not only does it show high accuracy in the simple examples considered this far, but we have obtained promising results for the application of the operator with regards to anisotropy parameter estimation, which is still a key problem in seismic data processing.

Part II

Amplitudes and migration: the dynamic problem

Chapter 7

Introduction

The motivation for a seismic experiment is to obtain information about the subsurface: what does it consist of, i.e. what are the material parameters, and how is it stratified. The result of the experiment is a seismic section, a time image of the subsurface. This image is, however, a distorted image that can not be directly translated into velocities and structure: the reflections present in the section do not show the correct positions and inclinations of the corresponding reflectors.

A corrected map of the subsurface can be obtained by inverting the seismic reflection data. One specific inversion process is the seismic migration, which moves[1] the reflections in the time section to the correct reflector positions, thus the migration output provides a focused image of the subsurface.

A specific type of migration, amplitude-preserving migration, also allows the reconstruction of the reflection amplitudes. Since reflection coefficients for one wave-type (e.g., an incident P wave) depend on the P and S velocities of the media above and below the reflector, the reconstructed PP reflection coefficient is a prime source of information: it provides estimates on the P and S velocities also below the reflector. Thus, information about shear properties can even be obtained without measuring shear waves, from PP reflections by examining the AVO (amplitude vs. offset) or AVA (amplitude vs. angle) behaviour. This feature makes amplitude-preserving migration an important technique in seismic imaging.

Amplitude-preserving migration is carried out in terms of a weighted summation of the seismic traces, which are stacked along the diffraction time surface for the image point under consideration. The stacking process yields the structural image, whereas the weight functions take care of the amplitudes. Unfortunately this process is very expensive with respect to computational time and storage, because

1. the diffraction time surface for each subsurface point must be computed and stored,
2. individual weight functions must be computed and stored for each source-subsurface-receiver point combination,
3. the summation stack has to be carried out over the whole experiment's aperture.

Therefore an efficient strategy is of utmost importance when dealing with migration, especially if amplitudes are concerned.

[1]to *migrate* means to *move*

Different approaches have been published to overcome these problems. I have already discussed traveltime generation and interpolation Part 1 of my thesis. In this second part, I will focus on amplitudes, or, more specifically, geometrical spreading and migration weight functions.

During the last decades, several approaches have led to different formulations for true-amplitude weight functions (e.g., Beylkin, 1985; Bleistein, 1987; Schleicher et al., 1993a), which are, however, found to be equivalent (Hanitzsch, 1997). According to Sollid (2000), true-amplitude migration has only been applied successfully in regions with relatively simple geology, whereas in complex media it is still unknown if any migration method can lead to trustworthy results for the amplitudes (Gray et al., 2001). Nevertheless, Gray et al. (2001) emphasise that attention must be paid to amplitudes because ignoring them bears the risk of introducing artifacts into the images, which may compromise the interpretation.

Despite its benefits, true-amplitude migration is not routinely applied, as it is a task of high computational effort, especially when 3D data are considered. As mentioned above, in addition to the traveltime tables for the generation of the stacking surfaces, further quantities are required to compute the true-amplitude weight functions. Whereas fast implementations like finite-difference Eikonal solvers (FDES, e.g., Vidale, 1990) or kinematic ray tracing (KRT, Červený, 2001) can be applied for the traveltimes, the computation of the weight functions requires more effort.

The standard way to compute the weights is the application of dynamic ray tracing (DRT, Gajewski and Pšenčík, 1987; Červený and de Castro, 1993; Hanitzsch et al., 1994). In addition to being slower than FDES and KRT, DRT has higher requirements on the model, i.e., smoothness. Furthermore, in the presence of anisotropy, DRT has additional issue, e.g., when shear wave splitting occurs, this can lead to problems not only for the S-waves but for P-wave computation as well.

Although efficient implementations for true-amplitude Kirchhoff migration exist (see, e.g., Thierry et al., 1999a,b), the dynamic ray tracing issue still holds, in particular when anisotropy needs to be considered. Correspondingly, much effort has gone into finding simplified, more economic expressions for the weights, as shown by, e.g., Dellinger et al. (2000) or Zhang et al. (2000). Hanitzsch et al. (2001) introduced an interesting method that applies the weight *after* the stacking. This solves the problem associated with the computation and storage of large weight function tables, but not with the aperture. Schleicher et al. (1997) have published a technique to carry out limited aperture migration. They compute the optimum migration aperture together with the weight functions using dynamic ray tracing.

In this part of my thesis, I present an approach to amplitude preserving migration that leads to considerable savings, up to a factor of 10^{-5}, in storage, as well as in CPU requirements. My strategy uses coarsely-gridded traveltime tables as only input information. These traveltime tables are in any event needed for the construction of the diffraction time surface. The information that is contained in the traveltimes provides a solution to all the three major problems stated above:

1. a fast and accurate traveltime interpolation algorithm (as I have already shown in Chapter 2),

2. an efficient technique for the determination of the weight functions, which will be introduced in Chapter 9,

3. a technique to determine an optimum and limited migration aperture, as I will show in Section 9.7.

The traveltime interpolation coefficients are determined from the coarsely-gridded input traveltimes. The coefficients are the input for the computation of the weight functions and the size of the optimum aperture. Since all quantities can be computed on-the-fly no additional storage is required. The following agenda gives a brief overview of the steps involved.

Since the method that I present in this part of my thesis is based on the ray concept, Appendix A summarises the basic principles of wave propagation in the high frequency limit, the asymptotic ray method. That appendix is mainly intended to recollect those foundations that are crucial for this thesis, focusing on the ray propagator formalism and the paraxial ray method.

The traveltime interpolation introduced in Chapter 2 is exact up to second order, thus acknowledging the wavefront curvature. This property translates directly into an expression for the geometrical spreading, which is a consequence of the wavefront curvature and a key ingredient to the weight function. I derive expressions for the spreading in Chapter 8. Examples for simple and complex velocity models including anisotropic examples illustrate that this technique for the computation of geometrical spreading leads to convincing results compared to spreading obtained with dynamic ray tracing.

With the results from the previous chapters it is now possible to formulate the technique of traveltime-based true-amplitude migration. Chapter 9 begins with a review of the concept of amplitude-preserving migration. I derive an expression for the weight functions in terms of the traveltime coefficients and give examples for the reconstruction of amplitudes for PP reflections and reflections from PS converted waves, beginning with simple isotropic and anisotropic models to evaluate the performance of the method. Application to complex synthetic and field data shows that the traveltime-based migration yields the same image quality as migration using dynamic ray tracing, thus also confirming the results from Chapter 8.

Although the computational effort required for amplitude-preserving migration can be considerably reduced by applying the traveltime-based technique, a further significant reduction is possible by limiting the migration aperture. Therefore, limited-aperture migration is considered in Section 9.7. I explain why use of a limited aperture is possible and how an optimum aperture can be defined, as well as determined. As for the migration weights, the traveltime coefficients provide a tool to estimate the optimum aperture. Examples illustrate the limited aperture migration and confirm the high potential savings in computational time as well as an enhanced image quality.

In Chapter 10, I discuss two suggestions for possible future work. One topic that I will already briefly address in Section 9.8 in the context of anisotropy is the influence of errors in the velocity model on the recovered amplitudes. Another future aspect is a migration implementation that allows for a better illumination of the image point in the subsurface. It was originally suggested by Brandsberg-Dahl et al. (2001) and is especially suited for a traveltime based implementation.

Chapter 11 draws the final conclusions of the work presented in this part of my thesis.

Chapter 8

Geometrical spreading

Geometrical spreading, together with traveltimes, plays an important role in many applications of reflection seismology, such as migration, tomography, and modelling. The traditional method of computing geometrical spreading is to perform dynamic ray tracing, as described by Červený et al. (1977) or Popov and Pšenčík (1978). Dynamic ray tracing, however, is a rather time consuming process. Therefore, other methods have been proposed. In 1990, Vidale and Houston suggested a technique to calculate amplitudes from traveltimes. Although it is very fast it suffers from problems with accuracy. The method proposed by VanTrier and Symes (1990) is based on a finite difference (FD) eikonal solver. An improved FD scheme that achieves higher order accuracy was suggested by Pusey and Vidale (1991). Another way to determine geometrical spreading is proposed by Buske (2000), by directly solving the transport equation with finite differences. All these techniques are more efficient than dynamic ray tracing. Lower order FD methods are, however, restricted to fine grids, whereas higher order schemes are less efficient. This restriction does not apply to the amplitude estimation using a wavefront construction method introduced by Vinje et al. (1993). Another ray-based approach is shown by Hubral et al. (1992a), who give an expression for the geometrical spreading that is directly related to second order traveltime derivatives in terms of the Bortfeld (1989) matrices.

The method of computing geometrical spreading that I suggest in this chapter is based on the traveltime coefficients introduced in Chapter 2, and closely related to the formula by Hubral et al. (1992a). The coefficient matrices that were introduced in Chapter 2 can be related to the submatrix $\underline{Q}_2$ of the $\underline{\underline{\Pi}}$ propagator, which provides the spreading. Therefore, the geometrical spreading can be determined from traveltimes. The resulting expression is equivalent to the result obtained by Hubral et al. (1992a).

After a short introduction to the cause of geometrical spreading I derive expressions for the spreading in terms of the second order traveltime derivative matrices. That section is followed by application to different isotropic velocity models, ranging from models, where the analytic solution is known to the highly complex Marmousi model. The spreading can be computed from both parabolic and hyperbolic traveltime coefficients. The results confirm again the superiority of the hyperbolic expression. In the final section, I expand the theory to anisotropic media and demonstrate that the method is equally applicable there.

a) b)

Figure 8.1: Geometrical spreading for a point source in a homogeneous medium. The wavefronts are circles in 2-D or spheres in 3-D. The energy flux through a solid angle element remains constant (a). The flux through a surface element depends on the radius of curvature of the wavefront (b).

8.1 Introduction

Conservation of energy is a fundamental rule that also applies to wave propagation. It means that, unless attenuation is caused by mechanisms like, e.g., absorption, the energy of a wavefront remains unchanged. Such mechanisms are not considered in this chapter and I assume an ideal elastic medium. While the wave propagates through the medium, its initial energy is "spread" on the expanding wavefront, causing a decrease in the wave amplitude. This phenomenon is called geometrical spreading.

Figure 8.1 displays a point source in a homogeneous medium and two corresponding wavefronts. Figure 8.1 a) states that the amount of energy, expressed by the flux through a section of the circular (in 2D) or spherical (in 3D) wavefront remains constant for a fixed solid angle. This means, however, that for the second wavefront with smaller curvature the same amount of energy is spread over a larger surface than for the first wavefront with high curvature. Since a detector measures the energy flux through a surface element, not through a solid angle, it will register a smaller amplitude for the second wavefront than for the first one (see Figure 8.1, b). The ratio of the measuring surface element to the complete wavefront is proportional to $1/r^2$ in 3-D, and $\propto 1/r$ in 2-D, where r is the radius of curvature of the wavefront. The amplitude corresponds to the square-root of the flux, therefore the amplitude of the wave in a 3-D medium decreases with $1/r$ and with $1/\sqrt{r}$ in 2-D. The relative geometrical spreading L is the inverse of the amplitude, thus $L \propto r$ in 3-D and $L \propto \sqrt{r}$ in 2-D. The curvature of the wavefront also determines the geometrical spreading in arbitrary media, as I illustrate in Figure 8.2. Furthermore, Figure 8.3 shows that the measured flux also depends on the incidence angle between the wavefront and the registration surface.

Knowing that the geometrical spreading is governed by wavefront curvature and that the curvature of a function is determined by its second order derivatives, a relationship between the spreading and the traveltime derivatives from Chapter 2 can be established. An expression for the spreading in terms of second order traveltime derivatives in a specific, ray centred coordinate system was already given in Appendix A. The following section will relate that result to the coefficients from the traveltime expansions in Chapter 2.

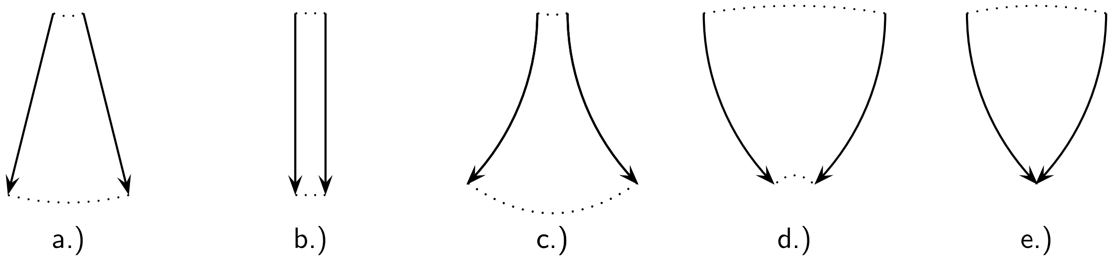

Figure 8.2: Geometrical spreading expressed by ray density and wavefront curvature for arbitrary isotropic media. (a) Homogeneous medium: the same situation as in Figure 8.1. The ray density decreases and the energy is distributed over a larger surface, leading to a decrease in amplitude. (b) Plane wave: the ray density as well as the surface remain constant, therefore the amplitude does not change either. (c) The rays diverge stronger than for the homogeneous medium, leading to a decrease in ray density and the energy is distributed over a larger surface; the amplitude decreases stronger than for the homogeneous case. (d) Converging rays lead to an increase of the amplitude. (e) Extreme case of (d), where two rays meet at a so-called caustic point. In this point, the amplitude grows infinite. Note, however, that in reality, we are not dealing with mathematical rays. For a physical ray, the energy is distributed over the Fresnel volume, not concentrated in a point, as implied in (e). Since the rays are perpendicular to the wavefronts, we can easily recognise that the curvature of the rays translates into the curvature of the corresponding wavefront, which determines the geometrical spreading.

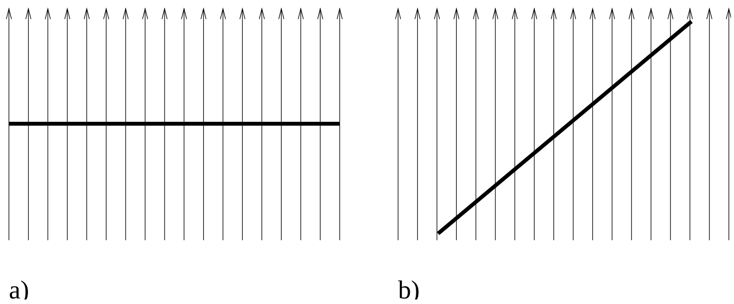

Figure 8.3: Energy flux through a surface. The arrows denote the flux and the thick lines the measuring surfaces. Both surfaces have equal size. In the case of vertical incidence, a), more flux lines pass through the surface than for oblique incidence, b). Therefore, the measured amplitude depends on the incidence angle.

8.2 Spreading and traveltime derivatives

From Equation (A.5.15) I take the modulus of the relative geometrical spreading, $L = |\det \underline{Q}|^{1/2}$. For a point source at s_0 and a receiver at g_0, Equation (A.6.18) with initial point source conditions (A.6.7) yields

$$\begin{pmatrix} \underline{Q}(g_0) \\ \underline{P}(g_0) \end{pmatrix} = \begin{pmatrix} \underline{Q}_1(g_0,s_0) & \underline{Q}_2(g_0,s_0) \\ \underline{P}_1(g_0,s_0) & \underline{P}_2(g_0,s_0) \end{pmatrix} \begin{pmatrix} \underline{0} \\ \underline{1} \end{pmatrix} = \begin{pmatrix} \underline{Q}_2(g_0,s_0) \\ \underline{P}_2(g_0,s_0) \end{pmatrix} \quad , \tag{8.2.1}$$

and therefore

$$L = |\det \underline{Q}_2(g_0,s_0)|^{1/2} \quad . \tag{8.2.2}$$

It is custom to use the normalised geometrical spreading $\mathcal{L}$ rather than the relative spreading L, which was introduced by Ursin (1990) to be

$$\mathcal{L}(g_0,s_0) = \frac{1}{V_s} L(g_0,s_0) \quad . \tag{8.2.3}$$

With $\underline{Q}(g_0,s_0) = -\underline{Q}^\top(s_0,g_0)$ the reciprocity relation for the normalised spreading reads

$$L(g_0,s_0) = V_s\,\mathcal{L}(g_0,s_0) = V_g\,\mathcal{L}(s_0,g_0) = L(s_0,g_0) \quad . \tag{8.2.4}$$

In Chapter 2, I have shown how the second order traveltime derivative matrices $\hat{\underline{G}}$, $\hat{\underline{S}}$, and $\hat{\underline{N}}$ can be determined from traveltime maps. Since $\underline{Q}_2$ is also a matrix of second order traveltime derivatives, a relationship can be established that links the matrix $\hat{\underline{N}}$ to $\underline{Q}_2$. For this reason, I compare the paraxial traveltime approximation in Cartesian coordinates (A.7.16) to the parabolic traveltime expansion introduced in (2.1.4), leading to

$$\hat{\underline{N}} = \hat{\underline{H}}_s\,\hat{\underline{Q}}_2^-\,\hat{\underline{H}}_g^\top \quad , \tag{8.2.5}$$

where the matrices $\hat{\underline{H}}$ are the transformation matrices from Cartesian to ray centred coordinates on the central ray. This can be solved for $\hat{\underline{Q}}_2^-$, which I define as

$$\hat{\underline{Q}}_2^- = \begin{pmatrix} \underline{Q}_2^{-1} & & 0 \\ & & 0 \\ 0 & 0 & 0 \end{pmatrix} = \hat{\underline{H}}_s^{-1}\,\hat{\underline{N}}\,\hat{\underline{H}}_g^{-\top} \quad . \tag{8.2.6}$$

The matrices $\hat{\underline{H}}_s$ and $\hat{\underline{H}}_g$ are defined by Equation (A.5.15). Matrix $\hat{\underline{H}}_s$ consists of the three column vectors $\vec{\boldsymbol{e}}_{1_s}$, $\vec{\boldsymbol{e}}_{2_s}$, and $\vec{\boldsymbol{e}}_{3_s} = \vec{\boldsymbol{t}}_s = V_s\hat{\boldsymbol{p}}_0$. The matrix $\hat{\underline{H}}_g$ is defined accordingly, but using the index g instead of s and $\hat{\boldsymbol{q}}_0$ instead of $\hat{\boldsymbol{p}}_0$. It can easily be shown that $\hat{\underline{H}}^\top = \hat{\underline{H}}^{-1}$. The slowness vectors in Cartesian coordinates (e.g., $\hat{\boldsymbol{p}}_0$) follow from Figure 8.4, and with the slowness vector in ray centred coordinates $\hat{\boldsymbol{p}}_0^{(q)} = (0,0,1/V_s)^\top$

$$\hat{\boldsymbol{p}}_0 = \hat{\underline{H}}(s_0)\,\hat{\boldsymbol{p}}_0^{(q)} = \begin{pmatrix} -\frac{1}{V_s}\sin\vartheta_s\,\cos\varphi_s \\ \frac{1}{V_s}\sin\vartheta_s\,\sin\varphi_s \\ \frac{1}{V_s}\cos\vartheta_s \end{pmatrix} \quad , \tag{8.2.7}$$

and $\hat{\boldsymbol{q}}_0$ accordingly.

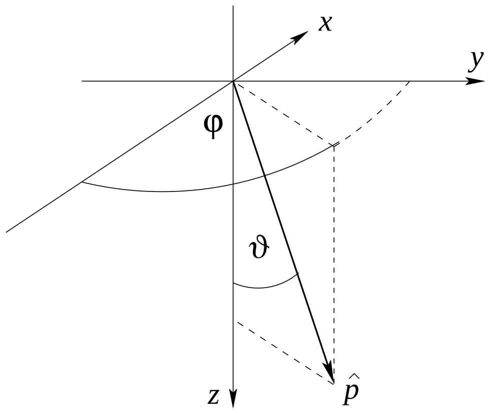

Figure 8.4: Slowness vector and angles in the Cartesian coordinate system. The angle ϑ is the azimuth, φ the polar angle.

Now I use again the constraints on the matrix elements of $\hat{\underline{\mathsf{N}}}$ given by the eikonal equations at the central source and receiver positions. They were already used to derive expressions for the z-components of $\hat{\underline{\mathsf{N}}}$ and $\hat{\underline{\mathsf{S}}}$ in Section 2.1. In addition to Equations (2.1.13) and (2.1.14), I use the following relations

$$\begin{aligned}
N_{xz} &= -\frac{q_{x_0}}{q_{z_0}} N_{xx} - \frac{q_{y_0}}{q_{z_0}} N_{xy} \quad , \\
N_{yz} &= -\frac{q_{x_0}}{q_{z_0}} N_{yx} - \frac{q_{y_0}}{q_{z_0}} N_{yy} \quad , \\
N_{zz} &= \frac{1}{p_{z_0}\, q_{z_0}} \left(p_{x_0}\, q_{x_0} N_{xx} + p_{x_0}\, q_{y_0} N_{xy} + p_{y_0}\, q_{x_0} N_{yx} + p_{y_0}\, q_{y_0} N_{yy} \right) \quad .
\end{aligned} \tag{8.2.8}$$

Equations (2.1.13), (2.1.14), and (8.2.8) can be rewritten to

$$\begin{aligned}
N_{K3} &= -\frac{H_{g_{I3}}}{H_{g_{33}}} N_{KI} \quad , \\
N_{3J} &= -\frac{H_{s_{I3}}}{H_{s_{33}}} N_{IJ} \quad , \\
N_{33} &= \frac{H_{s_{J3}}}{H_{s_{33}}} \frac{H_{g_{K3}}}{H_{g_{33}}} N_{JK}
\end{aligned} \tag{8.2.9}$$

(I, J, K=1,2 and summation convention is applied). Furthermore, in component notation Equation (8.2.6) reads

$$\begin{aligned}
Q^{-}_{2_{il}} &= H_{s_{ji}}\, N_{jk}\, H_{g_{kl}} \\
&= \left(\frac{H_{s_{Ji}}\, H_{s_{33}} - H_{s_{J3}}\, H_{s_{3i}}}{H_{s_{33}}} \right) N_{JK} \left(\frac{H_{g_{Kl}}\, H_{g_{33}} - H_{g_{K3}}\, H_{g_{3l}}}{H_{g_{33}}} \right)
\end{aligned} \tag{8.2.10}$$

(i, j, k, l=1,2,3), where Equation (8.2.9) has been applied. From Equation (8.2.10) follows immediately that

$$\begin{aligned}
Q^{-}_{2_{i3}} &= 0 \qquad (i = 1, 2, 3) \quad , \\
Q^{-}_{2_{3i}} &= 0 \qquad (i = 1, 2, 3) \quad .
\end{aligned} \tag{8.2.11}$$

For the remaining elements of $\underline{\hat{\mathsf{Q}}}_2^-$ I use the fact that the base vectors $\vec{e}_1$, $\vec{e}_2$, and $\vec{t}$ are an orthonormal system with $\vec{e}_1 \times \vec{e}_2 = \vec{t}$ etc. This leads to

$$\frac{H_{JI}\,H_{33} - H_{J3}\,H_{3I}}{H_{33}} = H_{JI}^{-1} \quad . \tag{8.2.12}$$

The element H_{JI}^{-1} is the $JI^{\rm th}$ element of the matrix $\underline{\mathsf{H}}^{-1}$, where

$$\underline{\mathsf{H}} = \begin{pmatrix} H_{11} & H_{12} \\ H_{21} & H_{22} \end{pmatrix} \quad , \tag{8.2.13}$$

is the upper left submatrix of matrix $\underline{\hat{\mathsf{H}}}$. Please mind that the inverse of $\underline{\mathsf{H}}$, $\underline{\mathsf{H}}^{-1}$, is *not* equal to the upper left submatrix of the matrix $\underline{\hat{\mathsf{H}}}^{-1}$, but

$$\underline{\mathsf{H}}^{-1} = \frac{1}{\det \underline{\mathsf{H}}} \begin{pmatrix} H_{22} & -H_{12} \\ -H_{21} & H_{11} \end{pmatrix} \quad , \tag{8.2.14}$$

where the absolute value of the determinant of $\underline{\mathsf{H}}_s$ is equal to $\cos\vartheta_s$, and $|\det\underline{\mathsf{H}}_g|$=$\cos\vartheta_g$. Introducing $\underline{\mathsf{N}}$ as the upper left 2×2 submatrix of $\underline{\hat{\mathsf{N}}}$, the 2×2 matrix $\underline{\mathsf{Q}}_2^{-1}$ results in

$$\underline{\mathsf{Q}}_2^{-1} = \underline{\mathsf{H}}_s^{-\top}\,\underline{\mathsf{N}}\,\underline{\mathsf{H}}_g^{-1} \quad . \tag{8.2.15}$$

With $\det\underline{\mathsf{Q}}_2 = 1/\det\underline{\mathsf{Q}}_2^{-1}$, the spreading in terms of matrix $\underline{\hat{\mathsf{N}}}$ can therefore be expressed as

$$\mathcal{L} = \frac{1}{V_s}\sqrt{\left|\frac{\cos\vartheta_s\,\cos\vartheta_g}{N_{xx}\,N_{yy} - N_{xy}\,N_{yx}}\right|} = \sqrt{\frac{V_g}{V_s}}\sqrt{\left|\frac{p_{0_z}\,q_{0_z}}{N_{xx}\,N_{yy} - N_{xy}\,N_{yx}}\right|} \quad . \tag{8.2.16}$$

Other expressions using different matrix elements of $\underline{\hat{\mathsf{N}}}$ can be found with the relationships between the matrix elements (8.2.8). Here I give only those depending on the elements of $\underline{\hat{\mathsf{N}}}$ that can be determined directly from traveltimes, i.e. not using the N_{3i} elements (see Section 2.1):

$$\begin{aligned} \mathcal{L} &= \sqrt{\frac{V_g}{V_s}}\sqrt{\left|\frac{p_{0_z}\,q_{0_y}}{N_{yx}\,N_{xz} - N_{xx}\,N_{yz}}\right|} \quad , \\ \mathcal{L} &= \sqrt{\frac{V_g}{V_s}}\sqrt{\left|\frac{p_{0_z}\,q_{0_x}}{N_{xy}\,N_{yz} - N_{yy}\,N_{xz}}\right|} \quad . \end{aligned} \tag{8.2.17}$$

These results are equivalent to a result given by Hubral et al. (1992a), who show that the geometrical spreading can be expressed by

$$\mathcal{L} = \frac{1}{V_s}\sqrt{|\cos\theta_s\,\cos\theta_g\,\det\underline{\mathsf{B}}|} \quad . \tag{8.2.18}$$

Here, θ_s is the emergence angle at the anterior surface and θ_g the incidence angle at the posterior surface. The 2×2 matrix $\underline{\mathsf{B}}$ is a submatrix of the ray propagator $\underline{\underline{\mathsf{T}}}$ (see Appendix A and Section 2.8). Using Equation (2.8.8) from Chapter 2.8 yields

$$\mathcal{L} = \frac{1}{V_s}\sqrt{\left|\frac{\cos\theta_s\,\cos\theta_g}{\tilde{N}_{11}\,\tilde{N}_{22} - \tilde{N}_{12}\,\tilde{N}_{21}}\right|} \quad . \tag{8.2.19}$$

If the anterior and posterior surfaces coincide with the x-y-surface of the Cartesian coordinate system, the angles θ_s and θ_g in Equation (8.2.18) equal the angles ϑ_s and ϑ_g. Since in this case the $\tilde{x}$-$\tilde{y}$-surface follows from the x-y-surface by a simple rotation (the determinant of the rotation matrix is equal to 1), the determinants of $\underline{\mathsf{N}}$ and $\tilde{\underline{\mathsf{N}}}$ are equal. Insertion into Equation (8.2.18) leads to

$$\mathcal{L} = \frac{1}{V_s} \sqrt{\left| \frac{\cos\theta_s \, \cos\theta_g}{\det \tilde{\underline{\mathsf{N}}}} \right|} = \frac{1}{V_s} \sqrt{\left| \frac{\cos\vartheta_s \, \cos\vartheta_g}{\det \underline{\mathsf{N}}} \right|} \quad , \tag{8.2.20}$$

which is the same result as in Equation (8.2.16). Results for other orientations of the anterior and posterior surfaces can be found accordingly.

8.3 Isotropic examples

To validate the method, this section starts with models whose analytic solution for the spreading and traveltimes is known. The first example is a homogeneous model with V_0=3 km/s. The input traveltimes were given on a 100m coarse grid. Two sets of input traveltimes were applied. The first contains analytic traveltimes. The second set was obtained with an FD eikonal solver using the Vidale (1990) algorithm on a 10m grid and subsequent resampling of the resulting traveltimes. Hyperbolic and parabolic traveltime coefficients were determined from the traveltimes. The spreading at the coarse grid points was computed with Equation (8.2.16). Trilinear interpolation was carried out onto a fine 10m grid using the spreading values at the coarse grid points. The results were compared to analytically computed geometrical spreading. The residual errors are displayed in Figure 8.5 for both sets of input traveltimes.

The spreading that was computed from the hyperbolic coefficients has smaller errors than that from the parabolic coefficients. This result agrees with the higher errors for the parabolic than for hyperbolic coefficients which was shown in Section 2.3. Also, Figure 8.5 shows that the errors in spreading computed from Vidale traveltimes follow the errors of these traveltimes (see Figure 8.6). The main contributions to the errors from analytic traveltimes come from the trilinear interpolation of the spreading onto the fine grid. Since the errors near the source are the highest, a region of 100m depth under the source was excluded from the statistics. Errors near the source are higher because of the high wavefront curvature there, however, for most applications, the source region is of lower interest. Also, since the geometrical spreading near the source is small, the relative error is rather sensitive there. The median and maximum errors are given in Table 8.1.

A constant velocity gradient model with V_0=3 km/s and $\partial V/\partial z$=0.5s^{-1} with the same dimensions as the homogeneous model is the second example. The resulting error distributions have the same properties as those of the homogeneous model. The errors are displayed in Figure 8.7. The maximum and median errors are also given in Table 8.1.

As an example for a complex velocity model, I have again chosen the Marmousi model (see Figure 2.10). Unlike for the traveltime example in Section 2.4, I have no reference solution to evaluate the resulting geometrical spreading. However, for a 2-D version of the Marmousi model the geometrical (line source) spreading was available for comparison from a wavefront construction implementation by Ettrich and Gajewski (1996). This program was also used to compute the input traveltimes, where 62.5m was chosen as coarse grid spacing. Hyperbolic traveltime coefficients and the geometrical spreading resulting from them were computed at the coarse grid points. The spreading was subsequently interpolated with bilinear interpolation onto a 12.5m fine grid. Figure

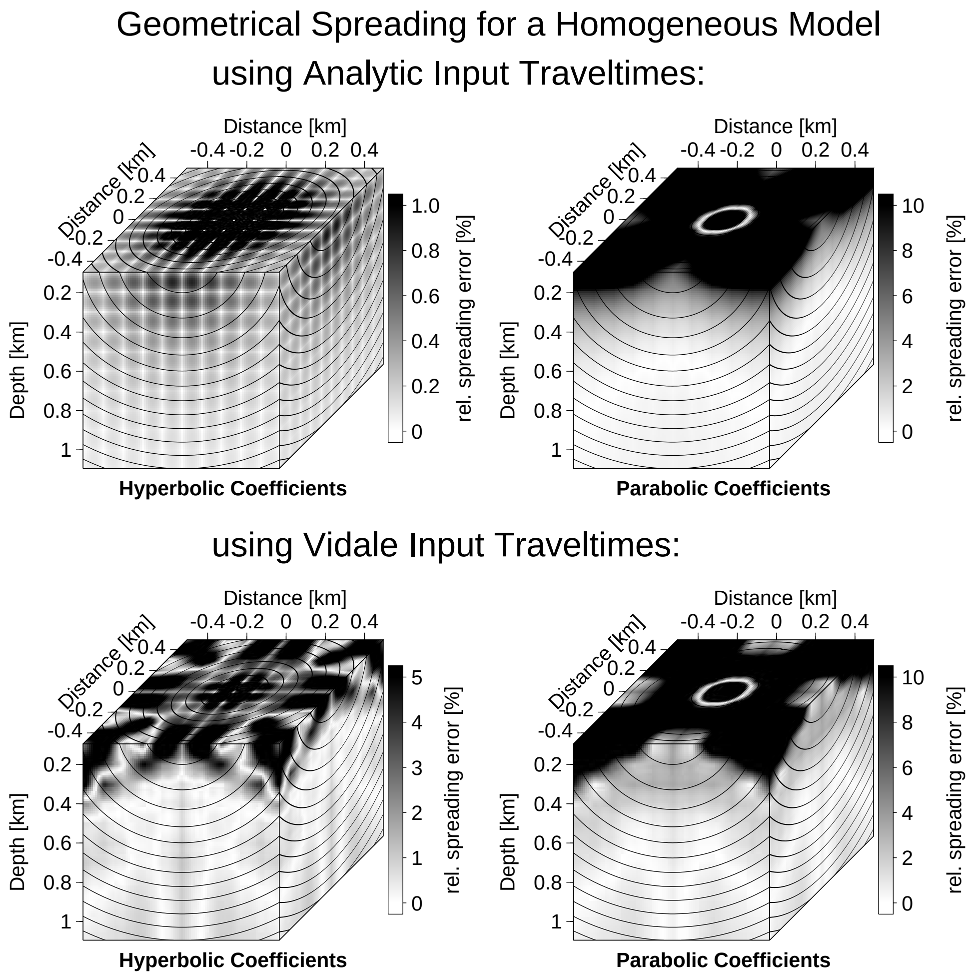

Figure 8.5: Relative errors in geometrical spreading for a homogeneous model, on the right for results from hyperbolic coefficients, left for parabolic coefficients. The top row shows results from analytic input traveltimes, the bottom row those from Vidale traveltimes. The errors of the "parabolic" spreading are larger than those from hyperbolic coefficients. The errors in spreading from Vidale traveltimes follow the traveltime errors of the Vidale algorithm (see Figure 8.6). Please note the different error scales.

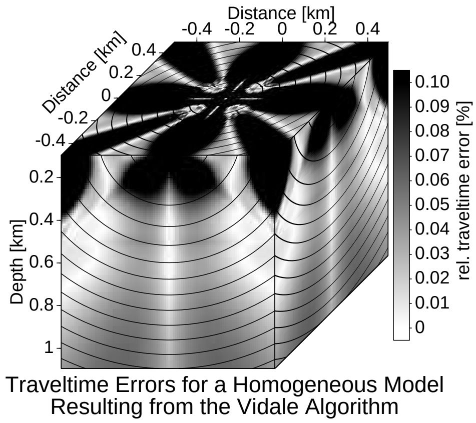

Figure 8.6: Relative errors in percent of Vidale traveltimes for a homogeneous model with V=3 km/s. The median error is 0.06% with a maximum relative error of 0.8%.

Table 8.1: Relative errors in percent of geometrical spreading for two generic models using analytic and numerical traveltimes as input data. A layer of 100m depth under the source was excluded from the statistics.

Model	Traveltimes	Coefficients	Median of rel. error [%]	Maximum rel. error [%]
Homogeneous	analytic	hyperbolic	0.301	14.5
Homogeneous	analytic	parabolic	1.01	61.8
Homogeneous	Vidale	hyperbolic	0.69	14.6
Homogeneous	Vidale	parabolic	1.55	61.4
Gradient	analytic	hyperbolic	0.251	14.1
Gradient	analytic	parabolic	1.03	61.8
Gradient	Vidale	hyperbolic	0.709	14.2
Gradient	Vidale	parabolic	1.61	61.5

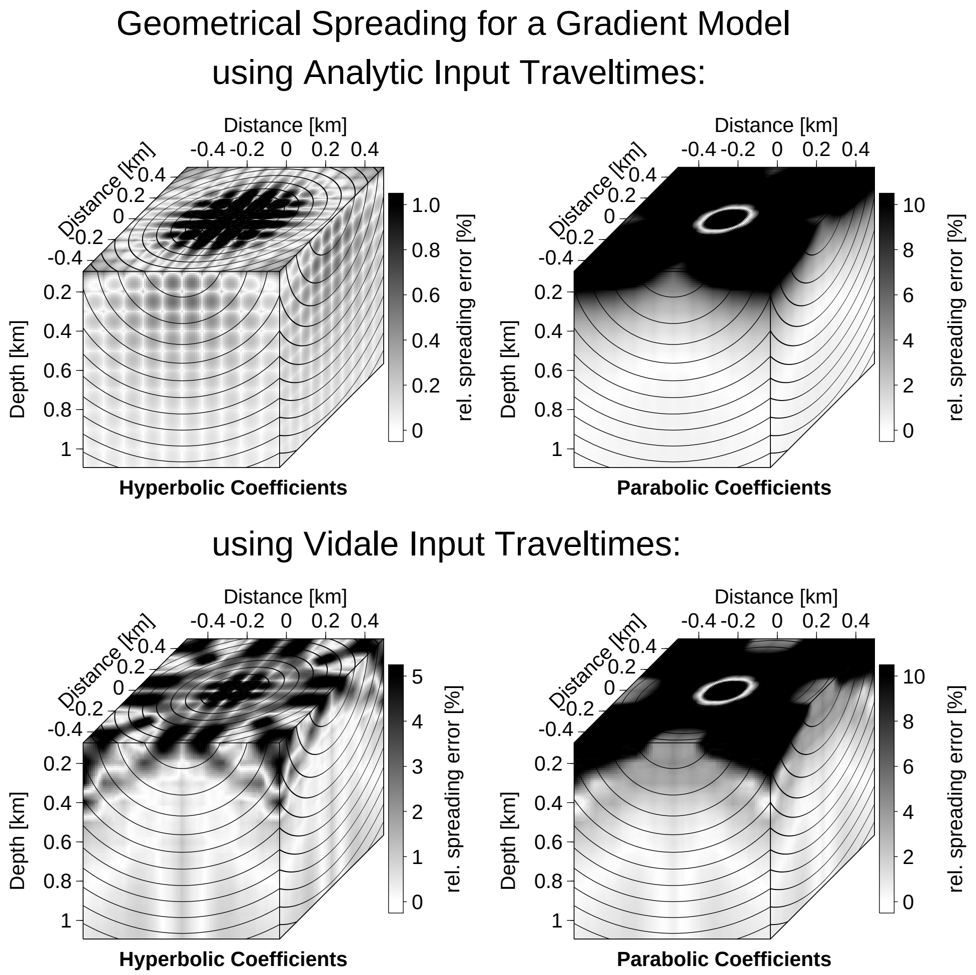

Figure 8.7: Relative errors in geometrical spreading for a gradient model, on the right for results from hyperbolic coefficients, left for parabolic coefficients. The top row shows spreading errors resulting from analytic traveltimes, the bottom row for Vidale traveltimes. Again, the hyperbolic coefficients yield better results than the parabolic ones. Please note the different error scales.

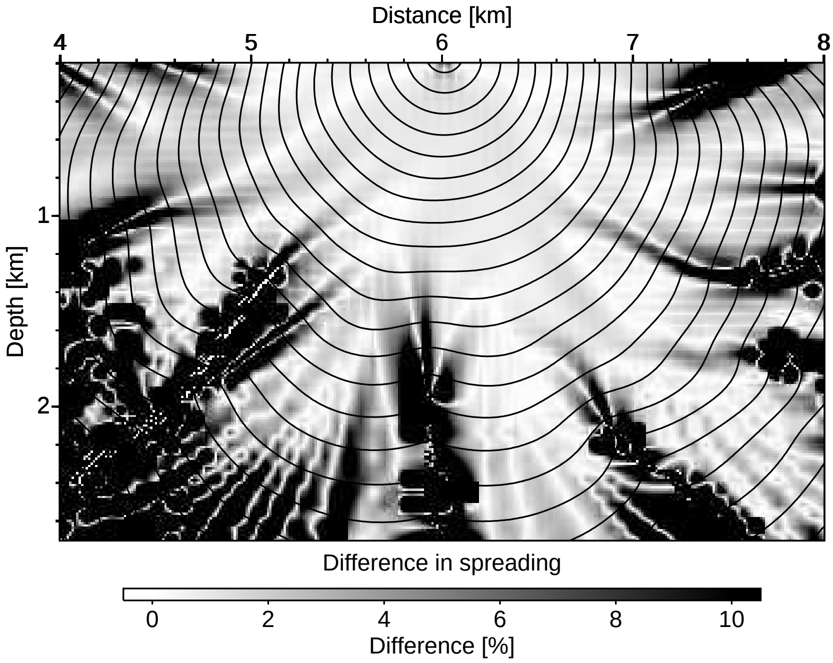

Figure 8.8: Comparison of spreading calculated from hyperbolic coefficients to spreading from a wavefront construction implementation. The difference between both is given in percent. Regions where both results deviate are addressed in the text.

8.8 shows the difference between the results from wavefront construction and hyperbolic coefficients. The median of the difference between the results from the two methods is below 1.8%. The two solutions coincide well apart from regions with discontinuous wavefronts where triplications occur. As described in Section 2.7, these must be detected and the individual branches must be treated separately, also using later arrivals. This was not implemented and therefore the spreading is not computed correctly in these regions. The difference of both solutions is also very distinct in the lower left corner of the image with a pattern that indicates to follow ray paths. Here I presume that the ray density in the wavefront construction algorithm was too small, leading to a failure in traveltime and spreading interpolation, and thus in the input data.

The geometrical spreading was also computed for the 3-D version of the Marmousi model. Input traveltimes were computed using the Vidale algorithm (see Section 2.4) on a 12.5m fine grid, and resampled onto a 125m coarse grid. Hyperbolic coefficients and spreading were computed at the coarse grid points. The spreading was then interpolated onto a 12.5m fine grid using trilinear interpolation. Figure 8.9 shows the results. As expected, the behaviour of the spreading follows the wavefront curvature indicated by the isochrones. In some regions (e.g., those pointed at by the arrows), a speckled pattern emerges. This is caused by a deficiency in the traveltimes due to the implementation of the Vidale scheme: the isochrones in these regions are "rippled". As a consequence, the traveltimes are not smooth, leading to errors in the determination of the coefficients.

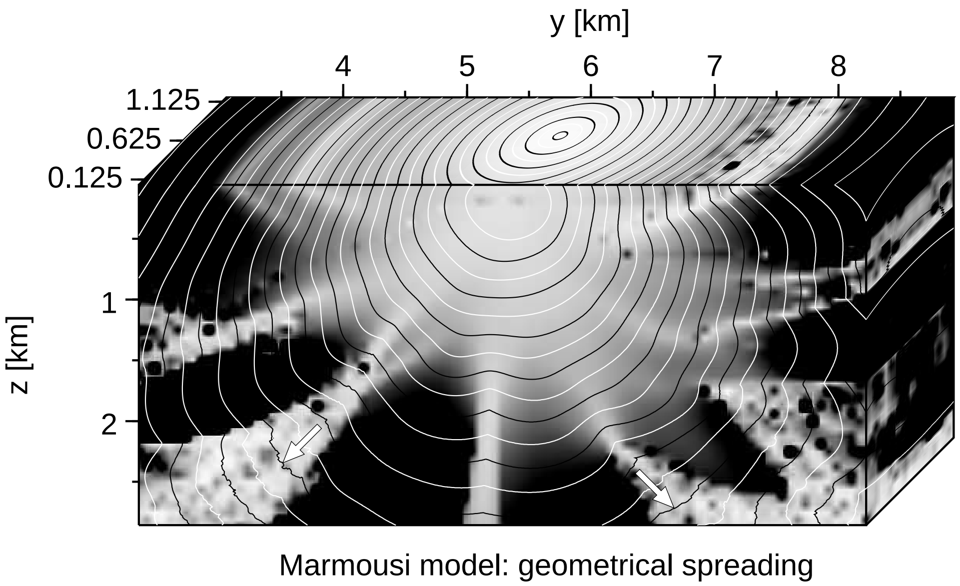

Figure 8.9: Geometrical spreading for the Marmousi model. The arrows indicate two of the regions where the input traveltime data is corrupt, therefore a speckled pattern in the spreading arises (see text). The reason is a deficiency in the FD implementation for the traveltime generation.

8.4 Anisotropy

As I have shown above, geometrical spreading in isotropic media can be determined from traveltime derivatives. In this section, I will show that the method can be extended to anisotropy. I begin with the derivation of the expression of spreading in terms of traveltime derivatives and then demonstrate the result with examples.

Method

As for isotropic media, the modulus of the relative geometrical spreading in anisotropic media is given by Červený (2001)

$$L = \sqrt{|\mathrm{det}\underline{\mathrm{Q}}_2|} \quad . \tag{8.4.1}$$

Our aim is thus again to develop a relationship between the matrix $\underline{\mathrm{Q}}_2$ and the matrix $\underline{\mathrm{N}}$. In contrast to the isotropic case, however, we must now take into consideration that the transformation from Cartesian to ray-centred coordinates involves not only the slowness angles ϑ_i and φ_i, but also the angles between group velocities and phase velocities (which coincide in the isotropic case) as well as the angles between the group velocities and the vertical axis.

The relationships can be derived in a similar fashion as I have applied in section 8.2. Since they were already derived by Schleicher et al. (2001), I give only their result for the determinant of $\underline{\mathrm{Q}}_2$ here:

$$|\mathrm{det}\underline{\mathrm{Q}}_2| = \frac{\cos\alpha_s \cos\alpha_g}{\cos\chi_s \cos\chi_g} \, |N_{11}N_{22} - N_{12}N_{21}|^{-1} \quad . \tag{8.4.2}$$

As already indicated above, α_s (α_g) is the acute angle between the ray or group velocity vector $\boldsymbol{v}_s$ ($\boldsymbol{v}_g$) at the source (receiver) and the s_3 (g_3) direction. The angle χ_s (χ_g) is made by the ray velocity vector and the slowness vector $\boldsymbol{p}$ ($\boldsymbol{q}$). It is given by the relationship

$$\cos \chi_s = \frac{V_s}{v_s} \quad , \tag{8.4.3}$$

and for $\cos \chi_g$ accordingly, where V_s (V_g) is the phase velocity at the source (receiver), which can be determined from the slowness components by $V_s^{-2} = \boldsymbol{p} \cdot \boldsymbol{p}$ ($V_g^{-2} = \boldsymbol{q} \cdot \boldsymbol{q}$). Thus, the relative geometrical spreading for arbitrary wave type in an anisotropic medium becomes

$$L = \sqrt{\frac{\cos \alpha_s \, \cos \alpha_g}{|N_{11}N_{22} - N_{12}N_{21}|} \frac{v_s}{V_s} \frac{v_g}{V_g}} \quad . \tag{8.4.4}$$

In isotropic media, $V = v$, and Equation (8.4.4) reduces to the result derived above.

The components v_{s_i} (i=1,2,3) of the ray velocity vector for an arbitrary anisotropic medium can be computed from the slowness vector $\boldsymbol{p}$ and the values of density normalised elasticity tensor a_{ijkl} at the source position (Červený, 2001):

$$v_{s_i} = a_{ijkl} \, p_l \, \frac{D_{jk}}{D} \quad . \tag{8.4.5}$$

In Equation (8.4.5) the p_l are the components of the slowness vector. The matrix elements D_{jk} are given by Červený (2001)

$$D_{jk} = \frac{1}{2} \, \epsilon_{jlm} \epsilon_{kno} (\Gamma_{ln} - \delta_{ln})(\Gamma_{mo} - \delta_{mo}) \quad , \tag{8.4.6}$$

where

$$\Gamma_{jk} = a_{ijkl} \, p_j \, p_l \tag{8.4.7}$$

is the Christoffel matrix. Furthermore,

$$D = D_{ii} \quad . \tag{8.4.8}$$

In Equations (8.4.5) to (8.4.8) summation convention is applied. The symbol ϵ_{jlm} denotes the Levi-Civitta tensor, and δ_{jk} is Kronecker's delta. Application of Equation (8.4.5) using the slowness vector and the elasticity tensor at the source and the receiver, respectively, leads to both ray velocities, v_s and v_g, as well as to the ray angles, α_s and α_g.

Equation (8.4.5) is following from the solution of the eigenvalue problem for the Christoffel matrix Γ_{jk}. If the Christoffel matrix is degenerate, Equation (8.4.5) cannot be applied since then D=0. This happens globally in isotropic media (where, however, the ray velocity equals the phase velocity and is known) and can also occur locally in anisotropic media, if the phase velocities of both quasi shear waves coincide. The problems with the resulting singularities are inherent to standard anisotropic high frequency methods and not a deficiency of our method in particular.

Equation (8.4.1) gives the *modulus* of the geometrical spreading. For the computation of proper migration weights, however, the phase shift due to caustics must also be considered. This is only possible, if later arrival traveltimes are available. These are important for migration in complex media (Geoltrain and Brac, 1993). Our method can also be applied to later arrivals. In that case, the individual traveltime branches which contribute to the resulting triplications must be treated separately, as suggested in section 2.7.

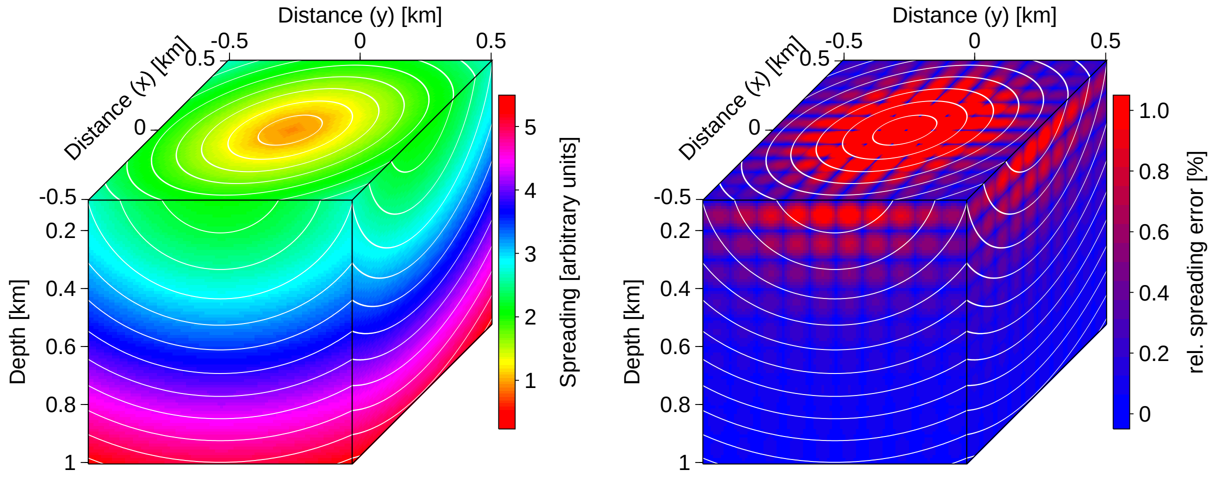

Figure 8.10: Geometrical spreading determined from traveltimes for a homogeneous model with elliptical symmetry (left) and errors of the geometrical spreading for this model. Relative errors are higher in the near-source vicinity because of the stronger local curvature and the trilinear interpolation onto the fine grid. Note that the major contributions to the errors come from the trilinear interpolation, whereas at the coarse grid-points the errors are of a smaller magnitude.

Examples

In this section we give examples for two anisotropic models, a homogeneous model with elliptical anisotropy where an analytic solution exists, and the triclinic velocity model already used to demonstrate the traveltime interpolation in section 2.5.

Our first example is a homogeneous model with elliptical anisotropy. We considered P-waves with the relevant density-normalised elastic coefficients $A_{11} = A_{22} = 15.96$ km^2/s^2 and $A_{33} = 11.4$ km^2/s^2. Coarsely-gridded traveltime tables were computed analytically on a 100 m coarse grid. The geometrical spreading was computed on the coarse grid using Equation (8.4.4) and the coefficients from Equation (2.2.2). Subsequent trilinear interpolation was then carried out to obtain the spreading on a 10 m fine grid. The results were compared to the analytical solution (see Appendix C). Figure 8.10 shows both the spreading itself and its relative errors. The median of the relative errors is 0.23 % and its maximum is 9.2 %. Note in Figure 8.10, that the main contributions to the errors come from the trilinear interpolation. This is especially true in the region near the source where the wavefront curvature is strongest. This region is, however, of minor interest for migration.

In the next example we show the geometrical spreading for the homogeneous triclinic model (Vosges sandstone) from section 2.5. Again, the spreading was computed from the traveltime coefficients and the elasticity tensor at the coarse grid points with a 100 m spacing and trilinearly interpolated onto the 10 m fine grid. Since no analytical solution exists for this model, and a suitable tool for the computation of geometrical spreading on a densely sampled 3-D grid is not available to us, the errors can not be quantified. The results are shown in Figure 8.11

Finally, we have embedded a low velocity lens in the triclinic medium. As for the traveltimes shown in Figure 2.16, we expect errors near the triplications of the wavefront in the centre of the model. Figure 8.12 shows the geometrical spreading for the whole model as well as a section through the triplicated wavefront region. Again, to obtain the correct coefficients in these regions, later-arrival

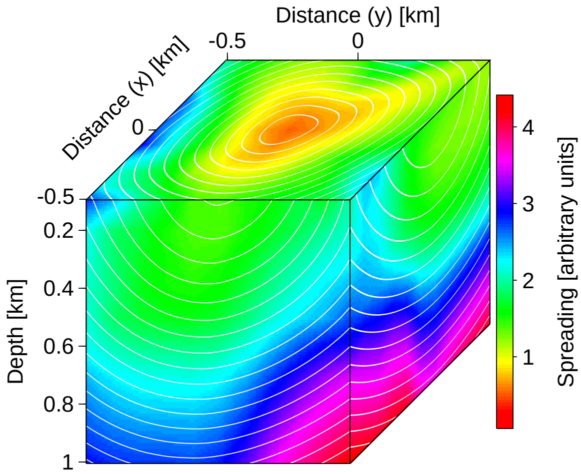

Figure 8.11: Geometrical spreading determined from traveltimes for a homogeneous model with triclinic symmetry.

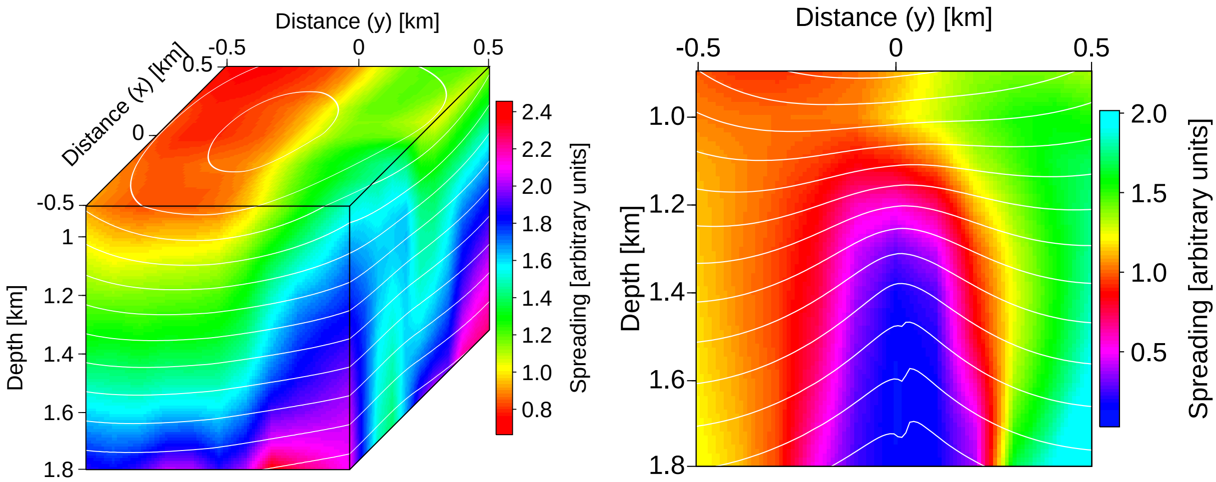

Figure 8.12: Geometrical spreading determined from traveltimes for a velocity lens model with a triclinic symmetry. The section on the right side cuts through a triplicated wavefront. In the blue centre region near the triplication the spreading values are wrong. To correctly determine the traveltime coefficients in these regions, later-arrivals are required. The shape of the isochrones in the centre of the model is caused by artifacts in the reference traveltimes.

traveltimes are required.

I conclusion, we find that geometrical spreading can also be obtained from traveltimes for anisotropic media.

Chapter 9

True-amplitude migration

Migration is an inversion operation that recovers the structure of the subsurface from seismic reflection data. It *moves* the reflections in the input data to their correct locations and inclinations. Although an initial velocity model must already exist migration provides a better focused image of the subsurface. This is also possible if lateral velocity variations exist, which makes it a powerful tool compared to other imaging techniques, as, e.g., NMO-DMO-stacking.

Amplitude preserving migration is a specific type of Kirchhoff migration. In addition to the structural image it also provides information on the reflection strength of the reflectors in the model, leading to estimates of the shear properties of the subsurface. This information is a key feature for reservoir characterisation.

I begin this chapter with a review of the existing concept of amplitude preserving migration, also named "true amplitude migration". Three different theoretical approaches have been published during the last 15 years. All of them apply weight functions to the diffraction stack to countermand the loss in amplitude that is caused by geometrical spreading. One method was introduced by Keho and Beydoun (1988), as an extension of the classical Kirchhoff theory (Gardner et al., 1974). It is based on the wave field concepts and gives results for the common shot (CS) and common receiver (CR) configurations. The weight functions were derived using WBKJ ray theoretical Green's function amplitudes. Another approach is that of Bleistein (1987) whose weight functions are based upon Beylkin's determinant (Beylkin, 1985). A work by Červený and de Castro (1993) relates the Beylkin determinant to quantities that can be computed by dynamic ray tracing. This approach can be applied to the common offset (CO) configuration in addition to CS and CR data. The theory behind the third approach was derived by Schleicher et al. (1993a). They propose a weight function that can be derived using paraxial ray theory for arbitrary configuration. A comparison of the three methods can be found in Hanitzsch (1997).

The chapter continues with a short introduction to migration, especially migration of the Kirchhoff type. The next section considers the derivation of a general expression for the weight functions in 3-D media. Since this thesis uses the approach of Schleicher et al. (1993a), I will give a summary of their work. Two quantities are the main ingredients to the weight functions, the geometrical spreading $\mathcal{L}$ and a matrix, $\underline{\mathrm{H}}_{\mathrm{F}}$, which will be explained in the following section, too. Both, $\mathcal{L}$ and $\underline{\mathrm{H}}_{\mathrm{F}}$ can be expressed in terms of the second order traveltime derivatives introduced in Chapter 2, which leads to the final weight function. The corresponding weights for migration in 2-D and 2.5-D are also given, although without derivation. This concludes the theoretical part of the chapter. The next two sections are dedicated to application of the method, first to PP data, including complex synthetic and field data, followed by a PS-converted wave example. A section dedicated to the determination of optimised migration apertures is given, before I extend the method to account for anisotropy.

9.1 Introduction to seismic depth migration

The aim of a seismic reflection experiment is to gain information about the subsurface. This concerns the material properties (densities and elastic parameters) as well as structural information, like geometry and position of reflectors. Although one can quite easily simulate the results from a seismic experiment if the velocities and structural information are given, the inverse process is much more complicated. A zero-offset time section will display an image of the subsurface. This image, however, is distorted: reflectors may not be shown at their correct positions and their inclinations will be wrong. Further confusion is added by diffraction events and later arrivals, e.g., from trough-like structures. Depth migration is an inversion technique which can reconstruct the true image of the subsurface. The term 'to migrate' has the meaning 'to move': the reflections which are present in the seismic data are moved to their correct positions and inclinations. At the same time, diffractions are collapsed. Therefore, the migrated image is a focused and corrected image of the subsurface.

Figure 9.1 shows schematically, how migration works. Each subsurface point under consideration is treated as a diffraction point. The diffraction traveltime curve for the point is constructed (how this can be done will be addressed below) and the traces are stacked along that curve. This process is called Kirchhoff migration. Figure 9.1 illustrates that the summation will only be constructive if the point under consideration lies on the reflector.

Consider now what would happen, if the event in Figure 9.1 were a diffracted event. In this case the stack would only give a non-vanishing result if the subsurface point and the scatterer which causes the diffracted event coincide. This means that a diffraction in the seismic section, which is caused by a point scatterer, is collapsed into a point at the correct position by the migration.

We can think of a reflector as an ensemble of point scatterers. Superposition of the individual points leads to the reconstructed reflector, as shown by Figures 9.2 and 9.3. The resulting image can be either in depth, if the migration output for the image point is written to its position, or in time, where the migration output is written to the apex of the stacking surface. Please note that the terms depth migration and time migration are not defined by either a depth or a time section. They are different concepts, which will be addressed now.

In order to construct the stacking surface, information is required on the velocities. The stacking surface in time migration is given by analytic diffraction traveltimes resulting from RMS velocities (Bancroft, 1998). This is a simplification which does not hold for complex models, especially if strong lateral velocity variations are present. Therefore it is better to consider the "real" velocity model to compute diffraction traveltime curves as stacking surfaces, e.g., with ray tracing or FD eikonal solvers. This process is called depth migration. It is much more complicated and time consuming than to carry out a time migration, but complex models can be considered.

Migration requires a velocity model. The reader may wonder why a technique is chosen to construct an image of the subsurface where the information one hopes to obtain must already exist. This is only partially true. Of course it appears to be paradox to use the hoped-for output as input information. But the demands on the input velocity model allow, for example, to use a long

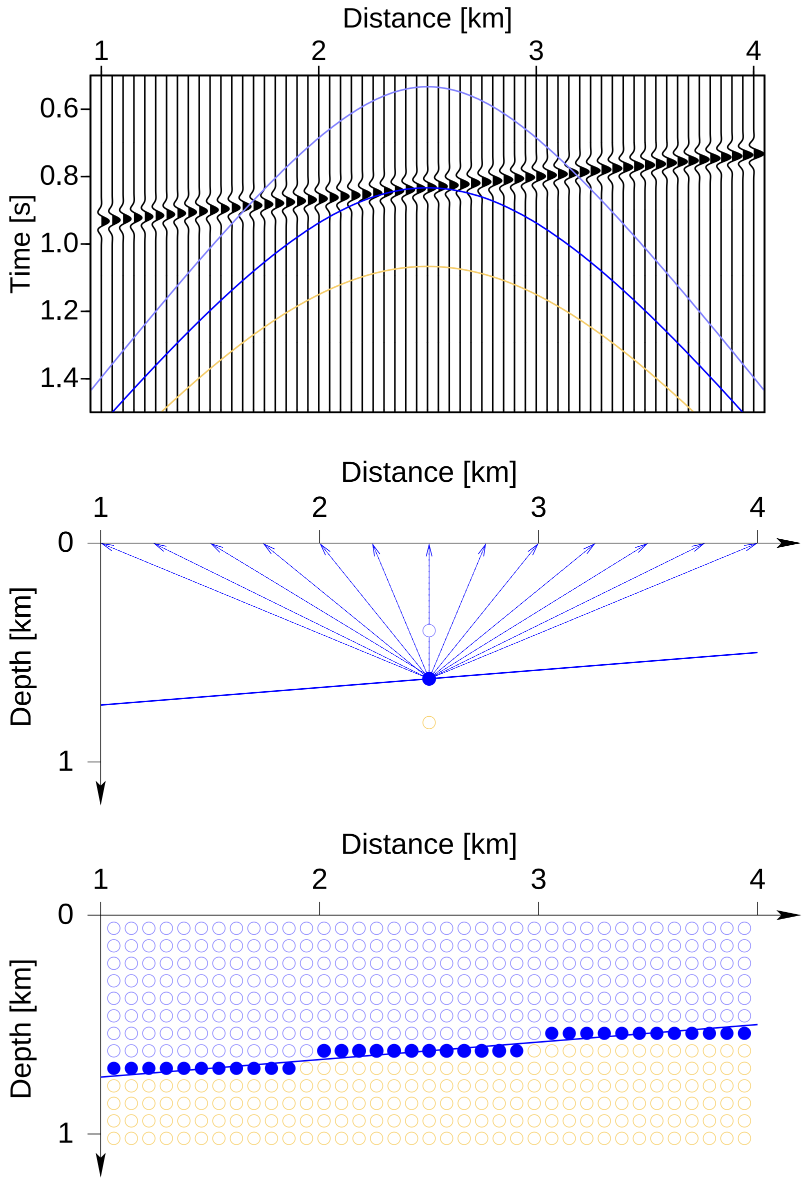

Figure 9.1: Principle of Kirchhoff migration. The top figure shows seismograms for an inclined reflector and diffraction traveltime curves for three different points in the subsurface. The middle figure shows the position of these points and raypaths. One of the points is located on the reflector, another above, and the third below the reflector. Summation of the seismogram traces along the traveltime curves only leads to a non-vanishing result if the traveltime trajectory is tangent to the events, which only happens if the subsurface point under consideration lies on a reflector or is a diffractor. This is displayed in the bottom figure, where only points on the reflector are marked solid, indicating non-zero summation results. This figure also illustrates that the resolution of the depth image depends on the subsurface sampling and frequency content of the data.

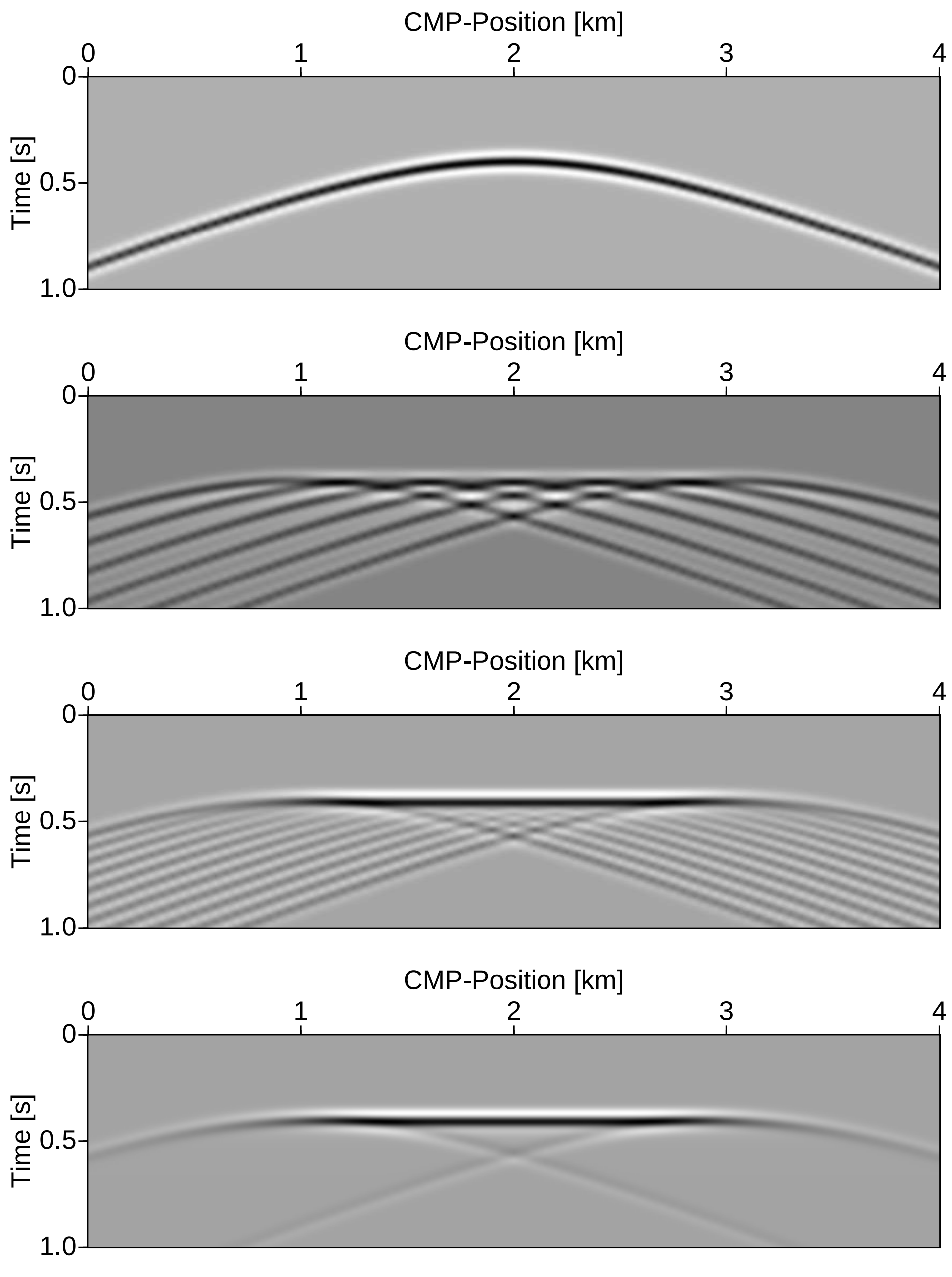

Figure 9.2: Construction of a reflector as a superposition of point scatterers. Every point scatterer leads to a diffraction event. If the density of the scatter points is high enough, superposition of the individual events results in cancellation of the diffraction tails except at the endpoints.

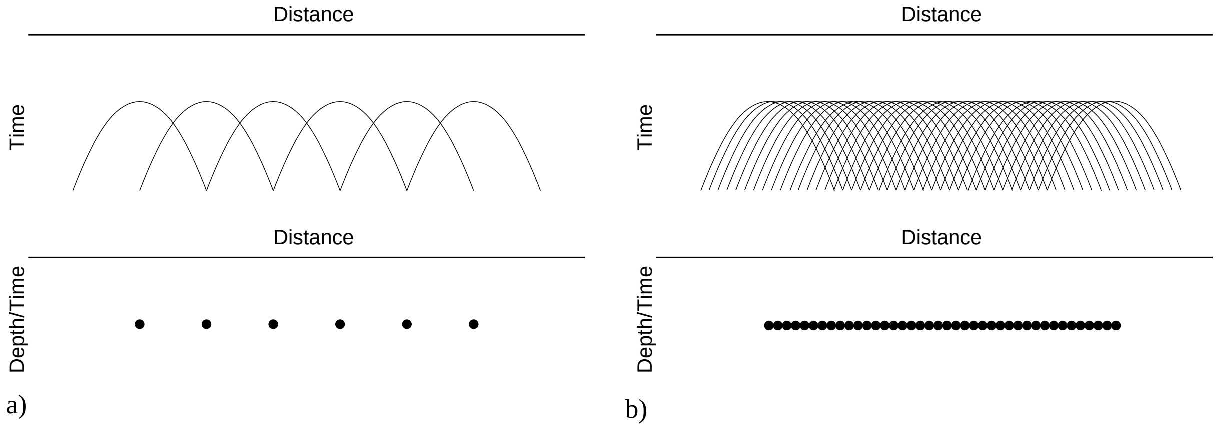

Figure 9.3: Migration as superposition of point scatterers. Figure a) shows diffraction events for individual point scatterers in a schematic seismic section (top, see also Figure 9.2). The bottom of a) shows the corresponding migration result, where the diffraction events are collapsed into points. If the spatial sampling of the reflector is dense enough, the shape of the reflector is reconstructed. This is indicated in the lower part of Figure b).

wavelength model as an initial velocity model. Such a model can be the result from a tomographic inversion or a simplified model assumed to match the data. The migrated section resulting from such a model will display details not present in the input velocity model. Consider, e.g., a constant velocity input model and and a reflection in the seismic data. The migrated section will show the reflector although it was not present in the constant velocity model. Thus migration yields an image where the structures are more distinct. Also, the better the initial model fits the real one, the better will the focusing of the migrated section be.

Although migration is already a very powerful tool to enhance image quality, there is one aspect which makes it even more important. If suitable weight functions are applied during the stack, the reflection amplitudes can be recovered (provided that the data acquisition and pre-processing has not destroyed amplitude information). This processing is named true-amplitude migration or amplitude-preserving migration. It means, that if, e.g., PP data was recorded, the migration output corresponds to the PP reflection coefficients. Their behaviour in terms of AVO (amplitude vs. offset) or AVA (amplitude vs. angle) yields information about shear properties because the PP reflection coefficient also depends on the shear properties. This is a very important feature of true-amplitude migration. Because it provides shear information without directly measuring shear waves true-amplitude migration has become a key technique nowadays. Therefore I will explain it in detail in the following section.

9.2 Derivation of true-amplitude weight functions

The term true amplitude migration (Bortfeld, 1982) describes primary reflections that are freed of the amplitude loss caused by geometrical spreading. This can be formally expressed by what Schleicher et al. (1993a) define to be a true amplitude trace: they assume an analytic true amplitude signal that can be written as

$$U_{TA}(t) = \mathcal{L}\, U(\boldsymbol{\xi}, t + \tau_R(\boldsymbol{\xi})) = \mathcal{R}\mathcal{A}\, F(t) \quad . \tag{9.2.1}$$

In this equation the normalised geometrical spreading is denoted by $\mathcal{L}$, $\mathcal{A}$ expresses transmission losses, $F(t)$ is the shape of the analytic source pulse, and τ_R is the reflection traveltime. The plane wave reflection coefficient is denoted by $\mathcal{R}$ and $U(\boldsymbol{\xi}, t)$ is the seismic data in terms of the trace coordinates $\boldsymbol{\xi} = (\xi_1, \xi_2)$ that describe the source and receiver locations depending on the acquisition geometry. The relationship between them and the vectors of the source and receiver coordinates $\boldsymbol{s}$ and $\boldsymbol{g}$ are given by

$$\begin{aligned} \boldsymbol{s} &= \boldsymbol{s}_0 + \underline{\Sigma}\,(\boldsymbol{\xi} - \boldsymbol{\xi}^*) \quad , \\ \boldsymbol{g} &= \boldsymbol{g}_0 + \underline{\Gamma}\,(\boldsymbol{\xi} - \boldsymbol{\xi}^*) \quad , \end{aligned} \tag{9.2.2}$$

where

$$\Sigma_{ij} = \frac{\partial s_i}{\partial \xi_j} \quad , \qquad \Gamma_{ij} = \frac{\partial g_i}{\partial \xi_j} \quad . \tag{9.2.3}$$

The coordinate $\boldsymbol{\xi}^*$ is that of the stationary point and the constants $\boldsymbol{s}_0, \boldsymbol{g}_0$ are given by

$$\boldsymbol{s}_0 = \boldsymbol{s}(\boldsymbol{\xi}^*) \quad \text{and} \quad \boldsymbol{g}_0 = \boldsymbol{g}(\boldsymbol{\xi}^*) \quad . \tag{9.2.4}$$

Examples for frequently used configurations are (Schleicher et al., 1993a)

- for a common shot configuration: $\underline{\Sigma} = \underline{0}$ and $\underline{\Gamma} = \underline{1}$,
- for a common receiver configuration: $\underline{\Sigma} = \underline{1}$ and $\underline{\Gamma} = \underline{0}$,
- for a common offset configuration: $\underline{\Sigma} = \underline{1}$ and $\underline{\Gamma} = \underline{1}$,
- for a common midpoint configuration: $\underline{\Sigma} = \underline{1}$ and $\underline{\Gamma} = -\underline{1}$.

More examples can be found in Vermeer (1995).

For the special case of 2.5-D, ξ_1 is taken to be the in-plane and ξ_2 the out-of-plane direction with the sources and receivers being both positioned at ξ_2^*. This corresponds to a zero-offset configuration in ξ_2-direction and therefore in this case the configuration matrices $\underline{\Sigma}$ and $\underline{\Gamma}$ reduce to

$$\underline{\Sigma} = \begin{pmatrix} \Sigma_{11} & 0 \\ 0 & 1 \end{pmatrix} \quad , \qquad \underline{\Gamma} = \begin{pmatrix} \Gamma_{11} & 0 \\ 0 & 1 \end{pmatrix} \quad , \tag{9.2.5}$$

where only the first elements are configuration-dependent. For example, in a common shot experiment

$$\Sigma_{11} = 0 \quad , \qquad \Gamma_{11} = 1 \quad . \tag{9.2.6}$$

The seismic data $U(\boldsymbol{\xi}, t)$ is assumed to have the form

$$U(\boldsymbol{\xi}, t) = \frac{\mathcal{R}\mathcal{A}}{\mathcal{L}}\, F(t - \tau_R(\boldsymbol{\xi})) \quad . \tag{9.2.7}$$

Schleicher et al. (1993a) show that if this is the case, a diffraction stack of the form

$$V(M) = -\frac{1}{2\pi} \iint_A \mathrm{d}\xi_1\, \mathrm{d}\xi_2\, W_{3\mathrm{D}}(\boldsymbol{\xi}, M) \frac{\partial U(\xi_1, \xi_2, t)}{\partial t}\Bigg|_{\tau_D(\boldsymbol{\xi}, M)} \tag{9.2.8}$$

yields a true amplitude migrated trace obeying (9.2.1) if proper weight functions $W_{3\mathrm{D}}(\boldsymbol{\xi}, M)$ are applied. In Equation (9.2.8), $V(M)$ is the migration output for an image point M, A is the aperture of the experiment (assumed to provide sufficient illumination), and $\partial U(\boldsymbol{\xi}, t)/\partial t$ is the time derivative of the input seismic trace. This derivative is evaluated at the diffraction traveltime $\tau_D(\boldsymbol{\xi}, M)$.

The integral (9.2.8) cannot generally be analytically solved. It can, however be transformed to the frequency domain and for high frequencies be approximately evaluated by the stationary phase method. First, the expression (9.2.7) is inserted into (9.2.8)

$$V(M) = -\frac{1}{2\pi} \iint\limits_A \mathrm{d}\xi_1\, \mathrm{d}\xi_2\, W_{3\mathrm{D}}(\boldsymbol{\xi}, M)\, \frac{\mathcal{RA}}{\mathcal{L}} \frac{\partial F(t+\tau_F(\boldsymbol{\xi}, M))}{\partial t} \quad , \tag{9.2.9}$$

where $\tau_F(\boldsymbol{\xi}, M) = \tau_D(\boldsymbol{\xi}, M) - \tau_R(\boldsymbol{\xi})$ is the difference between diffraction and reflection traveltime. Now (9.2.9) is transformed to the frequency domain where the tilde as in $\tilde{F}(\omega)$ denotes the Fourier transform of the function $F(t)$

$$\tilde{V}(M) = -\frac{i\omega}{2\pi} \tilde{F}(\omega) \iint\limits_A \mathrm{d}\xi_1\, \mathrm{d}\xi_2\, W_{3\mathrm{D}}(\xi_1, \xi_2, M)\, \frac{\mathcal{RA}}{\mathcal{L}}\, \mathrm{e}^{i\omega\tau_F(\xi_1,\xi_2,M)} \quad . \tag{9.2.10}$$

To solve this integral approximately, the stationary phase method can be applied (Bleistein, 1984). It yields a solution to an integral of the form

$$I(\omega) = \int\limits_A \mathrm{d}\boldsymbol{\xi}\, f(\boldsymbol{\xi})\, \mathrm{e}^{i\omega\tau_F(\boldsymbol{\xi})} \tag{9.2.11}$$

for a real valued function $\tau_F(\boldsymbol{\xi})$ and sufficiently high frequency ω, provided that there exists a stationary point at $\boldsymbol{\xi}^*$ with $\vec{\nabla}_\xi \tau_F(\boldsymbol{\xi}^*) = 0$. For the case of $\dim(\boldsymbol{\xi}) = 2$ as in (9.2.10), the integral (9.2.11) has the approximate solution

$$I(\omega) \approx \frac{2\pi}{\omega} \frac{f(\boldsymbol{\xi}^*)}{\sqrt{|\det \underline{\mathrm{H}}_\mathrm{F}|}}\, \mathrm{e}^{i\omega\tau_F(\boldsymbol{\xi}^*) + i\mathrm{sgn}\underline{\mathrm{H}}_\mathrm{F}} \quad , \tag{9.2.12}$$

corresponding to the leading term of an asymptotic expansion in ω. The 2×2 matrix $\underline{\mathrm{H}}_\mathrm{F}$ is given by

$$\underline{\mathrm{H}}_{F_{IJ}} = \frac{\partial^2 \tau_F(\boldsymbol{\xi}^*)}{\partial\xi_I\, \partial\xi_J} \quad . \tag{9.2.13}$$

I assume that the stationary point is isolated and unique within the aperture. I also assume that it is not a caustic point, i.e. $\det\underline{\mathrm{H}}_\mathrm{F} \neq 0$. The sign of the matrix $\underline{\mathrm{H}}_\mathrm{F}$, $\mathrm{sgn}\underline{\mathrm{H}}_\mathrm{F}$, is the number of positive minus the number of negative eigenvalues of $\underline{\mathrm{H}}_\mathrm{F}$. Application of the stationary phase method to (9.2.10) corresponds to an expansion of the phase function $\tau_F(\boldsymbol{\xi}, M)$ up to second order with respect to the stationary point

$$\tau_F(\boldsymbol{\xi}, M) = \tau_F(\boldsymbol{\xi}^*, M) + (\boldsymbol{\xi} - \boldsymbol{\xi}^*)^\top \underline{\mathrm{H}}_\mathrm{F} (\boldsymbol{\xi} - \boldsymbol{\xi}^*) \tag{9.2.14}$$

and yields the following result

$$\tilde{V}(M) \approx \tilde{F}(\omega)\, W_{3\mathrm{D}}(\boldsymbol{\xi}^*, M)\, \frac{\mathcal{RA}}{\mathcal{L}\sqrt{|\det\underline{\mathrm{H}}_\mathrm{F}|}}\, \mathrm{e}^{i\omega\tau_F(\boldsymbol{\xi}^*, M) - \frac{i\pi}{4}(2-\mathrm{sgn}\underline{\mathrm{H}}_\mathrm{F})} \quad . \tag{9.2.15}$$

If no stationary point exists inside the aperture, the integral will yield only a negligible result of the order ω^{-1} caused by contributions from the boundaries of the aperture. This can be suppressed by applying a taper (see Schleicher et al. 1993a). The result (9.2.15) transformed back into the time domain reads

$$V(M) \approx W_{3\mathrm{D}}(\boldsymbol{\xi}^*, M)\, \frac{\mathcal{RA}}{\mathcal{L}\, \sqrt{|\mathrm{det}\underline{\mathrm{H}}_{\mathrm{F}}|}}\, F(t + \tau_F(\boldsymbol{\xi}^*, M))\, \mathrm{e}^{-\frac{i\pi}{4}(2-\mathrm{sgn}\underline{\mathrm{H}}_{\mathrm{F}})} \quad . \tag{9.2.16}$$

If the point M lies on a reflector, the diffraction and reflection traveltime curves are tangent to each other in the stationary point, meaning that $\tau_F(\boldsymbol{\xi}^*, M) = 0$. This leads to

$$V(M) \approx W_{3\mathrm{D}}(\boldsymbol{\xi}^*, M)\, \frac{\mathcal{RA}}{\mathcal{L}\, \sqrt{|\mathrm{det}\underline{\mathrm{H}}_{\mathrm{F}}|}}\, F(t)\, \mathrm{e}^{-\frac{i\pi}{4}(2-\mathrm{sgn}\underline{\mathrm{H}}_{\mathrm{F}})} \quad . \tag{9.2.17}$$

If we consider a point M that does not lie on the reflector, $\tau_F(\boldsymbol{\xi}^*, M)$ will not be zero. Since the source pulse $F(t)$ will be zero outside a small time interval τ_ϵ, $F(t + \tau_F(\boldsymbol{\xi}^*, M))$ will become zero if $|\tau_F(\boldsymbol{\xi}^*, M)| > \tau_\epsilon$. Therefore, (9.2.16) will yield a non-vanishing result only for points on the reflector (or, more precisely, for points that are within the reflector's Fresnel zone). To get an expression for the weight function, the result (9.2.17) is compared to the expression for the true amplitude trace given by (9.2.1). Since both, $V(M)$ and U($\boldsymbol{\xi}$,t), have significant values only, if M is on a reflector, the comparison leads to the weight function for an image point on a reflector, denoted by $M{=}R$, where

$$W_{3\mathrm{D}}(\boldsymbol{\xi}^*, R) = \mathcal{L}\sqrt{|\mathrm{det}\underline{\mathrm{H}}_F|}\, \mathrm{e}^{i\frac{\pi}{2}\left(1-\frac{\mathrm{sgn}\underline{\mathrm{H}}_F}{2}\right)} \quad . \tag{9.2.18}$$

In the following sections I will give expressions for the matrix $\underline{\mathrm{H}}_{\mathrm{F}}$ and the geometrical spreading of the reflected event, $\mathcal{L}$. The final result for the weight function which employs these expressions will be better suited for an implementation than Equation (9.2.18) because both, $\mathcal{L}$, and $\underline{\mathrm{H}}_{\mathrm{F}}$, depend on the curvature of the reflector in the image point. The final weight function will not suffer from this disadvantage. As I will also show, the final weight function will be valid for all subsurface points, regardless of M actually being located at a reflector.

Application of the weight function (9.2.18) in its final form in the stacking process will yield a true-amplitude trace as defined by Equation (9.2.1). This migration output still contains transmission losses, $\mathcal{A}$, caused by the overburden. However, according to Hanitzsch (1995) transmission loss due to interfaces is negligible except for interfaces with strong impedance contrast. Therefore, transmission losses must be taken into account for these types of interfaces only. This is, for example, the case if a reflector under a salt structure is considered, because of the strong contrast in acoustic impedance between the salt and the surrounding medium. This problem can be dealt with by using layer stripping methods (Hanitzsch, 1995).

The matrix $\underline{\mathrm{H}}_{\mathrm{F}}$

Schleicher et al. (1993a) show how the matrix $\underline{\mathrm{H}}_{\mathrm{F}}$ can be expressed in terms of second order derivative matrices of the traveltimes. They split the traveltime from a source located at a position $\boldsymbol{s}$ to a receiver at $\boldsymbol{g}$ into the two corresponding branches, from $\boldsymbol{s}$ to a subsurface point M at the position $\bar{\boldsymbol{r}}$, and from $\bar{\boldsymbol{r}}$ to $\boldsymbol{g}$, and connect the two branches with the Bortfeld propagator (see Section A.9). Here, I follow the lines of derivation proposed in Schleicher (1993). I also make use of the fact that the traveltime $\tau(\bar{\boldsymbol{r}}, \boldsymbol{g})$ is equal to $\tau(\boldsymbol{g}, \bar{\boldsymbol{r}})$. The vectors $\boldsymbol{s}$ and $\boldsymbol{g}$ lie in the registration surface whose base vectors are assumed to coincide with the global Cartesian coordinate system introduced in Chapter 2. Therefore they have dimension two, which is distinguished from a 3-D vector carrying a hat $\hat{}$. Vector $\bar{\boldsymbol{r}}$ will be used to describe the reflection point. This makes sense only if $\bar{\boldsymbol{r}}$ lies in the reflector surface, therefore $\bar{\boldsymbol{r}}$ is a 2-D vector in a specific coordinate system associated with the reflector surface. This coordinate system is denoted with a bar $\bar{}$. Both $\tau(\boldsymbol{g}, \bar{\boldsymbol{r}})$ and $\tau(\boldsymbol{s}, \bar{\boldsymbol{r}})$ can be expressed in terms of a 2-D variant of the parabolic traveltime expansion Equation (2.1.4) with

$$\tau(\boldsymbol{s}, \bar{\boldsymbol{r}}) = \tau_1 - \boldsymbol{p}_{0_1}^{\top} \Delta \boldsymbol{s} + \bar{\boldsymbol{q}}_{0_1}^{\top} \Delta \bar{\boldsymbol{r}} - \Delta \boldsymbol{s}^{\top} \underline{\bar{\mathsf{N}}}_1 \, \Delta \bar{\boldsymbol{r}} - \frac{1}{2} \Delta \boldsymbol{s}^{\top} \underline{\mathsf{S}}_1 \, \Delta \boldsymbol{s} + \frac{1}{2} \Delta \bar{\boldsymbol{r}}^{\top} \underline{\bar{\mathsf{G}}}_1 \, \Delta \bar{\boldsymbol{r}} \tag{9.2.19}$$

and

$$\tau(\boldsymbol{g}, \bar{\boldsymbol{r}}) = \tau_2 - \boldsymbol{p}_{0_2}^{\top} \Delta \boldsymbol{g} + \bar{\boldsymbol{q}}_{0_2}^{\top} \Delta \bar{\boldsymbol{r}} - \Delta \boldsymbol{g}^{\top} \underline{\bar{\mathsf{N}}}_2 \, \Delta \bar{\boldsymbol{r}} - \frac{1}{2} \Delta \boldsymbol{g}^{\top} \underline{\mathsf{S}}_2 \, \Delta \boldsymbol{g} + \frac{1}{2} \Delta \bar{\boldsymbol{r}}^{\top} \underline{\bar{\mathsf{G}}}_2 \, \Delta \bar{\boldsymbol{r}} \quad . \tag{9.2.20}$$

The sums of Equations (9.2.19) and (9.2.20) yield τ_D and τ_R. For the diffraction traveltime, the diffractor position is fixed at $\bar{\boldsymbol{r}}_0$, and thus with $\Delta \bar{\boldsymbol{r}}=0$

$$\tau_D(\boldsymbol{s}, \boldsymbol{g}) = \tau_0 - \boldsymbol{p}_0^{\top} \Delta \boldsymbol{s} + \boldsymbol{q}_0^{\top} \Delta \boldsymbol{g} - \frac{1}{2} \Delta \boldsymbol{s}^{\top} \underline{\mathsf{S}}_1 \, \Delta \boldsymbol{s} - \frac{1}{2} \Delta \boldsymbol{g}^{\top} \underline{\mathsf{S}}_2 \, \Delta \boldsymbol{g} \quad , \tag{9.2.21}$$

where I have used the abbreviations $\tau_0 = \tau_1 + \tau_2$, $\boldsymbol{p}_0 = \boldsymbol{p}_{0_1}$, and $\boldsymbol{q}_0 = -\boldsymbol{p}_{0_2}$. For the reflection traveltime it must be taken into account that variation of source and/or receiver positions will result in a different reflection point $\bar{\boldsymbol{r}}$. Aiming for an expression containing $\Delta \boldsymbol{s}$ and $\Delta \boldsymbol{g}$ only, Snell's law is applied, stating that $\bar{\boldsymbol{q}}_{0_1} + \bar{\boldsymbol{q}}_{0_2} = \boldsymbol{\nabla}_{\bar{r}}^{*} \tau_R = \boldsymbol{0}$. This can be solved for $\bar{\boldsymbol{r}}$, and $\bar{\boldsymbol{r}}$ is then eliminated from the sum of Equations (9.2.19) and (9.2.20), resulting in

$$\tau_R(\boldsymbol{s}, \boldsymbol{g}) = \tau_0 - \boldsymbol{p}_0^{\top} \Delta \boldsymbol{s} + \boldsymbol{q}_0^{\top} \Delta \boldsymbol{g} - \frac{1}{2} \Delta \boldsymbol{s}^{\top} \underline{\mathsf{S}} \, \Delta \boldsymbol{s} + \frac{1}{2} \Delta \boldsymbol{g}^{\top} \underline{\bar{\mathsf{G}}} \, \Delta \boldsymbol{g} - \Delta \boldsymbol{s}^{\top} \underline{\bar{\mathsf{N}}} \, \Delta \boldsymbol{g} \quad , \tag{9.2.22}$$

where the matrices $\underline{\bar{\mathsf{N}}}$, $\underline{\mathsf{S}}$, and $\underline{\bar{\mathsf{G}}}$ are given by

$$\begin{aligned} \underline{\mathsf{S}} &= \underline{\mathsf{S}}_1 + \underline{\bar{\mathsf{N}}}_1 (\underline{\bar{\mathsf{G}}}_1 + \underline{\bar{\mathsf{G}}}_2)^{-1} \underline{\bar{\mathsf{N}}}_1^{\top} \quad , \\ \underline{\bar{\mathsf{G}}} &= -\underline{\mathsf{S}}_2 - \underline{\bar{\mathsf{N}}}_2 (\underline{\bar{\mathsf{G}}}_1 + \underline{\bar{\mathsf{G}}}_2)^{-1} \underline{\bar{\mathsf{N}}}_2^{\top} \quad , \\ \underline{\bar{\mathsf{N}}} &= \underline{\bar{\mathsf{N}}}_1 (\underline{\bar{\mathsf{G}}}_1 + \underline{\bar{\mathsf{G}}}_2)^{-1} \underline{\bar{\mathsf{N}}}_2^{\top} \quad . \end{aligned} \tag{9.2.23}$$

For further simplification, the matrix $\underline{\mathsf{H}}$ is introduced as an abbreviation for

$$\underline{\mathsf{H}} = \underline{\bar{\mathsf{G}}}_1 + \underline{\bar{\mathsf{G}}}_2 \quad . \tag{9.2.24}$$

In the following step, the difference τ_F between Equations (9.2.21) and (9.2.22) is built and at the same time $\Delta \boldsymbol{s} = \boldsymbol{s} - \boldsymbol{s}_0$ and $\Delta \boldsymbol{g} = \boldsymbol{g} - \boldsymbol{g}_0$ are expressed in trace coordinates $\boldsymbol{\xi}$ using the configuration matrices $\underline{\Sigma}$ and $\underline{\Gamma}$ (9.2.3)). The resulting expression for $\tau_F(\boldsymbol{\xi}, M)$ is

$$\tau_F(\boldsymbol{\xi}, M) = \frac{1}{2} (\boldsymbol{\xi} - \boldsymbol{\xi}^*)^{\top} \left[\underline{\Sigma}^{\top} \underline{\bar{\mathsf{N}}}_1 \underline{\mathsf{H}}^{-1} \, \underline{\bar{\mathsf{N}}}_1^{\top} \underline{\Sigma} + \underline{\Gamma}^{\top} \underline{\bar{\mathsf{N}}}_2 \underline{\mathsf{H}}^{-1} \, \underline{\bar{\mathsf{N}}}_2^{\top} \underline{\Gamma} + 2 \, \underline{\Sigma}^{\top} \underline{\bar{\mathsf{N}}}_1 \underline{\mathsf{H}}^{-1} \, \underline{\bar{\mathsf{N}}}_2^{\top} \underline{\Gamma} \right] (\boldsymbol{\xi} - \boldsymbol{\xi}^*) \quad . \tag{9.2.25}$$

Differentiation with respect to $\boldsymbol{\xi}$ yields $\underline{\mathsf{H}}_{\mathrm{F}}$

$$\underline{\mathsf{H}}_{\mathrm{F}} = \left(\underline{\Sigma}^{\top} \underline{\bar{\mathsf{N}}}_1 + \underline{\Gamma}^{\top} \underline{\bar{\mathsf{N}}}_2 \right) \underline{\mathsf{H}}^{-1} \left(\underline{\bar{\mathsf{N}}}_1^{\top} \underline{\Sigma} + \underline{\bar{\mathsf{N}}}_2^{\top} \underline{\Gamma} \right) \quad . \tag{9.2.26}$$

This leads to the determinant of $\underline{\mathsf{H}}_{\mathrm{F}}$

$$|\det \underline{\mathsf{H}}_{\mathrm{F}}| = \frac{|\det(\underline{\bar{\mathsf{N}}}_1^{\top} \underline{\Sigma} + \underline{\bar{\mathsf{N}}}_2^{\top} \underline{\Gamma})|^2}{|\det \underline{\mathsf{H}}|} \quad . \tag{9.2.27}$$

Furthermore, $\mathrm{sgn} \underline{\mathsf{H}}_{\mathrm{F}}$ equals $\mathrm{sgn} \underline{\mathsf{H}}$, since $\underline{\mathsf{H}}$ is a symmetric matrix.

Geometrical spreading and final weight function

I have shown in Chapter 8 how the geometrical spreading is related to the matrices $\hat{\underline{\mathsf{N}}}$ and $\underline{\mathsf{N}}$. These relationships also apply to the geometrical spreading of a reflected event. With Equation (9.2.23) the spreading can be expressed in terms of the matrices $\bar{\underline{\mathsf{N}}}_I$ and $\bar{\underline{\mathsf{G}}}_I$, or $\underline{\mathsf{H}}$, following from the decomposition of traveltimes, and resulting in

$$\begin{aligned}\mathcal{L} &= \frac{1}{V_s}\sqrt{\frac{\cos\vartheta_s\,\cos\vartheta_g}{|\mathrm{det}\bar{\underline{\mathsf{N}}}|}}\,\mathrm{e}^{-i\frac{\pi}{2}\kappa} && (9.2.28)\\ &= \frac{1}{V_s}\sqrt{\cos\vartheta_s\,\cos\vartheta_g}\sqrt{\frac{|\mathrm{det}\underline{\mathsf{H}}|}{|\mathrm{det}\bar{\underline{\mathsf{N}}}_1|\,|\mathrm{det}\bar{\underline{\mathsf{N}}}_2|}}\,\mathrm{e}^{-i\frac{\pi}{2}\kappa}\quad. && (9.2.29)\end{aligned}$$

The KMAH index κ of the reflected ray can be decomposed into the KMAH indices of the ray branches κ_I (Schleicher et al., 1993a)

$$\kappa = \kappa_1 + \kappa_2 + \left(1 - \frac{\mathrm{sgn}\underline{\mathsf{H}}}{2}\right)\quad. \tag{9.2.30}$$

The KMAH indices κ_I are known if a suitable traveltime generator is used, as, e.g., the method by Coman and Gajewski (2001), which outputs later-arrival traveltimes sorted for their KMAH index. The angles ϑ_s and ϑ_g are the emergence angle at the source and the incidence angle at the receiver. They can be computed from the slowness vectors at the source and receiver, i.e.,

$$\begin{aligned}\cos\vartheta_s &= \sqrt{1 - V_s^2\,\boldsymbol{p}_{0_1}\cdot\boldsymbol{p}_{0_1}}\quad,\\ \cos\vartheta_g &= \sqrt{1 - V_g^2\,\boldsymbol{p}_{0_2}\cdot\boldsymbol{p}_{0_2}}\quad.\end{aligned} \tag{9.2.31}$$

Equation (9.2.18) together with (9.2.27), (9.2.29), and (9.2.30) yields the final expression for the weight function:

$$W_{3\mathrm{D}}(\boldsymbol{\xi}^*, M) = \frac{1}{V_s}\sqrt{\cos\vartheta_s\,\cos\vartheta_g}\,\frac{|\mathrm{det}(\bar{\underline{\mathsf{N}}}_1^\top\underline{\boldsymbol{\Sigma}} + \bar{\underline{\mathsf{N}}}_2^\top\underline{\boldsymbol{\Gamma}})|}{\sqrt{|\mathrm{det}\bar{\underline{\mathsf{N}}}_1|\,|\mathrm{det}\bar{\underline{\mathsf{N}}}_2|}}\,\mathrm{e}^{-i\frac{\pi}{2}(\kappa_1+\kappa_2)}\quad. \tag{9.2.32}$$

Equation (9.2.32) contains only quantities which do not depend on whether the image point M is a reflection point or not. Therefore, Equation (9.2.32) can be applied for all subsurface points. Since the matrices $\bar{\underline{\mathsf{G}}}_I$ do not occur anymore, Equation (9.2.32) is furthermore independent of the reflector curvature. For the determination of the matrices $\bar{\underline{\mathsf{N}}}_I$ from $\hat{\underline{\mathsf{N}}}_I$ so far, however, the reflector inclination is required. It is possible to reformulate the weight functions in a reflector-independent way. This is addressed in Section 9.4.

All quantities in Equation (9.2.32) can be determined from traveltime tables. The matrices $\bar{\underline{\mathsf{N}}}_I$ are computed from the $\hat{\underline{\mathsf{N}}}_I$ which are also needed for the diffraction time surface, as are the slownesses that lead to the angles ϑ_I. Since all coefficients must be known for the computation of the diffraction time surface anyway, the determination of the weight functions takes only a small part of the computational time required for the migration. I name this approach traveltime-based true-amplitude migration because coarsely gridded traveltime tables are the only input required. Since very small additional effort must be spent for the weights, it is very efficient. The high accuracy of the coefficients has already been stated in Chapter 2. The accuracy of the geometrical spreading computed from the coefficients in Chapter 8 supports the expected high accuracy of the recovered reflection coefficients. Before I will demonstrate the method with applications, however, I will derive corresponding weight functions for 2-D media and situations, where a 2.5-D geometry is considered.

9.3 Weight functions for 2.5-D and 2-D

Sometimes seismic data is only available for sources and receivers constrained to a single straight acquisition line. Processing of this data with techniques based on 2-D wave propagation does not yield satisfactory results because the (spherical) geometrical spreading in the data caused by the 3-D earth does not agree with the cylindrical (i.e. line source) spreading implied by the 2-D wave equation. The problem can be dealt with by assuming the subsurface to be invariant in the off-line direction. This symmetry is called to be 2.5-dimensional (Bleistein, 1986). Apart from the geometrical spreading, the properties involved do not depend on the out-of-plane variable and can be computed with 2-D techniques. The geometrical spreading can be split into an in-plane part that is equal to the 2-D spreading and an out-of-plane contribution. For the described symmetry, the product of both equals the spreading following from the 3-D wave equation.

Equation (9.2.18) is an expression for a weight function if the diffraction stack is carried out over the aperture in ξ_1 and ξ_2. Since in the 2.5-D case the data comes from a single acquisition line (assumed to coincide with the ξ_1 coordinate), the stack is performed only over ξ_1. In this case the input data is $U(\xi_1, \xi_2, t) = U(\xi_1, \xi_2^*, t)$ where the asterisk denotes the stationary point (which is in this case the ξ_2 position of the source-receiver line). The weight functions for 2.5-D symmetry can be derived following the same lines as for 3-D. Equation (9.2.8) becomes

$$V(M) = -\frac{1}{2\pi} \int_A \mathrm{d}\xi_1 \int_{-\infty}^{\infty} \mathrm{d}\xi_2 \, W_{3\mathrm{D}}(\xi_1, \xi_2, M) \, \frac{\mathcal{R}A}{\mathcal{L}} \frac{\partial F(t)}{\partial t} \bigg|_{\tau_F(\xi_1, \xi_2, M)} \quad . \tag{9.3.1}$$

After carrying out the integration over ξ_2 in the frequency domain by applying stationary phase method (following Martins et al. 1997) $V(M)$ becomes

$$\begin{aligned} V(M) &= \frac{1}{\sqrt{2\pi}} \int_A \mathrm{d}\xi_1 \, W_{3\mathrm{D}}(\xi_1, \xi_2^*, M) \left(\frac{\partial^2 \tau_D}{\partial \xi_2^2}\bigg|_{\xi_2^*} \right)^{-\frac{1}{2}} \mathrm{e}^{-i\frac{\pi}{4}} \, \frac{\mathcal{R}A}{\mathcal{L}} \, f[F(t)] \Big|_{\tau_F(\xi_1, \xi_2^*, M)} \\ &= \frac{1}{\sqrt{2\pi}} \int_A \mathrm{d}\xi_1 \, W_{3\mathrm{D}}(\xi_1, \xi_2^*, M) \left(\frac{\partial^2 \tau_D}{\partial \xi_2^2}\bigg|_{\xi_2^*} \right)^{-\frac{1}{2}} \mathrm{e}^{-i\frac{\pi}{4}} \, f[U(\xi_1, \xi_2^*, t + \tau_D(\xi_1, \xi_2^*, M))] \\ &= \frac{1}{\sqrt{2\pi}} \int_A \mathrm{d}\xi_1 \, W_{2.5\mathrm{D}}(\xi_1, \xi_2^*, M) \, f[U(\xi_1, \xi_2^*, t + \tau_D(\xi_1, \xi_2^*, M))] \end{aligned} \tag{9.3.2}$$

Note, that in this case not the time derivative of the seismic trace is taken, but a $\sqrt{i\omega}$ filter operation in the frequency domain (commonly called 'half derivative') is applied instead. This is denoted by the function $f[U(t)]$ in (9.3.2). The 2.5-D weight function is related to the 3-D weight by

$$W_{2.5\mathrm{D}}(\xi_1, \xi_2^*, M) = W_{3\mathrm{D}}(\xi_1, \xi_2^*, M) \left(\frac{\partial^2 \tau_D}{\partial \xi_2^2}\bigg|_{\xi_2^*} \right)^{-\frac{1}{2}} \mathrm{e}^{-i\frac{\pi}{4}} \quad . \tag{9.3.3}$$

For the 2.5-D geometry simplifications apply to the matrix $\underline{\mathrm{H}}_{\mathrm{F}}$ and to the spreading, and therefore to the weight function. Let the out-of-plane direction (index 2) coincide with the y-axis of the Cartesian system defined by the traveltime tables with $y_0 = s_{20} = g_{20} = r_{20}$ as y-position of the sources and receivers. Then it follows that

$$N_{22}|_{y_0} = \hat{N}_{yy}|_{y_0}, \quad G_{22}|_{y_0} = \hat{G}_{yy}|_{y_0} \quad \text{and} \quad S_{22}|_{y_0} = \hat{S}_{yy}|_{y_0} \quad . \tag{9.3.4}$$

From the symmetry one can see that the y-components of the slownesses vanish at y_0 along the profile:

$$\left.\frac{\partial\tau}{\partial y_s}\right|_{y_0} = \left.\frac{\partial\tau}{\partial y_g}\right|_{y_0} = \left.\frac{\partial\tau}{\partial y_r}\right|_{y_0} = 0 \quad . \tag{9.3.5}$$

From this follows that the matrices $\underline{\mathsf{S}}, \bar{\underline{\mathsf{G}}}$ and $\bar{\underline{\mathsf{N}}}$ consist only of diagonal elements. Furthermore, the absolute values of the yy- or 22-components of all of the matrices are equal,

$$\left.N_{22}\right|_{y_0} = \left.G_{22}\right|_{y_0} = -\left.S_{22}\right|_{y_0} \tag{9.3.6}$$

and the sign of $\left.N_{22}\right|_{y_0}$ is positive; i.e., $\mathrm{sgn}(N_{22}|_{y_0}) = +1$.

As already indicated, the geometrical spreading can be written as the product of an in-plane and an out-of-plane contribution. The reason is that the matrix $\bar{\underline{\mathsf{N}}}$ consists only of the diagonal elements. Equation (9.2.28) becomes

$$\mathcal{L}_{2.5\mathrm{D}} = \frac{1}{V_s}\,\frac{\sqrt{\cos\vartheta_s\,\cos\vartheta_g}}{\sqrt{|\bar{N}_{11}|}}\,\sqrt{\frac{1}{|N_{22}|}}\;\mathrm{e}^{-i\frac{\pi}{2}\kappa} = \sqrt{\sigma}\,\mathcal{L}_{2\mathrm{D}} \quad , \tag{9.3.7}$$

where $\sqrt{\sigma} = \sqrt{N_{22}^{-1}}$ is the out-of-plane spreading. The in-plane contribution equals the (line source) spreading for 2-D wave propagation given by

$$\mathcal{L}_{2\mathrm{D}} = \frac{1}{V_s}\,\frac{\sqrt{\cos\vartheta_s\,\cos\vartheta_g}}{|\bar{N}|}\;\mathrm{e}^{-i\frac{\pi}{2}\kappa} \quad , \tag{9.3.8}$$

where the matrix $\bar{\underline{\mathsf{N}}}$ reduces to the scalar $\bar{N}$ $(=\bar{N}_{11})$. The second-order derivative of the diffraction traveltime with respect to the ξ_2 component can be determined from Equation (9.2.21). It is

$$\left.\frac{\partial^2\tau_D}{\partial\xi_2^2}\right|_{\xi_2^*} = -S_{1_{22}} - S_{2_{22}} \quad . \tag{9.3.9}$$

This leads to the final weight function for a 2.5-D symmetry

$$W_{2.5\mathrm{D}}(\xi_1,\xi_2^*,M) = \frac{\sqrt{\cos\vartheta_s\cos\vartheta_g}}{V_s}\,\frac{|\bar{N}_{1_{11}}\Sigma_{11} + \bar{N}_{2_{11}}\Gamma_{11}|}{\sqrt{|\bar{N}_{1_{11}}\bar{N}_{2_{11}}|}}\,\sqrt{\frac{N_{1_{22}}+N_{2_{22}}}{N_{1_{22}}N_{2_{22}}}}\;\mathrm{e}^{-i\frac{\pi}{2}(\kappa_1+\kappa_2)-i\frac{\pi}{4}} \quad . \tag{9.3.10}$$

If a 2-D medium with 2-D geometrical spreading (line source) is assumed, the stack (9.3.2) can be used with the 2-D weight function

$$W_{2\mathrm{D}}(\xi,M) = \mathcal{L}\sqrt{H_F}\,\mathrm{e}^{i\frac{\pi}{2}\left(1-\frac{\mathrm{sgn}H_F}{2}\right)} \quad . \tag{9.3.11}$$

In this case, the matrix $\underline{\mathsf{H}}_{\mathrm{F}}$ is reduced to a scalar H_F. The final weight function for 2-D reads

$$W_{2\mathrm{D}}(\xi,M) = \frac{\sqrt{\cos\vartheta_s\cos\vartheta_g}}{V_s}\,\frac{|\bar{N}_1\Sigma + \bar{N}_2\Gamma|}{\sqrt{|\bar{N}_1\bar{N}_2|}}\;\mathrm{e}^{-i\frac{\pi}{2}(\kappa_1+\kappa_2)-i\frac{\pi}{4}} \quad . \tag{9.3.12}$$

This 2-D weight function is equivalent to the one given by Hanitzsch et al. (1994).

9.4 Reflector-independent weight functions

The true-amplitude weight functions derived in this chapter can be expressed in a manner which is independent of a priori knowledge about the reflector. This is possible since the weights were derived for the stationary point, i.e., the actually reflected ray. For this specific ray terms which previously required knowledge of the reflector orientation can be expressed using Snell's law. In this section I derive a reflector independent formulation of the weight functions.

As a reminder, the general weight function valid for PP and PS data reads

$$W(\boldsymbol{\xi}^*, M) = \frac{1}{V_s}\sqrt{\cos\vartheta_s \cos\vartheta_g}\sqrt{\frac{\cos\theta_1}{\cos\theta_2}}\,\frac{|\det(\underline{\bar{\mathsf{N}}}_1^\top \underline{\Sigma} + \underline{\bar{\mathsf{N}}}_2^\top \underline{\Gamma})|}{\sqrt{|\det\underline{\bar{\mathsf{N}}}_1 \det\underline{\bar{\mathsf{N}}}_2|}}\, e^{-i\frac{\pi}{2}(\kappa_1+\kappa_2)} \quad , \tag{9.4.1}$$

where the angles ϑ_I are the emergence and incidence angles on the registration surface at the source $(I=s)$ and the receiver $(I=g)$. The angles θ_I are the incidence angle $(I=1)$ at the reflector and the reflection angle $(I=2)$. The $2{\times}2$ matrices $\underline{\bar{\mathsf{N}}}_I$ result from a rotation of the $3{\times}3$ matrices $\underline{\hat{\mathsf{N}}}_I$ into the tangent plane of the reflector (denoted by the bar$^-$). This rotation can only be carried out if the orientation of the reflector with respect to the global Cartesian system is known in which the matrices $\underline{\hat{\mathsf{N}}}_I$ are defined.

In the following I will show how the weight function (9.4.1) can be written in terms of of the matrices $\underline{\mathsf{N}}_I$ and the corresponding slowness vectors without needing to know the reflector orientation. The difference between the matrices $\underline{\mathsf{N}}_I$ and $\underline{\bar{\mathsf{N}}}_I$ is that the $\underline{\bar{\mathsf{N}}}_I$ are defined in the interface coordinate system associated with the reflector, whereas the matrices $\underline{\mathsf{N}}_I$ are the upper left submatrices of the mixed derivative matrices $\underline{\hat{\mathsf{N}}}_I$ in the global Cartesian coordinate system.

From Equation (8.2.15) I use the relationship between $\underline{\mathsf{N}}$ and the matrix $\underline{\mathsf{Q}}_2$ between two points (denoted by a and b, where index a is either s or g in the registration surface while index b is 1 or 2 at the interface):

$$\underline{\mathsf{Q}}_2^{-1} = \underline{\mathsf{H}}_a^{-\top}\,\underline{\mathsf{N}}\,\underline{\mathsf{H}}_b^{-1} \quad . \tag{9.4.2}$$

A similar relationship exists between $\underline{\mathsf{Q}}_2$ and $\underline{\bar{\mathsf{N}}}$ (Hubral et al., 1992a):

$$\underline{\bar{\mathsf{N}}} = \underline{\mathsf{G}}_a^\top\,\underline{\mathsf{Q}}_2^{-1}\,\underline{\mathsf{G}}_b \quad , \tag{9.4.3}$$

where the matrices $\underline{\mathsf{G}}_I$ are the upper left $2{\times}2$ submatrices of the transformation matrices between the interface and ray centred coordinates (see Section A.8). Combining Equations (9.4.2) and (9.4.3) leads to

$$\underline{\bar{\mathsf{N}}} = \underline{\mathsf{G}}_a^\top\,\underline{\mathsf{H}}_a^{-\top}\,\underline{\mathsf{N}}\,\underline{\mathsf{H}}_b^{-1}\,\underline{\mathsf{G}}_b \quad . \tag{9.4.4}$$

In the registration surface I assume that the global and interface coordinate systems coincide, see Figure 9.4. In this case the matrices $\underline{\mathsf{G}}_a$ and $\underline{\mathsf{H}}_a$ are equal, thus $\underline{\mathsf{G}}_a^\top\,\underline{\mathsf{H}}_a^{-\top}{=}\underline{1}$ at both the source and the receiver position. At the image point so far neither $\underline{\mathsf{G}}_b$ nor $\underline{\mathsf{H}}_b$ are determined since the orientation of the interface is unknown, as are the base vectors $\vec{\boldsymbol{e}}_i$ of the ray centred coordinate system. However, under the assumption that the two rays associated with the indices 1 and 2 correspond to a reflection, i.e. the stationary ray, I define the ray centred coordinate base vectors as illustrated in Figure 9.5. The vectors $\vec{\boldsymbol{\imath}}_i$ are the base vectors of the interface coordinate system, the $\vec{\boldsymbol{e}}_i^{(I)}$ are those of the ray centred coordinate systems for the rays denoted by $I{=}1,2$ in the weight function. The vectors $\vec{\boldsymbol{e}}_3^{(I)}$ are determined by the slownesses vectors. Since

$$\vec{\boldsymbol{e}}_2 = \vec{\boldsymbol{e}}_2^{(1)} = \vec{\boldsymbol{e}}_2^{(2)} = \vec{\boldsymbol{\imath}}_2 \tag{9.4.5}$$

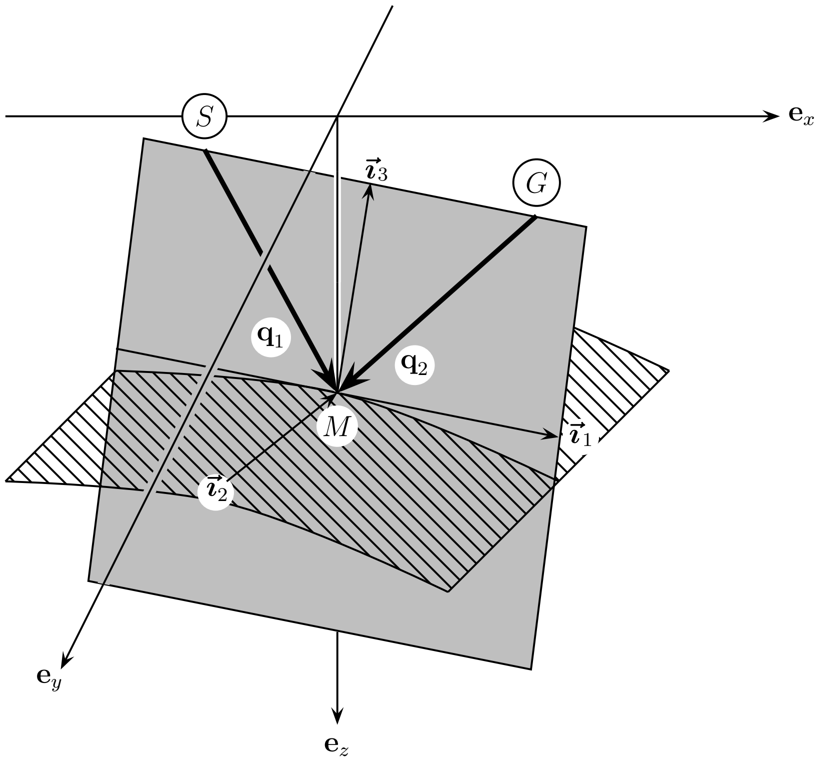

Figure 9.4: Coordinate systems. The unit base vectors $\vec{e}_x$, $\vec{e}_y$, and $\vec{e}_z$ form the Cartesian coordinate system in which the traveltime tables are given. It can, e.g., be chosen to coincide with the acquisition scheme. The unit base vectors $\vec{\imath}_1$, $\vec{\imath}_2$, and $\vec{\imath}_3$ define the reflector coordinate system. The hatched surface indicates the reflector. Vector $\vec{\imath}_3$ is normal to the reflector at the image point M and vectors $\vec{\imath}_1$ and $\vec{\imath}_2$ lie in the plane tangent to the reflector at M. The incidence plane (grey) spanned by $\vec{\imath}_1$ and $\vec{\imath}_3$ contains the slowness vectors $\boldsymbol{q}_1$ and $\boldsymbol{q}_2$ at M, where $\boldsymbol{q}_1$ is the slowness of the ray segment from the source at S to the image point, and $\boldsymbol{q}_2$ that of the ray segment from the receiver at G to M.

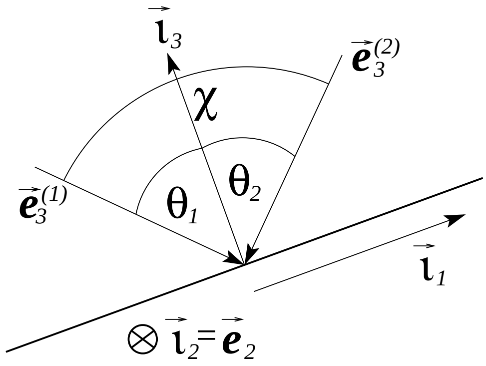

Figure 9.5: Definition of the ray centred coordinate system associated with the reflected ray: $\vec{\imath}_3$ is normal to the interface, $\vec{\imath}_1$ lies in the propagation plane as well as in the tangent plane of the interface, and $\vec{\imath}_2$ is given by $\vec{\imath}_3 \times \vec{\imath}_1$. The base vectors of the ray centred systems, $\vec{e}_i^{(I)}$ are defined such that $\vec{e}_2^{(I)}{=}\vec{\imath}_2$. The vectors $\vec{e}_3^{(I)}{=}\vec{t}^{(I)}$ are tangent to the rays. They are given by the directions of the slowness vectors. The angles θ_I are the incidence angles on the reflector, and the angle $\chi{=}\theta_1{+}\theta_2$.

is defined to be perpendicular to the plane of propagation (see Figure 9.5), it can be computed from the vector product of $\vec{e}_3^{(1)}$ and $\vec{e}_3^{(2)}$, which yields a vector perpendicular to both $\vec{e}_3^{(I)}$. Therefore $\vec{e}_2$ is given by

$$\vec{e}_2 = \frac{1}{\sin\chi}\,\vec{e}_3^{(1)} \times \vec{e}_3^{(2)} \quad , \tag{9.4.6}$$

where the factor $\sin^{-1}\chi$ ensures that $\vec{e}_2$ is a unit vector. Using the fact that the unit vectors $\vec{e}_i$ form a right-handed orthonormal system, it follows with $|\vec{e}_3^{(1)} \cdot \vec{e}_3^{(2)}|{=}\cos\chi$ that

$$\begin{aligned} \vec{e}_1^{(1)} &= \vec{e}_2 \times \vec{e}_3^{(1)} = \frac{1}{\sin\chi}\left(\vec{e}_3^{(1)} \times \vec{e}_3^{(2)}\right) \times \vec{e}_3^{(1)} = \frac{1}{\sin\chi}\left(\vec{e}_3^{(2)} - \vec{e}_3^{(1)}\cos\chi\right) \\ \vec{e}_1^{(2)} &= \vec{e}_2 \times \vec{e}_3^{(2)} = \frac{1}{\sin\chi}\left(\vec{e}_3^{(1)} \times \vec{e}_3^{(2)}\right) \times \vec{e}_3^{(2)} = \frac{1}{\sin\chi}\left(-\vec{e}_3^{(1)} + \vec{e}_3^{(2)}\cos\chi\right). \end{aligned} \tag{9.4.7}$$

With (see (8.2.7))

$$\vec{e}_3^{(I)} = V\,\boldsymbol{q}_0^{(I)} = \begin{pmatrix} -\sin\vartheta_I\cos\varphi_I \\ \sin\vartheta_I\sin\varphi_I \\ \cos\vartheta_I \end{pmatrix} \tag{9.4.8}$$

the matrices $\underline{\mathsf{H}}_I^{-1}$ are

$$\underline{\mathsf{H}}_1^{-1} = \frac{1}{\cos\vartheta_1 \sin\chi} \times$$

$$\begin{pmatrix} \sin\vartheta_1\cos\varphi_1\cos\vartheta_2 - \sin\vartheta_2\cos\varphi_2\cos\vartheta_1 & \sin\vartheta_2\sin\varphi_2\cos\vartheta_1 - \sin\vartheta_1\sin\varphi_1\cos\vartheta_2 \\ \sin\vartheta_1\sin\varphi_1\cos\chi - \sin\vartheta_2\sin\varphi_2 & \sin\vartheta_1\cos\varphi_1\cos\chi - \sin\vartheta_2\cos\varphi_2 \end{pmatrix}$$

$$\underline{\mathsf{H}}_2^{-1} = \frac{1}{\cos\vartheta_2 \sin\chi} \times$$

$$\begin{pmatrix} \sin\vartheta_1\cos\varphi_1\cos\vartheta_2 - \sin\vartheta_2\cos\varphi_2\cos\vartheta_1 & \sin\vartheta_2\sin\varphi_2\cos\vartheta_1 - \sin\vartheta_1\sin\varphi_1\cos\vartheta_2 \\ -\sin\vartheta_2\sin\varphi_2\cos\chi + \sin\vartheta_1\sin\varphi_1 & -\sin\vartheta_2\cos\varphi_2\cos\chi + \sin\vartheta_1\cos\varphi_1 \end{pmatrix} . \tag{9.4.9}$$

The matrices $\hat{\underline{\mathsf{G}}}_I$ are given by (see Section A.8)

$$G_{ij} = \vec{\boldsymbol{\imath}}_i \cdot \vec{\boldsymbol{e}}_j \quad . \tag{9.4.10}$$

This leads to (see also Figure 9.5)

$$\underline{\mathsf{G}}_1 = \underline{\mathsf{G}}_1^\top = \begin{pmatrix} -\cos\theta_1 & 0 \\ 0 & 1 \end{pmatrix} \quad \text{and} \quad \underline{\mathsf{G}}_2 = \underline{\mathsf{G}}_2^\top = \begin{pmatrix} -\cos\theta_2 & 0 \\ 0 & 1 \end{pmatrix} \quad . \tag{9.4.11}$$

The angles θ_I are the incidence angles on the interface. They cannot be computed without knowing the orientation of the interface. However, it is not necessary to know the angles θ_I themselves as I will now demonstrate. Inserting Equation (9.4.4) into the weight function (9.4.1) leads to

$$\begin{aligned} \frac{|\det(\bar{\underline{\mathsf{N}}}_1^\top \underline{\boldsymbol{\Sigma}} + \bar{\underline{\mathsf{N}}}_2^\top \underline{\boldsymbol{\Gamma}})|}{\sqrt{|\det\bar{\underline{\mathsf{N}}}_1 \det\bar{\underline{\mathsf{N}}}_2|}} &= \frac{|\det(\underline{\mathsf{G}}_1^\top \underline{\mathsf{H}}_1^{-\top} \underline{\mathsf{N}}_1^\top \underline{\boldsymbol{\Sigma}} + \underline{\mathsf{G}}_2^\top \underline{\mathsf{H}}_2^{-\top} \underline{\mathsf{N}}_2^\top \underline{\boldsymbol{\Gamma}})|}{\sqrt{|\det\left(\underline{\mathsf{G}}_1^\top \underline{\mathsf{H}}_1^{-\top} \underline{\mathsf{N}}_1\right) \det\left(\underline{\mathsf{G}}_2^\top \underline{\mathsf{H}}_2^{-\top} \underline{\mathsf{N}}_2\right)|}} \\ &= \sqrt{\cos\vartheta_1 \, \cos\vartheta_2} \sqrt{\frac{\cos\theta_1}{\cos\theta_2}} \, \frac{|\det(\underline{\mathsf{H}}_1^{-\top} \underline{\mathsf{N}}_1^\top \underline{\boldsymbol{\Sigma}} + \underline{\mathsf{G}}_1^{-1} \underline{\mathsf{G}}_2 \, \underline{\mathsf{H}}_2^{-\top} \underline{\mathsf{N}}_2^\top \underline{\boldsymbol{\Gamma}})|}{\sqrt{|\det\underline{\mathsf{N}}_1 \det\underline{\mathsf{N}}_2|}} \quad , \end{aligned} \tag{9.4.12}$$

where $|\det\underline{\mathsf{H}}_I|{=}\cos\vartheta_I$ and $|\det\underline{\mathsf{G}}_I|{=}\cos\theta_I$ was used. With

$$\underline{\mathsf{G}}_I^{-1} = \begin{pmatrix} -\frac{1}{\cos\theta_I} & 0 \\ 0 & 1 \end{pmatrix} \tag{9.4.13}$$

the matrix product $\underline{\mathsf{G}}_1^{-1}\underline{\mathsf{G}}_2$ in (9.4.12) becomes

$$\underline{\mathsf{G}}_1^{-1}\underline{\mathsf{G}}_2 = \begin{pmatrix} -\frac{1}{\cos\theta_1} & 0 \\ 0 & 1 \end{pmatrix} \begin{pmatrix} -\cos\theta_2 & 0 \\ 0 & 1 \end{pmatrix} = \begin{pmatrix} \frac{\cos\theta_2}{\cos\theta_1} & 0 \\ 0 & 1 \end{pmatrix} \quad . \tag{9.4.14}$$

This means that the angles θ_I themselves do not determine the weight function (9.4.1) but the ratio of their cosines does. Since for monotypic waves $\theta_1{=}\theta_2$, the new weight function in terms of matrices $\underline{\mathsf{N}}_I$ instead of $\bar{\underline{\mathsf{N}}}_I$ reads

$$W(\boldsymbol{\xi}^*, M) = \frac{1}{V_s} \sqrt{\cos\vartheta_s \cos\vartheta_g} \sqrt{\cos\vartheta_1 \, \cos\vartheta_2} \, \frac{|\det(\underline{\mathsf{H}}_1^{-\top} \underline{\mathsf{N}}_1^\top \underline{\boldsymbol{\Sigma}} + \underline{\mathsf{H}}_2^{-\top} \underline{\mathsf{N}}_2^\top \underline{\boldsymbol{\Gamma}})|}{\sqrt{|\det\underline{\mathsf{N}}_1 \det\underline{\mathsf{N}}_2|}} e^{-i\frac{\pi}{2}(\kappa_1+\kappa_2)} \quad . \tag{9.4.15}$$

To obtain a weight function suitable for migration of converted wave data, an expression for the ratio of the cosines of the angles θ_I is required which does not depend on a priori information about the reflector. This expression can be found with the transformation matrix $\hat{\underline{\mathsf{Z}}}$ between global and interface Cartesian coordinates

$$\hat{\underline{\mathsf{Z}}} = \hat{\underline{\mathsf{H}}}_1 \, \hat{\underline{\mathsf{G}}}_1^{-1} \; = \; \hat{\underline{\mathsf{H}}}_2 \, \hat{\underline{\mathsf{G}}}_2^{-1} \quad , \tag{9.4.16}$$

or, in index notation

$$Z_{ik} = H_{ij}^{(1)} G_{kj}^{(1)} \; = \; H_{ij}^{(2)} G_{kj}^{(2)} \quad , \tag{9.4.17}$$

where $\hat{\underline{\mathsf{G}}}^{-1} = \hat{\underline{\mathsf{G}}}^{\top}$ was used. With Snell's law, stating that

$$p = \frac{\sin\theta_1}{V_1} = \frac{\sin\theta_2}{V_2} \tag{9.4.18}$$

Equation (9.4.17) leads to the following system of equations:

$$\begin{aligned} Z_{i3} &= -H_{i3}^{(1)} \cos\theta_1 + H_{i1}^{(1)} \sin\theta_1 = -\, H_{i3}^{(2)} \cos\theta_2 + H_{i1}^{(2)} \sin\theta_2 \\ &= -H_{i3}^{(1)} \cos\theta_1 + H_{i1}^{(1)} \, V_1 \, p \; = -\, H_{i3}^{(2)} \cos\theta_2 + H_{i1}^{(2)} \, V_2 \, p \quad . \end{aligned} \tag{9.4.19}$$

Substituting the elements of $\hat{\underline{\mathsf{H}}}_I$ into the system (9.4.19) and elimination of p yields after some algebra

$$\frac{\cos\theta_1}{\cos\theta_2} = \frac{V_1 \, \cos\chi + V_2}{V_2 \, \cos\chi + V_1} \quad . \tag{9.4.20}$$

With this result the new weight function for the migration of converted waves is given by

$$\begin{aligned} W(\boldsymbol{\xi}^*, M) \;\; = \;\; & \frac{1}{V_s} \sqrt{\cos\vartheta_s \cos\vartheta_g} \, \sqrt{\cos\vartheta_1 \cos\vartheta_2} \, \frac{V_1 \, \cos\chi + V_2}{V_2 \, \cos\chi + V_1} \times \\ & \times \frac{|\det(\underline{\mathsf{H}}_1^{-\top} \underline{\mathsf{N}}_1^{\top} \underline{\boldsymbol{\Sigma}} + \underline{\mathsf{G}}_1^{-1} \underline{\mathsf{G}}_2 \, \underline{\mathsf{H}}_2^{-\top} \underline{\mathsf{N}}_2^{\top} \underline{\mathsf{\Gamma}})|}{\sqrt{|\det \underline{\mathsf{N}}_1 \, \det \underline{\mathsf{N}}_2|}} e^{-i \, \frac{\pi}{2} (\kappa_1 + \kappa_2)} \end{aligned} \tag{9.4.21}$$

with

$$\underline{\mathsf{G}}_1^{-1} \underline{\mathsf{G}}_2 = \begin{pmatrix} \frac{V_2 \, \cos\chi + V_1}{V_1 \, \cos\chi + V_2} & 0 \\ 0 & 1 \end{pmatrix} \quad . \tag{9.4.22}$$

For a 2.5-D symmetry, the situation simplifies as the non-diagonal elements of the matrices $\underline{\mathsf{H}}_I$ become zero (the angles φ_I are either 0° or 180°). We find that

$$\underline{\mathsf{H}}_I^{-1} = \begin{pmatrix} \frac{1}{\cos\vartheta_I} & 0 \\ 0 & 1 \end{pmatrix} \quad . \tag{9.4.23}$$

Furthermore, in 2-D and 2.5-D $\chi = \theta_1 + \theta_2 = \vartheta_1 + \vartheta_2$, and (see (8.2.8))

$$\frac{N_{xx}}{q_z} = -\frac{N_{xz}}{q_x} \quad . \tag{9.4.24}$$

In 2-D, the matrices reduce to scalars with

$$\begin{aligned} G_1 &= -\cos\theta_1 \\ G_2 &= -\cos\theta_2 \\ |H_1| &= \cos\vartheta_1 \\ |H_2| &= \cos\vartheta_2 \quad , \end{aligned} \tag{9.4.25}$$

where the sign of H_I depends on that of the x component of the slowness vector.

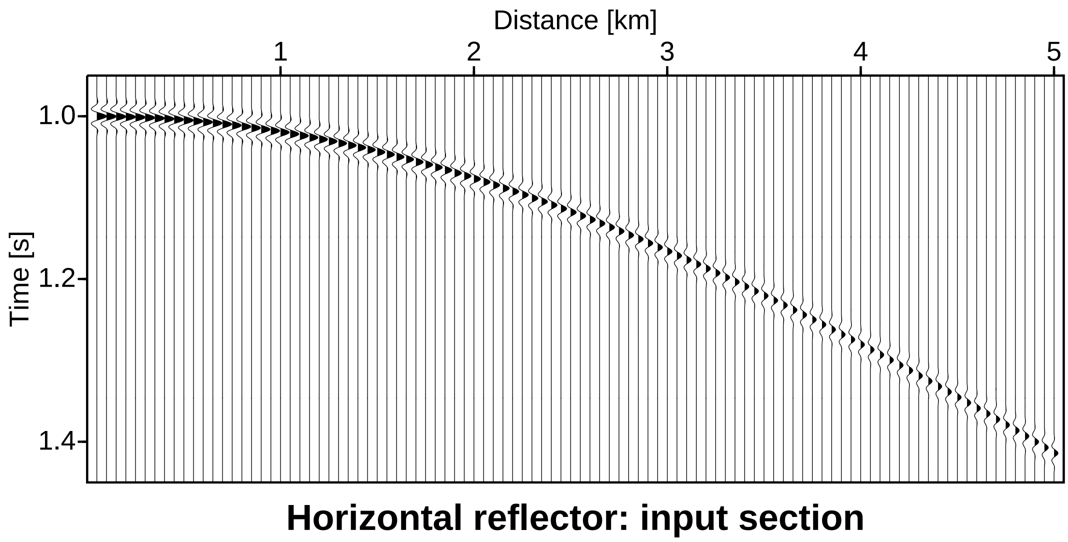

Figure 9.6: Synthetic common shot section for the first example, a two-layer model with a horizontal reflector.

9.5 Application to PP Data

In this section I will apply the new method to two generic velocity models first. Simple examples were chosen in order to allow for comparison of numerically and analytically computed amplitudes. The method is, however, not limited to homogeneous velocity layer models, which is why I show results for complex examples after evaluating that the new technique is indeed capable of reconstructing the reflectivity.

For convenience reasons all examples are restricted to 2.5-D. For the generic examples the velocity model was only used to compute the traveltimes with a finite difference eikonal solver (FDES, Vidale 1990) using an implementation of Leidenfrost (1998). These traveltimes were resampled from the original 10m fine grid required by FDES for sufficient accuracy and stored on a coarse grid of 50m in either direction. Diffraction traveltimes were interpolated from this coarse grid onto a fine migration grid of 5m in z-direction using the hyperbolic traveltime approximation (2.2.2). The migration weights were also computed from the coarse gridded traveltimes using the coefficients determined from the hyperbolic approximation, see Chapter 2.

The first model has a planar horizontal reflector at a depth of 2500m. The P velocity is V_{P_1}=5km/s in the upper part of the model and V_{P_2}=6km/s below the reflector. The S velocities $V_{S_i}=V_{P_i}/\sqrt{3}$ were used for reflection coefficients; only PP reflections were considered. The density is ρ[g/cm^3]=1.7+0.2V_P[km/s]. Ray synthetic seismograms were computed using the SEIS88 package (Červený and Pšenčík, 1984) for a receiver line consisting of 100 equidistantly positioned receivers with a spacing of 50m and the first receiver 50m away from the point source. The resulting common shot section is shown in Figure 9.6.

Figure 9.7 shows the relevant part of the resulting migrated depth section for this one shot together with the model. The reflector was migrated to the correct position and the source pulse, a Gabor

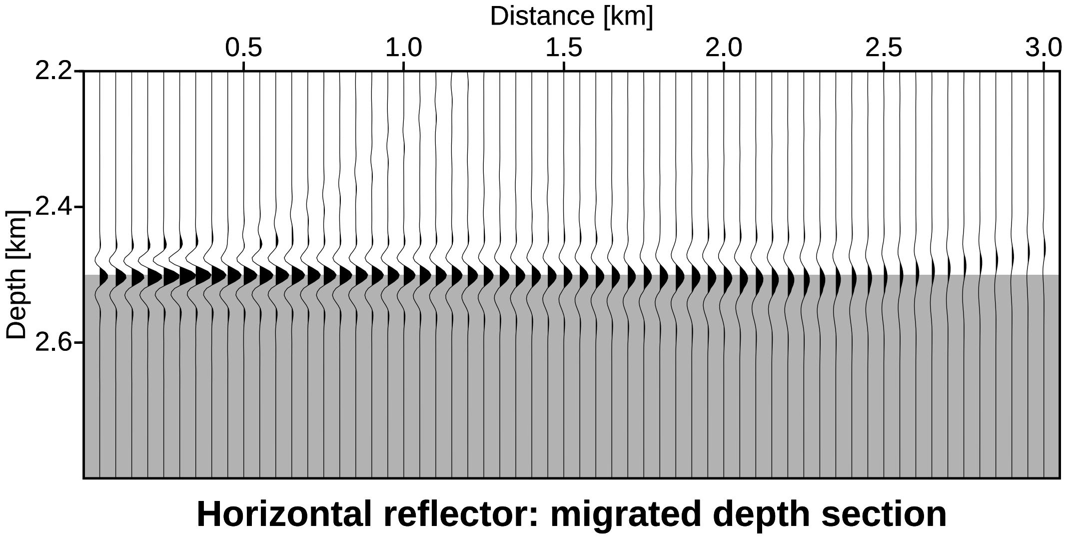

Figure 9.7: Migrated depth section of the common shot section shown in Figure 9.6. The grey area indicates the lower layer. The reflector was migrated to the correct position and the source pulse, a Gabor wavelet, was reconstructed.

wavelet, was reconstructed. Since there are no transmission losses caused by the overburden, the amplitudes of the migrated section coincide with the reflection coefficients. Figure 9.8 (top) shows the accordance between amplitudes picked from the migrated section in Figure 9.7 with theoretical values. Apart from the peaks at 300m and 2000m distance the two curves coincide, i.e. the correct AVO behaviour was reconstructed. The peaks are aperture effects caused by the limited extent of the receiver line and can be suppressed with a taper. Figure 9.8 (middle) displays relative errors of the reflection coefficients. As a comparison, errors of reflection coefficients that were computed with our migration routine, but using analytic traveltimes as input data instead of FD traveltimes, are also given in Figure 9.8 (middle). Whereas the average error in the reflection coefficients from FD traveltimes is 2%, the error from analytic traveltimes is a magnitude smaller (0.22%; for both cases only values that are not affected by aperture effects were considered). The higher error for FD traveltimes as input data is due to the systematical errors that are inherent to the Vidale algorithm. Figure 9.8 (bottom) illustrates that the maximum errors in the reflection coefficients coincide with the region of highest errors in the traveltimes.

The second model has the same velocities and densities as the first model, but here a dipping plane reflector with an inclination angle of 14° separates the two velocity layers. The reflector depth below the source is 2500m. Ray synthetic seismograms were computed using the SEIS88 package (Červený and Pšenčík, 1984) for 80 receivers with 50m distance starting at 50m from the point source. In order to ensure causality in the Vidale algorithm, this velocity model had to be 10-fold smoothed. Figure 9.9 shows the common shot section, and Figure 9.10 shows the migrated depth section together with the original reflector position. Again the reflector was migrated to the correct depth and inclination.

As for the first example the reflection coefficients were picked from the migrated section and compared

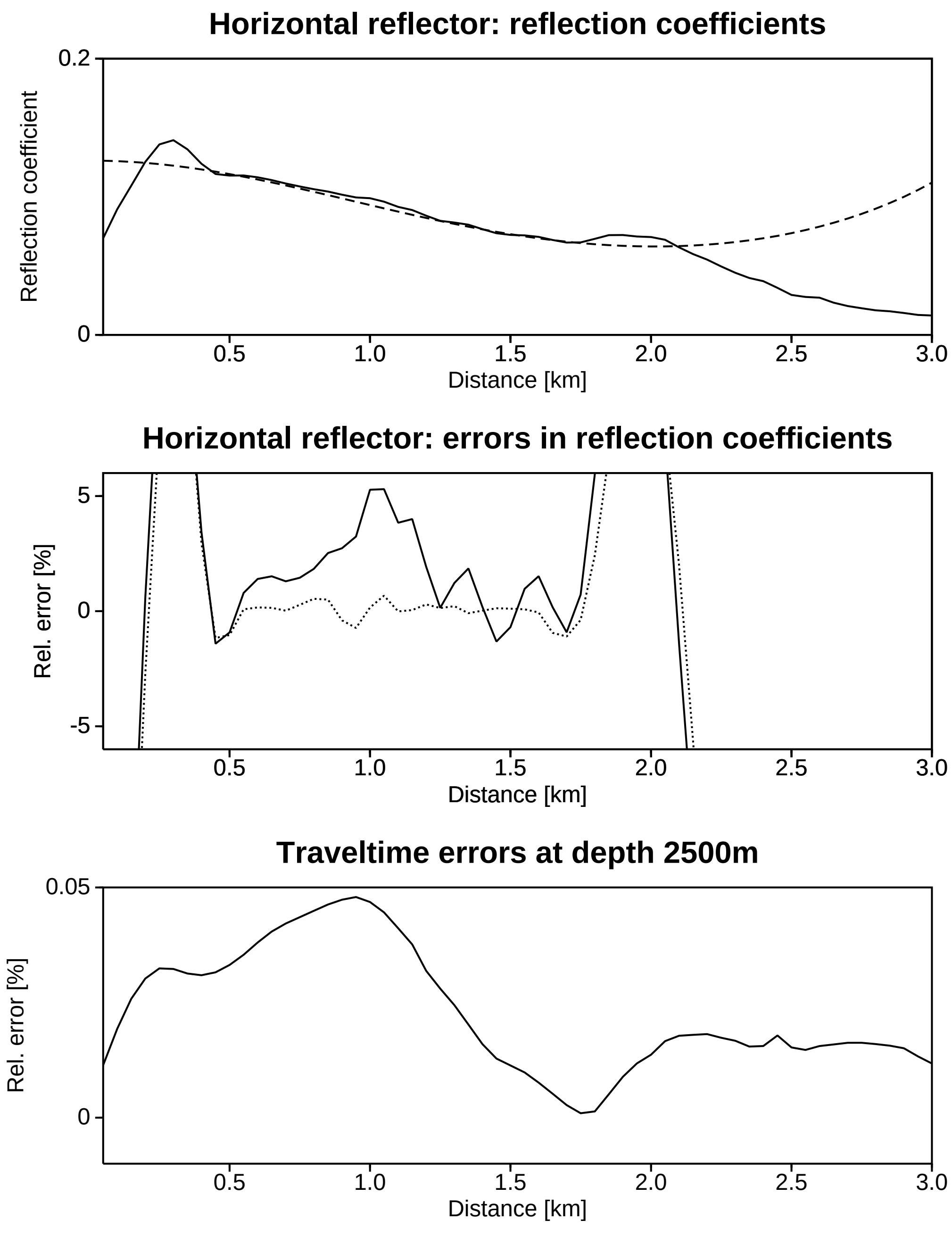

Figure 9.8: Top: solid line: picked reflection coefficients from the migrated section in Figure 9.7; dashed line: analytic values for the reflection coefficients. Middle: solid line: relative errors of the picked reflection coefficients; dotted line: relative errors of reflection coefficients if analytic traveltimes are used as input. Bottom: relative errors of the input traveltimes computed with an FD eikonal solver taken at the reflector at a depth of 2500m. The maximum traveltime error coincides with the maximum error in the reflection coefficients.

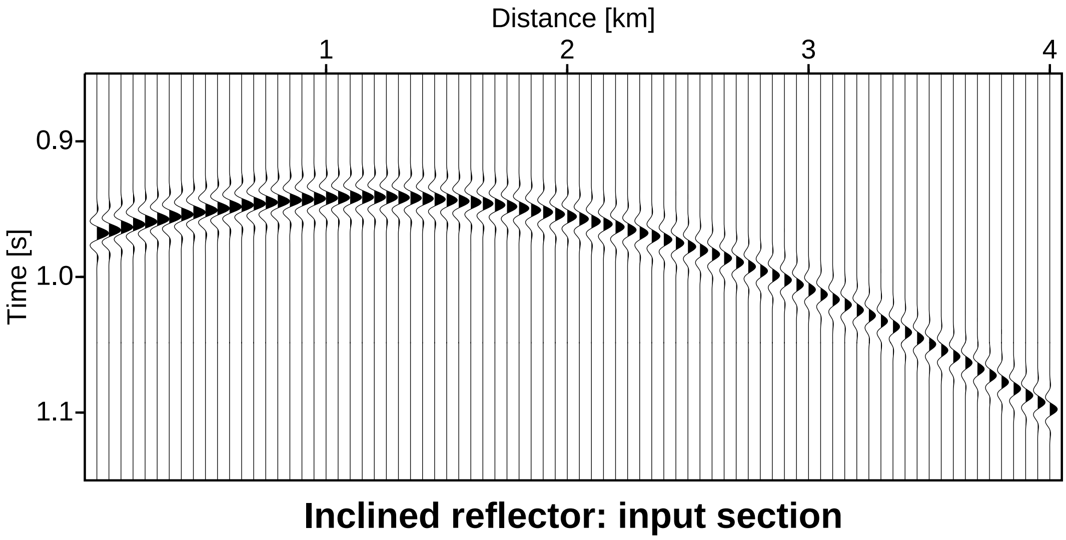

Figure 9.9: Synthetic common shot section for the second example, a two-layers model with an inclined reflector.

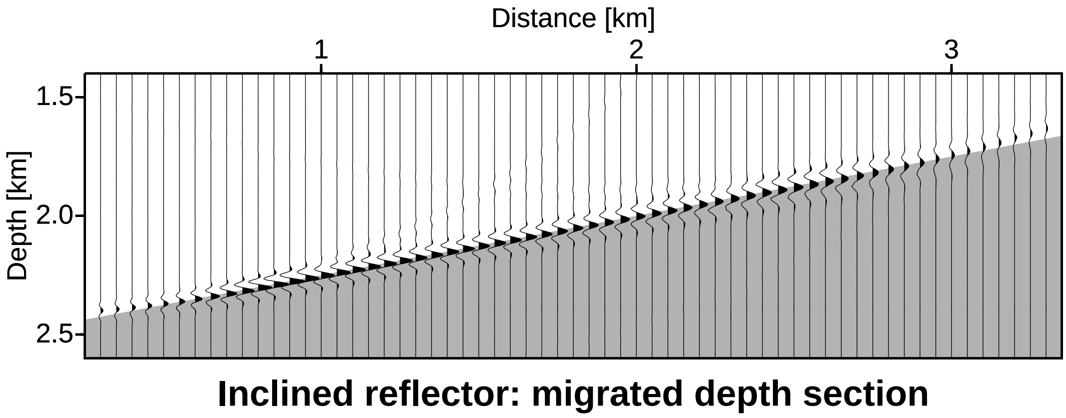

Figure 9.10: Migrated depth section for the second example. The cray area indicates the lower layer. The reflector was migrated to the correct depth and inclination. The source pulse was correctly reconstructed.

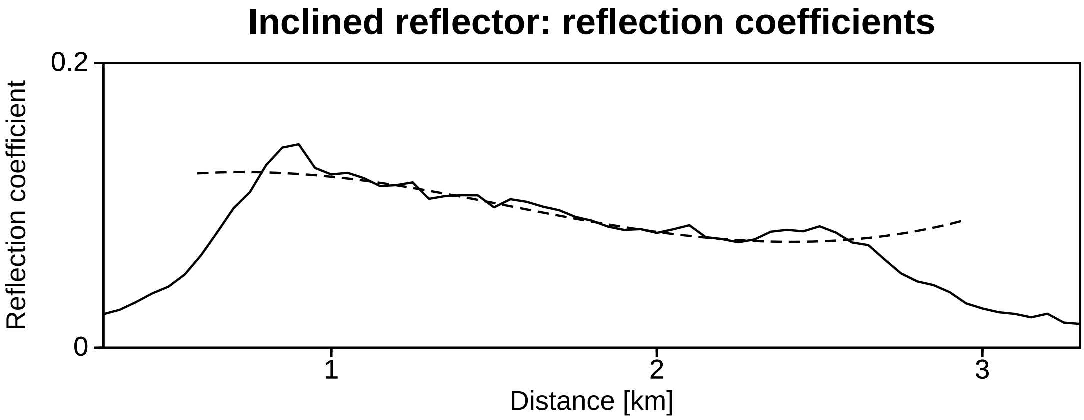

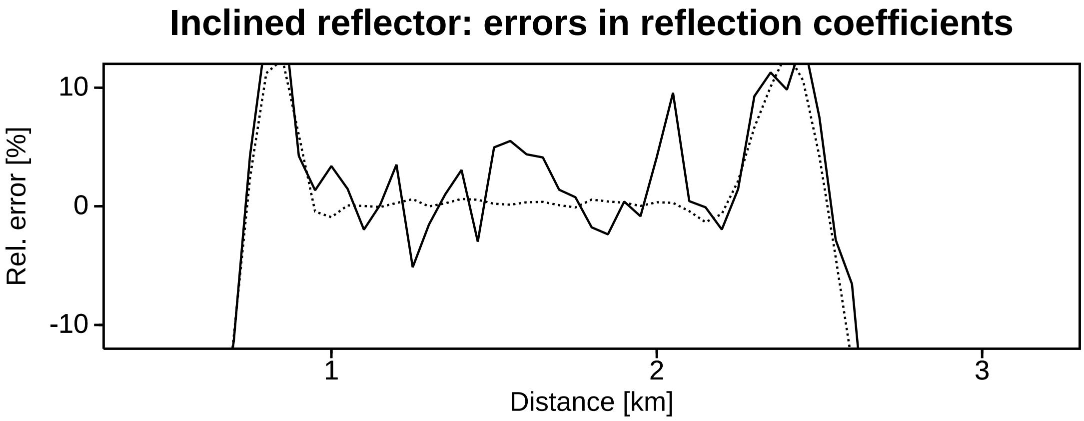

Figure 9.11: Top: solid line: picked reflection coefficients from the migrated section in Figure 9.10; dashed line: analytic values for the reflection coefficients. Bottom: solid line: relative errors of the picked reflection coefficients; dotted line: relative errors of reflection coefficients if analytic traveltimes are used.

to analytic values. Figure 9.11 (top) shows the result. The peaks at 900m and 2500m are again due to boundary effects. Figure 9.11 (bottom) displays the relative errors of the picked reflection coefficients. The average errors for reflection coefficients from FD traveltimes and from analytic traveltimes as input are 2.9% and 0.27%, respectively. In addition to the already discussed errors caused by the FD routine, the higher error compared to the first model can be attributed to the smoothing of the velocity model. Smoothing of V^{-1}, as was applied, preserves only the vertical traveltime. Changes in the traveltimes lead to changes in curvature and, thus, to changes in the weight functions.

Complex synthetic data set

To investigate the performance and quality of the traveltime-based strategy to true-amplitude migration, we have chosen a complex 2.5D synthetic model, shown in Figure 9.12. Ray synthetic seismograms were computed using two-point paraxial ray tracing. Transmission losses were not

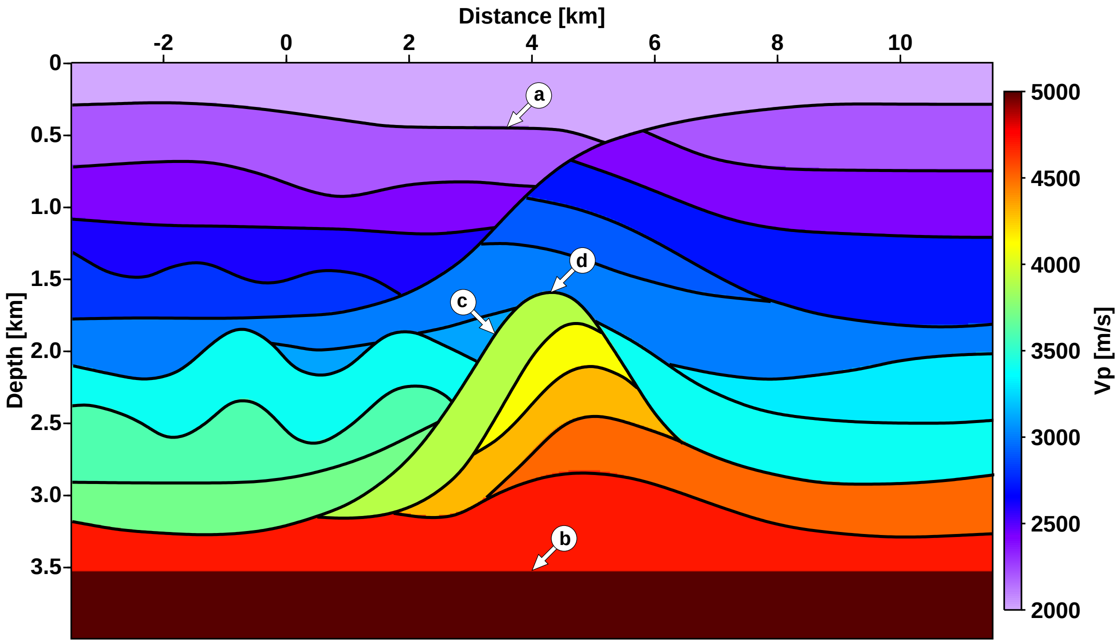

Figure 9.12: Velocity model for the synthetic data example. This figure shows the original blocky model in which the seismograms were computed. The arrows indicate locations where the reconstructed amplitudes will be investigated.

modelled. A total of 56 600 traces were generated and sorted in common-offset gathers with offsets ranging from 0 to 1980 m. The resulting zero-offset section is displayed in Figure 9.13. Although Figure 9.13 reveals modelling artifacts, such as missing diffractions at the pinch-outs and irregular amplitude behaviour in isolated spots, we have decided to use this complex model. For the verification of our method we will compare the results to those obtained from a true-amplitude migration using weights generated with dynamic ray tracing (DRT). Both results will be influenced by the artifacts in the input data, but their impact should be the same, thus making the comparison valid.

In order to compare our result to that from the DRT-based migration, a smooth velocity model was required. The velocity model we used is shown in Figure 9.14. It was obtained from an imaging workflow based on the Common-Reflection-Surface (CRS) stack (Mann et al., 2003; Hertweck, 2004) and subsequent tomographic inversion of the CRS attributes (Duveneck, 2004). Traveltime tables on grids with a spacing of 100 m in each dimension were generated using two-point paraxial ray tracing for sources distributed with a spacing of 100 m. These were the only input to the traveltime-based algorithm.

For the comparison to the DRT-based migration we have applied two-point paraxial ray tracing to compute the necessary Green's function tables (GFT's) on a 50 m grid with a shot spacing of also 50 m. The finer grid spacing was required for this implementation as it uses linear interpolation of the traveltimes. For the 2.5D common-offset weight function (Hanitzsch, 1997) the GFT consists of the following four quantities:

1. the traveltime,

2. the emergence angle,

3. the in-plane geometrical spreading, and

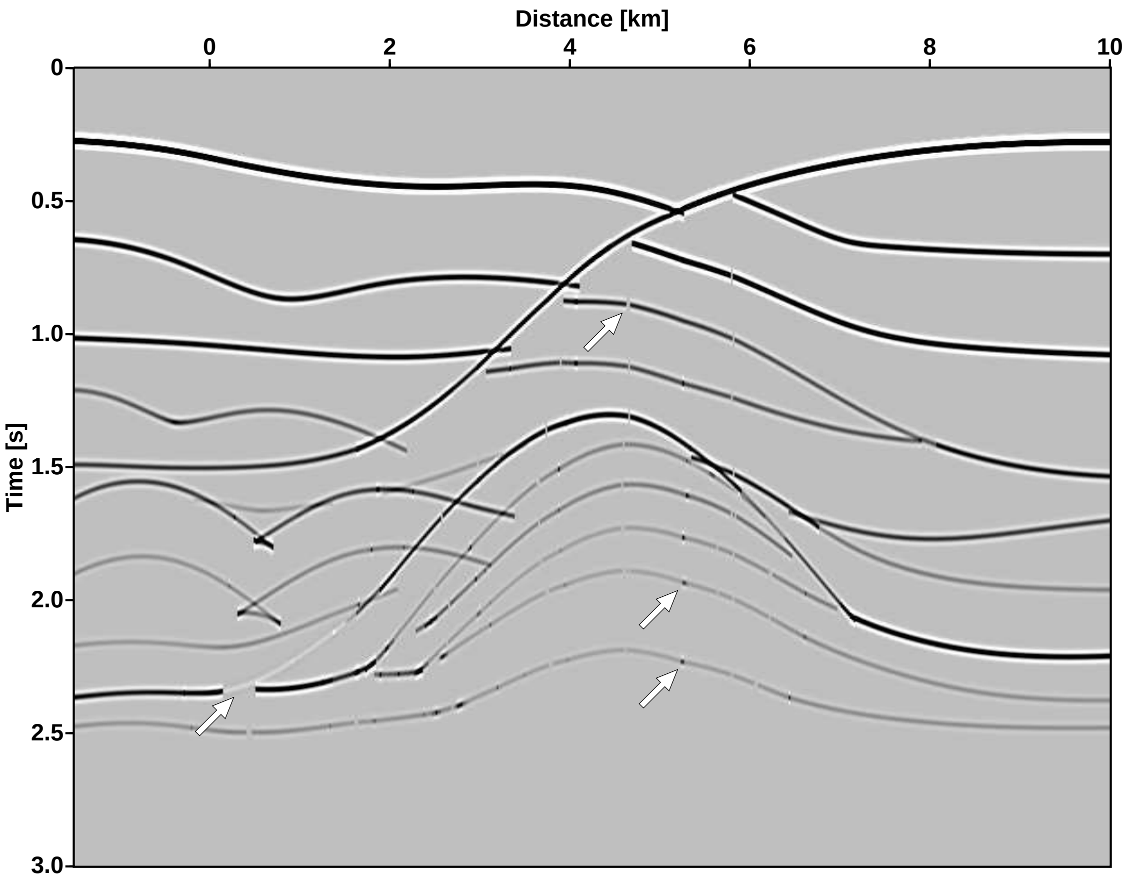

Figure 9.13: Unmigrated zero-offset section of the synthetic data set obtained by ray modelling. Note the missing diffractions at pinch-outs and changes in amplitudes along the reflectors, e.g., at the positions indicated by arrows.

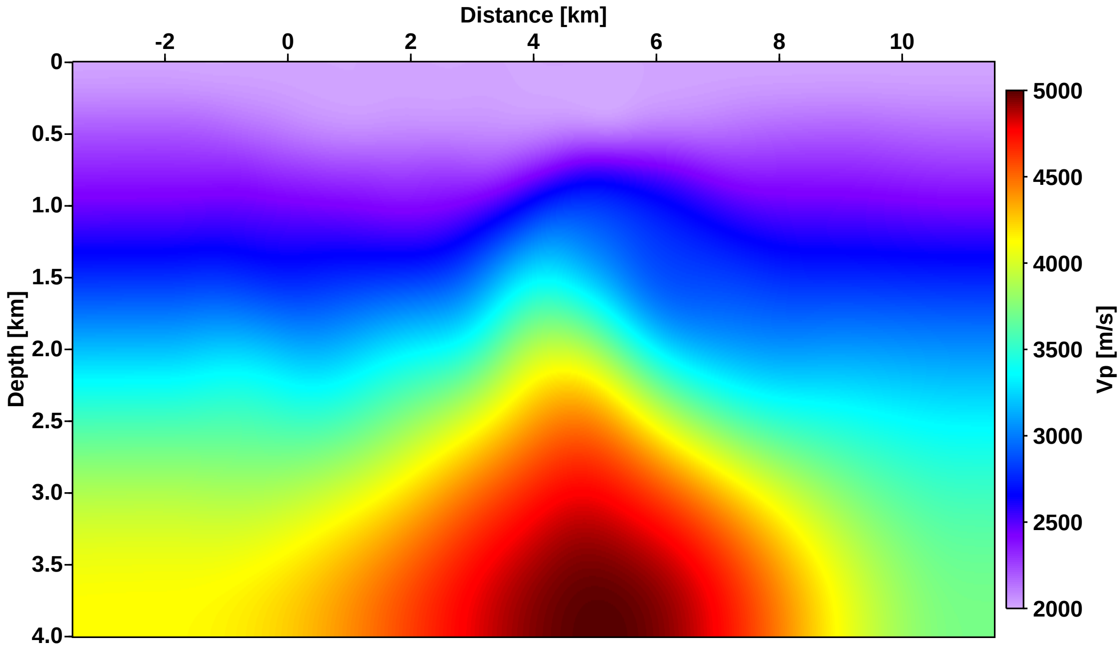

Figure 9.14: Velocity model for the synthetic data example. This figure shows the smooth model used for the generation of the traveltimes and GFT's.

4. the out-of-plane geometrical spreading.

Although both migration methods can include multi-arrival traveltimes, the codes we used are limited to single arrivals, e.g. first arrivals or arrivals with maximum amplitude. In this example, arrivals with maximum amplitude were used in both cases and a comparison is therefore valid. The discretisation of the migration grid was 10 m in x- and 5 m in z-direction.

Figure 9.15 shows the stacked migrated depth sections. At the shallower depths, a mute was applied to the larger offsets to avoid the distortions caused by pulse stretch (Tygel et al., 1994). Both results, i.e., for the migration with DRT weights (Figure 9.15a) and traveltime-based weights (Figure 9.15b), were displayed with the same plotting parameters. A comparison between them reveals no significant differences. Figure 9.16 displays common image gathers obtained from both migration methods. The comparison shows again no significant differences between the DRT weights (Figure 9.16a) and the traveltime-based weights (Figure 9.16b), indicating that the results from both methods coincide on the kinematic aspects. Whereas the CRS tomography yields a good initial model for migration, further model updating steps after migration velocity analysis were not carried out, thus explaining some residual move-out visible in both cases.

In addition to the structural image of the subsurface discussed in the previous paragraph, we have investigated the accuracy of the reconstructed amplitudes. We have picked amplitude versus offset (AVO) curves from the common image point gathers at the four different reflector positions indicated in Figure 9.12. Figure 9.17a shows the AVO for the topmost reflector at x=2.6 km. At this position, the reflector is plane and horizontal, and we could compute the corresponding analytical reflectivity. The amplitudes obtained from both migration methods coincide, and both match very well the analytical values. Figure 9.17b shows the AVO resulting from both methods on the flat bottom reflector, and Figures 9.17c and 9.17d display the AVO of an inclined and a curved reflector segment,

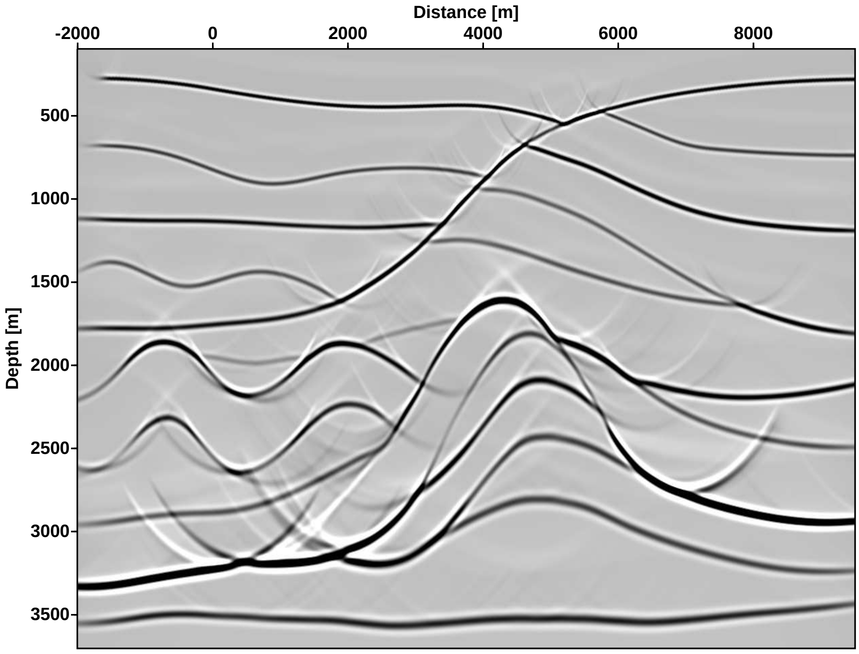

(a)

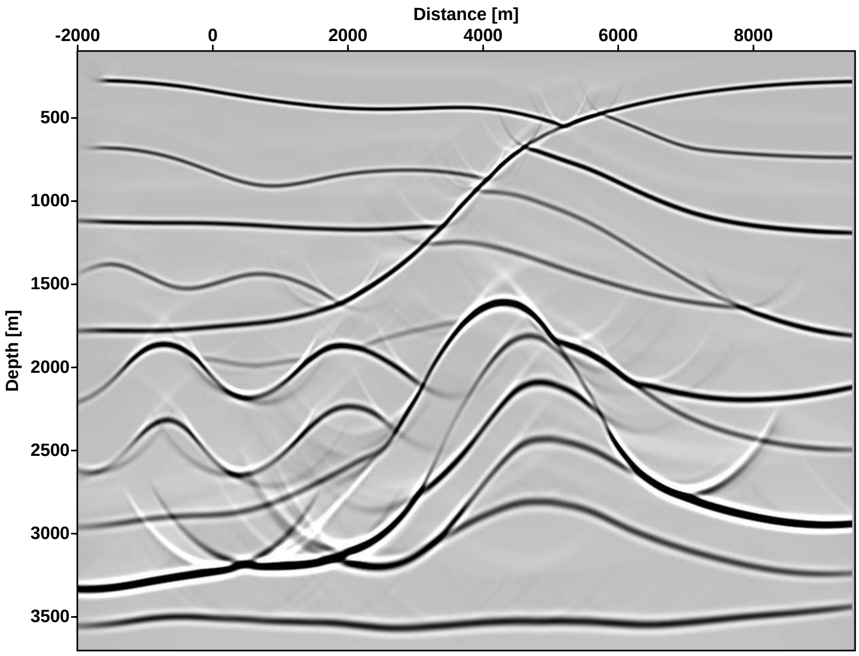

(b)

Figure 9.15: True-amplitude prestack-migrated stacked sections for the synthetic data set: (a) with weight functions from dynamic ray tracing, (b) from the traveltime-based approach. Both figures are displayed with the same grey scale. The smiles at pinch-outs occur because diffractions were not modelled, see Figure 9.13.

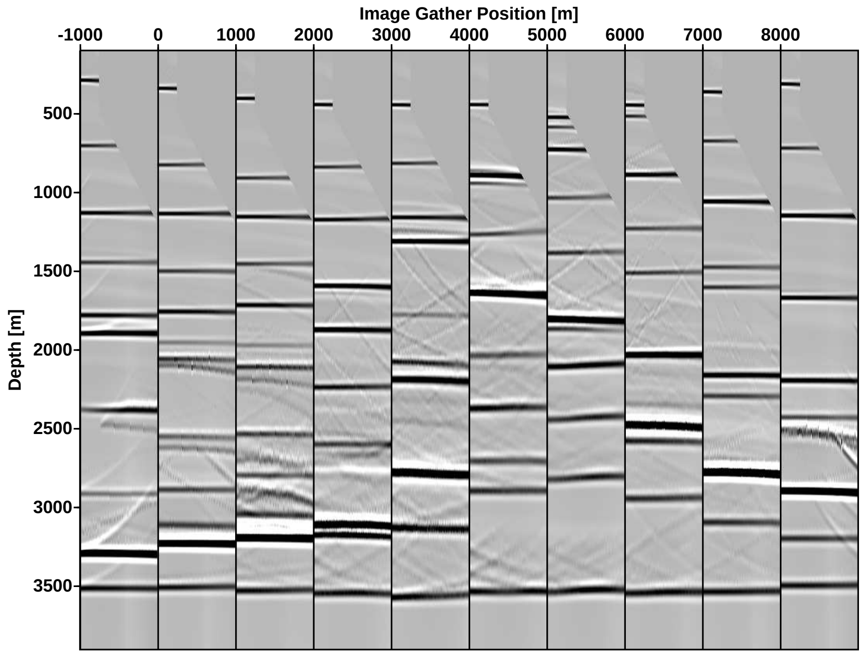

(a)

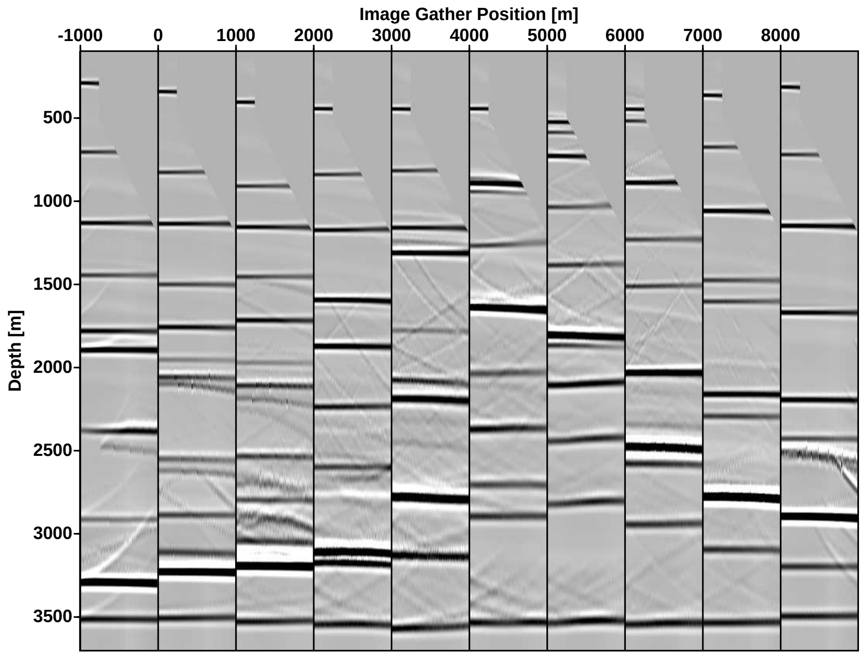

(b)

Figure 9.16: Common image gathers resulting from migration of the synthetic data, (a) with DRT weights and (b) traveltime-based weights. Both figures are displayed with the same grey scale.

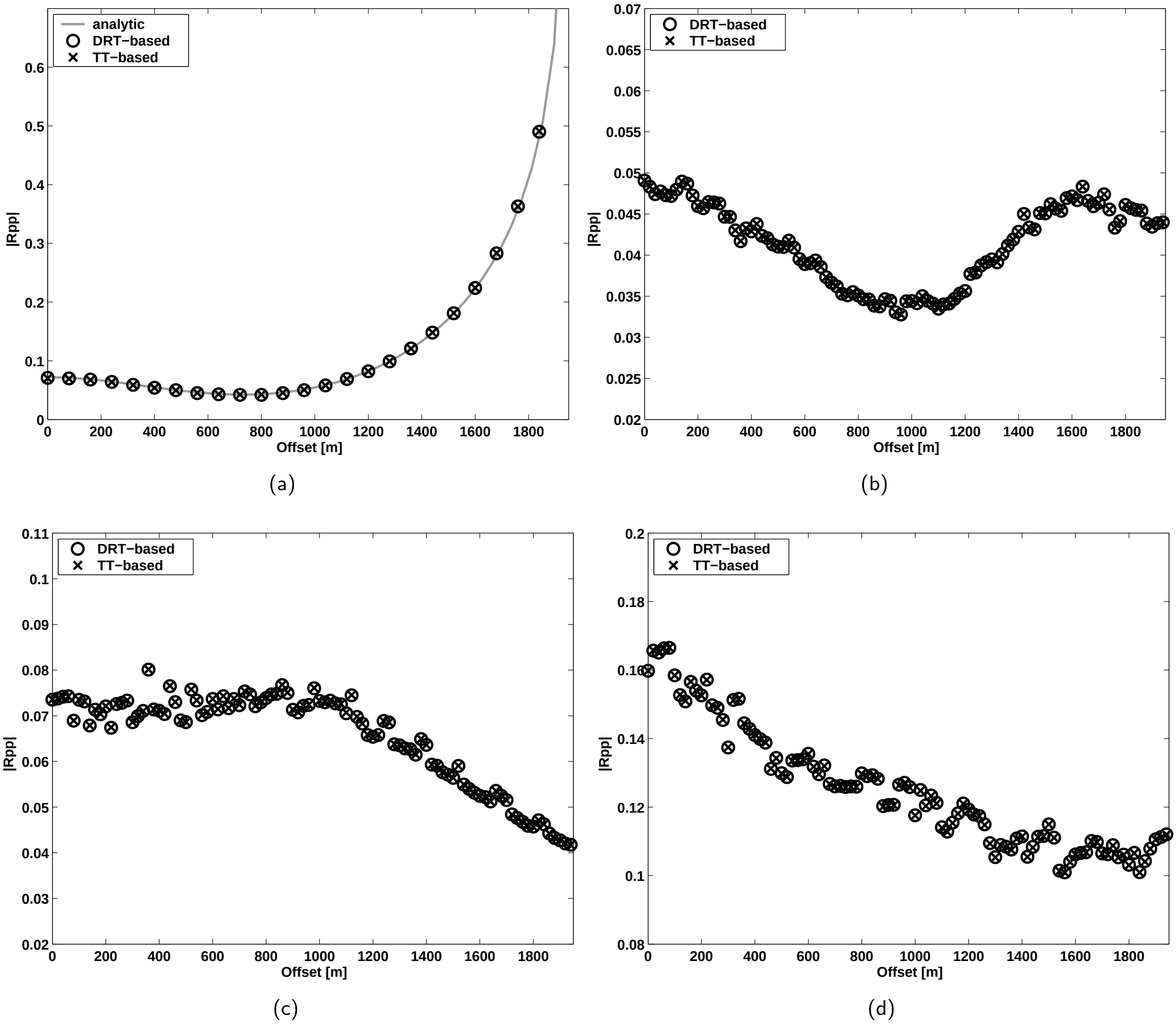

Figure 9.17: AVO curves picked in the common image gathers at the four positions indicated in Figure 9.12. (a) Top reflector, (b) bottom reflector, (c) steeply-inclined reflector, and (d) curved reflector.

respectively. These three last locations were chosen in order to investigate if the influence of the overburden, as well as slope and curvature of reflectors still lead to the same result with our method. We can see that the amplitudes resulting from both methods coincide in each case.

Application to field data

The seismic data used for the following case study were acquired by an energy resource company. They intend to carry out a project where a detailed knowledge of the subsurface structures is essential.

Standard pre-processing of the field data was carried out, where the following steps influenced the amplitudes: spherical divergence correction, minimum-phase transformation, automatic gain correction, and deconvolution. This means that the pre-processing did not preserve the amplitudes and the data are, therefore, not suited to recover the correct reflection amplitudes. The aim, however, is to show that our method yields the same result as true-amplitude migration using weights from dynamic ray tracing. Although the reconstructed amplitudes can not be considered in terms of reflectivity and AVO, the data set is nevertheless suited to demonstrate the equivalence between both migration schemes.

After the pre-processing of the data, an imaging workflow based on the Common-Reflection-Surface (CRS) stack (Mann et al., 2003; Hertweck, 2004) was carried out. The velocity model shown in Figure 9.18 was obtained from a tomographic inversion of the CRS attributes (Duveneck, 2004). This model was used to generate the input traveltimes and GFT's with two-point paraxial ray tracing. Again, only the maximum-amplitude arrival was considered. For the traveltime-based migration, the spacing of the input grid was 100 m, and the grid spacing of the GFT's for the DRT-based migration was 40 m. The finer grid spacing of the GFT's was necessary since the DRT-based migration applies

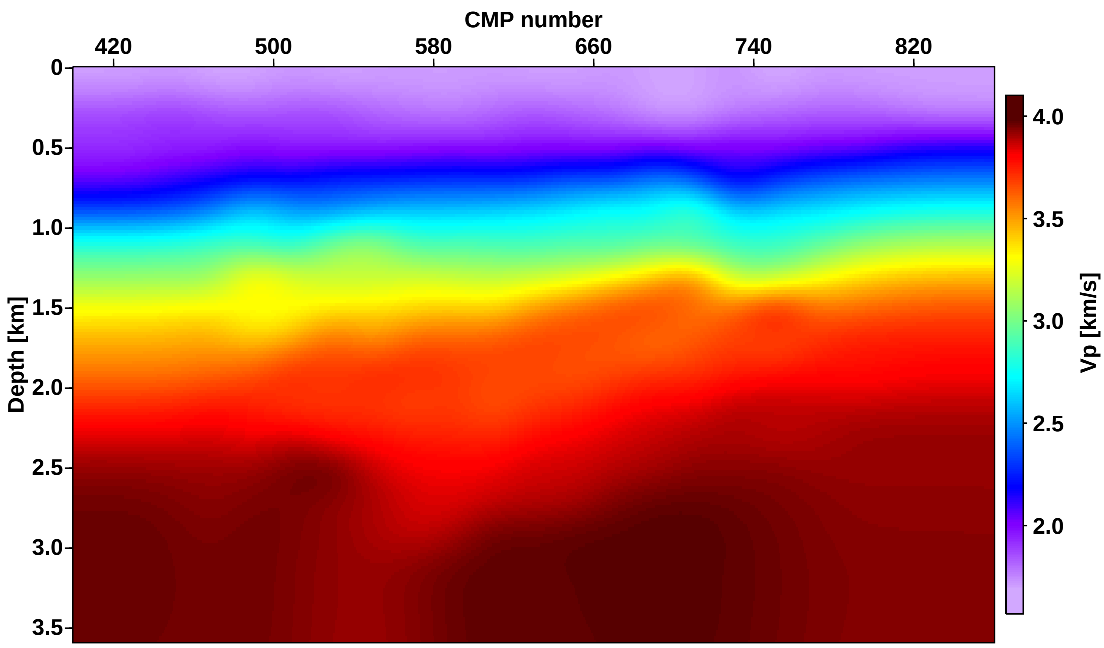

Figure 9.18: Velocity model for the real data set obtained from CRS tomography. The arrows indicate locations where the reconstructed amplitudes will be investigated.

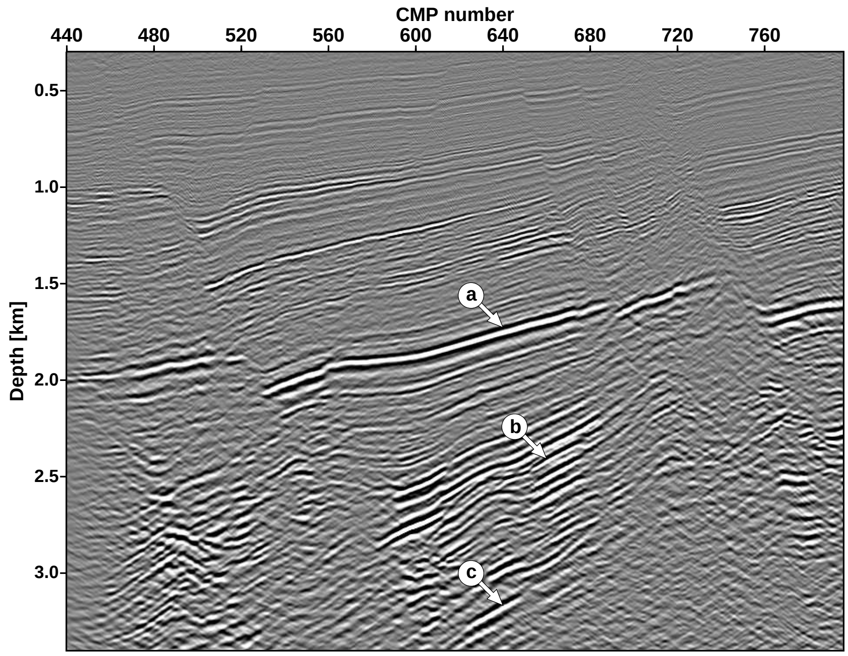

(a)

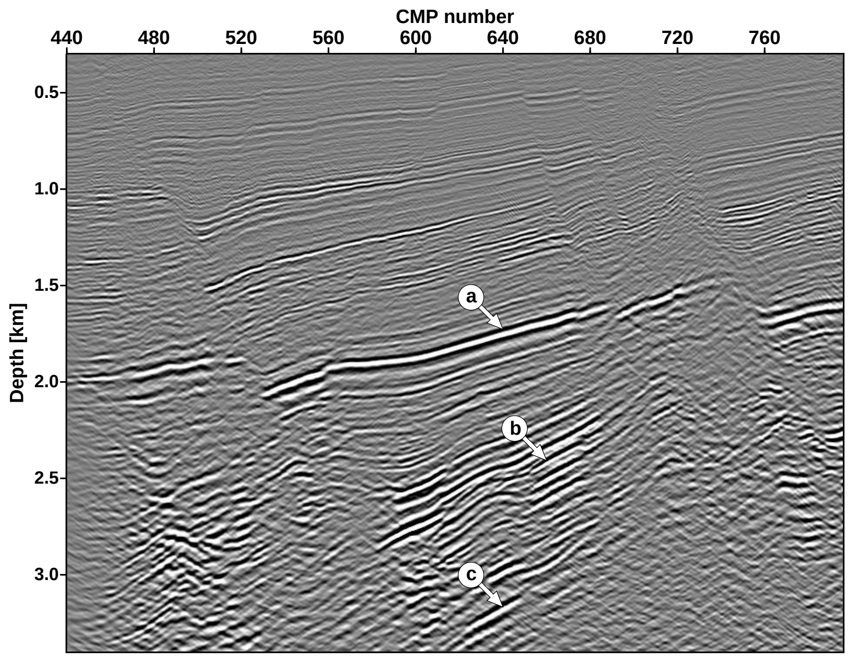

(b)

Figure 9.19: True-amplitude migrated and stacked sections of the real data set: (a) with weight functions from dynamic ray tracing, (b) with weight functions from the traveltime-based approach. Both figures are displayed with the same grey scale.

linear traveltime interpolation. The migration grid had a spacing of 10 m in x- and 5 m in z-direction.

Figures 9.19 and 9.20 show the stacked sections and the common-image gathers obtained from both

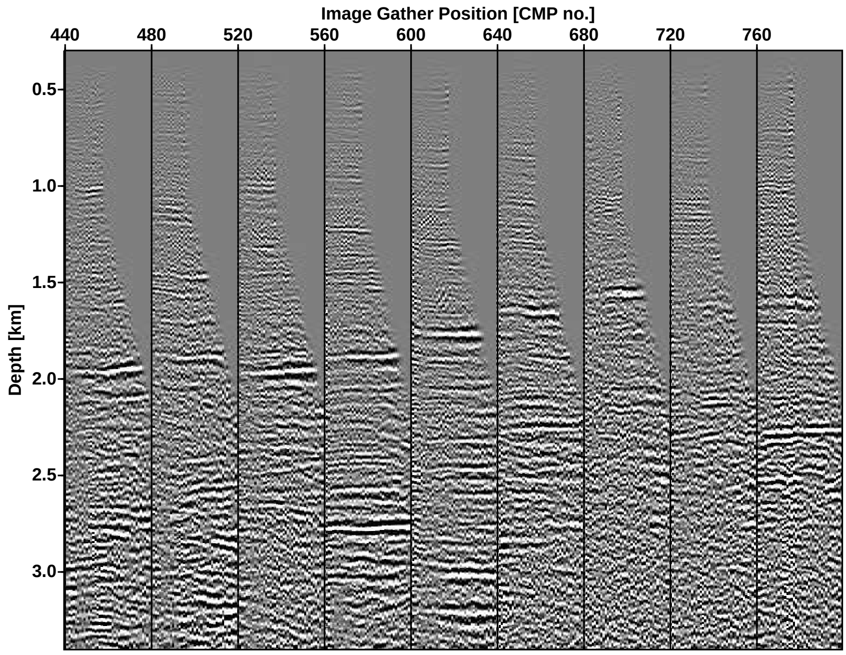

(a)

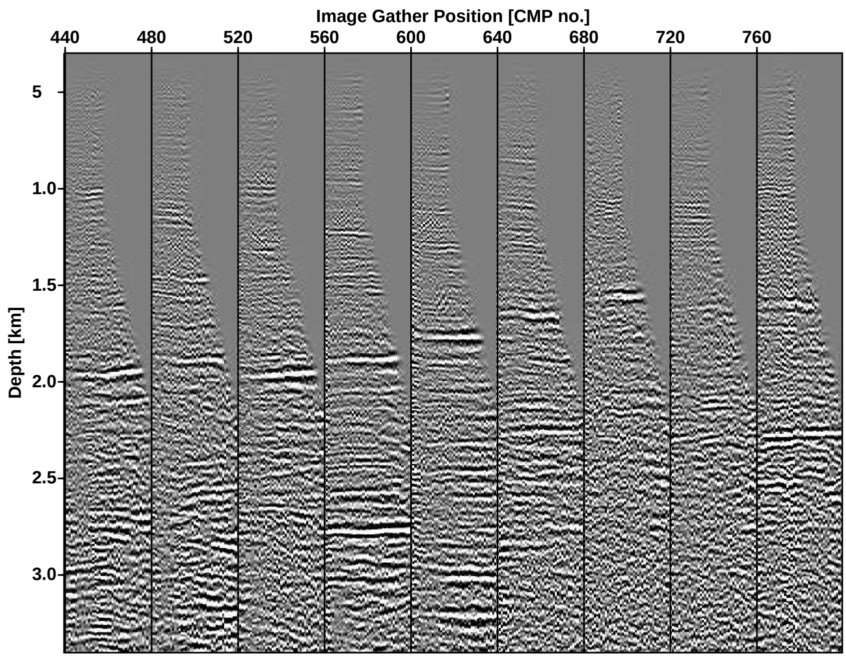

(b)

Figure 9.20: Common image gathers resulting from migration of the real data with (a) DRT weights, and (b) traveltime-based weights. Both figures are displayed with the same grey scale.

migration methods. As in the previous synthetic examples, visual inspection shows that the results are kinematically equivalent. Again, we observe residual move-out in the common image gathers, as a model update based on a migration velocity analysis was not carried out.

Although the recovered amplitudes do not correctly represent reflectivities, we have picked amplitudes from the common image point gathers at three different locations (see Figure 9.18) for comparison. The results are shown in Figure 9.21. We find once more that the amplitudes from both methods agree well. The higher scattering of the results compared with the synthetic data set may be caused by the noise in the real data.

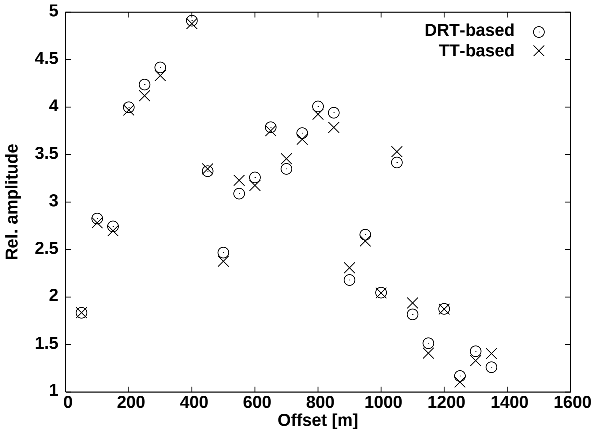

(a)

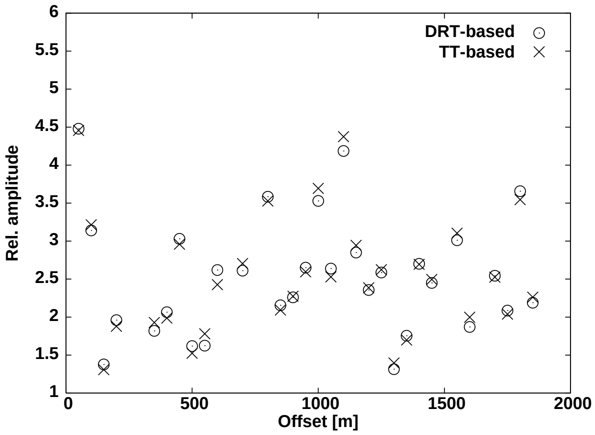

(b)

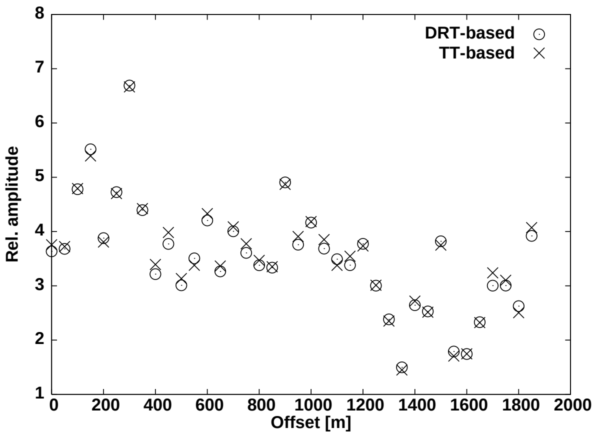

(c)

Figure 9.21: Amplitudes picked in the common image gathers at the three positions indicated in Figure 9.18. Note that these do not reflect the real AVO since the pre-processing of the data set was not carried out in an amplitude-preserving fashion.

9.6 Application to PS-converted waves

The algorithm can also be applied to PS converted waves. However, an additional factor must be considered in the weight function to allow for the discontinuity of the geometrical spreading at an interface (see Section A.8, or Červený et al. 1977). For a PS converted wave, the geometrical spreading (9.2.28) becomes

$$\mathcal{L} = \frac{1}{V_s} \sqrt{\frac{\cos\theta_1}{\cos\theta_2}} \sqrt{\frac{\cos\vartheta_s\,\cos\vartheta_g}{|\det\underline{\bar{\mathsf{N}}}|}}\,\mathrm{e}^{-i\frac{\pi}{2}\kappa} \quad , \tag{9.6.1}$$

where θ_1 is the incidence angle at the reflector and θ_2 is the reflection angle. For PP reflections, Snell's law requires that $\theta_1 = \theta_2$, yielding again Equation (9.2.28).

The resulting weight function for PS converted waves reads

$$W(\boldsymbol{\xi}^*, M) = \frac{1}{V_s}\sqrt{\cos\vartheta_s\cos\vartheta_g}\sqrt{\frac{\cos\theta_1}{\cos\theta_2}}\,\frac{|\det(\underline{\bar{\mathsf{N}}}_1^{\top}\underline{\boldsymbol{\Sigma}} + \underline{\bar{\mathsf{N}}}_2^{\top}\underline{\boldsymbol{\Gamma}})|}{\sqrt{|\det\underline{\bar{\mathsf{N}}}_1\,\det\underline{\bar{\mathsf{N}}}_2^{\top}|}}\,e^{-i\,\frac{\pi}{2}(\kappa_1+\kappa_2)} \quad . \tag{9.6.2}$$

Apart from the additional factor that acknowledges the discontinuity of spreading Equation (9.6.2) looks formally equal to the PP weight function, Equation (9.2.32). Note, however, that for PS converted waves, the matrices must be determined from the appropriate traveltime tables. The diffraction traveltime curve consists of the down-going P wave and the up-going S wave. Therefore, two sets of input traveltime tables are required for the construction of the diffraction time surface and the weight functions. Matrix elements carrying the index 1 are computed from the P wave traveltimes and those with index 2 from S wave traveltime tables.

I present a 2-D example: ray synthetic seismograms (Figure 9.22) were obtained using the SEIS88 package (Červený and Pšenčík, 1984) for a two-layers model with a horizontal interface in a common shot configuration. The P-velocity is V_{P_1}=5km/s in the upper layer and V_{P_2}=6km/s in the lower layer that lies at a depth of 2km below the source. The S-velocities are $V_{S_i} = V_{P_i}/\sqrt{3}$ and the density is given by $\rho = 1.7 + 0.2V_P$ (ρ in g/cm^3 and V_P in km/s). 300 receivers with a spacing of 10m were distributed starting 10m away from a line source. Only PS reflections were considered in this example.

The migrated depth section is shown in Figure 9.23. Reflection coefficients were picked from the section and are compared to analytic results. Figure 9.24 shows good accordance between the two curves. The (negative) peak at a distance of 1.8km is a boundary effect caused by the limited extent of the receiver line, which provides sufficient illumination of the reflector only for distances smaller than 1.8km. This also causes the diffraction that shows in the migrated section (cf. Figure 9.23).

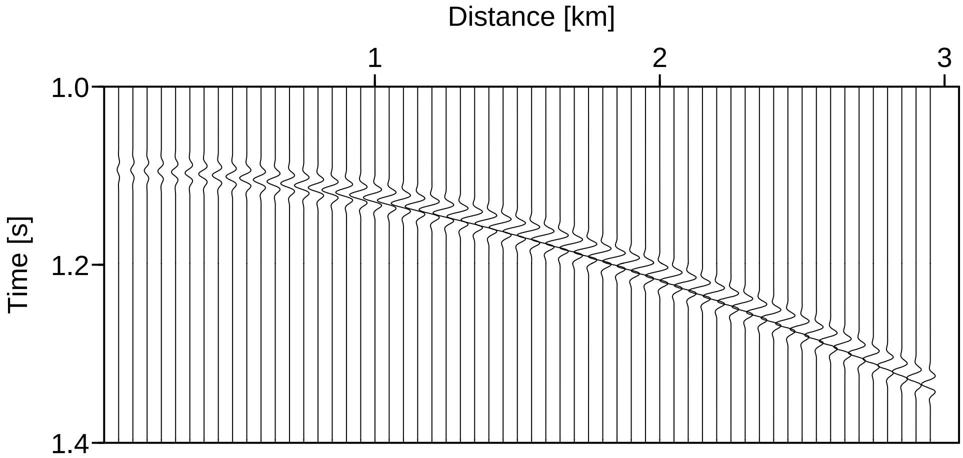

Figure 9.22: Synthetic common shot section: the receiver spacing is 10m but only every fifth trace is shown here.

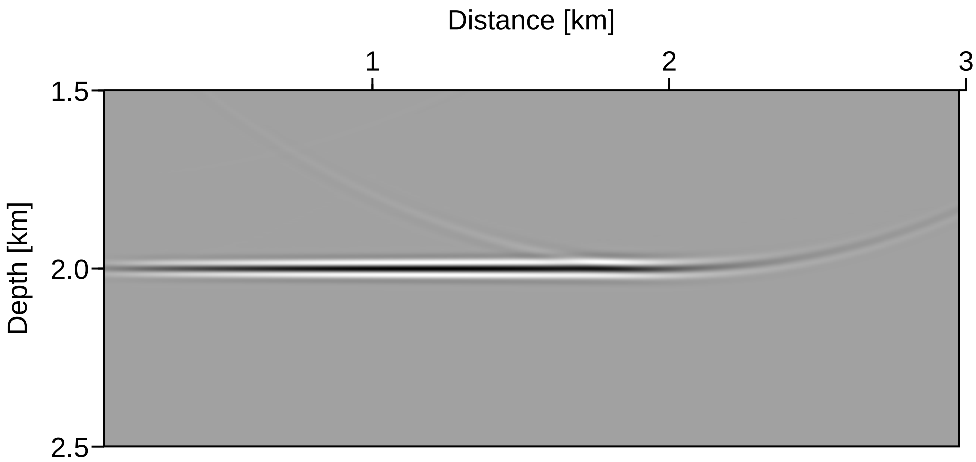

Figure 9.23: Migrated depth section: the reflector was migrated to the correct position. The amplitude matches the reflection coefficient. The diffraction is a boundary effect (see text).

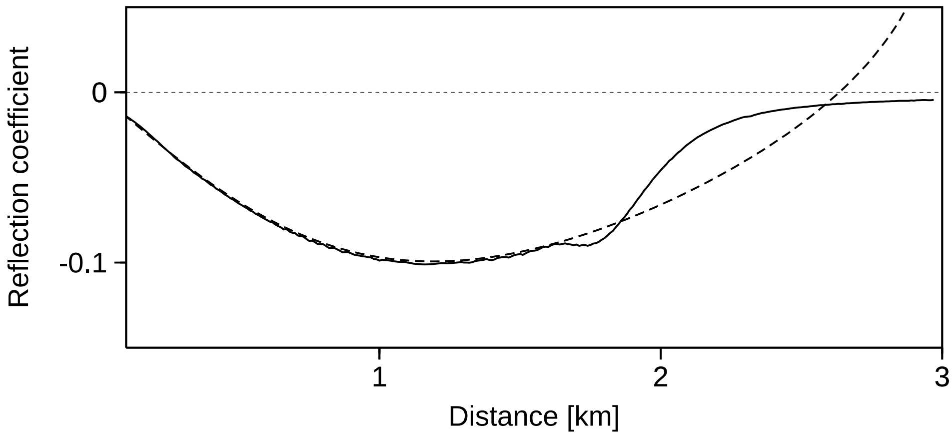

Figure 9.24: Solid line: picked reflection coefficients from the migrated section in Figure 9.23. The peak at 1.8km is a boundary effect (see text). Dashed line: analytic values for the reflection coefficients.

9.7 Limited-aperture migration

True amplitude migration as introduced in in this section is based on a summation stack along diffraction time surfaces. If the summation is carried out over the whole aperture of the experiment, this becomes a very time consuming process. A significant part of this time, however, is spent unnecessarily: traces where the diffraction time and the traveltime of the associated reflected event differ by more than the duration of the source pulse (this criterion defines the minimum migration aperture), do not contribute to the desired migration result, but only lead to an increase in migration noise. Thus, a restriction to the minimum aperture as an optimised migration aperture can significantly enhance the image quality as well as the computational efficiency. Also, once the minimum aperture is determined, boundary effects can be recognised as such.

Although it is a different physical concept, the definition of the optimised (minimum) aperture bears a strong formal relationship to the (first) Fresnel zone, the intersection surface of the Fresnel volume with the reflector surface. In 1992, Červený and Soares propose an algorithm for Fresnel volume ray tracing. They *"believe that Fresnel volume ray tracing will find [...] applications [...] in the inversion of seismic data in the near future"*. Hubral et al. (1993a) describe the Fresnel zone by paraxial approximation in terms of second order derivative matrices of traveltimes. For the zero-offset situation the projection of this paraxial Fresnel zone onto the earth's surface is given by Hubral et al. (1993b). Schleicher et al. (1997) derive an expression for the projected Fresnel zone for arbitrary measurement configurations. They also introduce an expression for the size of the optimum migration aperture, which is also derived using the paraxial approximation. They further show that in this approximation both projected Fresnel zone and optimum migration aperture coincide. Hertweck et al. (2003) illustrate imaging artifacts arising from aperture effects.

Schleicher et al. (1997) compute the optimum migration aperture by means of dynamic ray tracing. The quantities that are required are, however, as the weight functions, related to second-order traveltime derivatives. Therefore, the optimum aperture can be determined from traveltimes. In the first section an approximate expression for the optimum migration aperture will be derived. I will show that the quantities which determine the optimum aperture are the same as the matrix elements used in the weight functions and traveltime interpolation. I will give examples on limited aperture migration in the section thereafter. The section concludes with an estimate of possible savings in computational time.

Optimum migration aperture

Figure 9.25 shows an extract of a seismic section for a single reflector and a diffraction traveltime curve for a point on the reflector. One can easily see that only those traces contribute to the stack (9.2.8) where the diffraction traveltime curve τ_D is within the reflection traveltime τ_R, and τ_R plus the duration of the signal, τ_L. As in Chapter 9 which introduces amplitude-preserving migration it is assumed that the seismic experiment is designed to provide sufficient illumination of the target area. Schleicher et al. (1997) use this criterion to define the minimum aperture, which is also the optimum aperture:

$$|\tau_F| = |\tau_D - \tau_R| \leq \tau_L \quad , \tag{9.7.1}$$

where τ_F is the difference between diffraction and reflection traveltime.Please note that the terms minimum and optimum aperture as introduced by Schleicher et al. (1997) refer to the reconstruction of the amplitude. Sun (1999) uses the same terms but with respect to elimination of a specific type of migration noise. Therefore the optimum apertures of Schleicher et al. (1997) and Sun (1999) do not coincide. I use the term "optimum" aperture in the sense of Schleicher et al. (1997).

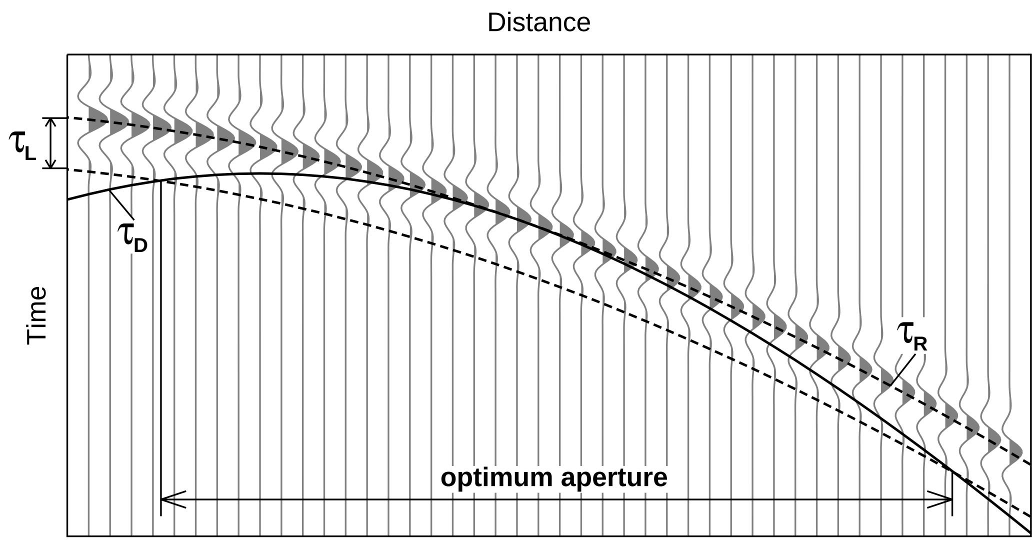

Figure 9.25: Schematic seismic section for a single reflector and traveltime curve for a diffraction point on the reflector. Dashed lines: reflection traveltime τ_R (coinciding with the events) and τ_R+τ_L, where τ_L is the duration of the source pulse. Solid line: diffraction traveltime τ_D. Traces outside the optimum aperture, which is given by the intersection points between the diffraction curve and the "end" of the signal, do not contribute to the diffraction stack.

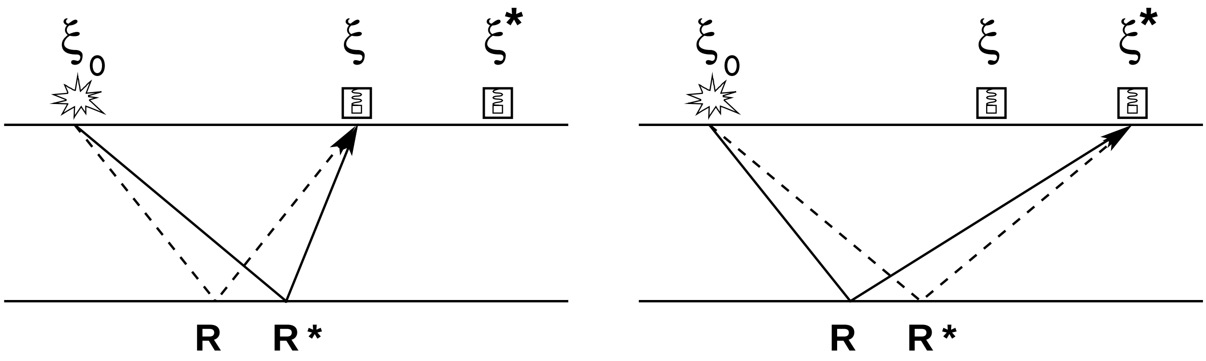

Figure 9.26: Minimum migration aperture (left) and Fresnel zone (right): the criterion for the minimum aperture (in the ξ-surface) is that the traveltimes $\tau(\overline{\xi_0 R^* \xi})$ and $\tau(\overline{\xi_0 R \xi})$ do not differ by more than the signal length τ_L. The Fresnel zone on the reflector is defined such that the difference between the traveltimes $\tau(\overline{\xi_0 R^* \xi^*})$ and $\tau(\overline{\xi_0 R \xi^*})$ is smaller than half a period $T/2$. The stationary ray is from ξ_0 to ξ^* passing R^* in both cases. Dashed lines indicate reflected rays and solid lines stand for diffracted rays.

Equation (9.7.1) bears a strong similarity to the definition of the (first) Fresnel zone. The difference between the two concepts is, that the Fresnel zone is defined on the reflector, whereas the minimum aperture criterion is applied in the registration surface. Figure 9.26 demonstrates this difference.

To find an expression for the optimum aperture as it is given by Equation (9.7.1), τ_F is expanded into a second-order Taylor series with respect to the 2-D source-receiver location coordinates $\boldsymbol{\xi} = (\xi_1, \xi_2)$. The expansion is centred at the stationary point $\boldsymbol{\xi}^*$, where $\tau_D = \tau_R$ and $\vec{\nabla}\tau_F = 0$:

$$\tau_F = \frac{1}{2}\,(\boldsymbol{\xi} - \boldsymbol{\xi}^*)^\top\, \underline{\mathrm{H}}_\mathrm{F}\, (\boldsymbol{\xi} - \boldsymbol{\xi}^*) \quad , \tag{9.7.2}$$

in which $\underline{\mathrm{H}}_\mathrm{F}$ is the Hessian matrix of the traveltime difference τ_F. It has already been introduced in Section 9.2, where it was required for the weight functions. With this equation and Equation (9.7.1), the optimum aperture in paraxial approximation is given by (Schleicher et al., 1997):

$$\frac{1}{2}\,|(\boldsymbol{\xi} - \boldsymbol{\xi}^*)^\top \underline{\mathrm{H}}_\mathrm{F} (\boldsymbol{\xi} - \boldsymbol{\xi}^*)| = \tau_L \quad . \tag{9.7.3}$$

For the evaluation of Equation (9.7.3), however, the centre of the aperture that corresponds to the stationary ray must be known. This can be determined from the slowness vectors. As I assume the velocity model to be known, information on the inclination angle of the reflector is available. The incidence angle θ_1 on the reflector is then given by

$$\cos\theta_1 = \sqrt{1 - V_1^2\; \bar{\boldsymbol{q}}_1 \cdot \bar{\boldsymbol{q}}_1} \quad , \tag{9.7.4}$$

where $\bar{\boldsymbol{q}}_1$ is the slowness vector of the ray from the source to the reflector. Similarly, $\bar{\boldsymbol{q}}_2$ is the slowness vector of a ray from the receiver to the reflector. The reflection angle θ_2 is expressed by an equivalent of (9.7.4) but using $\bar{\boldsymbol{q}}_2$ instead. Since the stationary ray obeys Snell's law, the centre of the aperture for PP data is the geophone position where the difference between θ_1 and θ_2 is minimal.

As for the weight functions the matrices $\underline{\bar{\mathrm{N}}}_I$ and $\underline{\bar{\mathrm{G}}}_I$ which are needed for the computation of $\underline{\mathrm{H}}_\mathrm{F}$ can be determined from $\underline{\hat{\mathrm{N}}}_I$ and $\underline{\hat{\mathrm{G}}}_I$ by rotating the latter onto the tangent planes of the recording surface and the reflector candidate. Moreover, the curvature of the recording surface and the reflector has to be considered. This procedure is described in Section 2.8. To do so, I assume that a priori information on the velocity model is available. For simple models the inclination of a reflector can be computed from the gradient of the velocity model. More generally, for example if the velocity model is smooth, it can be extracted from a previous migration. The determination of the reflector curvature follows similar lines. For image points that are not located on a reflector, this information will not be available. For these cases, however, the inclination and curvature are irrelevant, because the migration output will be negligible, regardless of inclination and curvature. For simplicity, I assume both to be zero for those points. If the reflector's inclination but not its curvature can be determined for a point which is located on the reflector, I expect that the approximation of the reflector by a locally plane surface will yield satisfactory results in many cases. This assumption appears to be acceptable since applicability of the ray method requires that the radius of reflector curvature is large compared to the wavelength. Moreover, the recovered reflection coefficient is a plane wave reflection coefficient.

Examples

I have applied the algorithm to simple generic models. These have the advantage of known analytic solutions for the involved quantities. Therefore they are very useful for the validation of the method. The example given here is a two-layer model with an inclined interface. The inclination angle is 63° and the model has a velocity of 5km/s above and 6km/s below the reflector. A ray-synthetic common-shot section was computed with the SEIS88 package (Červený and Pšenčík, 1984) using a Gabor wavelet with a signal length of 25ms and 10m distance between the receivers. The migration was carried out first using the original noise-free data, and then for the same dataset with white (random) noise added, having a signal-to-noise ratio of 2. The noisy input section is shown in Figure 9.27. In both cases the optimum aperture was applied as well as the complete aperture for comparison. In limiting the aperture one must, however, take

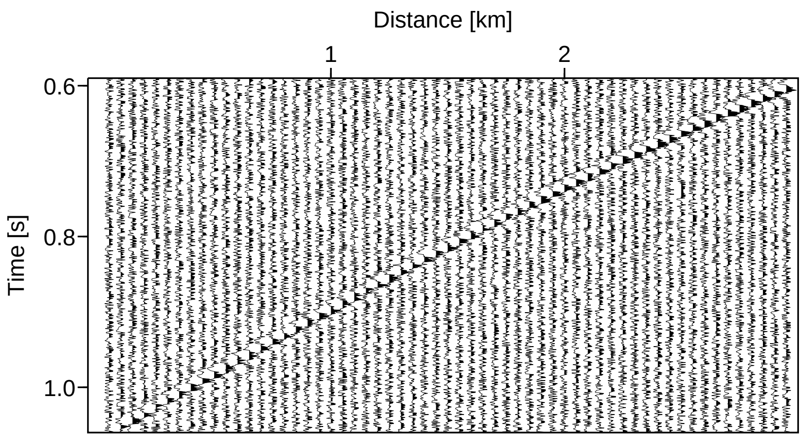

Figure 9.27: Synthetic common-shot section for a 63° inclined reflector: The receiver spacing is 10m but only every fifth trace is shown here. The signal-to-noise ratio is 2.

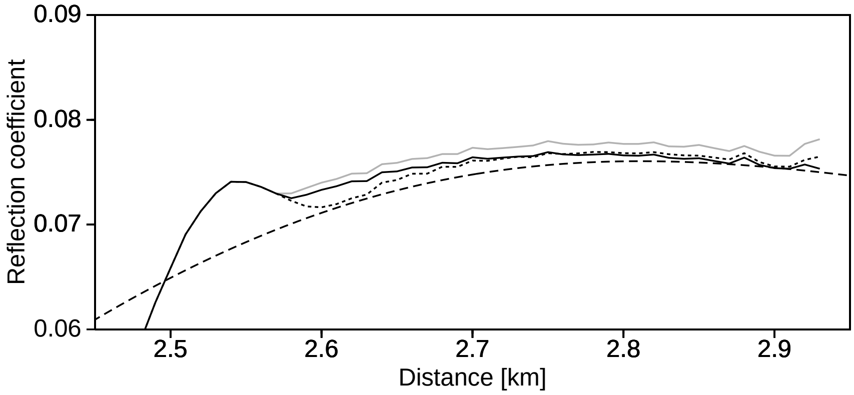

Figure 9.28: Recovered reflection coefficients from noise-free data for a 63° inclined reflector: Dashed line: analytic reflection coefficients. Dotted line: recovered coefficients if the whole aperture is used. Solid lines: recovered coefficients if the optimum aperture is used. The black line results from applying a taper to the aperture, the Grey line follows without tapering. The reflection coefficients from the optimised aperture migration are overestimated (see text). The peak near 2.5km is a boundary effect caused by insufficient illumination of the reflector due to the limited extent of the receiver line.

into account that boxcar filtering produces undesirable effects like ringing or overshooting in the migrated image. Therefore a taper was applied at the endpoints of the aperture. Please note that the taper was not applied in the sense of Sun (1999), but to serve a basic rule of signal processing.

Figure 9.28 shows the recovered reflection coefficients from the noise-free section and analytic values. Compared to the whole aperture result, application of the optimum aperture leads to slightly overestimated reflection coefficients. This effect is more pronounced if the taper is omitted. For example, at 2.7 km distance the error of the recovered reflection coefficient is 1.3% if the whole aperture is used, it is 1.7% for the tapered optimum aperture and 3.0% for the optimum aperture without taper. The reason for the overestimation of the reflection coefficients is that Equation (9.7.3) represents an approximation for the optimum aperture. Figure 9.29 demonstrates the difference between the exact optimum aperture (which can be computed for this type of model, but closed form solutions do not exist for arbitrary models) and the optimum aperture in paraxial approximation resulting from Equation (9.7.3). Please observe in Figure 9.29 that traces within the required aperture, but not within the paraxial aperture would give negative contributions to the stack. This is the reason why the reflection coefficients are overestimated. By applying the taper, additional traces outside of the paraxial aperture are allowed to contribute. This leads to a partial compensation of the overestimation caused by the errors of the paraxial aperture.

The AVO behaviour, however, by which I signify the gradient or the general shape of the AVO is of more interest for interpretation than the absolute value of the reflection coefficients. It is less affected by the effect described above than the absolute value: Figure 9.28 shows that the AVO trend is preserved for all three cases, whether the whole aperture is used or the optimum aperture, with or without taper. For reflectors with moderate or no inclination the effect takes place on a

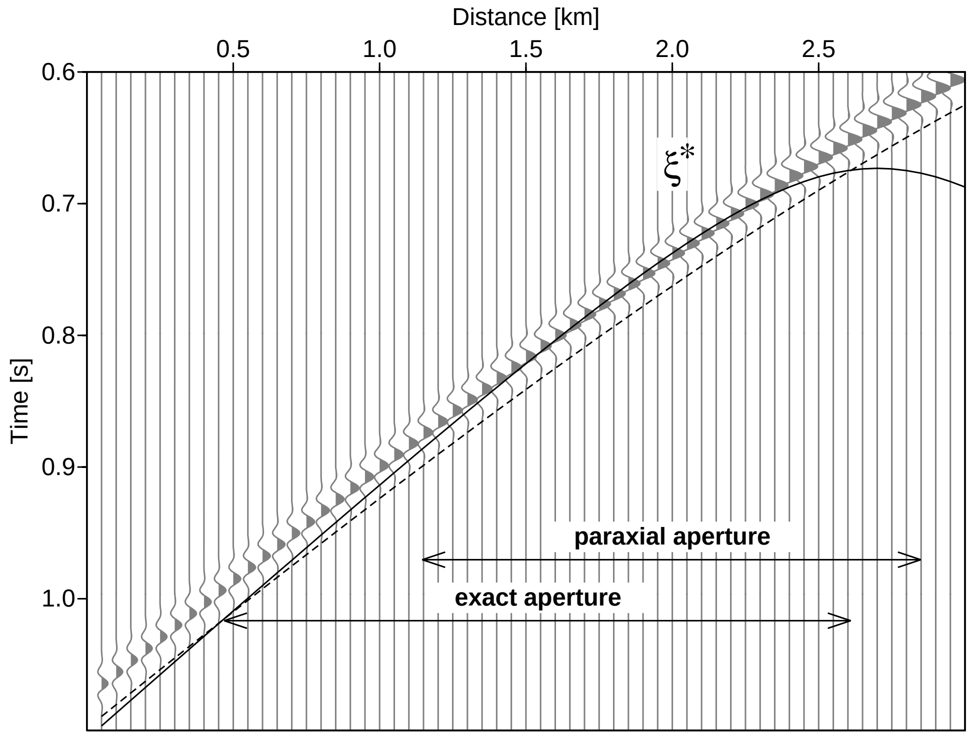

Figure 9.29: Exact and paraxial optimum migration aperture for a point on the 63° inclined reflector. Dashed line: reflection traveltime plus signal length $\tau_R + \tau_L$. Solid line: diffraction traveltime curve τ_D. The centre of the paraxial aperture that corresponds to the stationary ray is located at ξ^*.

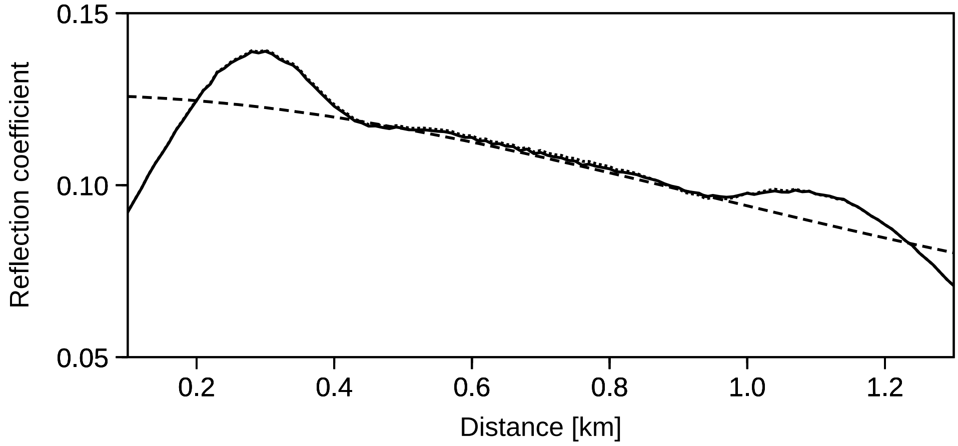

Figure 9.30: Recovered reflection coefficients from noise-free data for a horizontal reflector. The difference between the two results is very small. Dashed line: analytic reflection coefficients. Solid line: recovered coefficients if the optimum aperture is used. Dotted line: recovered coefficients if the whole aperture is used. The two peaks at 0.3 and 1.1km are again boundary effects.

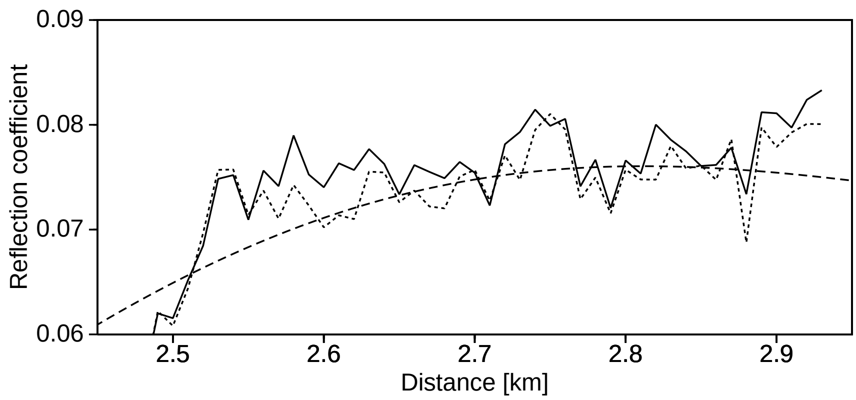

Figure 9.31: Results from noisy data for a 63° inclined reflector: Dashed line: analytic reflection coefficients. Solid line: recovered reflection coefficients if the optimum aperture is used. Dotted line: recovered coefficients if the whole aperture is used.

smaller scale. Figure 9.30 shows that the results for a horizontal reflector (at 2.5km depth and with the same velocities and wavelet as above) look virtually the same for both apertures.

The reflection coefficients that result from the noisy input data on the 63° reflector are shown in Figure 9.31 together with the analytic values. Please keep in mind that in this example the quality of the input section is very poor. For a better signal-to-noise ratio the scatter in the recovered reflection coefficients is significantly smaller. The migrated depth sections of the noisy data using the optimum aperture and the whole aperture are shown in Figure 9.32. In both cases the reflector has been migrated to the correct position but the image quality is improved if the optimum

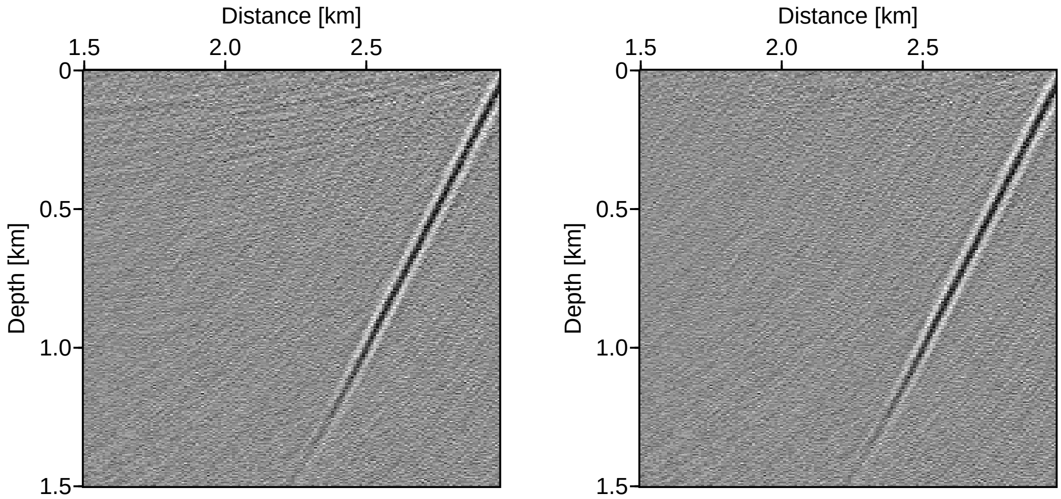

Figure 9.32: Migrated depth sections of noisy data for the 63° inclined reflector. Left: the whole aperture was used; right: only traces within the optimum aperture were used.

aperture is used. This effect may be more apparent if more than one arrival is present in the input section. If, e.g., another reflection event in the data would cut through the one under consideration, it would add unwanted contributions to the stack, thus increasing the noise. By limiting the aperture, this higher noise can at least be averted for unwanted events that lie outside of the aperture.

I have shown that application of the method to simple types of models yields good results in terms of image quality and recovered amplitude. The goal was to provide these good results and at the same time reduce the requirements in computational time and storage. The storage problem can be overcome by using coarse gridded traveltimes as only input data, as shown in Chapter 2 and 9. The determination of the weight function from traveltimes as well as the interpolation of the diffraction time surfaces lead to savings in computational time, see also Chapter 2 and 9. The following section discusses potential savings in computational time that result alone from the limited migration aperture.

Potential savings in computational time

The method of traveltime-based true-amplitude migration itself is very efficient in terms of computational time and storage, as already discussed in Chapter 2 and 9. The savings in computational time that result from the reduction of the migration aperture alone are difficult to estimate because of the various factors involved in the size of the required aperture. To give an idea about possible savings, I have compared the optimum aperture to the complete aperture for the case of a single, horizontal reflector. The results are shown for 2-D and 3-D in Figure 9.33. Three parameters were varied to demonstrate their influence on the aperture: the velocity in the upper part of the model, the reflector depth, and the signal length. For small cable lengths, the savings are moderate because the required apertures are not much smaller than the total cable length. If the cable length is increased, the ratio of required aperture to complete aperture decreases. The effect of the velocity and signal

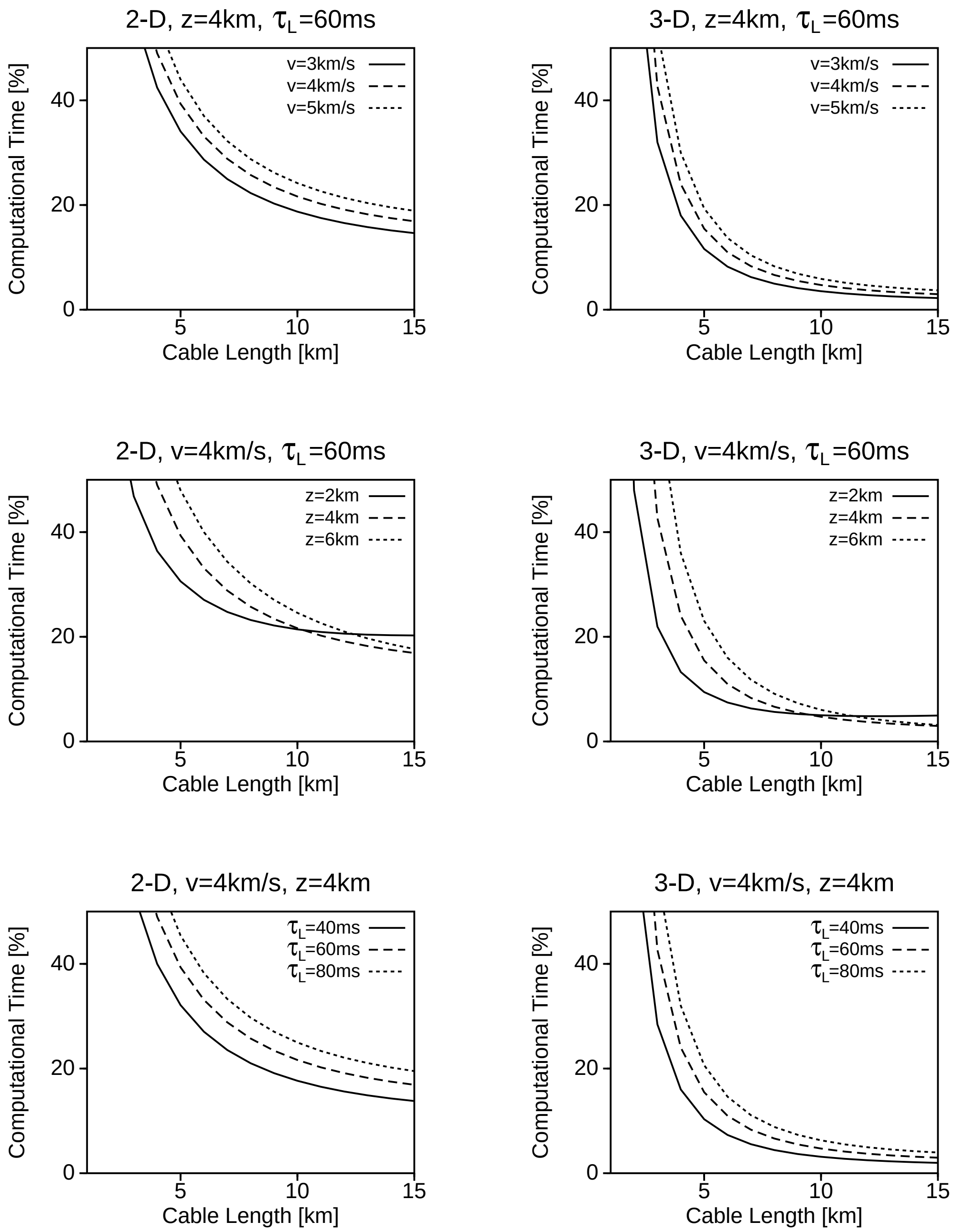

Figure 9.33: Potential savings in percent of computational time by using the optimum migration aperture (100% corresponds to the complete aperture). The velocity model used here is a horizontal reflector. The parameters that were varied in these plots are the velocity in the upper layer (top), the reflector depth (middle) and the length of the source pulse (bottom), on the left for 2-D and right for 3-D.

length are similar since both are closely related to the wavelength. For varying reflector depth a more pronounced change occurs in the behaviour of the required aperture. The shallower the reflector is, the higher is the incidence angle of the wave with the normal to the registration surface, leading to an increase in apparent wavelength. This requires a larger aperture.

9.8 Anisotropy

So far, amplitude-preserving migration has almost exclusively been applied to PP data, where an isotropic medium was assumed. Although anisotropy is recognised as important it is only considered with respect to kinematic aspects but not to amplitudes. Even the kinematics are in most cases reduced to simple types of media, e.g., media with transverse isotropy. If we are dealing with an anisotropic earth, however, the application of isotropic methods leads to problems.

Anisotropy can have several causes, as for example intrinsic anisotropy or layer-induced anisotropy. Other possibilities are oriented fluid-filled crack systems, and, of course, a combination of these causes, leading to an effective anisotropy. In summary, as soon as there exists an organised structure with a preferred orientation, anisotropy shows if the wavelength of the investigation method is larger than the scale of the structure. This problem of different scales has practical relevance if results from measurements on different scales are to be combined, e.g., surface and bore hole seismics. If anisotropy is not considered, these results will not coincide (i.e. leading to mis-ties etc.).

Anisotropic effects are not restricted to kinematics. They have considerable influence on the AVO- or AVA-behaviour of geological interfaces. One example are shales and sands with a similar acoustic impedance. The anisotropy of the shales can lead to a reversal in the polarity of the reflection coefficient that does not occur for isotropy. Another possibility are amplitude changes assigned to the presence of gas if a medium is assumed to be isotropic. In an anisotropic medium, this behaviour can be explained without gas (de Hoop et al., 1999). Therefore, anisotropy must also be acknowledged where amplitudes are considered.

A theoretical representation of Kirchhoff migration in anisotropic media was given by de Hoop and Bleistein (1997). This very complex theory is not very well suited for an implementation. Although Gerea et al. (2000) give an anisotropic example for amplitude-preserving migration of multi-component data, they use a simplified weight function and consider only a horizontally layered VTI medium. This approach is very restricted and will not be applicable to media with more complex anisotropy.

Since the anisotropy is often small, it may at a first look be tempting to use isotropic methods. The simple example of a horizontal reflector in a medium with elliptical symmetry and $\epsilon = \delta = 0.1$ shown in Figure 9.34 demonstrates that this is not a solution.

If the traveltime trajectories are computed for isotropic velocities, the depth image is distorted, as can be seen in Figure 9.35: use of the stacking (NMO) velocity (Figure 9.35a) leads to a horizontal reflector at the wrong depth and use of vertical velocities, e.g., from borehole measurements, in Figure 9.35b leads to the right depth for the zero-offset, but the shape of the reflector is no longer plane and horizontal. Only if the true anisotropic velocities are available, can the reflector depth and structure be correctly imaged (Figure 9.35c).

The same happens if we use isotropic weight functions, as demonstrated by Figure 9.36. Although the overall behaviour of the reflectivity obtained from the application of isotropic weights is similar to the real reflectivity, changes in AVO can lead to mis-interpretation. If we wish to constrain shear velocities with the help of PP reflectivity, anisotropy must be taken into account for the weight functions.

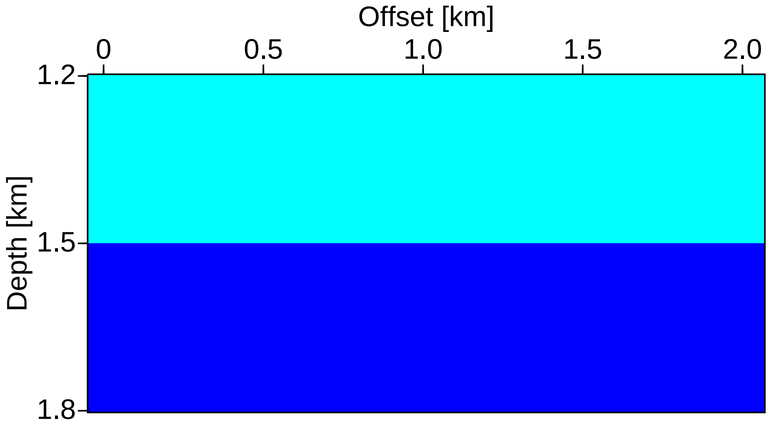

Figure 9.34: Anisotropic velocity model with elliptical symmetry and $\epsilon = \delta$=0.1. The reflector is located at a depth of 1.5 km.

In this section, I extend the traveltime-based approach to true-amplitude migration in isotropic media suggested in this Chapter to anisotropy. Since the derivation is formally identical to that for the isotropic case – in fact, the only difference is that now the anisotropic formulation for the geometrical spreading (see Section 8.4) must be used – I give only a shortened form of the derivation here before demonstrating the anisotropic true-amplitude migration with examples for PP and PS reflections.

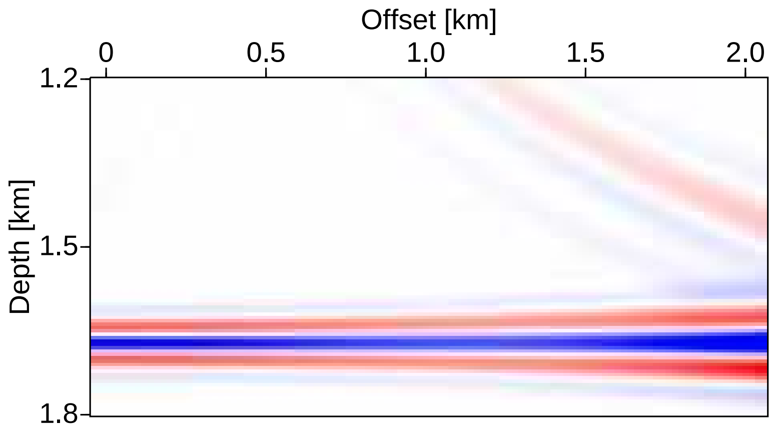

(a)

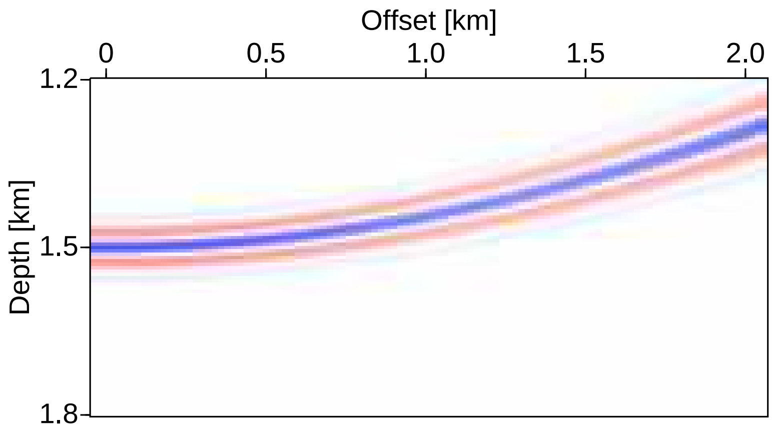

(b)

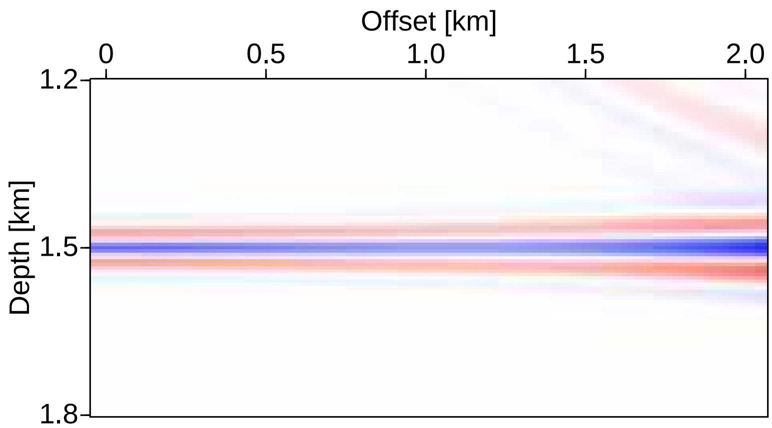

(c)

Figure 9.35: Migration results using (a) the isotropic stacking velocity, (b) the vertical velocity, (c) the anisotropic model. If isotropic models are used, the reflector cannot be correctly reconstructed: in (a) the depth is wrong, and in (b) the shape is wrong.

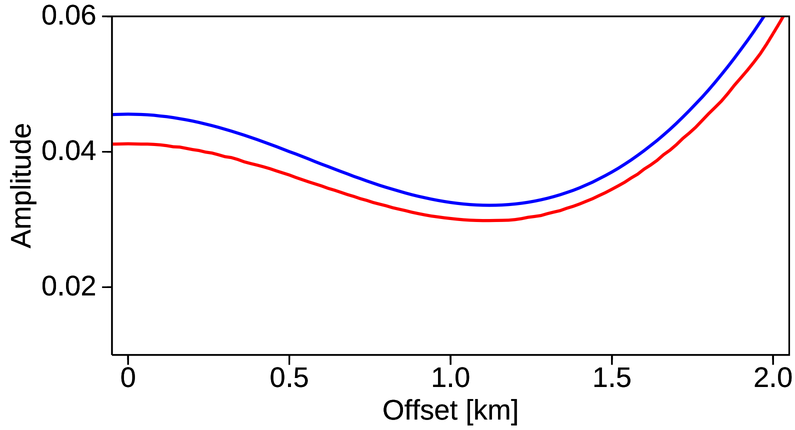

Figure 9.36: Reconstructed PP reflectivity using an isotropic weight (red) in comparison to the real reflectivity (blue).

Method

The displacement $\boldsymbol{u}(S,G,t)$ which results from an elastic wave generated by a source at S and registered by a receiver at R in an arbitrarily anisotropic heterogeneous medium can be expressed by

$$\boldsymbol{u}(S,G,t) = \sqrt{\frac{\rho(S)\,V(S)}{\rho(G)\,V(G)}}\,\frac{\mathcal{R}\,\mathcal{G}(S,\gamma_1,\gamma_2)}{\mathcal{L}(G,S)}\,\mathrm{e}^{i\frac{\pi}{2}\kappa}\,F\big(t-\tau_R(G,S)\big)\,\boldsymbol{g}(G) \tag{9.8.1}$$

(Červený, 2001). In (9.8.1) $\rho(S)$, $\rho(G)$, $V(S)$, and $V(G)$ are the densities and phase velocities at the source and receiver. The quantity $\mathcal{R}$ contains the reflection coefficient and transmission losses. The source signal has the temporal shape given by $F(t)$, and $\tau_R(G,S)$ is the traveltime of the reflected event. The radiation function $\mathcal{G}(S,\gamma_1,\gamma_2)$ at the source depends on the ray parameters γ_1 and γ_2 . The vector $\boldsymbol{g}(G)$ denotes the polarisation at the receiver. The relative geometrical spreading factor is expressed by $\mathcal{L}(G,S)$, and the factor $\mathrm{e}^{i\frac{\pi}{2}\kappa}$ describes phase changes from caustics.

As in the isotropic case we assume that the migration output $U(M)$ for the subsurface point M, the migration output $U(M)$, is proportional to $\mathcal{R}$. It can be obtained from the following integral:

$$U(M) = \frac{-1}{2\,\pi}\iint \mathrm{d}\xi_1\,\mathrm{d}\xi_2\,W(\boldsymbol{\xi},M)\,\left.\frac{\partial u(\boldsymbol{\xi},t)}{\partial t}\right|_{\tau_D(\boldsymbol{\xi},M)}\quad, \tag{9.8.2}$$

where the vector $\boldsymbol{\xi}$ describes the source and receiver positions in the chosen acquisition geometry, e.g., CMP, single shot, or common-offset section. The integral (9.8.2) corresponds to a diffraction stack with the weight function $W(\boldsymbol{\xi},M)$. After a transformation to the frequency domain, (9.8.2) can be solved in the high frequency limit by applying the method of stationary phase (e.g., Bleistein, 1984). This leads to the weight function

$$W(\boldsymbol{\xi},M) = \sqrt{\frac{\rho(G)}{\rho(S)}}\,\frac{\sqrt{v_z(G)\,v_z(S)}}{V(S)}\,\frac{1}{\mathcal{G}(S,\gamma_1,\gamma_2)}\,\frac{|\det\left(\underline{\tilde{\mathsf{N}}}_1^{\top}\underline{\Sigma}+\underline{\tilde{\mathsf{N}}}_2^{\top}\underline{\Gamma}\right)|}{\sqrt{|\det\underline{\tilde{\mathsf{N}}}_1|\,|\det\underline{\tilde{\mathsf{N}}}_2|}}\,\mathrm{e}^{-i\frac{\pi}{2}(\kappa_1+\kappa_2)}\quad. \tag{9.8.3}$$

The relation between $\boldsymbol{\xi}$ and S and G is described by the configuration matrices $\underline{\Sigma}$ and $\underline{\Gamma}$. Examples can be found in Schleicher et al. (1993a), and in Section 9.2. The radiation function at the source can be calculated after Gajewski (1993), or Pšenčík and Teles (1996). The vertical components v_z of the ray (group) velocities at the source and receiver are computed from the slowness vectors obtained from coarsely-gridded traveltimes as shown in Section 8.4 and the Appendices E and D. The matrices $\underline{\tilde{\mathrm{N}}}_1$ and $\underline{\tilde{\mathrm{N}}}_2$ are second-order mixed derivatives of the traveltimes in the reflector surface. These are obtained by a rotation of the second-order traveltime derivative matrices in global Cartesian coordinates into the reflector surface, see Section 9.4.

Special case: 2.5D

To carry out the stack in (9.8.2), data from a 3D coverage is required. Sometimes, data is only available for a single acquisition line. In the special case, where the medium is assumed to be invariant in the off-line (i.e. $\xi_2{=}y$) direction, a so-called 2.5D symmetry, the migration can be carried out by applying a modified stack, namely

$$U(M) = \sqrt{\frac{1}{2\,\pi}} \int \mathrm{d}\xi_1\, W_{\mathsf{2.5D}}(\xi_1, M)\, f\left[u\big(\xi_1, t+\tau_D(\xi_1,M)\big)\right] \tag{9.8.4}$$

(e.g., Martins et al., 1997). Here, $f[u]$ is a filter operation corresponding to a multiplication of u with $\sqrt{i\omega}$ in the frequency domain (applied instead of the time derivation of u in the 3D case). The 2.5D weight function is simpler than the 3D weight, as $\tilde{N}_{I_{12}}{=}\tilde{N}_{I_{21}}{=}0$. With $\sigma_I{=}\tilde{N}^{-1}_{I_{22}}$, the weight function becomes

$$W_{\mathsf{2.5D}}(\xi_1, M) = \sqrt{\frac{\rho(G)}{\rho(S)}}\, \frac{\sqrt{v_z(G)\; v_z(S)}}{V(S)}\, \frac{1}{\mathcal{G}(S,\gamma_1,\gamma_2)}\, \frac{|\tilde{N}_1\Sigma + \tilde{N}_2\Gamma|}{\sqrt{|\tilde{N}_1\,\tilde{N}_2|}}\, \sqrt{\sigma_1+\sigma_2}\; \mathsf{e}^{-i\frac{\pi}{2}(\kappa_1+\kappa_2)} \quad , \tag{9.8.5}$$

where $\tilde{N}_I$ is used as abbreviation for $\tilde{N}_{I_{11}}$.

As we do not a priori know the orientation of the reflector surface, it is assumed for each source-receiver combination that it corresponds to the stationary ray. Then the orientation can be obtained from the slowness vectors of the two ray segments at the image point, denoted by $\boldsymbol{q}_1$ and $\boldsymbol{q}_2$. Their horizontal components are determined from coarsely-gridded traveltimes (see Chapter 2), whereas the vertical components are computed by the method suggested in Appendix E. We find, that

$$\tilde{N}_I = N_{I_{xx}}\cos\beta - N_{I_{xz}}\sin\beta \quad , \tag{9.8.6}$$

with the mixed second-order traveltime derivatives in the global Cartesian coordinate system,

$$\begin{aligned} N_{1_{xx}} &= -\frac{\partial^2 T(S,M)}{\partial x_s\,\partial x_m} & \qquad N_{1_{xz}} &= -\frac{\partial^2 T(S,M)}{\partial x_s\,\partial z_m} \\ N_{2_{xx}} &= -\frac{\partial^2 T(G,M)}{\partial x_g\,\partial x_m} & \qquad N_{2_{xz}} &= -\frac{\partial^2 T(G,M)}{\partial x_g\,\partial z_m} \end{aligned} \tag{9.8.7}$$

(the indices s, g, and m denote the source, receiver, and image point, respectively). The angle β is given by

$$\tan\beta = -\frac{\cos\vartheta_2 - \cos\vartheta_1}{\sin\vartheta_2 - \sin\vartheta_1} = -\frac{V_2\;q_{z2} - V_1\,q_{z1}}{V_2\,q_{x2} - V_1\,q_{x1}} \quad , \tag{9.8.8}$$

where V_I are the phase velocities of the ray segments at the image point, and ϑ_I are the corresponding phase angles.

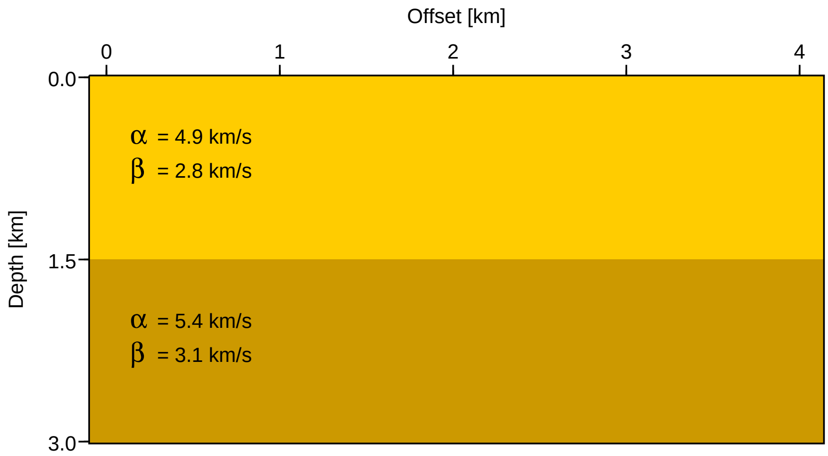

Figure 9.37: The anisotropic velocity model. Thomsen's parameters were chosen as $\epsilon = \delta = 0.1$ and $\gamma = 0.1$.

Examples

We have applied the method to the simple anisotropic velocity model displayed in Figure 9.37. In both layers we chose $\epsilon = \delta = 0.1$ and $\gamma = 0.1$ corresponding to elliptical symmetry because this symmetry enables us to compute the analytical reflectivity for comparison with the migration results. Ray synthetic seismograms were generated for an explosion source. The required traveltime tables for the qP- and qSV-waves were computed analytically. These were the only input data needed for the computation of the true-amplitude weight functions.

The depth-migrated PP section is shown in Figure 9.38a; the PS section in Figure 9.38b. As we have used the correct elastic parameters for the generation of the traveltimes, the migration result shows the reflector imaged in the correct location.

Since another aim of the true-amplitude migration is to recover the reflectivity, we have picked the amplitudes from the image gathers. The results are shown together with the analytic solutions in Figure 9.39a for the PP result, and in Figure 9.39b for the PS result. As we can see, both reconstructed AVO curves coincide with the analytic values. The deviations at higher offsets are caused by the limited extent of the receiver line. Due to the asymmetry of the ray paths, the offset range is different for the PP and the PS case.

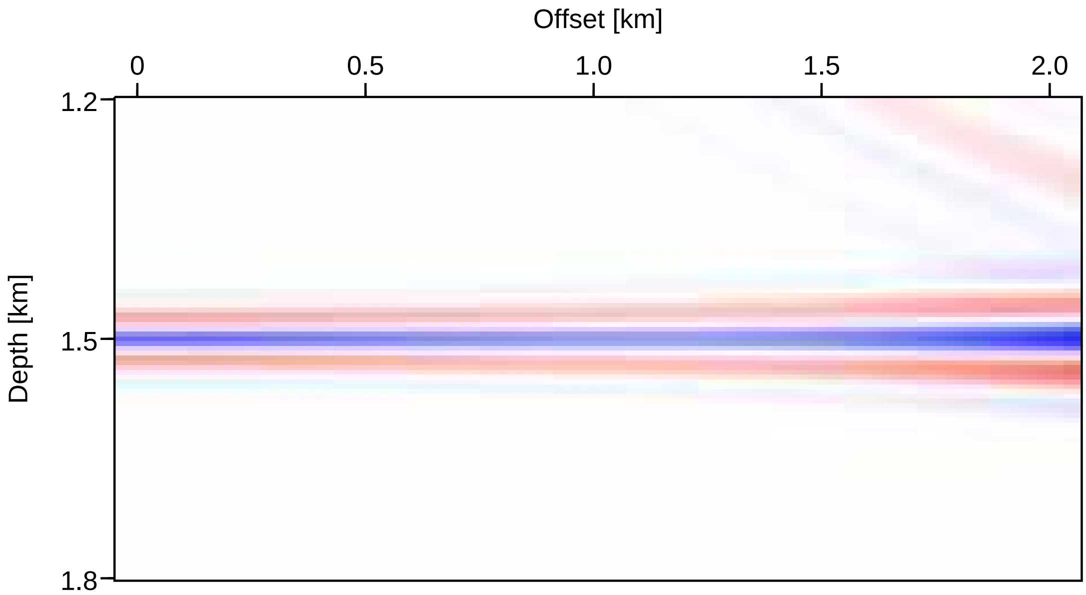

(a)

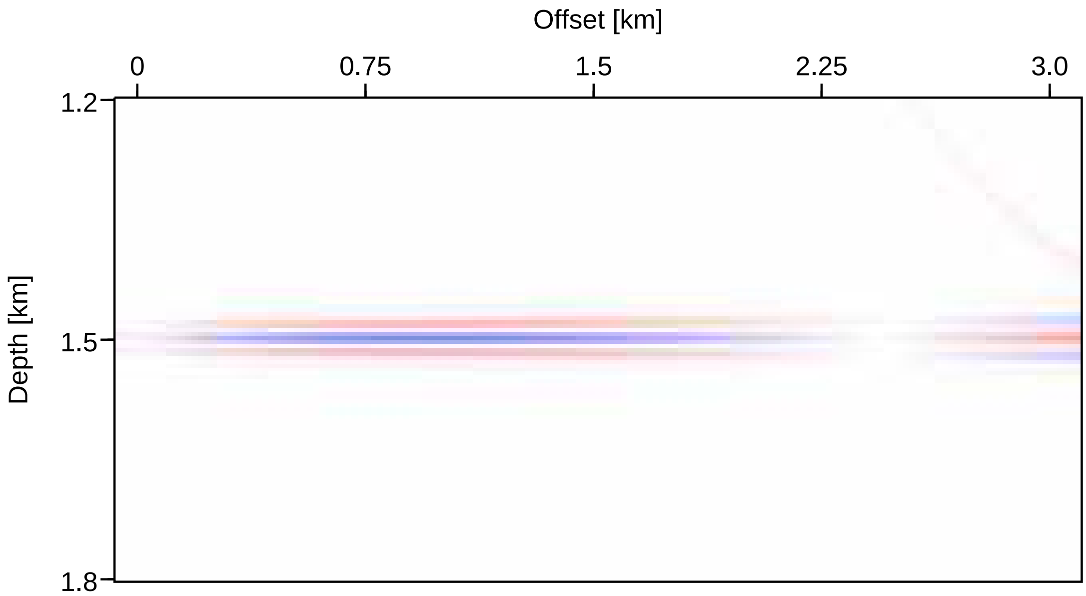

(b)

Figure 9.38: (a) The depth-migrated PP section, and (b) the depth-migrated PS section

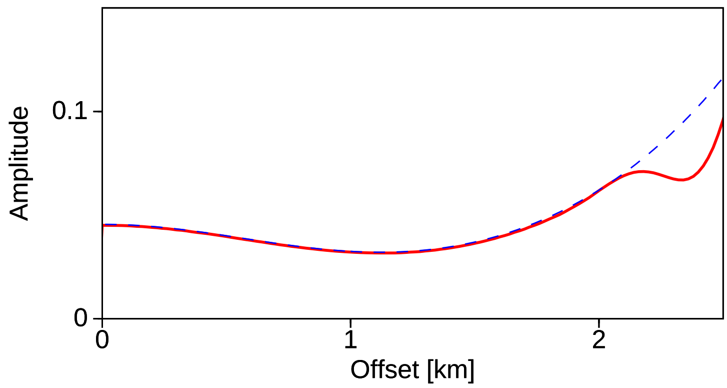

(a)

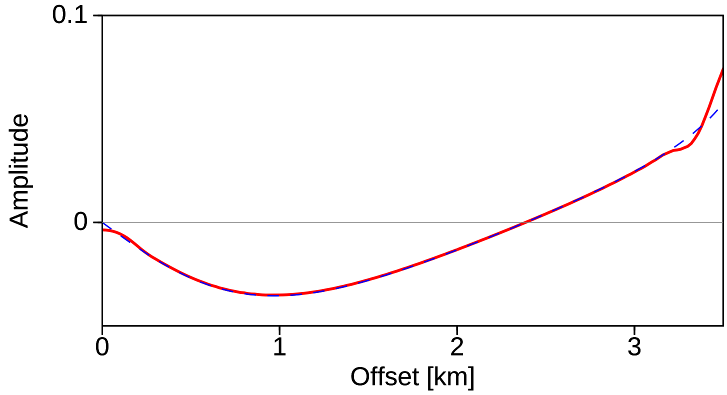

(b)

Figure 9.39: AVO for (a) PP reflections and (b) PS reflections: the reconstructed reflectivity (solid red line) coincides with the analytic solution (blue dashed line).

Conclusions

By applying the traveltime-based strategy for true-amplitude migration in anisotropic media we can obtain a dynamically correct depth migrated image without the need for dynamic ray tracing. Although the example shown was simple, we conclude that the method is equally suited for complex situations. This conclusion is supported by the application of our method to complex isotropic examples (see Section 9.5), as well as the accuracy of the determination of geometrical spreading from traveltimes for 3D anisotropic models (see Section 8.4), using the same coefficients as the weight function introduced in this section. The extension to three dimensions is straightforward.

Chapter 10

Outlook

In this second part of my thesis, I have introduced the technique of traveltime-based true-amplitude migration in isotropic and anisotropic media. Application to a multitude of examples illustrates that the method is indeed a powerful tool in seismic data processing. There remain, however, aspects which are worth a thorough investigation.

One key issue is the sensitivity of migration techniques with respect to errors in the available velocity model, or, speaking more widely in order to include anisotropy, the quality of the elastic parameters. Although we would like to obtain the 'correct' model as a final result of the processing, this is not generally possible. At best, we obtain a model that is consistent with the data, but it need not necessarily represent the real subsurface situation. Particularly in the anisotropic case, it is not always possible to find all parameters: e.g., the vertical velocities cannot be determined from surface observations alone.

I have shown in Section 9.8 how the use of isotropic velocities and isotropic weight functions leads to errors in the subsurface structure reconstructed from migration, as well as in the reflectivities. Although this is a very special case of an erroneous velocity model, it clearly demonstrates the dependence of migration on the quality of the velocity information.

It is, therefore, an important task to investigate the influence of the model errors on the output. In this chapter, I suggest how this influence could be quantified in a systematic study. I also consider one special case of velocity errors, namely when smooth models are used: the output from model-building tools are often blocks with constant velocity or gradients. In order to generate traveltimes by ray methods, and to a much lesser degree also by, e.g., finite difference eikonal solvers, however, the model representation must be smooth.

Only recently has a method been proposed how a smoothing process can be designed that maintains the traveltime through the original model to the layer boundary (Vinje et al., 2012). This process, however, results in an anisotropic medium. If conventional smoothing is applied, the traveltimes to the boundary are not conserved. In my examples, I am showing the influence of less sophisticated smoothing of the model.

Another related problem is the illumination – or lack thereof – of the image point under consideration. With growing complexity of the models, uniform illumination of the subsurface point under consideration becomes crucial. This concerns not only structural complexity, but also complexity for example in the sense of anisotropy where illumination is a key issue to recover the directional dependency. A migration implementation allowing for control of illumination would therefore serve to significantly enhance the quality of the resulting image and amplitudes. This can be achieved by traveltime-based migration with angular parametrisation.

In the final section of this chapter, I will show how the image quality following from such an algorithm can be enhanced in comparison to a scheme with equidistant receiver spacing. An implementation of the traveltime-based migration with angular parametrisation to include amplitudes is still pending, however, a kinematic comparison was carried out in a Ph.D. thesis under the author's supervision (Kaschwich, 2006). The example given in this section demonstrates the superiority of the angular parametrisation and strongly suggests to apply it in the amplitude-preserving fashion.

10.1 Complex models and sensitivity to velocity errors

Although I have shown examples of complex models, there are a few issues that we need to keep in mind when dealing with complex media. In this section, I take a closer look at some problems that may arise in the case of strong velocity variations.

The velocity model is needed for the computation of the traveltime tables and thus, indirectly, for the traveltime coefficients, i.e. slownesses and second-order derivative matrices. The velocity model also contains information on the inclination and curvature of reflectors. A typical candidate for a complex velocity model would contain several velocity layers as well as diffractors and synclinal or anticlinal structures, e.g., salt domes and faults, since these are the situations that are of most interest for exploration.

Complex structures in the velocity model express themselves in complex seismic sections that contain later arrivals, and, therefore, triplications. These are of considerable interest, because a lot of energy is contained in their reverse branches. Therefore the reconstruction of amplitudes with a true-amplitude migration makes sense only if later arrivals are accounted for. This has consequences for the choice of the algorithm used for the generation of the traveltime tables.

Finite-difference eikonal solvers (FDES) are not suited because they compute only first arrivals. The alternative to FDES are techniques which are based on the ray method. Currently, two such programs are available to the author. The first is based on the wavefront construction method (WFC, Vinje et al. 1993) and part of the NORSAR program package. The second program employs the wavefront oriented ray tracing technique (WRT) developed by Coman and Gajewski (2001) and extended to anisotropy by Kaschwich (2006).

Figure 10.1 shows (first arrival) traveltimes which were computed for the Picrocol model (Brokešová et al., 1994) with the NORSAR package. The relevant part of the model is also given by Figure 10.1. One can see that there are regions where no traveltimes have been computed. These are shadow zones, which were not covered with rays, therefore no traveltimes are available, and the values are set to zero. It is thus impossible to determine the traveltime coefficients which are required for the weight functions and the diffraction time surface in these regions.

This problem with incomplete traveltime tables is not inherent to the NORSAR code in particular or the wavefront construction method in general, but it applies to all ray tracing techniques. The

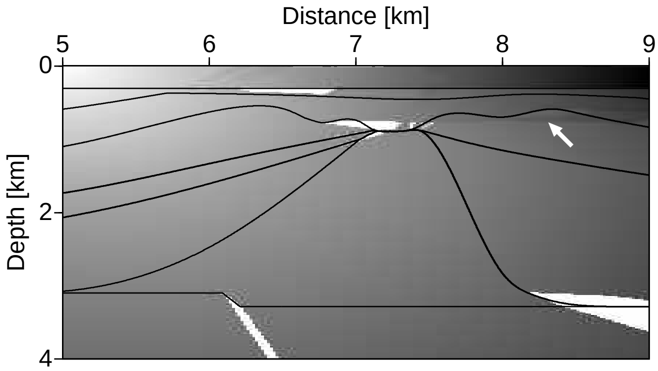

Figure 10.1: Traveltimes for the Picrocol model, computed with the NORSAR package. The values of the traveltimes are displayed by the greyscale with white corresponding to zero traveltime. The source is located in the upper left corner of the model. The black lines correspond to the interfaces of the model. White areas are regions, where the traveltime value is zero. These are shadow zones, that could not be covered with rays. In other regions (see the arrow) the traveltimes appear to be wrong, since there seems to be a discontinuity in them. It is possible that this traveltime belongs to a later arrival.

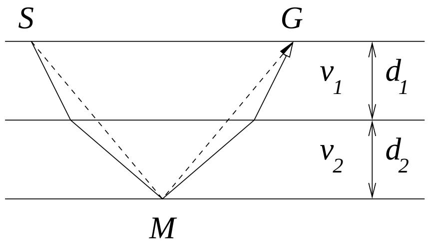

Figure 10.2: Ray paths from a source at S to a receiver at G via a subsurface point M assumed to lie on a reflector. Rays are shown for a two-layer medium (solid line) and a substitute medium (dashed line) with constant velocity. The constant velocity is chosen in such a way that the vertical traveltime is conserved.

reason is that for models with discontinuities of the velocity – as for the 'hard' reflectors in the Picrocol model – the scale length is no longer large compared to the wavelength (cf. Equation (A.1.7)): the velocity variations take place on a much smaller scale at the interfaces, especially for thin layers. If this is the case, ray tracing techniques reach their limit.

To adjust the scale length, smoothing of the velocity model is advised. The WRT technique by Coman and Gajewski (2001) yields complete traveltime tables including later arrivals only if small wavenumbers are removed from the velocity model. Smoothing of the velocity model, however, leads to deviations of the traveltimes and wavefront curvatures compared to those for the unsmoothed model. Consequently, errors in the weight functions, and therefore in the reconstructed amplitudes occur. I will illustrate this with a simple example.

Consider a reflector with an overburden that consists of two parallel constant velocity layers of equal thickness $d_1 = d_2$ (Figure 10.2). This model has a velocity discontinuity where the velocities v_1 and v_2 meet. The extreme case of a smoothed version of this model would be one layer with a constant

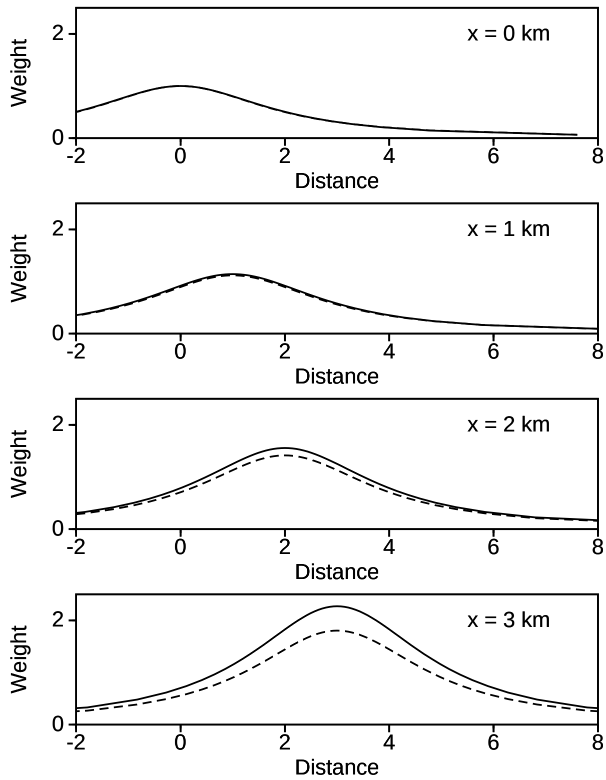

Figure 10.3: Weight functions for a two-layer overburden model as in Figure 10.2 (solid line) and the constant velocity substitute (dashed line) for a point at the distance x on the reflector. The source is located at zero. The error of the weight function which uses the substitute medium increases for growing x.

velocity v, where

$$v = (d_1 + d_2)\left(\frac{d_1}{v_1} + \frac{d_2}{v_2}\right)^{-1} = \frac{1}{2}\,\frac{v_1 v_2}{v_1 + v_2} \quad . \tag{10.1.1}$$

This form of v arises if slownesses are smoothed instead of velocities. It ensures that the vertical traveltime is conserved[1]. Figure 10.3 shows the weight functions for the original model and for the smoothed version. The error of the weights for the smoothed model increases with growing offset. This leads to an underestimation of the recovered reflection amplitude for higher offsets. Although in this example the smoothing was taken to its extreme, the effect has also been shown by Peles et al. (2001) for a model which was only reasonably smoothed.

The astute reader may now remark that, although I have reservations against the use of smoothed velocity models, I employ a different kind of smoothing myself for the weight functions: every interpolation corresponds to smoothing. Since the weight functions are determined at the coarse grid points only, trilinear interpolation is carried out onto all fine grid subsurface points, thereby smoothing the weight functions. The observation that this leads to errors in the weight functions is correct. However, the effect is small, as I will demonstrate with another simple example.

[1] This is the reason, why the slownesses are smoothed instead of velocities. Note, however, that the conservation of the vertical traveltime applies only to one depth point under the source at the depth z_0, if the model was smoothed between z=0 and z_0. E.g., for a point in the v_1-layer the vertical traveltime is $z/v_1 \neq z/v$, if v was determined from the v_i until reflector depth!

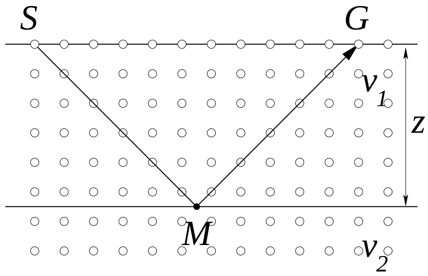

Figure 10.4: Representation of a two-layer medium. The circles denote coarse grid points where the weight functions are determined. At the depth z the weights need to be interpolated onto the reflector. This leads to errors.

Figure 10.4 shows a two-layer medium with a horizontal interface at the depth z. It is unlikely that the reflector will coincide with the coarse grid points at which the weight functions are determined. This situation is given in Figure 10.4. The correct, un-interpolated weight functions would be determined in the reflector surface. This means that only traveltimes to points on the reflector would enter the computation, which are in this case those for a constant velocity model with velocity v_1. Since traveltimes are not available in the reflector surface but only in planes below and above it, the weights for the points on the reflector are interpolated from the points below and above. In the model case the weights above the reflector are the correct ones since the velocity is constant v_1. Therefore the traveltimes from which the weights are computed are the correct ones. Below the reflector, the traveltimes behave different due to the discontinuous change in slowness at the interface, and the change in wavefront curvature (see, e.g., Leidenfrost et al. 1998). The weights at this depth are derived from traveltimes which were obtained by using velocity v_2 for the grid points below the reflector. They are, therefore, wrong with respect to the reflector. As a consequence, the weights on the reflector which result from interpolation of the values below and above the reflector are also wrong.

The errors in the weight functions which result from the interpolation of weight functions from below and above the reflector are very small. Figure 10.5 shows the weight functions and the relative errors for a model like the one in Figure 10.4 with v_1=4.5km/s, v_2=5km/s, and z=2km. The coarse grid spacing in this example is 100m, with the reflector in the middle between two coarse grid points. Only for higher offsets the errors increase. The move-out is smaller there, therefore the curvature in terms of the matrix $\underline{\bar{\mathrm{N}}}$ is small, as is the weight function. This lets the errors appear higher since they are relative errors.

So far, I have discussed the influence of smoothed models on the migration weights. This is, however, not the only way how migration is affected by errors in the velocities. The velocity model enters the migration in various ways. Errors in the velocity model cause not only wrong weights but also wrong traveltimes. These show in the migrated (kinematic) image in terms of under- and over-migration (i.e. smiles and frowns). However, even horizontal alignment of events in a common image gather does not signify that the velocity model which was used for the migration is correct, as, e.g., shown by Menyoli and Gajewski (2001). Therefore, one must always assume that the velocity model under consideration has errors. As shown above, the traveltime errors which result from the wrong velocities also cause errors in the true-amplitude migration weight functions, and, therefore in the recovered amplitudes. Since this is always the case, the correlation

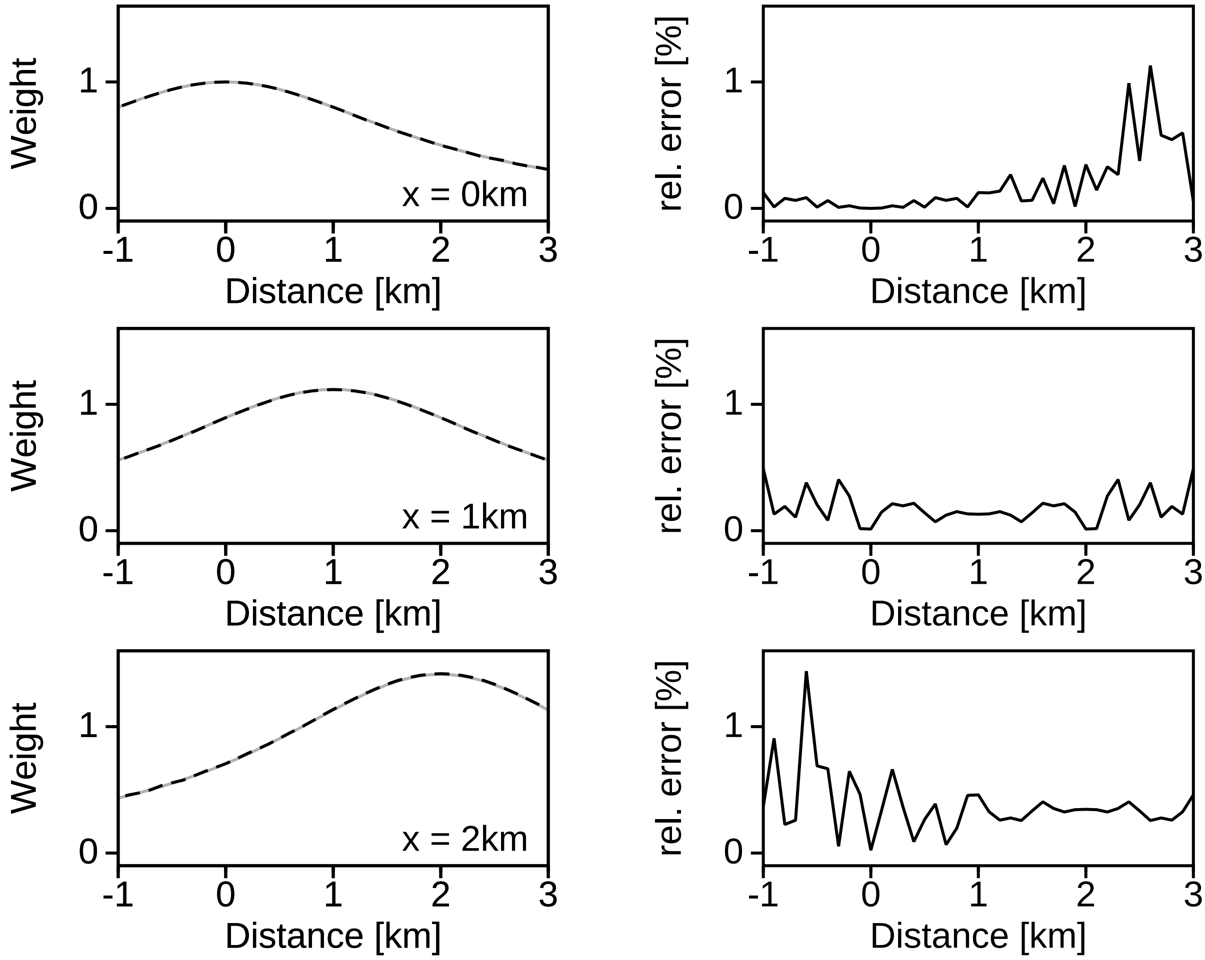

Figure 10.5: Weight functions for three points at the distance x on the reflector for the model given by Figure 10.4. Right: analytic weight function (gray lines) and interpolated weight function (dashed lines). Since both curves nearly coincide, the relative errors of the interpolated weight functions are given on the left. The slightly increasing error towards larger distance from the image point is caused by the smaller values of the weight function.

between the errors in the velocity model and those of the recovered amplitudes should be investigated.

Smoothing as one important error source has already been addressed above. A more general approach to study the influence of model errors would be to evaluate the traveltime error ΔT in terms of the velocity error Δv given by

$$\Delta T = \frac{\partial T}{\partial v} \Delta v \quad . \tag{10.1.2}$$

Subsequent differentiation of Equation (10.1.2) will then lead to expressions for the error of those traveltime derivatives which are involved in the weight functions. Since the main contribution to the stack comes from traces in the vicinity of the stationary ray, the deviation of the weights for these traces will give insight to the effect that velocity errors have on the recovered amplitudes.

To investigate the amplitude errors, the generalised NMO-equation (3.6.12) can be employed:

$$T^2 = T_0^2 + \frac{r^2}{v_{nmo}^2} = T_0^2 + T_0 N r^2 \quad . \tag{10.1.3}$$

This equation connects the traveltime T to the NMO velocity v_{NMO}. The quantity N contains second order derivatives which enter into the weight function. Therefore Equation (10.1.3) can be used to describe errors of N in terms of traveltime errors.

For arbitrary media the traveltime errors can be found by perturbation methods. The deviation of the traveltime T of the traveltime of the unperturbed medium T_{ref} is given by

$$\Delta T = T - T_{ref} = -\int_{s_0}^{s} \frac{\Delta v}{v^2} \, \mathrm{d}s \quad , \tag{10.1.4}$$

where v is the velocity of the unperturbed medium and Δv the deviation of it. The integration is carried out along the ray path of the unperturbed medium. As before, differentiation of Equation (10.1.4) leads to expression for the errors of the traveltime derivatives that are needed for the weight functions.

A similar approach can be followed for qP waves in weakly anisotropic media. Jech and Pšenčík (1989) give the traveltime error by

$$\Delta T = -\frac{1}{2} \int_{s_0}^{s} \frac{\Delta a_{ijkl} p_i p_l g_j g_k}{v} \, \mathrm{d}s \quad , \tag{10.1.5}$$

where the Δa_{ijkl} are the deviations of the density-normalised elastic parameters from those of the unperturbed medium, p_i are the slownesses and g_j the polarisation vectors. The subsequent procedure is the same as for isotropic media.

It may even be possible that the results of these investigations lead to criteria for a better focusing. If this would be the case, the results may be used to formulate a migration-based velocity analysis technique in addition to the evaluation of residual move-out in common image gathers. To predict such a method at this time, however, would be premature.

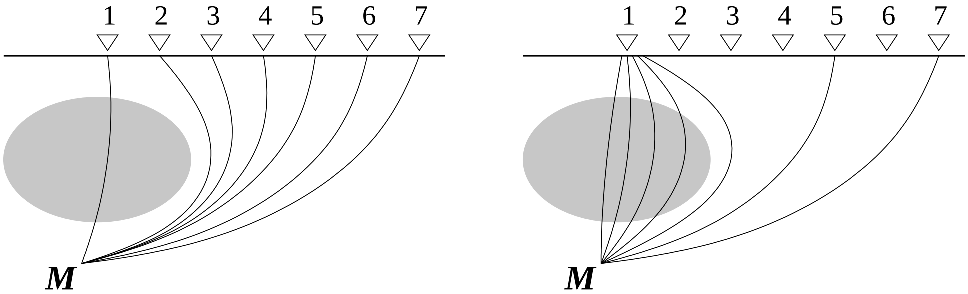

Figure 10.6: Schematic ray paths for a medium with a low velocity zone (gray) from an image point M to several receivers (triangles). Left: in conventional migration only a small angular region is well illuminated at M. On the right, the angles of the rays starting from M are evenly distributed. This leads to even illumination at the image point, which is especially important for shadow zones (see receivers 2–4).

10.2 Migration with angular parametrisation

In a typical seismic experiment, the sources and receivers are spaced as uniformly as possible in the recording surface. This line-up has, however, a vital disadvantage: the even coverage at the registration surface does not coincide with regular illumination at the image point, which is necessary for AVO or AVA studies. To achieve uniform illumination at the image point, rays with equal angular distance are required from the image point to the registration surface. Rays which leave the image point with equi-angular spacing, however, do not arrive with equidistant spacing at the recording surface. Therefore equidistant spacing of sources and receivers leads to high illumination in some angular regions, and poor illumination in others. Figure 10.6 (left) illustrates this effect. It has high impact in complex media, e.g., with shadow zones, or in the presence of anisotropy where illumination is crucial for parameter estimation.

To provide reliable AVO or AVA, the illumination of the image point should be evenly distributed over a large angular area. Since a model dependent registration can not be realised, a specific implementation of migration could compensate for this shortfall, the migration with angular parametrisation, which was suggested by Brandsberg-Dahl et al. (2001). In such an implementation, the traces in the registration surface are chosen to span a large angle at the image point as evenly as possible (see Figure 10.6, right). This is achieved by specifying the emergence angle, respectively the slowness at the image point. At the same time this procedure avoids the problematic triplications, because a ray is non-ambiguously characterised by its slowness.

Therefore, an implementation based on the hyperbolic traveltime interpolation will be also especially suited, because then, the uniform coverage at the image point will be particularly easy to realize. The slowness of a ray from the image point at $M = x_0$ to a source at $\boldsymbol{s}_0 + \Delta \boldsymbol{s}$ is given by

$$\boldsymbol{q} = \boldsymbol{q}_0 - T_0 \, \underline{\mathsf{N}} \Delta \boldsymbol{s} \quad . \tag{10.2.1}$$

The quantities T_0, $\boldsymbol{q}_0$, and $\underline{\mathsf{N}}$ correspond to the traveltime and its derivatives for a ray from x_0 to $\boldsymbol{s}_0$. The emergence angle at x_0 is given by the slowness $\boldsymbol{q}$ at x_0. Therefore, Equation (10.2.1) leads to the position $\boldsymbol{s}_0 + \Delta \boldsymbol{s}$ for a prescribed emergence angle. Since in some cases there will be no trace at this position, trace interpolation is required, which is discussed, e.g., in Spitz (1991) or Kabir and Verschuur (1995). An alternative to their techniques is the construction of a new trace by prestack data enhancement suggested by Baykulov and Gajewski (2009). On the other hand, if

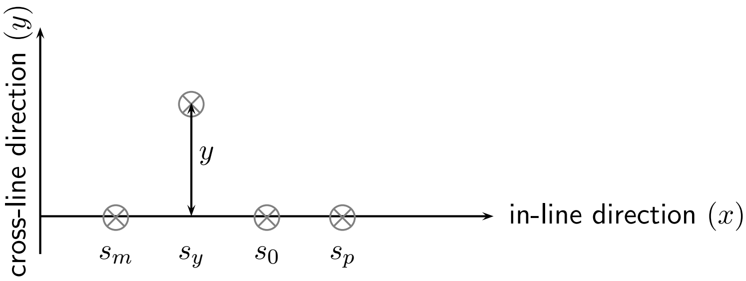

Figure 10.7: Ray end points in the acquisition surface. Due to the 2.5D symmetry rays emitted from the image point in $x-z$ direction reach the surface at y=0. For example, the rays emerging at s_m, s_0, and s_p were emitted in the $x-z$ plane under equidistant angles, but arrive at irregular distances. The ray arriving at (s_y, y) is required for the determination of the out-of-plane spreading σ.

the acquisition scheme provides a dense distribution of sources and receivers, trace interpolation may not be necessary as the nearest trace may be used.

Because the spacing of the ray endpoints in the registration surface will not be equidistant, the equations for the determination of the traveltime coefficients derived in Chapter 2 need to be adapted to the more general situation of irregular grids. In the following, I will describe such a scheme.

The traveltimes are generated by ray shooting. To obtain an even illumination at the image point, x_0, a fan of rays with a constant angular increment is emitted. The image points are sampled on a coarse grid. During the ray shooting, the positions of the intersections of the rays with the registration surface are computed and stored in addition to the traveltimes. Although the subsurface grid is chosen regularly, the distribution of the ray endpoints, i.e., sources and receivers in the registration surface, will not be regular.

For simplicity I consider a 2.5D symmetry here, however, the extension to 3D is straightforward. In the 2.5D case, we need the coefficients (see Section 9.3)

$p = p_x$	horizontal slowness at the source/receiver,
q_x, q_z	horizontal and vertical slowness at the image point,
$S = S_{xx}$	second-order traveltime derivative at the source/receiver,
G_{xx}, G_{zz}, G_{xz}	second-order traveltime derivatives at the image point,
N_{xx}, N_{xz}	second-order mixed traveltime derivative,
$\sigma = N_{yy}^{-1}$	for the computation of the out-of-plane spreading.

I begin with the determination of p, S, and σ. Consider the following endpoints $\otimes$ of the rays shot from the image point x_0 in the acquisition surface as shown in Figure 10.7

Let the ray from x_0 to s_0 be the expansion point with the traveltime T_0. Correspondingly, we denote $T(x_0, s_m)$ by T_m, $T(x_0, s_p)$ by T_p, and $T(x_0, s_y)$ by T_y. Then the coefficients p, S, and σ, i.e., the derivatives with respect to the acquisition coordinates are computed from the hyperbolic traveltime expression in Section 2.2 by

$$
\begin{aligned}
p &= -\frac{(T_0^2 - T_p^2)(s_m - s_0)^2 - (T_0^2 - T_m^2)(s_p - s_0)^2}{2\,T_0\,(s_p - s_0)(s_m - s_0)(s_p - s_m)} \quad , \\
S &= \frac{(T_0^2 - T_p^2)(s_m - s_0) - (T_0^2 - T_m^2)(s_p - s_0)}{T_0\,(s_p - s_0)(s_m - s_0)(s_p - s_m)} + \frac{p^2}{T_0} \quad , \\
\sigma &= \frac{T_0\,y^2}{T_y^2 - \big(T_0 - p(s - s_y)\big)^2 + T_0\,S(s - s_y)^2} \quad .
\end{aligned}
\tag{10.2.2}
$$

For the determination of the derivatives with respect to the image point coordinates, we need an intermediate step. An analogous derivation according to Equation (10.2.2) would require traveltimes from three image points to the same point s_0 in the registration surface. These are, however, not generally available since the rays emerging from the three image points will not all incide at s_0.

As suggested in Figure 10.8, rays are shot from the three subsurface points at x_m, x_0, and x_p to s_m, s_0, and s_p, respectively. They have the traveltimes T_{0m}, T_0, and T_{0p} and the coefficients p_m, p_p, S_m, and S_p, where the subscripts indicate to which x they belong. With these quantities we obtain the traveltimes $\tilde{T}_m{=}T(x_m, s_0)$ and $\tilde{T}_p{=}T(x_p, s_0)$ by applying the hyperbolic interpolation from Section 2.2:

$$
\begin{aligned}
\tilde{T}_m^2 &= \big((T_{0m} - p_m\,(s_m - s_0)\big)^2 - T_{0m} S_m (s_m - s_0)^2 \quad , \\
\tilde{T}_p^2 &= \big((T_{0p} - p_p\,(s_p - s_0)\big)^2 - T_{0p} S_p (s_p - s_0)^2 \quad .
\end{aligned}
$$

From these traveltimes we can now compute the coefficients q_x and G_{xx} with the expressions for regular grids given in Section 2.2,

$$
\begin{aligned}
q_x &= \frac{\tilde{T}_p^2 - \tilde{T}_m^2}{4\,T_0\,\Delta x} \quad , \\
G_{xx} &= \frac{\tilde{T}_p^2 + \tilde{T}_m^2 - 2\,T_0^2}{2\,T_0\,\Delta x^2} - \frac{q_x^2}{T_0} \quad ,
\end{aligned}
$$

where $\Delta x = x_p - x_0 = x_0 - x_m$. The coefficients q_z, G_{zz}, G_{xz}, N_{xx}, and N_{xz} are computed correspondingly after the $T(x,z,s)$ were obtained from interpolation to the according positions.

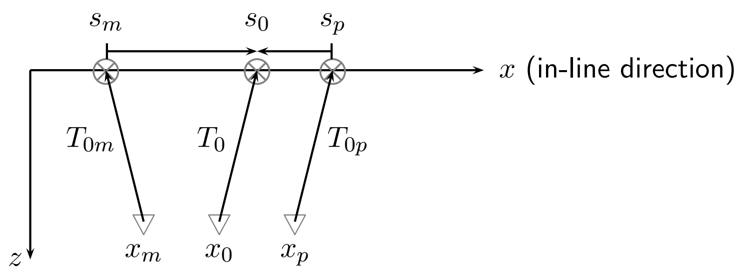

Figure 10.8: Positions of image points for the computation of the remaining coefficients after p, S, and σ have been determined.

Example

A kinematic traveltime-based migration with angular parametrisation was implemented in the context of the Ph.D. work by Kaschwich (2006) under the author's supervision. I will present the results in this section.

Figure 10.9 shows the velocity model Kaschwich (2006) used as input. It consists of a horizontal layer below a velocity lens, leading to an irregular illumination. Synthetic seismograms were modelled with an algorithm based on the Fourier method (Kosloff and Baysal, 1982).

Kaschwich (2006) has carried out a kinematic Kirchhoff migration with two different methods. The results are displayed in Figure 10.10. On the left in Figure 10.10, we observe that the reflector was

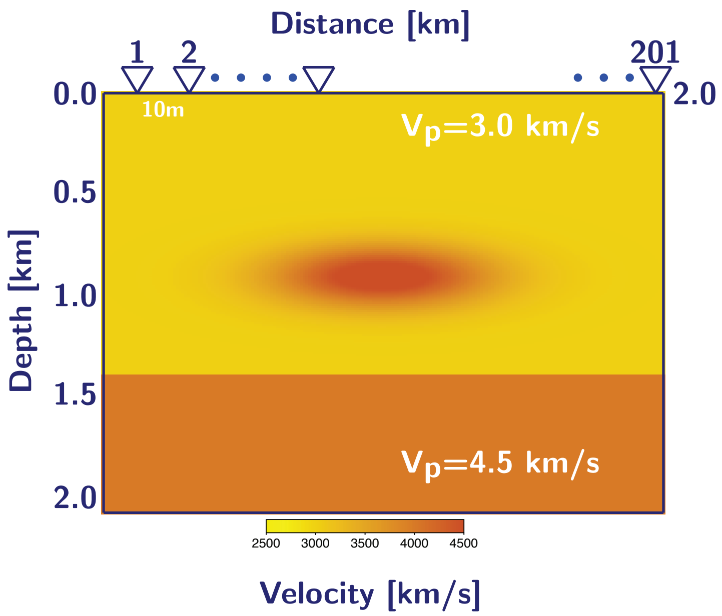

Figure 10.9: Velocity model and acquisition scheme used for the comparison of migration with angular parametrisation vs. conventional migration: a horizontal layer is placed under a lens-shaped velocity anomaly, which leads to irregular illumination. An end-on spread acquisition with the source on the left was used.

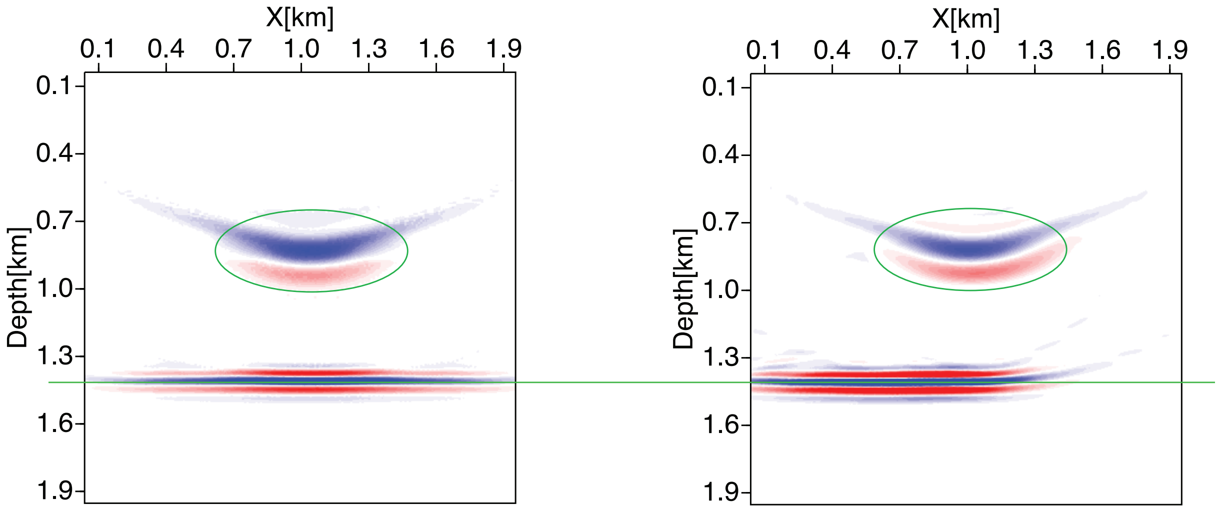

Figure 10.10: Migration with angular parametrisation (left) and conventional migration (right) of the data generated for the model shown in Figure 10.9. Green lines indicate the position of the horizontal reflector and the lens. The equal illumination resulting from the angular parametrisation leads to a continuously imaged reflector under the lens (left), whereas the lack of illumination of the conventional migration (right) causes severe artifacts, i.e., a large part of the reflector is missing on the right hand side, and the reflector continuity is distorted under the lens. Furthermore, the amplitudes do not coincide.

continuously imaged by the migration with angular parametrisation. On the right are results from a migration using a Seismic Un*x Kirchhoff migration code. In this case, only the left part of the reflector could be reconstructed. The right part is distorted or not visible because there was no sufficient ray coverage during the conventional migration.

We can also observe in Figure 10.10 that the reconstructed amplitudes along the reflector do not coincide for both migrations. The implementation and verification of the true-amplitude flavour of traveltime-based migration with angular parametrisation will be a future work.

Chapter 11

Conclusions

In this second part of my thesis I have presented an efficient strategy for amplitude-preserving migration of the Kirchhoff type. It is based on coarsely-gridded traveltimes as only input information and therefore only requires a small amount of computer storage. The traveltimes are employed for the computation of all quantities required for the migration process, namely the traveltime interpolation onto fine grids for the stacking surface, the true-amplitude weight functions, and the size of the optimum migration aperture. The method also provides a tool for the computation of geometrical spreading.

The matrices involved in the traveltime interpolation introduced in Chapter 2 bear a close relationship to the matrices describing dynamic wavefield properties in the context of the paraxial ray approximation. This relation leads to the determination of the complete ray propagator from traveltimes. The ray propagator can be used for various tasks including the computation of geometrical spreading and migration weights.

I have derived expressions for the spreading in terms of the traveltime coefficients and demonstrated their accuracy with several examples, ranging from isotropic and anisotropic homogeneous and constant velocity models to the highly complex Marmousi model. The results show clearly that the determination of geometrical spreading from traveltimes leads to high accuracy for all types of media.

The traveltime coefficients were also applied for the determination of migration weight functions. I have first investigated simple generic examples in order to evaluate the method. The results show good accordance between the reconstructed reflectors and theoretical values in terms of position as well as in amplitudes. This applies to PP and PS converted wave data, in isotropic as well as in anisotropic media.

Application of the traveltime-based strategy to two complex examples, a synthetic and a field data set, confirms the equivalence of the results to those obtained from dynamic ray tracing based weights. The recovered reflectivities coincide for all considered interfaces, regardless of their depth, inclination, or curvature.

Although the computational effort can already be considerably reduced by the traveltime-based strategy, a further significant reduction in computational time can achieved by limiting the migration aperture to a minimum. A simple example indicates potential savings of up to 80 percent in 2-D and more than 90 percent in 3-D. Moreover, I have shown that use of a limited aperture can enhance the image quality by reducing migration noise.The size of the optimum aperture can also be computed from the traveltime coefficients, however, assumptions on the reflector dips must be made unless a priori information on the inclinations is available.

Since the method works equally well for isotropic as well as anisotropic media, it has another advantage over migration techniques based on dynamic ray tracing (DRT). For the traveltime-based migration, only traveltimes are required as input information. This permits the use of kinematic ray tracing (KRT) as opposed to DRT, which has significantly higher restrictions to the models regarding smoothness. Furthermore, ray tracing in anisotropic media fails in the presence of shear wave singularities, i.e., when both shear velocities coincide. In this case, other means for traveltime computation like finite-difference eikonal solvers can still be used for the generation of traveltimes. This is not possible if the weight functions need to be determined by ray methods, and it is another significant advantage of the method.

I have addressed two additional issues in the outlook, Chapter 10. Section 10.1 deals with errors of the velocity model and suggests how the influence of these errors on the reconstructed image and recovered amplitudes can be investigated. This is a topic of great importance as the main problem nowadays still lies in the determination of the velocity model, not in the actual migration.

Another problem occurs in complex media if the regular discretisation of the acquisition does not reflect an irregular illumination in the subsurface, e.g., in the presence of velocity lenses. Here, the extension of the traveltime-based strategy to migration with angular parametrisation, which prescribes even illumination of the image point, leads to much better results already for the kinematic case. The theory of the extension to true-amplitudes is suggested in Section 10.2 but remains to be investigated in practice.

Part III

Appendices

Appendix A

Review of the ray method

This appendix gives an overview of the ray method. It introduces the basic equations of asymptotic ray theory and the paraxial ray method. Beginning with the elastodynamic equation, the eikonal equations, and the transport equations for arbitrary elastic anisotropic media will be derived and discussed. This is followed by a section on kinematic and dynamic ray tracing in Cartesian and ray centred coordinates to solve the eikonal and transport equations. The ray propagator formalism and its relation to the paraxial ray approximation is introduced for two different concepts. The first approach is based on a traveltime expansion into the wavefront. In the second, the traveltimes are expanded into reference surfaces, as, e.g., registration surfaces or reflectors.

Since there exists a large variety of texts on the basic concepts of the ray method, I have only given a few representative references at the end of each section. Those are by no means a complete list.

In this thesis I consider isotropic as well as anisotropic media. In order to retain the overview character of this appendix, some results in the following sections are derived for isotropic media only, although according formulations for anisotropic media exist. Often, e.g., for the ray propagator formalism, the anisotropic relations have the same form as in the isotropic case but I have not explicitly pointed this out in every case. However, corresponding relationships for anisotropic media can in detail be found in Červený (2001).

A.1 The elastodynamic equation and ray series

Consider a perfectly elastic, inhomogeneous medium that is described by the density ρ and the elasticity tensor c_{ijkl}. These are assumed to be continuous functions of space only and to have continuous first and piece-wise continuous second order derivatives. In this case the elastodynamic equation for the displacement $\hat{\boldsymbol{u}}$ (without voluminal forces) reads

$$\sigma_{ij,j} = \rho u_{i,tt} \quad , \tag{A.1.1}$$

where the stress tensor σ_{ij} is given by

$$\sigma_{ij} = c_{ijkl}\, \varepsilon_{kl} \quad , \tag{A.1.2}$$

and the strain tensor ε_{kl} by

$$\varepsilon_{kl} = \frac{1}{2}\left(u_{k,l} + u_{l,k}\right) \quad . \tag{A.1.3}$$

Both, stress and strain tensors are symmetric tensors. Their symmetry and energy considerations lead to symmetric properties for the elasticity tensor:

$$c_{ijkl} = c_{jikl} = c_{ijlk} = c_{klij} \quad . \tag{A.1.4}$$

As a consequence, the number of independent elastic parameters is reduced from 81 (=3^4) to 21.

Inserting Equations (A.1.2) and (A.1.3) into (A.1.1) leads to

$$(c_{ijkl}\, u_{k,l})_{,j} = \rho\, u_{i,tt} \quad . \tag{A.1.5}$$

Equation (A.1.5) is the elastodynamic equation for a perfectly elastic, inhomogeneous, anisotropic medium. One possible way to solve this equation is the ray series solution, an asymptotic series in powers of inverse frequency, which approximates the displacement

$$u_i(x_j, t) = \mathrm{e}^{-i\omega(t-\tau(x_j))} \sum_{n=0}^{\infty} \frac{1}{(-i\omega)^n}\, U_i^{(n)}(x_j) \quad . \tag{A.1.6}$$

The vectorial amplitude $U_i^{(n)}$ is of the order n term (the superscripted (n) does not denote differentiation) and can be complex valued. The quantity τ is a real scalar called the eikonal or phase function. Surfaces of constant τ with $\tau(\hat{\boldsymbol{x}}) = t_0$ represent the wavefront for a specified time t_0. Since τ and U_i are functions of space only, Equation (A.1.6) separates the spatial dependency from the temporal dependency of the displacement, making (A.1.5) easier to handle.

Equation (A.1.6) is a high frequency solution of (A.1.5), where "high" is large in a relative sense. This means, that the variation of the amplitude u_i, over the distance of a wavelength $\lambda = 2\pi V/\omega$ – more precisely, the maximum wavelength – must be negligible compared to the value of u_i. This also applies to other related quantities, as, e.g., the phase velocity V, and the slowness vector p_i which will be explained later. As for the displacement, their variation must also not take place on a smaller scale than that given by the maximum wavelength. This condition reads

$$\lambda \ll \frac{u_i}{|\vec{\nabla} u_i|} \quad , \qquad \lambda \ll \frac{p_i}{|\vec{\nabla} p_i|} \quad , \quad \text{and} \quad \lambda \ll \frac{V}{|\vec{\nabla} V|} \quad . \tag{A.1.7}$$

Denoting the minimum of the right hand sides in (A.1.7) by the scale length L, the three relations (A.1.7) can be summarised to

$$\frac{\lambda}{L} \ll 1 \quad . \tag{A.1.8}$$

If in this sense ω is large enough, only the leading term of the series (A.1.6), i.e. n=0, is of practical interest. This is the case for most applications, including those addressed in this work. Therefore from now on only the zero order solution will be considered and the index (0) will be omitted

$$u_i = U_i^{(0)}\, \mathrm{e}^{-i\omega(t-\tau)} = U_i\, \mathrm{e}^{-i\omega(t-\tau)} \quad . \tag{A.1.9}$$

Inserting Equation (A.1.9) into (A.1.5) leads to

$$(i\omega)^2\, N_i(\hat{\boldsymbol{U}}) + i\omega\, M_i(\hat{\boldsymbol{U}}) + L_i(\hat{\boldsymbol{U}}) = 0 \quad , \tag{A.1.10}$$

introducing the three vector operators

$$N_i(\hat{\boldsymbol{U}}) \;=\; \frac{c_{ijkl}}{\rho}\, \tau_{,j}\, \tau_{,l}\, U_k - U_i \quad , \tag{A.1.11}$$

$$M_i(\hat{\boldsymbol{U}}) \;=\; \frac{c_{ijkl}}{\rho}\, \tau_{,j}\, U_{k,l} + \frac{1}{\rho}(c_{ijkl}\, \tau_{,l}\, U_k)_{,j} \quad , \tag{A.1.12}$$

$$L_i(\hat{\boldsymbol{U}}) \;=\; \frac{1}{\rho}\, (c_{ijkl}\, U_{k,l})_{,j} \quad . \tag{A.1.13}$$

Since ω is assumed to be sufficiently large, the $L_i(\hat{\boldsymbol{U}})$ term in (A.1.10) can be neglected. Then $\tau(x_j)$ and $U_i(x_j)$ can be determined independent of the frequency by solving

$$N_i(\hat{\boldsymbol{U}}) = 0 \quad , \tag{A.1.14}$$
$$M_i(\hat{\boldsymbol{U}}) = 0 \quad . \tag{A.1.15}$$

Equation (A.1.14) leads to equations for τ, the eikonal equations, which will be discussed in the following section. The amplitude U_i obeys the transport equations that are derived from (A.1.15) and discussed thereafter.

Literature for Section A.1:

- Červený (1972),
- Pšenčík (1994).

A.2 The eikonal equations

Equation (A.1.14) can be rewritten to formulate an eigenvalue problem. Introducing the Christoffel matrix Γ_{ik} with

$$\Gamma_{ik} = \frac{c_{ijkl}}{\rho}\,\tau_{,j}\,\tau_{,l} \quad , \tag{A.2.1}$$

Equation (A.1.14) becomes

$$(\Gamma_{ik} - \delta_{ik})\,U_k = 0 \quad . \tag{A.2.2}$$

Nontrivial solutions of (A.2.2) require that

$$|\Gamma_{ik} - \delta_{ik}| = 0 \quad . \tag{A.2.3}$$

Therefore, the m eigenvalues $G^{(m)}$ given by

$$|\Gamma_{ik} - G^{(m)}\delta_{ik}| = 0 \tag{A.2.4}$$

must equal 1. The corresponding eigenvectors $g_k^{(m)}$ describe the polarisation. They are determined from

$$(\Gamma_{ik} - G^{(m)}\,\delta_{ik})\,g_k^{(m)} = 0 \quad . \tag{A.2.5}$$

Expression (A.2.4) yields a cubic equation, meaning that three independent solutions exist for m=1,2,3 with eigenvectors that are perpendicular to each other. If two eigenvalues coincide (degeneration, e.g., for the shear wave in an isotropic medium, see below), only the plane that contains the corresponding eigenvectors can be determined. It is perpendicular to the third eigenvector.

Multiplication of Equation (A.2.5) with $g_k^{(m)}$ leads to the eikonal equation for anisotropic media

$$G^{(m)} = 1 = \Gamma_{ik}\,g_i^{(m)}\,g_k^{(m)} = \frac{c_{ijkl}}{\rho}\,\tau_{,j}\,\tau_{,l}\,g_i^{(m)}\,g_k^{(m)} \quad . \tag{A.2.6}$$

Let us take a look at the isotropic case now. In isotropic media, the elasticity tensor reduces to

$$c_{ijkl} = \lambda\delta_{ij}\delta_{kl} + \mu(\delta_{ik}\delta_{jl} + \delta_{il}\delta_{jk}) \tag{A.2.7}$$

with the Lamé parameters λ and μ and Kronecker δ_{ij}. A more appealing form is (with $m \neq n$)

$$\begin{aligned} c_{nnnn} &= \lambda + \mu \quad , \\ c_{mnmn} = c_{mnnm} &= \mu \quad , \\ c_{mmnn} &= \lambda \end{aligned} \tag{A.2.8}$$

(no summation convention is applied here). The remaining elements of c_{ijkl} are zero. With (A.2.8), Equation (A.1.14) can be rewritten to

$$\frac{\lambda + \mu}{\rho} \tau_{,i} \tau_{,k} U_k + \frac{\mu}{\rho} \tau_{,k} \tau_{,k} U_i - U_i = 0 \quad , \tag{A.2.9}$$

or, in vectorial form

$$\frac{\lambda + \mu}{\rho} (\hat{\boldsymbol{U}} \cdot \vec{\nabla}\tau)\vec{\nabla}\tau + \frac{\mu}{\rho} (\vec{\nabla}^2 \tau) \hat{\boldsymbol{U}} - \hat{\boldsymbol{U}} = 0 \quad . \tag{A.2.10}$$

To determine the eikonal equations, the scalar product and the vector product of Equation (A.2.10) with $\vec{\nabla}\tau$ is built. The quantity

$$\hat{\boldsymbol{p}} = \vec{\nabla}\tau \tag{A.2.11}$$

is the slowness vector perpendicular to the wavefront. Its scalar and vector products with (A.2.10) yield

$$\hat{\boldsymbol{N}}(\hat{\boldsymbol{U}}) \cdot \vec{\nabla}\tau = [(-\rho + (\lambda + 2\mu)(\vec{\nabla}\tau)^2] (\hat{\boldsymbol{U}} \cdot \vec{\nabla}\tau) = 0 \tag{A.2.12}$$

$$\hat{\boldsymbol{N}}(\hat{\boldsymbol{U}}) \times \vec{\nabla}\tau = [(-\rho + \mu (\vec{\nabla}\tau)^2] (\hat{\boldsymbol{U}} \times \vec{\nabla}\tau) = 0 \quad . \tag{A.2.13}$$

Both Equations (A.2.12) and (A.2.13) must be fulfilled for all $\hat{\boldsymbol{U}}$ and τ. This leads to two independent solutions

1. $\hat{\boldsymbol{U}} \times \vec{\nabla}\tau = 0$ and

   $$(\vec{\nabla}\tau)^2 = \frac{\rho}{\lambda + 2\mu} = \frac{1}{V_\mathrm{P}^2} \quad . \tag{A.2.14}$$

   The first condition demands that $\hat{\boldsymbol{U}}$ is parallel to $\vec{\nabla}\tau$. The polarisation vector $g_k^{(3)} = V_\mathrm{P}\tau_{,k}$ is the tangent vector (m was assigned to be 3 as usual in the literature). This solution describes a P-wave with the propagation velocity V_P.

2. $\hat{\boldsymbol{U}} \cdot \vec{\nabla}\tau = 0$ and

   $$(\vec{\nabla}\tau)^2 = \frac{\rho}{\mu} = \frac{1}{V_\mathrm{S}^2} \quad . \tag{A.2.15}$$

   Here, the first condition demands that $\hat{\boldsymbol{U}}$ is perpendicular to $\vec{\nabla}\tau$, corresponding to a shear wave that has two components with the polarisation vectors $g_k^{(1)}$ and $g_k^{(2)}$ and the propagation velocity V_S. As mentioned before, in this case the polarisation vectors can be chosen arbitrarily, perpendicular to each other, in the plane perpendicular to $\vec{\nabla}\tau$. One particular choice are the base vectors $\vec{\boldsymbol{e}}_1$ and $\vec{\boldsymbol{e}}_2$ from the ray centred coordinate system (see below) which has advantages concerning the transport equations that will be derived in the next section.

Equations (A.2.14) and (A.2.15) are the isotropic eikonal equations for P and S waves, respectively. Equation (A.2.6) for isotropic media reads

$$G^{(m)} = 1 = V_m^2 \tau_{,k}\tau_{,k} \quad . \tag{A.2.16}$$

Here, the velocity V_m is the phase velocity of the corresponding wave, i.e., $V_3 = V_\mathrm{P}$ and $V_1 = V_2 = V_\mathrm{S}$.

Literature for Section A.2:

- Červený and Ravindra (1971),
- Gajewski and Pšenčík (1987).

A.3 The transport equations

The procedure for the determination of the transport equations in inhomogeneous anisotropic media is similar to the derivation of the eikonal equations in the previous section. The displacement vectors $U_i^{(m)}(x_j)$ can be written as

$$U_i^{(m)}(x_j) = U^{(m)}(x_j)\, g_i^{(m)}(x_j) \quad . \tag{A.3.1}$$

Since this applies to all three waves, m=1,2,3, the index m will be omitted from now on. Building the scalar product of the polarisation vector g_i and Equation (A.1.15) leads to

$$M_i(\hat{\boldsymbol{U}})\, g_i = 2\, U_{,j}\, v_j + \frac{U}{\rho}\, v_j\, \rho_{,j} + U\, v_{j,j} = 0 \quad , \tag{A.3.2}$$

introducing the group velocity vector

$$v_i = \frac{\mathrm{d}x_i}{\mathrm{d}\tau} = \frac{c_{ijkl}}{\rho}\, \tau_{,l}\, g_j\, g_k \quad . \tag{A.3.3}$$

In isotropic media, the group velocity $v = |\hat{\boldsymbol{v}}|$ equals the phase velocity V. Note that for shear waves (m=1,2) the choice of polarisation vectors is important. For arbitrary choice, there are additional terms in (A.3.2), leading to two coupled transport equations for m=1 and m=2. Only if $\mathrm{d}g_i^{(1,2)}/\mathrm{d}s \propto p_i$ is fulfilled (as it is the case for the ray centred coordinates, see Section A.5 below), Equations (A.3.2) decouple. Equations (A.3.2) for m=1,2,3 are the transport equations. They can be rewritten in terms of τ derivatives which is easier to be solved. To the first two terms in (A.3.2)

$$\Phi_{,j}\, v_j = \vec{\nabla}\Phi \cdot \frac{\mathrm{d}\hat{\boldsymbol{x}}}{\mathrm{d}\tau} = \frac{\mathrm{d}\Phi}{\mathrm{d}\tau} \tag{A.3.4}$$

applies. The divergence of the group velocity in the third term of (A.3.2) is given by

$$v_{j,j} = \lim_{\Delta V_\tau \to 0} \frac{1}{\Delta V_\tau} \oint \hat{\boldsymbol{v}} \cdot \mathrm{d}\hat{\boldsymbol{S}}_\tau = \lim_{\Delta V_\tau \to 0} \frac{1}{\Delta V_\tau} \oint \hat{\boldsymbol{v}} \cdot \hat{\boldsymbol{p}}\, V\, \mathrm{d}S_\tau \tag{A.3.5}$$

where the integration is carried out over the surface of a piece of a ray tube that is limited by the phase fronts t=τ_0 and t=$\tau_0 + \mathrm{d}\tau$=τ (see Figure A.1). A vectorial surface element $\mathrm{d}\boldsymbol{S}_{\gamma_3}$ is the cross-sectional area of the ray tube: the part of the surface γ_3=*const.* that is cut out by the ray tube. It is defined as

$$\mathrm{d}\hat{\boldsymbol{S}}_{\gamma_3} = \left(\frac{\partial \hat{\boldsymbol{x}}}{\partial \gamma_1} \times \frac{\partial \hat{\boldsymbol{x}}}{\partial \gamma_2} \right)_{\gamma_3} \mathrm{d}\gamma_1\, \mathrm{d}\gamma_2 \quad , \tag{A.3.6}$$

introducing the ray coordinates (ray parameters) γ_i, see also Figure A.1. The corresponding volume element is given by

$$\mathrm{d}V_{\gamma_3} = \mathcal{J}_{\gamma_3}\, \mathrm{d}\gamma_1\, \mathrm{d}\gamma_2\, \mathrm{d}\gamma_3 = \mathrm{d}\hat{\boldsymbol{S}}_{\gamma_3} \cdot \frac{\mathrm{d}\hat{\boldsymbol{x}}}{\mathrm{d}\gamma_3}\, \mathrm{d}\gamma_3 \quad , \tag{A.3.7}$$

where $\mathcal{J}_{\gamma_3}$ is the determinant of the Jacobian $\underline{\hat{\mathsf{X}}}$

$$X_{ij} = \frac{\partial x_i}{\partial \gamma_j} \quad . \tag{A.3.8}$$

Choice of the arc length s for γ_3 leads to

$$\mathcal{J}_s \,\mathrm{d}\gamma_1 \,\mathrm{d}\gamma_2 = \mathrm{d}\hat{\boldsymbol{S}}_s \cdot \frac{\mathrm{d}\hat{\boldsymbol{x}}}{\mathrm{d}s} = \mathrm{d}\hat{\boldsymbol{S}}_s \cdot \frac{\hat{\boldsymbol{v}}}{v} = \mathrm{d}S_s \quad , \tag{A.3.9}$$

and for $\gamma_3 = \tau$

$$\begin{aligned} \mathcal{J}_\tau \,\mathrm{d}\gamma_1 \,\mathrm{d}\gamma_2 &= \mathrm{d}\hat{\boldsymbol{S}}_\tau \cdot \frac{\mathrm{d}\hat{\boldsymbol{x}}}{\mathrm{d}s} = v \,\mathrm{d}\hat{\boldsymbol{S}}_\tau \cdot \frac{\mathrm{d}\hat{\boldsymbol{x}}}{\mathrm{d}s} = v \,\mathrm{d}S_s & \text{(A.3.10)} \\ &= \mathrm{d}S_\tau \, V \,\hat{\boldsymbol{p}} \cdot \hat{\boldsymbol{v}} = V \;\mathrm{d}S_\tau = \Omega \, V \;\mathrm{d}\gamma_1 \,\mathrm{d}\gamma_2 \quad , & \text{(A.3.11)} \end{aligned}$$

introducing the quantity Ω

$$\Omega = \left(\frac{\partial \hat{\boldsymbol{x}}}{\partial \gamma_1} \times \frac{\partial \hat{\boldsymbol{x}}}{\partial \gamma_2} \right)_\tau \cdot \hat{\boldsymbol{p}} \, V = \frac{\mathrm{d}S_\tau}{\mathrm{d}\gamma_1 \,\mathrm{d}\gamma_2} \quad . \tag{A.3.12}$$

Now the volume element ΔV_τ can be written as

$$\Delta V_\tau = V \,\mathrm{d}S_\tau \,\Delta\tau = V \,\mathrm{d}S_\tau \,(\tau - \tau_0) \quad . \tag{A.3.13}$$

Figure A.1 shows that $\hat{\boldsymbol{v}} \,\mathrm{d}\hat{\boldsymbol{S}}_\tau$ has only non-vanishing contributions at the cross sections of the ray tube with the phase fronts t=*const.*

$$\text{at} \quad \tau : \quad \hat{\boldsymbol{v}} \cdot \mathrm{d}\hat{\boldsymbol{S}}_\tau = V(\tau) \,\mathrm{d}S_\tau = \mathcal{J}_\tau(\tau) \,\mathrm{d}\gamma_1 \,\mathrm{d}\gamma_2 \quad , \tag{A.3.14}$$

and

$$\text{at} \quad \tau_0 : \quad \hat{\boldsymbol{v}} \cdot \mathrm{d}\hat{\boldsymbol{S}}_\tau = -V(\tau_0) \,\mathrm{d}S_\tau = -\mathcal{J}_\tau(\tau_0) \,\mathrm{d}\gamma_1 \,\mathrm{d}\gamma_2 \quad . \tag{A.3.15}$$

Inserting these and (A.3.13) into (A.3.5) yields

$$\begin{aligned} v_{j,j} &= \lim_{\tau \to \tau_0} \frac{\mathcal{J}_\tau(\tau) - \mathcal{J}_\tau(\tau_0)}{\mathcal{J}_\tau \cdot (\tau - \tau_0)} \\ &= \frac{1}{\mathcal{J}_\tau} \frac{\mathrm{d}\mathcal{J}_\tau}{\mathrm{d}\tau} \quad . \end{aligned} \tag{A.3.16}$$

With (A.3.16) and (A.3.4), Equation (A.3.2) becomes

$$2 \frac{\mathrm{d}U}{\mathrm{d}\tau} + \frac{U}{\rho} \frac{\mathrm{d}\rho}{\mathrm{d}\tau} + \frac{U}{\mathcal{J}_\tau} \frac{\mathrm{d}\mathcal{J}_\tau}{\mathrm{d}\tau} = 0 \tag{A.3.17}$$

or

$$\frac{\mathrm{d}}{\mathrm{d}\tau} \left(\sqrt{\rho \, \mathcal{J}_\tau} \, U \right) = 0 \quad . \tag{A.3.18}$$

The solution of Equation (A.3.18) is straightforward

$$U(\tau) = U(\tau_0) \sqrt{\frac{\rho(\tau_0) \, \mathcal{J}_\tau(\tau_0)}{\rho(\tau) \, \mathcal{J}_\tau(\tau)}} \quad . \tag{A.3.19}$$

Equation (A.3.19), however may lead to problems if, e.g., a point source at τ_0 is considered. For this case it is better to use the following solution of (A.3.18)

$$U(\tau) = \frac{\Psi(\gamma_1, \gamma_2)}{\sqrt{\rho(\tau) \, \mathcal{J}_\tau(\tau)}} = \frac{\Psi(\gamma_1, \gamma_2)}{\sqrt{\rho(\tau) \, V(\tau) \, \Omega(\tau)}} \quad , \tag{A.3.20}$$

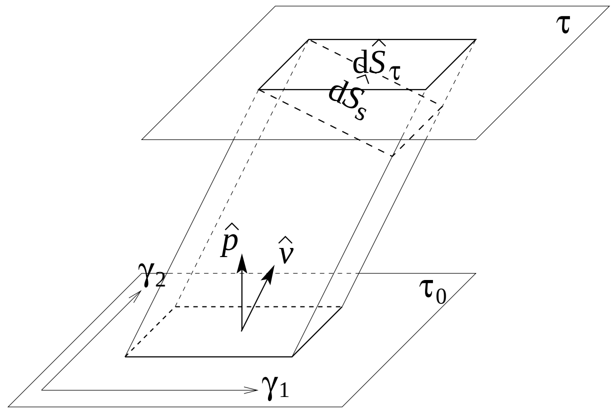

Figure A.1: A segment of a ray tube limited by cross sections with the phase front at $t = \tau = \tau_0 + \mathrm{d}\tau$ and $t = \tau_0$. The corners of the surface element $\mathrm{d}\hat{\boldsymbol{S}}_{\gamma_3}$ are given by rays with the ray parameters (γ_1, γ_2), $(\gamma_1 + \mathrm{d}\gamma_1, \gamma_2)$, $(\gamma_1 + \gamma_2 + \mathrm{d}\gamma_2)$, and $(\gamma_1 + \mathrm{d}\gamma_1, \gamma_2 + \mathrm{d}\gamma_2)$.

where the function $\Psi(\gamma_1, \gamma_2)$ is constant along the ray specified by the ray parameters (γ_1, γ_2), e.g., the take-off angles. If the arc length s is chosen as γ_3 instead of τ, Equation (A.3.20) becomes

$$U(\tau) = \frac{\Psi(\gamma_1, \gamma_2)}{\sqrt{\rho(\tau)\, v(\tau)\, \mathcal{J}_s(\tau)}} \quad , \tag{A.3.21}$$

since $\mathcal{J}_\tau = v\, \mathcal{J}_s$ follows from (A.3.10) and (A.3.9). At this point the relative geometrical spreading L is introduced as

$$L = \sqrt{\Omega} \quad . \tag{A.3.22}$$

Since the sign of $\mathcal{J}_{\gamma_3}$ may change, it is suitable to take the square root of $\mathcal{J}_{\gamma_3}$ as follows

$$\sqrt{\mathcal{J}_{\gamma_3}} = \sqrt{|\mathcal{J}_{\gamma_3}|}\; \mathrm{e}^{-i\frac{\pi}{2}\kappa} \quad , \tag{A.3.23}$$

where the quantity κ, the so-called KMAH-index is an index of the ray trajectory. It gives the number of points at which the sign of $\mathcal{J}_{\gamma_3}$ has changed. These points are called caustic points. A first order caustic increments κ by one, a second order caustic by two. The behaviour of a ray tube at caustic points of first and second order is illustrated in Figure A.2.
Literature for Section A.3:

- Červený (1972),
- Pšenčík (1994).

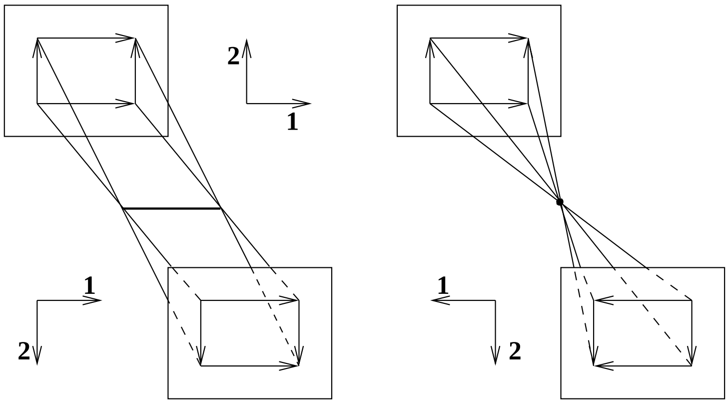

Figure A.2: Behaviour of a ray tube at caustic points: at a first order caustic (line caustic) the ray tube shrinks to an arc perpendicular to the direction of propagation (left). At a second order caustic (point caustic) the ray tube shrinks to a point (right). The vectors indicate that after going through a line caustic the direction of the surface element is changed, leading to a change in sign of $\mathcal{J}_{\gamma_3}$. If the ray passes a point caustic, the sign changes twice (resulting in the original sign).

A.4 Ray tracing

The phase function $\tau(x_i)$ can be found by solving the kinematic ray tracing (KRT) equations. They are easily obtained from applying the method of characteristics (Courant and Hilbert, 1962) to the eikonal Equation (A.2.6). If a Hamiltonian $\mathcal{H}(x_i, p_i, \tau)$=0 can be found, the characteristics in terms of the parameter u are described by

$$\frac{\mathrm{d}x_i}{\mathrm{d}u} = \frac{\partial \mathcal{H}}{\partial p_i} \quad , \qquad \frac{\mathrm{d}p_i}{\mathrm{d}u} = -\frac{\partial \mathcal{H}}{\partial x_i} \quad , \qquad \frac{\mathrm{d}\tau}{\mathrm{d}u} = p_i \frac{\partial \mathcal{H}}{\partial p_i} \quad . \tag{A.4.1}$$

One possible choice of a Hamiltonian is

$$\mathcal{H}(x_i, p_i) = G - 1 = a_{ijkl}\, p_j\, p_l\, g_i\, g_k = 0 \quad , \tag{A.4.2}$$

using an eigenvalue of the eikonal equation, G, and a_{ijkl}=c_{ijkl}/ρ, leading to the following KRT for the parameter τ

$$v_i = \frac{\mathrm{d}x_i}{\mathrm{d}\tau} = a_{ijkl}\, p_l\, g_j\, g_k \quad , \qquad \frac{\mathrm{d}p_i}{\mathrm{d}\tau} = -\frac{1}{2}\, a_{njkl,i}\, p_n\, p_l\, g_j\, g_k \quad , \tag{A.4.3}$$

where v_i is the i-th component of the group velocity vector. With $\mathrm{d}s/\mathrm{d}\tau = v$, the KRT system for the parameter s reads

$$\frac{\mathrm{d}x_i}{\mathrm{d}s} = \frac{1}{v}\, a_{ijkl}\, p_l\, g_j\, g_k \quad , \qquad \frac{\mathrm{d}p_i}{\mathrm{d}s} = -\frac{1}{2\,v}\, a_{njkl,i}\, p_n\, p_l\, g_j\, g_k \quad . \tag{A.4.4}$$

For isotropic media the systems (A.4.3) and (A.4.4) reduce to

$$\frac{\mathrm{d}x_i}{\mathrm{d}\tau} = V^2\, p_i \quad , \qquad \frac{\mathrm{d}p_i}{\mathrm{d}\tau} = -\frac{1}{V}\, \frac{\partial V}{\partial x_i} \quad , \tag{A.4.5}$$

$$\frac{\mathrm{d}x_i}{\mathrm{d}s} = V\, p_i \quad , \qquad \frac{\mathrm{d}p_i}{\mathrm{d}s} = -\frac{1}{V^2}\, \frac{\partial V}{\partial x_i} \quad . \tag{A.4.6}$$

To compute the ray amplitude, the quantity $\mathcal{J}_{\gamma_3} = \det\underline{\hat{X}}$ needs to be determined. Defining the matrix $\underline{\hat{Y}}$

$$Y_{ij} = \frac{\partial p_i}{\partial \gamma_j} \quad , \tag{A.4.7}$$

the dynamic ray tracing (DRT) equations are obtained from differentiating the KRT Equations (A.4.3) or (A.4.4) with respect to the ray parameters γ_J (J=1,2). For, e.g., γ_3=τ this yields

$$\begin{aligned}\frac{\mathrm{d}X_{iJ}}{\mathrm{d}\tau} &= \frac{1}{2}\left[\frac{\partial^2 G}{\partial p_i\,\partial x_k}\,X_{kJ} + \frac{\partial^2 G}{\partial p_i\,\partial p_k}\,Y_{kJ}\right] \quad , \\ \frac{\mathrm{d}Y_{iJ}}{\mathrm{d}\tau} &= -\frac{1}{2}\left[\frac{\partial^2 G}{\partial x_i\,\partial x_k}\,X_{kJ} + \frac{\partial^2 G}{\partial x_i\,\partial p_k}\,Y_{kJ}\right] \quad .\end{aligned} \tag{A.4.8}$$

The elements $X_{i3} = \frac{\partial x_i}{\partial \tau}$ and $Y_{i3} = \frac{\partial p_i}{\partial \tau}$ can be determined directly from the ray tracing Equations (A.4.3).

For isotropic media the DRT system looks as follows

$$\begin{aligned}\frac{\mathrm{d}X_{iJ}}{\mathrm{d}\tau} &= 2\,V\,\frac{\partial V}{\partial x_k}\,p_i X_{kJ} + V^2 Y_{iJ} \\ \frac{\mathrm{d}Y_{iJ}}{\mathrm{d}\tau} &= \left[\frac{1}{V^2}\,\frac{\partial V}{\partial x_i}\,\frac{\partial V}{\partial x_k} - \frac{1}{V}\,\frac{\partial^2 V}{\partial x_i \partial x_k}\right] X_{kJ} \quad .\end{aligned} \tag{A.4.9}$$

This equation and (A.4.5) require that the velocity function V must have continuous derivatives up to second order. The behaviour of rays at interfaces where this is not the case is discussed further below.

Literature for Section A.4:

- Červený (1972),
- Gajewski and Pšenčík (1990).

A.5 Ray-centred coordinates

Sometimes it is convenient to work with a ray centred coordinate system instead of global Cartesian coordinates. This is for example the case if so-called paraxial rays, rays in the near vicinity of a central ray, are to be computed. The radius vector in the ray centred system is given by

$$\hat{\boldsymbol{r}}(q_1, q_2, s) = \hat{\boldsymbol{r}}(0,0,s) + \vec{\boldsymbol{e}}_1(s)\,q_1 + \vec{\boldsymbol{e}}_2(s)\,q_2 \quad . \tag{A.5.1}$$

On the central ray q_1=q_2=0. Whether a ray is in a "near vicinity" of the central ray depends on the model under consideration. The vectors

$$\begin{aligned}\vec{\boldsymbol{e}}_1 &= \vec{\boldsymbol{n}}\cos\theta - \vec{\boldsymbol{b}}\sin\theta \\ \vec{\boldsymbol{e}}_2 &= \vec{\boldsymbol{n}}\sin\theta + \vec{\boldsymbol{b}}\cos\theta\end{aligned} \tag{A.5.2}$$

and the tangent vector $\vec{\boldsymbol{t}}$ form an orthogonal base. Vector $\vec{\boldsymbol{t}}$ is perpendicular to the wavefront, $\vec{\boldsymbol{e}}_I$ (I=1,2) lie in the wavefront. The vectors $\vec{\boldsymbol{n}}$ and $\vec{\boldsymbol{b}}$ are the normal and binormal vector (see Figure

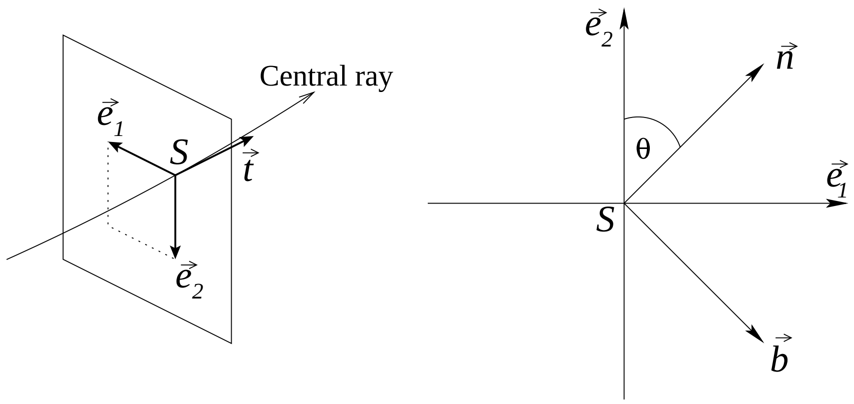

Figure A.3: Definition of the ray centred coordinate system: position of the base vectors with respect to the central ray and the wavefront. The surface indicates the tangent plane to the wavefront, perpendicular to the central ray (left). Right: unit vectors $\vec{e}_1$ and $\vec{e}_2$, and normal and binormal vectors, $\vec{n}$ and $\vec{b}$, respectively.

A.3). They and $\vec{t}$ obey Frenet's formulae. The angle θ between $\vec{e}_1$ and $\vec{b}$, as between $\vec{e}_2$ and $\vec{n}$ can be obtained from the integration over the torsion T along the ray

$$\theta(s) = \theta(s_0) + \int_{s_0}^{s} T(\sigma)\,\mathrm{d}\sigma \quad . \tag{A.5.3}$$

The scale parameters h_1 and h_2 (with $h_I = |\mathrm{d}\hat{\boldsymbol{r}}/\mathrm{d}q_I|$) are equal to one, and $h_3 = h$, with the curvature of the ray K, is

$$h_3 = h = \left|\frac{\mathrm{d}\hat{\boldsymbol{r}}}{\mathrm{d}s}\right| = 1 - K\cos\theta\, q_1 - K\sin\theta\, q_2 \quad . \tag{A.5.4}$$

Derivation of the base vectors yields

$$\begin{aligned}
\frac{\mathrm{d}\vec{e}_1}{\mathrm{d}s} &= \qquad -K\cos\theta\,\vec{t} \qquad = \left(\frac{\mathrm{d}\vec{t}}{\mathrm{d}s}\cdot\vec{e}_1\right)\vec{t} \\
\frac{\mathrm{d}\vec{e}_2}{\mathrm{d}s} &= \qquad -K\sin\theta\,\vec{t} \qquad = \left(\frac{\mathrm{d}\vec{t}}{\mathrm{d}s}\cdot\vec{e}_2\right)\vec{t} \\
\frac{\mathrm{d}\vec{t}}{\mathrm{d}s} &= K\cos\theta\,\vec{e}_1 + K\sin\theta\,\vec{e}_2 = \left(\frac{\mathrm{d}\vec{t}}{\mathrm{d}s}\cdot\vec{e}_I\right)\vec{e}_I
\end{aligned} \tag{A.5.5}$$

The derivatives of $\vec{e}_I$ point in the direction of $\vec{t}$. This means that – unlike the vectors $\vec{n}$ and $\vec{b}$ – the vectors $\vec{e}_I$ do not rotate during propagation along the central ray. Comparison of (A.5.5) to (A.5.4) leads to an expression for h

$$h = 1 - \left(\frac{\mathrm{d}\vec{t}}{\mathrm{d}s}\cdot\vec{e}_I\right) q_I \quad . \tag{A.5.6}$$

The scale parameter h can be expressed in terms of derivatives of the phase velocity. Because the ray tracing equations for isotropic media, (A.4.6), are employed in the following step, the resulting relation holds for isotropic media only. Using $\vec{\boldsymbol{t}} = V\,\hat{\boldsymbol{p}}$ and the ray tracing Equations (A.4.6), the derivative of the tangent vector in isotropic media becomes

$$\frac{\mathrm{d}\hat{\boldsymbol{t}}}{\mathrm{d}s} = -\frac{1}{V}\left.\frac{\partial V}{\partial q_I}\right|_{q_K=0} \vec{\boldsymbol{e}}_I \quad , \tag{A.5.7}$$

and therefore

$$h = 1 + \frac{1}{V}\left.\frac{\partial V}{\partial q_I}\right|_{q_K=0} q_I \quad . \tag{A.5.8}$$

On the central ray, the coordinates q_I are zero and therefore h=1.

In order to derive the ray tracing equations in ray centred coordinates, the Hamilton Equations (A.4.1) can be used. I will derive the ray tracing equations for isotropic media only, however, use of a Hamiltonian for anisotropic media will lead to an equivalent formulation for anisotropic media, see, e.g., Červený (2001). A suitable Hamiltonian for isotropic media in the ray centred coordinate system is

$$\mathcal{H}\left(q_I, p_I^{(q)}\right) = -\frac{h}{V}\left[1 - V^2\, p_I^{(q)} p_I^{(q)}\right]^{1/2} \quad , \tag{A.5.9}$$

where $p_I^{(q)}$ is the I-th slowness component in ray centred coordinates. To derive the ray tracing system for paraxial rays, this Hamiltonian is expanded in $p_I^{(q)}$ and q_I neglecting terms of higher than second order

$$\mathcal{H}\left(q_I, p_I^{(q)}\right) = -\frac{1}{V} + \frac{1}{2}\,V\,p_I^{(q)} p_I^{(q)} + \frac{1}{2V^2}\frac{\partial^2 V}{\partial q_I\,\partial q_J}\,q_I\,q_J \quad , \tag{A.5.10}$$

leading to the kinematic ray tracing equations

$$\begin{aligned} \frac{\mathrm{d}q_I}{\mathrm{d}s} &= \frac{\partial \mathcal{H}}{\partial p_I^{(q)}} = V\,p_I^{(q)} \quad , \\ \frac{\mathrm{d}p_I^{(q)}}{\mathrm{d}s} &= -\frac{\partial \mathcal{H}}{\partial q_I} = -\frac{1}{V}\,\frac{\partial^2 V}{\partial q_I\,\partial q_J}\,q_J \quad . \end{aligned} \tag{A.5.11}$$

For the determination of the ray amplitude, the matrix $\hat{\underline{\mathsf{X}}}$ is expressed as a product of two matrices $\hat{\underline{\mathsf{H}}}$ and $\hat{\underline{\mathsf{Q}}}$. The Jacobian of the transformation from Cartesian to ray centred coordinates along the central ray ($q_I = 0$) is denoted by $\hat{\underline{\mathsf{H}}}$. Then, the elements of $\hat{\underline{\mathsf{H}}}$ are given by

$$H_{ij} = \frac{\partial x_i}{\partial q_j} = \frac{\partial q_j}{\partial x_i} \quad , \tag{A.5.12}$$

where $q_3 = s$. On the central ray, $h = 1$, and therefore $\det\hat{\underline{\mathsf{H}}}$=1. The matrix $\hat{\underline{\mathsf{Q}}}$ is the Jacobian for the transformation from ray centred coordinates to ray coordinates on the central ray with

$$Q_{ij} = \frac{\partial q_i}{\partial \gamma_j} \quad . \tag{A.5.13}$$

Since $q_I = 0$ along the central ray, the components $Q_{13} = Q_{23} = 0$. Specifying $\gamma_3 = s$ yields Q_{33}=1 and thus

$$\det\hat{\underline{\mathsf{X}}} = \det\hat{\underline{\mathsf{H}}}\cdot\det\hat{\underline{\mathsf{Q}}} = Q_{11}\,Q_{22} - Q_{12}\,Q_{21} = \det\underline{\mathsf{Q}} \quad . \tag{A.5.14}$$

This means that the ray amplitude is determined by $\underline{\mathsf{Q}}$, which is the upper left 2×2 submatrix of $\hat{\underline{\mathsf{Q}}}$. For the geometrical spreading this means that

$$L = \sqrt{\det\underline{\mathsf{Q}}} \quad . \tag{A.5.15}$$

Note that Equation (A.5.15) is also valid in anisotropic media.

Introducing also the 2×2 matrix $\underline{\mathsf{P}}$ with

$$P_{IJ} = \frac{\partial p_I^{(q)}}{\partial \gamma_J} \tag{A.5.16}$$

and differentiation of Q_{IJ} and P_{IJ} with respect to s leads to the DRT system in ray centred coordinates

$$\frac{\mathrm{d}Q_{IJ}}{\mathrm{d}s} = V\, P_{IJ} \quad , \qquad \frac{\mathrm{d}P_{IJ}}{\mathrm{d}s} = -\frac{1}{V^2}\, V_{JK}\, P_{KJ} \quad . \tag{A.5.17}$$

The 2×2 matrix $\underline{\mathsf{V}}$ contains second order derivatives of the velocity

$$V_{IJ} = \left.\frac{\partial^2 V}{\partial q_I\, \partial q_J}\right|_{q_K=0} \quad . \tag{A.5.18}$$

The DRT system (A.5.17) can be rewritten to another form, if the matrix $\underline{\mathsf{M}} = \underline{\mathsf{P}}\,\underline{\mathsf{Q}}^{-1}$ is introduced. Differentiation of $\underline{\mathsf{M}}$ leads to

$$\frac{\mathrm{d}}{\mathrm{d}s}\,\underline{\mathsf{M}} + V\, \underline{\mathsf{M}}\,\underline{\mathsf{M}} + \frac{1}{V^2}\,\underline{\mathsf{V}} = \underline{0} \quad , \tag{A.5.19}$$

which is known as the Ricatti equation. Equation (A.5.19) can also be derived from the paraxial eikonal equation. The eikonal equation in ray centred coordinates reads

$$\tau_{,1}^2 + \tau_{,2}^2 + \frac{1}{h^2}\,\tau_{,s}^2 = \frac{1}{V^2} \quad . \tag{A.5.20}$$

Taking into consideration that $\tau_{,I} = p_I^{(q)}$, (A.5.20) can be solved for $\tau_{,s}$

$$\tau_{,s} = \frac{h}{V}\sqrt{1 - V^2\, p_I^{(q)}\, p_I^{(q)}} = -H\left(q_I, p_I^{(q)}\right) \quad , \tag{A.5.21}$$

where $H\left(q_I, p_I^{(q)}\right)$ is the Hamiltonian from Equation (A.5.9). Using the approximation of the Hamiltonian (A.5.10) and inserting $\tau_{,I}$ and $\tau_{,s}$ into (A.5.20), this leads to the paraxial eikonal equation

$$\left(\frac{\partial \tau}{\partial q_1}\right)^2 + \left(\frac{\partial \tau}{\partial q_2}\right)^2 + \left(\frac{\partial \tau}{\partial s}\right)^2 = \frac{1}{V^2} - \frac{1}{V^3}\, V_{IJ}\, q_I\, q_J \quad , \tag{A.5.22}$$

where the matrix $\underline{\mathsf{V}}$ was defined in (A.5.18). For the following step an expansion of the eikonal τ is required. Expansion of τ in q_I yields

$$\tau(q_1, q_2, s) = \tau(0, 0, s) + \frac{1}{2}\, M_{IJ}\, q_I\, q_J \quad , \tag{A.5.23}$$

where the matrix $\underline{\mathsf{M}}(s)$ is the second order derivative matrix of τ with respect to q_I

$$M_{IJ} = \left.\frac{\partial^2 \tau}{\partial q_I\, \partial q_J}\right|_{q_K=0} \quad . \tag{A.5.24}$$

From now on, $\tau(s)$ is used to abbreviate $\tau(0,0,s)$. The first order derivatives disappear because the expansion is carried out in the wavefront, where τ is constant. Building the derivative of (A.5.23) with respect to s yields

$$\frac{\partial \tau(q_1, q_2, s)}{\partial s} = \frac{\partial \tau(s)}{\partial s} + \frac{1}{2}\,\frac{\mathrm{d}M_{IJ}}{\mathrm{d}s}\, q_I\, q_J = \frac{1}{V} + \frac{1}{2}\,\frac{\mathrm{d}M_{IJ}}{\mathrm{d}s}\, q_I\, q_J \quad . \tag{A.5.25}$$

Similarly, derivation of (A.5.23) with respect to q_I yields

$$\left(\frac{\partial\tau}{\partial q_1}\right)^2 + \left(\frac{\partial\tau}{\partial q_2}\right)^2 = M_{IK}\, M_{KJ}\, q_I\, q_J \quad . \tag{A.5.26}$$

Inserting the found expressions for $\tau_{,s}$ and $\tau_{,I}$ into (A.5.22) gives again the Ricatti equation. Therefore, the matrix $\underline{\mathsf{M}}$ from (A.5.19) equals the second order derivative matrix introduced in (A.5.23) with

$$M_{IJ} = P_{IK}\, Q^{-1}_{KJ} = \left.\frac{\partial^2\tau}{\partial q_I\, \partial q_J}\right|_{q_K=0} \quad . \tag{A.5.27}$$

Literature for Section A.5:

- Popov and Pšenčík (1978),
- Červený and Hron (1980).

A.6 Propagator matrices

Introducing the 4×1 column matrix $\underline{\mathsf{W}}$

$$\underline{\mathsf{W}} = (q_1, q_2, p_1^{(q)}, p_2^{(q)})^\top \quad , \tag{A.6.1}$$

the ray tracing system (A.5.11) can be written as

$$\frac{\mathrm{d}}{\mathrm{d}s}\underline{\mathsf{W}} = \underline{\underline{\mathsf{S}}}\,\underline{\mathsf{W}} \quad , \tag{A.6.2}$$

where the 4×4 matrix $\underline{\underline{\mathsf{S}}}$ is given by

$$\underline{\underline{\mathsf{S}}} = \begin{pmatrix} \underline{\mathsf{0}} & \underline{\mathsf{1}} \\ -\frac{1}{V^2}\underline{\mathsf{V}} & \underline{\mathsf{0}} \end{pmatrix} \quad . \tag{A.6.3}$$

The matrices $\underline{\mathsf{0}}$ and $\underline{\mathsf{1}}$ are the zero and unit matrix (2×2 here). A ray tracing system for anisotropic media that corresponds to the system (A.5.11) can be derived yielding also Equation (A.6.2). In this case the matrix $\underline{\underline{\mathsf{S}}}$ is not given by Equation (A.6.3), but the following considerations also apply to anisotropic media.

A 4×4 matrix $\underline{\underline{\mathsf{A}}}$ is called an integral matrix, if it satisfies the relation

$$\frac{\mathrm{d}}{\mathrm{d}s}\underline{\underline{\mathsf{A}}} = \underline{\underline{\mathsf{S}}}\,\underline{\underline{\mathsf{A}}} \quad , \tag{A.6.4}$$

meaning that each column of $\underline{\underline{\mathsf{A}}}$ obeys Equation (A.6.2). If $\underline{\underline{\mathsf{A}}} = \underline{\underline{\mathsf{1}}}$ for $s = s_0$, $\underline{\underline{\mathsf{A}}}$ is also a propagator matrix (from s_0). If $\underline{\underline{\mathsf{A}}}$ is an integral matrix formed by four linear independent solutions of (A.6.2), it is called a fundamental matrix.

The ray propagator matrix $\underline{\underline{\Pi}}(s, s_0)$ is a fundamental matrix formed as follows

$$\underline{\underline{\Pi}}(s, s_0) = \begin{pmatrix} \underline{\mathsf{Q}}_1(s, s_0) & \underline{\mathsf{Q}}_2(s, s_0) \\ \underline{\mathsf{P}}_1(s, s_0) & \underline{\mathsf{P}}_2(s, s_0) \end{pmatrix} \quad , \tag{A.6.5}$$

where $\underline{Q}_1$, $\underline{Q}_2$, $\underline{P}_1$ and $\underline{P}_2$ are 2×2 matrices with the following meaning: $\underline{Q}_1$ and $\underline{P}_1$ are solutions of the dynamic ray tracing Equations (A.5.17) for the initial conditions

$$\underline{Q}_1(s_0) = \underline{1} \quad \text{and} \quad \underline{P}_1(s_0) = \underline{0} \quad , \tag{A.6.6}$$

that describe a line source. $\underline{Q}_2$ and $\underline{P}_2$ also solve the dynamic ray tracing Equations (A.5.17), but for initial conditions of a point source

$$\underline{Q}_2(s_0) = \underline{0} \quad \text{and} \quad \underline{P}_2(s_0) = \underline{1} \quad . \tag{A.6.7}$$

If $\underline{\underline{S}}$ is continuous, the ray propagator matrix satisfies the chain rule

$$\underline{\underline{\Pi}}(s, s_0) = \underline{\underline{\Pi}}(s, s_1)\, \underline{\underline{\Pi}}(s_1, s_0) \quad . \tag{A.6.8}$$

With

$$\underline{\underline{\Pi}}(s_0, s_0) = \underline{\underline{\Pi}}(s_0, s_1)\, \underline{\underline{\Pi}}(s_1, s_0) = \underline{\underline{1}} \quad , \tag{A.6.9}$$

it follows that

$$\underline{\underline{\Pi}}^{-1}(s_1, s_0) = \underline{\underline{\Pi}}(s_0, s_1) \quad , \tag{A.6.10}$$

which leads to

$$\underline{\underline{\Pi}}^{-1}(s, s_0) = \begin{pmatrix} \underline{P}_2^\top(s, s_0) & -\underline{Q}_2^\top(s, s_0) \\ -\underline{P}_1^\top(s, s_0) & \underline{Q}_1^\top(s, s_0) \end{pmatrix} \quad . \tag{A.6.11}$$

The propagator $\underline{\underline{\Pi}}$ is symplectic, meaning

$$\underline{\underline{\Pi}}^\top\, \underline{\underline{J}}\, \underline{\underline{\Pi}} = \underline{\underline{J}} \quad , \tag{A.6.12}$$

with the matrix

$$\underline{\underline{J}} = \begin{pmatrix} \underline{0} & \underline{1} \\ -\underline{1} & \underline{0} \end{pmatrix} \quad . \tag{A.6.13}$$

This property yields the following relations

$$\begin{aligned} \underline{Q}_1^\top \underline{P}_1 - \underline{P}_1^\top \underline{Q}_1 &= \underline{0} \quad , \\ \underline{Q}_2^\top \underline{P}_2 - \underline{P}_2^\top \underline{Q}_2 &= \underline{0} \quad , \\ \underline{P}_2^\top \underline{Q}_1 - \underline{Q}_2^\top \underline{P}_1 &= \underline{1} \quad , \\ \underline{Q}_1^\top \underline{P}_2 - \underline{P}_1^\top \underline{Q}_2 &= \underline{1} \quad . \end{aligned} \tag{A.6.14}$$

With $\underline{\underline{\Pi}}(s, s_0)$ the solution of Equation (A.6.2) can be written as

$$\underline{W}(s) = \underline{\underline{\Pi}}(s, s_0)\, \underline{W}(s_0) \tag{A.6.15}$$

for any initial conditions given at s_0 represented by $\underline{W}(s_0)$. A similar solution exists for a (A.6.2)-like equation for the 4×2 matrix $\underline{X}$

$$\underline{X} = \begin{pmatrix} \underline{Q} \\ \underline{P} \end{pmatrix} \quad , \tag{A.6.16}$$

which is not to be mistaken for the matrix $\underline{\hat{X}}$ defined in (A.3.8). The dynamic ray tracing system (A.5.17) can thus be rewritten as

$$\frac{\mathrm{d}}{\mathrm{d}s}\underline{X} = \underline{\underline{S}}\, \underline{X} \quad , \tag{A.6.17}$$

and is solved by

$$\underline{X}(s) = \underline{\underline{\Pi}}(s, s_0)\, \underline{X}(s_0) \quad . \tag{A.6.18}$$

Literature for Section A.6:

- Červený (1985),
- Červený (2001).

A.7 Paraxial traveltimes

Using Equation (A.5.23), the traveltime for a point (q_1, q_2, s) in a vicinity of a point $(0, 0, s_0)$ (see Figure A.4) can be written as

$$\tau(q_1, q_2, s) = \tau(s_0) + \left.\frac{\partial \tau}{\partial s}\right|_{s_0} (s - s_0) + \frac{1}{2} \left.\frac{\partial^2 \tau}{\partial s^2}\right|_{s_0} (s - s_0)^2 + \frac{1}{2} M_{IJ}(s_0) q_I q_J \quad . \tag{A.7.1}$$

The s-derivatives are evaluated with (A.5.25). Keeping only terms up to first order leads to

$$\left.\frac{\partial \tau}{\partial s}\right|_{s_0} = \frac{1}{V_0} \quad \Rightarrow \quad \left.\frac{\partial^2 \tau}{\partial s^2}\right|_{s_0} = -\frac{1}{V_0^2} \left.\frac{\partial V}{\partial s}\right|_{s_0} \quad , \tag{A.7.2}$$

where $V_0 = V(s_0)$. These expressions are inserted into (A.7.1) yielding

$$\tau(q_1, q_2, s) = \tau(s_0) + \frac{1}{V_0} (s - s_0) - \frac{1}{2\, V_0^2} \left.\frac{\partial V}{\partial s}\right|_{s_0} (s - s_0)^2 + \frac{1}{2} M_{IJ}(s_0) q_I q_J \quad . \tag{A.7.3}$$

The traveltime for a paraxial ray can also be expressed in local Cartesian coordinates $\hat{\boldsymbol{y}}$ with $y_I = q_I$ and $y_3 = h(s - s_0)$. Introducing the 3×3 matrix $\underline{\hat{\mathsf{M}}}$

$$\underline{\hat{\mathsf{M}}} = \begin{pmatrix} M_{11} & M_{12} & -\frac{1}{V_0^2} \left.\frac{\partial V}{\partial y_1}\right|_{s_0} \\ M_{21} & M_{22} & -\frac{1}{V_0^2} \left.\frac{\partial V}{\partial y_2}\right|_{s_0} \\ -\frac{1}{V_0^2} \left.\frac{\partial V}{\partial y_1}\right|_{s_0} & -\frac{1}{V_0^2} \left.\frac{\partial V}{\partial y_2}\right|_{s_0} & -\frac{1}{V_0^2} \left.\frac{\partial V}{\partial y_3}\right|_{s_0} \end{pmatrix} \tag{A.7.4}$$

and the slowness vector in local Cartesian coordinates

$$\hat{\boldsymbol{p}}^{(y)}(s_0) = \begin{pmatrix} 0 \\ 0 \\ \frac{1}{V_0} \end{pmatrix} \quad , \tag{A.7.5}$$

the paraxial traveltime becomes

$$\tau(y_i) = \tau(s_0) + p_i^{(y)}(s_0) y_i + \frac{1}{2} M_{ij} y_i y_j \quad . \tag{A.7.6}$$

To determine the slowness vector $\hat{\boldsymbol{p}}^{(y)}(s)$, the gradient of (A.7.6) with respect to y is taken:

$$p_i^{(y)}(s) = p_i^{(y)}(s_0) + M_{ij} y_j \quad . \tag{A.7.7}$$

This substituted in (A.7.6) yields another expression for $\tau(y_i)$:

$$\tau(y_i) = \tau(s_0) + \frac{1}{2} \left(p_i^{(y)}(s) + p_i^{(y)}(s_0) \right) y_i \quad . \tag{A.7.8}$$

In general Cartesian coordinates $\hat{\boldsymbol{x}}$ Equation (A.7.6) becomes

$$\tau(x_i) = \tau(s_0) + p_i^{(x)}(s_0) x_i + \frac{1}{2} H_{ik} M_{kl} H_{jl} x_i x_j \quad . \tag{A.7.9}$$

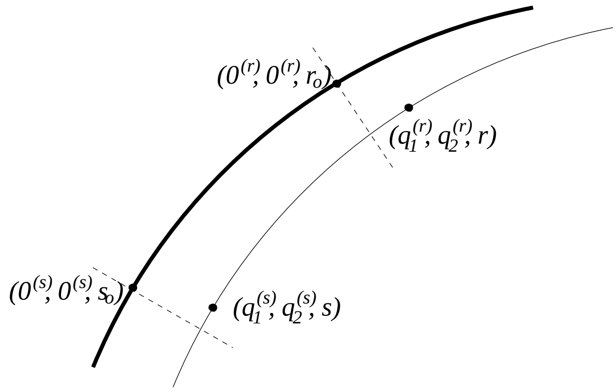

Figure A.4: Central ray (bold) and a paraxial ray. The dashed lines indicate the wavefronts.

Suppose now that the propagator matrix $\underline{\Pi}(r_0, s_0)$ for a ray from s_0 to r_0 be known (see Figure A.4). Let the slowness vectors $\boldsymbol{p}^{(q)}$ at $\boldsymbol{q}^{(r)}$ and $\boldsymbol{q}^{(s)}$ be denoted by the corresponding index. Then the relationship between $\boldsymbol{q}^{(r)}$, $\boldsymbol{p}^{(r)}$, $\boldsymbol{q}^{(s)}$ and $\boldsymbol{p}^{(s)}$ is given by (A.6.15):

$$\begin{aligned} \boldsymbol{q}^{(r)} &= \underline{Q}_1(r_0, s_0)\, \boldsymbol{q}^{(s)} + \underline{Q}_2(r_0, s_0)\, \boldsymbol{p}^{(s)} \quad , \\ \boldsymbol{p}^{(r)} &= \underline{P}_1(r_0, s_0)\, \boldsymbol{q}^{(s)} + \underline{P}_2(r_0, s_0)\, \boldsymbol{p}^{(s)} \quad . \end{aligned} \tag{A.7.10}$$

Using (A.6.14) and $\underline{M} = \underline{P}_2 \underline{Q}_2^{-1}$ for a point source, these equations can be solved for the slownesses, yielding

$$\begin{aligned} \boldsymbol{p}^{(s)} &= \underline{Q}_2^{-1}(r_0, s_0)\, \boldsymbol{q}^{(r)} + \underline{M}(s_0, r_0)\, \boldsymbol{q}^{(s)} \quad , \\ \boldsymbol{p}^{(r)} &= \underline{M}(r_0, s_0)\, \boldsymbol{q}^{(r)} \quad + \underline{Q}_2^{-\top}(r_0, s_0)\, \boldsymbol{q}^{(s)} \quad . \end{aligned} \tag{A.7.11}$$

With these expressions for the slownesses in ray centred coordinates, the according formulations in local Cartesian coordinates are

$$\begin{aligned} \hat{\boldsymbol{p}}^{(y)}(s) &= \hat{\boldsymbol{p}}^{(y)}(s_0) + \underline{Q}_2^{-1}(r_0, s_0)\, \boldsymbol{y}(r) + \underline{M}(s_0, r_0)\, \boldsymbol{y}(s) - \frac{1}{V_0^2} \left. \frac{\partial c}{\partial y_i} \right|_{s_0} y_i \\ &= \hat{\boldsymbol{p}}^{(y)}(s_0) + \underline{Q}_2^{-1}(r_0, s_0)\, \boldsymbol{y}(r) + \underline{\hat{M}}(s_0, r_0)\, \hat{\boldsymbol{y}}(s) \quad , \\ \hat{\boldsymbol{p}}^{(y)}(r) &= \hat{\boldsymbol{p}}^{(y)}(r_0) - \underline{Q}_2^{-\top}(r_0, s_0)\, \boldsymbol{y}(s) + \underline{\hat{M}}(r_0, s_0)\, \hat{\boldsymbol{y}}(r) \quad . \end{aligned} \tag{A.7.12}$$

Now $\tau(r, s) = \tau(r) - \tau(s)$ is built by using Equation (A.7.8)for $\tau(r)$ and $\tau(s)$ and inserting (A.7.12). This leads to

$$\begin{aligned} \tau(r, s) &= \tau(r_0) - \tau(s_0) + \hat{\boldsymbol{p}}^{(y)}(r_0) \cdot \hat{\boldsymbol{y}}(r) - \hat{\boldsymbol{p}}^{(y)}(s_0) \cdot \hat{\boldsymbol{y}}(s) \\ &\quad + \frac{1}{2}\, \hat{\boldsymbol{y}}(r) \cdot \underline{\hat{M}}(r_0, s_0) \hat{\boldsymbol{y}}(r) - \frac{1}{2}\, \hat{\boldsymbol{y}}(s) \cdot \underline{\hat{M}}(s_0, r_0) \hat{\boldsymbol{y}}(s) \\ &\quad - \frac{1}{2} \left[\hat{\boldsymbol{y}}(r) \cdot \underline{\hat{Q}}_2^{-\top}\, \hat{\boldsymbol{y}}(s) + \hat{\boldsymbol{y}}(s) \cdot \underline{\hat{Q}}_2^{-}\, \hat{\boldsymbol{y}}(r) \right] \quad , \end{aligned} \tag{A.7.13}$$

introducing the matrix $\underline{\hat{Q}}_2^{-}$ and its transposed $\underline{\hat{Q}}_2^{-\top}$ such that $\underline{Q}_2^{-1}$ is the upper left submatrix of $\underline{\hat{Q}}_2^{-}$ and the elements $\underline{\hat{Q}}_{2_{i3}}^{-}$ and $\underline{\hat{Q}}_{2_{3i}}^{-}$ are zero. With

$$\hat{\boldsymbol{y}}(r) \cdot \underline{\hat{Q}}_2^{-\top}\, \hat{\boldsymbol{y}}(s) = \hat{\boldsymbol{y}}(s) \cdot \underline{\hat{Q}}_2^{-}\, \hat{\boldsymbol{y}}(r) \tag{A.7.14}$$

and $\tau_0 = \tau(r_0) - \tau(s_0)$ the final result for the paraxial traveltime from s to r in local Cartesian coordinates becomes

$$\begin{aligned}\tau(r,s) &= \tau_0 + \hat{\boldsymbol{p}}^{(y)}(r_0)\cdot\hat{\boldsymbol{y}}(r) - \hat{\boldsymbol{p}}^{(y)}(s_0)\cdot\hat{\boldsymbol{y}}(s) - \hat{\boldsymbol{y}}(s)\cdot\hat{\underline{\mathsf{Q}}}_2^{-}\hat{\boldsymbol{y}}(r)\\ &\quad +\frac{1}{2}\,\hat{\boldsymbol{y}}(r)\cdot\hat{\underline{\mathsf{M}}}(r_0,s_0)\hat{\boldsymbol{y}}(r) - \frac{1}{2}\,\hat{\boldsymbol{y}}(s)\cdot\hat{\underline{\mathsf{M}}}(s_0,r_0)\hat{\boldsymbol{y}}(s) \quad . \end{aligned} \tag{A.7.15}$$

Again, this can also be written in general Cartesian coordinates $\hat{\boldsymbol{x}}$:

$$\begin{aligned}\tau(r,s) &= \tau_0 + \hat{\boldsymbol{p}}^{(x)}(r_0)\cdot\hat{\boldsymbol{x}}(r) - \hat{\boldsymbol{p}}^{(x)}(s_0)\cdot\hat{\boldsymbol{x}}(s) - \hat{\boldsymbol{x}}(s)\cdot\hat{\underline{\mathsf{H}}}(s_0)\hat{\underline{\mathsf{Q}}}_2^{-}\hat{\underline{\mathsf{H}}}^{\top}(r_0)\hat{\boldsymbol{x}}(r)\\ &\quad +\frac{1}{2}\,\hat{\boldsymbol{x}}(r)\cdot\hat{\underline{\mathsf{H}}}(r_0)\hat{\underline{\mathsf{M}}}(r_0,s_0)\hat{\underline{\mathsf{H}}}^{\top}(r_0)\hat{\boldsymbol{x}}(r)\\ &\quad -\frac{1}{2}\,\hat{\boldsymbol{x}}(s)\cdot\hat{\underline{\mathsf{H}}}(s_0)\hat{\underline{\mathsf{M}}}(s_0,r_0)\hat{\underline{\mathsf{H}}}^{\top}(s_0)\hat{\boldsymbol{x}}(s) \quad . \end{aligned} \tag{A.7.16}$$

Although isotropic equations were used for the derivation of the resulting traveltime expressions, they are also valid in anisotropic media, provided that the corresponding anisotropic matrices $\hat{\underline{\mathsf{M}}}$ and $\underline{\mathsf{Q}}_2$ are used, see Červený (2001).
Literature for Section A.7:

- Červený (1985),
- Červený (2001).

A.8 Interfaces

Until now velocities were assumed to be continuous functions with continuous first and second derivatives. This section describes the influence of a smooth curved interface, where the velocity has a discontinuity. If a ray arrives at a boundary between two different media, it will undergo an abrupt change in direction. This results in a discontinuity also in the matrix $\hat{\underline{\mathsf{M}}}$. The purpose of this section is to determine the transformation of slowness vectors and matrices $\hat{\underline{\mathsf{M}}}$ over interfaces.

Consider the traveltimes of incoming and outgoing (meaning reflected or transmitted) waves described by (A.7.6) in local Cartesian coordinates, where the point $s_0 = b$ lies on the boundary. Since the direction of the ray changes on impinging on the boundary, the base vectors of the ray centred coordinates associated with the incoming and outgoing wave do not coincide. Therefore, yet another set of Cartesian coordinates $\hat{\boldsymbol{z}}$ is introduced, that is associated with the interface. Its base vectors $\vec{\boldsymbol{\imath}}_i$ are defined as follows (see Figure A.5):

1. The normal to the interface corresponds to $\vec{\boldsymbol{\imath}}_3$. It points into the medium of the incident wave, meaning that $\hat{\boldsymbol{p}}\cdot\vec{\boldsymbol{\imath}}_3 <0$.
2. The base vector $\vec{\boldsymbol{\imath}}_1$ is oriented along the intersection of the interfaces tangent plane with the plane of incidence. Its direction is such that $\hat{\boldsymbol{p}}\cdot\vec{\boldsymbol{\imath}}_1 >0$.
3. Vector $\vec{\boldsymbol{\imath}}_2$ is tangent vector to the interface and perpendicular to the plane of incidence, $\vec{\boldsymbol{\imath}}_2 = \vec{\boldsymbol{\imath}}_3 \times \vec{\boldsymbol{\imath}}_1$.

The case of vertical incidence is not considered. Note that different directions are used throughout the literature. The transformation between this interface Cartesian coordinate system and the general Cartesian system is described by the matrix $\hat{\underline{\mathsf{Z}}}$ with

$$Z_{ij} = \frac{\partial x_i}{\partial z_j} = \frac{\partial z_j}{\partial x_i} \tag{A.8.1}$$

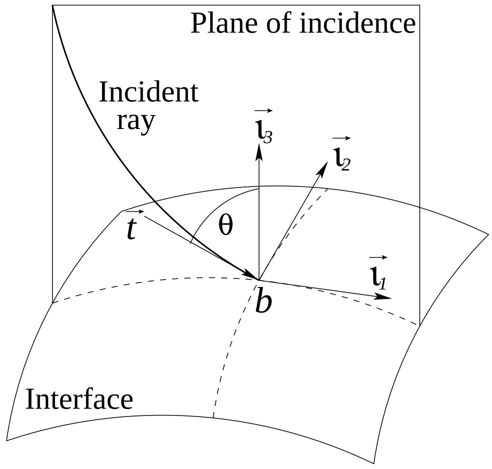

Figure A.5: Definition of the Cartesian coordinate system associated with an interface: $\vec{\imath}_3$ is normal to the interface, $\vec{\imath}_1$ lies in the incidence plane and the interface tangent plane at b, and $\vec{\imath}_2$ is given by $\vec{\imath}_3 \times \vec{\imath}_1$.

and the transformation from ray centred coordinates to interface Cartesian coordinates by a matrix $\underline{\hat{G}}$. This matrix can be expressed in two fashions, first as a product of the transformation matrices $\underline{\hat{Z}}$ and $\underline{\hat{H}}$

$$\underline{\hat{G}} = \underline{\hat{Z}}^\top \underline{\hat{H}} = \begin{pmatrix} \vec{e}_1 \cdot \vec{\imath}_1 & \vec{e}_2 \cdot \vec{\imath}_1 & \vec{t} \cdot \vec{\imath}_1 \\ \vec{e}_1 \cdot \vec{\imath}_2 & \vec{e}_2 \cdot \vec{\imath}_2 & 0 \\ \vec{e}_1 \cdot \vec{\imath}_3 & \vec{e}_2 \cdot \vec{\imath}_3 & \vec{t} \cdot \vec{\imath}_3 \end{pmatrix} \quad . \tag{A.8.2}$$

The matrix $\underline{\hat{G}} = \underline{\hat{G}}^{\parallel}\,\underline{\hat{G}}^{\perp}$ can also be expressed by the two rotation matrices $\underline{\hat{G}}^{\parallel}$ and $\underline{\hat{G}}^{\perp}$, where θ is the incidence angle between $\vec{\imath}_3$ and $\vec{t}$, and ϕ the angle between $\vec{\imath}_2$ and $\vec{e}_2$

$$\underline{\hat{G}}^{\parallel} = \begin{pmatrix} \cos\theta & 0 & \sin\theta \\ 0 & 1 & 0 \\ -\sin\theta & 0 & \cos\theta \end{pmatrix} \quad \text{and} \quad \underline{\hat{G}}^{\perp} = \begin{pmatrix} \cos\phi & -\sin\phi & 0 \\ \sin\phi & \cos\phi & 0 \\ 0 & 0 & 1 \end{pmatrix} \quad . \tag{A.8.3}$$

The traveltime expansion (A.7.9) expressed in interface coordinates is

$$\tau(z_i) = \tau_0 + p_i^{(x)} Z_{ij} z_j + \frac{1}{2} G_{ik} M_{kl} G_{jl} z_i z_j \quad . \tag{A.8.4}$$

Now, let the 3-component of a vector $\hat{\boldsymbol{z}}$ be described by

$$z_3 = \frac{1}{2} z_I \, D_{IJ} \, z_J \tag{A.8.5}$$

with $\underline{D}$ being the curvature matrix of the interface. Inserting this into Equation (A.8.4) and neglecting terms of higher order than two yields

$$\tau(z_I) = \tau_0 + p_i^{(x)} Z_{iJ} z_J + \frac{1}{2} F_{IJ} z_I z_J \quad . \tag{A.8.6}$$

The matrix $\underline{F}$ is given by

$$\underline{F} = \underline{G}\,\underline{M}\,\underline{G}^\top + \frac{\cos\theta}{V}\underline{D} + \underline{E} \quad , \tag{A.8.7}$$

where

$$
\begin{aligned}
E_{IJ} &= G_{I3}G_{JK}M_{3K} + G_{I3}G_{J3}M_{33} + G_{IK}G_{J3}M_{K3} \\
&= -\frac{1}{V^2}\left(G_{I3}G_{JK}\left.\frac{\partial V}{\partial q_K}\right|_b + G_{I3}G_{J3}\left.\frac{\partial V}{\partial q_3}\right|_b + G_{IK}G_{J3}\left.\frac{\partial V}{\partial q_K}\right|_b \right) \quad , \qquad \text{(A.8.8)}
\end{aligned}
$$

and the matrix $\underline{\mathsf{G}}$ is the upper left (2×2) submatrix of $\hat{\underline{\mathsf{G}}}$

$$
\underline{\mathsf{G}} = \begin{pmatrix} \cos\theta\cos\phi & -\cos\theta\sin\phi \\ \sin\phi & \cos\phi \end{pmatrix} \quad . \qquad \text{(A.8.9)}
$$

The terms in the matrix $\underline{\mathsf{F}}$ have simple physical meaning: the matrix $\underline{\mathsf{D}}$ describes the geometry of the interface, i.e. the curvature. For a plane reflector $\underline{\mathsf{D}}$ vanishes. The matrix $\underline{\mathsf{E}}$ describes the inhomogeneity of the medium. This term vanishes in a constant velocity medium.

Suppose that Equation (A.8.6) describes the traveltime of an incident wave at a point b on the interface, where all quantities in (A.8.6) are given at b. A similar equation can be written for reflected/transmitted waves. To distinguish between incident and reflected/transmitted wave, parameters of the reflected/transmitted wave will be denoted by a tilde. Phase matching along the interface in a near vicinity of b requires

$$
\tau + p_i^{(x)} Z_{iJ}\, z_J + \frac{1}{2} F_{IJ}\, z_I\, z_J = \tilde{\tau} + \tilde{p}_i^{(x)} Z_{iJ}\, z_J + \frac{1}{2} \tilde{F}_{IJ}\, z_I\, z_J \quad . \qquad \text{(A.8.10)}
$$

If this is to be fulfilled for any z_I, it leads to

$$
\begin{aligned}
\tau &= \tilde{\tau} \\
p_i^{(x)} Z_{iJ} &= \tilde{p}_i^{(x)} Z_{iJ} \\
F_{IJ} &= \tilde{F}_{IJ} \quad . \qquad \text{(A.8.11)}
\end{aligned}
$$

The second relation yields Snell's law. The third relation

$$
\underline{\mathsf{G}}\,\underline{\mathsf{M}}\,\underline{\mathsf{G}}^\top + \frac{\cos\theta}{V}\,\underline{\mathsf{D}} + \underline{\mathsf{E}} = \tilde{\underline{\mathsf{G}}}\,\tilde{\underline{\mathsf{M}}}\,\tilde{\underline{\mathsf{G}}}^\top + \frac{\cos\tilde{\theta}}{\tilde{V}}\,\underline{\mathsf{D}} + \tilde{\underline{\mathsf{E}}} \qquad \text{(A.8.12)}
$$

can be rewritten to an expression for the transformation of the matrix $\underline{\mathsf{M}}$ across the interface

$$
\tilde{\underline{\mathsf{M}}} = \tilde{\underline{\mathsf{G}}}^{-1}\left[\underline{\mathsf{G}}\,\underline{\mathsf{M}}\,\underline{\mathsf{G}}^\top + u\,\underline{\mathsf{D}} + \underline{\mathsf{E}} - \tilde{\underline{\mathsf{E}}}\right]\tilde{\underline{\mathsf{G}}}^{-\top} \quad , \qquad \text{(A.8.13)}
$$

where the abbreviation

$$
u = \frac{\cos\theta}{V} - \frac{\cos\tilde{\theta}}{\tilde{V}} \qquad \text{(A.8.14)}
$$

was used.

The following step, the transformation of the matrices $\underline{\mathsf{Q}}$ and $\underline{\mathsf{P}}$, is straightforward. Since the ray parameters γ_I must not change for reflection or transmission, they can be matched as was done for the phases in (A.8.11)

$$
\left.\frac{\partial \gamma_I}{\partial z_J}\right|_b = \left.\frac{\partial \gamma_I}{\partial q_K}\right|_b \left.\frac{\partial q_K}{\partial z_J}\right|_b \quad . \qquad \text{(A.8.15)}
$$

This relation must be the same for the incident and outgoing wave and therefore

$$
\underline{\mathsf{Q}}^{-1}\underline{\mathsf{G}}^\top = \tilde{\underline{\mathsf{Q}}}^{-1}\tilde{\underline{\mathsf{G}}}^\top \quad \Rightarrow \quad \tilde{\underline{\mathsf{Q}}} = \tilde{\underline{\mathsf{G}}}^\top \underline{\mathsf{G}}^{-\top}\underline{\mathsf{Q}} \quad . \qquad \text{(A.8.16)}
$$

For the geometrical spreading, this means that with det$\underline{\mathsf{G}}$=$\cos\theta$

$$\det\tilde{\underline{\mathsf{Q}}} = \frac{\cos\tilde{\theta}}{\cos\theta}\,\underline{\mathsf{Q}} \quad . \tag{A.8.17}$$

The corresponding relation for $\tilde{\underline{\mathsf{P}}}$ follows from (A.8.13), (A.8.16), and $\underline{\mathsf{M}} = \underline{\mathsf{P}}\,\underline{\mathsf{Q}}^{-1}$

$$\tilde{\underline{\mathsf{P}}} = \tilde{\underline{\mathsf{G}}}^{-1}\left[\underline{\mathsf{G}}\,\underline{\mathsf{P}} + \left(u\,\underline{\mathsf{D}} + \underline{\mathsf{E}} - \tilde{\underline{\mathsf{E}}}\right)\underline{\mathsf{G}}^{-\top}\underline{\mathsf{Q}}\right] \quad . \tag{A.8.18}$$

Equations (A.8.16) and (A.8.18) can be summarised using the 4×2 matrix $\underline{\mathsf{X}}$ that was defined in (A.6.16)

$$\tilde{\underline{\mathsf{X}}} = \underline{\underline{\mathsf{F}}}\,\underline{\mathsf{X}} \tag{A.8.19}$$

by introducing a 4×4 interface matrix $\underline{\underline{\mathsf{F}}}$ with

$$\underline{\underline{\mathsf{F}}} = \begin{pmatrix} \tilde{\underline{\mathsf{G}}}^{\top} & \underline{0} \\ \underline{0} & \tilde{\underline{\mathsf{G}}}^{-1} \end{pmatrix} \begin{pmatrix} \underline{1} & \underline{0} \\ u\,\underline{\mathsf{D}} + \underline{\mathsf{E}} - \tilde{\underline{\mathsf{E}}} & \underline{1} \end{pmatrix} \begin{pmatrix} \underline{\mathsf{G}}^{-\top} & \underline{0} \\ \underline{0} & \underline{\mathsf{G}} \end{pmatrix} \quad . \tag{A.8.20}$$

Similar to (A.6.18), ray propagator matrices can be used to describe the ray from a starting point b_0 passing the interface at b and arriving at s by

$$\underline{\mathsf{X}}(s) = \underline{\underline{\Pi}}(s,b)\;\underline{\underline{\mathsf{F}}}(b)\;\underline{\underline{\Pi}}(b,b_0)\;\underline{\mathsf{X}}(b_0) \quad . \tag{A.8.21}$$

For the transformation of displacement amplitudes across the interface, the reflection/transmission coefficient needs to be included. This can be done in terms of the matrix $\hat{\underline{\mathsf{R}}}$ of reflection/transmission coefficients, yielding

$$\tilde{\hat{U}} = \hat{\underline{\mathsf{R}}}\,\hat{\underline{\mathsf{G}}}^{\perp}\hat{\boldsymbol{U}} \quad . \tag{A.8.22}$$

The 1-component of the vector $\hat{\boldsymbol{U}}$ corresponds to a P-wave (as defined in Section A.2), the 2-component is an SH-wave and the 3-component an SV-wave. This means that, e.g., the 11-component of the matrix $\hat{\underline{\mathsf{R}}}$ is the P-P reflection/transmission coefficient. The final expression for the displacement vector reads

$$\hat{\boldsymbol{U}}(s) = \frac{1}{\sqrt{V(s)\,\rho(s)\,\det\underline{\mathsf{Q}}(s)}}\sqrt{\frac{\tilde{V}(b)\,\tilde{\rho}(b)\,\det\tilde{\underline{\mathsf{Q}}}(b)}{V(b)\,\rho(b)\,\det\underline{\mathsf{Q}}(b)}}\;\hat{\underline{\mathsf{R}}}(b)\;\hat{\underline{\mathsf{G}}}^{\perp}(b)\,\hat{\boldsymbol{\Psi}}(b_0) \quad . \tag{A.8.23}$$

If not only one but N interfaces are involved, Equations (A.8.21) and (A.8.23) change as follows: the chain rule (A.6.8) for propagator matrices applied to (A.8.21) immediately leads to

$$\underline{\mathsf{X}}(s) = \underline{\underline{\Pi}}(s,b_N)\;\prod_{i=N}^{1}\left[\underline{\underline{\mathsf{F}}}(b_i)\;\underline{\underline{\Pi}}(b_i,b_{i-1})\right]\;\underline{\mathsf{X}}(b_0) \quad . \tag{A.8.24}$$

The according expression for the displacement becomes

$$\hat{\boldsymbol{U}}(s) = \frac{\mathrm{e}^{i\delta\tau(s,b_0)}}{\sqrt{V(s)\,\rho(s)\,\det\underline{\mathsf{Q}}(s)}}\;\prod_{i=N}^{1}\sqrt{\frac{\tilde{V}(b_i)\,\tilde{\rho}(b_i)\,\det\tilde{\underline{\mathsf{Q}}}(b_i)}{V(b_i)\,\rho(b_i)\,\det\underline{\mathsf{Q}}(b_i)}}\;\prod_{i=N}^{1}\left[\hat{\underline{\mathsf{R}}}(b_i)\;\hat{\underline{\mathsf{G}}}^{\perp}(b_i)\right]\;\hat{\boldsymbol{\Psi}}(b_0) \quad , \tag{A.8.25}$$

where $\delta\tau(s,b_0)$=$-\pi/2\kappa(s,b_0)$ is a phase shift due to caustics. The KMAH index κ of the ray trajectory was introduced in (A.3.23). It is convenient to rewrite Equation (A.8.25) by introducing the following notations: let the scalar quantity $\mathcal{A}(s)$ cover the transmission losses

$$\mathcal{A}(s) = \frac{1}{\sqrt{V(s)\,\rho(s)}}\;\prod_{i=N}^{1}\sqrt{\frac{\tilde{V}(b_i)\,\tilde{\rho}(b_i)}{V(b_i)\,\rho(b_i)}} \quad . \tag{A.8.26}$$

The reflection/transmission matrix $\hat{\underline{\mathsf{R}}}$ is summarised by

$$\hat{\underline{\mathsf{R}}}(s) = \prod_{i=N}^{1} \hat{\underline{\mathsf{R}}}(b_i)\ \hat{\underline{\mathsf{G}}}^{\perp}(b_i) \quad , \tag{A.8.27}$$

and the relative geometrical spreading $L(s)$ is given by

$$L(s) = \left| \det\underline{\mathsf{Q}}(s) \prod_{i=N}^{1} \frac{\cos\theta(b_i)}{\cos\tilde{\theta}(b_i)} \right|^{\frac{1}{2}} \mathrm{e}^{i\delta\tau(s,b_0)} = \left| \det\underline{\mathsf{Q}}(s) \prod_{i=N}^{1} \frac{\det\underline{\mathsf{Q}}(b_i)}{\det\tilde{\underline{\mathsf{Q}}}(b_i)} \right|^{\frac{1}{2}} \mathrm{e}^{i\delta\tau(s,b_0)} \quad . \tag{A.8.28}$$

With these, Equation (A.8.25) becomes

$$\hat{\boldsymbol{U}}(s) = \frac{\mathcal{A}(s)}{L(s)} \hat{\underline{\mathsf{R}}}(s)\, \hat{\boldsymbol{\Psi}}(b_0) \quad . \tag{A.8.29}$$

Literature for Section A.8:

- Červený (1985),
- Červený (2001).

A.9 The Bortfeld propagator

The propagator $\underline{\underline{\mathsf{T}}}$ that was introduced by Bortfeld obeys similar relations as the $\underline{\underline{\Pi}}$ propagator. However, the $\underline{\underline{\mathsf{T}}}$ propagator is defined in reference surfaces as opposed to the $\underline{\underline{\Pi}}$ formalism which is based on an expansion into the wavefront. Consider a central ray that emerges from a point s_0 in a surface, the so-called anterior surface and arrives at a point r_0 in the posterior surface. Both surfaces have local Cartesian coordinate systems fixed with their origins at s_0 and r_0, respectively. Let the orientation of the systems be such that the 3-component coincides with the normal to the surfaces at s_0 and r_0. The corresponding slowness vectors are

$$\hat{\boldsymbol{p}}(s_0) = \frac{\vec{\boldsymbol{t}}(s_0)}{V(s_0)} \quad \text{and} \quad \hat{\boldsymbol{p}}(r_0) = \frac{\vec{\boldsymbol{t}}(r_0)}{V(r_0)} \quad . \tag{A.9.1}$$

A paraxial ray at a point s has the coordinates

$$\hat{\boldsymbol{x}}(s) = (x_1,\, x_2,\, f(x_1, x_2))^{\top} \tag{A.9.2}$$

and the slowness

$$\hat{\boldsymbol{p}}(s) = \frac{\vec{\boldsymbol{t}}(s)}{V(s)} \quad . \tag{A.9.3}$$

Points in a near vicinity of s are described by $\hat{\boldsymbol{x}} + \mathrm{d}\hat{\boldsymbol{x}}$ with

$$\mathrm{d}\hat{\boldsymbol{x}} = (\mathrm{d}\boldsymbol{x}, \vec{\nabla} f \cdot \mathrm{d}\boldsymbol{x})^{\top} \quad . \tag{A.9.4}$$

In the x_1-x_2 plane the 3-D vectors $\hat{\boldsymbol{x}}(s)$ and $\hat{\boldsymbol{p}}(s)$ are represented by 2-D vectors $\boldsymbol{x}(s)$ and $\boldsymbol{p}(s)$. The vector $\boldsymbol{x}(s)$ is simply the projection of $\hat{\boldsymbol{x}}(s)$ onto the x_1-x_2 plane and was already used in Equation (A.9.4). To obtain the slowness vector $\boldsymbol{p}(s)$, two cascaded projections are required (see Figure A.6): in the first step, $\hat{\boldsymbol{p}}(s)$ is projected onto the tangent plane of the anterior surface at s. This yields the tangential slowness vector $\hat{\boldsymbol{p}}_T(s)$ parallel to the tangent plane with

$$\mathrm{d}\hat{\boldsymbol{p}}_T = (\mathrm{d}\boldsymbol{p}, \vec{\nabla} f \cdot \mathrm{d}\boldsymbol{p})^{\top} \quad . \tag{A.9.5}$$

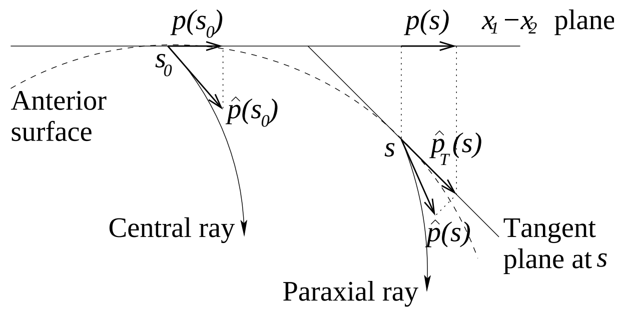

Figure A.6: Projection of the slowness into the x_1-x_2 plane.

The vector $\boldsymbol{p}(s)$ is the projection of $\hat{\boldsymbol{p}}_T(s)$ onto the x_1-x_2 plane. The same applies to the properties in the posterior surface.

The relationship between the initial vectors $\boldsymbol{x}(s)$ and $\boldsymbol{p}(s)$ and the final vectors $\boldsymbol{x}(r)$ and $\boldsymbol{p}(r)$ is expressed by a first order approximation that is valid in a near vicinity of the central ray

$$\begin{aligned} \boldsymbol{x}(r) &= \underline{\mathsf{A}}\,\boldsymbol{x}(s) + \underline{\mathsf{B}}\,\left(\boldsymbol{p}(s) - \boldsymbol{p}(s_0)\right) \quad , \\ \boldsymbol{p}(r) - \boldsymbol{p}(r_0) &= \underline{\mathsf{C}}\,\boldsymbol{x}(s) + \underline{\mathsf{D}}\,\left(\boldsymbol{p}(s) - \boldsymbol{p}(s_0)\right) \quad , \end{aligned} \tag{A.9.6}$$

where the 2×2 matrices are the derivatives

$$\begin{aligned} A_{IJ} &= \left.\frac{\partial x(r)}{\partial x(s)}\right|_{r_0,s_0} \quad , \qquad B_{IJ} = \left.\frac{\partial x(r)}{\partial p(s)}\right|_{r_0,s_0} \quad , \\ C_{IJ} &= \left.\frac{\partial p(r)}{\partial x(s)}\right|_{r_0,s_0} \quad , \qquad D_{IJ} = \left.\frac{\partial p(r)}{\partial p(s)}\right|_{r_0,s_0} \quad . \end{aligned} \tag{A.9.7}$$

Since (A.9.6) bears a close similarity to (A.7.10), (A.9.6) can be rewritten to

$$\begin{pmatrix} \boldsymbol{x}(r) \\ \boldsymbol{p}(r) - \boldsymbol{p}(r_0) \end{pmatrix} = \underline{\underline{\mathsf{T}}}(r_0, s_0) \begin{pmatrix} \boldsymbol{x}(s) \\ \boldsymbol{p}(s) - \boldsymbol{p}(s_0) \end{pmatrix} \quad , \tag{A.9.8}$$

introducing the propagator matrix $\underline{\underline{\mathsf{T}}}(r_0, s_0)$

$$\underline{\underline{\mathsf{T}}}(r_0, s_0) = \begin{pmatrix} \underline{\mathsf{A}}(r_0, s_0) & \underline{\mathsf{B}}(r_0, s_0) \\ \underline{\mathsf{C}}(r_0, s_0) & \underline{\mathsf{D}}(r_0, s_0) \end{pmatrix} \quad . \tag{A.9.9}$$

The first order approximation of $\boldsymbol{x}$ and $\boldsymbol{p}$ corresponds to a second order approximation of the traveltime. The total differential of the traveltime is given by

$$\begin{aligned} \mathrm{d}\tau &= \vec{\nabla}_r \tau \cdot \mathrm{d}\hat{\boldsymbol{x}}(r) + \vec{\nabla}_s \tau \cdot \mathrm{d}\hat{\boldsymbol{x}}(s) \\ &= \hat{\boldsymbol{p}}(r) \cdot \mathrm{d}\hat{\boldsymbol{x}}(r) - \hat{\boldsymbol{p}}(s) \cdot \mathrm{d}\hat{\boldsymbol{x}}(s) \\ &= \hat{\boldsymbol{p}}_T(r) \cdot \mathrm{d}\hat{\boldsymbol{x}}(r) - \hat{\boldsymbol{p}}_T(s) \cdot \mathrm{d}\hat{\boldsymbol{x}}(s) \\ &= \left(\boldsymbol{p}(r),\, \vec{\nabla}_r f \cdot \boldsymbol{p}(r)\right) \cdot \begin{pmatrix} \mathrm{d}\boldsymbol{x}(r) \\ \vec{\nabla}_r f \cdot \boldsymbol{x}(r) \end{pmatrix} - \left(\boldsymbol{p}(s),\, \vec{\nabla}_s f \cdot \boldsymbol{p}(s)\right) \cdot \begin{pmatrix} \mathrm{d}\boldsymbol{x}(s) \\ \vec{\nabla}_s f \cdot \boldsymbol{x}(s) \end{pmatrix} \\ &\approx \boldsymbol{p}(r) \cdot \mathrm{d}\boldsymbol{x}(r) - \boldsymbol{p}(s) \cdot \mathrm{d}\boldsymbol{x}(s) \quad . \end{aligned} \tag{A.9.10}$$

The last approximation is motivated by the aim for a second order approximation of τ, therefore terms containing products of f derivatives are neglected. The signs were chosen in a way that the traveltime increases for growing distance in the direction of propagation of the ray. Now $\boldsymbol{p}(r)$ and $\boldsymbol{p}(s)$ are expressed in terms of the $\underline{\underline{\mathsf{T}}}$-submatrices from (A.9.6)

$$\begin{aligned} \boldsymbol{p}(s) &= \boldsymbol{p}(s_0) - \underline{\mathsf{B}}^{-1}\underline{\mathsf{A}}\boldsymbol{x}(s) + \underline{\mathsf{B}}^{-1}\boldsymbol{x}(r) \quad , && \text{(A.9.11)} \\ \boldsymbol{p}(r) &= \boldsymbol{p}(r_0) + \underline{\mathsf{D}}\underline{\mathsf{B}}^{-1}\boldsymbol{x}(r) + \left[\underline{\mathsf{C}} - \underline{\mathsf{D}}\underline{\mathsf{B}}^{-1}\underline{\mathsf{A}}\right]\boldsymbol{x}(s) \quad . && \text{(A.9.12)} \end{aligned}$$

Inserting these slownesses into Equation (A.9.10), the latter can be integrated, leading to

$$\begin{aligned} \tau &= \tau_0 + \boldsymbol{p}(r_0)\cdot\boldsymbol{x}(r) - \boldsymbol{p}(s_0)\cdot\boldsymbol{x}(s) - \boldsymbol{x}(s)\cdot\underline{\mathsf{B}}^{-1}\boldsymbol{x}(r) \\ &\quad + \frac{1}{2}\,\boldsymbol{x}(s)\cdot\underline{\mathsf{B}}^{-1}\underline{\mathsf{A}}\boldsymbol{x}(s) + \frac{1}{2}\,\boldsymbol{x}(r)\cdot\underline{\mathsf{D}}\,\underline{\mathsf{B}}^{-1}\boldsymbol{x}(r) && \text{(A.9.13)} \end{aligned}$$

($\tau_0 = \tau(s_0, r_0)$). This requires that

$$\underline{\mathsf{B}}^{-1}\underline{\mathsf{A}} = \underline{\mathsf{A}}^\top\underline{\mathsf{B}}^{-\top}\,, \qquad \underline{\mathsf{D}}^\top\underline{\mathsf{B}}^{-1} = \underline{\mathsf{B}}^{-\top}\underline{\mathsf{D}}^\top\,, \qquad \underline{\mathsf{A}}^\top\underline{\mathsf{D}} - \underline{\mathsf{C}}^\top\underline{\mathsf{B}} = \underline{\mathsf{1}} \quad , \tag{A.9.14}$$

following from the demand that the order of differentiation of τ must be arbitrary. These relations yield the symplecticity of $\underline{\underline{\mathsf{T}}}$ and

$$\underline{\mathsf{B}}^\top\underline{\mathsf{D}} = \underline{\mathsf{D}}^\top\underline{\mathsf{B}}\,, \qquad \underline{\mathsf{A}}^\top\underline{\mathsf{C}} = \underline{\mathsf{C}}^\top\underline{\mathsf{A}} \quad . \tag{A.9.15}$$

As for the propagator matrix $\underline{\underline{\Pi}}$, the inverse can be computed for $\underline{\underline{\mathsf{T}}}$

$$\underline{\underline{\mathsf{T}}}^{-1}(r_0, s_0) = \underline{\underline{\mathsf{T}}}(s_0, r_0) = \begin{pmatrix} \underline{\mathsf{D}}(r_0, s_0)^\top & -\underline{\mathsf{B}}(r_0, s_0)^\top \\ -\underline{\mathsf{C}}(r_0, s_0)^\top & \underline{\mathsf{A}}(r_0, s_0)^\top \end{pmatrix} \quad . \tag{A.9.16}$$

The $\underline{\underline{\Pi}}$ and $\underline{\underline{\mathsf{T}}}$ propagator matrices can be transformed into each other. The relation between them can be found by applying Equation (A.7.9) to the anterior and posterior surfaces, leading to

$$\begin{aligned} \tau &= \tau_0 + \boldsymbol{p}(r_0)\cdot\boldsymbol{x}(r) - \boldsymbol{p}(s_0)\cdot\boldsymbol{x}(s) - \boldsymbol{x}(s)\cdot\underline{\mathsf{G}}(s_0)\underline{\mathsf{Q}}_2^{-1}\underline{\mathsf{G}}^\top(r_0)\boldsymbol{x}(r) \\ &\quad - \frac{1}{2}\,\boldsymbol{x}(s)\cdot\underline{\mathsf{G}}(s_0)\underline{\mathsf{F}}(s_0)\underline{\mathsf{G}}^\top(s_0)\boldsymbol{x}(s) + \frac{1}{2}\,\boldsymbol{x}(r)\cdot\underline{\mathsf{G}}(r_0)\underline{\mathsf{F}}(r_0)\underline{\mathsf{G}}^\top(r_0)\boldsymbol{x}(r) \quad . \end{aligned} \tag{A.9.17}$$

Comparison of (A.9.13) and (A.9.17) leads to

$$\underline{\underline{\mathsf{T}}}(r_0, s_0) = \underline{\underline{\mathsf{X}}}(r_0)\,\underline{\underline{\mathsf{G}}}(r_0)\,\underline{\underline{\Pi}}(r_0, s_0)\,\underline{\underline{\mathsf{G}}}^\top(s_0)\,\underline{\underline{\mathsf{X}}}^\top(s_0) \quad , \tag{A.9.18}$$

with

$$\underline{\underline{\mathsf{G}}}(r_0) = \begin{pmatrix} \underline{\mathsf{G}}^{-1}(r_0) & \underline{\mathsf{0}} \\ \underline{\mathsf{0}} & \underline{\mathsf{G}}^\top(r_0) \end{pmatrix} \quad , \qquad \underline{\underline{\mathsf{G}}}(s_0) = \begin{pmatrix} \underline{\mathsf{G}}^\top(s_0) & \underline{\mathsf{0}} \\ \underline{\mathsf{0}} & \underline{\mathsf{G}}^{-1}(s_0) \end{pmatrix} \quad , \tag{A.9.19}$$

and

$$\underline{\underline{\mathsf{X}}}(r_0) = \begin{pmatrix} \underline{\mathsf{1}} & \underline{\mathsf{0}} \\ \frac{\cos\theta(r_0)}{V(r_0)}\,\underline{\mathsf{D}}(r_0) + \underline{\mathsf{E}}(r_0) & \underline{\mathsf{1}} \end{pmatrix} \quad , \qquad \underline{\underline{\mathsf{X}}}(s_0) = \begin{pmatrix} \underline{\mathsf{1}} & \underline{\mathsf{0}} \\ \frac{-\cos\theta(s_0)}{V(s_0)}\,\underline{\mathsf{D}}(s_0) - \underline{\mathsf{E}}(s_0) & \underline{\mathsf{1}} \end{pmatrix} \quad . \tag{A.9.20}$$

The matrices $\underline{\mathsf{D}}$ and $\underline{\mathsf{E}}$ are taken from (A.8.7) at s_0 and r_0 accordingly.

Literature for Section A.9:

- Bortfeld (1989),
- Hubral et al. (1992a).

Appendix B

Analytic traveltime coefficients for simple media

This appendix contains expressions for the traveltimes and their first and second-order derivatives for simple cases where the analytic solution is known. For the generic examples in isotropic media I have chosen a model with a constant vertical velocity gradient and a homogeneous (constant velocity) medium, which is a special case of the constant velocity gradient medium. Expressions for the traveltime and the coefficients are also given for a homogeneous medium with elliptical anisotropy. For both homogeneous models given here, the hyperbolic traveltime expression yields the exact traveltime. This is explicitly shown for the isotropic homogeneous model.

For all three models I denote the source position by (s_x, s_y, s_z) and the receiver position by (g_x, g_y, g_z). I use the following abbreviations: $x = g_x - s_x$, etc., and $r = \sqrt{x^2 + y^2 + z^2}$.

B.1 Constant velocity gradient medium

This velocity model is described by the vertical gradient b and

$$V(z) = a + bz \quad . \tag{B.1.1}$$

Form this follow the velocity at the source $V_s = a + bs_z$ and at the receiver $V_g = a + bg_z$. The traveltime from $\hat{\boldsymbol{s}}$ to $\hat{\boldsymbol{g}}$ is

$$\tau = \frac{1}{b}\,\mathrm{arcosh}\left(1 + \frac{b^2 r^2}{2\,V_s V_g}\right) \quad . \tag{B.1.2}$$

The geometrical spreading in two and three dimensions is

$$\begin{aligned} \mathcal{L}_{\mathrm{2D}} &= \frac{1}{V_s}\sqrt{\frac{W}{2}} \quad , \quad \text{and} \\ \mathcal{L}_{\mathrm{3D}} &= \frac{1}{V_s}\,\frac{W}{2} \quad , \end{aligned} \tag{B.1.3}$$

where the abbreviation

$$W = \sqrt{b^2 r^4 + 4\,V_s V_g r^2} \tag{B.1.4}$$

was used. To simplify the expressions for the coefficients, another abbreviation is introduced here:

$$F = b^2 r^2 + 2\,V_s V_g \quad . \tag{B.1.5}$$

The first order derivatives of Equation (B.1.2) lead to the slowness components are

$$
\begin{aligned}
p_{x_0} = q_{x_0} &= \frac{1}{W}\, 2\,x \quad , \\
p_{y_0} = q_{y_0} &= \frac{1}{W}\, 2\,y \quad , \\
p_{z_0} &= \frac{1}{W}\left(2\,z + \frac{br^2}{V_s}\right) \quad , \\
q_{z_0} &= \frac{1}{W}\left(2\,z - \frac{br^2}{V_g}\right) \quad .
\end{aligned}
\tag{B.1.6}
$$

The second order derivative matrix elements are

$$
\begin{aligned}
S_{xx} = -G_{xx} = -N_{xx} &= \frac{1}{W^3}\left(4\,Fx^2 - 2W^2\right) \quad , \\
S_{yy} = -G_{yy} = -N_{yy} &= \frac{1}{W^3}\left(4\,Fy^2 - 2W^2\right) \quad , \\
S_{xy} = -G_{xy} = -N_{xy} = -N_{yx} &= \frac{1}{W^3}\left(4\,Fx\,y\right) \quad , \\
S_{yz} = -N_{zy} &= \frac{1}{W^3}\left(4\,Fy\,z - 4\,V_g br^2 y\right) \quad , \\
G_{yz} = N_{yz} &= \frac{1}{W^3}\left(-4\,Fy\,z - 4\,V_s br^2 y\right) \quad , \\
S_{zx} = -N_{zx} &= \frac{1}{W^3}\left(4\,Fz\,x - 4\,V_g br^2 x\right) \quad , \\
G_{zx} = N_{xz} &= \frac{1}{W^3}\left(-4\,Fz\,x - 4\,V_s br^2 x\right) \quad ,
\end{aligned}
$$

and

$$
\begin{aligned}
S_{zz} &= \frac{1}{W^3}\left(4\,Fz^2 - 2\,W^2 - \frac{b^4r^6}{V_s^2} - \frac{6\,V_g b^2 r^4}{V_s} + 8\,V_g(V_s - V_g)r^2\right) \quad , \\
G_{zz} &= \frac{1}{W^3}\left(-4\,Fz^2 + 2\,W^2 + \frac{b^4r^6}{V_g^2} + \frac{6\,V_s b^2 r^4}{V_g} - 8\,V_s(V_g - V_s)r^2\right) \quad , \\
N_{zz} &= \frac{8\,V_g V_s}{W^3}\left(r^2 - z^2\right) \quad .
\end{aligned}
\tag{B.1.7}
$$

B.2 Homogeneous isotropic medium

This model is a special case of the constant velocity gradient model with $b = 0$. The constant velocity is denoted by V. Application of the formula of l'Hospital to Equation (B.1.2) leads to the well-known result

$$
\tau = \frac{r}{V} \quad . \tag{B.2.1}
$$

With $W = 2Vr$, the geometrical spreading for this homogeneous model is given by

$$
\begin{aligned}
\mathcal{L}_{2\mathrm{D}} &= \sqrt{\frac{r}{V}} \quad , \quad \text{and} \\
\mathcal{L}_{3\mathrm{D}} &= r \quad ,
\end{aligned}
\tag{B.2.2}
$$

in two and three dimensions, respectively. Furthermore, with $F = 2V^2$, Equation (B.1.6) leads to

$$
\begin{aligned}
p_{x_0} = q_{x_0} &= \frac{x}{Vr} \quad , \\
p_{y_0} = q_{y_0} &= \frac{y}{Vr} \quad , \\
p_{z_0} = q_{z_0} &= \frac{z}{Vr} \quad .
\end{aligned}
\tag{B.2.3}
$$

Equations (B.1.7) and (B.1.7) yield

$$
\begin{aligned}
-S_{xx} = G_{xx} = N_{xx} &= \frac{y^2 + z^2}{Vr^3} \quad , \\
-S_{yy} = G_{yy} = N_{yy} &= \frac{z^2 + x^2}{Vr^3} \quad , \\
-S_{zz} = G_{zz} = N_{zz} &= \frac{x^2 + y^2}{Vr^3} \quad , \\
-S_{xy} = G_{xy} = N_{xy} = N_{yx} &= -\frac{xy}{Vr^3} \quad , \\
-S_{yz} = G_{yz} = N_{yz} = N_{zy} &= -\frac{yz}{Vr^3} \quad , \\
-S_{zx} = G_{zx} = N_{zx} = N_{xz} &= -\frac{zx}{Vr^3} \quad .
\end{aligned}
\tag{B.2.4}
$$

I will now prove that the hyperbolic traveltime expansion Equation (2.2.2) is the exact solution for a model with constant velocity. Instead of vector notation I will use index notation here (summation convention is applied) with the index 1 for x, 2 for y, and 3 for z. Abbreviating $r_i = g_i - s_i$ leads to $r^2 = r_i r_i$ and $V^2\tau^2(\hat{\boldsymbol{s}}, \hat{\boldsymbol{g}}) = r_i\, r_i$. Equation (2.2.2) in index notation reads

$$
\tau^2(\hat{\boldsymbol{s}}, \hat{\boldsymbol{g}}) = (\tau_0 + q_{0i}\Delta g_i - p_{0i}\Delta s_i)^2 - 2\tau_0 \Delta s_i N_{ij} \Delta g_j + \tau_0(\Delta g_i G_{ij} \Delta g_j - \Delta s_i S_{ij} \Delta s_j)
\tag{B.2.5}
$$

where the traveltime τ_0 is taken in the expansion point and s_{i_0}, g_{i_0}

$$
\tau_0^2 = \frac{r_{i_0} r_{i_0}}{V^2} = \frac{(g_{i_0} - s_{i_0})(g_{i_0} - s_{i_0})}{V^2}.
\tag{B.2.6}
$$

In this context the coefficients of Equation (B.2.5) are written as

$$
\begin{aligned}
p_{i_0} = q_{i_0} &= \frac{r_{i_0}}{V^2\,\tau_0} \\
S_{ij} &= \frac{p_{i_0} p_{j_0}}{\tau_0} - \frac{\delta_{ij}}{V^2\,\tau_0} \\
G_{ij} &= \frac{\delta_{ij}}{V^2\,\tau_0} - \frac{q_{i_0} q_{j_0}}{\tau_0} \\
N_{ij} &= \frac{\delta_{ij}}{V^2\,\tau_0} - \frac{p_{i_0} q_{j_0}}{\tau_0}.
\end{aligned}
\tag{B.2.7}
$$

Inserting these into Equation (B.2.5) and expanding the square on the right side of the equation yields

$$
\begin{aligned}
\tau^2(\hat{\boldsymbol{s}},\hat{\boldsymbol{g}}) &= \tau_0^2 + 2\tau_0(q_{i_0}\Delta g_i - p_{i_0}\Delta s_i) + q_{i_0}\Delta g_i\, q_{j_0}\Delta g_j + p_{i_0}\Delta s_i\, p_{j_0}\Delta s_j \\
&\quad -2p_{i_0}\Delta s_i\, q_{j_0}\Delta g_j - q_{i_0}\Delta g_i\, q_{j_0}\Delta g_j - p_{i_0}\Delta s_i\, p_{j_0}\Delta s_j + 2p_{i_0}\Delta s_i\, q_{j_0}\Delta g_j \\
&\quad +\frac{\Delta g_i\Delta g_i}{V^2} + \frac{\Delta s_i\Delta s_i}{V^2} - 2\frac{\Delta s_i\Delta g_i}{V^2} \\
&= \tau_0^2 + 2\tau_0 q_{i_0}\Delta g_i - 2\tau_0 p_{i_0}\Delta s_i + \frac{1}{V^2}\left(\Delta g_i\Delta g_i + \Delta s_i\Delta s_i - 2\Delta s_i\Delta g_i\right) \\
&= \frac{1}{V^2}\left(r_{i_0}r_{i_0} + 2r_{i_0}\Delta g_i - 2r_{i_0}\Delta s_i + \Delta g_i\Delta g_i + \Delta s_i\Delta s_i - 2\Delta s_i\Delta g_i\right) \\
&= \frac{1}{V^2}\left(r_{i_0} + \Delta g_i - \Delta s_i\right)\left(r_{i_0} + \Delta g_i - \Delta s_i\right). \qquad \text{(B.2.8)}
\end{aligned}
$$

This last result is the square of Equation (B.2.5) and thus the hyperbolic approximation (2.2.2) yields the exact result for an isotropic medium with constant velocity.

B.3 Homogeneous medium with elliptical anisotropy

Elliptical anisotropy is a special case of transversal isotropic (TI) media. A TI medium is characterised by the density ρ and six non-zero elastic parameters, where five of them are independent:

$$
\begin{aligned}
c_{1111} &= c_{2222} \quad , \\
c_{3333} & \quad , \\
c_{1122} & \quad , \\
c_{3311} &= c_{2233} \quad , \\
c_{2323} &= c_{3131} \quad , \quad \text{and} \\
c_{1212} &= \frac{c_{1111} - c_{1122}}{2} \quad . \qquad \text{(B.3.1)}
\end{aligned}
$$

For elliptical anisotropy it is furthermore necessary that (Helbig, 1983)

$$
(c_{1111} - c_{2323})(c_{3333} - c_{2323}) - (c_{3311} + c_{2323})^2 = 0 \quad . \qquad \text{(B.3.2)}
$$

Following Daley and Hron (1979a,b), the traveltime in a homogeneous elliptical anisotropic medium is

$$
\tau = \sqrt{\frac{x^2}{v_x^2} + \frac{y^2}{v_x^2} + \frac{z^2}{v_z^2}} \quad . \qquad \text{(B.3.3)}
$$

The velocity v_z is that of a wave which travels in z direction, and v_x is that of a wave travelling in x direction, or, more precisely, in the x-y plane, since the medium shows rotational symmetry with respect to the z axis. Please note that in this type of medium ray (group) and phase velocity coincide for waves that travel in z direction or in the x-y plane. The velocities v_x and v_z depend on the wave-type. For a qP wave they are given by

$$
v_x = \sqrt{\frac{c_{1111}}{\rho}} \quad \text{and} \quad v_z = \sqrt{\frac{c_{3333}}{\rho}} \quad . \qquad \text{(B.3.4)}
$$

For a qSH wave the velocities are

$$
v_x = \sqrt{\frac{c_{1212}}{\rho}} \quad \text{and} \quad v_z = \sqrt{\frac{c_{2323}}{\rho}} \quad . \qquad \text{(B.3.5)}
$$

In the case of a qSV wave both velocities are equal:

$$v_x = v_z = \sqrt{\frac{c_{2323}}{\rho}} \quad . \tag{B.3.6}$$

The slownesses for this model are

$$\begin{aligned} p_{x_0} = q_{x_0} &= \frac{x}{v_x^2\,\tau} \quad , \\ p_{y_0} = q_{y_0} &= \frac{y}{v_x^2\,\tau} \quad , \\ p_{z_0} = q_{z_0} &= \frac{z}{v_z^2\,\tau} \quad . \end{aligned} \tag{B.3.7}$$

The second-order derivatives are

$$\begin{aligned} -S_{xx} = G_{xx} = N_{xx} &= \frac{v_x^2\tau^2 - x^2}{v_x^4\,\tau^3} \quad , \\ -S_{yy} = G_{yy} = N_{yy} &= \frac{v_x^2\tau^2 - y^2}{v_x^4\,\tau^3} \quad , \\ -S_{zz} = G_{zz} = N_{zz} &= \frac{v_z^2\tau^2 - z^2}{v_z^4\,\tau^3} \quad , \\ -S_{xy} = G_{xy} = N_{xy} = N_{yx} &= -\frac{xy}{v_x^4\,\tau^3} \quad , \\ -S_{yz} = G_{yz} = N_{yz} = N_{zy} &= -\frac{yz}{v_x^2\,v_z^2\,\tau^3} \quad , \\ -S_{zx} = G_{zx} = N_{zx} = N_{xz} &= -\frac{zx}{v_z^2\,v_x^2\,\tau^3} \quad . \end{aligned} \tag{B.3.8}$$

Similarly as for isotropic homogeneous media, it can be shown that the hyperbolic traveltime expansion yields the exact solution for a homogeneous medium with elliptical anisotropy.

Appendix C

Elliptical anisotropy

C.1 Summary

This appendix gives a short summary of the properties of anisotropic media with elliptical symmetry. It was motivated by the need for analytic expressions for the evaluation and verification of related computer algorithms. After a brief introduction and derivation of the phase and ray (group) velocities and the polarisation vectors I give expressions for the plane wave reflection and transmission coefficients at a boundary between two elliptically anisotropic half-spaces. These are followed by expressions for the traveltimes and the geometrical spreading for homogeneous media with elliptical anisotropy. Please note, that the resulting expressions are equally valid for isotropic media if the elastic coefficients are chosen accordingly.

In order to compile this summary on elliptical anisotropy, I referred to the following publications:

- Červený (2001)
- Daley and Hron (1979a)
- Pšenčík and Teles (1996)

C.2 Introduction

A medium with elliptical anisotropy and a vertical symmetry axis is characterised by the density-normalised elasticity tensor ($A_{ik} = C_{ik}/\rho$)

$$\underline{\mathsf{A}} = \begin{pmatrix} A_{11} & A_{12} & A_{13} & & & \\ A_{12} & A_{11} & A_{13} & & & \\ A_{13} & A_{13} & A_{33} & & & \\ & & & A_{44} & & \\ & & & & A_{44} & \\ & & & & & A_{66} \end{pmatrix} \qquad \text{(C.2.1)}$$

with the additional constraints

$$\begin{aligned} A_{12} &= A_{11} - 2\,A_{66} \\ (A_{13} + A_{44})^2 &= (A_{11} - A_{44})(A_{33} - A_{44}) \quad . \end{aligned} \qquad \text{(C.2.2)}$$

Let the slowness vector be denoted by $\boldsymbol{p}$. Since $\underline{\mathrm{A}}$ displays rotational symmetry with respect to the vertical (z- or 3-) axis I choose $\boldsymbol{p}$ in a way that $p_y = p_2 = 0$ and

$$\boldsymbol{p} = \left(\frac{\sin\phi}{V},\, 0,\, \frac{\cos\phi}{V} \right) \quad , \tag{C.2.3}$$

where ϕ is the phase angle made by $\boldsymbol{p}$ and the vertical (z- or 3-) axis, and V is the phase velocity. I introduce the abbreviations d_{11} and d_{33} with

$$d_{11} = A_{11} - A_{44} \quad \text{and} \quad d_{33} = A_{33} - A_{44} \quad . \tag{C.2.4}$$

This leads to the following non-vanishing elements of the Christoffel matrix $\Gamma_{ik} = a_{ijkl}p_j p_l$:

$$\begin{aligned}
\Gamma_{11} &= A_{11}\,p_1^2 + A_{44}\,p_3^2 \;=\; A_{11}\frac{\sin^2\phi}{V^2} + A_{44}\frac{\cos^2\phi}{V^2} \quad , \\
\Gamma_{22} &= A_{66}\,p_1^2 + A_{44}\,p_3^2 \;=\; A_{66}\frac{\sin^2\phi}{V^2} + A_{44}\frac{\cos^2\phi}{V^2} \quad , \\
\Gamma_{33} &= A_{44}\,p_1^2 + A_{33}\,p_3^2 \;=\; A_{44}\frac{\sin^2\phi}{V^2} + A_{33}\frac{\cos^2\phi}{V^2} \quad , \\
\Gamma_{13} &= (A_{13} + A_{44})\,p_1\,p_3 \;=\; \sqrt{d_{11}d_{33}}\,\frac{\sin\phi\,\cos\phi}{V^2} \quad .
\end{aligned} \tag{C.2.5}$$

C.3 Phase velocities

The solution of the Christoffel equation for the displacement vector $\boldsymbol{u}$,

$$(\Gamma_{ik} - \delta_{ik})u_k = 0 \quad , \tag{C.3.1}$$

where δ_{ik} is Kronecker's delta, requires that

$$\left| \Gamma_{ik} - G^{(n)}\delta_{ik} \right| = 0 \quad . \tag{C.3.2}$$

This determinant leads to the characteristic polynomial of third order, whose three solutions are the eigenvalues $G^{(n)} = 1$, with $n = 1, 2,\, 3$. I define the index 1 to be a *q*SV wave, 2 an SH wave, and 3 a *q*P wave. The physical meaning of these definitions will become apparent in the next section on the polarisation vectors. For simplicity, the indices are abbreviated by SV, SH, and P, omitting the *q*.

Insertion of Γ_{ik} for the elliptic case yields three phase velocities $V^{(n)}$:

$$\begin{aligned}
V^{SV} &= \sqrt{A_{44}} \quad , \\
V^{SH} &= \sqrt{A_{66}\sin^2\phi^{SH} + A_{44}\cos^2\phi^{SH}} \quad , \\
V^{P} &= \sqrt{A_{11}\sin^2\phi^{P} + A_{33}\cos^2\phi^{P}} \quad .
\end{aligned} \tag{C.3.3}$$

C.4 Polarisation

The three eigenvectors $\boldsymbol{g}^{(n)}$ that obey

$$(\Gamma_{ik} - \delta_{ik})g_k^{(n)} = 0 \tag{C.4.1}$$

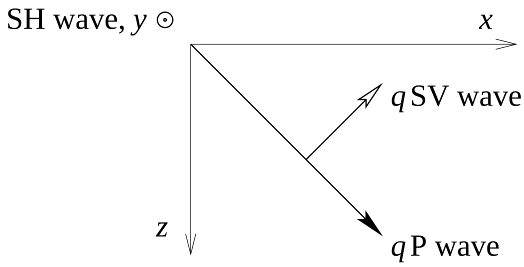

Figure C.1: Polarisation vectors in a medium with elliptical anisotropy. The *q*P and *q*SV waves propagate in the x-z plane, the SH wave polarisation vector is oriented along the y axis, pointing to the reader.

are the polarisation vectors of the three waves with the phase velocities $V^{(n)}$. The polarisations are given by

$$\begin{aligned} \boldsymbol{g}^{SV} &= \left(m^{SV}\cos\phi^{SV},\, 0,\, -l^{SV}\sin\phi^{SV}\right) \quad , \\ \boldsymbol{g}^{SH} &= (0,\, 1,\, 0) \quad , \\ \boldsymbol{g}^{P} &= \left(l^{P}\sin\phi^{P},\, 0,\, m^{P}\cos\phi^{P}\right) \quad , \end{aligned} \tag{C.4.2}$$

where the abbreviations $l^{(n)}$ and $m^{(n)}$ are introduced:

$$\begin{aligned} l^{(n)} &= \sqrt{\frac{d_{11}}{d_{11}\sin^2\phi^{(n)} + d_{33}\cos^2\phi^{(n)}}} \quad , \\ m^{(n)} &= \sqrt{\frac{d_{33}}{d_{11}\sin^2\phi^{(n)} + d_{33}\cos^2\phi^{(n)}}} \quad . \end{aligned} \tag{C.4.3}$$

The signs of the polarisation vectors are chosen in a way that the $\boldsymbol{g}^{(n)}$ form an orthonormal system, see Figure C.1. The wave associated with index 3 is a *q*P wave, which I have abbreviated with P for shortness. The index 1 corresponds to a quasi shear wave, abbreviated with SV. The SH wave has index 2.

C.5 Ray (group) velocities

The components of the ray or group velocity vectors for the three wave types, $\boldsymbol{v}^{(n)}$ (denoted by lower case letters to distinguish the group velocities from the phase velocities $V^{(n)}$) are given by

$$v_i^{(n)} = a_{ijkl}\, g_j^{(n)}\, g_k^{(n)}\, p_l^{(n)} \quad , \tag{C.5.1}$$

leading to

$$\begin{aligned} \boldsymbol{v}^{SV} &= \left(\sqrt{A_{44}}\sin\phi^{SV},\, 0,\, \sqrt{A_{44}}\cos\phi^{SV}\right) \quad , \\ \boldsymbol{v}^{SH} &= \left(\frac{A_{66}}{V^{SH}}\,\sin\phi^{SH},\, 0,\, \frac{A_{44}}{V^{SH}}\,\cos\phi^{SH}\right) \quad , \\ \boldsymbol{v}^{P} &= \left(\frac{A_{11}}{V^{P}}\,\sin\phi^{P},\, 0,\, \frac{A_{33}}{V^{P}}\,\cos\phi^{P}\right) \quad . \end{aligned} \tag{C.5.2}$$

Introducing the ray angle $\theta^{(n)}$ with $\tan\theta^{(n)} = v_x^{(n)}/v_z^{(n)}$ yields

$$\begin{aligned}
\tan\theta^{SV} &= \tan\phi^{SV} \quad , \\
\tan\theta^{SH} &= \frac{A_{66}}{A_{44}}\tan\phi^{SH} \quad , \\
\tan\theta^{P} &= \frac{A_{11}}{A_{33}}\tan\phi^{P} \quad ,
\end{aligned} \tag{C.5.3}$$

and

$$\begin{aligned}
v^{SV} &= \sqrt{A_{44}} &&= V^{SV} \quad , \\
v^{SH} &= \frac{\sqrt{A_{66}^2\sin^2\phi^{SH} + A_{44}^2\cos^2\phi^{SH}}}{V^{SH}} &&= \left[\frac{\sin^2\theta^{SH}}{A_{66}} + \frac{\cos^2\theta^{SH}}{A_{44}}\right]^{-\frac{1}{2}} \quad , \\
v^{P} &= \frac{\sqrt{A_{11}^2\sin^2\phi^{P} + A_{33}^2\cos^2\phi^{P}}}{V^{P}} &&= \left[\frac{\sin^2\theta^{P}}{A_{11}} + \frac{\cos^2\theta^{P}}{A_{33}}\right]^{-\frac{1}{2}} \quad .
\end{aligned} \tag{C.5.4}$$

C.6 Reflection and transmission coefficients

The displacement vector for a plane wave of type n is expressed by

$$\boldsymbol{u}^{(n)} = U^{(n)}\,\boldsymbol{g}^{(n)}\,\mathrm{e}^{-i\omega(t-\tau^{(n)})} \quad . \tag{C.6.1}$$

where $U^{(n)}$ is the scalar amplitude associated with the wavetype n. The eikonal or phase function $\tau^{(n)}$ is

$$\tau^{(n)} = \nabla\tau^{(n)}\cdot\boldsymbol{r} = \boldsymbol{p}^{(n)}\cdot\boldsymbol{r} \quad . \tag{C.6.2}$$

Consider now a plane boundary between two homogeneous elliptically anisotropic half spaces at the depth $z = 0$ (see Figure C.2). Depending on the type of the incident wave, reflected and transmitted waves of different types are generated. An incident SH wave leads to reflected and transmitted SH waves, whereas in the cases of incident *q*SV or *q*P waves conversion from *q*SV to *q*P and vice versa can also occur. Therefore, an incident *q*SV wave will generate not only reflected and transmitted *q*SV waves, but also reflected and transmitted *q*P waves. The same applies to an incident *q*P wave which will lead to reflected and transmitted *q*SV and *q*P waves. Each of these waves can be written in terms of Equation (C.6.1). In addition to the upper index n for the wavetype, the individual displacement vectors will be denoted with the lower index 0 for the incident wave, R for the reflected wave, and T for the transmitted wave.

To determine the reflection and transmission coefficients of the displacement, the following boundary conditions must be fulfilled:

Continuity of displacement : $u_x, u_y, u_z \quad ,$

Continuity of shear stress : $\sigma_{xz} = \rho A_{44}(\frac{\partial u_x}{\partial z} + \frac{\partial u_z}{\partial x}) \quad ,$

$\sigma_{yz} = \rho A_{44}\frac{\partial u_y}{\partial z} \quad ,$

Continuity of normal stress : $\sigma_{zz} = \rho(A_{13}\frac{\partial u_x}{\partial x} + A_{33}\frac{\partial u_z}{\partial z}) \quad .$

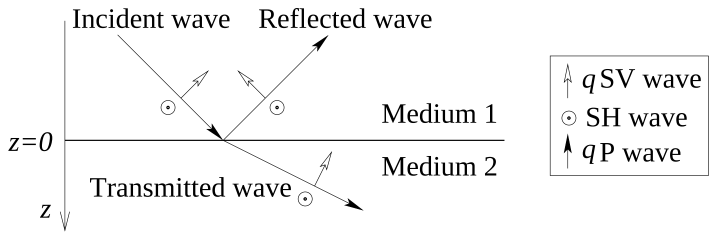

Figure C.2: Boundary between two homogeneous elliptical media and orientation of the polarisation vectors of the incident, reflected, and transmitted waves.

The spatial derivatives of the displacement components are

$$\frac{\partial u_i}{\partial x_j} = i\omega\, \mathrm{e}^{-i\omega(t-\boldsymbol{p}\cdot\boldsymbol{r})}\, u_i\, p_j \quad . \tag{C.6.3}$$

The slowness vectors of the incident, reflected, and transmitted waves are given by

$$\begin{aligned}
\text{incident wave} \quad &: \quad \boldsymbol{p}_0^{(n)} &=& \quad \frac{1}{V_0^{(n)}}\,(\sin\phi_0^{(n)},\,0,\,\cos\phi_0^{(n)}) \quad ,\\
\text{reflected wave} \quad &: \quad \boldsymbol{p}_R^{(n)} &=& \quad \frac{1}{V_R^{(n)}}\,(\sin\phi_R^{(n)},\,0,\,-\cos\phi_R^{(n)}) \quad ,\\
\text{transmitted wave} \quad &: \quad \boldsymbol{p}_T^{(n)} &=& \quad \frac{1}{V_T^{(n)}}\,(\sin\phi_T^{(n)},\,0,\,\cos\phi_T^{(n)}) \quad .
\end{aligned} \tag{C.6.4}$$

Snell's law requires that the horizontal slowness $p = \sin\phi/V$ remains constant. This can lead to imaginary angles ϕ. In that case the displacement given by Equation (C.6.1) will show exponential behaviour along z. To avoid an increase in amplitude, the cosine of the angle ϕ must be either a real or a positive imaginary number.

Application of the boundary conditions and phase matching leads to equations for the reflection and transmission coefficients. Since the SH wave is decoupled from the *q*P and *q*SV waves, the SH and *q*P/*q*SV cases can be treated separately.

SH waves

Continuity of the y component of the displacement, u_y, and the shear stress σ_{yz} leads to

$$\begin{aligned}
R_{SH-SH} &= \frac{U_R^{SH}}{U_0^{SH}} = \frac{\rho^{(1)}\,A_{44}^{(1)}\,V_2\,\cos\phi_1 - \rho^{(2)}\,A_{44}^{(2)}\,V_1\,\cos\phi_2}{\rho^{(1)}\,A_{44}^{(1)}\,V_2\,\cos\phi_1 + \rho^{(2)}\,A_{44}^{(2)}\,V_1\,\cos\phi_2} \quad ,\\
T_{SH-SH} &= \frac{U_T^{SH}}{U_0^{SH}} = \frac{2\,\rho^{(1)}\,A_{44}^{(1)}\,V_2\,\cos\phi_1}{\rho^{(1)}\,A_{44}^{(1)}\,V_2\,\cos\phi_1 + \rho^{(2)}\,A_{44}^{(2)}\,V_1\,\cos\phi_2} \quad ,
\end{aligned} \tag{C.6.5}$$

where index 1 describes the properties of medium 1 (with the incident/reflected wave) and index 2 those of medium 2 with the transmitted wave. The reflection angle, ϕ_R^{SH} is equal to the incidence angle $\phi_0^{SH} = \phi_1$, and the transmission angle $\phi_T^{SH} = \phi_2$ can be computed from Snell's law, leading to

$$\phi_T^{SH} = \arctan\left[\frac{A_{44}^{(2)}}{\frac{1}{p^2} - A_{66}^{(2)}}\right]^{\frac{1}{2}} \quad , \tag{C.6.6}$$

where p can be computed from the quantities of the incident wave, i.e. $p = \sin\phi_0^{SH}/V_0^{SH}$.

qP-qSV waves

Continuity of the x and z components of the displacement vectors, the shear stress σ_{xz} and the normal stress σ_{zz} leads to two linear system of equations with four unknowns, one system for an incident SV wave,

$$\begin{pmatrix} X_{11} & X_{12} & X_{13} & X_{14} \\ X_{21} & X_{22} & X_{23} & X_{24} \\ X_{31} & X_{32} & X_{33} & X_{34} \\ X_{41} & X_{42} & X_{43} & X_{44} \end{pmatrix} \begin{pmatrix} R_{SV-P} \\ T_{SV-P} \\ R_{SV-SV} \\ T_{SV-SV} \end{pmatrix} = \begin{pmatrix} Y_1^{SV} \\ Y_2^{SV} \\ Y_3^{SV} \\ Y_4^{SV} \end{pmatrix} \quad , \tag{C.6.7}$$

and a second for an incident P wave:

$$\begin{pmatrix} X_{11} & X_{12} & X_{13} & X_{14} \\ X_{21} & X_{22} & X_{23} & X_{24} \\ X_{31} & X_{32} & X_{33} & X_{34} \\ X_{41} & X_{42} & X_{43} & X_{44} \end{pmatrix} \begin{pmatrix} R_{P-P} \\ T_{P-P} \\ R_{P-SV} \\ T_{P-SV} \end{pmatrix} = \begin{pmatrix} Y_1^{P} \\ Y_2^{P} \\ Y_3^{P} \\ Y_4^{P} \end{pmatrix} \quad . \tag{C.6.8}$$

As for the SH case, the reflection coefficients $R_{nn'}$ and transmission coefficients $T_{nn'}$ of the displacement are given by the amplitude ratio between the reflected/transmitted wave (of type n) and the incident wave (of type n'):

$$R_{nn'} = \frac{U_R^n}{U_0^{n'}} \quad \text{and} \quad T_{nn'} = \frac{U_T^n}{U_0^{n'}} \quad . \tag{C.6.9}$$

The 4×4 matrix $\underline{X}$ is the same in both Equations, (C.6.7) and (C.6.8). Its elements are

$$
\begin{aligned}
X_{11} &= \;\; U_R^P\, l_R^P\, \sin\phi_R^P \quad , \\
X_{12} &= -\, U_T^P\, l_T^P\, \sin\phi_T^P \quad , \\
X_{13} &= -\, U_R^{SV}\, m_R^{SV}\, \cos\phi_R^{SV} \quad , \\
X_{14} &= -\, U_T^{SV}\, m_T^{SV}\, \cos\phi_T^{SV} \quad , \\
\\
X_{21} &= -\, U_R^P\, m_R^P\, \cos\phi_R^P \quad , \\
X_{22} &= -\, U_T^P\, m_T^P\, \cos\phi_T^P \quad , \\
X_{23} &= -\, U_R^{SV}\, l_R^{SV}\, \sin\phi_R^{SV} \quad , \\
X_{24} &= \;\; U_T^{SV}\, l_T^{SV}\, \sin\phi_T^{SV} \quad , \\
\\
X_{31} &= -\, \frac{U_R^P}{V_R^P}\, C_{55}^{(1)}\, \sin\phi_R^P\, \cos\phi_R^P\, (l_R^P + m_R^P) \quad , \\
X_{32} &= -\, \frac{U_T^P}{V_T^P}\, C_{55}^{(2)}\, \sin\phi_T^P\, \cos\phi_T^P\, (l_T^P + m_T^P) \quad , \\
X_{33} &= -\, \frac{U_R^{SV}}{V_R^{SV}}\, C_{55}^{(1)}\, (l_R^{SV} \sin^2\phi_R^{SV} - m_R^{SV} \cos^2\phi_R^{SV}) \quad , \\
X_{34} &= \;\; \frac{U_T^{SV}}{V_T^{SV}}\, C_{55}^{(2)}\, (l_T^{SV} \sin^2\phi_T^{SV} - m_T^{SV} \cos^2\phi_T^{SV}) \quad , \\
\\
X_{41} &= \;\; \frac{U_R^P}{V_R^P}\, (C_{13}^{(1)}\, l_R^P\, \sin^2\phi_R^P + C_{33}^{(1)}\, m_R^P\, \cos^2\phi_R^P) \quad , \\
X_{42} &= -\, \frac{U_T^P}{V_T^P}\, (C_{13}^{(2)}\, l_T^P\, \sin^2\phi_T^P + C_{33}^{(2)}\, m_T^P\, \cos^2\phi_T^P) \quad , \\
X_{43} &= -\, \frac{U_R^{SV}}{V_R^{SV}}\, \sin\phi_R^{SV}\, \cos\phi_R^{SV}\, (C_{13}^{(1)}\, m_R^{SV} - C_{33}^{(1)}\, l_R^{SV}) \quad , \\
X_{44} &= -\, \frac{U_T^{SV}}{V_T^{SV}}\, \sin\phi_T^{SV}\, \cos\phi_T^{SV}\, (C_{13}^{(2)}\, m_T^{SV} - C_{33}^{(2)}\, l_T^{SV}) \quad .
\end{aligned}
\tag{C.6.10}
$$

The right hand sides of Equations (C.6.7) and (C.6.8) are given by

$$
\begin{aligned}
Y_1^{SV} &= -\, U_0^{SV}\, m_0^{SV}\, \cos\phi_0^{SV} \quad , \\
Y_2^{SV} &= \;\; U_0^{SV}\, l_0^{SV}\, \sin\phi_0^{SV} \quad , \\
Y_3^{SV} &= \;\; \frac{U_0^{SV}}{V_0^{SV}}\, C_{55}^{(1)}\, (l_0^{SV} \sin^2\phi_0^{SV} - m_0^{SV} \cos^2\phi_0^{SV}) \quad , \\
Y_4^{SV} &= -\, \frac{U_0^{SV}}{V_0^{SV}}\, \sin\phi_0^{SV}\, \cos\phi_0^{SV}\, (C_{13}^{(1)}\, m_0^{SV} - C_{33}^{(1)}\, l_0^{SV}) \quad .
\end{aligned}
\tag{C.6.11}
$$

and

$$
\begin{aligned}
Y_1^P &= -\, U_0^P\, l_0^P\, \sin\phi_0^P \quad , \\
Y_2^P &= -\, U_0^P\, m_0^P\, \cos\phi_0^P \quad , \\
Y_3^P &= -\, \frac{U_0^P}{V_0^P}\, C_{55}^{(1)}\, \sin\phi_0^P\, \cos\phi_0^P\, (l_0^P + m_0^P) \quad , \\
Y_4^P &= -\, \frac{U_0^P}{V_0^P}\, (C_{13}^{(1)}\, l_0^P\, \sin^2\phi_0^P + C_{33}^{(1)}\, m_0^P\, \cos^2\phi_0^P) \quad .
\end{aligned}
\tag{C.6.12}
$$

The reflection and transmission angles are again determined from Snell's law:

$$
\begin{aligned}
\phi_R^P &= \arctan\left[\frac{A_{33}^{(1)}}{\frac{1}{p^2} - A_{11}^{(1)}}\right]^{\frac{1}{2}} \quad , \\
\phi_T^P &= \arctan\left[\frac{A_{33}^{(2)}}{\frac{1}{p^2} - A_{11}^{(2)}}\right]^{\frac{1}{2}} \quad , \\
\phi_R^{SV} &= \arcsin(p\, V_R^{SV}) \quad , \\
\phi_T^{SV} &= \arcsin(p\, V_T^{SV}) \quad ,
\end{aligned}
\tag{C.6.13}
$$

where again, $p = \sin\phi_0^{(n)}/V_0^{(n)}$ is computed from the incident wave with n equal to P or SV.

Equations (C.6.7) and (C.6.8) can be solved for the individual coefficients by the usual methods for systems of linear equations.

Normalised R/T coefficients

Another possibility is to express the coefficients normalised with respect to the energy flux perpendicular to the interface. The normalised reflection and transmission coefficients $\mathcal{R}_{nn'}$ and $\mathcal{T}_{nn'}$ are obtained from the standard coefficients $R_{nn'}$ and $T_{nn'}$ by

$$
\begin{aligned}
\mathcal{R}_{nn'} &= \left|\frac{\rho_R\, v_R^{n'}\, \cos\phi_R^{n'}}{\rho_0\, v_0^n\, \cos\phi_0^n}\right|^{\frac{1}{2}} R_{nn'} \quad , \\
\mathcal{T}_{nn'} &= \left|\frac{\rho_T\, v_T^{n'}\, \cos\phi_T^{n'}}{\rho_0\, v_0^n\, \cos\phi_0^n}\right|^{\frac{1}{2}} T_{nn'} \quad .
\end{aligned}
\tag{C.6.14}
$$

The wavetype denoted by n' is again that of the incident wave, index n corresponds to the reflected or transmitted wave.

C.7 Traveltimes

Consider a homogeneous medium with the vector $\boldsymbol{r} = (x, y, z) = (g_x - s_x, g_y - s_y, g_z - s_z)$ describing the distance between the source ($\boldsymbol{s}$) and receiver ($\boldsymbol{g}$) positions, and its modulus, $r = \sqrt{x^2 + y^2 + z^2}$. The traveltime $\tau^{(n)}$ of a wave of type n propagating from the source to the receiver is given by $\tau^{(n)} = r/v^{(n)}$. This results in the following traveltimes:

$$
\begin{aligned}
\tau^{SV} &= \sqrt{\frac{x^2+y^2+z^2}{A_{44}}} \quad , \\
\tau^{SH} &= \sqrt{\frac{x^2+y^2}{A_{66}} + \frac{z^2}{A_{44}}} \quad , \\
\tau^{P} &= \sqrt{\frac{x^2+y^2}{A_{11}} + \frac{z^2}{A_{33}}} \quad .
\end{aligned}
\tag{C.7.1}
$$

C.8 Geometrical Spreading

The relative geometrical spreading $L^{(n)}$ that a wave of type n undergoes in a homogeneous medium can be expressed by

$$
L^{(n)} = \frac{\cos\theta^{(n)}}{\sqrt{\left|\mathrm{det}\underline{\mathsf{N}}^{(n)}\right|}} \frac{v^{(n)}}{V^{(n)}} \quad , \tag{C.8.1}
$$

where the 2×2 matrix $\underline{\mathsf{N}}^{(n)}$ is the second-order mixed derivative matrix of the traveltimes $\tau^{(n)}$ with respect to the source and receiver positions:

$$
N_{IJ}^{(n)} = -\frac{\partial^2 \tau^{(n)}}{\partial s_I \, \partial g_J} \quad . \tag{C.8.2}
$$

(Indices I and J take the values 1 and 2.) Differentiation of Equation (C.7.1) leads to the following expressions for the relative geometrical spreading:

$$
\begin{aligned}
L^{SV} &= \sqrt{A_{44}}\, r \quad , \\
L^{SH} &= \frac{\sqrt{A_{44}}\, A_{66}}{v\, V}\, r \quad , \\
L^{P} &= \frac{A_{11}\, \sqrt{A_{33}}}{v\, V}\, r \quad .
\end{aligned}
\tag{C.8.3}
$$

Appendix D

Determination of sectorially best-fitting isotropic background media

D.1 Summary

Computations in anisotropic media are commonly simplified by applying perturbation methods. These require suitable background media, that are often chosen to be isotropic. In this appendix we present expressions for sectorially best-fitting isotropic P- and S-velocities. The equations follow from a generalisation of a technique suggested by Fedorov (1968). Examples for media with polar (VTI) and triclinic symmetry confirm the superiority of the results over the commonly used globally best-fitting isotropic velocities by Fedorov (1968). This makes the method particularly suited for any application associated with perturbation techniques for anisotropic wave propagation.

D.2 Introduction

Computations in anisotropic media are usually very cumbersome. Many techniques developed for isotropic media will fail or have to be altered in the presence of anisotropy. Therefore, computations in anisotropic media are commonly simplified by applying perturbation methods (e.g., Jech and Pšenčík, 1989), where the anisotropic medium is described by a linear combination of a suitable background or reference medium, and a small perturbation with respect to the background medium. Often an isotropic background is assumed, where the perturbations account for the anisotropy. This has the advantage that isotropic techniques can be used for the computations in the background medium. In the simplest case, the isotropic velocities can be obtained from averaging the elastic constants over all phase directions, leading to the well-known result by Fedorov (1968). For applications like the generation of traveltimes with finite-difference methods in combination with perturbation (e.g., Ettrich and Gajewski, 1998; Soukina et al., 2003; Ettrich et al., 2001) have derived expressions for background media with elliptical anisotropy that permit to consider media with stronger anisotropy than isotropic backgrounds. However, their results are restricted to P-waves.

The results from Ettrich et al. (2001) were not only derived for averaging over all phase directions, but also for an average over a cone around the vertical axis, thus leading to a sectorially best-fitting elliptical background medium. Intuitively a sectorial fit permits a closer approximation when information on the phase directions can be restricted to a sector instead of the whole unit sphere. This is often possible, for example in the reflection/transmission problem, where Snell's law has to be evaluated at a boundary between two anisotropic media. In this case the horizontal slowness, and thus the azimuth angle is known, therefore averaging could be restricted to be carried out over the inclination only. Formulae for this type of averaging are provided in this work.

We have derived expressions for sectorially best-fitting isotropic velocities following the approach suggested by Fedorov (1968). These are closely related to the velocities resulting from the weak anisotropy approximation (Backus, 1965). In contrast to the work by Ettrich et al. (2001) we give also expressions for best-fitting shear velocities. Also, the averaging can take place over any region desired, not only over a cone around the vertical axis, although this important case is a subset of our solution.

In the first section of this appendix, we describe the averaging approach by Fedorov (1968) to obtain the globally best-fitting isotropic medium. We use a generalisation of his approach to determine a sectorially best-fitting medium. We demonstrate the superiority of the resulting expressions over the global average in the following section with examples on compressional and shear velocities and slowness surfaces for media with polar and triclinic symmetry. Finally, we summarise our conclusions and give an outlook.

D.3 Method

For the derivation of expressions for best-fitting isotropic background (or reference) velocities we follow the derivation for the globally best-fitting isotropic medium given in Fedorov (1968). We begin with the Christoffel matrix $\underline{\Lambda}$

$$\Lambda_{ik} = a_{ijkl} n_j n_l \quad , \tag{D.3.1}$$

where the a_{ijkl} are the elements of the density-normalised elasticity tensor, and the n_j are the components of the phase normal vector,

$$\boldsymbol{n} = \begin{pmatrix} \sin\theta\,\cos\phi \\ \sin\theta\,\sin\phi \\ \cos\theta \end{pmatrix} \quad , \tag{D.3.2}$$

where θ is the inclination and ϕ the azimuth angle. The eigenvalue problem for $\underline{\Lambda}$ leading to the three phase velocities V_m (m=1,2,3) is

$$(\Lambda_{ik} - V_m^2\,\delta_{ik})\,g_i^{(m)} = 0 \quad . \tag{D.3.3}$$

In (D.3.3), the eigenvector $g_i^{(m)}$ is the polarisation vector of the wave corresponding to the phase velocity V_m, which, in turn, is the m-th eigenvalue of $\underline{\Lambda}$. If the phase normal n_j is known, (D.3.3) can be solved and the phase velocities can be obtained in a closed form from $|\Lambda_{ik} - V_m^2\,\delta_{ik}| = 0$ (e.g., with Cardani's formula).

Now we express the elasticity tensor a_{ijkl} in a linearised form by the sum of the elasticity tensor of an isotropic background medium, $a_{ijkl}^{(0)}$, and the deviations Δa_{ijkl} of the anisotropic medium from the isotropic background:

$$a_{ijkl} = a_{ijkl}^{(0)} + \Delta a_{ijkl} \quad . \tag{D.3.4}$$

Remembering that the elasticity tensor for an isotropic medium is given by

$$a_{ijkl}^{(0)} = (V_P^2 - 2\,V_S^2)\delta_{ij}\delta_{kl} + V_S^2(\delta_{ik}\delta_{jl} + \delta_{il}\delta_{jk}) \tag{D.3.5}$$

we want to find the P- and S-wave velocities V_P and V_S that give the best isotropic approximation for an arbitrarily anisotropic medium.

To obtain this best-fitting isotropic background medium, it is required that

$$\langle(\Lambda_{ik} - \Lambda_{ik}^{(0)})^2\rangle \stackrel{!}{=} \text{Min.} \tag{D.3.6}$$

becomes minimal (Fedorov, 1968). The brackets $\langle\rangle$ denote the averaging process

$$\langle A(\theta,\phi)\rangle_{\theta,\phi} = \frac{\int\limits_{\phi_1}^{\phi_2}\int\limits_{\theta_1}^{\theta_2} A(\theta,\phi)\sin\theta\,\mathrm{d}\theta\,\mathrm{d}\phi}{\int\limits_{\phi_1}^{\phi_2}\int\limits_{\theta_1}^{\theta_2} \sin\theta\,\mathrm{d}\theta\,\mathrm{d}\phi} \quad . \tag{D.3.7}$$

Expanding the square in (D.3.6) leads to

$$\langle(\Lambda_{ik} - \Lambda_{ik}^{(0)})^2\rangle = \langle\Lambda_{ik}\Lambda_{ik}\rangle + \langle\Lambda_{ik}^{(0)}\Lambda_{ik}^{(0)}\rangle - 2\,\langle\Lambda_{ik}\Lambda_{ik}^{(0)}\rangle \quad , \tag{D.3.8}$$

where

$$\Lambda_{ik}^{(0)}\Lambda_{ik}^{(0)} = V_P^4 + 2\,V_S^4 \quad , \tag{D.3.9}$$

and

$$\Lambda_{ik}\Lambda_{ik}^{(0)} = (V_P^2 - V_S^2)a_{ijkl}n_in_jn_kn_l + V_S^2 a_{ijil}n_jn_l \quad . \tag{D.3.10}$$

To minimise the objective function (D.3.6), the derivatives of (D.3.6) with respect to V_P and V_S must be zero. The resulting linear system of equations leads to

$$\begin{aligned} V_P^2 &= a_{ijkl}\langle n_in_jn_kn_l\rangle \quad , \\ V_S^2 &= \frac{1}{2}\left(a_{ijkl}\langle n_jn_l\rangle - V_P^2\right) \quad . \end{aligned} \tag{D.3.11}$$

These isotropic phase velocities yield the best-fitting background velocities in a least-square sense.

The same result was originally derived by Fedorov (1968) following the same approach, but minimising (D.3.6) not for the velocities but for the Lamé-parameters λ and μ instead. Fedorov derived his results in order to find *that isotropic medium that is most similar to the given crystal not only as regards the propagation of elastic waves but also as regards elastic properties generally*. To do so, he averaged the phase normals n_j over the entire unit sphere, i.e. $\theta = [0\ldots\pi]$ and $\phi = [0\ldots 2\pi]$, in (D.3.7), resulting in

$$\begin{aligned} V_P^2 &= \frac{1}{15}\left(a_{iikk} + 2\,a_{ikik}\right) \quad , \\ V_S^2 &= \frac{1}{30}\left(3\,a_{ikik} - a_{iikk}\right) \quad . \end{aligned} \tag{D.3.12}$$

Fedorov (1968) has also determined the best-fitting isotropic velocities for the case that the direction of the phase normal was fixed, i.e. no averaging was carried out in Equation (D.3.11). In this case the resulting velocities coincide with those obtained from the weak anisotropy approximation (Backus, 1965). More precisely, for the S-wave the best-fitting isotropic velocity is the geometric mean of the weak anisotropy qS_1- and qS_2-velocities:

$$\begin{aligned} V_{P_{WA}}^2 &= a_{ijkl}\,n_in_jn_kn_l \\ V_{S_{WA}}^2 &= \frac{1}{2}\left(a_{ijik}\,n_jn_k - V_{P_{WA}}^2\right) \quad . \end{aligned} \tag{D.3.13}$$

This result is not surprising as the weak anisotropy approximation is based on a linear (first-order) perturbation of the elasticity tensor, as is Equation (D.3.4).

There are, however, situations where neither the average over the whole unit sphere nor the result for a given phase direction is the best choice for a background medium. This is, for example, the case when only two of the three components of p_j are available, as for the reflection-transmission problem at an interface, where a sixth-order polynomial must be solved to evaluate Snell's law (Henneke, 1971). Another example is the second-order interpolation of traveltimes (see Chapter 2) in the presence of topography. Here, the vertical slowness is required for the interpolation, but only the horizontal components are available. The same problem occurs in the determination of geometrical spreading from traveltimes (see Chapter 8). In all these cases, only the horizontal slowness is known. Since the phase velocity is also unknown, the vertical slowness can not simply be obtained from the eikonal equation. Here, it would be a better choice to use a background medium that is obtained only from averaging over the inclination angle θ since the azimuth angle ϕ is known.

Also, for other applications using perturbation methods, it can be favourable to use a sectorially best-fitting background medium rather than the global one given by (D.3.12). This has been recognised before, for example by Ettrich et al. (2001) who have published equations for approximate P-wave velocities that yield the best fit for a cone around the vertical axis.

Therefore we have generalised the result by Fedorov (1968) for the cases in between averaging over the whole unit sphere and no averaging at all. We present our results in the following sections, first for an average over a sectorial fit in θ and ϕ (Equations (D.4.1) and (D.4.2)), followed by expressions where the average is only taken over the inclination for those applications where the azimuth is known (Equations (D.5.1) and (D.5.2)), and, finally, followed by the special case of a weakly anisotropic medium with polar symmetry (VTI medium) in terms of Thomsen's parameters (Thomsen, 1986).

D.4 Averaging over inclination and azimuth

In this section we provide the expressions for best-fitting isotropic background velocities, if the averaging is carried out over the inclination (θ) and the azimuth (ϕ) in the intervals $[\theta_1 \ldots \theta_2]$ and

$[\phi_1 \dots \phi_2]$. If $-\theta_1 \neq \theta_2$, we find for the best-fitting P-velocity

$$
\begin{aligned}
V_P^2 &= V_P^2(\theta_1, \theta_2, \phi_1, \phi_2) = a_{ijkl} \langle n_i n_j n_k n_l \rangle_{\theta,\phi} \\
&= A_{11} \left(\frac{C_1 - 2\,C_3 + C_5}{C_1} \right) \left(\frac{3\,\Delta_0 + \Delta_2 + \Delta_4}{8\,\Delta_0} \right) + A_{22} \left(\frac{C_1 - 2\,C_3 + C_5}{C_1} \right) \left(\frac{3\,\Delta_0 - \Delta_2 + \Delta_4}{8\,\Delta_0} \right) \\
&+ A_{33} \frac{C_5}{C_1} \\
&+ (4\,A_{44} + 2\,A_{23}) \left(\frac{C_3 - C_5}{C_1} \right) \left(\frac{4\,\Delta_0 - \Delta_2}{8\,\Delta_0} \right) + (4\,A_{55} + 2\,A_{13}) \left(\frac{C_3 - C_5}{C_1} \right) \left(\frac{4\,\Delta_0 + \Delta_2}{8\,\Delta_0} \right) \\
&+ (4\,A_{66} + 2\,A_{12}) \left(\frac{C_1 - 2\,C_3 + C_5}{C_1} \right) \left(\frac{\Delta_0 - \Delta_4}{8\,\Delta_0} \right) \\
&- 4\,A_{16} \left(\frac{C_1 - 2\,C_3 + C_5}{C_1} \right) \left(\frac{\Gamma_4}{8\,\Delta_0} \right) + 4\,A_{26} \left(\frac{C_1 - 2\,C_3 + C_5}{C_1} \right) \left(\frac{\Sigma_4}{8\,\Delta_0} \right) \\
&+ 4\,A_{24} \left(\frac{S_5}{C_1} \right) \left(\frac{\Gamma_1 - \Gamma_3}{8\,\Delta_0} \right) - 4\,A_{15} \left(\frac{S_5}{C_1} \right) \left(\frac{\Sigma_1 - \Sigma_3}{8\,\Delta_0} \right) \\
&+ 4\,A_{34} \left(\frac{S_3 - S_5}{C_1} \right) \left(\frac{\Gamma_1}{8\,\Delta_0} \right) - 4\,A_{35} \left(\frac{S_3 - S_5}{C_1} \right) \left(\frac{\Sigma_1}{8\,\Delta_0} \right) \\
&+ (4\,A_{14} + 8\,A_{56}) \left(\frac{S_5}{C_1} \right) \left(\frac{\Gamma_3}{8\,\Delta_0} \right) - (4\,A_{25} + 8\,A_{46}) \left(\frac{S_5}{C_1} \right) \left(\frac{\Sigma_3}{8\,\Delta_0} \right) \\
&- (4\,A_{36} + 8\,A_{45}) \left(\frac{C_3 - C_5}{C_1} \right) \left(\frac{\Gamma_2}{8\,\Delta_0} \right) , \qquad \text{(D.4.1)}
\end{aligned}
$$

and for the best-fitting shear velocity

$$
\begin{aligned}
V_S^2 &= V_S^2(\theta_1, \theta_2, \phi_1, \phi_2) = \frac{1}{2} \left(a_{ijkl} \langle n_j n_l \rangle_{\theta,\phi} - V_P^2 \right) \\
&= A_{11} \left(\frac{C_1 - C_3}{2\,C_1} \right) \left(\frac{4\,\Delta_0 + \Delta_2}{8\,\Delta_0} \right) + A_{22} \left(\frac{C_1 - C_3}{2\,C_1} \right) \left(\frac{4\,\Delta_0 - \Delta_2}{8\,\Delta_0} \right) + A_{33} \left(\frac{C_3}{2\,C_1} \right) \\
&+ A_{44} \left[\left(\frac{C_1 - C_3}{2\,C_1} \right) \left(\frac{4\,\Delta_0 - \Delta_2}{8\,\Delta_0} \right) + \frac{C_3}{2\,C_1} \right] + A_{55} \left[\left(\frac{C_1 - C_3}{2\,C_1} \right) \left(\frac{4\,\Delta_0 + \Delta_2}{8\,\Delta_0} \right) + \frac{C_3}{2\,C_1} \right] \\
&+ A_{66} \left(\frac{C_1 - C_3}{2\,C_1} \right) + 2\,(A_{16} + A_{26} + A_{45}) \left(\frac{C_1 - C_3}{2\,C_1} \right) \left(\frac{\Sigma_2}{8\,\Delta_0} \right) \\
&+ 2\,(A_{24} + A_{34} + A_{56}) \left(\frac{S_3}{2\,C_1} \right) \left(\frac{\Gamma_1}{8\,\Delta_0} \right) - 2\,(A_{15} + A_{35} + A_{46}) \left(\frac{S_3}{2\,C_1} \right) \left(\frac{\Sigma_1}{8\,\Delta_0} \right) \\
&- \frac{V_P^2}{2} . \qquad \text{(D.4.2)}
\end{aligned}
$$

The abbreviations C_n, S_n, Γ_n, Σ_n, and Δ_n are introduced further below. In the special case that $\theta_1 = 0$, $\theta_2 = \pi$, $\phi_1 = 0$, and $\phi_2 = 2\pi$, these expressions reduce to the global average of Fedorov (1968) given by (D.3.12). For $\theta_1 = 0$, $\theta_2 = \theta$, $\phi_1 = 0$, and $\phi_2 = 2\pi$, Equation (D.4.1) is equal to the sectorially best-fitting isotropic P-velocity derived by Ettrich et al. (2001).

If $-\theta_1 = \theta_2 = \theta$, Equations (D.4.1) and (D.4.2) must be used in a variant as C_1 becomes zero: In (D.4.1) and (D.4.2) we must replace C_n by C_n^0 and S_n by zero. The abbreviations C_n^0 are introduced further below.

D.5 Averaging over inclination only

If the phase normals are averaged over the inclination (θ) only, we only integrate over θ in (D.3.7). As result we find for the best-fitting P-velocity in the case that $-\theta_1 \neq \theta_2$

$$\begin{aligned}
V_P^2 &= V_P^2(\theta_1,\theta_2) = a_{ijkl}\langle n_i n_j n_k n_l\rangle_\theta \\
&= A_{11}\left(\frac{C_1 - 2\,C_3 + C_5}{C_1}\right)\cos^4\phi \,+\, A_{22}\left(\frac{C_1 - 2\,C_3 + C_5}{C_1}\right)\sin^4\phi \,+\, A_{33}\,\frac{C_5}{C_1} \\
&+ (4\,A_{44} + 2\,A_{23})\left(\frac{C_3 - C_5}{C_1}\right)\sin^2\phi \,+\, (4\,A_{55} + 2\,A_{13})\left(\frac{C_3 - C_5}{C_1}\right)\cos^2\phi \\
&+ (4\,A_{66} + 2\,A_{12})\left(\frac{C_1 - 2\,C_3 + C_5}{C_1}\right)\sin^2\phi\cos^2\phi \\
&+ 4\,A_{16}\left(\frac{C_1 - 2\,C_3 + C_5}{C_1}\right)\sin\phi\cos^3\phi \,+\, 4\,A_{26}\left(\frac{C_1 - 2\,C_3 + C_5}{C_1}\right)\cos\phi\sin^3\phi \\
&- 4\,A_{24}\left(\frac{S_5}{C_1}\right)\sin^3\phi \,-\, 4\,A_{15}\left(\frac{S_5}{C_1}\right)\cos^3\phi \\
&- 4\,A_{34}\left(\frac{S_3 - S_5}{C_1}\right)\,\sin\phi \,-\, 4\,A_{35}\left(\frac{S_3 - S_5}{C_1}\right)\cos\phi \\
&- (4\,A_{14} + 8\,A_{56})\left(\frac{S_5}{C_1}\right)\sin\phi\cos^2\phi \,-\, (4\,A_{25} + 8\,A_{46})\left(\frac{S_5}{C_1}\right)\cos\phi\sin^2\phi \\
&+ (4\,A_{36} + 8\,A_{45})\left(\frac{C_3 - C_5}{C_1}\right)\sin\phi\cos\phi\,,
\end{aligned} \tag{D.5.1}$$

and for the best-fitting shear velocity

$$\begin{aligned}
V_S^2 &= V_S^2(\theta_1,\theta_2) = \frac{1}{2}\,\left(a_{ijkl}\langle n_j n_l\rangle_\theta - V_P^2\right) \\
&= A_{11}\left(\frac{C_1 - C_3}{2\,C_1}\right)\cos^2\phi \,+\, A_{22}\left(\frac{C_1 - C_3}{2\,C_1}\right)\sin^2\phi \,+\, A_{33}\left(\frac{C_3}{2\,C_1}\right) \\
&+ A_{44}\left[\left(\frac{C_1 - C_3}{2\,C_1}\right)\sin^2\phi + \frac{C_3}{2\,C_1}\right] \,+\, A_{55}\left[\left(\frac{C_1 - C_3}{2\,C_1}\right)\cos^2\phi + \frac{C_3}{2\,C_1}\right] \,+\, A_{66}\left(\frac{C_1 - C_3}{2\,C_1}\right) \\
&+ 2\,(A_{16} + A_{26} + A_{45})\left(\frac{C_1 - C_3}{2\,C_1}\right)\sin\phi\cos\phi \\
&- 2\,(A_{24} + A_{34} + A_{56})\left(\frac{S_3}{2\,C_1}\right)\sin\phi \,+\, 2\,(A_{15} + A_{35} + A_{46})\left(\frac{S_3}{2\,C_1}\right)\cos\phi \\
&- \frac{V_P^2}{2}\,.
\end{aligned} \tag{D.5.2}$$

The abbreviations C_n and S_n are introduced in further below..

If $-\theta_1 = \theta_2 = \theta$, Equations (D.5.1) and (D.5.2) must be used in a variant as C_1 becomes zero: In (D.5.1) and (D.5.2) we must replace C_n by C_n^0 and S_n by zero. The abbreviations C_n^0 can also be found further below.

D.6 Sectorially best-fitting velocities for VTI media

In this section we rewrite the expressions for the sectorially best-fitting velocities for the special case of an anisotropic medium with polar symmetry in terms of Thomsen's parameters (Thomsen, 1986). An anisotropic medium with polar symmetry, also commonly addressed as vertical transverse isotropic (VTI) symmetry, is characterised by the elastic tensor

$$\underline{\mathsf{A}} = \begin{pmatrix} A_{11} & A_{11} - 2A_{66} & A_{13} & 0 & 0 & 0 \\ & A_{11} & A_{13} & 0 & 0 & 0 \\ & & A_{33} & 0 & 0 & 0 \\ & & & A_{55} & 0 & 0 \\ & & & & A_{55} & 0 \\ & & & & & A_{66} \end{pmatrix} .$$

We use Thomsen's parameters (Thomsen, 1986) and the weak anisotropy approximation for δ (Thomsen, 1993) to express the elastic parameters as

$$\begin{aligned} A_{11} &= \alpha^2(1+2\epsilon)\,, & A_{33} &= \alpha^2\,, \\ A_{55} &= \beta^2\,, & A_{66} &= \beta^2(1+2\gamma)\,, \\ A_{13} &= \alpha^2(1+\delta) - 2\beta^2\,. \end{aligned}$$

Since the velocity is independent of the azimuth in this type of medium, Equations (D.4.1) and (D.4.2) lead to the same result as Equations (D.5.1) and (D.5.2), namely for the best-fitting P-wave velocity we get

$$V_P^2 = \alpha^2 \left[1 + 2\,\frac{C_1 - 2C_3 + C_5}{C_1}\,\epsilon + 2\,\frac{C_3 - C_5}{C_1}\,\delta\right] , \qquad \text{(D.6.1)}$$

and for the best-fitting S-wave velocity

$$V_S^2 = \beta^2 \left[1 + \frac{C_1 - C_3}{C_1}\,\gamma\right] + \alpha^2\,\frac{C_3 - C_5}{C_1}\,(\epsilon - \delta)\,. \qquad \text{(D.6.2)}$$

The abbreviations C_1, C_3, and C_5 are introduced in the following section.

D.7 Abbreviations

In this section we introduce the abbreviations used in the results. The averaging process described by Equation (D.3.7) leads to a set of integrals of trigonometric functions. In order to make the expressions for the velocities more legible we introduce the abbreviations

$$
\begin{aligned}
C_5 &= \frac{\cos^5\theta_2 - \cos^5\theta_1}{5}\,, & S_5 &= \frac{\sin^5\theta_2 - \sin^5\theta_1}{5}\,, \\
C_3 &= \frac{\cos^3\theta_2 - \cos^3\theta_1}{3}\,, & S_3 &= \frac{\sin^3\theta_2 - \sin^3\theta_1}{3}\,, \\
C_1 &= \cos\theta_2 - \cos\theta_1\,, & \Delta_0 &= \frac{\phi_2 - \phi_1}{8}\,, \\
\Delta_2 &= \frac{\sin 2\phi_2 - \sin 2\phi_1}{4}\,, & \Delta_4 &= \frac{\sin 4\phi_2 - \sin 4\phi_1}{32}\,, \\
\Gamma_1 &= \cos\phi_2 - \cos\phi_1\,, & \Sigma_1 &= \sin\phi_2 - \sin\phi_1\,, \\
\Gamma_2 &= \frac{\cos^2\phi_2 - \cos^2\phi_1}{2}\,, & \Sigma_2 &= \frac{\sin^2\phi_2 - \sin^2\phi_1}{2}\,, \\
\Gamma_3 &= \frac{\cos^3\phi_2 - \cos^3\phi_1}{3}\,, & \Sigma_3 &= \frac{\sin^3\phi_2 - \sin^3\phi_1}{3}\,, \\
\Gamma_4 &= \frac{\cos^4\phi_2 - \cos^4\phi_1}{4}\,, & \Sigma_4 &= \frac{\sin^4\phi_2 - \sin^4\phi_1}{4}
\end{aligned}
$$

to express the results of these integrals. The abbreviations were chosen in a way that the angular dependency can still be recognised, as C_n and Γ_n correspond to the n-th powers of the cosine of θ and ϕ, respectively, and S_n and Σ_n indicate the n-th powers of the sine of θ and ϕ.

For the results from averaging over the inclination from $-\theta$ to θ we use the abbreviations

$$
C_1^0 = \cos\theta - 1 \quad , \quad C_3^0 = \frac{\cos^3\theta - 1}{3} \quad , \quad C_5^0 = \frac{\cos^5\theta - 1}{5} \quad .
$$

In the next section we will give examples for the quality of the fit that can be obtained by using a sectorial approximation.

D.8 Examples for sectorially best-fitting isotropic background media

We consider two different types of anisotropic media to demonstrate the sectorially best-fitting isotropic background velocities. The first is a medium with polar symmetry and the vertical axis as symmetry axis (this symmetry is also known as vertically transverse isotropic, VTI). The density-normalised elastic parameters for this synthetic medium matching a shale (see, e.g., Thomsen, 1986) are

$$
\underline{\mathsf{A}} = \begin{pmatrix}
13.59 & 6.795 & 5.44 & 0. & 0. & 0. \\
 & 13.59 & 5.44 & 0. & 0. & 0. \\
 & & 10.873 & 0. & 0. & 0. \\
 & & & 2.72 & 0. & 0. \\
 & & & & 2.72 & 0. \\
 & & & & & 3.4
\end{pmatrix} \,, \tag{D.8.1}
$$

(values in km^2/s^2) or, in Thomsen's parameters:

$$
\begin{aligned}
\alpha &= 3.2974\,\text{km/s}\,, & \beta &= 1.6492\,\text{km/s}\,, \\
\epsilon &= 0.1249\,, & \gamma &= 0.1250\,, \\
\delta &= 0.0006 \quad .
\end{aligned}
$$

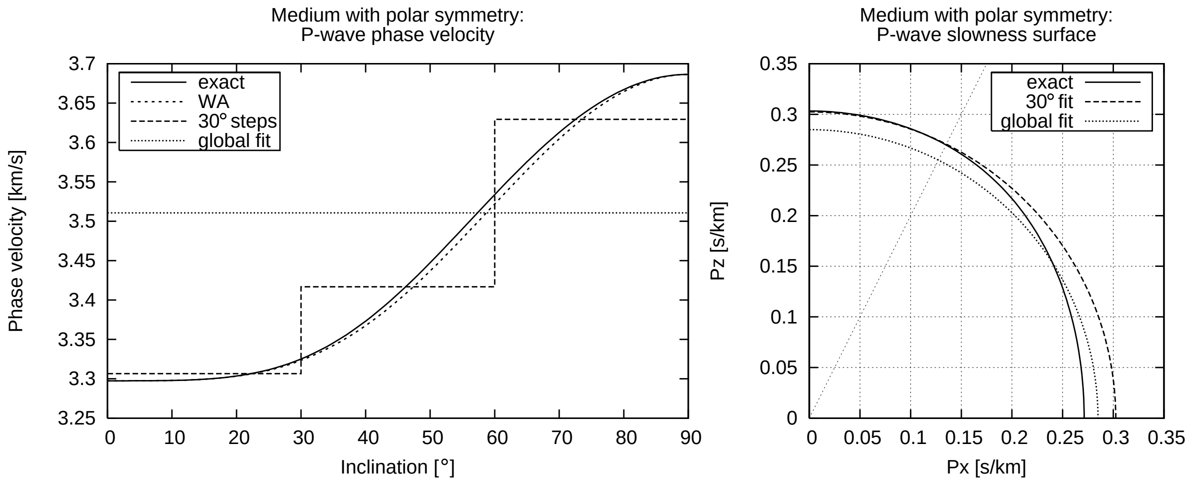

Figure D.1: P-wave phase velocities (left) and slowness surfaces (right) for a medium with polar symmetry. In the phase velocity plot, WA is short for the weak anisotropy approximation. In the slowness surface plot, the 30° line corresponds to an average over θ in the range $[0^\circ \ldots 30^\circ]$. The thin dotted line indicates the 30° cone.

We have computed the globally best-fitting isotropic velocities and the isotropic velocities for fixed inclination and azimuth angles from Equations (D.3.12) and (D.3.13). As mentioned above, the latter correspond to the weak-anisotropy approximation. Finally, we have applied Equations (D.5.1) and (D.5.2) to obtain the sectorially best-fitting velocities for sectors of 30° width in inclination. (Due to the rotational symmetry around the vertical axis the results from (D.5.1) and (D.5.2), and (D.4.1) and (D.4.2) coincide.) All results are displayed together with the exact solution in Figure D.1 for the P-wave and Figure D.2 for the shear wave.

It can be immediately seen that for the P-wave the 30° width sectorial fit is far superior to the global approximation (Figure D.1, left). This is also confirmed by the slowness surface plot in the right of Figure D.1. Here, only the result for the averaging from 0° to 30° is shown together with the exact values and the global approximation. It is obvious from Figure D.1 that in the 30° cone around the vertical axis the sectorial fit yields a much better approximation than the global one. For P-waves this was also shown by Ettrich et al. (2001).

At a first glance, the results appear less convincing for the shear wave in Figure D.2, however, we should not expect that we can approximate two different anisotropic shear velocities with one isotropic velocity that fits both well. Also, the velocity range displayed in the shear velocity plot is smaller than that in the P-velocity plot, therefore the deviations appear even larger. If we take a closer look, we still find that the sectorial fit matches the exact velocities better than the global one. This can also be seen in the plot of the slowness surface in the right of Figure D.2.

We have computed phase velocities and slowness surfaces in the same manner for a second example, a sandstone with triclinic symmetry (Mensch and Rasolofosaon, 1997). It is described by the density-

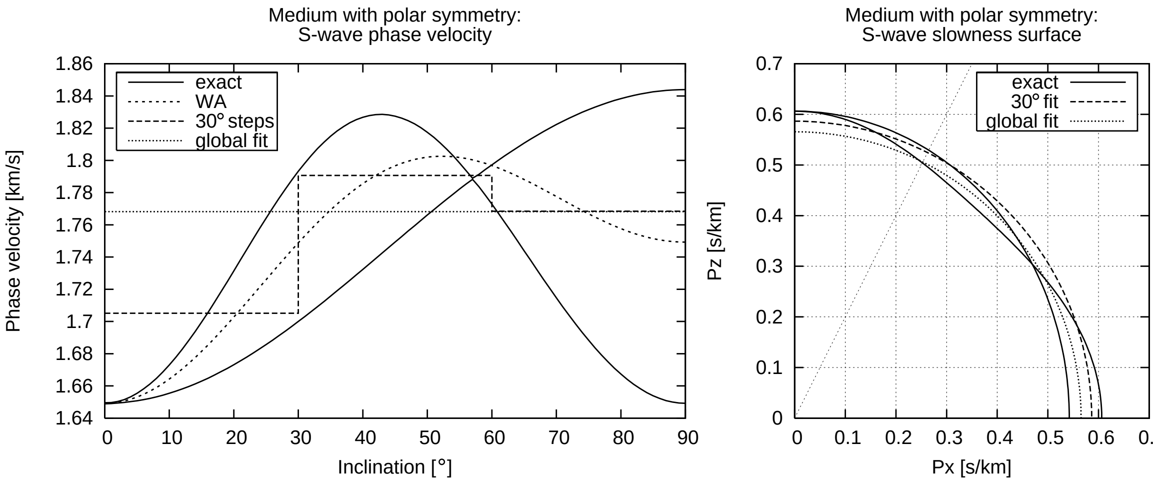

Figure D.2: Shear wave phase velocities (left) and slowness surfaces (right) for a medium with polar symmetry. In the phase velocity plot, WA is short for the weak anisotropy approximation. In the slowness surface plot, the 30° line corresponds to an average over θ in the range $[0^\circ \ldots 30^\circ]$. The thin dotted line indicates the 30° cone.

normalised elastic parameters

$$\underline{\mathsf{A}} = \begin{pmatrix} 4.95 & 0.43 & 0.62 & 0.67 & 0.52 & 0.38 \\ & 5.09 & 1.00 & 0.09 & -0.09 & -0.28 \\ & & 6.77 & 0.00 & -0.24 & -0.48 \\ & & & 2.45 & 0.00 & 0.09 \\ & & & & 2.88 & 0.00 \\ & & & & & 2.35 \end{pmatrix} \tag{D.8.2}$$

(values are given in km^2/s^2). We have only considered the x_1-direction with the azimuth angle $\phi = 0$ here. Figure D.3 shows the resulting P-wave phase velocities (left) and slowness surfaces (right), Figure D.4 shows the same for the shear waves.

As for the polar medium, we can see in Figure D.3 (left) that again the sectorial fit for the P-wave is a much better approximation to the real phase velocity than the global fit. In the slowness surface plot (right), we have displayed two sectorial fits. First, we have averaged θ from $[-30^\circ \ldots 30^\circ]$ and ϕ from $[-15^\circ \ldots 15^\circ]$. The second fit (denoted as 30° fit) results from averaging in θ over the interval $[-30^\circ \ldots 30^\circ]$ while keeping ϕ constant, i.e. $\phi = 0^\circ$. Although in this case both sectorial fits are very close to each other, larger differences can and do occur, for example if an azimuth angle of 60° is considered (not shown here). Both are superior to the approximation that results from averaging over all azimuths within the 30° cone around the vertical axis. For the shear wave we find again confirmed in Figure D.4 that a single velocity value cannot correctly describe both anisotropic shear velocities although the sectorial fit is still a better approximation than the global one.

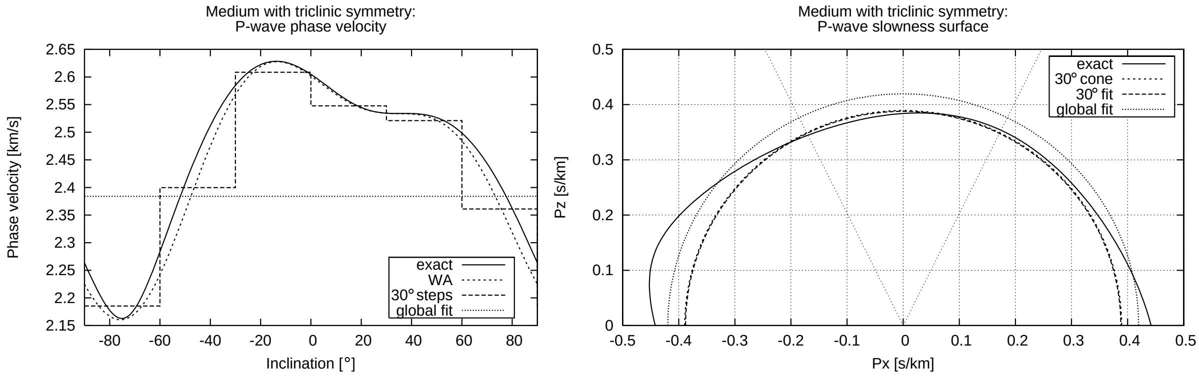

Figure D.3: P-wave phase velocities (left) and slowness surfaces (right) for a medium with triclinic symmetry. In the phase velocity plot, WA is short for the weak anisotropy approximation. In the slowness surface plot, the 30° line corresponds to an average over θ in the range $[0^\circ \ldots 30^\circ]$. The thin dotted line indicates the 30° cone.

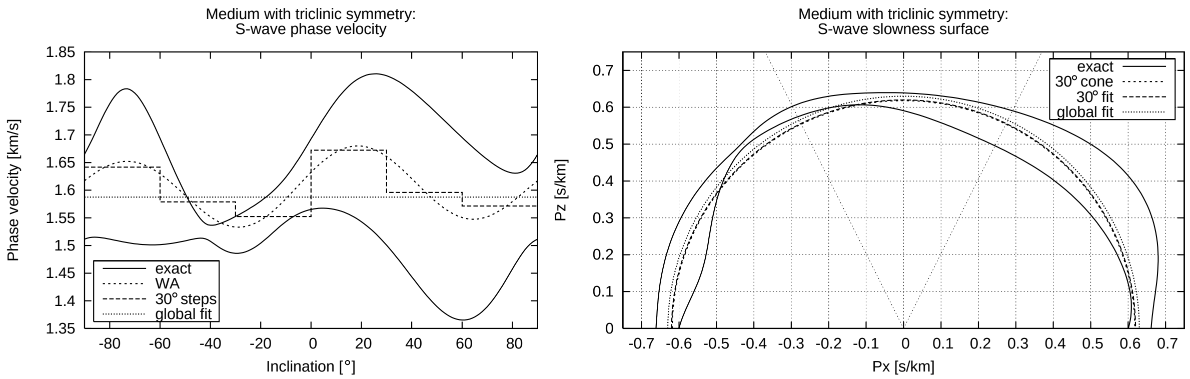

Figure D.4: Shear wave phase velocities (left) and slowness surfaces (right) for a medium with triclinic symmetry. In the phase velocity plot, WA is short for the weak anisotropy approximation. In the slowness surface plot, the 30° line corresponds to an average over θ in the range $[0^\circ \ldots 30^\circ]$. The thin dotted line indicates the 30° cone.

D.9 Conclusions and Outlook

We have presented expressions for sectorially best-fitting isotropic background media. These were obtained from a generalisation of the method by Fedorov (1968). Examples confirm that the sectorial approximation is generally superior to the global one. This conclusion is of special interest for applications within seismic exploration as here we are mainly concerned about a region restricted to inclinations below about 30°. Particularly for the P-waves we find good agreement between the real and the best-fitting isotropic background velocity resulting from the sectorial fit. But despite the fact that we cannot outwit physics by replacing two different shear velocities in the anisotropic medium by one isotropic background shear velocity, the results for the shear wave velocities are still very useful with regards to applications based on perturbation methods.

Possible applications are the second-order traveltime interpolation in anisotropic media when topography occurs and the determination of geometrical spreading from traveltimes. Here, the sectorially best-fitting background media can be combined with perturbation method in an iterative procedure to determine the third, missing, slowness component. The initial results are very promising. They are of particular interest as the method can also be applied to shear waves. In a similar way, we can solve the reflection/transmission problem at an interface between two anisotropic media. Generally, the expressions for sectorially best-fitting isotropic background media are of interest for any application associated with perturbation methods for anisotropic wave propagation.

Appendix E

Application of Snell's law in weakly anisotropic media

E.1 Summary

Snell's law describes the relationship between phase angles and velocities during the reflection or transmission of waves. It states that the horizontal slowness with respect to an interface is preserved during reflection or transmission. Evaluation of this relationship at an interface between two isotropic media is straight-forward. For anisotropic media, it is a complicated problem because the phase velocity depends on the angle, and in the anisotropic reflection/transmission problem neither is known. Solving Snell's law in the anisotropic case requires the numerical solution of a sixth-order polynomial. In addition to finding the roots, they have to be assigned to the correct reflected or transmitted wavetype. We show that if the anisotropy is weak, an approximate solution based on first-order perturbation theory can be obtained. This approach permits the computation of the full slowness vector and, therefore, the phase velocity and angle. In addition to replacing the need for solving the sixth-order polynomial, the resulting expressions allow us to prescribe the desired reflected or transmitted wavetype. The method is best implemented iteratively to increase accuracy. The result can be applied to anisotropic media with arbitrary symmetry. It converges toward the weak-anisotropy solution and provides overall good accuracy for media with weak to moderate anisotropy.

E.2 Introduction

A wave impinging on a boundary between two elastic media will change its direction such that the horizontal slowness remains constant. This statement is, in essence, Snell's law. Its evaluation in isotropic media is simple and straightforward when the incidence angle and the velocities are known. In anisotropic media, however, where the velocities are directionally dependent, the determination of the vertical slowness involves the solution of a sixth-order polynomial. Furthermore, the six roots of the polynomial need to be assigned to the vertical slownesses of the three reflected and three transmitted waves. Since the direction of energy flow may differ considerably from the orientation of the slowness vector, this task is by no means trivial.

Snell's law has a large variety of applications in imaging and modelling of reflection seismic data. It comes in different guises such as the search for the vertical slowness, the determination of the reflection or transmission angle, and the phase velocity of a reflected or transmitted event. All of these are equivalent and laborious to solve as soon as anisotropy has to be taken into account.

Computations in anisotropic media are generally cumbersome, and isotropic methods usually fail to provide suitable solutions. Since, however, it has been observed that the anisotropy is often weak, various approximations have been suggested over the years in an attempt to simplify the computations. Many of these works focus on transversely isotropic media with a vertical symmetry axis (VTI media). Thomsen (1986) suggested linearised expressions for phase and group velocities in VTI media. A representative overview of approximate expressions for the phase velocities in VTI media is given, for example, by Fowler (2003).

Furthermore, in VTI media, Snell's law can be solved analytically, i.e., the exact value of the vertical slowness can be computed from the horizontal component (Červený and Pšenčík, 1972). In order to avoid the computationally-expensive square-root in the resulting expression, several authors have introduced approximations for the slowness components; see, e.g., Schoenberg and de Hoop (2000) or Pedersen et al. (2007), and the references therein.

For media with arbitrary symmetry, the perturbation approach can be applied. Here, the anisotropic medium is represented by the elasticity tensor of a suitable background or reference medium, e.g., an isotropic medium or an anisotropic medium with a higher symmetry, such as VTI. Computations are carried out in the background medium. Then, correction terms based on the perturbations of the reference medium are applied to obtain results for the original medium.

Applications of first-order perturbation methods were suggested by Červený and Jech (1982) and Jech and Pšenčík (1989). In the latter work, the authors already noted the potential of an iterative procedure to determine the vertical slowness, but have not applied their idea. It is also possible to consider higher-order perturbation theory as shown by, e.g., Farra (2001).

Most authors focus on the determination of approximate expressions for phase velocities. In contrast to these works, our aim is to directly solve for the vertical slowness, assuming that the horizontal slowness components are known.

In this appendix, we introduce an extension of the iterative method suggested by Jech and Pšenčík (1989). We derive an alternate formulation that contains only the P- or S-wave velocity in the background medium instead of the complete isotropic elasticity tensor. This property simplifies the updating of the isotropic velocities required for the iteration process. Furthermore, we show that the iteration converges toward the weak-anisotropy solution. The resulting expressions for the phase velocities coincide with those derived by Mensch and Rasolofosaon (1997) in their generalisation of the work by Thomsen (1986). For VTI media, our results correspond to Thomsen's if the parameter δ is taken in the weak-anisotropy limit suggested by Sayers (1994). Therefore, the accuracy of our method is prescribed by that of the first-order perturbation method.

After a brief summary of the framework of first-order perturbation theory provided by Jech and Pšenčík (1989), we introduce our extension of that method. We corroborate this technique with numerical examples demonstrating the accuracy of the procedure.

E.3 First-order perturbation method

In first-order perturbation method, the density-normalised elastic parameters of the anisotropic medium, a_{ijkl}, are represented by the sum of the elastic parameters of a suitable background medium, $a^{(0)}_{ijkl}$, and perturbations Δa_{ijkl}:

$$a_{ijkl} = a^{(0)}_{ijkl} + \Delta a_{ijkl} \quad . \tag{E.3.1}$$

For perturbations assumed to be small ($\Delta a_{ijkl} \ll a^{0}_{ijkl}$), the first-order perturbation method yields an approximation for weak anisotropy. In this work, we consider only isotropic background media, where the elasticity tensor is given by

$$a^{(0)}_{ijkl} = (\alpha^2 - 2\,\beta^2)\,\delta_{ij}\delta_{kl} + \beta^2\,(\delta_{ik}\delta_{jl} + \delta_{il}\delta_{jk}) \quad . \tag{E.3.2}$$

In Equation (E.3.2), α and β are the isotropic compressional and shear-wave velocities, respectively.

The aim of this work is to determine the full slowness vector $\boldsymbol{p}$ in an anisotropic medium when the horizontal slowness components are known. In terms of the first-order perturbation method, $\boldsymbol{p}$ is represented by the sum of the slowness vector in the isotropic background, $\boldsymbol{p}^{(0)}$, and its perturbation $\Delta\boldsymbol{p}$.

Snell's law states that the horizontal slowness with respect to an interface is preserved. This means that the horizontal slowness components are not affected by the reflection or transmission of a wave at an interface, and only the vertical slowness is changed. Therefore, the perturbation appears only in the vertical component. Note that in this work, we use the terms 'horizontal' and 'vertical' with respect to the interface, represented by its normal vector $\boldsymbol{z}$. In this sense, the registration surface can also be considered to be an interface. The anisotropic slowness vector in the perturbed medium, $\boldsymbol{p}$, is thus written as

$$\boldsymbol{p} = \boldsymbol{p}^{(0)} + \boldsymbol{\Delta p} = \boldsymbol{p}^{(0)} + \Delta p\,\boldsymbol{z} \quad , \tag{E.3.3}$$

where the scalar quantity Δp is the perturbation of the vertical slowness.

Because we apply a result by Jech and Pšenčík (1989) to relate the perturbation of the slowness to the perturbation of the medium parameters, below we give a short summary of their derivation leading to the equations serving as the basis for our work.

Let $\boldsymbol{g}^{(0m)}$ denote the polarisation vectors in the unperturbed medium (indicated by the superscript (0)). The index m defines the wavetype, where $m = 3$ is a P-wave and $m = 1, 2$ are S-waves. In the isotropic case, the polarisation vector of a P-wave equals the phase normal $\boldsymbol{n}$. The S-wave polarisation vectors are not unique since their only condition is that they are orthogonal to each other and lie in the plane perpendicular to $\boldsymbol{n}$. This degeneration of the S-wave polarisation, however, can be removed with first-order perturbation theory. Consider the two vectors $\boldsymbol{e}^{(1)}$ and $\boldsymbol{e}^{(2)}$, where

$$\boldsymbol{e}^{(1)} = \begin{pmatrix} \cos\vartheta\,\cos\varphi \\ \cos\vartheta\,\sin\varphi \\ -\sin\varphi \end{pmatrix} \qquad \text{and} \qquad \boldsymbol{e}^{(2)} = \begin{pmatrix} -\sin\varphi \\ \cos\varphi \\ 0 \end{pmatrix} \quad .$$

These vectors form an orthonormal base with $\boldsymbol{e}^{(3)} = \boldsymbol{g}^{(03)} = \boldsymbol{n}$. Then, the polarisation vectors of the S-waves in the unperturbed, i.e., background, medium are given by (Jech and Pšenčík, 1989)

$$\begin{aligned} \boldsymbol{g}^{(01)} &= \boldsymbol{e}^{(1)}\,\cos\chi + \boldsymbol{e}^{(2)}\,\sin\chi \\ \boldsymbol{g}^{(02)} &= -\boldsymbol{e}^{(1)}\,\sin\chi + \boldsymbol{e}^{(2)}\,\cos\chi \quad . \end{aligned} \tag{E.3.4}$$

The angle χ is determined from the weak-anisotropy matrix (Pšenčík, 1998)

$$B_{MN} = \Delta a_{ijkl}\, e_i^{(M)}\, e_k^{(N)}\, n_j\, n_l \quad , \tag{E.3.5}$$

by

$$\tan 2\chi = \frac{2\, B_{12}}{B_{11} - B_{22}} \quad . \tag{E.3.6}$$

Jech and Pšenčík (1989) have shown that the first-order perturbation of the anisotropic eikonal equation,

$$G = 1 = a_{ijkl}\, p_i\, p_l\, g_j\, g_k \quad , \tag{E.3.7}$$

leads to

$$\Delta a_{ijkl}\, p_i^{(0)}\, p_l^{(0)}\, g_j^{(0)}\, g_k^{(0)} + 2\, a_{ijkl}^{(0)}\, \Delta p_i\, p_l^{(0)}\, g_j^{(0)}\, g_k^{(0)} = 0 \quad . \tag{E.3.8}$$

Using the representation of the perturbed slowness vector, Equation (E.3.3), to express Δp_i and solving for the perturbation of the vertical slowness results in (Jech and Pšenčík, 1989)

$$\Delta p = -\frac{\Delta a_{ijkl}\, p_i^{(0)}\, p_l^{(0)}\, g_j^{(0)}\, g_k^{(0)}}{2\, a_{ijkl}^{(0)}\, z_i\, p_l^{(0)}\, g_j^{(0)}\, g_k^{(0)}} \quad . \tag{E.3.9}$$

Jech and Pšenčík (1989) have indicated that Equation (E.3.9) can be used iteratively to increase the accuracy of the slowness vector but they do not pursue this approach any further. The procedure can be outlined as follows: assuming that suitable isotropic background velocities are available, the vertical slowness in the reference medium is computed from the isotropic eikonal equation by

$$p_3^{(0)} = \pm\sqrt{\frac{1}{V_0^2} - p_1^2 - p_2^2} \quad . \tag{E.3.10}$$

Here, the sign of p_3 is chosen according to whether we consider an incident or emerging wave, or a reflected or transmitted wave. After the first iteration step using Equation (E.3.9), the background velocity for the next step is updated with

$$\frac{1}{V_0^2} = p_1^2 + p_2^2 + p_3^2 \quad . \tag{E.3.11}$$

Following this update, Equation (E.3.9) is applied again, and the procedure is repeated until the desired accuracy is reached.

With the original expression for the slowness perturbation, Equation (E.3.9), both P- and S-wave velocities have to be updated simultaneously even if only one wavetype is considered. In order to avoid this problem, we have developed an alternative formulation of Equation (E.3.9), which contains only the isotropic velocity of the wavetype under consideration.

E.4 Separation of qP- and qS-waves

The equation for the perturbed slowness, (E.3.9), can be applied for qP- and qS-waves. In this section, we introduce a new formulation of Equation (E.3.9) that depends only on α for the application to qP-waves, and only on β for the qS-waves. This formulation also includes an alternative expression for the weak-anisotropy matrix $\underline{\mathsf{B}}$ defined in Equation (E.3.5) to make the expression for shear-wave polarisation required for the iteration given by Equation (E.3.9) independent of α.

Replacing Δa_{ijkl} in the numerator of Equation (E.3.9) we get

$$\begin{aligned} \Delta a_{ijkl}\, p_i^{(0)}\, p_l^{(0)}\, g_j^{(0)}\, g_k^{(0)} &= a_{ijkl}\, p_i^{(0)}\, p_l^{(0)}\, g_j^{(0)}\, g_k^{(0)} - a_{ijkl}^{(0)}\, p_i^{(0)}\, p_l^{(0)}\, g_j^{(0)}\, g_k^{(0)} \\ &= a_{ijkl}\, p_i^{(0)}\, p_l^{(0)}\, g_j^{(0)}\, g_k^{(0)} - 1 \quad , \end{aligned} \tag{E.4.1}$$

where we have substituted the eikonal Equation (E.3.7) for the isotropic background medium in the second term. Substituting the isotropic elasticity tensor $a_{ijkl}^{(0)}$ (Equation (E.3.2)) into the denominator, we obtain

$$2\, a_{ijkl}^{(0)}\, z_i\, p_l^{(0)}\, g_j^{(0)}\, g_k^{(0)} = 2\,(\alpha^2 - \beta^2)\, z_i\, g_i^{(0)}\, p_l^{(0)}\, g_l^{(0)} + 2\,\beta^2\, z_i\, p_i^{(0)} \quad . \tag{E.4.2}$$

For P-waves in isotropic media, the polarisation vector is $\boldsymbol{g}^{(03)} = \boldsymbol{n}$. Furthermore, $\boldsymbol{p}^{(0)} = \boldsymbol{n}/\alpha = \boldsymbol{g}^{(03)}/\alpha$, and the expression for the denominator, (E.4.2), reduces to

$$2\, a_{ijkl}^{(0)}\, z_i\, p_l^{(0)}\, g_j^{(0)}\, g_k^{(0)} = 2\,\alpha^2\, z_i\, p_i^{(0)} \quad . \tag{E.4.3}$$

With this result for P-waves, Equation (E.3.9) becomes

$$\Delta p = \frac{1 - a_{ijkl}\, p_i^{(0)}\, p_l^{(0)}\, g_j^{(0)}\, g_k^{(0)}}{2\,\alpha^2\, z_i\, p_i^{(0)}} \quad . \tag{E.4.4}$$

To derive a corresponding expression for the S-waves, we make use of the fact that the polarisation vectors $\boldsymbol{g}^{(01)}$ and $\boldsymbol{g}^{(02)}$ are perpendicular to $\boldsymbol{n}$. We obtain

$$2\, a_{ijkl}^{(0)}\, z_i\, p_l^{(0)}\, g_j^{(0)}\, g_k^{(0)} = 2\,\beta^2\, z_i\, p_i^{(0)} \quad , \tag{E.4.5}$$

and thus,

$$\Delta p = \frac{1 - a_{ijkl}\, p_i^{(0)}\, p_l^{(0)}\, g_j^{(0)}\, g_k^{(0)}}{2\,\beta^2\, z_i\, p_i^{(0)}} \quad . \tag{E.4.6}$$

In summary, Equation (E.3.9) can be rewritten as

$$\Delta p = \frac{1 - a_{ijkl}\, p_i^{(0)}\, p_l^{(0)}\, g_j^{(0)}\, g_k^{(0)}}{2\,V_0^2\, z_i\, p_i^{(0)}} \quad , \tag{E.4.7}$$

where V_0 is the isotropic background velocity of the wavetype under consideration, i.e., $V_0 = \alpha$ for qP-waves, and $V_0 = \beta$ for qS-waves.

With $\boldsymbol{g}^{(03)} = \boldsymbol{n}$ for P-waves, Equation (E.4.7) is independent of β in this case. To make expression (E.4.7) independent of α for the application to qS-waves, we need to rewrite the weak-anisotropy matrix $\underline{\mathsf{B}}$ such that it also becomes independent of α. This can be achieved by substituting the perturbation of the elasticity tensor into the weak-anisotropy matrix given by Equation (E.3.5). With the isotropic elasticity tensor (E.3.2), we find that

$$\begin{aligned} a_{ijkl}^{(0)}\, e_i^{(M)}\, e_k^{(N)}\, n_j\, n_l &= (\alpha^2 - 2\,\beta^2)\, e_i^{(M)}\, n_i\, e_k^{(N)}\, n_k + \beta^2\,(e_i^{(M)}\, e_i^{(N)}\, n_k\, n_k + e_i^{(M)}\, n_i\, e_k^{(N)}\, n_k) \\ &= \beta^2\, \delta_{MN} \quad . \end{aligned} \tag{E.4.8}$$

Now B_{MN} can be expressed by

$$B_{MN} = a_{ijkl}\, e_i^{(M)}\, e_k^{(N)}\, n_j\, n_l - \beta^2\, \delta_{MN} \quad , \tag{E.4.9}$$

which is independent of α. With Equations (E.4.7) and (E.4.9) we therefore have a new formulation of Equation (E.3.9) that contains only the isotropic background velocity of the desired wavetype. This formulation considerably simplifies the updating of the reference velocities during the iteration since only one isotropic velocity needs to be updated if these new expressions are applied instead of Equation (E.3.9).

As we show in the next section, however, iterative application of Equation (E.3.9) does not converge toward the real anisotropic slowness vector, but instead toward its weakly-anisotropic counterpart. Therefore, repeated application of Equation (E.3.9) will increase the accuracy only within the weak-anisotropy limit.

E.5 Convergence toward the weak-anisotropy approximation

Let us assume that the iterative determination of the perturbed slowness with Equation (E.3.9) leads to the anisotropic slowness vector $\boldsymbol{p}$. Then, after convergence has been achieved, we would expect Δp to be zero in further iteration steps, as $\boldsymbol{p}$ and $\boldsymbol{p}^{(0)}$ are then equal. Substituting the anisotropic eikonal Equation (E.3.7) into expression (E.3.9), we find that

$$\Delta p = \frac{a_{ijkl}\, p_i^{(0)}\, p_l^{(0)}\, (g_j\, g_k - g_j^{(0)}\, g_k^{(0)})}{2\, a_{ijkl}^{(0)}\, z_i\, p_l^{(0)}\, g_j^{(0)}\, g_k^{(0)}} \quad . \tag{E.5.1}$$

Only for a weakly anisotropic medium do the polarisation vectors $\boldsymbol{g}$ coincide with those in the isotropic background, $\boldsymbol{g}^{(0)}$, and Δp becomes zero. Therefore, the iterative use of Equation (E.3.9) converges toward the slowness vector in the weak-anisotropy approximation.

E.6 Examples

We have chosen an anisotropic medium with triclinic symmetry to demonstrate our method. The density-normalised elastic parameters of this rock, Vosges sandstone (given in km^2/s^2), were taken from a paper by Mensch and Rasolofosaon (1997):

$$\underline{\mathsf{A}} = \begin{pmatrix} 4.95 & 0.43 & 0.62 & 0.67 & 0.52 & 0.38 \\ & 5.09 & 1.00 & 0.09 & -0.09 & -0.28 \\ & & 6.77 & 0.00 & -0.24 & -0.48 \\ & & & 2.45 & 0.00 & 0.09 \\ & & & & 2.88 & 0.00 \\ & & & & & 2.35 \end{pmatrix} \quad . \tag{E.6.1}$$

In terms of generalised Thomsen parameters (Mensch and Rasolofosaon, 1997), this medium is described by

$$
\begin{array}{lll}
\epsilon_x = -0.124 & \epsilon_y = -0.135 & \epsilon_z = 0 \\
\delta_x = -0.213 & \delta_y = -0.057 & \delta_z = -0.241 \\
\chi_x = 0.099 & \chi_y = 0.014 & \chi_z = -0.069 \\
\epsilon_{15} = 0.075 & \epsilon_{24} = 0.014 & \epsilon_{34} = 0 \\
\epsilon_{16} = 0.057 & \epsilon_{26} = -0.043 & \epsilon_{35} = -0.035 \\
\gamma_x = -0.075 & \gamma_y = -0.02 & \gamma_z = 0.088 \\
\epsilon_{56} = 0 & \epsilon_{46} = 0.118 & \epsilon_{45} = 0
\end{array}
$$

In our example, we have considered the azimuth angle $\phi = 0$. For this direction, the anisotropy leads to variations of the qP-wave velocity of about 20 % and up to 30 % for the shear waves (see Figure 1). Although this rock does not qualify as a weakly anisotropic medium, it serves to investigate the range of applicability of our method.

The unit normal to the reference surface in our example, $\boldsymbol{z}$, coincides with the vertical direction (depth), i.e., $\boldsymbol{z} = (0, 0, 1)$. This means that we know the horizontal slowness components p_1 and p_2 and wish to determine the vertical slowness p_3 with the iteration procedure in Equation (E.4.7).

The exact slowness surfaces as well as their approximation under the weak-anisotropy assumption are shown in Figure E.1. For this medium, Mensch and Rasolofosaon (1997) found that the velocity errors introduced by the weak-anisotropy approximation are typically less than 1.5 % for the qP-wave and less than 2.5 % for the qS-waves. In order to find a suitable isotropic reference medium, we have computed sectorially best-fitting isotropic velocities. The determination procedure is an extension of the averaging method suggested by Fedorov (1968). It is briefly outlined in Appendix D. The slowness surfaces corresponding to two isotropic background velocities resulting from averaging over a range of 60° and 180° in inclination, respectively, are also shown in Figure (E.1).

We have carried out the iteration procedure for qP- and qS-waves with two sets of initial background velocities. The first example uses as the initial reference medium the sectorially best-fitting velocities obtained from an average over inclinations from -90 to 90 degrees with the fixed azimuth $\phi = 0$. The results of the first two iteration steps are shown in Figure E.2; in Figure E.2(a) for the qP-wave and in Figure E.2(b) for the qS-waves. For comparison, the weak-anisotropy solution is also shown in these figures. We find that already after just the second iteration, the numerical result matches the weak-anisotropy solution satisfactorily in most regions.

Closer inspection of the result shows that the vertical slowness is not well-behaved at larger inclination angles. There are two possible reasons for this behaviour. The first is that the denominator in Equation (E.4.7) becomes zero for $p_3^{(0)} = 0$. We observe that small values of $p_3^{(0)}$ can lead to large correction terms Δp and thus make the algorithm unstable. Problems can also occur for larger horizontal slownesses when the background velocity is higher than the anisotropic phase velocity. It is even possible that $p_3^{(0)}$ becomes imaginary if the inverse of the background velocity is smaller than the horizontal slowness. For these phase directions, the initial velocity must be chosen smaller.

We have, therefore, repeated our experiment with initial background velocities that are just below the minimum phase velocities in the anisotropic medium to ensure that the vertical slowness in the initial isotropic reference medium is real and non-zero. The results from the first two iteration steps with this initial reference medium are displayed in Figures E.3(a) and E.3(b) for the qP- and qS-waves, respectively.

Our first observation in Figure E.3 is that the convergence of vertical slowness is slower for these

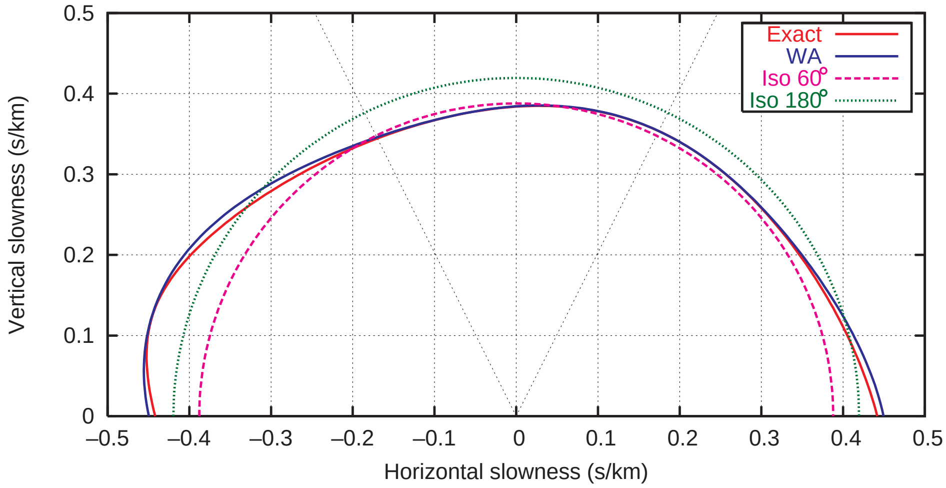

(a) Slowness surfaces of the qP-wave

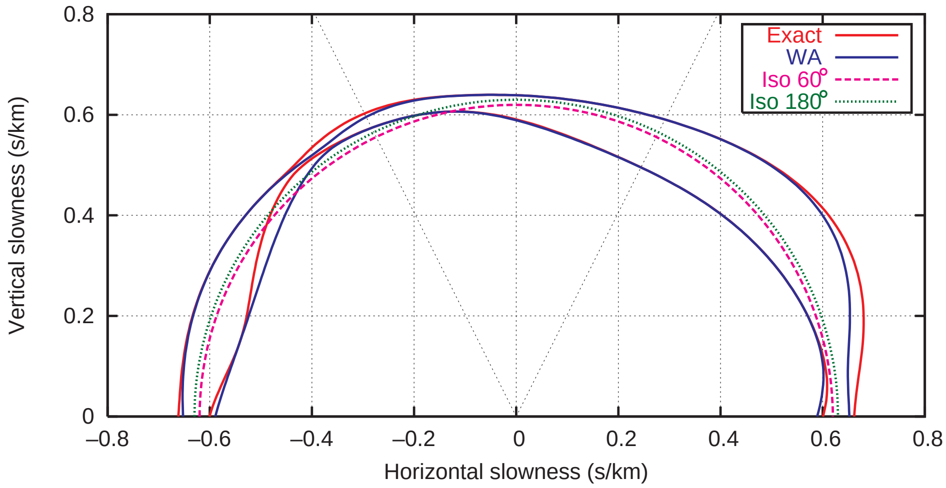

(b) Slowness surfaces of the qS-waves

Figure E.1: Slowness surfaces for a triclinic medium: the exact solution is given by the solid red lines; the solid blue lines show the approximation for weak anisotropy. The dashed pink and dotted green lines depict the sectorially best-fitting isotropic velocities averaged over an inclination range of 60° (indicated by the thin dotted straight lines) and 180°, respectively.

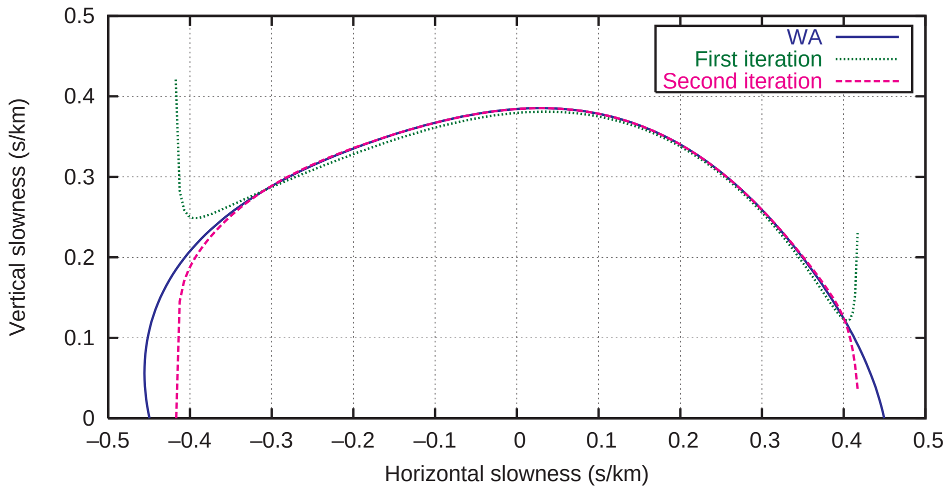

(a) Slowness surfaces of the qP-wave

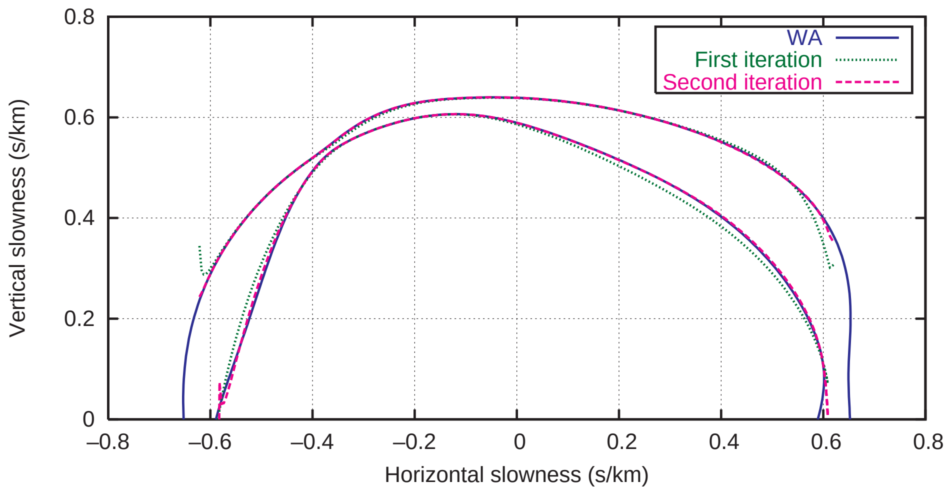

(b) Slowness surfaces of the qS-waves

Figure E.2: Slowness surfaces for a triclinic medium: the weak-anisotropy solution is given by the solid blue lines; the dotted green and dashed pink lines depict the first and second iteration of our technique, respectively. In this example, the sectorially best-fitting isotropic background velocities were used as initial reference medium. The second iteration matches the weak-anisotropy approximation closely, except for high inclination angles where the process becomes unstable (see text for details).

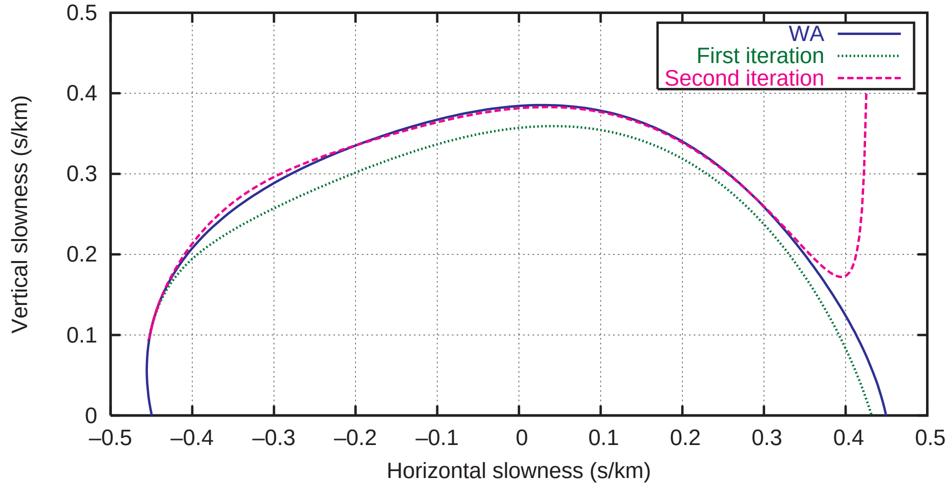

(a) Slowness surfaces of the qP-wave

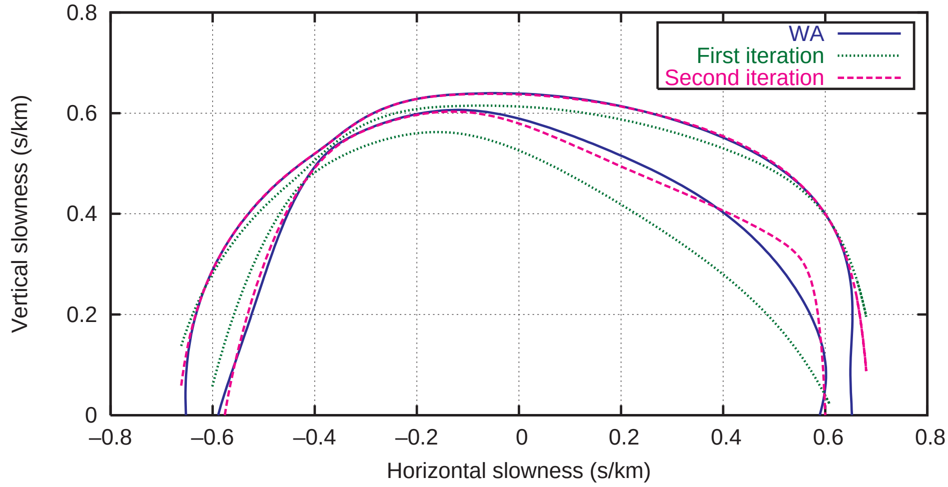

(b) Slowness surfaces of the qS-waves

Figure E.3: Slowness surfaces for a triclinic medium: the weak-anisotropy solution is given by the solid blue lines; the dotted green and dashed pink lines depict the first and second iteration of our technique, respectively. In this example, minimum velocities were used as initial reference medium. The stability problem has been reduced to some extent, but the convergence is slower than for the sectorially best-fitting velocities as initial background medium.

minimum velocities: the error after the second iteration is still larger than the error after the first iteration using the sectorially best-fitting velocities. Particularly for the faster $q\mathrm{S}_1$-wave, the second iteration does not yield a satisfactory result. On the other hand, the problems at higher inclination angles have been partly resolved.

Since high incidence angles often lead to post-critical reflections, they would not be considered in reflection seismics. We would then suggest using the sectorially best-fitting velocities as the initial reference medium. Furthermore, when inclination angles are limited to a given range, the sectorial fit can be restricted to that range and might give a better approximation than a fit over 180°. For example, the 60° average for the qP-wave shown in Figure E.1(a) matches the true slowness surface much better than does the 180° fit. For this smaller sector, already a single iteration would suffice. For the qS-waves, the situation is different because the isotropic velocity cannot properly approximate both anisotropic shear velocities at the same time. Therefore, at least a second iteration is always recommended. If high inclination angles need to be considered, minimum velocities should be chosen for the initial reference medium. Then, however, a larger number of iteration steps is required.

E.7 Conclusions

We have developed and applied a method to solve Snell's law in a weakly anisotropic medium. The objective of the method is the determination of the vertical slowness for a reflected or transmitted wave from the horizontal slowness components. To increase the accuracy, the procedure is best implemented in an iterative fashion.

Since for many practical applications the anisotropy is weak, our method provides an alternative to solving the sixth-order polynomial for the vertical slowness. Furthermore, the cumbersome assignation of the six roots to the three reflected and three transmitted events is no longer required because our algorithm allows the specification of just one particular wavetype.

With proper choice of the initial background velocity, the iteration converges quickly; however, the resulting vertical slowness pertains to the limit of the weak-anisotropy approximation, and not the exact value. This may lead to significant deviations in regions with shear-wave singularities. Because of numerical instabilities, the method is not reliable for high incidence angles.

Outside these regions, a good agreement between the analytic and numeric solution can be observed. We suggest applying the method for imaging rather than modelling. In imaging, the errors observed at large incidence angles are less meaningful since wide angle reflections are rarely taken into account.

Appendix F

Reflections from a spherical interface

In this chapter, I derive an equation for the traveltime of a wave reflected from a spherical interface in a homogeneous medium. Since the derivation for this traveltime from Snell's law leads to a polynomial of order six, which cannot be solved analytically, I use results from a related problem, the reflection of a wave from an inclined interface. In combination with these results, I obtain a polynomial of order four for the spherical interface, which has an analytical solution. I will, therefore, first discuss reflections from an inclined interface before turning to the problem of the spherical reflector.

F.1 Reflections from an inclined interface

Figure F.1 shows the geometry of the problem considered in this section. A dipping interface with the inclination angle ϕ_0 starts at the origin 0. The raypath from a source at S to a receiver at G leads to a reflection point at R. The traveltime of the ray $\overline{SRG}$ is $T = \overline{SRG}/V$, where V is the velocity. As can be seen in Figure F.1, the length of the ray $\overline{SRG}$ is the same as the distance $\overline{XG}$, where X is the mirror point of S with respect to the reflector.

From the geometry in Figure F.1, we immediately see that

$$\overline{SX} = 2\,S\sin\phi_0 \quad , \tag{F.1.1}$$

$$\overline{SG} = G - S \quad , \tag{F.1.2}$$

and

$$\angle GSX = 90^\circ + \phi_0 \quad \Rightarrow \quad \cos\angle GSX = -\sin\phi_0 \quad . \tag{F.1.3}$$

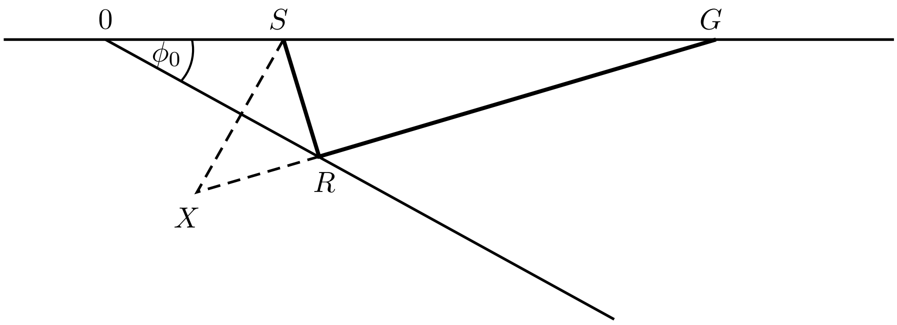

Figure F.1: Geometry of a reflection from an inclined interface.

The law of cosines yields

$$
\begin{aligned}
\overline{XG}^2 &= (G-S)^2 + 4\,S^2 \sin^2\phi_0 + 4\,S(G-S)\sin^2\phi_0 \\
&= (G-S)^2 + 4\,SG\sin^2\phi_0 \\
&= V^2T^2 \quad . \qquad \text{(F.1.4)}
\end{aligned}
$$

As we will see in the next section, the traveltime from S to R, $T_s = \overline{SR}/V$, as well as the traveltime from R to G, $T_g = \overline{RG}/V$, are also required for the spherical reflector problem. I use the law of sines in the triangle SXG, leading to

$$\frac{\sin\angle GSX}{\overline{XG}} = \frac{\sin(90^\circ + \phi_0)}{VT} = \frac{\cos\phi_0}{VT} = \frac{\sin\angle XGS}{\overline{SX}} = \frac{\sin\angle XGS}{2\,S\sin\phi_0} \quad , \qquad \text{(F.1.5)}$$

and with $\angle XGS = \angle RGS$

$$\sin\angle RGS = \frac{2\,\sin\phi_0\cos\phi_0}{VT}\,S \quad . \qquad \text{(F.1.6)}$$

In a similar fashion, I find that

$$\sin\angle GSR = \frac{2\,\sin\phi_0\cos\phi_0}{VT}\,G \quad . \qquad \text{(F.1.7)}$$

The angles $\angle RGS$ and $\angle GSR$ together with the distance $\overline{SG} = G - S$ are sufficient to describe the triangle SRG. With the law of sines in SRG,

$$\frac{\sin\angle RGS}{VT_s} = \frac{\sin\angle GSR}{VT_g} = \frac{\sin\angle GSR}{V(T-T_s)} \qquad \text{(F.1.8)}$$

I arrive at the following expressions for T_s and T_g in terms of T, S, and G:

$$T_s = \frac{S\,T}{S+G} \quad , \qquad T_g = \frac{G\,T}{S+G} \quad . \qquad \text{(F.1.9)}$$

These expressions are a result that we will need in the following section for the derivation of the traveltime of a spherical reflection.

F.2 Reflections from a spherical interface

Again, I begin by introducing the geometry of the problem. For simplicity, I consider only the 2D case. The extension from the circle to the sphere is straightforward. The circle has the radius ρ. Its centre is located at $(0,H)$. The reflection point R for a ray from the source at S to the receiver at G is described by (x_R, z_R), where

$$x_R = \rho\sin\phi \quad , \qquad z_R = H - \rho\cos\phi \quad . \qquad \text{(F.2.1)}$$

Note that the angle ϕ is not known at this point. The traveltimes from S to R, $T_s = \overline{SR}/V$, and that from R to G, $T_g = \overline{RG}/V$, are given by

$$
\begin{aligned}
V\,T_s &= \sqrt{(S-\rho\sin\phi)^2 + (H-\rho\cos\phi)^2} \quad , \\
V\,T_g &= \sqrt{(G-\rho\sin\phi)^2 + (H-\rho\cos\phi)^2} \quad . \qquad \text{(F.2.2)}
\end{aligned}
$$

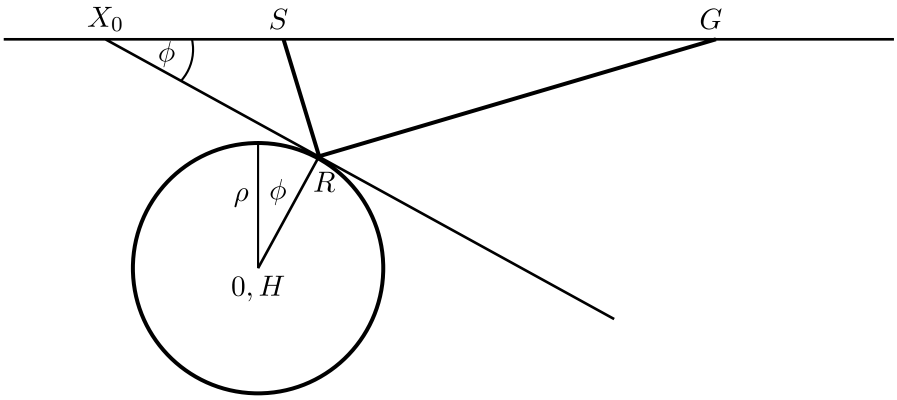

Figure F.2: Geometry of a reflection from a spherical interface: for a fixed reflection point R, the spherical reflector can be replaced by an auxiliary plane and inclined reflector that is tangent to the sphere in R.

In order for the traveltime from S to G, $T = T_s + T_g$ to be that of a reflected ray, I evaluate Snell's law, demanding that $\partial T/\partial\phi = 0$. Carrying out the derivative, I find that

$$\frac{S\rho\cos\phi - H\rho\sin\phi}{T_s} + \frac{G\rho\cos\phi - H\rho\sin\phi}{T_g} = 0 \quad . \tag{F.2.3}$$

Substituting the expressions for T_s and T_g, (F.2.2) leads to a polynomial of sixth order, which cannot be solved analytically. There is, however, an alternative for using (F.2.2): once the reflection point R is fixed by (F.2.3), the circle can be replaced by an inclined reflector that is tangent to the circle in the reflection point R. The inclination angle of this auxiliary reflector is ϕ, and its origin at X_0, as depicted in Figure F.2. In this case, we can use the expressions for T_s and T_g derived in the previous section, Equation (F.1.9). Taking the change of origin to X_0 into consideration, we find that

$$T_s = \frac{(S - X_0)\,T}{S + G - 2\,X_0} \quad , \qquad T_g = \frac{(G - X_0)\,T}{S + G - 2\,X_0} \quad . \tag{F.2.4}$$

If these are substituted into (F.2.3), after some tedious algebra, I obtain the fourth-order polynomial

$$ax^4 + bx^3 + cx^2 + dx + e = 0 \quad , \tag{F.2.5}$$

where $x = \sin\phi$ and

$$\begin{aligned}
a &= -4\,[H^2(S+G)^2 + (H^2 - SG)^2] \\
b &= 4\,\rho(S+G)(H^2 + SG) \\
c &= 4\,(SG - H^2)^2 - 4\,H^2\rho^2 - (\rho^2 - 4\,H^2)(S+G)^2 \\
d &= -4\,\rho SG(S+G) \\
e &= (\rho^2 - H^2)(S+G)^2 \quad .
\end{aligned} \tag{F.2.6}$$

The polynomial (F.2.5) has four solutions. Only two of them fulfill Snell's law (F.2.3). The reason is that (F.2.3) had to be squared in order to obtain (F.2.5). Of the two solutions obeying (F.2.3), one describes the reflection from the top of the circle, and the other the reflection from the bottom of the circle.

Once the angle ϕ has been determined from (F.2.3), T_s and T_g, and therefore the reflection traveltime for the given source-receiver combination can be computed.

Appendix G

NIP-wave tomography for converted waves

G.1 Introduction

Ever since the introduction of ocean bottom acquisition converted waves have gained importance in exploration seismics (e.g. Tsvankin, 2001). Excitation of shear waves requires significantly more effort than generation of P waves. It is not only difficult but also costly. Since shear information is also contained in the data of PS converted waves, these have been the focus of shear wave exploration for quite some time now.

There are many advantages of taking shear waves into consideration. For example, the presence of gas clouds leads to high absorption for the P waves and makes imaging under such regions inadequate for PP surveys. Shear waves, on the other hand, do not suffer from the absorption (Stewart et al., 2003). Another example where converted waves are beneficial is imaging of targets with weak PP and strong PS impedance contrasts, e.g., for certain types of shale-sand boundaries (Stewart et al., 2003). Due to the smaller velocity of shear waves they can be used to enhance the seismic resolution. This is particularly interesting for the investigation of steeply-inclined near-surface structures (Stewart et al., 2003). Finally, shear waves are essential for the detection and quantification of seismic anisotropy (e.g. Tsvankin, 2001).

Shear waves are also important for reservoir characterisation because parameters like porosity and permeability have strong influence on shear velocities (e.g. Nelson, 2001). Thus, the determination of shear velocities provides a direct means for the prediction of reservoir parameters. For example, it is possible to obtain information on the density and orientation of fractures from converted waves (e.g. Gaiser and Van Dok, 2003) since these fractures lead to seismic anisotropy.

Despite their advantages, shear waves also exhibit serious disadvantages. As already pointed out, for practical reasons the acquisition is usually restricted to converted waves. However, standard techniques for the processing of PP data cannot always be applied to these data.

In contrast to monotypic (i.e. PP or SS) reflections, the ray paths of converted waves are asymmetric with respect to interchanging sources and receivers. In particular in the presence of lateral inhomogeneities or anisotropy, the move-out of a converted wave becomes asymmetric because it contains a linear term, the so-called diodic move-out (Thomsen, 1999). This prevents the application of NMO correction in CMP gathers, which is based on the assumption of symmetric ray paths.

This problem is closely-related to the conversion point dispersal. Although there is a similar phenomenon for monotypic waves, the reflection point dispersal, that effect has a larger magnitude for converted waves.

For these reasons, PS data are sorted in common conversion point (CCP) gathers instead of CMP. Unfortunately, the determination of the CCP itself can be rather complicated (e.g. Tessmer et al., 1990; Thomsen, 1999). Also, it is by no means trivial to obtain a velocity model from the subsequent processing. For example, neglecting the sign of the offset during the CCP binning can lead to a bimodal velocity spectrum due to the diodic move-out (Thomsen, 1999).

Migration-based velocity model-building techniques (e.g. Al-Yahya, 1989) can be used for converted waves. In these methods, residual move-out in the CRP gathers is evaluated for a model update. However, one has to be cautious: due to the asymmetric ray paths in the case of converted waves, the gathers can appear horizontal even though the velocity may be wrong (Menyoli, 2002).

In conclusion, velocity model building with converted waves is much more elaborate than in the monotypic case. Although the effort could be reduced by processing SS data instead of PS, the resulting simplifications would be compensated with the problems arising during the acquisition.

One technique for the determination of P velocities was recently introduced by Duveneck (2004). It evaluates wave field attributes obtained from a common reflection surface (CRS) stack of PP data in a tomographic procedure. We suggest to extend the method such that we combine the wave field attributes for PP and PS data in order to simulate SS wave field attributes.

After a very brief introduction to NIP wave tomography, we present our method. Due to the already mentioned properties of converted waves the combination of PP and PS parameters is not straightforward. We will explain the specific problems in more detail and, following that section, present solutions.

G.2 Zero-offset CRS and NIP wave tomography for monotypic waves

The CRS stacking technique was described in Chapter 3. There, it was already mentioned that the method and in particular its parameters or wavefield attributes have a wide range of applications.

The application we focus on in this appendix is the NIP wave tomography suggested by Duveneck (2004). According to that work, 'in a correct model, all considered NIP waves when propagated back into the Earth along the normal ray focus at zero traveltime'. The concept of focusing NIP waves was already introduced by Hubral and Krey (1980), and cast into a tomographic inversion by Duveneck (2004).

With the traveltime, emergence angle, and NIP wave curvature given by the CRS stack, dynamic ray tracing is performed in an initial model. Subsequent evaluation of the resulting NIP wave radius leads to an update of the velocity model, which then serves as input for the next iteration step. The procedure is repeated until convergence is achieved.

G.3 Offset CRS formulation

The physical interpretation of the attributes, e.g. K_{NIP}, which is evaluated in the NIP wave tomography is based on a one-way process. This is possible for monotypic waves because the up- and down-going ray paths coincide in the zero offset case. This assumption is not valid if converted waves are considered. In consequence, the corresponding expression for the CRS operator has five parameters now instead of three for the monotypic zero offset case (see Chapter 3). Since it is formally identical with the common offset CRS formulation, we will use this general form from now on.

In source (s) and receiver (g) coordinates, the common offset CRS formula reads,

$$T^2(s', g') = (T_0 + q\,\Delta g - p\,\Delta s)^2 + T_0\,(G\,\Delta g^2 - S\,\Delta s^2 - 2\,N\,\Delta s\,\Delta g) \quad , \tag{G.3.1}$$

where the first-order derivatives,

$$p = -\frac{\partial T}{\partial s} \quad \text{, and} \qquad q = \frac{\partial T}{\partial g} \quad , \tag{G.3.2}$$

are the horizontal slownesses at the source and receiver, respectively. The second-order derivatives are given by

$$S = -\frac{\partial^2 T}{\partial s^2} \quad , \quad G = \frac{\partial^2 T}{\partial g^2} \quad \text{, and} \qquad N = -\frac{\partial^2 T}{\partial s\,\partial g} \quad . \tag{G.3.3}$$

In three dimensions, the first-order derivatives are vectors and the second-order derivatives are matrices (see Chapter 2).

Equation (G.3.1) is equal to the common offset CRS expression given by Bergler et al. (2002) (their Equation (1)). The first- and second-order derivatives can also be expressed by incidence and emergence angles β_G and β_S, and the velocities V_S and V_G, where the indices S and G denote source and receiver; and the scalar elements A, B, C, D of the surface-to-surface propagator matrix introduced by Bortfeld (1989). The relations between these parameters are,

$$A = -\frac{S}{N} \quad , \quad B = \frac{1}{N} \quad , \quad C = -N - \frac{SG}{N} \quad \text{, and} \qquad D = \frac{G}{N} \quad , \tag{G.3.4}$$

and

$$p = \frac{\sin\beta_S}{V_S} \quad , \qquad q = \frac{\sin\beta_G}{V_G} \quad , \tag{G.3.5}$$

or,

$$S = -\frac{A}{B} \quad , \qquad G = \frac{D}{B} \quad , \qquad N = \frac{1}{B} \quad , \tag{G.3.6}$$

and

$$\sin\beta_S = p\,V_S \quad , \qquad \sin\beta_G = q\,V_G \quad , \tag{G.3.7}$$

respectively.

For zero offset and monotypic waves, it follows from the symmetry that $p = -q$ and $G = -S$. With $g = x_m + h, s = x_m - h$, Equation (G.3.1) reduces to

$$\begin{aligned} T^2 &= (T_0 + 2q_0\,\Delta x_m)^2 + 2T_0[(G-N)\,\Delta x_m^2 + (G+N)\,\Delta h^2] \\ &= \left(t_0 + \frac{2\,\sin\beta_0}{v_0}\,(x_m - x_0)\right)^2 + 2\,\frac{t_0\cos^2\beta_0}{v_0}\left(\frac{(x_m-x_0)^2}{R_N} + \frac{h^2}{R_{NIP}}\right) \\ &= \left(t_0 + \frac{2\,\sin\beta_0}{v_0}\,(x_m - x_0)\right)^2 + 2\,\frac{t_0\cos^2\beta_0}{v_0}\left(K_N\,(x_m-x_0)^2 + K_{NIP}\,h^2\right) \end{aligned} \tag{G.3.8}$$

in that case, and the zero offset attributes can be expressed by

$$q = -p = \frac{\sin\beta_0}{V_0} \quad , \qquad G = -S = \frac{\cos^2\beta_0}{2\,V_0}\,(K_{NIP} + K_N) \quad , \qquad N = \frac{\cos^2\beta_0}{2\,V_0}\,(K_{NIP} - K_N) \quad , \tag{G.3.9}$$

or

$$\sin\beta_0 = q\,V_0 \quad , \qquad K_N = \frac{V_0}{\cos^2\beta_0}(G - N) \quad , \qquad K_{NIP} = \frac{V_0}{\cos^2\beta_0}(G + N) \quad , \tag{G.3.10}$$

respectively.

G.4 Ray segment decomposition

Since there is no equivalent one-way process in the case of converted waves, we have to consider the individual ray segments in order to find a way of combining the PP and PS wave field attributes. In the following, we will use a parabolic variant of (G.3.1). It is valid for the traveltime of a reflected or converted event as well as for each of the individual segments if a reflection point with the coordinate r is introduced.

A PP zero offset event consists of two identical P segments from s to r (or from r to g). Let S_{PP}, G_{PP}, N_{PP} denote the parameters of the reflected, i.e. PP, event, and $S_P \neq G_P, N_P$ those of the single P segment, i.e., the traveltime of the reflected event can be expressed by

$$\begin{aligned} T_{PP}(s', g') &= T_{0-PP} + q_{PP}\,\Delta g - p_{PP}\,\Delta s + \frac{1}{2}\left(G_{PP}\,\Delta g^2 - S_{PP}\,\Delta s^2 - 2\,N_{PP}\,\Delta s\,\Delta g\right) \\ &= 2\,(T_{0\,P} + q_P^r\,\Delta r - p_P\,\Delta s) + G_P\,\Delta r^2 - S_P\,\Delta s^2 - 2\,N_P\,\Delta s\,\Delta r \\ &= 2\,T_P(s', r') \quad , \end{aligned} \tag{G.4.1}$$

where q_P^r is the slowness at the reflector. In (G.4.1), $q_{PP} = -p_{PP}$ and $G_{PP} = -S_{PP}$ due to the symmetry.

Similarly, a zero offset SS event with parameters S_{SS}, G_{SS}, N_{SS} has two identical individual S segments with $S_S \neq G_S, N_S$:

$$\begin{aligned} T_{SS}(s', g') &= T_{0-SS} + q_{SS}\,\Delta g - p_{SS}\,\Delta s + \frac{1}{2}\left(G_{SS}\,\Delta g^2 - S_{SS}\,\Delta s^2 - 2\,N_{SS}\,\Delta s\,\Delta g\right) \\ &= 2\,(T_{0\,S} + q_S\,\Delta g - p_S^r\,\Delta r) + G_S\,\Delta g^2 - S_S\,\Delta r^2 - 2\,N_S\,\Delta r\,\Delta g \\ &= 2\,T_S(r', g') \quad , \end{aligned} \tag{G.4.2}$$

where p_S^r is the slowness at the reflector. In (G.4.2), $q_{SS} = -p_{SS}$ and $G_{SS} = -S_{SS}$ due to the symmetry.

Finally, a zero offset PS event described by S_{PS}, G_{PS}, N_{PS} consists of two individual different segments, the P and S segments, with S_P, G_P, N_P and S_S, G_S, N_S, respectively:

$$\begin{aligned}
T_{PS}(s',g') &= T_{0-PS} + q_{PS}\,\Delta g - p_{PS}\,\Delta s + \frac{1}{2}\left(G_{PS}\,\Delta g^2 - S_{PS}\,\Delta s^2 - 2\,N_{PS}\,\Delta s\,\Delta g\right) \\
&= T_{0\,P} + q_P^r\,\Delta r - p_P\,\Delta s + \frac{1}{2}\left(G_P\,\Delta r^2 - S_P\,\Delta s^2 - 2\,N_P\,\Delta s\,\Delta r\right) \\
&+ T_{0\,S} + q_S\,\Delta g - p_S^r\,\Delta r + \frac{1}{2}\left(G_S\,\Delta g^2 - S_S\,\Delta r^2 - 2\,N_S\,\Delta r\,\Delta g\right) \\
&= T_P(s',r') + T_S(r',g')
\end{aligned} \tag{G.4.3}$$

Elimination of the reflector coordinate in Equations (G.4.1), (G.4.2), and (G.4.3) by evaluating Snell's law leads to relationships between the coefficients of the single and reflected rays. For the PP case, we find

$$p_{PP} = p_P = -q_{PP} \quad , \qquad S_{PP} = S_P + \frac{N_P^2}{2\,G_P} = -G_{PP} \quad , \qquad N_{PP} = \frac{N_P^2}{2\,G_P} \quad . \tag{G.4.4}$$

Correspondingly, for the SS case it follows that

$$q_{SS} = q_S = -p_{SS} \quad , \qquad S_{SS} = S_S + \frac{N_S^2}{2\,G_S} = -G_{SS} \quad , \qquad N_{SS} = \frac{N_S^2}{2\,G_S} \quad . \tag{G.4.5}$$

Finally, for the converted wave,

$$\begin{gathered}
p_{PS} = p_P \quad , \qquad q_{PS} = q_S \quad , \\
S_{PS} = S_P + \frac{N_P^2}{G_P + G_S} \quad , \qquad G_{PS} = -S_S - \frac{N_S^2}{G_P + G_S} \quad , \qquad N_{PS} = \frac{N_P\,N_S}{G_P + G_S} \quad .
\end{gathered} \tag{G.4.6}$$

The same result can be obtained with the propagator formalism (Bortfeld, 1989). Combining Equations (G.3.9) and (G.4.5), we find that the NIP wave curvature corresponding to the zero-offset SS reflection is given by

$$K_{NIP-SS} = -\frac{V_{0\,S}}{\cos^2\beta_{0\,S}}\,S_S \quad . \tag{G.4.7}$$

According to (G.4.5), the angle $\beta_{0\,S}$ is the incidence angle at the receiver for the PS case, i.e., $\sin\beta_{0\,S} = q_{PS}\,V_{S\,0}$. With (G.4.6), we can now express S_S in Equation (G.4.7) by

$$S_S = -G_{PS} - \frac{N_{PS}^2}{S_{PS} - S_P} \quad , \tag{G.4.8}$$

where S_P follows from Equations (G.3.9) and (G.4.4) as

$$S_P = -\frac{\cos^2\beta_{0\,P}}{V_{0\,P}\,K_{NIP-PP}} \quad . \tag{G.4.9}$$

Equations (G.4.7) to (G.4.9) provide the NIP wave curvature of a simulated SS wave. To perform NIP wave tomography, we also require the emergence angle for the ray tracing, $\beta_{0\,S}$, which is given by q_{PS}, and the traveltime T_{0-SS}, which can be obtained from the difference between T_{0-PS} and T_{0-PP} by

$$T_{0-SS} = 2\,T_{0-PS} - T_{0-PP} \quad . \tag{G.4.10}$$

In conclusion, by combining the parameters from the PP and PS zero-offset CRS stacks, we can now, in theory, apply NIP wave tomography to obtain the shear velocity model. In practice, however, the determination of K_{NIP-SS} is not as straight-forward as described here. We discuss the reasons and other practical issues in the following section.

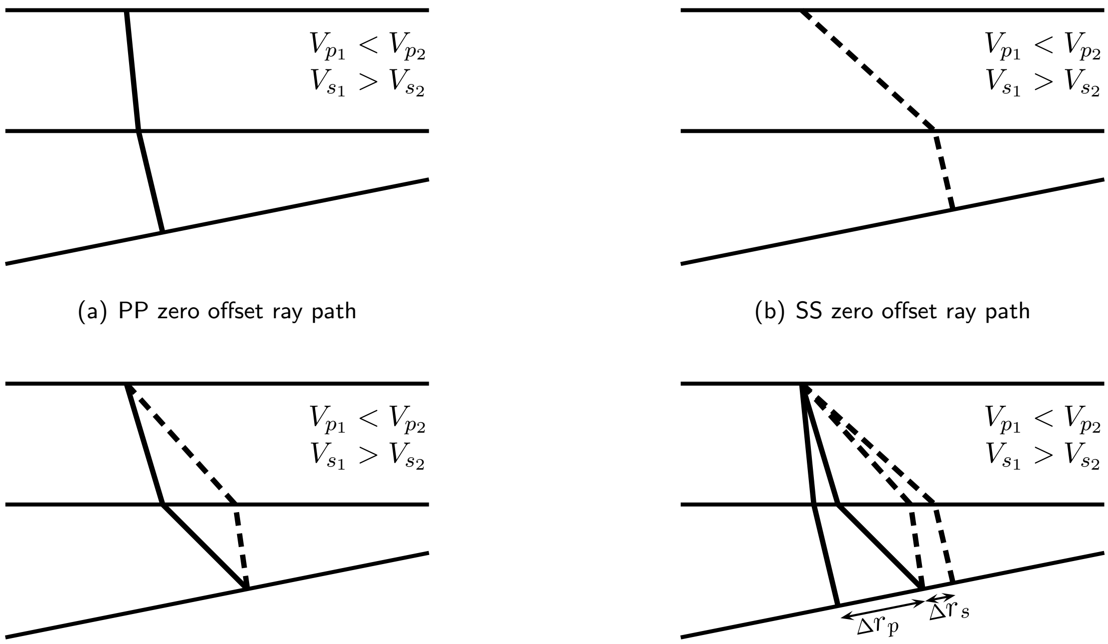

(a) PP zero offset ray path

(b) SS zero offset ray path

(c) PS zero offset ray path

(d) Distances between ray end points

Figure G.1: Zero-offset ray paths for (a) PP, (b) SS, and (c) PS reflections, where $V_{p_1}/V_{s_1} \neq V_{p_2}/V_{s_2}$. Solid lines indicate P-waves; dashed lines correspond to S-waves. (d) The distances Δr_p and Δr_s between ray end points.

G.5 Reflection point dispersal

For the derivation of the relationship between K_{NIP-SS} and the CRS parameters of the PP and PS data we have implicitly assumed that the ray paths for PP, PS, and SS coincide. Whereas in the monotypic case, the up- and down-going ray segments coincide and are normal to the reflector, this is not generally true for the zero offset converted wave, as demonstrated by Figure G.1. The P and S ray path segments are only then identical when the ratio of P and S velocities remains constant throughout the medium. If that were the case, however, we could simply compute our shear velocity model by applying a scale factor to the P model.

To address this problem, we assume that the distance Δr_p between the reflection point of the zero-offset PP reflection and the conversion point of the zero-offset PS reflection lies within a paraxial vicinity, i.e. the distance Δr_p in Figure G.1(d) is small. (Given that the distance Δr_s is smaller than Δr_p because of the steeper reflection angle, we suggest to ignore the deviations of the ray end points for the shear waves.) In that case, Δr_p can be expressed by (after Bortfeld, 1989)

$$\Delta r_p = \frac{p_{PS} - p_{PP}}{N_P} \quad . \tag{G.5.1}$$

In (G.5.1), the one-way parameter N_P for the P wave is not directly available from the PP CRS parameters, but it can be easily computed with dynamic ray tracing (DRT). In fact, computing N_P does not even require an additional effort as DRT is already performed within the NIP wave tomography. Considering the traveltime of the P wave to the conversion point, with

$$T_P^2(s, r') = \left(\frac{T_{0-PP}}{2} + q_P^r \, \Delta r_p\right)^2 + G_P \Delta r_p^2 \quad , \tag{G.5.2}$$

where q_P^r and G_P are also known from the DRT for the NIP wave tomography, we can now carry out DRT with the take-off angle corresponding to the PS wave and compute the value of S_P for this ray path to be combined with the PS parameters and obtain K_{NIP-SS}. Although this step requires additional DRT, the effort is negligible since only a single ray needs to be traced. Furthermore, the ray end point gives us a measure of the accuracy as it should coincide with $r' = r + \Delta r_p$, and therefore provides a means for quality control.

G.6 Identification of events

Combining parameters from PP and PS CRS stacks requires that the events under consideration need to be identified in both sections. The technique that springs to mind for solving this issue is slope matching, i.e., comparing the slowness vectors of the P segments of the PP and PS rays, p_{PP} and P_{PS}. However, as we have seen above, the ray paths do not coincide for media where the V_P/V_S ratio is not constant. In conclusion, the slownesses do not coincide either. In contrast to the 'PP+PS=SS' method (Grechka and Tsvankin, 2002), where slope matching in the pre-stack domain is performed to obtain SS traveltimes from combining PP and PS measurements, we are working in the post-stack domain, where their algorithm cannot be applied.

Although it is possible to manually identify key events in the sections and use these to assign weaker events, such a procedure would countermand one of the major advantages of NIP wave tomography, namely that user intervention, e.g., picking, is kept to a minimum. We recognise that this challenging step needs further investigation if it is intended to be carried out in a fully-automatic fashion.

There are additional issues related to the CRS stacking of converted waves that also occur in CCP stacking, like the polarity reversal of the shear wave or wave field separation prior to the stacking. Since the emphasis of this work is on the combination of the PP and PS parameters to obtain SS parameters, we refer the reader to the literature suggested in the introduction.

G.7 Conclusions

We have introduced a new method to obtain the NIP wave curvature of an SS reflection from CRS stacking of PP and PS data. Knowledge of the NIP wave curvature allows to perform NIP wave tomography for shear waves. Since the necessary parameters are available from the PP and PS sections, the shear model can now be determined without acquiring SS data.

As soon as the V_P/V_S ratio is not constant throughout the medium, an additional ray tracing step is required to account for the difference in the PP and PS emergence angles. Since only single rays need to be traced in the P model, this step does not degrade the numerical efficiency. Furthermore, dynamic ray tracing is already embedded in the NIP wave tomography.

Bibliography

Abakumov, I., Schwarz, B., Vanelle, C., Kashtan, B., and Gajewski, D., 2011, Double square root traveltime approximation for converted waves: 15th Annual WIT report.

Al-Yahya, K. M., 1989, Velocity analysis by iterative profile migration: Geophysics, **54**, 718–729.

Backus, G. E., 1965, Possible forms of seismic anisotropy of the uppermost mantle under oceans: Journal of Geophysical Research, **70**, 3429–3439.

Bancroft, J. C., 1998, A practical understanding of pre- and poststack migrations, Volume 2 (Prestack): SEG, Tulsa.

Bauer, A., Untersuchungen mit einem neuen Stapelverfahren: i-CRS und konvertierte Wellen:, B.Sc. thesis, University of Hamburg (in preparation), 2012.

Baykulov, M., and Gajewski, D., 2009, Prestack seismic data enhancement with partial common reflection surface (crs) stack: Geophysics, **74**, V49–V58.

Baykulov, M., Dümmong, S., and Gajewski, D., 2011, From time to depth with CRS attributes: Geophysics, **76**, S151–S155.

Baykulov, M., 2009, Seismic imaging in complex media with the common reflection surface stack: Ph.D. thesis, University of Hamburg.

Bergler, S., Duveneck, E., Höcht, G., Zhang, Y., and Hubral, P., 2002, Common-reflection-surface stack for converted waves: Stud. geophys. geod., **46**, 165–175.

Beylkin, G., 1985, Imaging of discontinuities in the inverse scattering problem by inversion of a causal generalized Radon transform: Journal of Mathematical Physics, **26**, 99–108.

Bleistein, N., 1984, Mathematical methods for wave phenomena: Academic Press.

Bleistein, N., 1986, Two-and-one-half dimensional in-plane wave propagation: Geophysical Prospecting, **34**, 686–703.

Bleistein, N., 1987, On the imaging of reflectors in the earth: Geophysics, **52**, 931–942.

Bortfeld, R., 1982, Phänomene und Probleme beim Modellieren und Invertieren, in Modellverfahren bei der Interpretation seismischer Daten: DVGI, Fachausschuß Geophysik.

Bortfeld, R., 1989, Geometrical ray theory: rays and traveltimes in seismic systems (second-order approximations of the traveltimes): Geophysics, **54**, 342–349.

Brandsberg-Dahl, S., de Hoop, M. V., and Ursin, B., 2001, AVA analysis and compensation on common image gathers in the angle domain: 63th Ann. Internat. Mtg., Eur. Assn. Expl. Geophys., Expanded Abstracts.

Brokešová, J., Dekker, S., and Duijndam, A., 1994, Applicability of high-frequency asymptotic methods for the model PICROCOL: 64th Ann. Internat. Mtg., Soc. Expl. Geophys., Expanded Abstracts, 783–786.

Brokešová, J., 1996, Construction of ray synthetic seismograms using interpolation of traveltimes and ray amplitudes: Pure and Applied Geophysics, **148**, 481–502.

Buske, S., 2000, Finite difference solution of the ray theoretical transport equation: Ph.D. thesis, Universitt Frankfurt.

Červený, V., and de Castro, M. A., 1993, Application of dynamic ray tracing in the 3-D inversion of seismic reflection data: Geophysical Journal International, **113**, 776–779.

Červený, V., and Hron, F., 1980, The ray series method and dynamic ray tracing systems for 3D inhomogeneous media: Bulletin of the Seismological Society of America, **70**, 47–77.

Červený, V., and Jech, J., 1982, Linearized solutions of kinematic problems of seismic body waves in inhomogeneous slightly anisotropic media: Journal of Geophysics, **51**, 96–104.

Červený, V., and Pšenčík, I., 1972, Rays and travel-time curves in inhomogeneous anisotropic media: Journal of Geophysics, **38**, 565–577.

Červený, V., and Pšenčík, I., 1984, Numerical modelling of seismic wave fields in 2-D laterally varying layered structures by the ray method *in* Engdahl, E., Ed., Documentation of Earthquake Algorithms: World Data Center for Solid Earth Geophysicists, Rep. SE-35, 36–40.

Červený, V., and Ravindra, R., 1971, Theory of seismic head waves: University of Toronto Press.

Červený, V., and Soares, J. E. P., 1992, Fresnel volume ray tracing: Geophysics, **57**, 902–911.

Červený, V., Molotkov, I. A., and Pšenčík, I., 1977, Ray method in seismology: Univerzita Karlova, Praha.

Červený, V., 1972, Seismic rays and ray intensities in inhomogeneous anisotropic media: Geophysical Journal of the Royal astronomical Society, **29**, 1–13.

Červený, V., 1985, The application of ray tracing to the numerical modeling of seismic wavefields in complex structures, *in* Dohr, G., Ed., Seismic shear waves, Part A: Theory: Geophysical Press, London – Amsterdam, 1–124.

Červený, V., 2001, Seismic ray theory: Cambridge University Press.

Coman, R., and Gajewski, D., 2001, Estimation of multivalued arrivals in 3-D models using wavefront ray tracing: 71th Ann. Internat. Mtg., Soc. Expl. Geophys., Expanded Abstracts.

Coman, R., and Gajewski, D., 2005, Traveltime computation by wavefront-oriented ray tracing: Geophysical Prospecting, **53**, 23–36.

Courant, R., and Hilbert, D., 1962, Methods of mathematical physics, vol.2: Partial differential equations: Interscience, New York.

Daley, P. F., and Hron, F., 1979a, Reflection and transmission coefficients for seismic waves in ellipsoidally anisotropic media: Geophysics, **44**, 27–38.

Daley, P. F., and Hron, F., 1979b, SH waves in layered transversely isotropic media – an asymptotic expansion approach: Bulletin of the Seismological Society of America, **69**, 689–711.

Das, V., and Gajewski, D., 2011, Comparison between normalized cross-correlation and semblance coherency measures in velocity analysis: 15th Annual WIT Report, pages 318–325.

de Bazelaire, E., 1988, Normal moveout revisited – inhomogeneous media and curved interfaces: Geophysics, **53**, 143–157.

de Hoop, M., and Bleistein, N., 1997, Generalized Radon transform inversions for reflectivity in anisotropic elastic media: Inverse Problems, **13**, 669–690.

de Hoop, M., Spencer, C., and Burridge, R., 1999, The resolving power of seismic amplitude data: an anisotropic inversion/migration approach: Geophysics, **64**, 852–873.

Dell, S., and Gajewski, D., 2011, Common-reflection-surface-based workflow for diffraction imaging: Geophysics, **76**, S187–S195.

Dellinger, J. A., Gray, S. H., Murphy, G. E., and Etgen, J. T., 2000, Efficient 2.5-D true-amplitude migration: Geophysics, **65**, 943–950.

Dix, H. C., 1955, Seismic velocities from surface measurements: Geophysics, pages 68–86.

Dümmong, S., 2006, Alternative Implementation des Common Reflection Surface Stapelverfahrens: Master's thesis, University of Hamburg.

Dümmong, S., 2010, Seismic data processing with an expanded common reflection surface workflow: Ph.D. thesis, University of Hamburg.

Duveneck, E., 2004, Velocity model estimation with data-derived wavefront attributes: Geophysics, **69**, 265–274.

Ettrich, N., and Gajewski, D., 1996, Wave front construction in smooth media for prestack depth migration: Pure and Applied Geophysics, **148**, 481–502.

Ettrich, N., and Gajewski, D., 1998, Traveltime computation by perturbation with fd-eikonal solvers in isotropic and weakly anisotropic media: Geophysics, **63**, 1066–1078.

Ettrich, N., Gajewski, D., and Kashtan, B. M., 2001, Reference ellipsoids for anisotropic media: Geophysical Prospecting, **49**, 321–334.

Farra, V., 2001, High-order perturbations of the phase velocity and polarization of qp and qs-waves in anisotropic media: Geophysical Journal International, **147**, 93–104.

Fedorov, F. I., 1968, Theory of elastic waves in crystals: Plenum Press, New York.

Fowler, P., 2003, Practical VTI approximations: A systematic anatomy: Journal of Applied Geophysics, **54**, 347–367.

Gaiser, J. E., and Van Dok, R. R., 2003, Converted shear-wave anisotropy attributes for fractured-reservoir management: AAPG Annual Convention, Abstracts.

Gajewski, D., and Pšenčík, I., 1987, Computation of high frequency wavefields in 3-D laterally inhomogeneous anisotropic media: Geophysical Journal of the Royal Astronomical Society, **91**, 383–411.

Gajewski, D., and Pšenčík, I., 1990, Vertical seismic profile synthetics by dynamic ray tracing in laterally varying layered anisotropic structures: Journal of Geophysical Research, **95**, 11,301–11,315.

Gajewski, D., 1993, Radiation from point sources in general anisotropic media: Geophysical Journal International, **113**, 299–317.

Gajewski, D., 1998, Determining the ray propagator from traveltimes: 68th Ann. Internat. Mtg., Soc. Expl. Geophys., Expanded Abstracts, 1900–1903.

Gardner, G. H. F., French, W. S., and Matzuk, T., 1974, Elements of migration and velocity analysis: Geophysics, **39**, 811–825.

Gelchinsky, B., Berkovitch, A., and Keydar, S., 1999, Multifocusing homeomorphic imaging. Part 1: Basic concepts and formulas: Journal of Applied Geophysics, **42**, 229–242.

Geoltrain, S., and Brac, J., 1993, Can we image complex structures with first arrival traveltime?: Geophysics, **58**, 564–575.

Gerea, C., Nicoletis, L., and Granger, P.-Y., 2000, Multi component true amplitude anisotropic imaging: Anisotropy 2000: Fractures, converted waves and case studies (9. International Workshop on Seismic Anisotropy), Soc. Expl. Geophys., Expanded Abstracts.

Gjøystdal, H., Reinhardsen, J. E., and Ursin, B., 1984, Traveltime and wavefront curvature calculations in three-dimensional inhomogeneous layered media with curved interfaces: Geophysics, **49**, 1466–1494.

Gray, S. H., Etgen, J., Dellinger, J., and Whitmore, D., 2001, Seismic migration problems and solutions: Geophysics, **66**, 1622–1640.

Grechka, V., and Tsvankin, I., 2002, PP+PS=SS: Geophysics, **67**, 1961–1971.

Hanitzsch, C., Schleicher, J., and Hubral, P., 1994, True-amplitude migration of 2D synthetic data: Geophysical Prospecting, **42**, 445–462.

Hanitzsch, C., Jin, S., Tura, A., and Audebert, F., 2001, Efficient amplitude-preserved prestack depth migration: 63th Ann. Internat. Mtg., Eur. Assn. Expl. Geophys., Expanded Abstracts, A–25.

Hanitzsch, C., 1995, Amplitude preserving prestack depth migration/inversion in laterally inhomogeneous media: Ph.D. thesis, Universitt Karlsruhe.

Hanitzsch, C., 1997, Comparison of weights in prestack amplitude-preserving depth migration: Geophysics, **62**, 1812–1816.

Helbig, K., 1983, Elliptical anisotropy – its significance and meaning: Geophysics, **48**, 825–832.

Henneke, E. G., 1971, Reflection-refraction of a stress wave at a plane boundary between anisotropic media: The Journal of the Acoustical Society of America, **51**, 210–217.

Hertweck, T., Jäger, C., Goertz, A., and Schleicher, J., 2003, Aperture effects in 2.5D Kirchhoff migration: A geometrical explanation: Geophysics, **68**, 1673–1684.

Hertweck, T., 2004, True-amplitude Kirchhoff migration: analytical and geometrical considerations: Ph.D. thesis, Logos-Verlag Berlin.

Höcht, G., de Bazelaire, E., Majer, P., and Hubral, P., 1999, Seismics and optics: hyperbolae and curvatures: Journal of Applied Geophysics, **42**, 261–281.

Hubral, P., and Krey, T., 1980, Interval velocities from seismic reflection time measurements: SEG, Tulsa.

Hubral, P., Schleicher, J., and Tygel, M., 1992a, Three-dimensional paraxial ray properties, Part 1: Basic relations: Journal of Seismic Exploration, **1**, 265–279.

Hubral, P., Schleicher, J., and Tygel, M., 1992b, Three-dimensional paraxial ray properties, Part 2: Applications: Journal of Seismic Exploration, **1**, 347–362.

Hubral, P., Schleicher, J., and Tygel, M., 1993a, Three dimensional primary zero offset reflections: Geophysics, **58**, 692–702.

Hubral, P., Schleicher, J., Tygel, M., and Hanitzsch, C., 1993b, Determination of Fresnel zones from traveltime measurements: Geophysics, **58**, 703–712.

Hubral, P., 1983, Computing true amplitude reflections in a laterally inhomogeneous earth: Geophysics, **48**, 1051–1062.

Jäger, R., Mann, J., Höcht, G., and Hubral, P., 2001, Common-reflection-surface stack: Image and attributes: Geophysics, **66**, 97–109.

Jech, J., and Pšenčík, I., 1989, First order perturbation method for anisotropic media: Geophysical Journal International, **99**, 369–376.

Kabir, N., and Verschuur, E., 1995, Reconstruction of missing offsets by parabolic Radon transform: Geophysical Prospecting, **43**, 347–368.

Kaschwich, T., 2006, Traveltime computation and migration in anisotropic media: Ph.D. thesis, University of Hamburg.

Keho, T. H., and Beydoun, W. B., 1988, Paraxial Kirchhoff migration: Geophysics, **53**, 1540–1546.

Kosloff, D., and Baysal, E., 1982, Forward modeling by a fourier method: Geophysics, **47**, 1402–1412.

Landa, E., Keydar, S., and Moser, T. J., 2010, Multifocusing revisited – inhomogeneous media and curved interfaces: Geophysical Prospecting, **58**, 925–938.

Leidenfrost, A., Kosloff, D., and Gajewski, D., 1998, A 3D FD eikonal solver for non-cubical grids: 60th Ann. Internat. Mtg., Eur. Assn. Expl. Geophys., Expanded Abstracts.

Leidenfrost, A., Ettrich, N., Gajewski, D., and Kosloff, D., 1999, Comparison of six different methods for calculating traveltimes: Geophysical Prospecting, **47**, 269–297.

Leidenfrost, A., 1998, Fast computation of traveltimes in two and three dimensions: Ph.D. thesis, University of Hamburg.

Mann, J., Duveneck, E., Hertweck, T., and Jäger, C., 2003, A seismic reflection imaging workflow based on the Common Reflection Surface stack: Journal of Seismic Exploration, **12**, 283–295.

Mann, J., 2002, Extensions and applications of the common-reflection-surface stack method: Ph.D. thesis, University of Karlsruhe.

Martins, J. L., Schleicher, J., Tygel, M., and Santos, L., 1997, 2.5-D true-amplitude migration and demigration: Journal of Seismic Exploration, **6**, 159–180.

Mayne, W. H., 1962, Common reflection point horizontal data stacking techniques: Geophysics, **27**, 927–938.

Mendes, M., 2000, Green's function interpolation for prestack imaging: Geophysical Prospecting, **48**, 49–62.

Mensch, T., and Rasolofosaon, P. N. J., 1997, Elastic wave velocities in anisotropic media of arbitrary anisotropy – generalisation of Thomsen's parameters ϵ, δ, and γ: Geophysical Journal International, **128**, 43–63.

Menyoli, E. M., and Gajewski, D., 2001, Kirchhoff migration of converted waves applying perturbation method for computing Greens functions: 63th Ann. Internat. Mtg., Eur. Assn. Expl. Geophys., Expanded Abstracts.

Menyoli, E. M., 2002, Model building and imaging with reflection data: Ph.D. thesis, University of Hamburg.

Minarto, E., 2012, Optimization of Common Reflection Surface (CRS) attributes based on hybrid method: EAGE Annual meeting, Student poster SP12.

Müller, T., 1999, The common reflection surface stack method – seismic imaging without explicit knowledge of the velocity model: Ph.D. thesis, University of Karlsruhe.

Nelder, J., and Mead, R., 1965, A simplex method for function minimization: Computer Journal, **7**, 308–313.

Nelson, R. A., 2001, Geologic analysis of naturally fractured reservoirs: Gulf Professional Publishing, Houston.

Operto, S., Xu, S., and Lambaré, G., 2000, Can we image quantitatively complex models with rays?: Geophysics, **65**, 1223–1238.

Pedersen, O., Ursin, B., and Stovas, A., 2007, Wide-angle phase-slowness approximations in VTI media: Geophysics, **72**, S177–S185.

Peles, O., Kosloff, D., Koren, Z., and Tygel, M., 2001, A practical approach to amplitude preserving migration: WIT Workshop 2001 on Seismic True-Amplitude Reflections.

Popov, M. M., and Pšenčík, I., 1978, Ray amplitudes in inhomogeneous media with curved interfaces: Geofysikální Sborník, **24**, 111–129.

Pusey, L. C., and Vidale, J. E., 1991, Accurate finite-difference calculation of WKBJ traveltimes and amplitudes: 61st Ann. Internat. Mtg., Soc. Expl. Geophys., Expanded Abstracts, 1513–1516.

Pšenčík, I., and Teles, T. N., 1996, Point source radiation in inhomogeneous anisotropic structures: Pure and Applied Geophysics, **148**, 591–623.

Pšenčík, I., 1994, Introduction to seismic methods: Lecture notes, PPPG/UFBa.

Pšenčík, I., 1998, Green's functions for inhomogeneous weakly anisotropic media: Geophysical Journal International, **135**, 279–288.

Sager, K., Untersuchungen mit einem neuen Stapelverfahren: i-CRS und Anisotropie:, B.Sc. thesis, University of Hamburg (in preparation), 2012.

Sayers, C. M., 1994, P-wave propagation in weakly anisotropic media: Geophysical Journal International, **116**, 799–805.

Schleicher, J., Tygel, M., and Hubral, P., 1993a, 3D true-amplitude finite-offset migration: Geophysics, **58**, 1112–1126.

Schleicher, J., Tygel, M., and Hubral, P., 1993b, Parabolic and hyperbolic paraxial two-point traveltimes in 3D media: Geophysics, **41**, 495–513.

Schleicher, J., Hubral, P., Tygel, M., and Jaya, M. S., 1997, Minimum apertures and Fresnel zones in migration and demigration: Geophysics, **62**, 183–194.

Schleicher, J., Tygel, M., Ursin, B., and Bleistein, N., 2001, The Kirchhoff-Helmholtz integral for anisotropic elastic media: Wave Motion, pages 353–364.

Schleicher, J., 1993, Bestimmung von Reflexionskoeffizienten aus Reflexionsseismogrammen: Ph.D. thesis, University of Karlsruhe.

Schoenberg, M. A., and de Hoop, M. V., 2000, Approximate dispersion relations for qp-$q$sv-waves in transversely isotropic media: Geophysics, **65**, 919–933.

Schwarz, B., 2011, A new nonhyperbolic multi-parameter stacking operator: Master's thesis, University of Hamburg.

Shah, P. M., 1973, Use of wavefront curvature to relate seismic data with subsurface parameters: Geophysics, **38**, 812–825.

Sollid, A., 2000, Imaging of ocean-bottom seismic data: Ph.D. thesis, Norwegian University of Science and Technology.

Soukina, S. M., Gajewski, D., and Kashtan, B. M., 2003, Traveltime computation for 3D anisotropic media by a dinite difference perturbation method: Geophysical Prospecting, **51**, 431–441.

Spinner, M., 2007, CRS-based minimum-aperture Kirchhoff migration in the time domain: Ph.D. thesis, University of Karlsruhe.

Spitz, S., 1991, Seismic trace interpolation: Geophysics, **50**, 785–794.

Stewart, R. R., Gaiser, J. E., Brown, R. J., and Lawton, D. C., 2003, Converted-wave seismic exploration: Applications: Geophysics, **68**, 40–57.

Sun, J., 1999, On the aperture effect in 3D Kirchhoff-type migration: Geophysical Prospecting, **47**, 1045–1076.

Taner, M. T., and Koehler, F., 1969, Velocity spectra – digital computer derivation and application of velocity functions: Geophysics, **34**, 859–881.

Tessmer, G., Krajewski, P., Fertig, J., and Behle, A., 1990, Processing of PS-reflection data applying a common conversion-point stacking technique: Geophysical Prospecting, **38**, 267–286.

Thierry, P., Lambaré, G., Podvin, P., and Noble, M. S., 1999a, 3-D preserved amplitude prestack depth migration on a workstation: Geophysics, **64**, 222–229.

Thierry, P., Lambaré, G., Podvin, P., and Noble, M. S., 1999b, Fast 2-D ray+Born migration/inversion in complex media: Geophysics, **64**, 162–181.

Thomsen, L., 1986, Weak elastic anisotropy: Geophysics, **51**, 1954–1966.

Thomsen, L., 1999, Converted-wave reflection seismology over inhomogeneous, anisotropic media: Geophysics, **64**, 678–690.

Tsvankin, I., 2001, Seismic signatures and analysis of reflection data in anisotropic media: Pergamon (Elsevier).

Tygel, M., Schleicher, J., and Hubral, P., 1994, Pulse distortion in depth migration: Geophysics, **59**, 1561–1569.

Ursin, B., 1982, Quadratic wavefront and traveltime approximations in inhomogeneous layered media with curved interfaces: Geophysics, **47**, 1012–1021.

Ursin, B., 1990, Offset dependent geometrical spreading in a layered medium: Geophysics, **55**, 492–496.

VanTrier, J., and Symes, W. W., 1990, Upwind finite-difference calculation of seismic traveltimes: 70th Ann. Internat. Mtg., Soc. Expl. Geophys., Expanded Abstracts, 1000–1003.

Vermeer, G. J. O., 1995, Discussion on "3-D true-amplitude finite-offset migration" by J. Schleicher, M. Tygel and P. Hubral (Geophysics, **58**, 1112–1126) with reply by the authors: Geophysics, **60**, 921–923.

Versteeg, R., and Grau, G., 1991, The Marmousi experience: 1990 EAEG workshop on Practical Aspects of Seismic Data Inversion, EAEG, Zeist, The Netherlands, Proceedings.

Vidale, J., and Houston, H., 1990, Rapid calculation of seismic amplitudes: Geophysics, **55**, 1504–1507.

Vidale, J., 1990, Finite-difference calculation of traveltimes in three dimensions: Geophysics, **55**, 521–526.

Vieth, K. U., 2001, Kinematic wavefield attributes in seismic imaging: Ph.D. thesis, University of Karlsruhe.

Vinje, V., Iversen, E., and Gjøystdal, H., 1993, Traveltime and amplitude estimation using wavefront construction: Geophysics, **58**, 1157–1166.

Vinje, V., Stovas, A., and Reynaud, D., Preserved-traveltime smoothing:, Submitted to Geophysical Prospecting, 2012.

Zhang, Y., Gray, S., and Young, J., 2000, Exact and approximate weights for Kirchhoff migration: 70th Ann. Internat. Mtg., Soc. Expl. Geophys., Expanded Abstracts, 1036–1039.

Zhang, Y., Bergler, S., and Hubral, P., 2001, Common-reflection-surface (CRS) stack for common offset: Geophysical Prospecting, **49**, 709–718.

Acknowledgements

Over the past 15 years, I'm afraid I've lost count of the number of all the people who have helped me with my life, my science, and everything else. If you can't find your name on this list, please forgive my failing memory and be assured that you nevertheless have a place in my heart!

First of all, I want to thank my family, my parents **Heide and Gérard Vanelle** as well as my brothers and sister, **Stefan, Martin, and Monique Vanelle**. I wouldn't be here without you!

This said, I am grateful to

- **Prof. Dr. Dirk Gajewski** for the opportunity to work with him and his invitation to share and teach me his enthusiasm in science. His support and trust gave the fledgling scientist the courage to fly. Since then, he's kept me grounded as well as in the air, not only as my supervisor, but also as one of the best friends I can ever imagine.

- **Prof. Dr. Martin Tygel** for his inspiring work and for honouring me by accepting to review this thesis.

- **Prof. Dr. Matthias Hort** for his support and sharing his enthusiasm with me, amongst others over a cappuccino at Stuttgart airport on a day I'll never forget, and for agreeing to serve on my habilitation board.

- **Prof. Dr. Angelika Humbert** for her encouragement. She opened my eyes with regards to many things, in particular that and how being a woman and a scientist can work. I miss you and I am so happy to have you – literally – on board for my habilitation committee.

- **Prof. Dr. Ulrich Bismayer** for spending a share of his precious time on my examination committee – now, and already ten years ago for my Ph.D.

- **Dr. Christian Hanitzsch** for reviewing my Ph.D. thesis.

- **Dr. Radu Coman** and **Dr. Tim Bergmann** for proof-reading my Ph.D. thesis and many shared laughs.

- All reviewers of my works and colleagues everywhere in the world for discussions and their constructive criticism.

- All past and present members of the **Applied Seismics Group** Hamburg for continuous discussion.

- **Dr. Ekkehart Tessmer** – not only for his invaluable help with computer troubles, but also for keeping me informed on Microsoft job offers! *wink*

- **Prof. Dr. Christian Hübscher** for his practical insight and a hug when I really needed it.
- **Dr. Ali Dehghani** for his generosity and humour.
- **Denis Anikiev**, **Ivan Abakumov**, **Dipl. Geophys. Oksana Zhebel**, **Dipl. Geophys. Sergius Dell**, **Dipl. Geophys. Benedikt Weiss**, **Dipl. Geophys. Sarah Wichmann**, **Dipl. Geophys. Jan Dettmer**, **Dipl. Geophys. Kerstin Sommer**, **Dipl. Geophys. André Koopmann**, **Dipl. Geophys. Benjamin Brezing**, **Dr. Mikhail Baykulov**, **Dr. Tina Kaschwich**, **Dr. Svetlana Golovnina**, **Dr. Elive Menyoli**, **Dr. Radu Coman**, **Dr. Stefan Dümmong**, **Dr. Andree Leidenfrost**, **Dr. Matthias Zillmer**, **Dr. Norman Ettrich**, **Martina Bobsin**, and **Khawar Ahmed** for many inspiring discussions, about science and more.
- **Korbinian Sager** for contributing his preliminary results for the anisotropic i-CRS.
- **Dipl. Geophys. Benjamin Schwarz** for his work, the (sometimes very passionate ;-) discussions – GMTA! – and meticulous proof-reading of a part of this thesis. All remaining mistakes are mine.
- **Dipl. Geol. Sönke Reiche** for challenging me to step away from the safety of my equations and return to more intuitive and descriptive understanding and explanations. After more than a decade of wallowing in theory, this was a most refreshing experience, which I hope to never forget again.
- **Robert Pfau** for his help with the Internet – not only for his neverending support with the WIT web server, but also for suggesting a google search keyword that really takes the cake. :-P
- **Christel Mynarik** for everything: you did so much more for me than just supporting me with the daily struggles with the administration. *hug*
- **Paola Dal Corso** for taking over when Christel left.
- All 'my' students for allowing me to learn from them while teaching.
- **Prof. Dr. Peter Hubral** for his inspiring work and support.
- **Prof. Dr. Boris Kashtan** for years of discussions during his many summer visits to Hamburg. As much as I was sometimes frustrated by his deep mathematical understanding compared to mine, I cannot but admire the eloquence of his derivations. Once I grasped them, the elegance of his inventions was usually very aesthetically pleasing – and has never failed to provide an interesting new research path.
- **Prof. Dr. Ivan Pšenčík** for his patience in letting me annoy him until I finally saw the light – sort of... ;-)
- **Prof. Dr. Klaus Helbig** for our shared passion over Merula and his enthusiasm for vacuum cleaners.
- **Prof. Dr. Martin Tygel**, **Prof. Dr. Jörg Schleicher**, **Prof. Dr. Amélia Novais**, **Prof. Dr. Lucio Santos**, **Prof. Dr. Jessé Costa**, **Prof. Dr. Lou Leite**, and all the other guys and gals from and around the Campinas University Department of Applied Mathematics for countless fruitful discussions and their friendship.

- **Dr. Miriam Spinner**, **Dr. Thomas Hertweck**, **Dr. Christoph Jäger**, and the rest of the Karlsruhe migration gang for our joint project and making me feel at home.
- **Gabi Melo** for interesting talks and tons of fun.
- **Carola Kauhs** for ensuring comfortable access to literature and help in finding less famous but equally important papers.
- The **CIS-IT helpdesk and staff** for fixing my myriads of minor and major computer woes.
- **Rainer Senke** and the Friday lunch crowd for keeping me well-fed.
- **Antje Newig** for her friendship and support with faculty and equal opportunity matters.

Furthermore, I acknowledge financial support from

- the European Commission (JOF3-CT97-0029),
- the German-Israeli-Foundation (I-524-018.08/97),
- the German Research Foundation (DFG, Ga 350-10 and Va 207),
- the sponsors of the Wave Inversion Technology (WIT) consortium,
- and the University of Hamburg.

Outside the ivory tower, I thank you for being there:

- The one and only **Pam Ehli** for having the same screws loose as I have.
- The **Hoffmann** family for the occasionally required reminder that there's life outside my lab, often accompanied by gorgeous food for my stomach and heart, and plenty more.
- **Alejandra**, **Ana**, **Argentine**, **Beth**, **Bijou**, **Brigitte**, **Carol**, **Dea**, **Helena**, **Jeanne**, **Joe**, **Kitty**, **Oran**, **Silv**, **Zack** – and last, not least, **Ian**, my better half :-P – and my boys and girls for allowing me to be myself.
- **Dr. Norbert Eckhardt** for stopping the tumble before it turned ballistic.
- **Dr. Nina Gartmann** for teaching me how to tame the hamster.